DOE/ER--0313/24

DOE/ER-0313/24

Fusion Materials

Semiannual Progress Report for Period Ending June 30, 1998

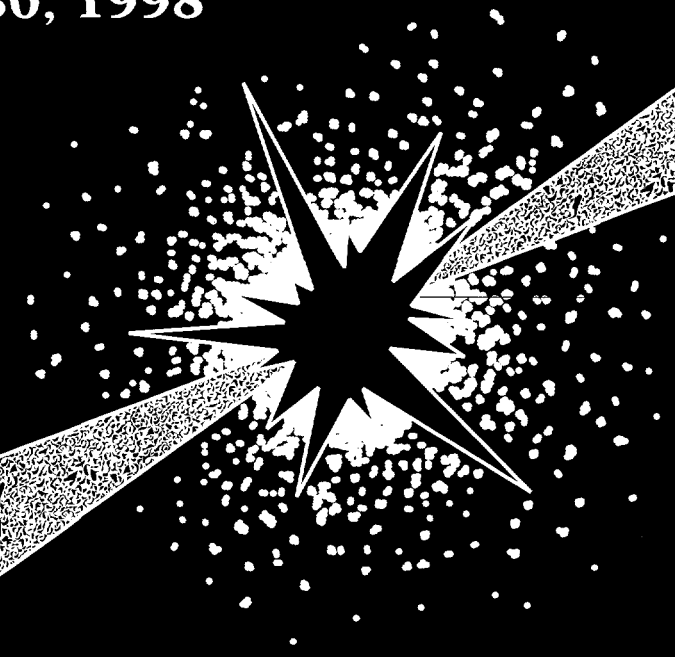

U. S. Department of Energy
Office of Fusion Energy Sciences

JAT

MASTER

DISTRIBUTION OF THIS DOCUMENT IS UNLIMITED

ORNL 98-6975/jcp

DOE/ER-0313/24
Distribution
Categories
UC-423, -424

FUSION MATERIALS
SEMIANNUAL PROGRESS REPORT
FOR THE PERIOD ENDING
June 30, 1998

Prepared for
DOE Office of Fusion Energy Sciences
(AT 60 20 00 0)

DATE PUBLISHED: SEPTEMBER 1998

Prepared for
OAK RIDGE NATIONAL LABORATORY
Oak Ridge, Tennessee 37831
Managed by
Lockheed Martin Energy Research Corp.
for the
U.S. DEPARTMENT OF ENERGY
under Contract DE-AC05-96OR22464

FOREWORD

This is the tweny-fourth in a series of semiannual technical progress reports on fusion materials. This report combines the full spectrum of research and development activities on both metallic and non-metallic materials with primary emphasis on the effects of the neutronic and chemical environment on the properties and performance of materials for in-vessel components. This effort forms one element of the materials program being conducted in support of the Fusion Energy Sciences Program of the U.S. Department of Energy. The other major element of the program is concerned with the interactions between reactor materials and the plasma and is reported separately.

The Fusion Materials Program is a national effort involving several national laboratories, universities, and industries. A large fraction of this work, particularly in relation to fission reactor experiments, is carried out collaboratively with our partners in Japan, Russia, and the European Union. The purpose of this series of reports is to provide a working technical record for the use of the program participants, and to provide a means of communicating the efforts of materials scientists to the rest of the fusion community, both nationally and worldwide.

This report has been compiled and edited under the guidance of A. F. Rowcliffe by Gabrielle Burn, Oak Ridge National Laboratory. Their efforts, and the efforts of the many persons who made technical contributions, are gratefully acknowledged.

F. W. Wiffen
International and Technology Division

Reports previously listed in this series are as follows:

DOE/ER-0313/1	Period ending September 30, 1986
DOE/ER-0313/2	Period ending March 31, 1987
DOE/ER-0313/3	Period ending September 30, 1987
DOE/ER-0313/4	Period ending March 31, 1988
DOE/ER-0313/5	Period ending September 30, 1988
DOE/ER-0313/6	Period ending March 31, 1989
DOE/ER-0313/7	Period ending September 30, 1989
DOE/ER-0313/8	Period ending March 31, 1990
DOE/ER-0313/9	Period ending September 30, 1990
DOE/ER-0313/10	Period ending March 31, 1991
DOE/ER-0313/11	Period ending September 30, 1991
DOE/ER-0313/12	Period ending March 31, 1992
DOE/ER-0313/13	Period ending September 30, 1992
DOE/ER-0313/14	Period ending March 31, 1993
DOE/ER-0313/15	Period ending September 30, 1993
DOE/ER-0313/16	Period ending March 31, 1994
DOE/ER-0313/17	Period ending September 30, 1994
DOE/ER-0313/18	Period ending March 31, 1995
DOE/ER-0313/19	Period ending December 31, 1995
DOE/ER-0313/20	Period ending June 30, 1996
DOE/ER-0313/21	Period ending December 31, 1996
DOE/ER-0313/22	Period ending June 30, 1997
DOE/ER-0313/23	Period ending December 31, 1997
DOE/ER-0313/100	Technical Evaluation of the Technology of Vanadium Alloys for Use as Blanket Structural Materials in Fusion Power Systems

CONTENTS

1.0 VANADIUM ALLOYS

TENSILE AND IMPACT PROPERTIES OF GENERAL ATOMICS 832864 HEAT OF V-4Cr-4Ti ALLOY - H. Tsai, L. J. Nowicki, J. Gazda, M. C. Billone, and D. L. Smith (Argonne National Laboratory), W. R. Johnson and P. Trester (General Atomics)

SUMMARY

A 1300-kg heat of V-4Cr-4Ti alloy was procured by General Atomics (GA) for the DIII-D radiative divertor program. To determine the mechanical properties of this alloy, tensile and Charpy tests were conducted on specimens prepared from pieces of 4.8-mm-thick as-rolled plates, a major product form for the DIII-D application. The tensile tests were conducted at three temperatures, 26, 280 and 380°C, the last two being the anticipated peak temperatures during DIII-D boronization and postvent bake-out, respectively. Results from these tests show that the tensile and impact properties of the 832864 heat are comparable to those of the other smaller V-(4-5)Cr-(4-5)Ti alloy heats previously developed by the U.S. Fusion Materials Program and that scale-up of vanadium alloy production can be successfully achieved as long as reasonable process control is implemented.

OBJECTIVE

The objective of this task was to determine the tensile and impact properties of the 832864 heat of V-4Cr-4Ti in the temperature regime of importance to the DIII-D radiative divertor program.

BACKGROUND

Vanadium-base alloys are promising candidates for fusion reactor applications because of their low activation and good thermal-mechanical properties and radiation resistance at high temperature. To demonstrate the in-service behavior of vanadium alloys in a typical tokamak environment, and to develop knowledge and experience on the design, processing, and fabrication of full-scale vanadium alloy components, GA developed a plan to fabricate a vanadium alloy structure in the DIII-D radiative divertor modification [1,2]. As part of this project, a 1300-kg heat of V-4Cr-4Ti alloy was procured by GA. This heat was produced by Teledyne Wah-Chang of Albany according to specifications developed by GA with input from ANL and ORNL. Particular attention was given to control of impurities in order to meet the immediate goals for the DIII-D radiative divertor program and future goals for development of vanadium alloys used in advanced fusion systems. The requirements included minimization of Nb, Mo, and Ag for low neutron activation; optimization of Si (400-1000 ppm) to suppress neutron-induced swelling; and control of O, N, C and other impurities to avoid grain-boundary segregation and precipitation of embrittling phases [3]. A detailed report on the production of this heat can be found elsewhere [4,5].

GA has conducted six tensile tests on the 832864-heat material at room temperature [6]. The specimens, with gauge dimensions of 4.06 mm (thick) x 6.35 mm (width) x 25.4 mm (length), were machined from either plate stock (4.8 mm thick) or rod stock (10.2 mm dia.). All specimens were annealed at 1000°C for 1 h in vacuum (<1 x 10^{-5} torr, cryopumped) before the tests. The tests were performed with attached gauge extensometers at a strain rate of 5 x 10^{-4}/s. Results of these tests are summarized in Table 1.

*Work supported by U.S. Department of Energy, Office of Fusion Energy Research, under Contract W31-109-Eng-38.

Table 1. Room-temperature tensile properties of Heat 832864 determined by GA

Specimens Made from	Yield Strength (MPa)	Ultimate Tensile Strength (MPa)	Total Elongation (%)	Reduction in Area (%)
Plate Stock	306	398	41	93
Rod Stock	299	408	42	88

EXPERIMENTAL PROCEDURE

Specimen Preparation

The ANL test specimens were prepared from two 4.8-mm-thick plates supplied by GA. They were the trimmed edges from two as-rolled plates. To avoid altering the as-rolled microstructure, the test specimens were electro-discharge machined with no further rolling of the pieces.

The tensile specimens were of the SS-3 design, which is the de facto standard for the fusion materials program. The nominal dimensions of the gauge were 0.76 (t) x 1.52 (w) x 7.6 (l) mm, and the longitudinal direction of the gauge was parallel to the final rolling direction of the plate.

The Charpy impact specimens were 1/3-size, 3.3 mm (t) x 3.3 mm (w) x 25.4 mm (l), with a 30°, 0.61-mm-deep, 0.08-mm-root radius machined notch. The notch orientation (i.e., crack propagation direction) was perpendicular to the final rolling direction and into the thickness of the plate. This Charpy specimen design is also a de facto standard and has been used extensively in previous fusion materials tests.

After the machining and cleaning, all specimens were annealed in an ion-pumped vacuum (<1 x 10^{-7} torr) at 1000°C for 1 h before the testing.

Test Procedure

One tensile test each was conducted at room temperature, 280, and 380°C, the last two being the anticipated peak temperatures during the DIII-D boronization and postvent bake-out, respectively. The room-temperature test was conducted in air; the elevated-temperature tests were conducted in high-purity flowing argon. The tests were performed with an Instron machine without an extensometer attached to the specimen gauge. Extensions due to slack in the grip and deformation of the load frame were subtracted from the crosshead displacement to obtain the correct gauge-section extension. The strain rate for all tests was 1.1 x 10^{-3}/s, which is the reference used in many previous fusion materials tensile tests.

All Charpy impact tests were conducted in air with a Dynatup drop-weight tester. Specimen temperature during the impact test was measured with a thermocouple spot-welded to the end of the specimen. For the above-ambient-temperature tests, a hot-air blower was used to provide the heating. For the below-room-temperature tests, liquid nitrogen was used to chill the specimens.

RESULTS AND DISCUSSION

Tensile Tests

The results of the tensile tests are summarized in Table 2 and Fig. 1. The individual tensile curves are shown in Fig. 2. Reduction-in-area measurements and fractographic examinations have not yet been conducted.

Table 2. Tensile properties of 832864 heat determined at ANL

Test Temp. (°C)	Yield Strength[a] (MPa)	Ultimate Tensile Strength (MPa)	Uniform Elongation (%)	Total Elongation (%)
26	315	410	19.3	28.5
280	228	345	16.7	23.2
380	228	355	15.3	22.8

[a] Lower yield point.

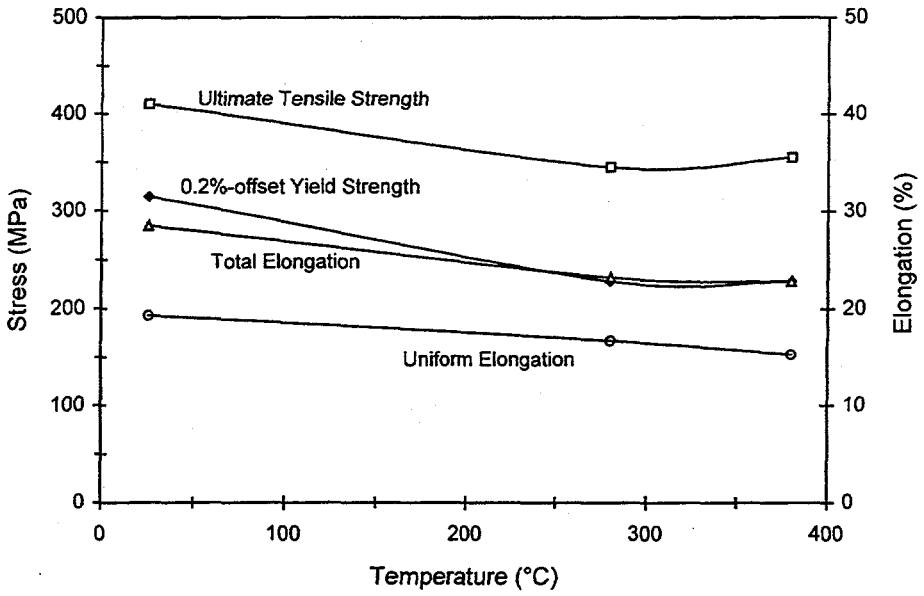

Fig. 1. Tensile properties of Heat 832864 as functions of test temperature

Compared to the data determined by GA (Table 1), the agreement in the room-temperature strengths is good. The slight difference in strain rates (1.1×10^{-3}/s in the ANL tests and 5×10^{-4}/s in the GA tests) appeared to be a nonfactor, as previous studies have indicated [7]. The room-temperature total elongation data from the ANL test, however, were notably lower than those from the GA tests, ≈29 vs. 41%. The cause of this discrepancy is probably related to differences in specimen size and geometry but has not been fully determined.

Possibly the most insightful assessment of the 832864 heat is to compare its properties with those of the previous V-4Cr-4Ti heats that have been extensively studied. In this regard, the 832864 heat appears to be fairly similar to the other heats, as described below.

In Fig. 3, ultimate tensile strength of the 832864 heat is compared to that in the existing V-4Cr-4Ti data base. The 832864 data are near the center of the established data band. The data also display the characteristic upturn with temperature in the ≈300-600°C range.

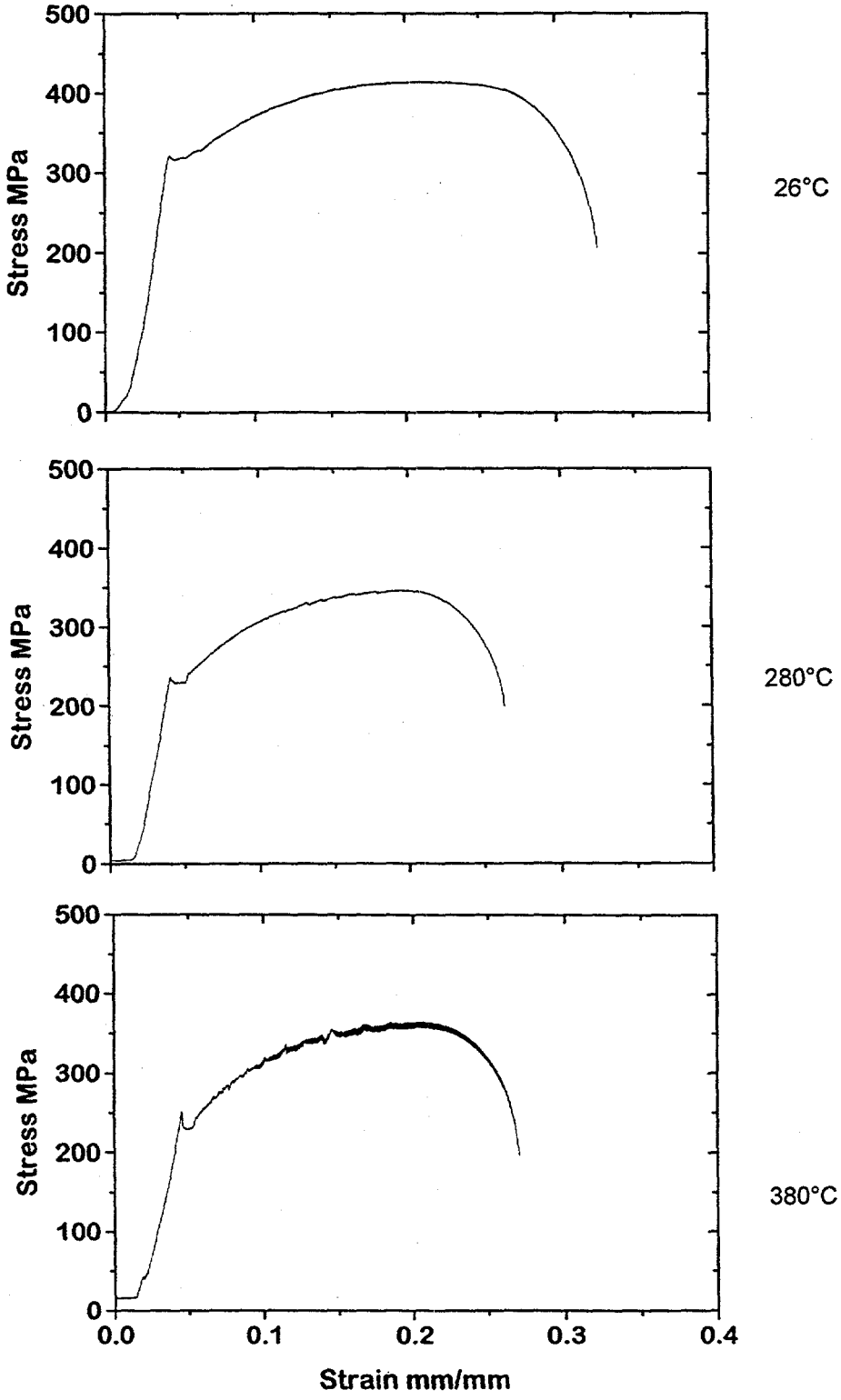

Fig. 2. Tensile plots for individual tests. Note occurrence of dynamic strain aging at 380°C.

Comparison of the yield strength and uniform elongation of the 832864 heat with those in the existing V-4Cr-4Ti data base is shown in Fig. 4. Again, the data for the 832864 heat are comparable with those of the previous heats. The yield strength of the 832864 heat is slightly lower than the group average, possibly because of its lower impurity and Si contents.

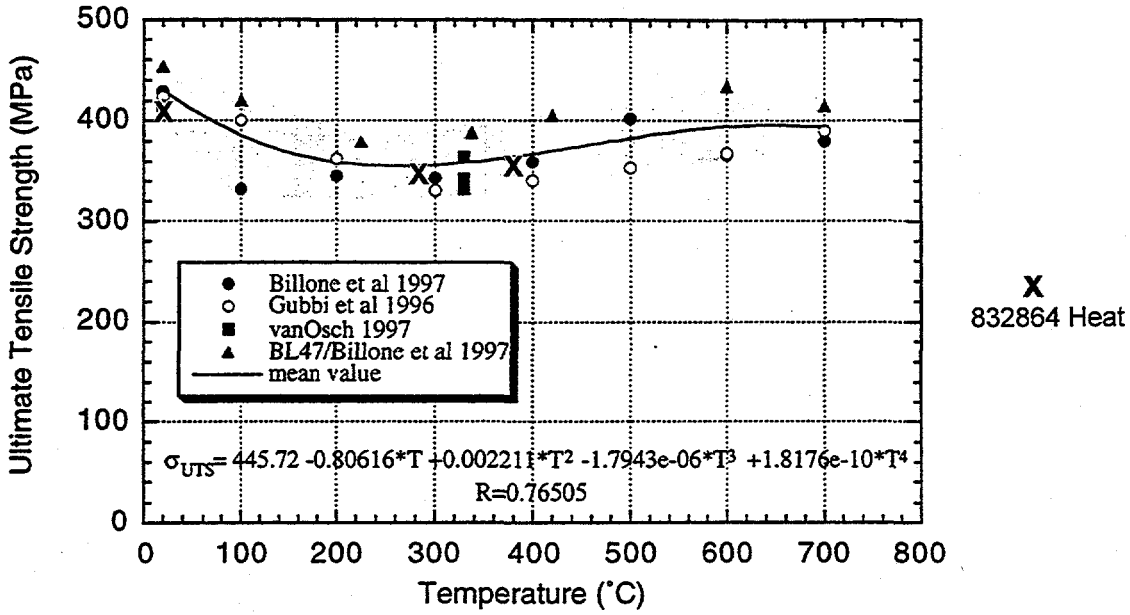

Fig. 3. Comparison of ultimate tensile strength of 832864 heat with that in existing data base [8].

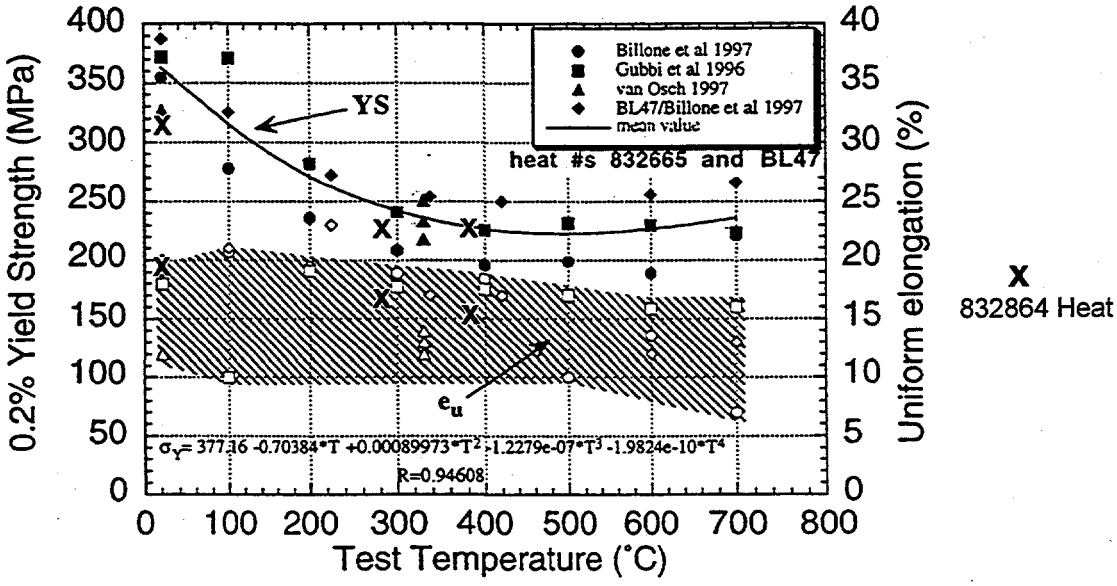

Fig. 4. Comparison of yield strength and uniform elongation of 832864 heat with those in existing database [8].

Likewise, comparison of total elongation data (Fig. 5) revealed no significant differences between 832864 and the other heats.

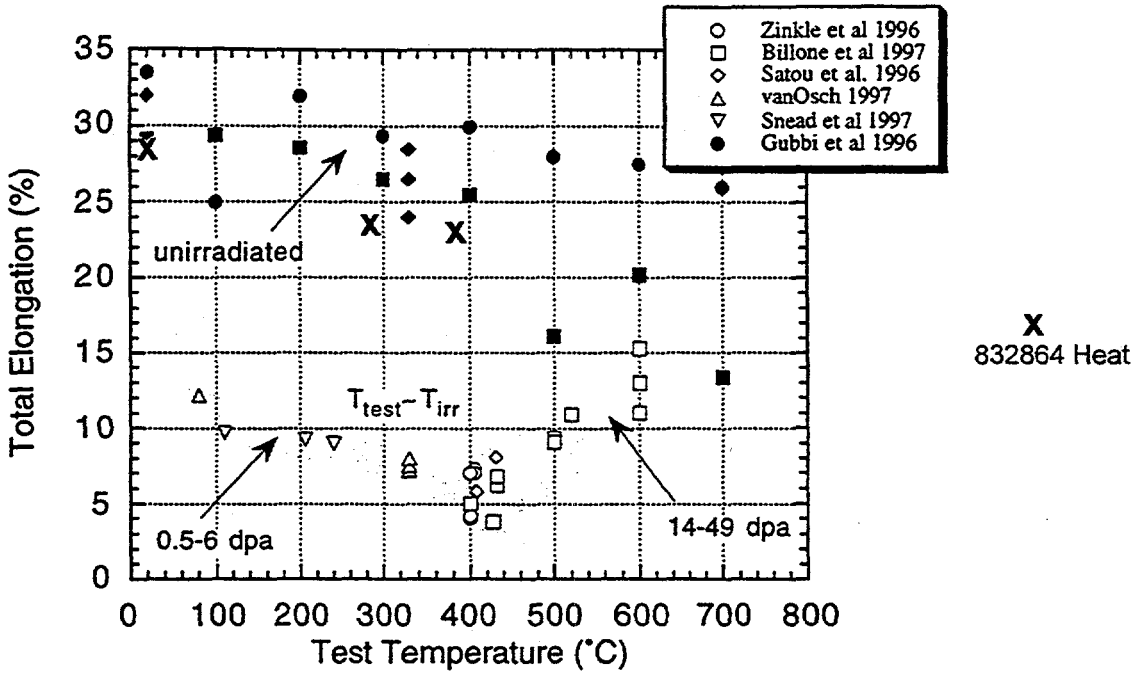

Fig. 5. Comparison of total elongation of 832864 heat with that in existing data base [8]. Neglect open-symbol irradiated data in lower part of chart.

Charpy Impact Tests

The results of the Charpy tests are shown in Fig. 6 along with prior data from the 832665 sibling heat of V-4Cr-4Ti. The upper-shelf energy of ≈10-12 J of the 832864 heat is slightly lower than that of the 832665 heat. Again, this may be due to differences in impurity contents. A transition from upper-shelf to lower-shelf, in good agreement with the data trend, appears to occur at a low temperature, ≈ -180°C. From Fig. 6, we can concluded that the impact properties of the 832864 heat are good and comparable to those of the sibling 832665 heat.

FUTURE ACTIVITIES

Fractographic examination of the test specimens will be completed to determine the fracture mode and reduction-in-area data.

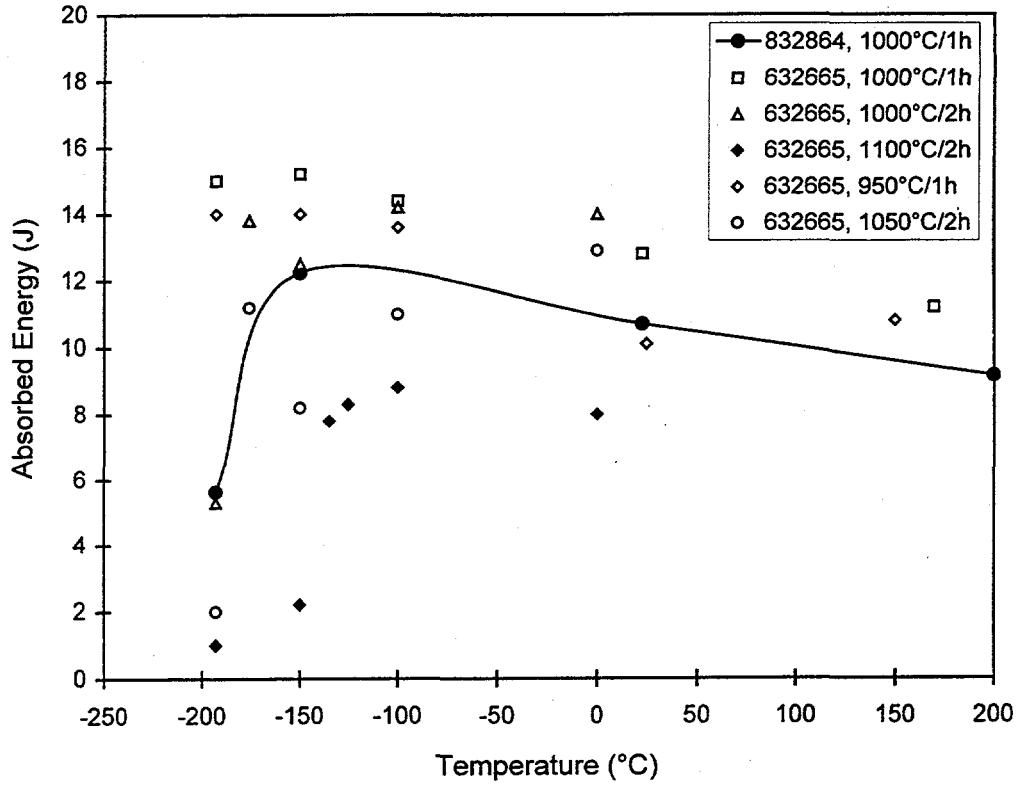

Fig. 6. Comparison of Charpy impact properties of 832864 heat with existing data base [9,10].

REFERENCES

1. J. P. Smith et al., "Vanadium Alloys for the Radiative Divertor Program of DIII-D," Proc. of the 16th IEEE/NPSS Symposium on Fusion Engineering, Champaign IL Sept 30-Oct 5, 1995.

2. J. P. Smith et al., "Utilizatiion of Vanadium Alloys in the DIII-D Radiative Divertor Program," Proc. of 7th International Conf. on Fusion Reactor Materials, Obninsk, Russia, Sept. 25-29, 1995.

3. H. M. Chung et al., "Fabrication of 500-kg Heat of V-4Cr-4Ti," Fusion Reactor Materials Semiannual Report, Sept. 30, 1994, DOE/ER-0313/17, pp.178-182.

4. W. R. Johnson, J. P. Smith, and R. D. Stambaugh, "Production and Fabrication of Vanadium Alloy for the Radiative Divertor Program of DIII-D," Fusion Reactor Materials Semiannual Report, Dec. 31, 1995, DOE/ER-0313/19, pp. 5-11.

5. W. R. Johnson, J. P. Smith, and R. D. Stambaugh, "Production and Fabrication of Vanadium Alloy for the Radiative Divertor Program of DIII-D – Annual Report Input for 1996," Fusion Reactor Materials Semiannual Report, June 30, 1996, DOE/ER-0313/20, pp. 3-10.

6. Personal communication, P. Trester to D. L. Smith, Feb. 26, 1998

7. A. N. Gubbi et al., "Effects of Strain Rate, Test Temperature, and Test Environment on Tensile Properties of Vanadium Alloys," Fusion Reactor Materials Semiannual Report, June 30, 1996, DOE/ER-0313/20, pp.38-52.

8. S. Zinkle, "Thermophysical and Mechanical Properties of V-(4-5)%Cr-(4-5)%Ti Alloys," Fusion Reactor Materials Semiannual Report, Dec. 31, 1997, DOE/ER-0313/23, pp. 99-108.

9. H. M. Chung et al., "Impact Properties of 500-kg Heat of V-4Cr-4Ti," Fusion Reactor Materials Semiannual Report, Sept. 30, 1994, DOE/ER-0313/17, pp.183-186.

10. H. M. Chung, L. Nowicki, and D. L. Smith, "Impact Properties of Precracked V-4Cr-4Ti Charpy Specimens," Fusion Reactor Materials Semiannual Report, March 31, 1995, DOE/ER-0313/18, pp. 253-258.

HIGH TEMPERATURE TENSILE PROPERTIES OF V-4Cr-4Ti — S. J. Zinkle, A. F. Rowcliffe and C. O. Stevens (Oak Ridge National Laboratory)

OBJECTIVE

The objective of this report is to summarize recent high temperature data on the tensile properties of V-4Cr-4Ti.

SUMMARY

Tensile tests have been performed on V-4Cr-4Ti at 750 and 800°C in order to extend the data base beyond the current limit of 700°C. From comparison with previous measurements, the yield strength is nearly constant and tensile elongations decrease slightly with increasing temperature between 300 and 800°C. The ultimate strength exhibits an apparent maximum near 600°C (attributable to dynamic strain aging) but adequate strength is maintained up to 800°C. The reduction in area measured on tensile specimens remained high (~80%) for test temperatures up to 800°C, in contrast to previous reported results.

PROGRESS AND STATUS

Introduction

The maximum operating temperature limit for vanadium alloys in fusion reactor design studies is typically assumed to be ~700°C [1,2]. Alternatively, it was recently suggested that vanadium alloys might be capable of operation at temperatures up to 750°C [3]. Although the maximum operating temperature will likely be determined by creep (thermal and irradiation), helium embrittlement, or corrosion effects, there are no known tensile data for V-4Cr-4Ti alloys at temperatures above 700°C. High temperature tensile data would be beneficial to help guide planned thermal creep experiments on V-4Cr-4Ti, and may provide some insight into the maximum allowable operating temperature based on mechanical strength considerations.

Experimental Procedure

The specimens were prepared from the 500 kg US fusion program heat of V-4Cr-4Ti (heat 832665). A 50% cold-rolled plate (6.4 mm thickness) supplied by Teledyne Wah Chang Albany was annealed at 1000°C for 2 h and then cross-rolled to a thickness of 3.81 mm (40% cold work). Type SS3 miniature sheet tensile specimens (nominal gage dimensions 0.76 × 1.52 × 7.6 mm) were electrodischarge machined and subsequently annealed at 1000°C for 2 h in a vacuum of ~2×10^{-7} torr. The specimens were engraved with ID codes (RC and RD series) prior to annealing. The tensile specimens were tested in vacuum (~2×10^{-7} torr) at a constant crosshead speed of 0.46 mm/minute, which corresponds to an initial strain rate of 1.0×10^{-3} s^{-1}. The specimens were held at the test temperature for 20 to 30 minutes prior to the start of the tensile test. Data were digitally acquired at an acquisition rate of 20 points per second. Following tensile testing, the fracture surfaces were examined in a scanning electron microscope in order to determine the reduction in area.

Results and Discussion

The tensile properties of the V-4Cr-4Ti specimens are listed in Table 1, and the load-elongation tensile curves are shown in Fig. 1. Slight yield drops were observed at all three test temperatures, similar to what was previously observed at test temperatures up to 700°C [4]. The difference between the upper and lower yield points was approximately 10 MPa in all three cases. The

Table 1. Summary of tensile data on V-4Cr-4Ti specimens.

Test temperature	Yield strength	Ultimate strength	Uniform elongation	Total elongation	Reduction in area
600°C	228 MPa	387 MPa	11.5%	22%	—
750°C	235 MPa	397 MPa	10.0%	17%	77%
800°C	234 MPa	337 MPa	10.5%	20%	82%

Luders band elongation was less than 2% at all three temperatures. The yield strength was determined at the lower yield point, which occurred at 0.2-0.5% plastic extension. Serrations in the stress-strain tensile curves were observed in specimens tested at temperatures up to 750°C, although the amplitude of the serrations observed at 750°C was much smaller than that observed at 600-700°C [4]. The amplitude of the serrations was very small (~1 MPa) at a test temperature of 800°C. The Portevin-Le Chatelier serrations fell below the general level of the stress-strain curve (Type C behavior [4]) at all three test temperatures.

The present tensile data are plotted along with previously reported tensile data [4-6] in Figs. 2-4. The strength data shown in Fig. 2 were fitted to a 4th order polynomial, and the resulting equations are given in the figure. The yield strength is nearly independent of test temperature between 300 and 800°C. The ultimate strength exhibits a local maximum at test temperatures near 600°C, and begins to significantly decrease at 800°C. As shown in Fig. 3, the uniform and total elongation decrease slowly with increasing temperature. High tensile elongations are observed at all temperatures up to 800°C. The reduction in area measured in the present study (Fig. 4) was ~80% at both 750 and 800°C. Ductile dimple fracture surfaces were observed at

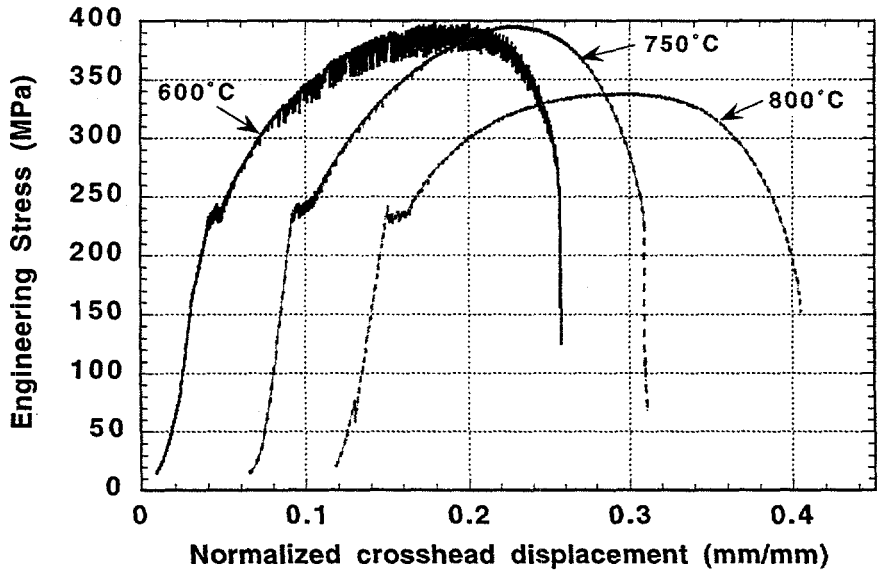

Fig. 1. Load-elongation curves for V-4Cr-4Ti tensile specimens tested at 600-800°C. The tensile curves have been horizontally offset for clarity.

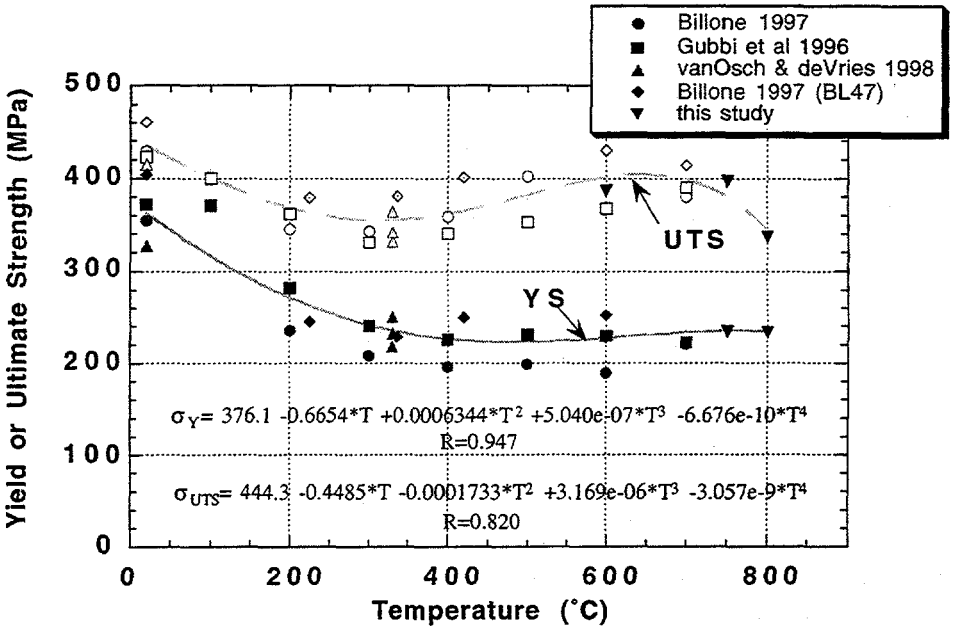

Fig. 2. Temperature dependence of the tensile strength of V-4Cr-4Ti [4-6]. Unless otherwise indicated, all of the data were obtained on the US Fusion program heat #832665.

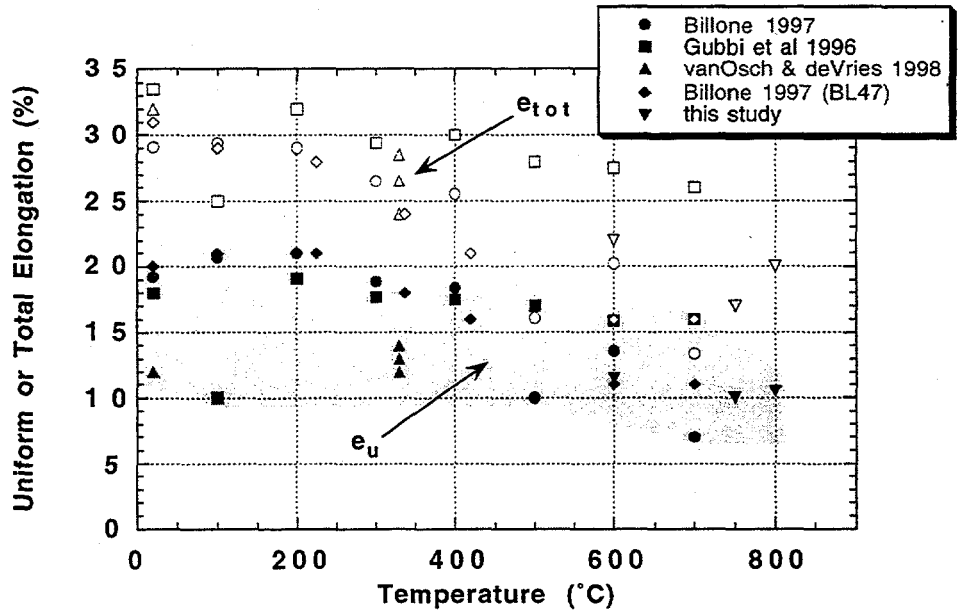

Fig. 3. Temperature dependence of the tensile elongations of V-4Cr-4Ti [4-6]. Unless otherwise indicated, all of the data were obtained on the US Fusion program heat #832665.

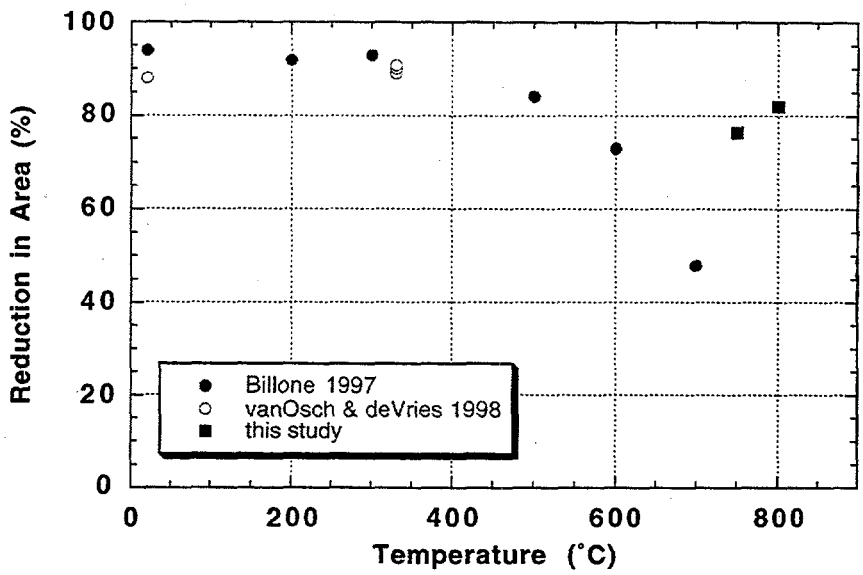

Fig. 4. Temperature dependence of the reduction in area of the US Fusion program heat (#832665) of V-4Cr-4Ti tensile tested at ~1 × 10^{-3} s^{-1} [5,6].

all temperatures investigated in this study. Previous studies [5,6] reported that the reduction in area for V-4Cr-4Ti was nearly constant between 20 and 500°C with a value of ~90%, and decreased rapidly at temperatures above 600°C. The reason for the apparent discrepancy in high temperature reduction in area values between the present study and the values summarized in ref. [5] is uncertain. Differences in the quality of the testing vacuum may be one possibility.

ACKNOWLEDGEMENTS

The authors thank A. M. Williams for providing the scanning electron microscopy measurements.

REFERENCES

1. D. L. Smith et al., Argonne National Laboratory Report ANL/FPP-84-1 (1984).
2. H. Matsui et al., Fusion Technology 30 (1996) 1293.
3. D. L. Smith et al., 8th Int. Conf. on Fusion Reactor Materials, Sendai, J. Nucl. Mater. (1998) in press.
4. A. N. Gubbi, A. F. Rowcliffe, W. S. Eatherly and L. T. Gibson, in Fusion Materials Semiannual Progress Report for Period ending June 30, 1996, DOE/ER-0313/20 (Oak Ridge National Lab, 1996) p. 38.
5. M. C. Billone, in Fusion Materials Semiann. Prog. Report for period ending Dec. 31 1997, DOE/ER-0313/23 (Oak Ridge National Lab, 1997) p. 3.
6. E. V. van Osch and M. I. de Vries, 8th Int. Conf. on Fusion Reactor Materials, Sendai, J. Nucl. Mater. (1998) in press.

TENSILE PROPERTIES OF VANADIUM-BASE ALLOYS IRRADIATED IN THE FUSION-1 LOW-TEMPERATURE EXPERIMENT IN THE BOR-60 REACTOR - H. Tsai, J. Gazda, L. J. Nowicki, M. C. Billone, and D. L. Smith (Argonne National Laboratory)

TIVE

60 is a sodium-cooled fast reactor in Russia with the low coolant inlet temperature of 300-
:. The objective of the Fusion-1 experiment in BOR-60 was to study the effects of neutron
ge in vanadium-base alloys in the 300-350°C temperature regime. Prior to this experiment,
ation testing of vanadium-base alloys in mixed-spectrum reactors and the fast reactor EBR-II
nperatures below ≈400°C had shown significant radiation hardening and embrittlement of
ials even at a relatively low neutron dose. The Fusion-1 experiment, a joint U.S.-Russia
to develop fusion materials, was designed to evaluate this low-temperature sensitivity at the
rate neutron fluence of ≈20 displacements per atom (dpa).

SUMMARY

The irradiation has been completed and the test specimens have been retrieved from the lithium-bonded capsule at the Research Institute of Atomic Reactors (RIAR) in Russia [1]. During this reporting period, the Argonne National Laboratory (ANL) tensile specimens were received from RIAR and initial testing and examination of these specimens at ANL has been completed. The results, corroborating previous findings [2-5], showed a significant loss of work hardening capability in the materials. There appears to be no significant difference in behavior among the various heats of vanadium-base alloys in the V-(4-5)Cr-(4-5)Ti composition range. The variations in the preirradiation annealing conditions also produced no notable differences.

EXPERIMENTAL PROCEDURE

Test Specimens

The tensile specimens submitted by ANL for the Fusion-1 experiment were 1/3-sized sheet specimens, with an overall length of 25.4 mm and a gauge section that was 7.62 mm long x 1.52 mm wide x 0.76 mm thick. The long direction of the gauge section was parallel to the final rolling direction of the sheets.

The primary test variable of the ANL specimens was alloy composition: V-4Cr-4Ti (Heat 832665), V-5Cr-5Ti (Heat T87), V-4Cr-4Ti with addition of 250 appm of boron (QN74), and a Russian heat of V-4Cr-4Ti (VX8). Table 1 shows the nominal compositions of these alloys. Also included in the test were weldment specimens from bead-on-plate laser welds of the Heat 832665 material. The purpose of adding boron to the QN74 alloy was to study the effects of helium generation from the B(n,α)Li reactions.

The secondary test variable was preirradiation thermal-mechanical treatment: all specimens except the weldment were annealed in vacuum at 950 or 1000°C for 1 or 2 h to remove the prior cold work (≈50%). The laser weldment specimens received only a hydrogen outgassing at 400°C for 1 h in vacuum after the welding, i.e., without a postweld heat treatment or the nominal 1000°C annealing.

* Work supported by the U.S. Department of Energy, Office of Fusion Energy Research, under Contract W-31-109-ENG-38.

Table 1. Nominal composition of the four alloys investigated

Heat Number	Ingot Size (kg)	Nom. Composition (wt.%)	Impurity Content (wppm)			
			O	N	C	Si
832665	500	V-3.8Cr-3.9Ti	310	85	80	780
T87	30	V-5.0Cr-5.0Ti	380	90	110	550
QN74[a]	15	V-4.0Cr-4.1Ti-B	350	220	200	870
VX8[b]	100	V-3.7Cr-3.9Ti	350	70	300	500

[a]Contains ≈250 appm of ^{10}B.
[b]From Russia. Contains (in wppm) 1120 Al, 280 Fe, 500 Co, 270 Mo, 1280 Nb, and 19 Zr.

Irradiation Summary

The Fusion-1 test vehicle was a single, 508-mm-long, lithium-bonded stainless steel capsule with a 36-mm OD and 32-mm ID. [1]. Inside the capsule, the test specimens were arranged in 10 equal-height tiers over the middle 361-mm region of the core. The ANL tensile specimens were placed below the core midplane, in Tiers 2, 3, and 4 (Tier 1 being at the bottom of the capsule) to attain the desired low specimen temperatures.

During the irradiation, which started in July 1995 and ended in June 1996, the reactor power and sodium inlet temperature were allowed to vary from time to time to comply with seasonal power output demands. Consequently, the specimen temperatures fluctuated during these operations. Based on the results of thermal analyses, the deviation from the time-averaged means was approximately ±16°C. The calculated time-averaged temperatures for specimens in tiers 2, 3, and 4 were 318, 320, and 323°C, respectively.

Displacement damage and transmutations in the specimens were calculated from the neutron flux and spectrum data determined from prior in-depth spectrometry measurements and the flux monitors incorporated in the Fusion-1 capsule. For Tiers 2, 3, and 4, the calculated displacement damage in the specimens was 17, 18, and 19 dpa, respectively. Because of the lack of thermal neutrons, atypical transmutations were insignificant. For specimens with added boron, the calculated helium generation rate in the material was ≈500 appm per dpa.

Capsule Disassembly

Because of the relatively large size of the fusion-1 capsule, the conventional method of using liquid ammonia to dissolve the lithium bond was impractical. An alternative technique of using heated mineral oil to melt and remove the lithium bond was adopted. (This method had been used before at RIAR to disassemble similar lithium-bonded capsules.) To ascertain that the exposure to oil at a temperature of ≈250°C for several hours would not adversely affect the properties of the specimens, extensive confirmatory tests were conducted at ANL. The results of these confirmatory tests showed only benign effects from the oil exposure and no measurable uptake of interstitial impurities.

The capsule disassembly was completed in an air cell at the RIAR. After the top and bottom end plugs of the capsule were removed with a low-speed saw, the capsule was immediately immersed in a bath of mineral oil at room temperature. The oil was then heated to 250°C to melt the lithium, which floated to the surface of the oil bath. The oil was then cooled to room temperature and the specimens were retrieved from the bath. The specimens were then repeatedly rinsed in alcohol at room temperature to remove residual oil and lithium and other possible surface contaminants.

RESULTS OF TENSILE TESTS

Thirteen tensile tests have been completed. The tests were conducted either at room temperature in air or at the irradiation temperature in high-purity flowing argon. Because the tests were performed without a specimen extensometer, the gauge elongation was determined from the crosshead displacement with the extension due to the slack in the grip and the deformation of the load frame subtracted. The strain rate for all tests was 1.1×10^{-3}/s. The results of these tests are summarized in Table 2.

Table 2. Tensile data for ANL specimens irradiated in Fusion-1 experiment[a,b]

Specimen ID No.	Material/Heat	Preirrad. Heat Treatment (°C/h)	Test Temp. (°C)	YS[c] (MPa)	UTS[c] (MPa)	UE[c] (%)	TE[c] (%)	RA[c,g] (%)
71-2	V-4Cr-4Ti/832655	1000/1	23	1115	1120	0.3	0.4	<≈3
71-1	V-4Cr-4Ti/832655	1000/1	318	913	932	0.7	1.3	tbd
71-2H2	V-4Cr-4Ti/832655	1000/2	23	1100	1115	0.3	0.5	<≈3
71-2H1	V-4Cr-4Ti/832655	1000/2	318	892	926	0.4	2.2	tbd
71-B	V-4Cr-4Ti/832655	950/2	23	1120	1125	0.5	0.8	<≈3
71-A	V-4Cr-4Ti/832655	950/2	318	953	962	0.4	1.3	tbd
72-2	V-5Cr-5Ti/T87	1000/1	23	1145	1150	0.4	0.4	<≈3
72-1	V-5Cr-5Ti/T87	1000/1	323	953	955	0.1	1.8	tbd
70-2	V-4Cr-4Ti-B/QN74	1000/1	23	[d]	[d]	[d]	[d]	[d]
70-1	V-4Cr-4Ti-B/QN74	1000/1	323	[e]	842	[e]	[e]	tbd
69-2	V-4Cr-4Ti/RF VX8	1000/1	23	1135	1170	1.4	2.8	<≈4
69-1	V-4Cr-4Ti/RF VX8	1000/1	323	909	936	0.5	2.3	tbd
71-LZ-1	832665/Laser	400/1	320	[f]	782	0.0	0.0	tbd

[a] All specimens were irradiated in the narrow temperature range of 318-323°C (time-averaged) and the dpa range of 17-19.
[b] All tests were conducted at a strain rate of 1.1×10^{-3}/s.
[c] YS: 0.2% offset yield strength; UTS: ultimate tensile strength; UE: uniform elongation; TE: total elongation; RA: reduction in area, tbd: to be determined.
[d] Specimen failed at grip at 727 MPa with no measurable plastic deformation before failure.
[e] Chart-drive malfunction prevented determination of these quantities.
[f] No measurable plastic deformation; offset yield strength could not be determined.
[g] See Ref. 6.

The yield strength of all of the materials was found to have increased significantly (by a factor of 3 to 4) over those of the nonirradiated materials. At the same time, there was a notable loss of work hardening ability, manifested by the small measured uniform elongation. All specimens failed rapidly due to plastic instability after yielding. Figure 1 shows the recorded tensile loading curves for Specimens 71-2 (Heat 832665) and 69-2 (Heat VX8), both of which were tested at room temperature. The load-displacement profiles of other specimens are similar. When tested at room temperature, the specimen with added boron broke at the grip before reaching the yield point, attesting to the material's brittleness after irradiation. The laser weldment specimens, although fractured at the gauge section, was also brittle and showed no measurable elongation. Uniform elongations for all other specimens were small (typically <1%). The Heat VX8 specimen

showed a marginally greater uniform elongation at room temperature; however, when tested at the irradiation temperature, its uniform elongation was essentially the same as those of the other specimens. Within the data scatter, therefore, it appears that all of the heats of vanadium-base alloys included in this test behaved similarly. The minor variations of the preirradiation heat treatment of the Heat 832665 specimens produced little effects.

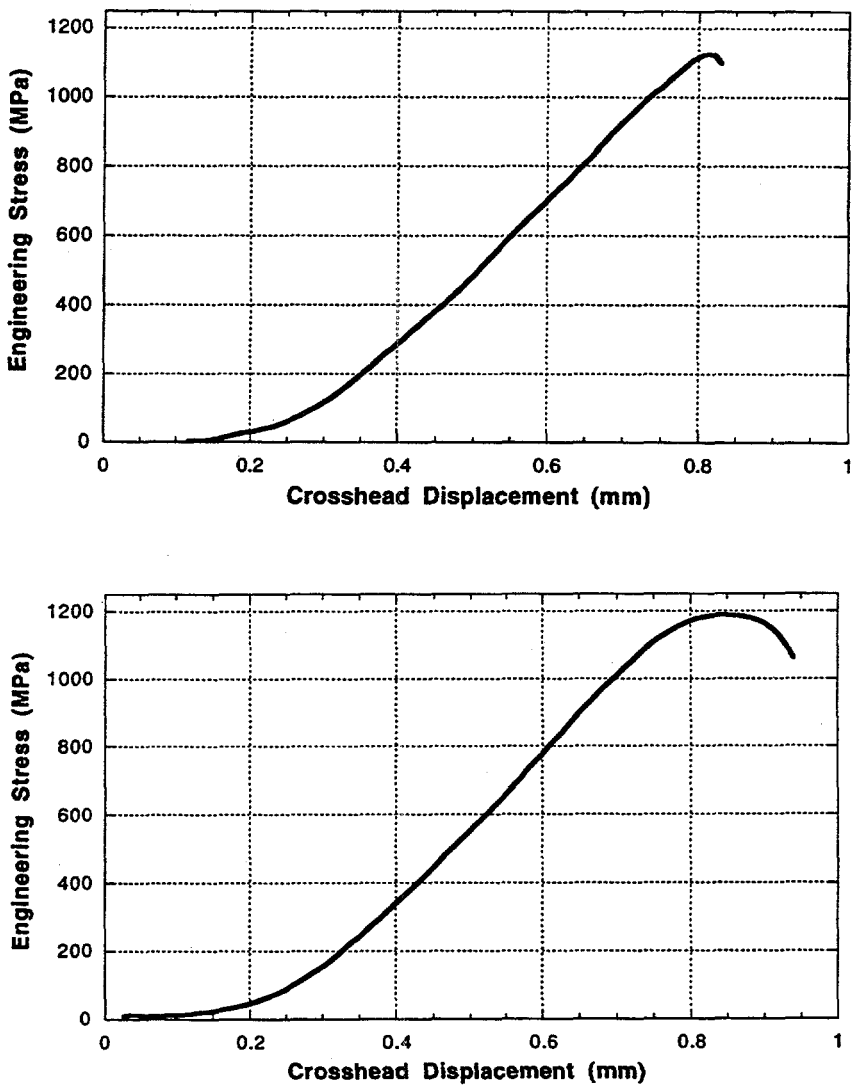

Fig. 1. Tensile loading curves for Specimens 71-2 (top, Heat 832665) and 69-2 (bottom, Heat VX8), both tested at room temperature. The gauge length of both specimens was 7.62 mm.

Fractographic examination with a scanning electron microscope is in progress. The objective of the examination is to determine the mode of fracture and the reduction of gauge cross-sectional area. The fractography of the room-temperature specimens has been completed. All fractures appear to be a mixture of ductile shear and brittle cleavage. Consistent with the elongation data, the reduction-in-area values were all small, as shown in Table 2. A more complete report of the fracture examination can be found in Ref. 6.

FUTURE ACTIVITIES

Fractographic examination will be completed. Additional tests will be conducted at lower strain rates to study dislocation channeling effects. The results from the present and future tests will be compared with X530, ATR-A1 and HFBR test data to better define the low-temperature irradiation effects.

REFERENCES

1. V. Kazakov et al., "Experience in Irradiation Testing of Low-Activation Structural Materials in Fast Reactor BOR-60," 8th Int. Conf. on Fusion Reactor Mater., Sendai, Japan, Oct. 26-31, 1998 (Proc. to be published).

2. H. Chung, H. Tsai, L. J. Nowicki, and D. L. Smith, "Tensile Properties of Vanadium Alloys Irradiated at 390°C in EBR-II," Fusion Materials Semiannual Progress Report for Period Ending June 30, 1997, DOE/ER-0313/22, pp.18-21.

3. S. J. Zinkle et al., "Effects of Fast Neutron Irradiation to 4 dpa at 400°C on the Properties of V-(4-5)Cr-(4-5)Ti Alloys," Fusion Materials Semiannual Progress Report for Period Ending December 31, 1996, DOE/ER-0313/21, pp.73-78.

4. D. J. Alexander et al., "Effects of Irradiation at Low Temperature on V-4Cr-4Ti," Fusion Materials Semiannual Progress Report for Period Ending June 30, 1996, DOE/ER-0313/20, pp.87-95.

5. H. Tsai et al., "Tensile and Impact Properties of Vanadium-Base Alloys Irradiated at Low Temperatures in the ATR-A1 Experiment," Fusion Materials Semiannual Progress Report for Period Ending December 31, 1997, DOE/ER-0313/23, pp.70-76.

6. J. Gazda, M. Meshii and H. Tsai, "Room Temperature Fracture in V-(4-5)Cr-(4-5)Ti Tensile Specimens Irradiated in Fusion-1 BOR-60 Experiment," ibid.

ROOM-TEMPERATURE FRACTURE IN V-(4-5)CR-(4-5)TI TENSILE SPECIMENS IRRADIATED IN FUSION-1 BOR-60 EXPERIMENT*

J. Gazda and M. Meshii (Northwestern University) and H. Tsai (Argonne National Laboratory)

SUMMARY

Specimens of V-(4-5)Cr-(4-5)Ti alloys were irradiated to ≈18 dpa at 320°C in the Fusion-1 capsule inserted into the BOR-60 reactor. Tensile tests at 23°C indicated dramatic yield strength increase (>300%), lack of work hardening, and minimal (<1%) total elongations. SEM analysis of fracture and side surfaces were conducted to determine reduction in area and the mode of fracture. The reduction of area was negligible. All but one specimen failed by a combination of ductile shear deformation and cleavage crack growth. Transgranular cleavage cracks were initiated by stress concentrations at the tips of the shear bands. In side-view observations, evidence was found of slip bands typically associated with dislocation channeling. No differences due to pre-irradiation heat treatment and heat-to-heat composition variations were detected. The only deviation from this behavior was found in V-4Cr-4Ti-B alloy, which failed in the grip portion by complete cleavage cracking.

OBJECTIVE

The objective of this study was to determine the room temperature tensile properties and fracture mode of tensile specimens of V-(4-5)Cr-(4-5)Ti alloys irradiated at ≈320°C in the BOR-60 reactor.

INTRODUCTION

Low-temperature irradiation performance data of V-4C-4Ti alloys are needed to establish guidance on the low-temperature limit of fusion reactors operation. These temperatures are also required for transient operation of the reactors in start-up, shut-down, and idle modes. Recently, a series of irradiation experiments was performed in various irradiation facilities to evaluate the irradiation performance of V-4Cr-4Ti alloys at low doses (0.1-6 dpa) [1-5]. The present irradiation experiment was designed to complement the low-dose data with information on the irradiation performance of V-(4-6)Cr-(4-6)Ti alloys in the temperature range of 310-350°C and at neutron fluences of 15 to 20 dpa. The irradiation was a part of the Russian Federation (RF)-U.S. collaborative Fusion-1 experiment in BOR-60 reactor. Specimens were delivered to Argonne National Laboratory and testing was initiated in this reporting period. The six fractured tensile specimens tested at 23°C were provided for our examination by the ANL Vanadium Alloy Development Program.

In this study, three specimens of the 500kg heat (#832665) of V-4Cr-4Ti alloy after various annealing treatments (1 h at 1000°C, 2 h at 1000°C, and 2 h at 950°C) were evaluated. The three additional specimens were V-4Cr-4Ti-250wppm ^{10}B (heat QN74) and V-5Cr-5Ti (heat T87) U.S. alloys, and the V-4Cr-4Ti alloy manufactured in the RF (heat VX8). The goals of the present work were to evaluate the mode of fracture and establish reasons for the dramatic yield strength increase, loss of macroscopic work hardening, and lack of elongation. The results of the tensile tests on these specimens are reported in a separate submission [6]. Here, we report on the findings of scanning electron microscopy (SEM) analysis of the fracture and side surfaces of the tensile specimens tested at 23°C.

---

*Work supported by U.S. Department of Energy Office of Fusion Energy Research and Argonne National Laboratory Division of Educational Programs, under Contract W-31-109-Eng-38.

EXPERIMENTAL PROCEDURES

The ANL tensile specimens included in the Fusion-1 experiment were machined from sheet stock to SS-3 geometry specifications (gauge dimensions: 7.62 mm length, 1.52 mm width, 0.76 mm thickness). The long direction of the specimens was parallel to the final rolling direction of the sheets. Two variables were investigated in the Fusion-1 experiment. First was the alloy's composition effects (listed in Table 1) and the second was the preirradiation heat treatment (listed in Table 2). The purpose of boron addition to the heat QN74 was to evaluate the effects of He generated by B(n,α)Li reactions. The ANL specimens were irradiated at ≈320°C to ≈18 dpa. The temperature varied by ±16°C during the irradiation period from July 1995 through June 1996 due to changes in sodium coolant inlet temperature. The coolant inlet temperature was dictated by the reactor's seasonal output demands. BOR-60, a fast breeder reactor, is used to generate electric power for the city of Dimitrovgrad, and in summer the power demands are lower. Following irradiation, the capsule was disassembled at the Research Institute of Atomic Reactors (RIAR). During disassembly specimens were exposed to mineral oil at 250°C followed by alcohol rinses at room temperature to dissolve the residual Li. Cleaned specimens were shipped to the USA.

Table 1. Nominal compositions of the four investigated alloys

Heat ID	Nominal	Major Impurities (wppm)			
	Composition (wt.%)	O	N	C	Si
832665	V-3.8Cr-3.9Ti	310	85	80	780
T87	V-5Cr-5Ti	380	90	110	550
QN74 [a]	V-4Cr-4.1Ti-B	350	220	200	870
VX8 [b]	V-3.7Cr-3.9Ti	350	70	300	500

[a] Contains 250 appm of ^{10}B.

[b] Manufactured in Russia; contains (in wppm) 1120 Al, 280 Fe, 500 Co, 270 Mo, 1280 Nb, and 19 Zr.

Table 2. Preirradiation heat treatments of investigated specimens

Specimen ID	Heat ID	Pre-Irradiation Annealing
BL71-2	832665	1 h at 1000°C
BL71-2H-2	832665	2 h at 1000°C
BL71-B	832665	2 h at 950°C
BL70-2	QN74	1 h at 1000°C
BL72-2	T87	1 h at 1000°C
BL69-2	VX8	1 h at 1000°C

Details of specimen handling and the testing procedures are given in the accompanying report [6]. The tensile tests were conducted at 23°C and a 0.0011 s^{-1} strain rate. In all tests, yield strengths were dramatically higher (≈300%) than in an unirradiated control specimens (≈350-400 MPa at 23°C). Slip bands formed and led to minimal work hardening and limited total elongations in specimens from heats 832665, T87 and VX8. The only specimen with appreciable macroscopic plastic deformation was the VX8 alloy. The specimen of QN74 failed in the grip area with no plastic deformation. The results of the tensile tests are given in Table 3.

After tensile testing, the specimens were examined by SEM in the ANL Alpha-Gamma Hot Cell Facility. For the reduction-in-area determinations, specimens were mounted in a vertical clip holder and oriented with cross-section parallel to the image plane. For the side-view observations, specimens were tilted ≈45°. Photomicrographs were acquired on Type 55 Polaroid film producing

both a positive print and a negative. The negatives were digitized by a Leafscan45 prepress negative scanner. The areas of deformed cross-sections were measured on digitized images. Figures for this report were prepared with Adobe PhotoShop software, and photographic quality output was generated by a Codonics NP-1600 die sublimation printer.

Table 3. Tensile data for ANL specimens irradiated in the Fusion-1 experiment in BOR-60

Specimen ID	YS (MPa)	UTS (MPa)	UE (%)	TE (%)
BL71-2	1115	1120	0.3	0.4
BL71-2H-2	1100	1115	0.3	0.5
BL71-B	1120	1125	0.5	0.8
BL70-2 [a]	-	-	-	-
BL72-2	1145	1150	0.4	0.4
BL69-2	1135	1170	1.4	2.8

[a] Specimen failed within the grip portion at 727 MPa with no plastic deformation.

RESULTS

SEM Fractography

Low magnification (≈40X) head-on orientation fractographs of the five tensile specimens that fractured within the gauge-length portion are presented in Fig. 1(a-e). A perspective view of the QN74 specimen is shown in Fig. 1(f). Reduction-of-area values obtained from these photomicrographs are listed in Table 4; all of these values are negligible. The slight variations from the pretesting values in the cross-sectional areas measured from photomicrographs of the fractured specimens are within the experimental error arising from misalignment of the specimens (≈3%). In all cases, however, fracture occurred by a combination of ductile shear and transgranular brittle cracking. Percentages of the cross-sectional area showing cleavage fracture are also listed in Table 4. Ductile shear fracture predominated in the specimens of V-4Cr-4Ti alloys (832665 and VX8). The percentage of brittle area in the VX8 specimen was higher than in the BL71-2. The difference in fracture behavior of these two specimens becomes apparent in observations with a perspective view (Fig. 2). Shear fracture occurred in BL71-2, while the VX8 alloy fractured transversely after limited necking. In both specimens, cleavage cracks propagated transversely to the loading direction.

Higher-magnification fractographs were obtained to evaluate the direction of cleavage crack propagation. The transitional regions, where cracks transformed from ductile to brittle mode were also examined. Typical examples are shown in Fig. 3. In all five cases, the flow direction of the "river pattern" indicates that the cleavage cracks initiated at a tip of shear band and propagated toward the surface of the specimen. This crack propagation direction suggests that the cleavage cracks were initiated by stress concentrations at the tip of the dislocation pileups impinging on grain boundaries.

The specimen of QN74 alloy fractured within the grip portion, as shown in Fig. 1(f). Close examination of the fracture surface revealed that the cleavage crack initiated at an outer edge of the specimen and propagated toward the pinhole. The "river pattern" visible in Fig. 4 flows to the pinhole. The average plane of the fracture surface was perpendicular to the loading direction. However, the crack changed the local orientation from grain to grain, following randomly oriented cleavage planes. Intergranular cracks were not observed.

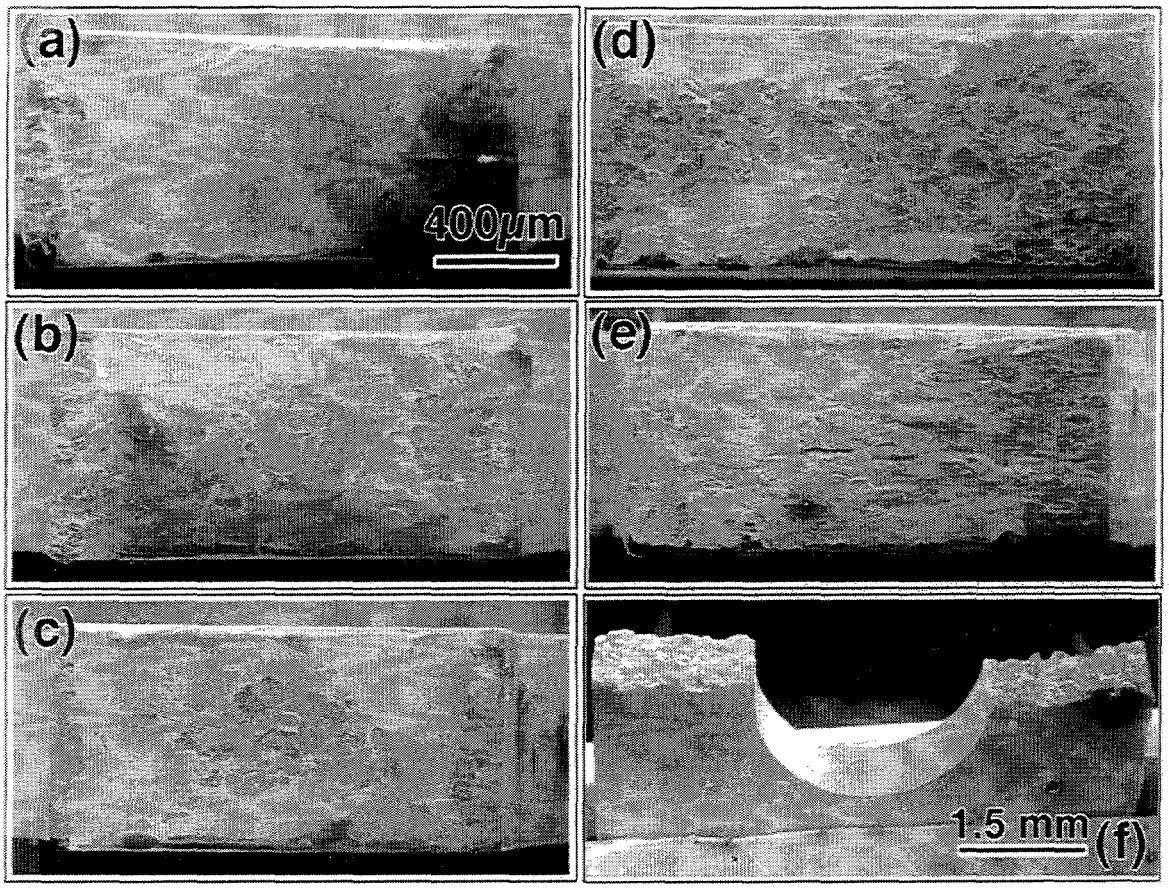

Fig. 1. SEM fractographs showing both ductile and brittle fracture areas of ANL tensile specimens irradiated in Fusion-1 experiment and tested at 23°C. Head-on views used to determine reduction in area: (a) BL71-2, (b) BL71-2H-2, (c) BL71-B, (d) BL72-2, (e) BL69-2, and (f) side view of grip portion of BL70-2 specimen.

Table 4. Reduction in cross-sectional area and fraction of brittle fracture surface in specimens of V-(4-5)-(4-5)Ti alloys irradiated in Fusion-1 capsule in BOR-60 reactor and tested at 23°C

Specimen ID	Cross-Sectional Area (mm^2)		Reduction	Percentage of
	Unirradiated	Post-irradiation	in Area (%)	Cleavage Fracture (%)
BL71-2	1.162	1.150	<< 3	15.83
BL71-2H-2	1.116	1.102	<< 3	65.78
BL71-B	1.185	1.178	<< 3	31.37
BL69-2	1.040	0.997	≈ 4	23.97
BL72-2	1.071	1.065	<< 3	72.05

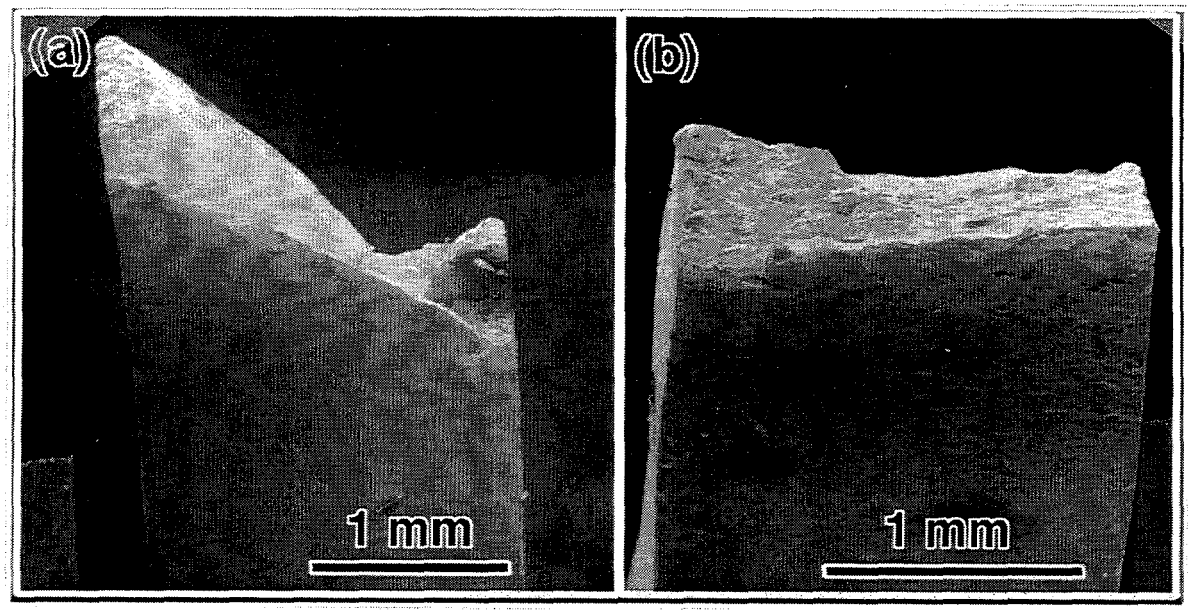

Fig. 2. Perspective views of specimens of V-4Cr-4Ti alloys with same preirradiation annealing schedule (1 h at 1000°C): (a) shear fracture in Heat 832665 (BL71-2) and (b) mixed-mode fracture in VX8 (BL69-2).

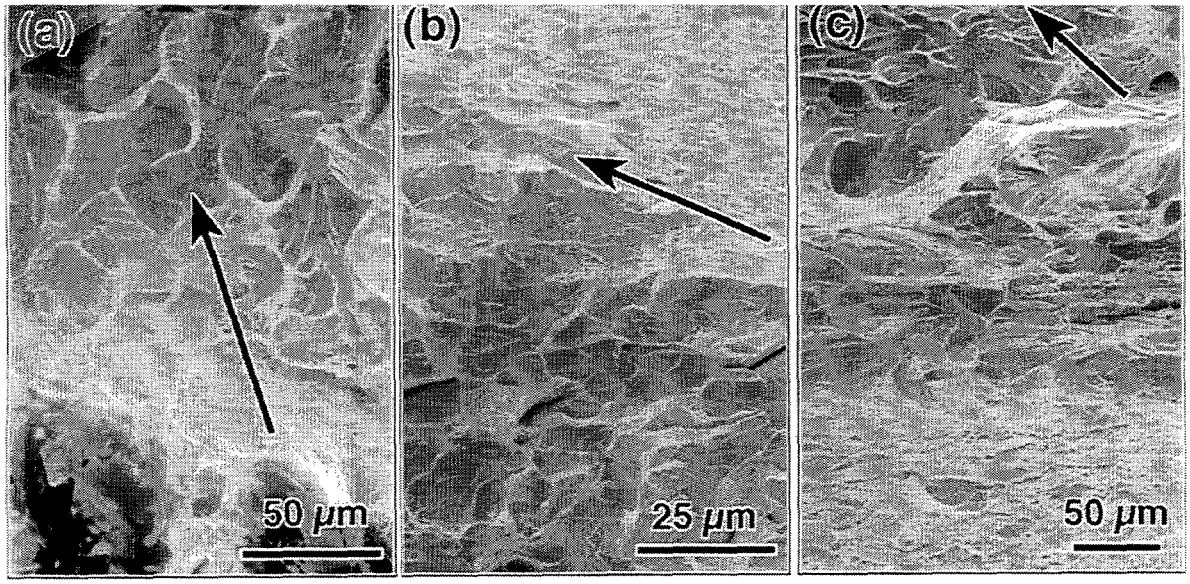

Fig. 3. SEM fractographs illustrating transformation from shear ductile to cleavage cracks: (a) BL71-2, (b)BL72-2, and (c) BL69-2. Arrows indicate directions of cleavage crack propagation.

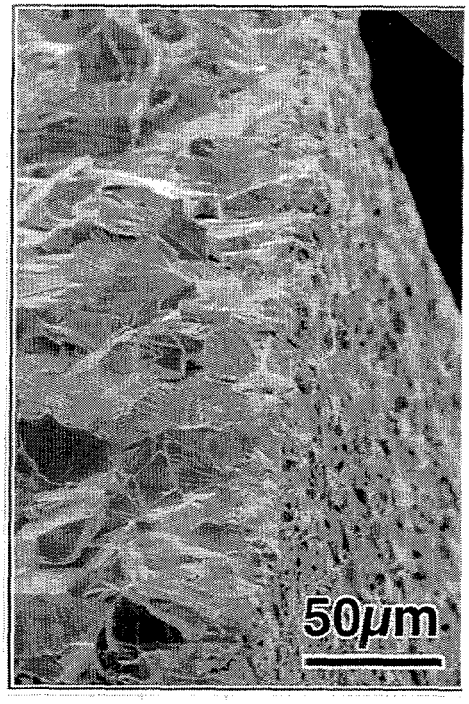

Fig. 4. View of inner surface of pinhole and fracture surface of QN74 specimen. Crack grew from outer specimen surface towards pinhole.

Side Surface Examinations

Side surfaces were examined to determine if slip bands characteristic of dislocation channeling formed during testing. They were observed in all five specimens that fractured in the gauge portion. Typical examples from the BL71-2H-2 and from the VX8 specimens are shown in Fig. 5. Short transverse cracks initiated at the surface were also found; they grew perpendicular to the direction of the applied tensile load, but did not extend far into the specimens. These cracks and slip bands were observed only in the necked regions.

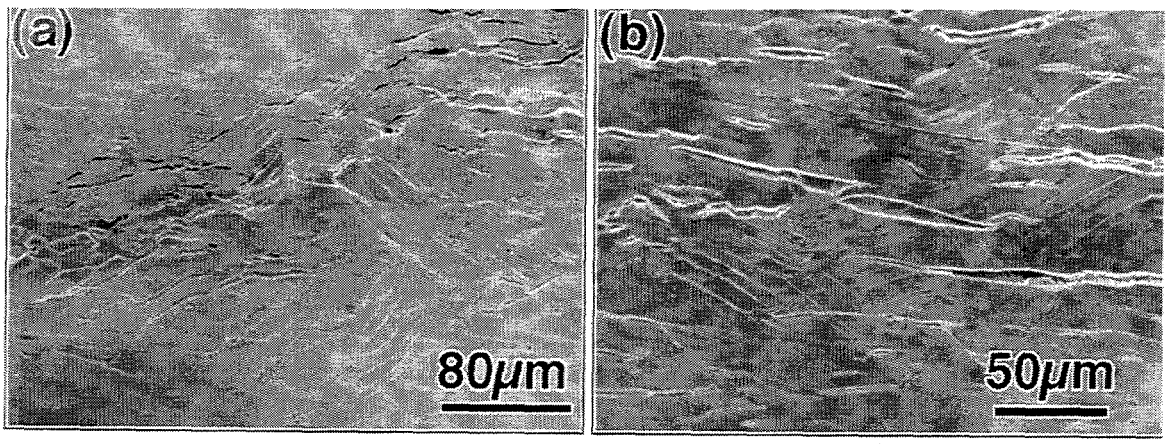

Fig. 5. Typical examples of surface steps indicating occurrence of dislocation channeling found on the side surfaces of the (a) heat 832665 - 2h anneal at 950°C, and (b) in VX8 specimen. The surface cracks also visible in these photomicrographs are perpendicular to tensile direction.

DISCUSSION

The occurrence of slip bands, shear bands, and shear cracks indicate that dislocation channels play a major role in the fracture of low-temperature-irradiated V-4Cr-4Ti alloys. Yield strengths observed in the present test are only slightly higher than those found in the earlier investigations of V-4Cr-4Ti alloy specimens irradiated to ≈6 dpa at 325°C in the HFR reactor [7], to ≈4 dpa at 390°C in the X530 experiment in the EBR-II reactor [8], and to ≈4 dpa at 280°C in the ATR-A1 experiment [9]. The same specimen geometry as in the present study was used in the EBR-II and ATR work. The HFR irradiation study used bar specimens with 4-mm-diameter gauge portions. All of these irradiations led to increased yield strength, lack of work hardening, and minimal elongations. In fractography evaluations of specimens from the X530 and ATR-A1 experiments, surface steps were found [10]. Dislocation channels were observed by TEM in the specimens irradiated at 390°C [11]. In the HFR study, a combination of cleavage and shear cracking was found [7]. Those data, combined with the results of the current study, indicate that irradiation of V-4Cr-4Ti below 400°C leads to detrimental hardening. They also indicate that dislocation channeling is not an effect of specimen geometry but rather an intrinsic response of the radiation-hardened alloy to the applied stress. From an engineering point of view, even the limited plastic deformation provided by the shear bands is preferred to complete brittle fracture. In additional papers, we identified the platelet precipitates formed in V-4Cr-4Ti during heavy ion and fast neutron irradiations at low temperatures (≤420°C). We also described their role in irradiation hardening [12, 13]. Further alloy design work to prevent irradiation-induced precipitate formation or to change the particle geometry will be necessary to improve ductility of V-4Cr-4Ti after low-temperature irradiation.

Heat-to-heat compositional variations did not play a major role in the response of the specimens to loading. Although the V-5Cr-5Ti alloy (T87) showed a considerably higher percentage of brittle fracture than did the V-4Cr-4Ti alloys, both ductile shear and brittle cracking contributed to its failure. Variations of annealing treatment of V-4Cr-4Ti (heat 832665) did not suppress the brittle cracking.

FUTURE WORK

Fractography study will be continued to evaluate the tensile specimens tested at irradiation temperatures. TEM investigations of cross-sections of irradiated and deformed specimens will also be conducted to determine effects of irradiation on the microstructure and the interaction mode of glide dislocations with radiation defects. The 3-mm discs irradiated in BOR-60 have not yet been delivered to ANL. Evaluations of these specimens will commence as soon as they arrive.

CONCLUSIONS

1. Both ductile-shear and transgranular cleavage fracture were observed in V-(4-5)Cr-(4-5)Ti alloys irradiated in the Fusion-1 capsule in the BOR-60 reactor after tensile testing at 23°C. The reductions of area were negligible except for that in the VX8 alloy which showed ≈4% reduction in area. A V-4Cr-4Ti-250appm ^{10}B specimen fractured by cleavage within the grip portion with no significant plastic deformation in the gauge length. Intergranular fracture was not observed in any of the specimens.
2. Heat-to-heat compositional variations and preirradiation annealing treatments had no effects on the fracture behavior. In all specimens, slip localization by shear bands and dislocation channeling was observed. Cleavage cracks initiate at the shear bands and propagate toward the surfaces of the specimens.
3. Slip localization and dislocation channeling provide the only plastic deformation found in these specimens. Occurrence of any plastic flow in radiation-hardened V-(4-5)Cr-(4-5)Ti alloys with yield strengths ≥1000 MPa is noteworthy.

REFERENCES

1. Tsai, H.-C., R. V. Strain, A. G. Hins, H. M. Chung, L. J. Nowicki, and D. L. Smith, Fusion Reactor Materials, Semiannual Progress Report for Period Ending September 30, 1994, Oak Ridge National Laboratory, DOE/ER-0313/17, 8-14.
2. Tsai, H., R. V. Strain, I. Gomes, A. G. Hins, and S. D. L., ATR-A1 Irradiation Experiment on Vanadium Alloys and Low-Activation Steels, Fusion Materials - Semiannual Progress Report for Period Ending December 31, Oak Ridge National Laboratory, DOE/ER-0313/19, 314-320.
3. Alexander, D. J., L. L. Snead, S. J. Zinkle, A. N. Gubbi, and A. F. Rowcliffe, Fusion Materials, 1996, DOE/ER-0313/20, Oak Ridge National Laboratory, DOE/ER-0313/20, 87-95.
4. van Osch, E. V., M. G. Horsten, M. I. de Vries, W. van Witzenburg, R. Conrad, G. Sordon, and G. P. Tartaglia, J. Nucl. Mater., **233-237** (1996), 1541-1546.
5. Rowcliffe, A. F., H. C. Tsai, D. L. Smith, V. Kazakov, and V. Chakin, Fusion Materials - Semiannual Progress Report for Period Ending June 30, Oak Ridge National Laboratory, DOE/ER-0313/22, 284-299.
6. Tsai, H. C., J. Gazda, L. J. Nowicki, and D. L. Smith, *Tensile Properties of Vanadium Base Alloys After A Low-temperature Irradiation in the Fusion-1 Experiment in the BOR-60 Reactor,* Fusion Materials - Semiannual Progress Report for Period Ending June 30, 1998, Oak Ridge National Laboratory, DOE/ER-0313/24, *in this issue.*
7. van Osch, E. and M. I. de Vries, *Irradiation Hardening of V-4Cr4Ti,* J. Nucl. Mater., (1998), Proceedings ICFRM-8, *in press*
8. Chung, H. M., H.-C. Tsai, L. J. Nowicki, and D. L. Smith, Tensile Properties of Vanadium alloys Irradiated at 390°C in EBR-II, Fusion Materials Semiannual Progress Report for Period Ending June 30, Oak Ridge National Laboratory, October 1997, DOE/ER-0313/22, 18-21.
9. Tsai, H., L. J. Nowicki, M. C. Billone, H. M. Chung, and D. L. Smith, Fusion Materials - Semiannual Progress Report for Period Ending December 31, 1997, Oak Ridge National Laboratory, DOE/ER-0313/23, 70-77.
10. Gazda, J., M. Meshii, H. M. Chung, and S. J. Zinkle. *Slip Localization by Dislocation Channeling in Low Temperature Irradiated Vanadium Base Alloys.* Presented at 19th ASTM International Symposium on Effects of Radiation on Materials, Seattle, June 16-18, 1998.
11. Gazda, J., M. Meshii, and H. M. Chung, *Microstructure of V-4Cr-4Ti after Low-Temperature Irradiation by Ions and Neutrons,* J. Nucl. Mater., (1998), Proceedings ICFRM-8, *in press.*
12. Gazda, J., M. Meshii, and H. M. Chung, *Low-Temperature Irradiation Induced Precipitation in V-4Cr-4Ti Alloy - The Mechanism,* J. Nucl. Mater., (1998), *submitted*
13. Chung, H. M., J. Gazda, and D. L. Smith, *Irradition-Induced Precipitation and Mechanical Properties of Vanadium-Based Alloys at <430°C,* Fusion Materials - Semiannual Progress Report for Period Ending June 30, Oak Ridge National Laboratory, DOE/ER-0313/24, *in this issue.*

EFFECTS OF IRRADIATION TO 4 DPA AT 390°C ON THE FRACTURE TOUGHNESS OF VANADIUM ALLOYS*

E. E. Gruber, T. M. Galvin, and O. K. Chopra (Argonne National Laboratory)

OBJECTIVE

The objective of this task is to study the effects of neutron irradiation on the fracture toughness of vanadium–base alloys.

SUMMARY

Fracture toughness J–R curve tests were conducted at room temperature on disk-shaped compact-tension DC(T) specimens of three vanadium alloys having a nominal composition of V-4Cr-4Ti. The alloys in the nonirradiated condition showed high fracture toughness; J_{IC} could not be determined but is expected to be above 600 kJ/m^2. The alloys showed very poor fracture toughness after irradiation to 4 dpa at 390°C, e.g., J_{IC} values of ≈10 kJ/m^2 or lower.

EXPERIMENTAL PROGRAM

The heats of vanadium alloy selected for the study had compositions of V-3.8 wt.%Cr-3.9 wt.%Ti (Heat #832665, designated BL-71, 783 wppm Si, 310 wppm O, 85 wppm N, 80 wppm C); V-4.1 wt.%Cr-4.3 wt.%Ti (Heat #9144, designated BL-47, 870 wppm Si, 350 wppm O, 220 wppm N, 200 wppm C); and V-4.0 wt.%Cr-4.1 wt.%Ti-B (designated BL-70 or QN74, 350 wppm Si, 480 wppm O, 79 wppm N, 54 wppm C, ≈250 appm B-10). Prior to testing, the alloys were annealed in high-purity vacuum for 1 h (at 1025-1050°C for BL-47, and at 1000°C for BL-71 and BL-70). Alloy BL-71 was tested in the nonirradiated condition and alloys BL-47 and BL-70 were irradiated to ≈4 dpa at 390°C in lithium in the EBR-II reactor experiment X530 (located in subcapsule S2 for BL-47 and S14 for BL-70). The room–temperature tensile properties of the various vanadium alloys [1] before and after irradiation are given in Table 1. The tensile properties of BL-47 were also used to determine the flow stress for irradiated alloy BL-70.

Table 1. Room-temperature tensile properties of nonirradiated and irradiated vanadium alloys

Alloy Designation	Irradiation Experiment	Yield Strength (MPa)	Ultimate Stress (MPa)
BL-47	–	404	460
BL-71	–	355	429
BL-47[a]	X530[b]	880	935

[a]Prior to irradiation, the alloy was warm-rolled at 400°C and annealed at 950°C.
[b]DC(T) specimens irradiated to ≈4 dpa at 390°C in EBR II reactor.

Fracture toughness J–R curve tests were conducted according to ASTM Specification E 1737 (Standard Test Method for J–Integral Characterization of Fracture Toughness) at room temperature on disk-shaped compact-tension DC(T) specimens of the various vanadium-base alloys. The method involves pin loading of fatigue-precracked specimens and determination of the J-integral as a function of crack growth. A detailed description of the facility is presented in Ref. 2. The facility is designed for conducting fracture toughness J-R or fatigue crack growth tests on 1/4 T DC(T) or C(T) specimens in air or light water reactor (LWR) environments at temperatures up to 300°C. Specimen extension is monitored and controlled outside of the high-temperature zone. The displacement of load points (center of the loading pins) is determined by subtracting the machine compliance from the measured

extension. Crack length was determined by the elastic unloading compliance method. The configuration of the 1/4T DC(T) specimens used in the present study is shown in Fig. 1. Crack length and J–integral were calculated by using the correlations recommended for DC(T) specimens in ASTM Specification E 1737.

Several validation tests were conducted in which the actual displacements of load points were measured optically and compared with the estimated loadline displacements. Measured loadline displacements showed very good agreement with the estimated values [3]; for loadline displacements of up to 2 mm, the error in the estimated values was <0.02 mm. Fracture toughness J–R curve tests were also conducted at room temperature and 288°C on 1/4-T C(T) specimens of two heats of thermally aged CF-8M cast stainless steel; the results were compared with data obtained on 1-T C(T) specimens to validate the test procedure [3].

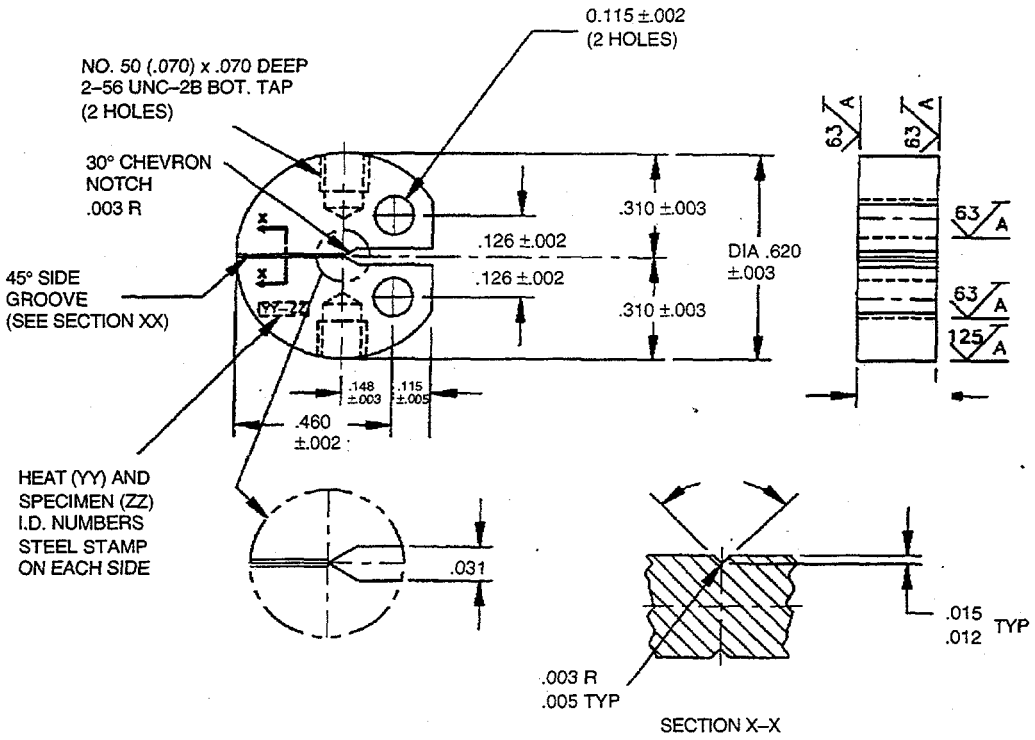

Figure 1. Configuration of disk–shaped compact–tension specimen for this study

Prior to testing, the specimens were fatigue–precracked at room temperature and at loads based on the maximum allowable load P_m given by the relation

$$P_m = (0.4\,\sigma_f\,B_N\,b^2)/(2W + a), \qquad (1)$$

where W is specimen width, a is crack length, B_N is net specimen thickness (distance between roots of the side grooves), b is noncracked ligament (distance from the crack front to the back edge of the specimen, i.e., $W - a$), and σ_f is flow stress expressed as the mean of the yield and ultimate stress. The final fatigue precrack extension was carried out at loads $\leq P_m$, or a load such that the ratio of the maximum stress intensity applied during fatigue precracking to the elastic modulus (K_{max}/E) was $\leq 1.6 \times 10^{-4}\ m^{1/2}$ ($\leq 0.001\ in.^{1/2}$).

The fatigue-precracked specimens were loaded at a constant extension rate and the tests were interrupted periodically to determine the crack length. The maximum range of unload/reload for crack extension measurements was the smaller of $0.5P_m$ or 50% of the current load. The final crack size was marked by fatigue cycling. After the test, the specimens were fractured and the initial (i.e., fatigue-precrack) and final (test) crack lengths were measured optically on both halves of the fractured specimen. The crack lengths were determined by the 9/8 averaging technique, i.e., the two–near–surface measurements were averaged and the resultant value was averaged with the remaining seven measurements.

RESULTS AND DISCUSSION

The load-versus-loadline displacement curves and fracture toughness J–R curves for nonirradiated specimens of alloy BL-71 are shown in Figures 2 and 3, and for irradiated specimens of alloys BL-47 and BL-70 in Figures 4 and 5. A slope of two times the flow stress was used to define the blunting and offset lines. Also, because displacement was monitored and controlled away from the specimen, loadline displacement is not constant during periods of unstable crack growth (observed in irradiated alloys) but is increased because of the accompanying load drop.

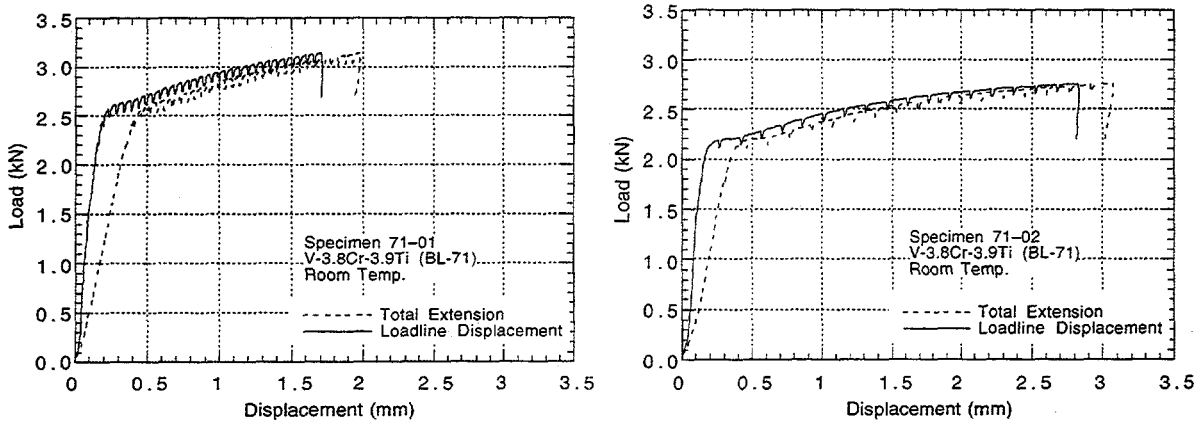

Figure 2. Load versus loadline displacement for specimens V71–01 and V71–02 of nonirradiated Heat 71 tested at room temperature

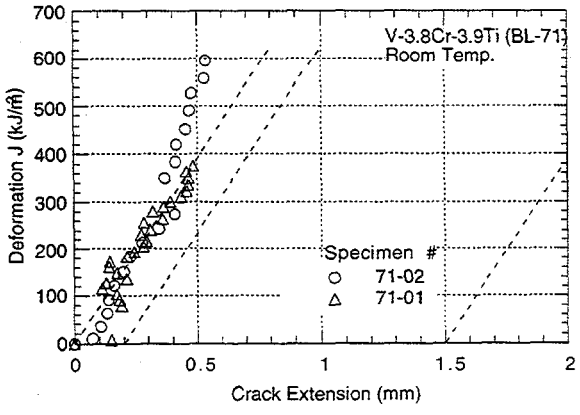

Figure 3. Fracture toughness J–R curves for specimens V71–01 and V71–02 of nonirradiated Heat 71 tested at room temperature

For the nonirradiated alloy BL-71, maximum load or displacement limit for the test facility was reached before the onset of stable crack extension, i.e., J_{IC} could not be determined but is expected to be above 600 kJ/m^2. The results for alloy BL-71 (Fig. 3) show excellent agreement with the data obtained earlier on production-scale Heat 832665 of V-4Cr-4Ti alloy [4].

Alloys BL-47 and BL-70 irradiated to ≈4 dpa at 390°C show very poor room-temperature fracture toughness. The J_{IC} values are 6 and 11 kJ/m^2 for BL-47 and BL-70, respectively. Both alloys showed several bursts of unstable crack extension. A detailed metallographic evaluation of the fracture surface has not been conducted; however, preliminary examination indicates that fracture occurred predominantly by cleavage.

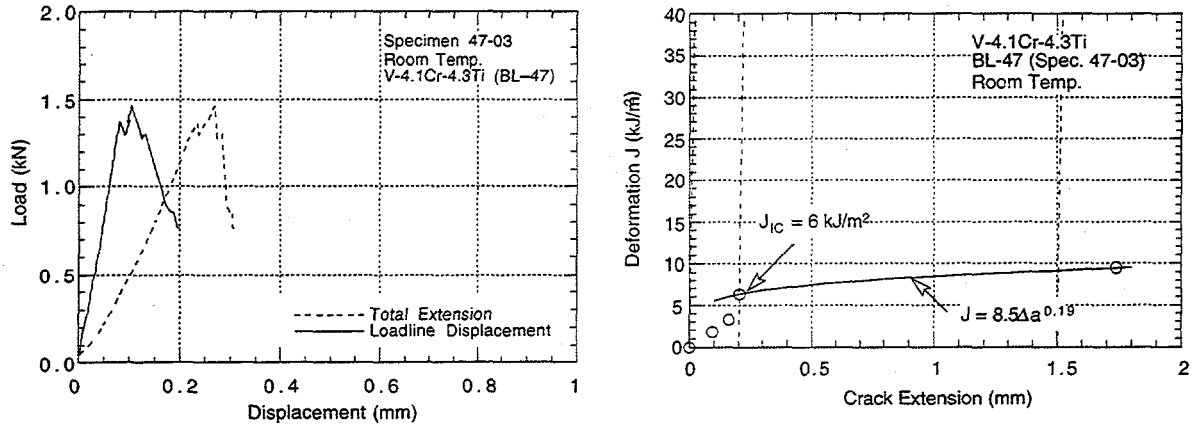

Figure 4. Load versus loadline displacement and fracture toughness J–R curve for irradiated Heat 47 tested at room temperature

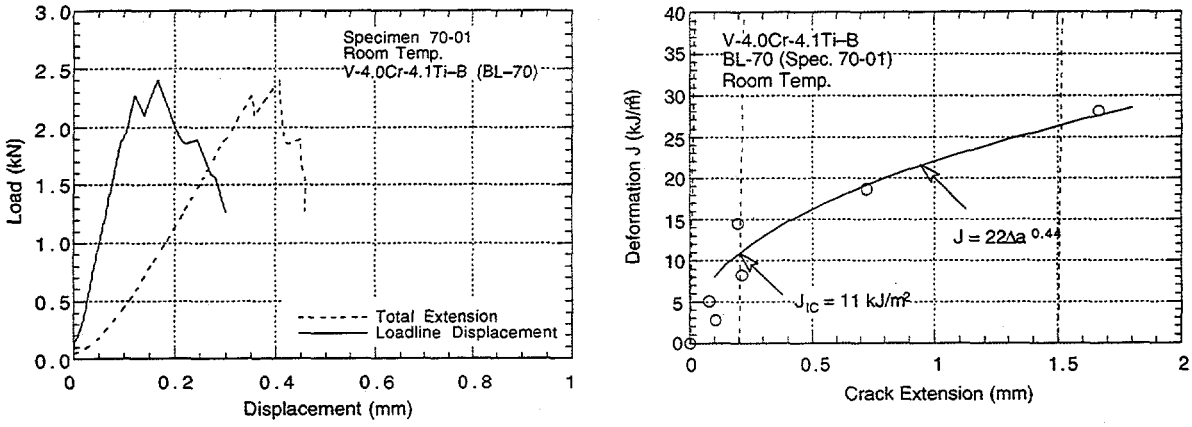

Figure 5. Load versus loadline displacement and fracture toughness J–R curve for irradiated Heat 70 tested at room temperature

REFERENCES

1. M. Billone, private communication April 1998.

2. T. H. Hughes and E. E. Gruber, "Development of Hot–Cell J–R Test Facility," Environmentally Assisted Cracking in Light Water Reactors Semiannual Report July 1996–December 1996, NUREG/CR-4667, Vol. 23, ANL–97/10, p. 42, Oct. 1997.

3. E. E. Gruber and O. K. Chopra, "Fracture Toughness J–R Test of Austenitic Stainless steels Irradiated in Halden Reactor," Environmentally Assisted Cracking in Light Water Reactors Semiannual Report January 1997 – June 1997, NUREG/CR-4667, Vol. 24, ANL–98/6, p. 54, April 1998.

4. H. Li, R. J. Kurtz, and R. H. Jones, "Mode I and Mixed Mode I/III Crack Initiation and Propagation Behavior of V-4Cr-4Ti Alloy at 25°C," Fusion Materials Semiannual Progress Report for the Period Ending December 31, 1996, DOE/ER-0313/21, p. 27, April 1997.

EFFECT OF IRRADIATION TEMPERATURE AND STRAIN RATE ON THE MECHANICAL PROPERTIES OF V-4Cr-4Ti IRRADIATED TO LOW DOSES IN FISSION REACTORS — S. J. Zinkle, L. L. Snead, A. F. Rowcliffe, D. J. Alexander, and L. T. Gibson (Oak Ridge National Laboratory)

OBJECTIVE

The objective of this report is to summarize recent data on the temperature-dependent tensile and fracture toughness properties of V-Cr-Ti alloys irradiated in the HFBR, ATR and BOR-60 fission reactors.

SUMMARY

Tensile tests performed on irradiated V-(3-6%)Cr-(3-6%)Ti alloys indicate that pronounced hardening and loss of strain hardening capacity occurs for doses of 0.1-20 dpa at irradiation temperatures below ~330°C. The amount of radiation hardening decreases rapidly for irradiation temperatures above 400°C, with a concomitant increase in strain hardening capacity. Low-dose (0.1-0.5 dpa) irradiation shifts the dynamic strain aging regime to higher temperatures and lower strain rates compared to unirradiated specimens. Very low fracture toughness values were observed in miniature disk compact specimens irradiated at 200-320°C to ~1.5-15 dpa and tested at 200°C.

PROGRESS AND STATUS

Introduction

Several recent studies have shown that V-4Cr-4Ti alloys exhibit significant radiation hardening and a dramatic decrease in strain hardening capacity following neutron irradiation at temperatures up to ~400°C [1-6]. The radiation hardening produces large increases in the ductile to brittle transition temperature, as measured by Charpy impact testing [1,2,6]. Further work is needed to accurately determine the minimum acceptable operating temperature for vanadium alloys in a fusion reactor environment (currently estimated to be 400°C), which will be determined by radiation hardening/embrittlement considerations. In order to provide additional mechanical properties data, we have recently measured the tensile properties of V-(3-6%)Cr-(3-6%)Ti alloys irradiated in the HFBR, ATR, and BOR-60 reactors at relatively low irradiation temperatures ($\leq$505°C). In addition, a limited number of fracture toughness tests were performed on irradiated V-4Cr-4Ti.

Experimental Procedure

Tensile measurements were performed on type SS-3 sheet tensile specimens (nominal gage dimensions 0.76 x 1.52 x 7.6 mm) from three recent neutron irradiation experiments. The first set of specimens were fabricated from the 500 kg US fusion program heat of V-4Cr-4Ti (heat 832665) and were irradiated at 160-504°C to doses of 0.1-0.5 dpa in the High Flux Beam Reactor (HFBR) [2]. Most of the HFBR specimens were vacuum annealed at 1000°C for 2 h prior to irradiation. Several specimens were given an alternative heat treatment of 900°C for 2 h prior to the HFBR irradiation. The second set of specimens consisted of V-4Cr-4Ti (heat 832665) and small (14 kg) heats [7] of V-3Cr-3Ti (heat T91), V-6Cr-3Ti (heat T92), and V-6Cr-6Ti (heat T90), all of which were irradiated in the Advanced Test Reactor (ATR) as part of the Gd-shielded ATR-A1 irradiation experiment [6]. All of the tested ATR specimens were vacuum annealed at 1000°C for

2 h prior to irradiation. The specimens were irradiated in ATR-A1 subcapsules AS5, AS6, AS11, or AS12 to doses of 3.0-3.5dpa at calculated temperatures of 205-230 and 4.5-4.7 dpa at 290-295°C. The third set of specimens included V-4Cr-4Ti (heats 832665 and T89), V-3Cr-3Ti (heat T91), V-6Cr-3Ti (heat T92), and V-6Cr-6Ti (heat T90), all of which were irradiated in the Li-bonded BOR-60 Fusion 1 irradiation experiment [8]. The V-4Cr-4Ti tensile specimens were annealed at either 1000°C for 2 h or 1050°C for 1 h prior to irradiation. The small heat tensile specimens (heats T89, T90, T91, T92) were annealed at 1050°C for 2 h prior to irradiation. Tensile specimens fabricated from gas tungsten arc and electron beam welds (fusion zone in the center of the gage length) in the as-welded and vacuum annealed (950°C, 2h) condition were also included in the BOR-60 capsule. The BOR-60 specimens tested in the present study were irradiated at tiers 1-5 of the Fusion 1 capsule at 316-325°C to doses of 15-20 dpa (2.2-2.9x10^{26} n/m^2, E>0.1 MeV). Further details of the specimen preparation and irradiation conditions for the HFIR [2], ATR [6], and BOR-60 [8] capsules are given elsewhere.

Miniature disk compact tension specimens with dimensions 12.5 mm diameter by 4.6 mm thickness (DCT) or 9.6 mm diameter by 3.56 mm thickness (DCT-A) were fabricated from the 500 kg heat of V-4Cr-4Ti in the T-L orientation. The specimens were annealed at 1000°C for 2 h and then fatigue pre-cracked at room temperature and side-grooved 10% of their thickness on each side prior to irradiation in ATR-A1 [6] and BOR-60 Fusion 1 [8] capsules. The ATR-A1 specimens (DCT-A geometry) were irradiated in subcapsules AS3 and AS13 at ~190°C,1.5 dpa and ~250°C, 2.3 dpa, respectively. The BOR-60 specimens (DCT geometry) were irradiated in tier 1 of the Fusion 1 capsule at 316°C to a dose of 15 dpa (2.2×10^{26} n/m^2, E>0.1 MeV).

Following irradiation, the tensile specimens were tested in vacuum (<2.5×10^{-6} torr) at the irradiation temperature at constant crosshead speeds ranging from 0.025 to 12.7 mm/minute, which corresponds to initial strain rates of 5.6×10^{-5} to 0.028 s^{-1}. The lower yield point was recorded as the yield strength in cases where a yield drop was observed. In specimens with very low uniform elongation (<0.5%), the lower yield point was determined by graphical analysis of the load-elongation curve . The irradiated DCT specimens were tested in air under stroke control on a 445 kN capacity servohydraulic test machine in general accordance with ASTM E813-89, Standard Test Method for J_{1C} and ASTM 1152-87, Standard Test Method for Determining J-R Curves. Further details of the DCT test technique are given elsewhere [9].

Results and Discussion

The tensile properties of the irradiated V-4Cr-4Ti specimens are listed in Tables 1-3. The relatively low irradiation temperatures used for this study caused considerable radiation hardening with an accompanying reduction in strain hardening capacity. The uniform elongation ranged from ~0.1-0.5% in the specimens irradiated at temperatures below 325°C, even for irradiation doses as low as 0.1 dpa. High uniform elongation (~7-11%) was observed in V-4Cr-4Ti irradiated to 0.1 dpa at 390 and 505°C and to 0.5 dpa at 415°C (Table 1). The unirradiated uniform elongations in V-4Cr-4Ti is15-20% at test temperatures of 200-400°C It is worth noting that the fine-grained specimens (900°C/2 h anneal) had 30 to 80 MPa higher irradiated strengths than the coarse-grained (1000°C/2 h) HFBR specimens for irradiation temperatures up to 300°C. As an aside, there was a typing mistake in the HFBR irradiated reduction in area measurements reported in Table 3 of ref. [2]. The reduction in area listed for specimen WH25 (87%) should be deleted, and a value of 78% should be inserted for specimen WH23.

The tensile curves in the specimens irradiated at temperatures below 325°C were characterized by a yield peak at elongations <0.2%, followed by a monotonically decreasing engineering stress with increasing elongation. As shown in Fig. 1 and in previous studies [2], a significant change in the slope of the irradiated load-elongation curve typically occurred at elongations of ~0.5%. The stress at the transition point was recorded as the yield stress (lower yield point), since the 0.2% plastic offset stress was typically equal to the ultimate stress. The V-3Cr-3Ti specimen XC01 irradiated in BOR 60 (Table 3) did not exhibit an observable yield drop/ macroscopic plastic

instability, although the strain hardening capacity was very low. The 0.2% plastic offset stress was used as the yield stress in Table 3 for this specimen.

Figure 2 shows the dose dependence of the yield strength in V-4Cr-4Ti irradiated at low temperatures, based on the present study and previous studies by several investigators. The data suggest that the radiation hardening approaches a saturation level for doses of ~5 dpa for irradiation temperatures of ~300 and ~400°C. There are no data available at doses between ~0.5 and 4 dpa to determine if saturation occurs at doses lower than 5 dpa. The data in Fig. 2 suggest that the yield strength decreases slightly with increasing dose above 5 dpa for irradiation temperatures of 400-430°C. However, further studies (particularly at doses of 1-10 dpa) are needed to determine the detailed dose dependence of the radiation hardening. It is possible that the apparent "radiation softening" that occurs at doses above 5 dpa at 400-430°C may be due to the higher irradiation temperatures (425-430°C)of the available data at doses >10 dpa compared to that at 4-10 dpa (400°C). Alternatively, coarsening of the microstructure may be occurring at doses above ~5 dpa which may lead to a reduction in the amount of radiation hardening at high doses.

Table 1. Summary of recent tensile data on V-4Cr-4Ti specimens irradiated in HFBR. The yield strength was determined at 0.2% plastic offset for the specimens irradiated at ≥325°C, whereas the lower yield point (typically occurring at ~0.5% plastic deformation) was used for the low irradiation temperature (<325°C) data marked with an asterisk. The data in italics refer to specimens which were given the alternate heat treatment of 900°C/2h prior to irradiation.

Specimen ID, dpa, T_{irr}	Test conditions	Yield strength	Ultimate strength	Uniform elongation	Total elongation
WH28, 0.5dpa, 160°C	160°C, 5.6×10^{-5} s^{-1}	700 MPa*	739 MPa[a]	0.1%	10.0%
WH29, 0.5dpa, 160°C	160°C, 0.028 s^{-1}	735 MPa*	766 MPa[a]	0.2%	9.8%
WH30, 0.5dpa, 160°C	160°C, 0.028 s^{-1}	750 MPa*	777 MPa[a]	0.2%	9.3%
ST14, 0.5dpa, 160°C	160°C, 1.1×10^{-3} s^{-1}	684 MPa*	752 MPa[a]	0.1%	10.0%
ST15, 0.5dpa, 160°C	160°C, 1.1×10^{-3} s^{-1}	672 MPa*	770 MPa[a]	0.1%	9.3%
ST45, 0.5dpa, 160°C	*160°C, 1.1×10^{-3} s^{-1}*	*764 MPa**	*840 MPa[a]*	*0.2%*	*8.7%*
ST21, 0.5dpa, 268°C	270°C, 1.1×10^{-3} s^{-1}	639 MPa*	706 MPa[a]	0.1%	9.3%
ST41, 0.5dpa, 268°C	*270°C, 1.1×10^{-3} s^{-1}*	*707 MPa**	*752 MPa[a]*	*0.1%*	*8.7%*
ST23, 0.5dpa, 260°C	260°C, 1.1×10^{-3} s^{-1}	647 MPa*	712 MPa[a]	0.2%	9.5%
ST42, 0.5dpa, 260°C	*260°C, 1.1×10^{-3} s^{-1}*	*702MPa**	*773 MPa[a]*	*0.1%*	*7.7%*
ST27, 0.5dpa, 324°C	325°C, 1.1×10^{-3} s^{-1}	592 MPa*	635 MPa[a]	0.2%	9.2%
ST43, 0.5dpa, 324°C	*325°C, 1.1×10^{-3} s^{-1}*	*605 MPa*	*605 MPa*	*0.5%*	*9.0%*
ST44, 0.5dpa, 307°C	*305°C, 1.1×10^{-3} s^{-1}*	*597 MPa*	*601 MPa*	*0.7%*	*9.2%*
ST33, 0.5dpa, 414°C	415°C, 1.1×10^{-3} s^{-1}	354 MPa	449 MPa	8.2%	17.8%
ST34, 0.5dpa, 414°C	415°C, 1.1×10^{-3} s^{-1}	352 MPa	443 MPa	6.6%	16.7%
ST49, 0.1dpa, 105°C	*105°C, 1.1×10^{-3} s^{-1}*	*632 MPa**	*669 MPa*	*0.2%*	*9.3%*
ST61, 0.1dpa, 256°C	255°C, 1.1×10^{-3} s^{-1}	491 MPa*	504 MPa	0.2%	11.8%
ST51, 0.1dpa, 256°C	*255°C, 1.1×10^{-3} s^{-1}*	*526 MPa**	*533 MPa*	*0.2%*	*11.3%*
ST68, 0.1dpa, 391°C	390°C, 5.6×10^{-5} s^{-1}	348 MPa	425 MPa	11.0%	22.3%
ST69, 0.1dpa, 391°C	390°C, 0.028 s^{-1}	348 MPa	415 MPa	9.0%	18.0%
ST58, 0.1dpa, 504°C	505°C, 5.6×10^{-5} s^{-1}	271 MPa	434 MPa	9.5%	19.2%
ST75, 0.1dpa, 504°C	505°C, 0.028 s^{-1}	281 MPa	407 MPa	12.1%	21.7%

*lower yield point
[a]upper yield point

Table 2. Summary of tensile test results on vanadium alloys irradiated in the ATR-A1 capsule. All tests were performed at a strain rate of $1.1x10^{-3}$ s^{-1}. The yield strength was determined at the lower yield point and the ultimate strength was measured at the upper yield point in all specimens.

Alloy, ID number	Irradiation conditions	Test temperature (°C)	Yield Strength (MPa)	Ultimate Strength (MPa)	Uniform Elongation (%)	Total Elongation (%)
V-3Cr-3Ti , XC08	3.0 dpa, 205°C	200	857	894	0.1	7.1
V-6Cr-3Ti , UC08	3.5 dpa, 230°C	200	863	906	0.15	7.0
V-6Cr-6Ti , ZC08	3.0 dpa, 205°C	200	943	957	0.3	7.3
V-3Cr-3Ti , XC06	4.5 dpa, 290°C	300	775	777	0.1	6.1
V-6Cr-3Ti , UC07	4.7 dpa, 295°C	300	882	897	0.1	5.7
V-6Cr-6Ti , ZC06	4.7 dpa, 295°C	300	869	876	0.2	8.2
V-6Cr-3Ti , UC06	4.7 dpa, 295°C	200	903	944	0.2	5.7

Table 3. Summary of tensile test results on vanadium alloys irradiated in BOR-60 ($1.1x10^{-3}$ s^{-1} strain rate). The yield strength was determined at the lower yield point and the ultimate strength was measured at the upper yield point in all base-metal specimens except XC01.

Alloy, ID number	Irradiation conditions	Test temperature (°C)	Yield Strength (MPa)	Ultimate Strength (MPa)	Uniform Elongation (%)	Total Elongation (%)
V-4Cr-4Ti (1000°C,2h), WE01	15 dpa, 316°C	320	949	979	0.1	5.1
V-4Cr-4Ti (1050°C,1h), WE21	19 dpa, 323°C	320	962	975	0.2	4.3
V-4Cr-4Ti-.1Si (T89), YC01	19 dpa, 323°C	320	977	993	0.15	5.7
V-6Cr-3Ti, UC01*	19 dpa, 323°C	320	960	980	0.1	6.0
V-3Cr-3Ti, XC01	20 dpa, 325°C	320	931	935	0.3	4.0
V-6Cr-6Ti, ZC01*	20 dpa, 325°C	320	940	942	0.2	5.4
V-4Cr-4Ti (GTA as-welded), WF08	18 dpa, 320°C	320	976	976	0.1	0.3
V-4Cr-4Ti (GTA+950°C,2h), WF01	18 dpa, 320°C	320	(882)	(882)	0.0	0.0
V-4Cr-4Ti (EB+950°C,2h), WF16	18 dpa, 320°C	320	(329)	(329)	0.0	0.0

*the UC and ZC specimens were mislabeled in earlier loading lists [8]; the UC tensile series is V-6Cr-3Ti (heat T-92) and the ZC series is V-6Cr-6Ti (heat T-90)

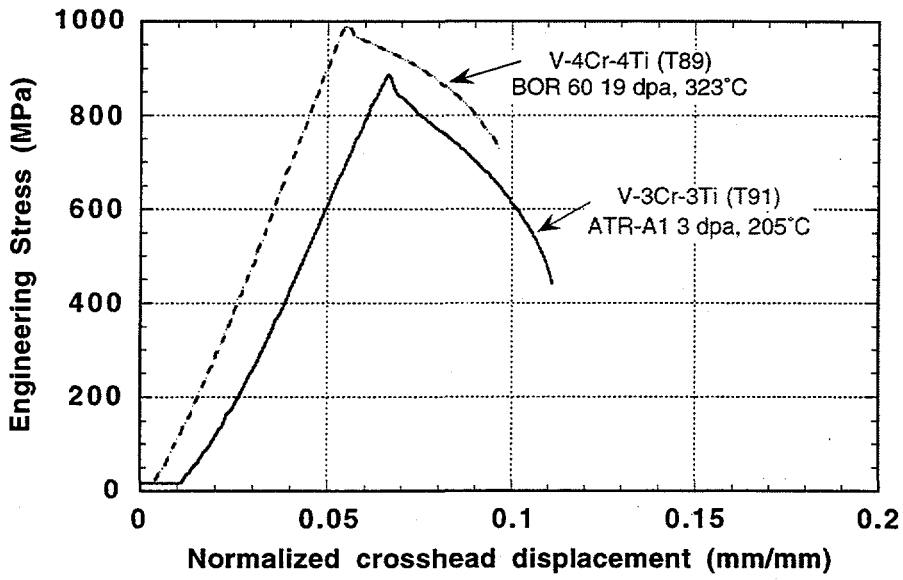

Fig. 1. Typical load-elongation tensile curves for V-Cr-Ti alloys irradiated in the ATR-A1 and BOR-60 Fusion 1 irradiation experiments. The tensile curves have been horizontally offset for clarity.

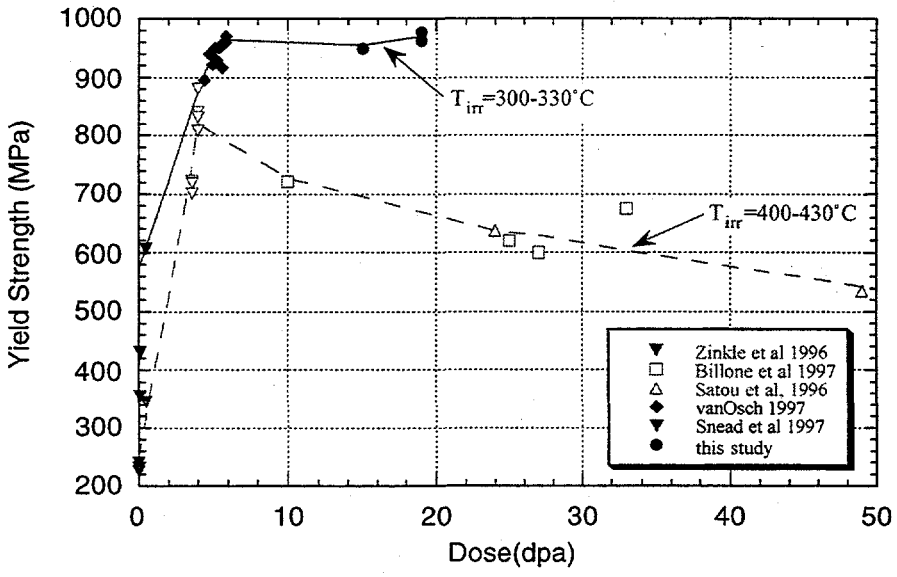

Fig. 2. Dose dependence of radiation hardening in V-(4-5%)Cr-(4-5%)Ti irradiated at low temperatures [1-3,10,11].

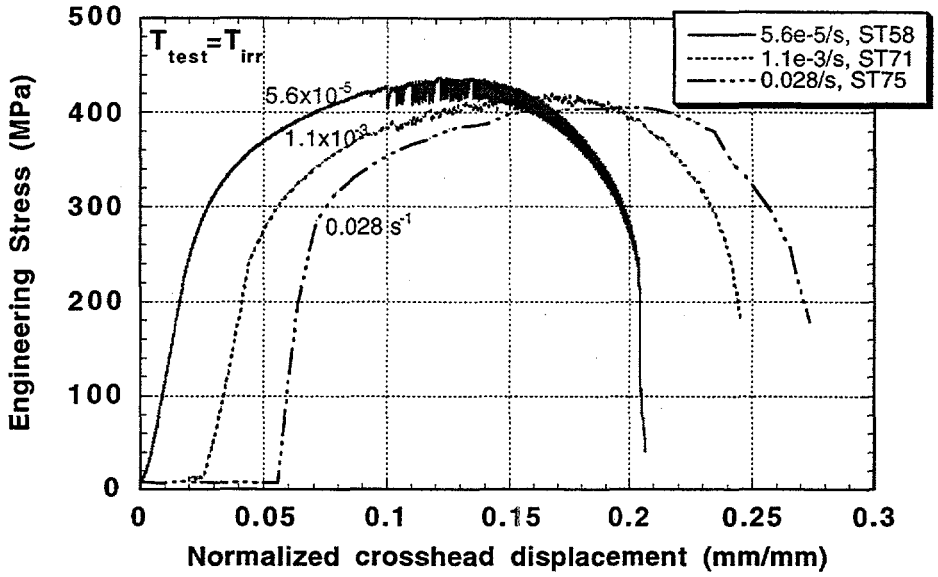

Fig. 3. Load-elongation curves for V-4Cr-4Ti tensile specimens irradiated in HFBR to 0.1 dpa at 504°C and tensile tested at 505°C. The tensile curves have been horizontally offset for clarity. The tensile data for specimen ST71 are tabulated elsewhere [2].

Somewhat lower yield strengths were reported by Kazakov and coworkers [4] for V-4Cr-4Ti irradiated to ~18 dpa at ~330°C in the same Fusion 1 capsule as the present BOR-60 specimens listed in Table 3. Since the total elongation was reported to be nearly zero (<1%, with brittle transgranular or mixed-mode fracture surfaces), the lower strength in their study may be attributable to embrittlement effects. Differences in the impurity content or differences in experimental technique (shoulder loaded Russian tests vs. pin-loaded ORNL tests, etc.) are possible explanations for the difference in tensile behavior. Recently reported tensile data on pin-loaded type SS-3 tensile specimens of V-4Cr-4Ti (heats 832665 and BL47) irradiated in the ATR-A1 capsule [6] are in agreement with the yield strength data shown in Fig. 2.

Serrations in the stress-strain tensile curves were only observed in specimens irradiated and tested at relatively high temperatures (>400°C). Figure 3 shows stress-strain curves for V-4Cr-4Ti irradiated to a dose of 0.1 dpa at 504°C in HFBR. The Portevin-Le Chatelier serrations fell below the general level of the stress-strain curve at the lowest strain rate (5.6×10^{-5} s^{-1}) investigated (Type C behavior [12]), whereas the serrations oscillated about the mean level of the stress-strain curve at higher strain rates (Type B behavior [12]). A similar transition from Type C to Type B serrations was observed in unirradiated V-4Cr-4Ti tested at 500°C at the same strain rates [12-14]. The amplitude of the oscillations decreased with increasing strain rate in both the unirradiated and irradiated specimens.

Previous work on unirradiated [12-14] and irradiated [14] V-4Cr-4Ti has found that the tensile strength increases with increasing strain rate at low temperatures and decreases with increasing strain rate at high temperatures (where dynamic strain aging is observed). The transition from a negative to a positive strain rate dependence occurs at 300°C in unirradiated V-4Cr-4Ti, with negative strain rate exponents observed at strain rates below 1×10^{-3} s^{-1} and positive strain rate exponents observed at strain rates above 1×10^{-3} s^{-1}. The measured value of the hardening strain rate exponent in the HFBR specimens irradiated to 0.1 dpa at 504°C (Fig. 3) is m=-0.010, where m is defined by [15]

$$m = \frac{1}{\sigma} \frac{\partial \sigma}{\partial \ln \dot{\varepsilon}} \qquad (1)$$

where σ is the stress and $\dot{\varepsilon}$ is the strain rate. This strain rate exponent is of slightly lower magnitude than that observed in unirradiated V-4Cr-4Ti specimens (m~-0.014 at 500°C). Previous work found that the strain rate exponent was reduced to m= -0.004 at 400°C following neutron irradiation to 4 dpa at 400°C, compared to the unirradiated value of m=-0.013 at 400°C [14]. The presence of a negative strain rate exponent is an indication of a significant interstitial solute concentration in the matrix which is free to migrate to dislocations during tensile testing. This implies that some of the C, O, N solute in the irradiated V-Cr-Ti alloys remains dissolved in the matrix and is not contained in titanium oxycarbonitride precipitates or solute-point defect clusters produced during irradiation [16], although the concentration of free interstitial solute is lower in irradiated specimens compared to unirradiated specimens. Since defect clusters introduce a weakly positive component to the strain rate exponent [17], the presence of defect clusters may be partially responsible for the reduced magnitude of the negative strain rate exponent in irradiated V-4Cr-4Ti specimens compared to unirradiated material. Interstitial solute bound to defect clusters or small precipitates would also decrease the magnitude of the irradiated strain rate exponent at 400-500°C compared to unirradiated values.

Table 4 summarizes the fracture toughness data obtained on V-4Cr-4Ti disk compact tension specimens irradiated in the ATR-A1 and BOR-60 Fusion 1 capsules. The result from an unirradiated BOR-60 control specimen is also included in Table 1 for purposes of comparison. Although the fracture toughness measured on the unirradiated control specimen does not meet the ASTM validity criteria, the high value is indicative of a high toughness. Similar high toughness values have been reported on larger unirradiated V-4Cr-4Ti specimens [18]. All of the irradiated specimens exhibited very low fracture toughness compared to unirradiated control specimens. Sample QA05 broke during preloading at an applied load of 14 pounds. The other two irradiated samples broke during the first three cycles of testing.

Table 4. Fracture toughness measured on irradiated and unirradiated disk compact tension specimens of V-4Cr-4Ti.

Sample ID	Irradiation conditions	Test temperature (°C)	K_J (MPa-$m^{1/2}$)
QA05 (ATR-A1)	190°C, 1.5 dpa	200	(~3)
QA01(ATR-A1)	250°C, 2.3 dpa	200	30
WC01(BOR-60)	316°C, 15 dpa	200	32
WC12	unirradiated	20	233

ACKNOWLEDGEMENTS

The authors thank H. Tsai (Argonne National Lab) for his assistance in the ATR and BOR-60 irradiations.

REFERENCES

1. S.J. Zinkle et al., in Fusion Materials Semiannual Progress Report for Period ending December 31, 1996, DOE/ER-0313/21 (Oak Ridge National Lab, 1996) p. 73.
2. L.L. Snead et al., in Fusion Materials Semiann. Prog. Report for period ending Dec. 31 1997, DOE/ER-0313/23 (Oak Ridge National Lab, 1997) p. 81.
3. E.V. van Osch, 8th Int. Conf. on Fusion Reactor Materials, Sendai, J. Nucl. Mater. (1997) submitted.
4. V.A. Kazakov, V.P. Chakin, Y.D. Goncharenko and Z.E. Ostrovsky, 8th Int. Conf. on Fusion Reactor Materials, Sendai, J. Nucl. Mater. (1997) submitted.
5. H.M. Chung and D.L. Smith, in Fusion Materials Semiann. Prog. Report for period ending June 30 1997, DOE/ER-0313/22 (Oak Ridge National Lab, 1997) p. 33.
6. H. Tsai et al., in Fusion Materials Semiann. Prog. Report for period ending Dec. 31 1997, DOE/ER-0313/23 (Oak Ridge National Lab, 1997) p. 70.
7. M.L. Grossbeck, in Fusion Materials Semiann. Prog. Report for period ending Dec. 31 1997, DOE/ER-0313/23 (Oak Ridge National Lab, 1997) p. 157.
8. A.F. Rowcliffe et al., in Fusion Materials Semiann. Prog. Report for period ending June 30 1997, DOE/ER-0313/22 (Oak Ridge National Lab, 1997) p. 284.
9. D.J. Alexander, in Small Specimen Test Techniques Applied to Nuclear Vessel Thermal Annealing and Plant Life Extension, ASTM STP 1204, eds. W.R. Corwin, F.M. Haggag and W.L. Server (American Society for Testing and Materials, Philadelphia, 1993) p. 130.
10. M.C. Billone, in Fusion Materials Semiann. Prog. Report for period ending Dec. 31 1997, DOE/ER-0313/23 (Oak Ridge National Lab, 1997) p. 3.
11. M. Satou et al., J. Nucl. Mater. 233-237 (1996) 447.
12. A.N. Gubbi, A.F. Rowcliffe, W.S. Eatherly and L.T. Gibson, in Fusion Materials Semiannual Progress Report for Period ending June 30, 1996, DOE/ER-0313/20 (Oak Ridge National Lab, 1996) p. 38.
13. A.N. Gubbi and A.F. Rowcliffe, presented at 8th Int. Conf. on Fusion Reactor Materials, Sendai, J. Nucl. Mater. (1997).
14. S.J. Zinkle, L.L. Snead, J.P. Robertson and A.F. Rowcliffe, in Fusion Materials Semiann. Prog Rep. for period ending Dec. 31 1997, DOE/ER-0313/23 (Oak Ridge National Lab, 1997) p. 77.
15. P. Haasen, Physical Metallurgy (Cambridge Univ. Press, New York, 1978) p. 26.
16. P.M. Rice and S.J. Zinkle, 8th Int. Conf. on Fusion Reactor Materials, Sendai, J. Nucl. Mater. (1998) in press.
17. T.J. Koppenaal and R.J. Arsenault, Metall. Reviews 16 (1971) 175.
18. H. Li, R.J. Kurtz and R.H. Jones, 8th Int. Conf. on Fusion Reactor Materials, Sendai, J. Nucl. Mater. (1998) in press.

MICROSTRUCTURAL EXAMINATION OF V-(3-6%)Cr-(3-5%)Ti IRRADIATED IN THE ATR-A1 EXPERIMENT - D. S. Gelles (Pacific Northwest National Laboratory)*

OBJECTIVE

The objective of this effort is to provide understanding of microstructural evolution in irradiated vanadium alloys for first wall applications in a fusion reactor.

SUMMARY

Microstructural examination results are reported for four heats of V-(3-6%)Cr-(3-5%)Ti irradiated in the ATR-A1 experiment to ~4 dpa at ~200 and 300°C to provide an understanding of the microstructural evolution that may be associated with degradation of mechanical properties. Fine precipitates were observed in high density intermixed with small defect clusters for all conditions examined following the irradiation. The irradiation-induced precipitation does not appear to be affected by preirradiation heat treatment or composition.

PROGRESS AND STATUS

Introduction

Vanadium-based alloys are being developed for application as a first wall material for magnetic fusion power system. It has been shown that alloys of composition V-(4-5%)Cr-(4-5%)Ti have very promising physical and mechanical properties.[1] Recent attention in this alloy class has focused on several issues, such as the effect of low-temperature irradiation on fracture toughness, the effect of helium generation, the effect of minor impurities, and heat-to-heat variation in work-hardening behavior at low irradiation temperatures. While other classes of alloys are still considered, the V-(4-5%)Cr-(4-5%)Ti alloys are being optimized to suppress their susceptibility to loss of work-hardening capability following irradiation at low temperatures by consideration of minor changes in major alloying levels. Susceptibility of the alloy class to this process under fusion-relevant conditions is considered to be a major factor in governing the minimum operating temperature of magnetic fusion devices.

Recent irradiation experiments at <430°C have shown that the loss of work-hardening capability and uniform elongation of V-4Cr-4Ti vary from heat to heat.[2] The present effort is a continuation of the effort to provide an understanding of the microstructural evolution in these alloys under irradiation with an expansion of the composition range to V-(3-6%)Cr-(3-5%)Ti by examination of specimens irradiated at low temperatures in the recent ATR-A1 experiment along with corresponding mechanical properties specimens.[3,4]

Experimental Procedure

Specimens in the form of microscopy disks 3 mm in diameter were included in the ATR-A1 test. Companion miniature tensile specimens were also irradiated providing the opportunity for comparison with shear punch and tensile response[4] at a later date. Twelve specimen conditions were selected for examination comprising four heats of material irradiated side-by-side at two

---

*Pacific Northwest National Laboratory (PNNL) is operated for the U.S. Department of Energy by Battelle Memorial Institute under contract DE-AC06-76RLO-1830.

irradiation temperatures with corresponding unirradiated control specimens. The compositions of the heats are given in Table 1[5,6] and the specimen conditions examined are shown in Table 2. Compositions covered the range V-(3-6%)Cr-(3-5%)Ti based on the availability of two heats recently prepared by ORNL.[3] All were heat treated at 1000°C for 1 or 2 h under vacuum (<10^{-7} torr) at ANL. Specimens were irradiated in ATR-A1 Subcapsules AS5 and AS11.[6] Temperatures and fluences have been estimated for these subcapsules as 284-300°C to 4.1 dpa and 223-234°C to 3.5 dpa, respectively,[5] but will be referred to as 300 and 200°C to 4 dpa in subsequent text. Specimen preparation and examination involved standard procedures. All images were computer processed and printed from scanned negative information.

Table 1. Compositions of heats examined

Heat #	Nominal Composition, wt%	Minor Impurities [appm]				
		O	N	C	Si	Other
832665, BL-71	V-3.8Cr-3.9Ti	310	85	80	783	220 Fe, 190 Al
T87, BL-72	V-5.0Cr-5.0Ti	380	90	110	550	
T91	V-2.84Cr-3.02Ti	230	62	120	940	130 Fe, 200 Al
T92	V-5.97Cr-2.94Ti	280	95	105	950	165 Fe, 255 Al

Table 2. Conditions of specimens examined by TEM

Specimen ID	Heat #	Heat treatment	Irradiation Temperature	Irradiation Dose
P8	832665, BL-71	1000°C/1h	na	0 dpa
P837			223-234°C	3.5 dpa
P811, P832			284-300°C	4.1 dpa
P7	T87, BL-72	1000°C/1h	na	0 dpa
P706			223-234°C	3.5 dpa
P710			284-300°C	4.1 dpa
P1	T91	1000°C/2h	na	0 dpa
P113			223-234°C	3.5 dpa
P107, P123			284-300°C	4.1 dpa
P2	T92	1000°C/2h	na	0 dpa
P224			223-234°C	3.5 dpa
P215			284-300°C	4.1 dpa

na: not applicable

Results

Pre-irradiation microstructures

The purpose of this work was to provide information on effects of radiation on microstructure in order to provide interpretation of mechanical properties response. As a result, emphasis was placed on examination of irradiated specimens. However, sufficient information was obtained to provide some comparison of the preirradiation microstructures for all four heats. All preirradiation microstructures appeared similarly, consisting, in general, of large equiaxed grains with large Ti,V(O,C,N) precipitate particles non-uniformly distributed. The particles observed were as large as 500 nm in heats 832665 and T87, but were generally 200-300 nm with many smaller particles. However, due to the non-uniform distribution, it is difficult to compare precipitate volume fraction from heat to heat based on electron microscopy. Grain boundaries were often distorted in the vicinity of such particles and many examples could be found where small grains were distributed amongst the larger grains, often where triple points would normally be found. In heats T87 and T92, areas were found where recrystallization had not occurred retaining a relaxed subgrain structure, but the volume fraction is expected to be low. This may be an indication that higher chromium contents discourage recrystallization.

Grain boundaries were often decorated with fine non-equiaxed precipitation on the order of 50 nm, but size and distributions varied from one grain boundary to another. Such precipitation is typically produced during cooling following the 1000°C annealing treatment.[8]

Microstructures following irradiation

The major effects of irradiation both at 200 and at 300°C were development of fine structure and evidence of increased internal strain based on lack of Kikuchi band structure. The fine structure was apparent under strain contrast conditions and can be expected to be the cause of the internal strain. Diffraction patterns showed little detail, but evidence for streaking at approximately ⅔<222>, found previously,[9] could be identified easily whereas streaking at ¾<200> was very faint and usually impossible to see. Images using ⅔<222> were very weak, but the scale of the structure matched that found in matrix dark field images approaching weak beam conditions. Therefore, it is apparent that precipitation due to ⅔<222> is responsible for the fine structure and internal strain observed.

Examples

Examples of these microstructures are provided in Figures 1, 2 and 3. Figure 1 shows two low magnification examples for each alloy of interest in the heat treated condition. In all cases, areas were selected to show grain boundary structure. Detailed inspection reveals fine precipitates on grain boundaries, with different size and spacial distributions on neighboring boundaries near triple points. Several examples are included where grain boundaries have been distorted due to associated large precipitate particles. Note that examples of smaller grains at triple points are shown in Figures 1a and 2h, and examples of unrecrystallized grain substructure can be found in Figures 2d and 2g, demonstrating further features of these microstructures prior to irradiation.

Figure 2 provides an example for each of the irradiated conditions at low magnification. The structures appear similar to those found in the unirradiated conditions except that fine precipitates on grain boundaries are no longer visible, and fine structure can be seen within grains. Large precipitate particles, present prior to irradiation, are retained.

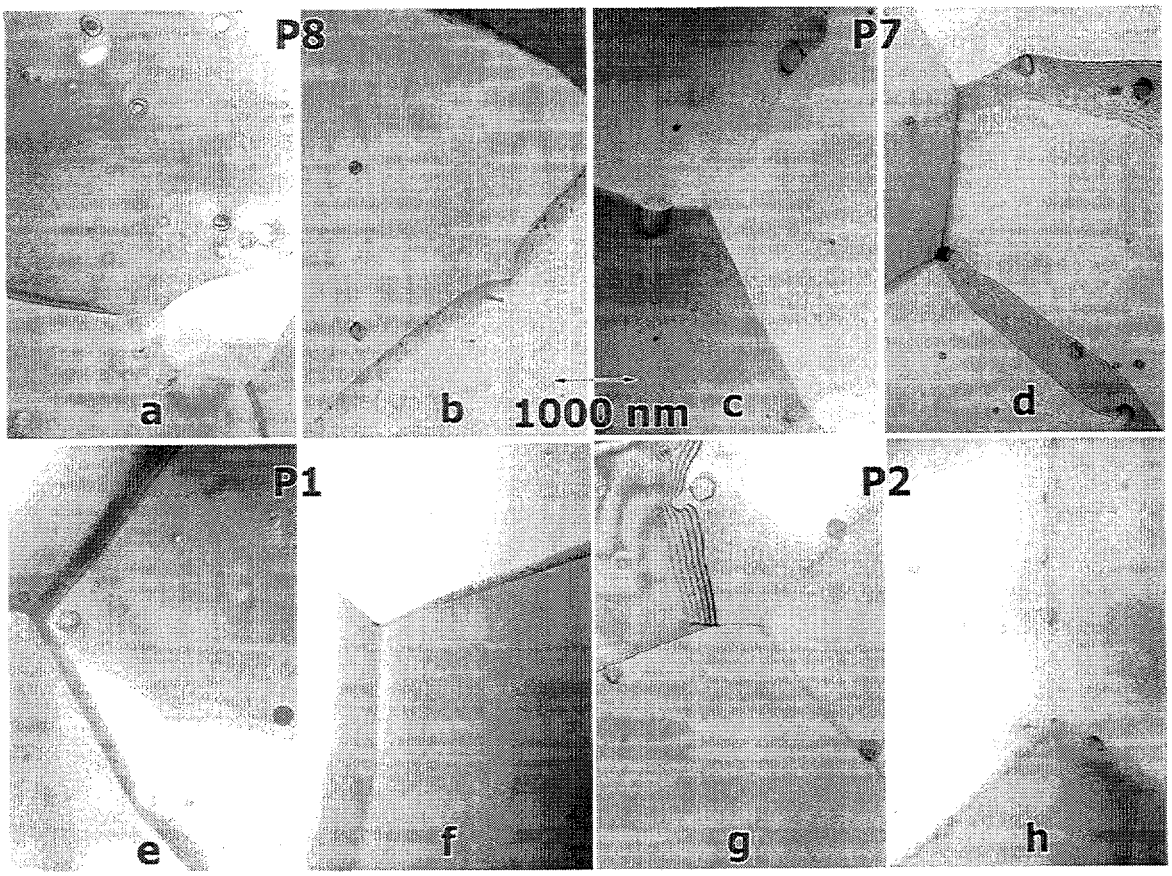

Figure 1. Low magnification examples of microstructures in specimens of V-(3-6%)Cr-(3-5%)Ti prior to irradiation showing the large heat 832665 in a and b, heat T87 in c and d, heat T91 in e and f, and heat T92 in g and h.

Figure 3 was prepared to show features of the fine structure within grains at higher magnification. For each irradiation condition, weak beam dark field images for the same area are shown using $\vec{g}$=[01$\bar{1}$] and [200], respectively, for foil conditions near (011) so that the corresponding $\vec{g}$ vectors are orthogonal with <200> horizontal. Where the information was available, the (011) pattern, with 000 on the lower left, has been inset. Also of note is that under the specimen identification code P224 a precipitate dark field image with $\vec{g}$= ~⅔[2$\bar{2}$2] has been inset. From this figure, the following can be demonstrated. Diffraction information only indicates the presence of intensity in the vicinity of ⅔<222>; intensity in the vicinity of ~¾<200> is very weak. Precipitate dark field images formed using $\vec{g}$=⅔<222> are very weak but indicate the presence of very small particles. Similar features can be seen in all weak beam images, indicating that the responsible precipitate particles provide strain fields visible under strain contrast conditions (or that matrix [200] and [011] reflections superimpose on precipitate reflections.) Comparison of [200] and [011] images consistently shows fine structure in both, but coarser structure as well in the [200] images. Figure 3f in particular can be interpreted to indicate the presence of dislocation loops approximately 20 nm in diameter. Therefore, the dislocation density is likely to be significantly lower than the precipitate particle density.

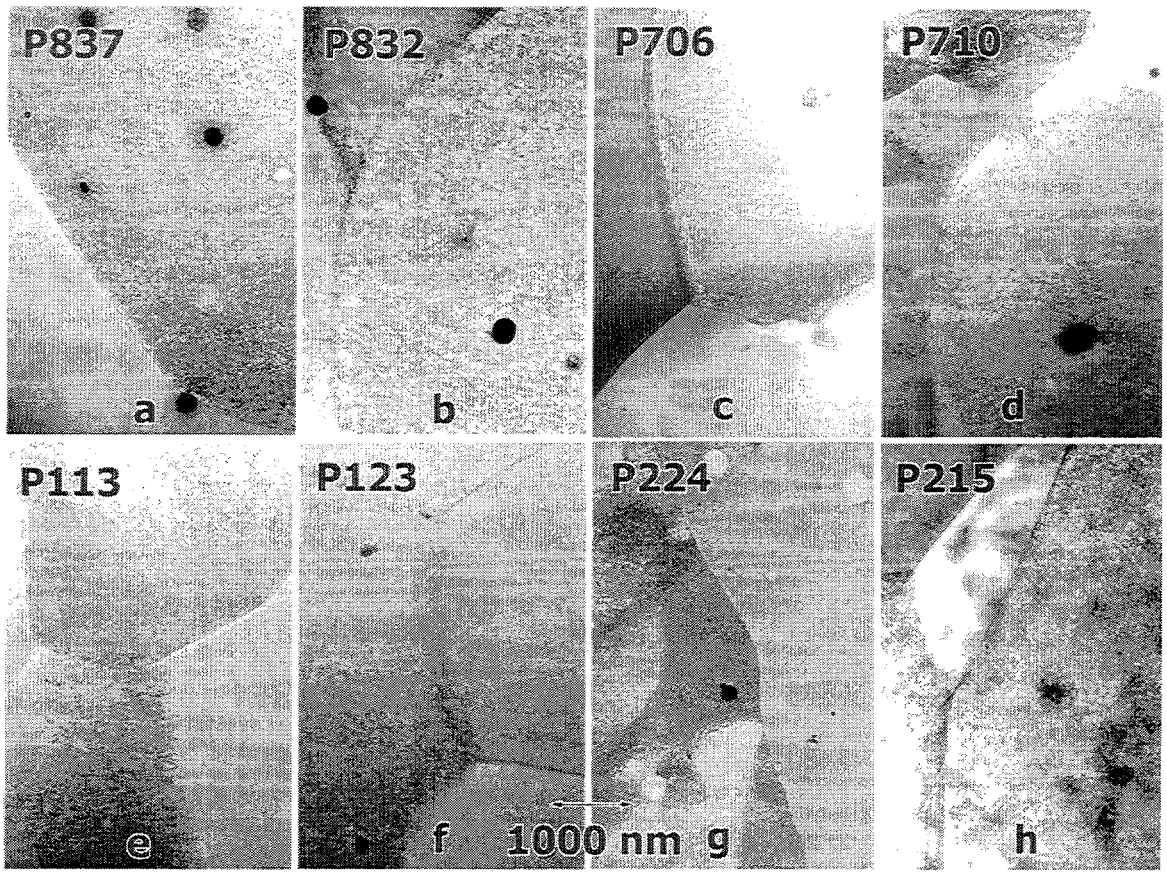

Figure 2. Low magnification examples of irradiated microstructures in specimens of V-(3-6%)Cr-(3-5%)Ti irradiated in the ATR-A1 experiment showing the large heat 832665 at 200 and 300°C in a and b, heat T87 at 200 and 300°C in c and d, heat T91 at 200 and 300°C in e and f, and heat T92 at 200 and 300°C in g and h.

Quantification of precipitation

As all weak beam images presented in Figure 3 were taken with matching stereo pairs, it is possible to quantify the precipitate features in order to estimate the consequences of such features on mechanical properties. Table 3 provides results from measurements of the fine structure observed on <011> images, assuming the particles are spherical. Based on examination of stereo information in thin areas, it can be noted that the precipitates are non-uniformly distributed. Precipitation is in patches, with areas of similar size separating the patches. The results in Table 3 indicate that precipitates are between 3 and 4 nm in average diameter at number densities between 1 and 3 $x10^{17}$ cm^{-3} corresponding to volume fractions on the order of 0.5%. Surprisingly, the observed response appears to be insensitive to irradiation temperature.

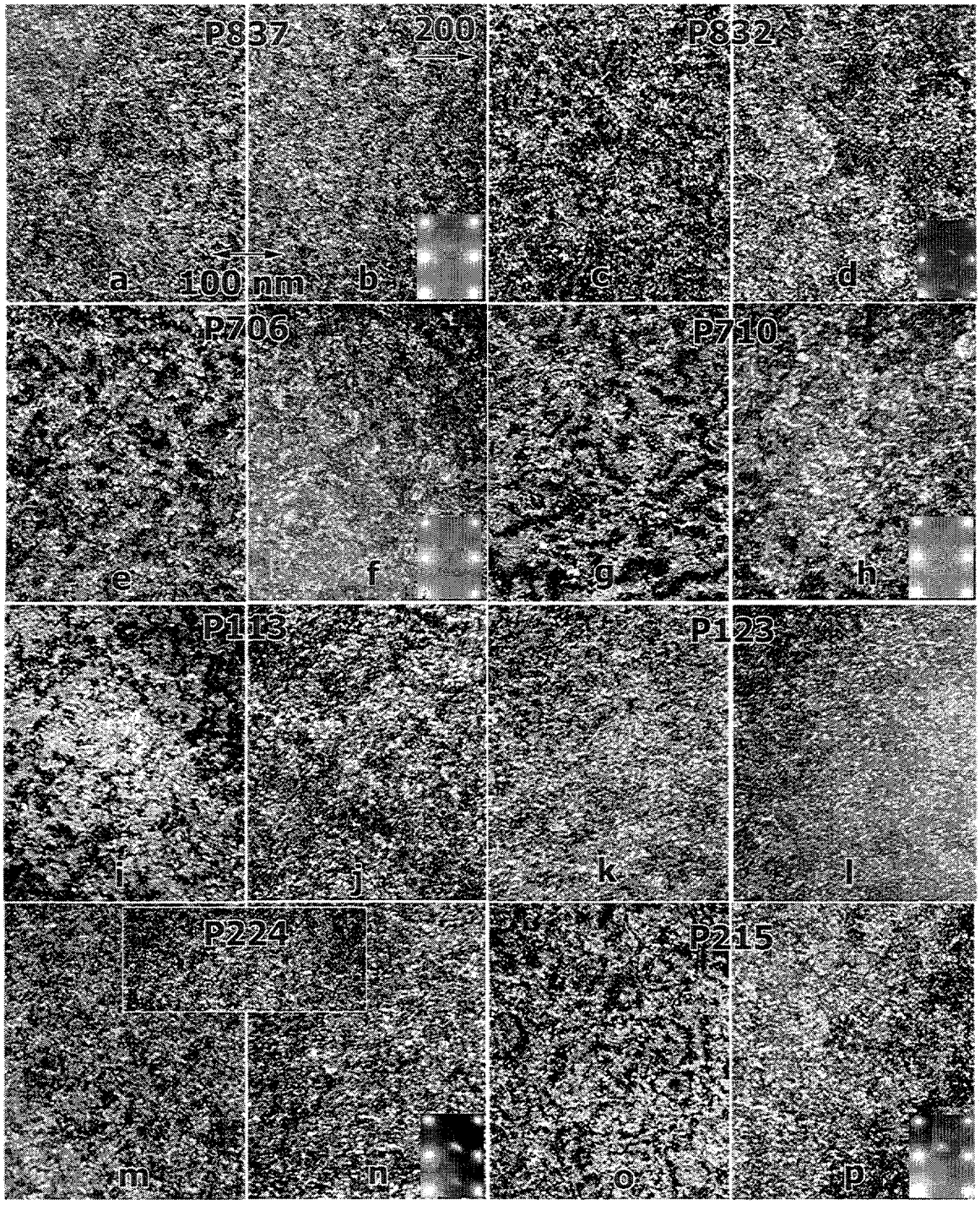

Figure 3. Dark field images using $\vec{g}$=[01$\bar{1}$] and [200], respectively, of irradiated microstructures in specimens of V-(3-6%)Cr-(3-5%)Ti from the ATR-A1 experiment showing the large heat 832665 at 200°C in a and b and at 300°C in c and d, heat T87 at 200°C in e and f and 300°C in g and h, heat T91 at 200°C in i and j and at 300°C in k and l, and heat T92 at 200°C in m and n and at 300°C in o and p. Where available, (011) diffraction patterns have been inserted and P224 contains an insert showing precipitate dark field contrast.

Discussion

The purpose of this work is to provide microstructural information allowing interpretation of test results for mechanical properties measurements including those on miniature tensile specimens and disks tested by shear punch procedures.[3,4] Results are not yet available, but preliminary results[10] indicate that all materials showed large degradation in properties following irradiation.

Based on the present and previous microstructural observations,[9] mechanical property degradation appears to be due to precipitation during irradiation. Unfortunately, the composition of the precipitate has not yet been established, so that it is not yet possible to provide recommendations for composition modifications for improved properties. However, recent results[11,12] indicate that precipitation of interstitial elements with titanium is likely responsible. This discussion is provided as further speculation on the likely causes for the behavior observed.

Table 3. Irradiation induced precipitate size and density as determined from weak beam images

Specimen ID	Conditions: Heat/dose/temp.	Mean diameter (nm)	Number density (10^{17} cm^{-3})	Volume fraction (%)
P837	BL-71/4 dpa/200°C	3.29	3.2	0.6
P832	BL-71/4 dpa/300°C	3.46	2.5	0.6
P706	T87/4 dpa/200°C	3.89	1.6	0.6
P710	T87/4 dpa/300°C	3.64	1.6	0.5
P113	T91/4 dpa/200°C	3.83	1.8	0.6
P123	T91/4 dpa/300°C	3.01	1.1	0.2
P224	T92/4 dpa/200°C	3.89	1.6	0.5
P215	T92/4 dpa/300°C	3.80	2.0	0.7

It is noteworthy that diffraction response for precipitates formed during irradiation is found to vary with irradiation temperature. Following irradiation at 400°C to 4.5 dpa in HFIR, streaks were found both at ¾<200> and ⅔<222>, whereas the present results following irradiation at 200 and 300°C to 4 dpa show streaks only at ⅔<222>. Therefore, two types of precipitation formed at 400°C, but at lower temperatures, one of those precipitates is not found, at least following irradiation to doses on the order of 4 dpa.

The precipitation identified following irradiation in the ATR-A1 experiment at 200 and 300°C is found to consist of particles on the order of 3 nm in diameter at densities in the range 1 to 3 $x10^{17}$ cm^{-3} corresponding to volume fractions on the order of 0.5%. As the precipitates are best imaged using strain contrast, it is likely that strain centers of this size and density would have a major effect on hardening and embrittlement. It is not yet understood why precipitation is similar in size following irradiation at both 200 and 300°C. Nor is it understood why number densities are found to vary as a function of composition such that heat 832665 gave higher densities by about a factor of two. Given the very small sizes of the precipitates, perhaps the best explanation lies in experimental uncertainty. Errors on the order of a factor of 2 are not unreasonable with such fine microstructures.

CONCLUSIONS

Eight specimen conditions from the ATR-A1 experiment irradiated at ~200 and 300°C to ~4 dpa, comprising four heats of V-(3-6%)Cr-(3-5%)Ti given similar preirradiation heat treatments and directly corresponding to mechanical properties specimens, have been examined to identify the cause of irradiation hardening. It is found that hardening is due to precipitation of a high density of small particles, but differs from response at 400°C, because one precipitate type dominates at the lower irradiation temperatures. Particle sizes are on the order of 3 nm in diameter at densities in the range 1 to 3 $x10^{17}$ cm^{-3} corresponding to volume fractions on the order of 0.5%. The irradiation-induced precipitation appears to be insensitive (to within a factor of ~2) to preirradiation heat treatment and composition.

FUTURE WORK

This work will be continued within the confines of funding and specimen availability.

REFERENCES

1. B. A. Loomis, A. B. Hull, and D. L. Smith, J. Nucl. Mater., 179-181 (1992) 148.

2. S. J. Zinkle, D. J. Alexander, J. P. Robinson, L. L. Snead, A. F. Rowcliffe, L. T. Gibson, W. S. Eatherly and H. Tsai, DOE/ER-0313/21, 73.

3. To be reported by S. J. Zinkle, etal, ORNL.

4. To be reported by M. L. Hamilton, etal, PNNL.

5. H. Tsai, L. J. Nowicki, M. C. Billone, H. M. Chung and D. L. Smith, DOE/ER-0313/23, 70.

6. M. L. Grossbeck, DOE/ER-0313/23, 157.

7. H. Tsai, R. V. Strain, I. Gomes, and D. L. Smith, DOE/ER-0313/22, 303.

8. D. S. Gelles and H. Li, DOE/ER-0313/19, 22.

9. D. S. Gelles and H. M. Chung DOE/ER-0313/22, 39.

10. S. J. Zinkle, ORNL, private communication.

11. D. S. Gelles, P. M. Rice, S. J. Zinkle and H. M. Chung, to be published in J. Nucl. Mater. as part of the proceedings of ICFRM-8.

12. S. J. Zinkle, A. F. Rowcliffe, L. L. Snead, and D. J. Alexander, "Physical Metallurgy of Vanadium Alloys," presented at the 19th ASTM Symposium on Effects of Radiation on Materials held 16-18 June 1998 in Seattle, WA.

IRRADIATION-INDUCED PRECIPITATION AND MECHANICAL PROPERTIES OF VANADIUM ALLOYS AT <430°C, H. M. Chung, J. Gazda, and D. L. Smith (Argonne National Laboratory)

OBJECTIVE

The objective of this study is to identify dense irradiation-induced precipitation of very fine particles that causes severe dislocation channeling and poor work-hardening capability in V-4Cr-4Ti at <430°C.

ABSTRACT

Recent attention to V-base alloys has focused on the effect of low-temperature (<430°C) irradiation on tensile and impact properties of V-4Cr-4Ti. In previous studies, dislocation channeling, which causes flow localization and severe loss of work-hardening capability, has been attributed to dense, irradiation-induced precipitation of very fine particles. However, efforts to identify the precipitates were unsuccessful until now. In this study, analysis by transmission electron microscopy (TEM) was conducted on unalloyed V, V-5Ti, V-3Ti-1Si, and V-4Cr-4Ti specimens that were irradiated at <430°C in conventional and dynamic helium charging experiments. By means of dark-field imaging and selected-area-diffraction analysis, the characteristic precipitates were identified to be $(V,Ti_{1-x})(C,O,N)$. Evidence indicates that severe dislocation channeling and poor work-hardening capability in V-4Cr-4Ti occur at <430°C as a result of dense precipitation of $(V,Ti_{1-x})(C,O,N)$. In V-3Ti-1Si, precipitation of $(V,Ti_{1-x})(C,O,N)$ was negligible at <430°C, and as a result, dislocation channeling did not occur and work-hardening capability was high.

INTRODUCTION

Recently, attention to vanadium alloy development for fusion reactor application has focused on the performance of V-(4-5)Cr-(4-5)Ti after low-temperature irradiation; tensile[1-7] and impact[4,6,7] properties after irradiation at <430°C have been of special interests. It has been reported that a 500-kg heat (832665) and a 30-kg heat BL-47 of V-4Cr-4Ti and a 80-kg heat BL-63 of V-5Cr-5Ti exhibited low uniform elongation as a result of virtual loss of work-hardening capability after irradiation at 80-430°C in several fission-reactor experiments, i.e., in HFBR,[1] HFIR,[2,3] EBR-II X530,[4,5] ATR,[6] FFTF MOTA,[7] and FFTF COBRA-1A2[7] experiments. In contrast to the tensile behavior at <430°C, V-Cr-Ti, V-Ti, and V-Ti-Si alloys exhibited generally good work-hardening capability after irradiation at ≥500°C.[8] The 500-kg heat of V-4Cr-4Ti also exhibited poor impact properties after irradiation at ≤390°C.[4,6,7] This was surprising, in view of a previous report that the 30-kg heat of V-4Cr-4Ti exhibited good impact properties after irradiation at ≥430°C in the FFTF,[9] and that the 500-kg heat exhibited excellent impact properties in the nonirradiated state.[8] In subsequent studies of the tensile behavior of the 500-kg heat, the poor work-hardening capability was found to be due to dislocation channeling that occurred extensively in the alloy after irradiation at ≤390°C.[10-12] Furthermore in these studies, severe dislocation channeling was attributed to dense precipitation of very fine particles (<10 nm in size) during irradiation at the low temperatures.[10-12] Therefore, identification of the irradiation-induced precipitates and understanding the mechanism of dislocation channeling have been of major importance in understanding the irradiation performance of V alloys at <430°C. However, initial efforts to gain information on the composition of the very fine precipitates by electron energy loss spectroscopy were inconclusive.[11,12]

In this work, TEM selected-area-diffraction (SAD) analysis and dark-field imaging techniques were utilized to identify the very fine irradiation-induced precipitates in the 500-kg heat of V-4Cr-4Ti that was irradiated in an Li environment in the EBR-II at ≈390°C, and in laboratory heats of V, V-5Ti, V-3Ti-1Si, and V-4Cr-4Ti (BL-47) that were irradiated at ≈420-600°C in the dynamic helium charging experiment (DHCE) in the FFTF.[8,13] In contrast to the poor work-hardening capability of the large-scale and laboratory heats of V-4Cr-4Ti irradiated in the conventional irradiation experiments (i.e., non-DHCE) at ≈390 and ≈430°C, respectively, work-

hardening capabilities of the laboratory heats of V-4Cr-4Ti and V-3Ti-1Si were significantly higher after irradiation in the DHCE at ≈430°C. This variation in work-hardening capability is manifested by significant variation in uniform elongation as shown in Fig. 1.[7] Therefore, of particular interest in this study was not only identification of the irradiation-induced precipitates but also relationship among degree of precipitation, dislocation channeling, and work-hardening capability of several alloys that were irradiated at <430°C.

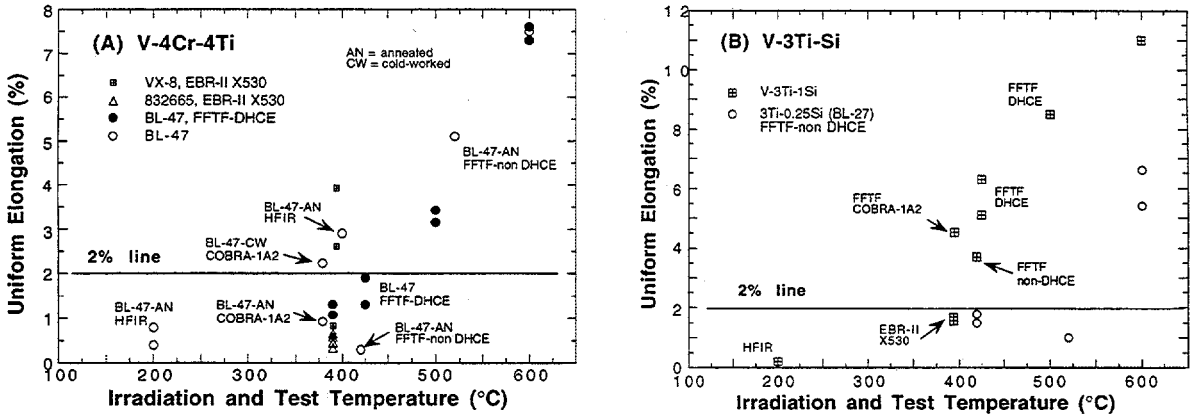

Fig. 1. Uniform elongation as a function of irradiation temperature (same as test temperature) of V-4Cr-4Ti (A) and V-3Ti-Si (B), showing significant variation in work-hardening capability, depending on heat and irradiation condition.

EXPERIMENTAL PROCEDURES

The elemental composition of the alloys investigated in this study, determined prior to irradiation, is given in Table 1. TEM analysis was not conducted on Heat VX-8 (V-3.7Cr-3.9Ti; O, 350 wppm; N, 70; C, 300; Si, 500; Nb, 1280; Al, 1120; Co, 500; Fe, 280; Mo, 270; and Zr, 19 wppm) and Heat BL-27 (V-3.1Ti-0.25Si; O, 210; N, 310; and C, 310 wppm), although uniform elongation of the heats was relatively high, as shown in Fig. 1. Details of conventional and DHCE irradiation experiments, in which TEM disks and tensile specimens of these alloys were irradiated, are summarized in Table 2. TEM disks and tensile specimens were machined out of cold-worked sheets ≈0.3 and ≈1 mm thick, respectively, followed by annealing at 1050–1125°C for 1 h in ion-pumped vacuum. The irradiated specimens were then retrieved from the irradiation capsules, and Li that was bonded onto the specimens was cleaned off in a bath of liquid ammonia. Then, the specimens were further cleaned ultrasonically in a bath of ethyl alcohol. TEM disks were also prepared out of the gage area of broken tensile specimens. All TEM disks were jet-thinned at -10°C in a solution of 15% sulfuric acid, 72% methanol, and 13% butyl cellulose. TEM was conducted with a JEOL 100CX-II scanning transmission electron microscope (100 keV) or with a Philips CM-30 analytical electron microscope (300 keV).

Table 1. Chemical composition of vanadium alloys

	Nominal Comp.	Impurity Concentration (wt. ppm)			
Heat ID	(wt.%)	O	N	C	Si
BL-19[a]	V	1101	161	360	–
BL-46[a]	4.6Ti	305	53	85	160
BL-45[a]	2.5Ti-1Si	345	125	90	9900
BL-47[b]	4.1Cr-4.3Ti	350	220	200	870
832665[c]	3.8Cr-3.9Ti	310	85	80	783

[a]15-kg laboratory heat
[b]30-kg laboratory heat
[c]500-kg production-scale heat

RESULTS

A typical bright-field image of dislocation channels, shown in Fig. 2, was obtained from the 500-kg Heat 832665 of V-4Cr-4Ti that was irradiated to ≈4 dpa and tensile-tested at 390°C. Several SAD patterns were obtained from the precipitate-rich regions, such as those in Fig. 2, in one orientation, e.g., (110) zone of the matrix. Using reflections from the precipitates, we obtained many dark-field images in this orientation . Then, the specimen was tilted to several

Table 2. Summary of conditions under which TEM disks and tensile specimens were irradiated

Alloy Type	Alloy Heat	Irradiation	Environment	Temperature (°C)	dpa
V-4Cr-4Ti	832665	EBR-II X530	Li	≈390	4
V	BL-19	FFTF-DHCE	Li	430-600	13-27
V-5Ti	BL-46	FFTF-DHCE	Li	430-600	13-27
V-3Ti-1Si	BL-45	FFTF-DHCE	Li	430-600	13-27
V-4Cr-4Ti	BL-47	FFTF-DHCE	Li	430-600	13-27

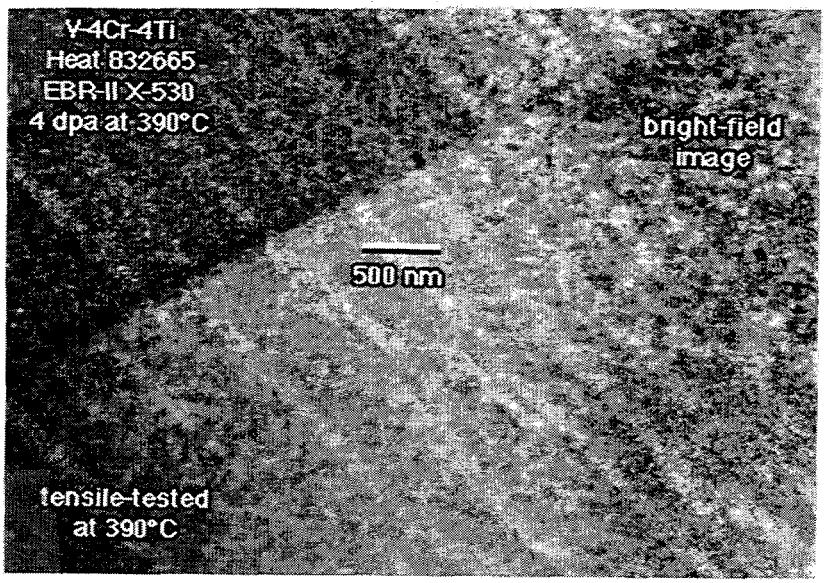

Fig. 2.

Bright–field image of dislocation channels in 500–kg V-4Cr-4Ti Heat 832665 tensile specimen irradiated to ≈4 dpa at 390°C in EBR-II X530 experiment and tensile–tested at 390°C

other orientations, e.g., (100), (120), and (310) zones of the matrix, and more SAD patterns and dark-field images of the precipitates were obtained at the new orientation. Because Heat 832665 V-4Cr-4Ti specimens that were irradiated at ≈390°C in the EBR-II X530 experiment contained a significantly high volume fraction of the precipitates,[11] dark-field images of the unknown precipitates could be obtained without much difficulty. Typical examples of SAD patterns are shown in Figs. 3-5, which correspond, respectively, to the (110), (310), and (320) zones of the matrix. For most SAD patterns, many double- diffraction spots are present, and, at the same time, precipitate reflections are superimposed on most matrix reflections. As a result, "pure" matrix reflections were difficult to find. Because of these two factors, significant difficulty was commonly encountered in isolating and identifying the operating precipitate zone in a given SAD pattern.

A typical example of a dark-field image of the precipitates, observed in a TEM disk of the 500-kg V-4Cr-4Ti heat after irradiation to ≈4 dpa at ≈390°C in the EBR-II, is given in Fig. 6. Very fine (size 3-10 nm), dense precipitates are visible; number density and volume fraction of precipitates in the figure correspond to ≈3.5 x 10^{17} cm^{-3} and ≈1.2%, respectively.

The SAD pattern in Fig. 3 shows numerous double-diffraction spots and precipitate reflections that correspond to the (111) zone of an fcc structure that is parallel to the (110) zone of the bcc matrix. Exactly the same orientational relationship was observed for relatively larger

precipitates in unalloyed V (BL-19) irradiated in the FFTF-DHCE to ≈18 dpa at 600°C (see the SAD pattern and dark-field image in Fig. 7). Furthermore, the lattice spacing of the fcc structure measured from the (111) zones of the SAD patterns in Figs. 2 (V-4Cr-4Ti, 832665) and 7 (unalloyed V, BL-19) was identical, i.e., $a_0 \approx 0.415–0.420$ nm. This finding shows that the same type of precipitation occurred in unalloyed V and V-4Cr-4Ti, although irradiation conditions and the size and density of the precipitates differed significantly.

The type of fcc precipitates that exhibited exactly the same diffraction characteristics and orientational relationship as those of the very fine precipitates, produced at ≈390°C in EBR-II, were observed in other alloys that were irradiated in the FFTF-DHCE, i.e., V-5Ti (BL-46) (Fig. 8), 30-kg V-4Cr-4Ti (BL-47) (Fig. 9), and V-3Ti-1Si (BL-45) (Fig. 10). For the orientation shown in Fig. 8, i.e., the (100) zone of the precipitate parallel to the (100) zone of the matrix, all precipitate reflections are hidden behind the matrix reflections. Therefore, the presence of

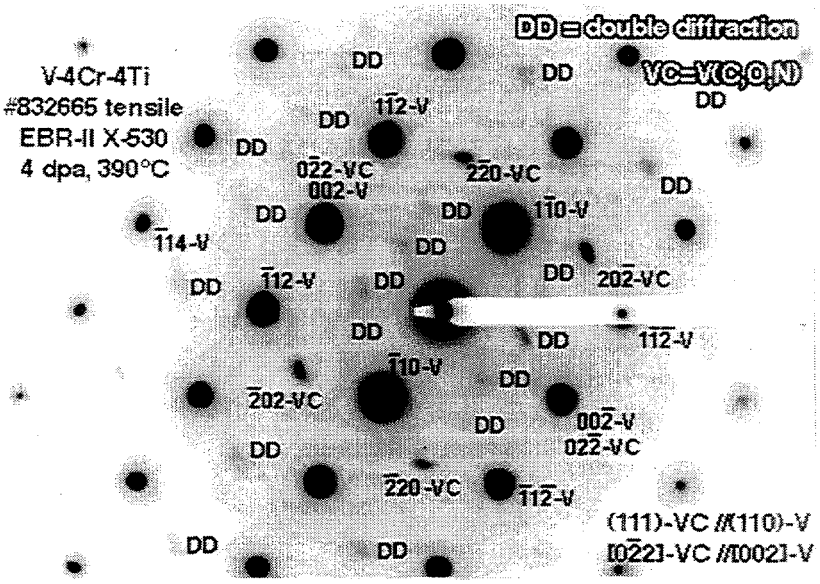

Fig. 3.

SAD pattern from V-4Cr-4Ti Heat 832665 TEM disk irradiated to ≈4 dpa at 390°C in EBR-II X530, showing (111) zone of $(V,Ti_{1-x})(C,O,N)$ precipitates parallel to (110) zone of matrix. Letters V, VC, and DD denote, respectively, matrix, $(V,Ti_{1-x})(C,O,N)$, and double diffraction spots.

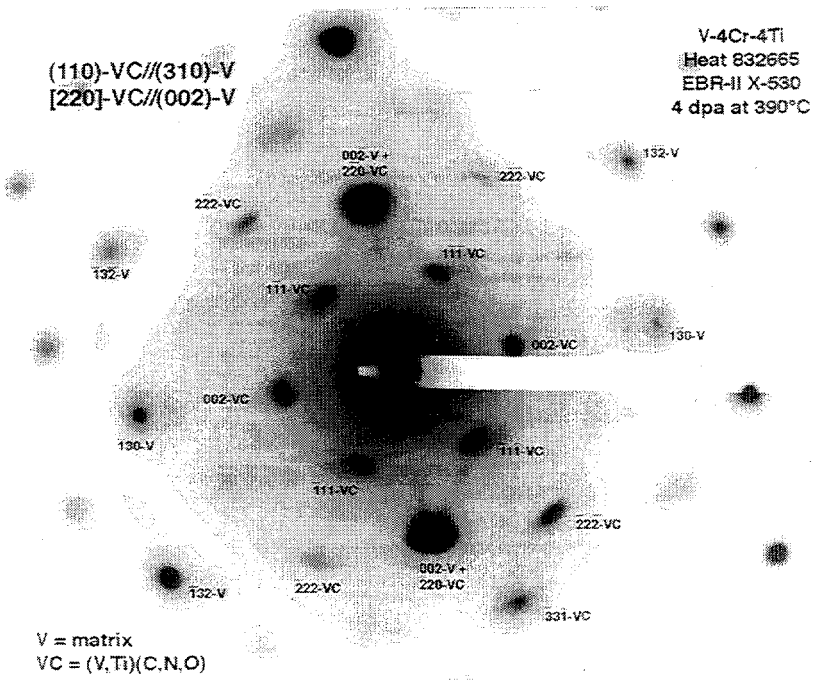

Fig. 4.

SAD pattern from V-4Cr-4Ti Heat 832665 TEM disk irradiated to ≈4 dpa at 390°C in EBR-II X530, showing (110) zone of $(V,Ti_{1-x})(C,O,N)$ precipitates nearly parallel to (310) zone of matrix. Letters V, VC, and DD denote, respectively, matrix, $(V,Ti_{1-x})(C,O,N)$, and double diffraction

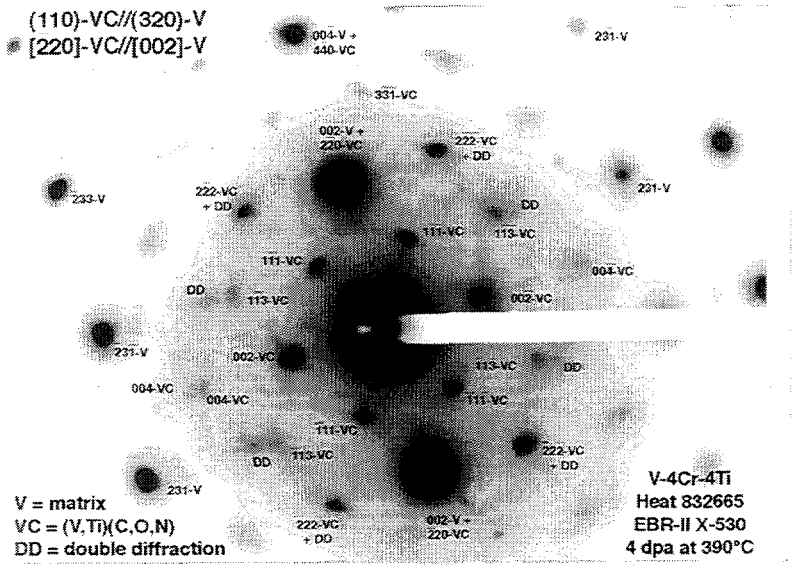

Fig. 5.

SAD pattern from V-4Cr-4Ti Heat 832665 TEM disk irradiated to ≈4 dpa at 390°C in EBR-II X530, showing (110) zone of $(V,Ti_{1-x})(C,O,N)$ precipitates nearly parallel to (320) zone of matrix. Letters V, VC, and DD denote, respectively, matrix, $(V,Ti_{1-x})(C,O,N)$, and double diffraction.

irradiation-induced precipitates is indicated only by the streaks, and dark-field images could be obtained only with the streaks that are visible near the matrix reflections. Such streaks are absent in the (100) zone of V-3Ti-1Si irradiated in the FFTF-DHCE to ≈27 dpa at ≈430°C (Fig. 10), indicating that precipitation in this alloy was insignificant under the irradiation conditions.

Initially, it was suspected that the characteristic precipitates could be either irradiation-enhanced precipitates of α-Ti (hcp, a_0 = 0.29504 nm, c_0 = 0.46833 nm), Ti_2O (hcp, a_0 = 0.2959 nm, c_0 = 0.4845 nm), Ti_3O (hcp, a_0 = 0.4991 nm, c_0 = 0.2879 nm), or metastable ω-phase (hcp, a_0 = 0.4573-0.4598 nm, c_0 = 0.2804-0.2818 nm). A Ti-rich Ti-V phase has been observed in Ti-V alloys by several investigators.[14,15] However, the diffraction behavior, such as that manifested in the SAD patterns in Figs. 2-4 and 6-9, was not consistent with any of these systems. Of particular importance is fact that the characteristic precipitates that exhibit the same diffraction behavior were also observed in unalloyed vanadium (BL-19, Fig. 6). Therefore, we searched for an fcc compound based on V.

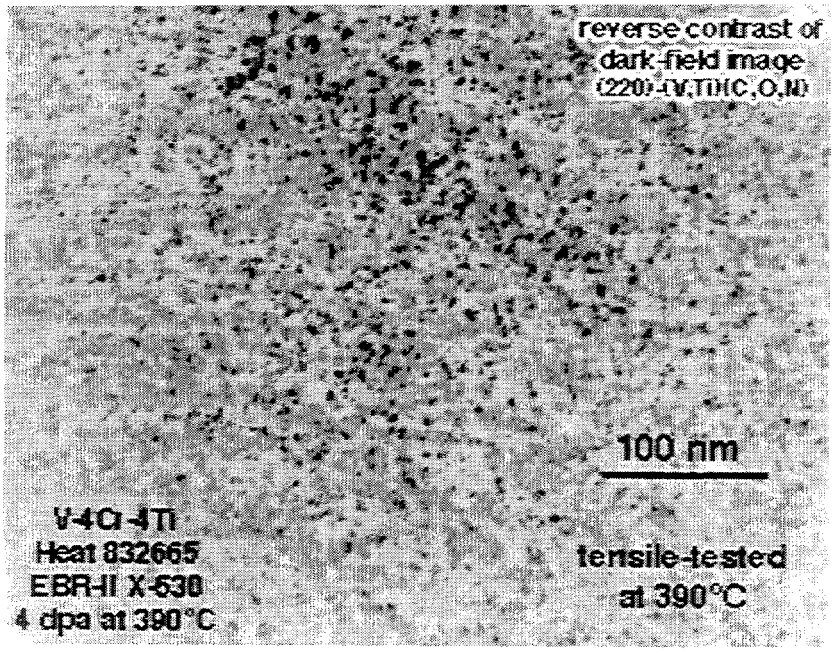

Fig. 6.

Reverse-contrast dark-field image of $(V,Ti_{1-x})(C,O,N)$ precipitates in V-4Cr-4Ti Heat 832665 TEM disk irradiated to ≈4 dpa at 390°C in EBR-II X530 experiment.

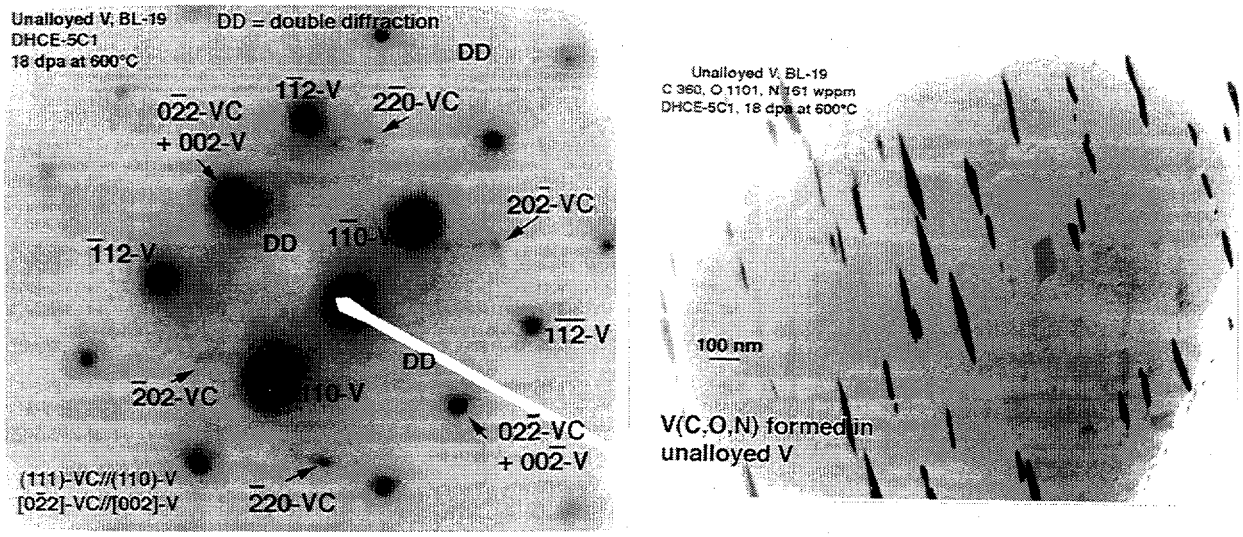

Fig. 7. SAD pattern (left) and reverse-contrast dark-field image (right) of V(C,O,N) precipitates observed in unalloyed V Heat BL-19 TEM disk irradiated to ≈18 dpa at 600°C in FFTF-DHCE, showing (111) zone of precipitate parallel to (110) zone of matrix. Letters V, VC, and DD denote, respectively, matrix, V(C,O,N), and double diffraction spots.

The SAD patterns shown in Figs. 3-5 and 7-10 could be indexed precisely only on the basis of the structure of VC, an fcc compound with a lattice constant of a_o = 0.4168-0.4169 nm.[16,17] Meanwhile, VO (fcc, a_o = 0.409 nm) and VN (fcc, a_o = 0.413 nm) are isostructural with VC, and lattice constants of the three phases are similar.[16,17] Considering this and the fact that the three compounds are mutually soluble, we conclude that the precipitates are V(C,O,N), an fcc (NaCl) structure (space group Fm3m) with a lattice constant a_o = 0.415-0.420 nm.

This measured lattice spacing is ≈1.5-2.0% smaller than the lattice spacings reported for TiC (fcc, a_o = 0.4313-0.4330 nm), TiO (fcc, a_o = 0.422-0.425 nm), or TiN (fcc, a_o = 0.4182-0.4243 nm).[16,17] However, this small difference in lattice spacing cannot be discerned conclusively from TEM SAD patterns. Therefore, based on measured lattice spacing alone, it is not possible to conclude whether the precipitates are V- or Ti-based precipitates, i.e., V(C,O,N) or Ti(C,O,N). However, the fact that the characteristics precipitates were observed in unalloyed V (BL-19, Fig. 7) provides conclusive evidence that they are of the V(C,O,N) type. This is supported further by the following observations.

The diffraction characteristics and morphology of the precipitates that formed at higher irradiation temperatures, such as those shown in Figs. 7 (unalloyed V at 600°C), 8 (V-5Ti at 600°C), and 10 (V-3Ti-1Si at 500°C), are essentially the same as the $(V_{0.75}Ti_{0.25})$(C,O,N) precipitates that were observed in laser and electron-beam welds of V-4Cr-4Ti Heat 832665 after postwelding annealing at 1000°C for 1 h.[18] Kazakov et al. reported that carbides of V (VC or V_2C) were observed in the fusion and heat-affected zones of gas-tungsten-arc welds of V-2.5Zr-0.35C.[19] The morphology of these carbides is essentially the same as that of V(C,O,N) precipitates observed in V, V-5Ti, and V-3Ti-1Si in this study and in the laser and electron-beam welds of Ref. 18. The morphology of V carbides observed by Kazakov et al. in the V-2.5Zr-0.35C welds was in distinct contrast to the spherical morphology of ZrC, which was observed only in the fusion zone of the alloy. Hence, we believe that the irradiation-induced precipitates observed in this study have essentially the fcc (NaCl) structure of VC that is modified in elemental composition; namely, O, and to a lesser extent, N atoms replacing some C atoms and Ti replacing some V in the Ti-containing V alloys.

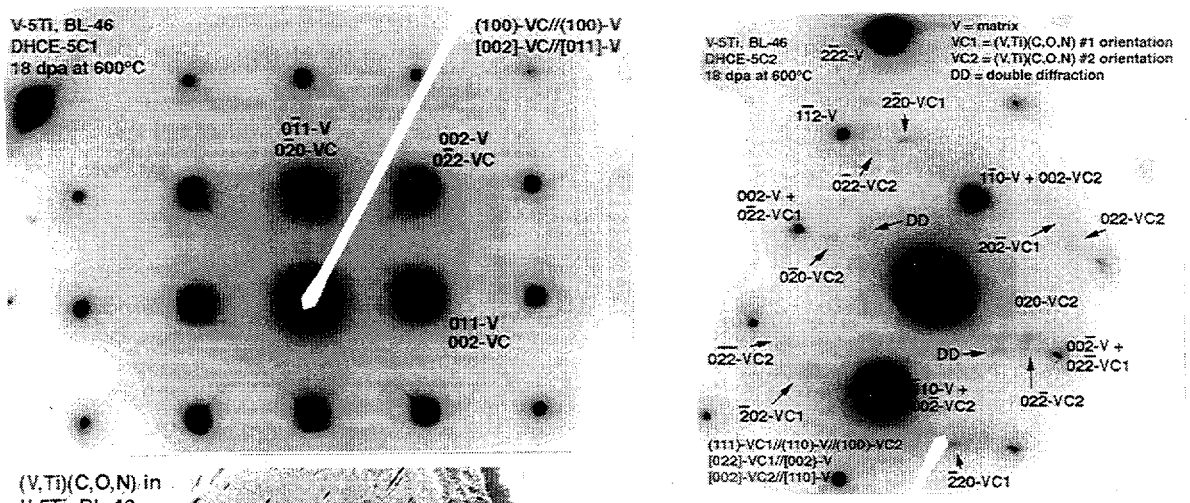

Fig. 8.

SAD patterns and reverse-contrast dark-field image of $(V,Ti_{1-x})(C,O,N)$ observed in V-5Ti BL-46 TEM disk irradiated to ≈18 dpa at 600°C in FFTF-DHCE. Upper left and right SAD patterns show, respectively, $(100)_{VC}//(100)_V$ and $(111)_{VC}//(110)_V$. Letters V, VC, and DD denote, respectively, matrix, $(V,Ti_{1-x})(C,O,N)$, and double diffraction.

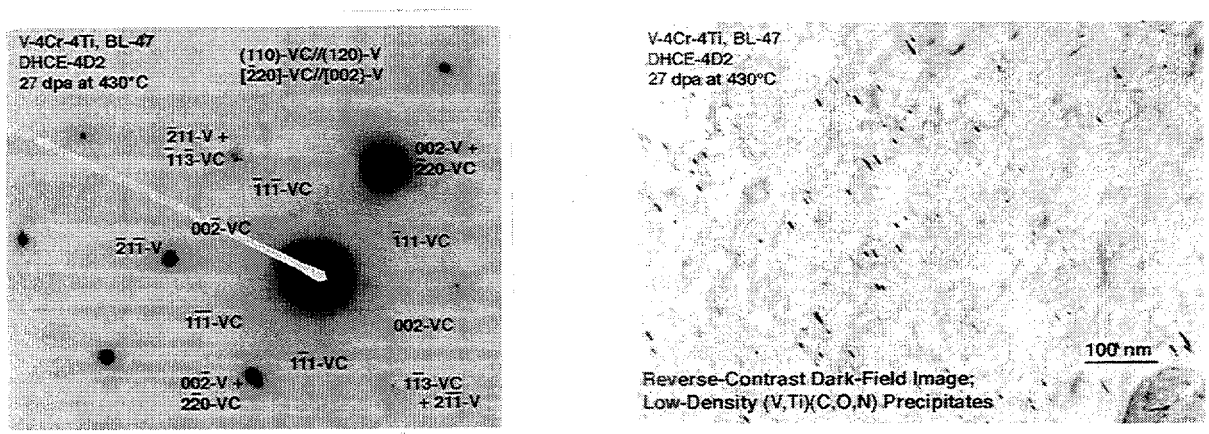

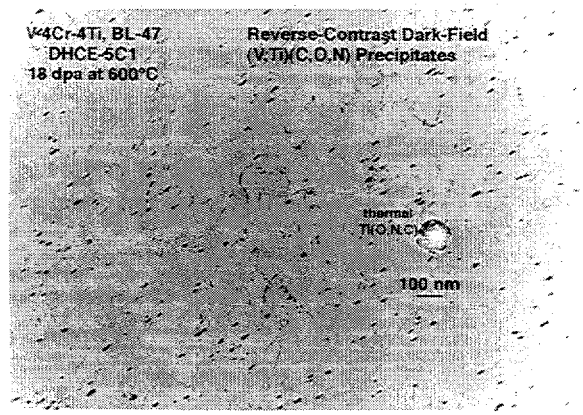

Fig. 9.

SAD pattern (top left, ≈27 dpa at 430°C) and reverse-contrast dark-field images (top right ≈27 dpa at 430°C; bottom left ≈18 dpa at 600°C) of $(V,Ti_{1-x})(C,O,N)$ from V-4Cr-4Ti BL-47 TEM disk irradiated in FFTF-DHCE. The SAD pattern shows $(110)_{VC}//(120)_V$. Letters V, VC, and DD denote, respectively, matrix, $(V,Ti_{1-x})(C,O,N)$, and double diffraction spots.

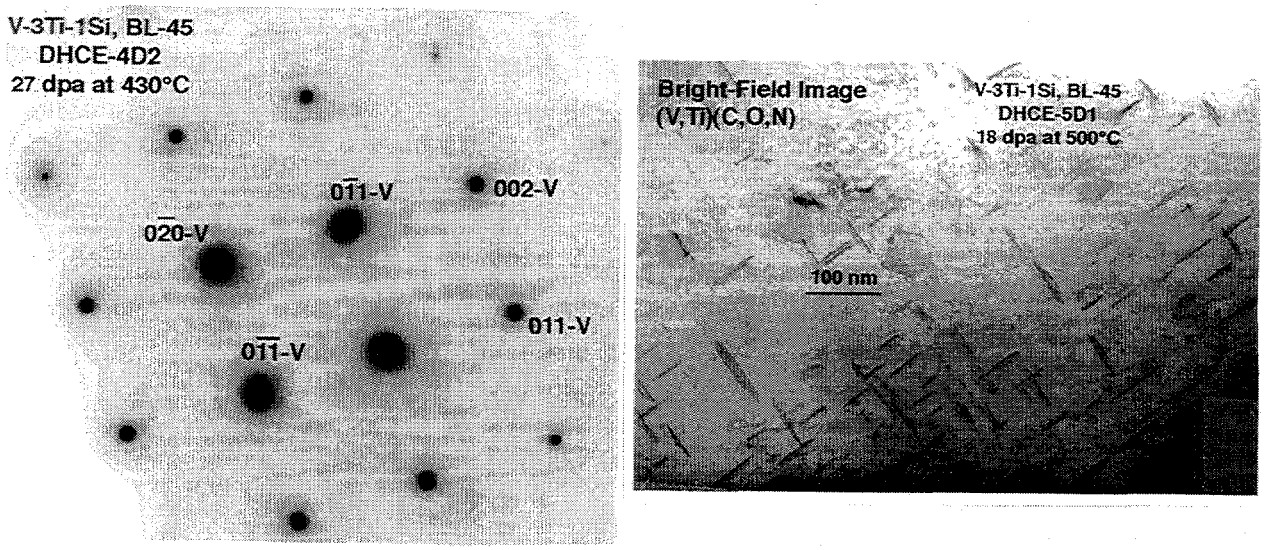

Fig. 10. SAD pattern (TEM disk, ≈27 dpa at 430°C) and dark-field image (TEM disk, ≈18 dpa at 500°C) of $(V,Ti_{1-x})(C,O,N)$ precipitates from V-3Ti-1Si BL-45 irradiated in FFTF-DHCE. The SAD pattern shows (100) zone of matrix free of streaks, indicating that $(V,Ti_{1-x})(C,O,N)$ precipitation at ≈27 dpa at 430°C was insignificant.

Thermal Ti(O,N,C) precipitates form in Ti-containing V alloys during ingot melting and fabrication when combined concentrations of O, N, and C exceed ≈400 wppm.[20] The morphology of this type of mostly 300-500-nm Ti(O,N,C) is invariably ellipsoidal or spherical, which is in distinct contrast to the elongated morphology of V(C,O,N) type precipitates such as those shown in Figs. 7, 8, and 10 in this study and those observed in welds in Refs. 18 and 19. Furthermore, thermally formed Ti(O,N,C) exhibits an orientational relationship of $(100)_{Ti(O,N,C)}//(110)_V$.

In contrast to this, the irradiation-induced precipitates of $(V,Ti_{1-x})(C,O,N)$ analyzed in this study exhibit two orientational relationships, i.e., $(111)_{V(C,O,N)}//(110)_V$ (Figs.3, 7, and 9) and $(100)_{V(C,O,N)}//(100)_V$ (Fig. 8). The latter orientation is identical to the orientation $(110)_{V(C,O,N)}//(110)_V$ that was observed for the $(VTi_{1-x})(C,O,N)$ precipitated in the welds of the 500–kg V-4Cr-4Ti.[18] The diffraction spots from the very fine $(V,Ti_{1-x})(C,O,N)$ precipitates in the 500–kg V-4Cr-4Ti specimens, irradiated to ≈4 dpa at 390°C, exhibit, as shown in Figs. 4 and 5, streaks in the <110> and <111> directions of the precipitate, indicating that they are extremely thin, needlelike precipitates. In contrast to this, the relatively large $(V,Ti_{1-x})(C,O,N)$ precipitates in V-5Ti, irradiated to ≈18 dpa at 600°C, exhibit streaks in the <110> direction only, showing that they are thin platelets (≈10 nm thick and 50-120 nm in diameter).

The diffraction characteristics of $(V,Ti_{1-x})(C,O,N)$ in the (100) orientation, such as those shown in Fig. 8, are in sharp contrast to those of the irradiation-induced Ti_5Si_3 precipitates at the same matrix orientation.[20] For example, diffraction patterns that are characteristic of the latter type of precipitates are shown in Fig. 11 [Ti_5Si_3 on the (100) and (111) zones of the matrix], which was obtained from V-3Ti-1Si (BL-45) irradiated to ≈18 dpa at 600°C in the FFTF-DHCE. Although the morphology of the Ti_5Si_3 precipitates shown in the figure is similar to that of thermally formed ellipsoidal Ti(O,N,C), their diffraction patterns differ from those of Ti(C,O,N)[20] and $(V,Ti_{1-x})(C,O,N)$, e.g., those on the (100) zone of the matrix shown in Fig. 8.

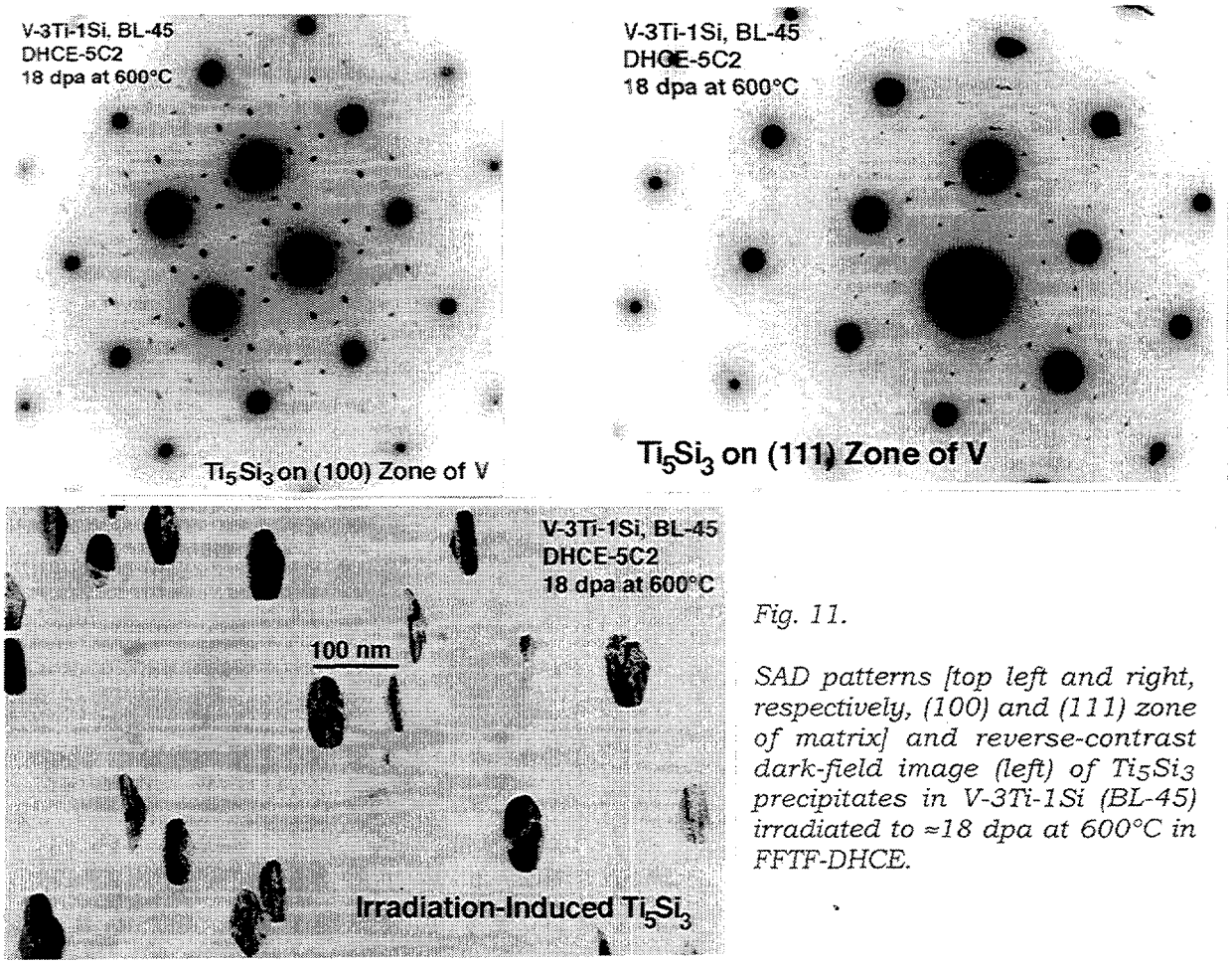

Fig. 11.

SAD patterns [top left and right, respectively, (100) and (111) zone of matrix] and reverse-contrast dark-field image (left) of Ti_5Si_3 precipitates in V-3Ti-1Si (BL-45) irradiated to ≈18 dpa at 600°C in FFTF-DHCE.

DISCUSSION

For the specimens of the 500-kg V-4Cr-4Ti (Heat 832665) that was irradiated to ≈4 dpa at 390°C in the EBR-II X530 experiment, the number density of the $(V,Ti_{1-x})(C,O,N)$ precipitates was extremely high, as shown in Fig. 6, whereas irradiation–induced precipitation of other phases in the same specimens, such as Ti_5Si_3, was negligible. It seems quite possible that irradiation-induced hardening of the material is mostly due to the high–density $(V,Ti_{1-x})(C,O,N)$ precipitates rather than to defect clusters or dislocation loops that act as primary barriers to dislocation motion. In agreement with a previous investigation,[11] it was difficult to obtain dark-field images of pure defect clusters (dislocation loops free of precipitate) in TEM disks or tensile specimens of this material, because most precipitate reflections were superimposed on matrix reflections. The size and number density of $(V,Ti_{1-x})(C,O,N)$ precipitates that were visible in dark-field images, and the size and number density of all types of barriers (defect clusters, dislocation loops, and precipitates) that were visible in the bright-field image were similar. This observation indicates that $(V,Ti_{1-x})(C,O,N)$ precipitated on or near most defect clusters and dislocation loops in the material.

From bright–field images (e.g., Fig. 2) alone, we cannot obtain direct evidence that helps clarify the role of the precipitates in dislocation channeling, nor can we gain insight into what alloying or impurity elements are responsible for precipitation-induced microstructural modification. However, the dark-field images (e.g., Fig. 12) provide more direct evidence for the role of $(V,Ti_{1-x})(C,O,N)$ precipitates in dislocation channeling. The dark-field image in Fig. 12 shows that $(V,Ti_{1-x})(C,O,N)$ precipitates, contained in a tensile specimen of the 500-kg V-4Cr-4Ti (Heat 832665) that was irradiated to ≈4 dpa at 390°C in the EBR-II X530 and tested at

390°C, were either sheared or plowed out of dislocation channels. Therefore, the severe dislocation channeling and poor work-hardening capability (manifested by uniform elongation <0.8%, Fig. 1A) of the material did, indeed, seem to be a direct consequence of extensive irradiation-induced precipitation of $(V,Ti_{1-x})(C,O,N)$ in the material. Likewise, the poor impact property of the material[7] is believed due to the same precipitation-induced microstructural degradation.

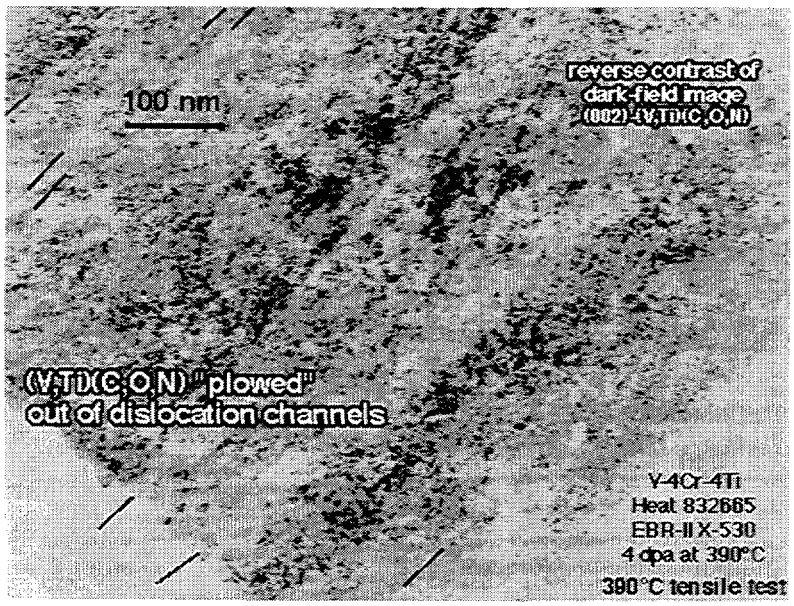

Fig. 12.

Reverse-contrast dark-field image of $(V,Ti_{1-x})(C,O,N)$ precipitates and dislocation channels in 500-kg V-4Cr-4Ti (Heat 832665) irradiated to ≈4 dpa at 390°C in EBR-II X530 and tensile tested at 390°C, showing that the precipitates were sheared or plowed out of dislocation channels.

In contrast to the case of the 500–kg heat V–4Cr–4Ti that was irradiated in the EBR–II, uniform elongation (i.e., 1.4–2.0 %) and work–hardening capability of the 30–kg V–4Cr–4Ti heat were relatively higher after irradiation to ≈27 dpa at ≈430°C in the FFTF–DHCE (see Fig. 1A).[7] This finding is consistent with the dark–field image of the microstructure of the latter material, shown in Fig. 9. The density of the fine $(V,Ti_{1-x})(C,O,N)$ precipitates produced in the 30–kg heat was more than an order of magnitude lower than that of the 500–kg heat, and as a consequence, the 30–kg heat seems to be more resistant to dislocation channeling, and hence, to flow localization. Similarly, a 15–kg heat of V–3Ti–1Si (BL–45) exhibited no sign of $(V,Ti_{1-x})(C,O,N)$ precipitation after irradiation at 430°C in the FFTF–DHCE or at 390°C in the COBRA–1A2 experiment. This observation is also consistent with the relatively higher work–hardening capability of the BL–45 specimens that is manifested by uniform elongations as high as 3.8–6.5% (see Fig. 1B). Thus, at least for three irradiated materials, i.e., V–4Cr–4Ti Heat 832665 irradiated to ≈4 dpa at 390°C in the EBR–II X530, V–4Cr–4Ti Heat BL–47 irradiated to ≈27 dpa at 430°C in the FFTF–DHCE, and V–3Ti–1Si Heat BL–45 irradiated to ≈27 dpa at 430°C in the FFTF–DHCE, we observed direct evidence for good correlation among the number density of the fine $(V,Ti_{1-x})(C,O,N)$ precipitates, the degree of dislocation channeling, and work–hardening capability.

Obviously, one way to improve work–hardening capability (and, at the same time, impact properties) of V–base alloys that are to be irradiated at <430°C is to suppress or prevent irradiation–induced precipitation of $(V,Ti_{1-x})(C,O,N)$. As shown in Fig. 1A, the coldworked specimen of BL–47 V–4Cr–4Ti exhibited better work–hardening capability than the annealed material (i.e., uniform elongation ≈2.3 vs. 0.9% after irradiation at 390°C), indicating that coldwork improves work–hardening capability. However, optimizing alloy or specimen fabrication procedures, such as coldworking, keeping C, O, and N concentrations at a sufficiently low level, or maximizing thermal precipitation, is probably either insufficient, too costly, or impractical. Alternatively, it may be feasible, by adding certain doping element(s), to shift the range of temperature of irradiation–induced $(V,Ti_{1-x})(C,O,N)$ precipitation to

sufficiently lower temperatures, e.g., <350°C, or even entirely eliminate precipitation in the temperature range of interest for fusion application.

Doping V–4Cr–4Ti with >1% Si appears to be an attractive idea. As shown in Fig. 1B, the work–hardening capability of BL–27 V–3Ti–0.25Si was significantly inferior to that of BL–45 V–3Ti–1Si. Although not conclusive at this time, this difference in work-hardening capability may be a manifestation of a beneficial effect of sufficiently high Si concentration in V–3Ti–Si alloys; e.g., $(V,Ti_{1-x})(C,O,N)$ precipitation and dislocation channeling is suppressed in the high–Si heat but is still active in the low–Si heat. Likewise, a sufficiently high Si concentration could also help to suppress or prevent $(V,Ti_{1-x})(C,O,N)$ precipitation in V–4Cr–4Ti at temperatures <450°C.

CONCLUSIONS

1. Dislocation channeling and poor work–hardening capability of the 500–kg heat of V–4Cr–4Ti, observed after irradiation at low temperatures (e.g., at <400°C), are caused by high–density irradiation-induced precipitation of very fine <10-nm particles. By dark-field imaging and selected area diffraction analysis, the characteristic precipitates were identified as $(V,Ti_{1-x})(C,O,N)$, which has an fcc structure and modified composition of VC, with some V replaced by Ti and some C replaced by O, and, to a lesser extent, by N. The same type of precipitates were also observed in unalloyed V, V–5Ti, V3Ti–1Si, and a 30–kg heat of V–4Cr–4Ti irradiated at 430–600°C in the dynamic helium charging experiment; precipitation behavior was influenced strongly by irradiation temperature.

2. Irradiation–induced precipitates of $(V,Ti_{1-x})(C,O,N)$ exhibited two orientations: $(111)_{V(C,O,N)}//(110)_V$, $[0-22]_{V(C,O,N)}//[002]_V$; and $(100)_{V(C,O,N)}//(100)_V$, $[002]_{V(C,O,N)}//[011]_V$. Diffraction spots from the <10–nm $(V,Ti_{1-x})(C,O,N)$ precipitates in the 500–kg V-4Cr-4Ti, irradiated to ≈4 dpa at 390°C, exhibited streaks in the <110> and <111> directions, indicating that they are very fine needlelike precipitates. In contrast, relatively large $(V,Ti_{1-x})(C,O,N)$ precipitates produced during irradiation at 600°C exhibited streaks in the <110> direction only, showing that they are thin platelets (≈10 nm thick and 50-120 nm in diameter). Thermally formed platelet $(V,Ti_{1-x})(C,O,N)$ precipitates were also observed in unirradiated postwelding–annealed laser and electron–beam welds of the 500–kg V–4Cr–4Ti.

3. In V–4Cr–4Ti at <27 dpa, $(V,Ti_{1-x})(C,O,N)$ precipitation is predominant for irradiation at <430°C, whereas Ti_5Si_3 precipitation is favored at >500°C.

4. Dark-field images provided direct evidence that $(V,Ti_{1-x})(C,O,N)$ precipitates in tensile specimens of the 500-kg V-4Cr-4Ti (Heat 832665) that were irradiated and tested at 390°C were either sheared or plowed out of dislocation channels. The severe dislocation channeling and poor work-hardening capability of the material is a direct consequence of extensive irradiation-induced precipitation of $(V,Ti_{1-x})(C,O,N)$. The poor impact property of the heat observed after irradiation at <390°C is probably also due to the same precipitation-induced microstructural degradation.

5. The number density of $(V,Ti_{1-x})(C,O,N)$ precipitates in the 30–kg heat V–4Cr–4Ti, irradiated to ≈27 dpa at ≈430°C in the dynamic helium charging experiment, was more than an order of magnitude lower than that of the 500–kg V–4Cr–4Ti heat that was irradiated at 390°C in a conventional experiment, and as a consequence, the heat was more resistant to dislocation channeling, and work–hardening capability was higher.

6. A 15–kg heat of V–3Ti–1Si showed no sign of $(V,Ti_{1-x})(C,O,N)$ precipitation after irradiation at <430°C in either conventional or dynamic helium charging experiments, indicating that the heat is inherently resistant to dislocation channeling. This finding is consistent with high work–hardening capability (uniform elongation of 3.8–6.5% at <27 dpa) that was observed for the alloy.

7. The work–hardening capability and impact properties of V–base alloys irradiated at <430°C can be improved by preventing irradiation–induced precipitation of $(V,Ti_{1-x})(C,O,N)$. Optimizing alloy or specimen fabrication procedures, e.g., coldworking, keeping C, O, and N concentrations sufficiently low, or maximizing thermal precipitation, is probably either insufficient, too costly, or impractical. Alternatively, it may be feasible to suppress or prevent $(V,Ti_{1-x})(C,O,N)$ precipitation by adding certain doping element(s). Doping V–4Cr–4Ti with >1% Si appears to be an attractive idea.

ACKNOWLEDGMENTS

The authors thank L. J. Nowicki for specimen retrieval, hot–cell mechanical testing, and preparation of specimens for microstructural examination.

REFERENCES

1. D. J. Alexander, L. L. Snead, S. J. Zinkle, A. N. Gubbi, A. F. Rowcliffe, and E. E. Bloom, "Effects of Irradiation at Low Temperature on V-4Cr-4Ti," in Fusion Reactor Materials, Semiannual Prog. Rep. DOE/ER-0313/20, Oak Ridge National Laboratory, Oak Ridge, TN (1996), pp. 87-95.
2. H. M. Chung, L. Nowicki, and D. L. Smith, "Tensile Properties of Vanadium Alloys Irradiated at 400°C in the HFIR," in Fusion Reactor Materials, Semiannual Prog. Rep. DOE/ER-0313/20, Oak Ridge National Laboratory, Oak Ridge, TN (1996), pp. 84-86.
3. H. M. Chung, L. Nowicki, and D. L. Smith, "Tensile Properties of Vanadium Alloys Irradiated at 200°C in the HFIR," in Fusion Reactor Materials, Semiannual Prog. Rep. DOE/ER-0313/22, Oak Ridge National Laboratory, Oak Ridge, TN (1997), pp. 29-32.
4. S. J. Zinkle, D. J. Alexander, J. P. Robertson, L. L. Snead, A. F. Rowcliffe, L. T. Gibson, W. S. Eatherly, and H.-C. Tsai, "Effect of Fast Neutron Irradiation to 4 dpa at 400°C on the Properties of V-(4-5)Cr-(4-5)Ti Alloys," in Fusion Reactor Materials, Semiannual Prog. Rep. DOE/ER-0313/21, Oak Ridge National Laboratory, Oak Ridge, TN (1997), pp. 73-78.
5. H. M. Chung, H.-C. Tsai, L. J. Nowicki, and D. L. Smith, "Tensile Properties of Vanadium Alloys Irradiated in EBR-II," in Fusion Reactor Materials, Semiannual Prog. Rep. DOE/ER-0313/22, Oak Ridge National Laboratory, Oak Ridge, TN (1997), pp. 18-21.
6. H.-C. Tsai, L. J. Nowicki, M. C. Billone, H. M. Chung, and D. L. Smith, "Tensile and Impact Properties of Vanadium Alloys Irradiated at Low Temperatures in the ATR-A1 Experiment," in Fusion Reactor Materials, Semiannual Prog. Rep. DOE/ER-0313/23, Oak Ridge National Laboratory, Oak Ridge, TN (1998), pp. 70-76.
7. H. M. Chung and D. L. Smith, "Tensile and Impact Properties of Vanadium Alloys Irradiated at <430°C," J. Nucl. Mater., 1998, (Proc. 8th Intl. Conf. Fusion Reactor Materials, Oct. 26-31, 1997, Sendai, Japan), in press.
8. H. M. Chung, B. A. Loomis, and D. L. Smith, J. Nucl. Mater. 239 (1996) 139.
9. B. A. Loomis, H. M. Chung, L. Nowicki, and D. L. Smith, J. Nucl. Mater. 212-215 (1994) 799-803.
10. J. Gazda, M. Meshii, and H. M. Chung, "Microstructure of V-4Cr-4Ti Alloy After Low Temperature Irradiation by Ions and Neutrons," J. Nucl. Mater., 1998, (Proc. 8th Intl. Conf. Fusion Reactor Materials, Oct. 26-31, 1997, Sendai, Japan), in press.
11. D. S. Gelles, P. M. Rice, S. J. Zinkle, and H. M. Chung, "Microstructural Examination of Irradiated V-4Cr-4Ti," ibid.
12. P. M. Price and S. J. Zinkle "Temperature Dependence of the Radiation-Damage Microstructure in V-4Cr-4Ti Neutron-Irradiated to Low Dose," ibid.

13. H. M. Chung, M. C. Billone, and D. L. Smith, "Effect of Helium on Tensile Properties of Vanadium Alloys," in Fusion Reactor Materials, Semiannual Prog. Rep. DOE/ER-0313/22, Oak Ridge National Laboratory, Oak Ridge, TN (1997), pp. 22-28.
14. B. S. Hickman, J. Inst. Met. 96 (1968) 330-337.
15. Ch. Leibovich, A. Rabinkin, and M. Talikaner, Met. Trans. A12 (1981) 1513-1519.
16. M. Hansen, Constitution of Binary Alloys, McGraw-Hill Book Co., 2nd Ed., New York, 1958.
17. F. A. Shunk, Constitution of Binary Alloys, 2nd Supplement, McGraw-Hill Book Co., New York, 1969.
18. H. M. Chung, J.-H. Park, R. V. Strain, K. H. Leong, and D. L. Smith, "Mechanical Properties and Microstructural Characteristics of Laser and Electron-Beam Welds in V-4Cr-4Ti Alloy After Low Temperature Irradiation by Ions and Neutrons," J. Nucl. Mater., 1998, (Proc. 8th Intl. Conf. Fusion Reactor Materials, Oct. 26-31, 1997, Sendai, Japan), in press.
19. V. Kazakov, V. Chakin, and Z. Ostrovsky, J. Nucl. Mater. 233-237 (1996) 364.
20. H. M. Chung, B. A. Loomis, and D. L. Smith, ASTM STP-1175 (1993) 1185.

REACTIONS OF HYDROGEN WITH V-Cr-Ti ALLOYS — J. R. DiStefano, J. H. DeVan, L. D. Chitwood (Oak Ridge National Laboratory), and D. H. Röhrig (Projektleitung Kernfusion, Forschungszentrum Karlsruhe)

OBJECTIVE

The objective of this task is to assess the effects of hydrogen on the mechanical properties of V-Cr-Ti alloys.

SUMMARY

In the absence of increases in oxygen concentration, additions of up to 400 ppm hydrogen to V-4 Cr-4 Ti did not result in significant embrittlement as determined by room temperature tensile tests. However, when hydrogen approached 700 ppm after exposure at 325°C, rapid embrittlement occurred. In this latter case, hydride formation ins the presumed embrittlement cause. When oxygen was added during or prior to hydrogen exposure, synergistic effects led to significant embrittlement by 100 ppm hydrogen.

PROGRESS AND STATUS

Experimental Program

Two alloys, V-5 Cr-5 Ti and V-4 Cr-4 Ti, were exposed to hy vironments. Samples were given various heat treatments before and after exposure to to evaluate their effects on hydrogen embrittlement. The alloys were exposed to hydro apparatus consisting of a gas supply, an alumina reaction tube coupled to an ultra high ystem, and a high temperature furnace around the reaction tube. High purity h as (99.9999%) was admitted through a controllable leak valve while the system w vacuated by the vacuum system. Temperatures of exposure were in the range 325 to some cases specimens were rapidly cooled after exposure by withdrawing them to a cold zone above the furnace, while other specimens remained in the furnace zone as it was cooled to room temperature. Hydrogen flow was maintained during cool down. The amounts of hydrogen picked up were monitored by weight changes and selective chemical analyses. Room temperature tensile tests were used to determine the effect of hydrogen on the mechanical properties of the two vanadium alloys.

Initially, tests in hydrogen were conducted on two heats of V-5 Cr-5 Ti (Table 1) at 450-500°C. Specimens were generally vacuum-annealed at 1125°C prior to hydrogen exposure. Hydrogen pressures were in the range 10^{-2} to 10 Pa (10^{-4} to 10^{-1} torr) and exposures were for 24 or 100 h. Subsequently, hydrogen uptake by V-4 Cr-4 Ti (Table 1) was determined at 10 Pa (~10^{-1} torr) and 450°C or at 325°C between 25-250 Pa (0.2-2 torr). In the latter tests on V-4 Cr-4 Ti, the gas supply system was modified by the addition of a hydrogen gas purifier that contained a Pd-Ag membrane to exclude oxygen and water vapor from the system, and the pre-test annealing temperature was lowered to 1050°C.

Table 1. Compositions of V-Cr-Ti Alloys

Nominal composition (wt %)	Heat ID	Concentration (wt %)			Concentration (wppm)			
		Cr	Ti	Fe	O	N	C	Si
V-5Cr-5Ti	ORNL	4.0	5.6	0.11	324	512	204	1100
V-5Cr-5Ti	832394	4.2	5.4	<0.045	427	52	40	<310
V-4Cr-4Ti	8326	3.1	4.1	0.022	310	85	86	780

Results and Discussion

In the initial tests on the two heats of V-5 Cr-5 Ti, exposures at 10^{-2}-10^{-1} Pa resulted in only minor hydrogen uptake and weight change, with minimal effects on mechanical properties. However, at hydrogen pressures of 1-10 Pa, weight gains generally exceeded those attributable to hydrogen alone, and selected chemical analyses indicated a concomitant increase in oxygen content. For any given exposure condition, the uptake of hydrogen was similar for the two heats. However, as shown in Fig. 1, specimen furnace (slowly) cooled under the hydrogen exposure pressure showed higher hydrogen concentrations than companion specimens moved quickly to a relatively cool region of the furnace. Some effect of grain size on tensile ductility was noted as indicated in Fig. 2. (Numbers refer to oxygen concentration associated with hydrogen concentration.) The heat of V-5 Cr-5 Ti identified as 832394 exhibited a larger grain size for a given annealing temperature and, in general, was more susceptible to hydrogen (plus oxygen) embrittlement. Hydrogen concentrations <50 wppm seriously embrittled this heat, while 70-80 wppm hydrogen resulted in only slight embrittlement of the finer-grained ORNL heat. Post-exposure heat treating the V-5 Cr-5 Ti alloys in vacuum for 100 h at 500°C was effective in removing hydrogen, as shown in Table 2. Although this treatment recovered most of the ductility in the finer-grained ORNL heat, heat 832394 remained brittle, an indication that oxygen contamination was a significant factor in the embrittlement of the latter heat.

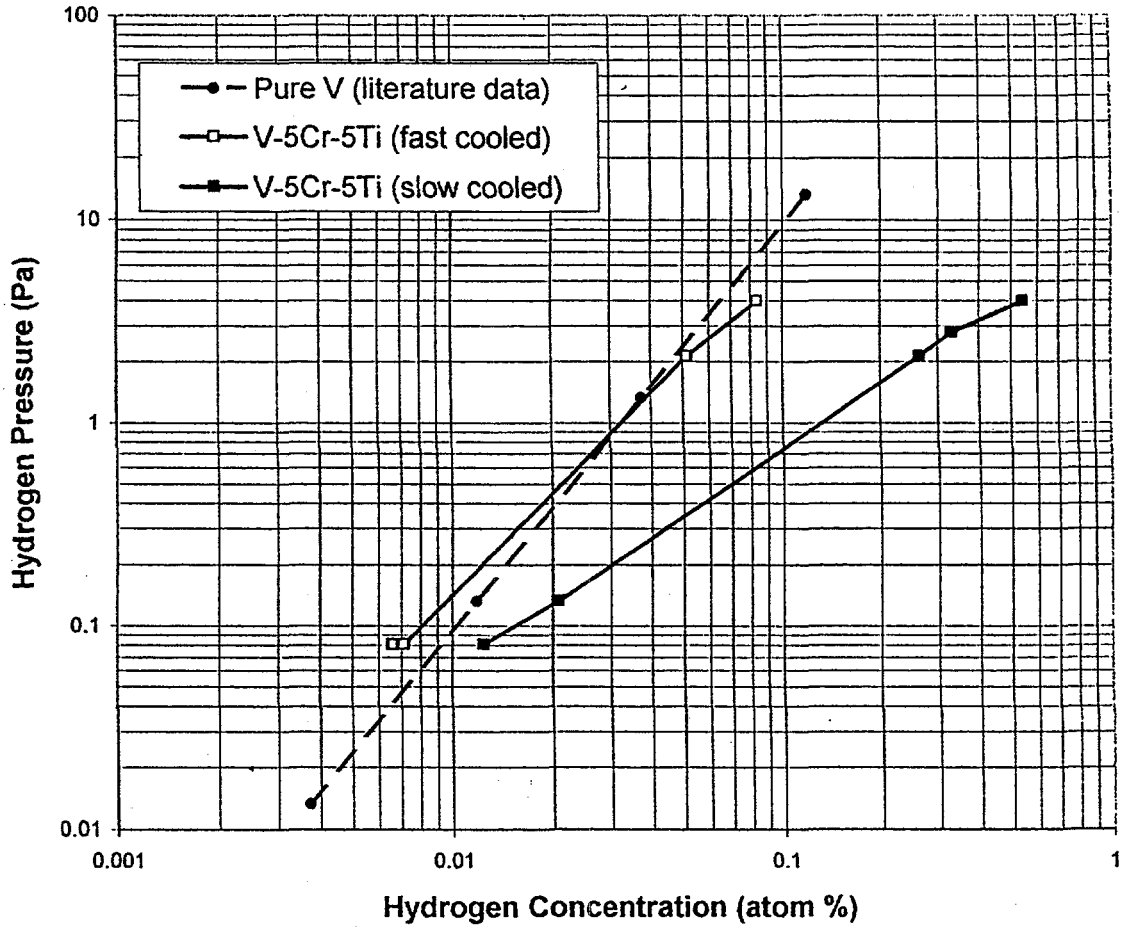

Fig. 1. Hydrogen concentrations in V-5 Cr-5 Ti and unalloyed vanadium [9,10] after exposure to low-pressure hydrogen at 500°C.

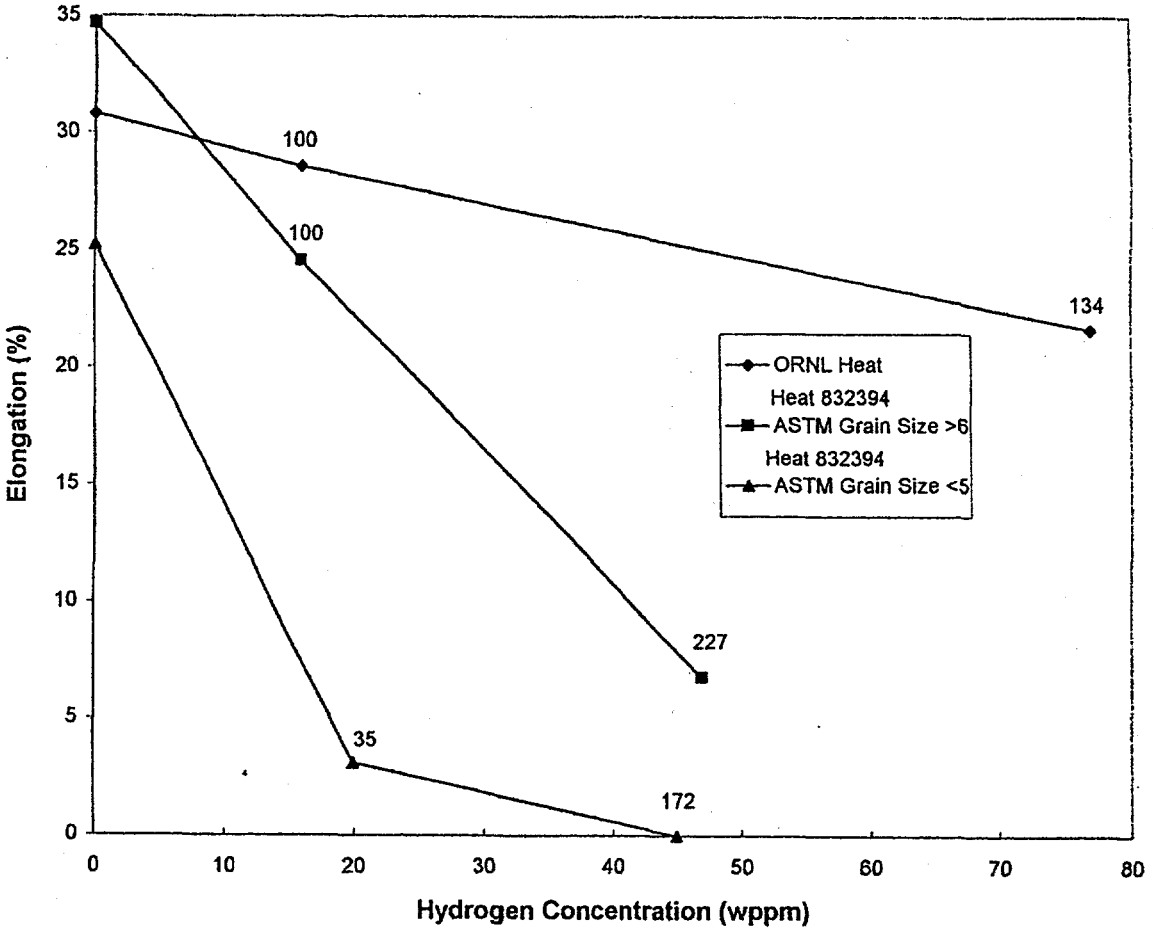

Fig. 2. Room temperature elongation (a) and yield strength (b) of two heats of V-5 Cr-5 Ti annealed at 1125°C prior to exposure to high purity hydrogen gas at 500°C. Numbers above data points show increases in oxygen concentration (ppm) accompanying hydrogen exposures.

Table 2. Effect of hydrogen exposure at 3 x 10^{-2} torr on V-5Cr-5Ti at 500C before and after vacuum heat treating at 500C[a] (Exposure and heat treating times were 100 h, respectively)

Heat	Cooling rate in hydrogen	Vacuum heat treat	Concentration (ppm)		Yield strength (MPa)	Ultimate strength (MPa)	Elongation (%)
			Hydrogen	Oxygen			
832394	Fast	No	45	172	FBY[b]	FBY[b]	0.0
832394	Slow	No	107	245	FBY[b]	FBY[b]	0.0
832394	Slow	Yes	2.4	185	506	515	0.3
ORNL	Fast	No	59	284	476	515	18.0
ORNL	Slow	No	150	332	493	533	7.0
ORNL	Slow	Yes	0.8	246	453	561	22.6

[a]Samples annealed at 1125C prior to exposure to hydrogen.
[b]Failed before yield.

To avoid the complexity of oxygen contamination effects, the test system was modified by the addition of a hydrogen purifier. The Pd-Ag alloy membrane in the purifier permitted only hydrogen to pass through, effectively eliminating oxygen as an impurity. This was verified by a residual gas analyzer which indicated that, except for a small amount of residual water vapor, hydrogen was the only gas that could be detected in the system.

Hydrogen uptake by V-4 Cr-4 Ti was then determined as shown in Fig. 3. The data in Fig. 3 for hydrogen concentration in V-4 Cr-4 Ti as a function of pressure at 325°C can be described by a Sievert's law relation and correlate with the data for fast-cooled V-5 Cr-5 Ti at 500°C, shown in Fig. 1. The agreement of the present data (shown as individual points in Fig. 3) with isotherms (lines in Fig. 3) derived from the literature for the V-H system,[1,2] demonstrates that V-Cr-Ti behaves similarly to pure vanadium with respect to hydrogen uptake at a given hydrogen pressure and temperature.

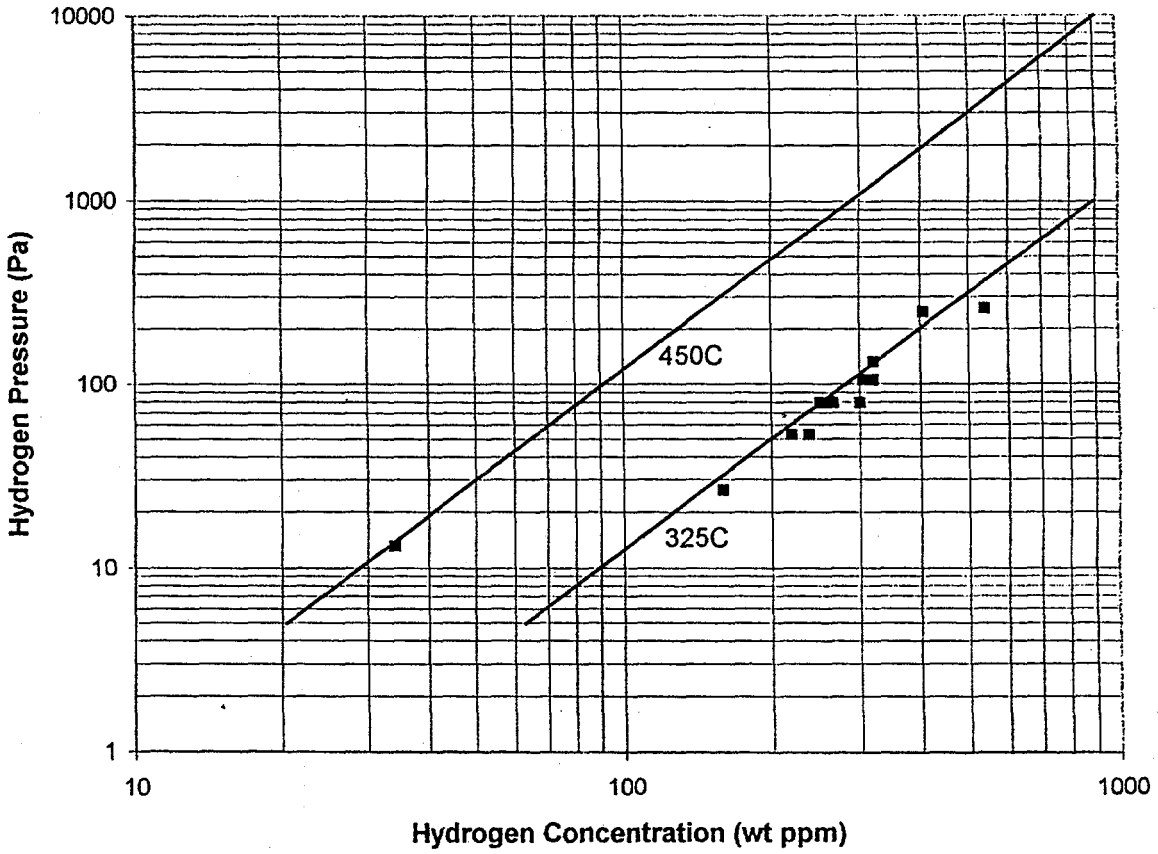

Fig. 3. Comparison of hydrogen concentrations in V-4 Cr-4 Ti with calculated concentrations in unalloyed vanadium at 450 and 300°C [9,10].

Results of room temperature tensile tests on V-4 Cr-4 Ti after exposure to hydrogen at 325°C are shown in Fig. 4. When oxygen was excluded, the addition of up to 400 ppm hydrogen increased the room temperature tensile strength slightly with only a small decrease in tensile elongation (Fig. 4). The fractures tended to be the cup/cone type, similar to that of the as-received alloys. However, a further increase in hydrogen concentration to 700 ppm resulted in complete embrittlement (Fig. 4). As shown in Fig. 5, this hydrogen concentration corresponds to the solubility threshold for hydride formation in pure vanadium below 80°C and is indicative that the ductile-brittle transition for specimens containing more than 400 ppm hydrogen is most likely associated with hydride formation.

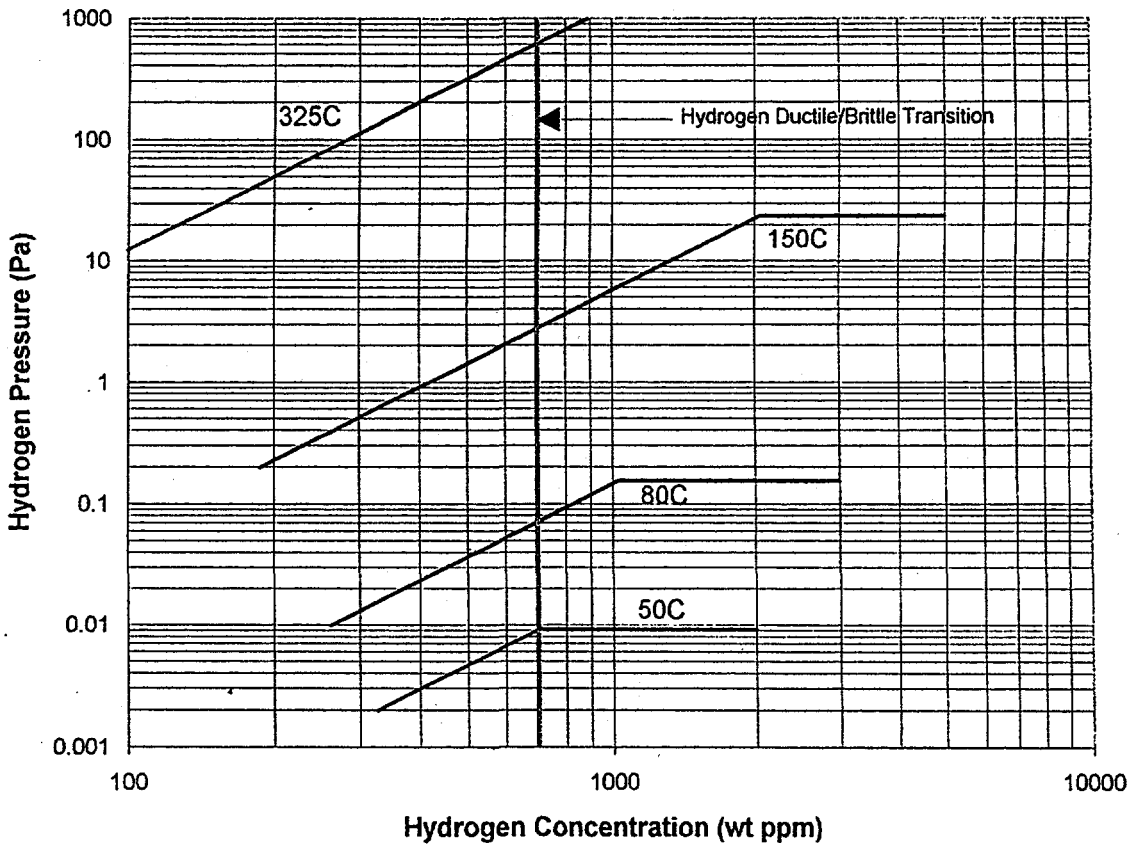

Fig. 4. Effect of hydrogen on room temperature elongation of V-4 Cr-4 Ti.

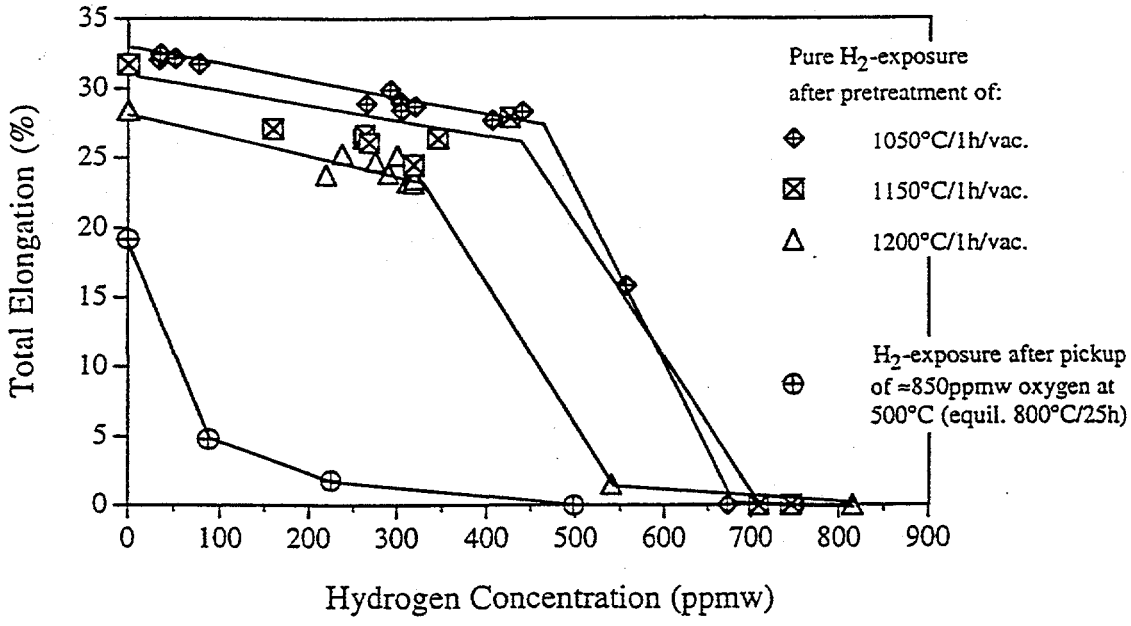

Fig. 5. Hydrogen concentrations in unalloyed vanadium at 50-325°C [10]. Horizontal portions represent two-phase regions (hydride + solid solution).

The synergistic effect of oxygen in combination with hydrogen was determined for V-4 Cr-4 Ti by first exposing the specimens to oxygen at 500°C, heat treating in vacuum at 800°C and then exposing the oxygenated specimens to hydrogen (Fig. 4). The initial addition of ~850 wppm oxygen reduced room temperature elongation from approximately 30 to 20%. However, subsequent exposure of a similar specimen to hydrogen drastically reduced its elongation to 5% after only 100 wppm hydrogen was added, whereas, in the absence of oxygen, >500 ppm hydrogen was generally required before room temperature ductility fell precipitously. Fracture cross sections indicated that the oxygen-doped specimens retained a relatively ductile core until the hydrogen concentration approached its solubility limit (Fig. 6). Oxygen was confined to a fixed depth below the surface, and embrittlement appeared to be associated with the combined effects of oxygen and hydrogen in this outer case. However, initiation of cracks in the outer case could also affect the fracture toughness of the hydrogen strengthened, ductile core, thereby further reducing the ductility.

Where embrittlement is due to the combined effects of oxygen and hydrogen, desorbing hydrogen by vacuum heat treating will generally improve the ductility, although embrittlement induced by oxygen is not reversed by heat treatments in the range normally used to remove hydrogen (<500°C). In fact, embrittlement by oxygen is exacerbated by heat treating in the 400-500°C temperature range,[3] and the desorption of hydrogen advisedly should be conducted above or below this range. The heat treatment needed to counter embrittlement by oxygen, when it is absorbed at 400-500°C, was shown to be in the range of 950°C and higher,[3] where the oxygen is precipitated from the matrix in the form of TiO_2.

Based on the present results, serious embrittlement of the reference V-Cr-Ti alloys by hydrogen isotopes would not be expected under nominal fusion reactor operating conditions, providing that oxygen pickup is carefully controlled. Given present estimates of plasma leakage to the first wall, our calculations of the deuterium-tritium pressures behind the currently proposed light element coatings (i.e., in cracks or crevices) show them to be on the order of 10^{-1} Pa (10^{-3} torr). At this pressure, as shown by the present results and those of Natesan,[4] hydrogen concentrations in V-Cr-Ti alloys are well within the solid solution range, and the principal mechanical property effect would be limited to slight hardening. One caveat is a possible additive effect with radiation damage, where protium produced in the alloys by transmutation reactions and radiation hardening may lead to an increase in the ductile-to-brittle transition temperature. Also, depending on design, hydrogen isotopes could affect the properties of V-Cr-Ti alloys if used for components on which plasma directly impinges, such as the divertor.

One of the major concerns in the application of V-Cr-Ti alloys to fusion reactors will be oxygen pickup, particularly in welds during reactor construction and during system bake-out prior to operation. As shown earlier,[3,5] oxidation that occurs internally at lower temperatures (e.g., 500°C) can of itself cause serious embrittlement, and, as shown here, the uptake of relatively small concentrations of hydrogen further increases the degree of embrittlement for a given level of oxygen. Accordingly, the permissible level of oxygen contamination will be strongly impacted by the uptake of hydrogen isotopes expected during reactor operation.

REFERENCES

1. L. A. Charlot, A. B. Johnson, and R. E. Westerman, "Solubilities and Diffusivities of Hydrogen Isotopes in Niobium, Niobium-Zirconium alloys, and Vanadium," *Technology of Controlled Thermonuclear Fusion Experiments and the Engineering Aspects of Fusion Reactors*, CONF-721111-23 (1973).
2. E. Fromm and E. Gebhardt, *Gase und Kohlenstoff in Metallen, 441-460, Springer-Verlag, Berlin-Heidelberg* (1976).
3. J. R. DiStefano and J. H. DeVan, "Reactions of Oxygen with V-Cr-Ti Alloys," *Journal of Nuclear Materials*, 249, 150-158 (1997).
4. K. Natesan, "Tensile Properties of V-Cr-Ti Alloys After Exposure in Hydrogen-Containing Environments," *Fusion Materials Semiannual Progress Report for Period Ending December 31, 1997*, DOE/ER-0313/23, pp. 127-129, March 1998.
5. K. Natesan and W. K. Soppet, "Tensile Properties of V-Cr-Ti Alloys After Exposure in Oxygen-Containing Environments," *Fusion Materials Semiannual Progress Report for Period Ending December 31, 1997*, DOE/ER-0313/23, pp. 130-135, March 1998.

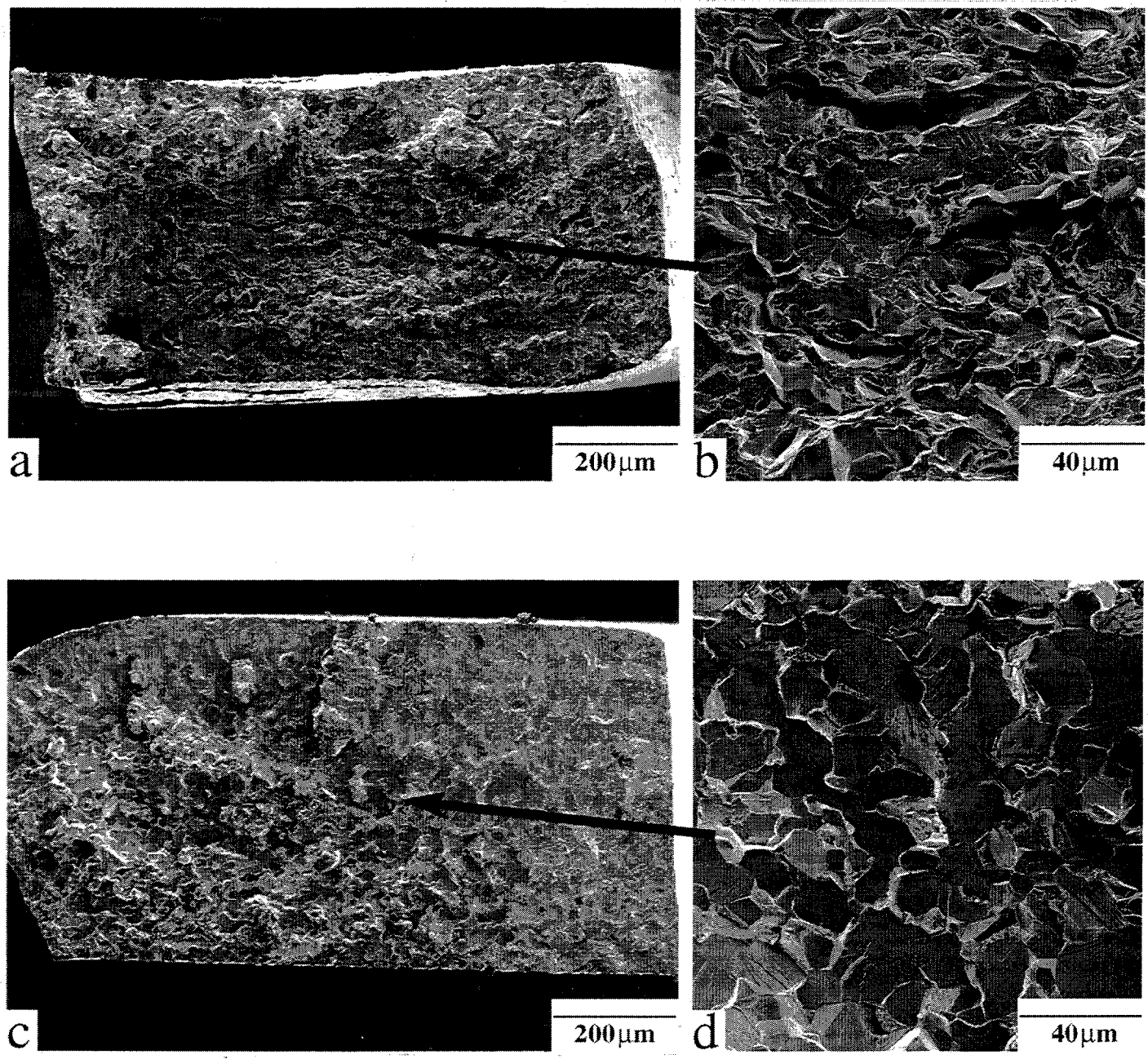

Fig. 6. SEM secondary electron images of V-4 Cr-4 Ti tensile fracture sections. Specimens were pre-exposed to oxygen (≈850 ppm) and aged at 800°C prior to hydrogen exposure at 325°C. The region of brittle cleavage and intergranular cracking increased in depth as H concentration increased from (a,b) 900 ppm to (c,d) 500 ppm.

TENSILE PROPERTIES OF V-Cr-Ti ALLOYS AFTER EXPOSURE IN HYDROGEN-CONTAINING ENVIRONMENTS*

K. Natesan and W. K. Soppet (Argonne National Laboratory)

OBJECTIVE

The objectives of this task are to (a) determine the hydrogen uptake of V-Cr-Ti alloys as a function of temperature and partial pressure of hydrogen (pH_2) in the exposure environment, (b) examine the microstructural characteristics of surfaces and cross sections of the alloys after exposure, (c) evaluate the influence of hydrogen uptake in low-pH_2 environments on the tensile properties and cracking propensity of the alloys at room and elevated temperatures, and (d) determine the effects of oxygen/hydrogen interactions on the tensile properties of the alloys.

SUMMARY

A systematic study has been initiated at Argonne National Laboratory to evaluate the performance of several V-Cr-Ti alloys after exposure to environments containing hydrogen at various partial pressures. The goal is to correlate the chemistry of the exposure environment with hydrogen uptake in the samples and its influence on the microstructure and tensile properties of the alloys. At present, the principal effort has focused on the V-4Cr-4Ti alloy of heat identified as BL-71; however other alloys (V-5Cr-5Ti alloy of heats BL-63, and T87, plus V-4Cr-4Ti alloy from General Atomics [GA]) are also being evaluated. Other variables of interest are the effect of initial grain size on hydrogen uptake and tensile properties, and the synergistic effects of oxygen and hydrogen on the tensile behavior of the alloys. Experiments conducted on specimens of various V-Cr-Ti alloys exposed to pH_2 levels of 0.01 and 3×10^{-6} torr showed negligible effect of H_2 on either maximum engineering stress or uniform and total elongation. However, uniform and total elongation decreased substantially when the alloys were exposed to 1.0 torr H_2 pressure. Preliminary data from sequential exposures of the materials to low-pO_2 and several low-pH_2 environments did not reveal an adverse effect on the maximum engineering stress or on uniform and total elongation. Further, tests in H_2 environments on specimens annealed at different temperatures showed that grain-size variation by a factor of ≈2 had little or no effect on tensile properties.

EXPERIMENTAL PROGRAM

The heats of vanadium alloy selected for the study had nominal compositions of V-5 wt.%Cr-5 wt.%Ti (designated as BL-63 and T87) and V-4 wt.%Cr-4 wt.%Ti (designated as BL-71 and 44 from the GA heat). Detailed chemical analyses of these heats were given in an earlier report (1). The tensile specimens were fabricated according to ASTM Standard E8-69 specifications and had a gauge length of ≈19 mm and a gauge width of ≈4.5 mm. Specimens were annealed for 1 h at 1050°C prior to hydrogen exposure and tensile testing. Some specimens of BL-63 and BL-71 heats were also annealed for 2 h at 1200°C to obtain a larger grain size before hydrogen exposure.

Tensile samples of the alloys were exposed for 100 h at 500°C to environments containing H_2 at partial pressures of 3×10^{-6} and 1.0 torr and subsequently tensile-tested at a strain rate of 1.8×10^{-4} s^{-1} in room-temperature air. The specimens were loaded by means of pins that pass through holes in the grips and enlarged end sections of the specimen, thus minimizing misalignment. Total elongation was measured with a vernier caliper and load/elongation chart records. The fracture surfaces and longitudinal and axial cross sections of the tested specimens are being examined by scanning electron microscopy.

RESULTS AND DISCUSSION

Effect of Hydrogen Exposure

The engineering stress/engineering strain plots at room temperature for V-4Cr-4Ti and V-5Cr-5Ti materials in as-annealed condition and after exposure to H_2 at partial pressures of 3×10^{-6} and 0.01 torr were reported in Ref. 1. The results showed that in the pH_2 range of the present study, BL-63 exhibited a negligible effect of H_2 on tensile properties, while BL-71 exhibited a small decrease in uniform and total elongation after H_2 exposure. During this period, additional tensile specimens of the two alloys were exposed for 100 h at 500°C to H_2 gas at pressures of 1×10^{-4}, 1×10^{-2}, 5×10^{-2}, and 1 torr.

Engineering stress/engineering strain curves from different tests at room temperature were analyzed to evaluate several tensile properties for the alloys after several H_2 treatments. Table 1 shows the values for maximum engineering stress and uniform and total elongation in the two materials after exposure at different pH_2 levels. Figure 1 shows the maximum engineering stress values as a function of H concentration for both the alloys. The results show that H_2 pressures in the range of the present study have little or no effect on the maximum engineering stress for either alloy. The uniform and total elongation values for the two alloys are 0.14-0.19 and 0.18-0.31, respectively, at H_2 pressures of 3×10^{-6} to 5×10^{-2} torr. After exposure at an H_2 pressure of 1 torr, both alloys showed significant decrease in uniform and total elongation, indicating that this H_2 pressure may be the threshold for embrittlement of the alloys. Figure 2 is a plot of uniform and total elongation values as a function of H_2 concentration for both alloys. The hydrogen concentrations in the BL-63 and BL-71 alloys after exposure for 100 h at 500°C in 1 torr H_2 pressure were 330 and 358 wppm, respectively.

Effect of Oxygen Pretreatment

To examine the synergistic effect, if any, of oxygen and hydrogen in the alloy on the tensile behavior of V-Cr-Ti alloys, tensile specimens of the two alloys were pretreated in several low-pO_2 environments for 100 h at 500°C. Subsequently, the exposure gas was changed from O_2 to H_2 at the same temperature and exposure of the specimens was continued for another 100 h. The preexposure of the specimens to the low-pO_2 environments resulted in different concentrations of O in the alloys, which were subsequently exposed to different H_2 pressures. The specimens exposed to the dual treatment were analyzed for O and H by the vacuum fusion technique. Table 2 lists the O and H concentrations for specimens with different treatments. The O concentrations ranged from 550 to 2230 wppm, while the H concentration was 6 to 16 wppm. It should be noted

Table 1. Effects of 100 h hydrogen exposure at 500°C on room-temperature tensile properties of V-Cr-Ti alloys, initially annealed for 1 h at 1050°C in vacuum

pH_2 in exposure environment	Maximum engineering stress (MPa)		Uniform elongation		Total elongation	
(torr)	BL-63	BL-71	BL-63	BL-71	BL-63	BL-71
-	469	424	0.165	0.186	0.303	0.322
3×10^{-6}	437	440	0.189	0.174	0.313	0.263
1×10^{-4}	523	467	0.157	0.154	0.182	0.227
1×10^{-4} (repeat)	487	491	0.169	0.148	0.249	0.206
1×10^{-2}	445	459	0.194	0.169	0.313	0.263
5×10^{-2}	483	477	0.143	0.142	0.223	0.191
1	481	468	0.0077	0.0016	0.020	0.0016

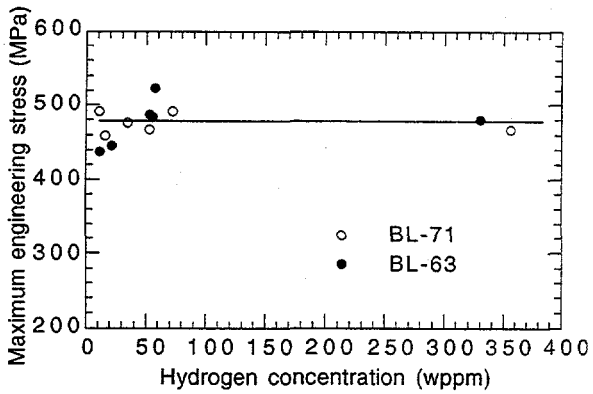

Figure 1. Maximum engineering stress as a function of H concentration for V-4Cr-4Ti and V-5Cr-5Ti alloys tested at room temperature

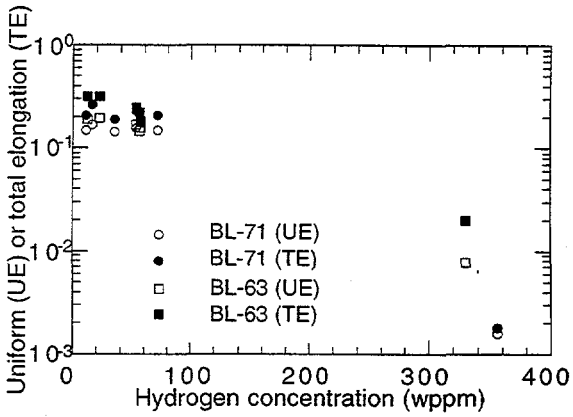

Figure 2. Uniform and total elongation as a function of H concentration for V-4Cr-4Ti and V-5Cr-5Ti alloys tested at room temperature

Table 2. Oxygen and hydrogen concentrations in pretreated tensile specimens

pO_2 in pre-exposure environment[a] (torr)	pH_2 in exposure environment[b] (torr)	Concentration (in wppm) of Oxygen		Hydrogen	
		BL-63	BL-71	BL-63	BL-71
-	3×10^{-6}	550	670	12	11
3×10^{-7}	1×10^{-6}	625	620	16	16
1×10^{-6}	1×10^{-6}	730	820	6	7
1×10^{-4}	3×10^{-6}	2230	2020	15	13

[a]Preexposure time was 100 h at 500°C.

[b]Exposure time in hydrogen was 100 h at 500°C.

that the diffusion coefficient for O is a few orders of magnitude lower than that for H in these alloys; as a result, after the 100-h exposures the measured H concentration will be uniformly distributed over the entire 1-mm-thick section of the specimens, while the O concentration will be confined to a depth of ≈50 μm from the surface [2,3].

The pretreated tensile specimens were tensile-tested at a strain rate of 1.8×10^{-4} s^{-1} in room-temperature air. Engineering stress/engineering strain curves from different tests were analyzed to evaluate several tensile properties for the alloys after the dual treatments. Table 3 shows the values for maximum engineering stress and uniform and total elongation for the two materials after the dual treatments. Figures 3 and 4 show the maximum engineering stress and the uniform and total elongation as a function of O concentration for both the alloys. It is evident that O concentration up to ≈2300 wppm, even though confined to the surface regions of the specimens, has a negligible effect on tensile properties; no synergistic effect of O and H on the properties is observed, based on the present study. Additional experiments are planned to examine this issue at higher O and H concentrations in the material, as well as at temperatures above room temperature.

Effect of Initial Grain Size

To examine the effect of initial grain size on subsequent H_2 uptake and tensile properties, specimens of BL-71 and BL-63 were annealed for 2 h at 1200°C; this increased the grain size by at

Table 3. Effects of 100 h hydrogen exposure at 500°C on room-temperature tensile properties of V-Cr-Ti alloys, initially annealed for 1 h at 1050°C in vacuum and pretreated in low-pO_2 environment

pO_2 in pre-exposure environment[a] (torr)	pH_2 in exposure environment (torr)	Maximum engineering stress (MPa)		Uniform elongation		Total elongation	
		BL-63	BL-71	BL-63	BL-71	BL-63	BL-71
-	-	469	424	0.165	0.186	0.303	0.322
-	3×10^{-6}	437	440	0.189	0.174	0.313	0.263
3×10^{-7}	1×10^{-6}	452	453	0.173	0.162	0.297	0.266
1×10^{-6}	1×10^{-6}	507	475	0.165	0.146	0.268	0.228
1×10^{-4}	3×10^{-6}	484	451	0.132	0.136	0.184	0.177

[a]Preexposure time was 100 h at 500°C.

Table 4. Effects of 100 h hydrogen exposure at 500°C on room-temperature tensile properties of enlarged-grain V-Cr-Ti alloys, initially annealed for 2 h at 1200°C in vacuum

pH_2 in exposure environment (torr)	Maximum engineering stress (MPa)		Uniform elongation		Total elongation	
	BL-63	BL-71	BL-63	BL-71	BL-63	BL-71
3×10^{-6}	515	472	0.144	0.159	0.250	0.225
1×10^{-2}	524	479	0.160	0.153	0.244	0.227
5×10^{-2}	544	509	0.129	0.082	0.188	0.082

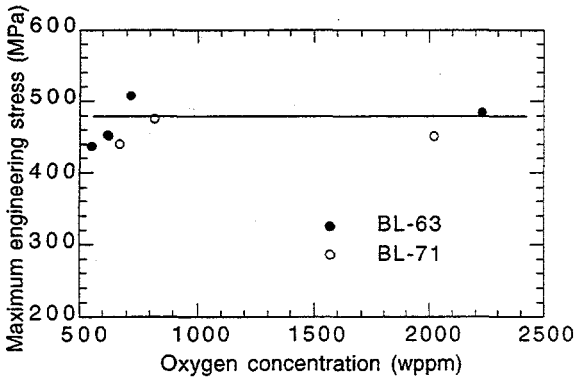

Figure 3. Maximum engineering stress as a function of O uptake during preoxidation and subsequent H_2 exposure for V-4Cr-4Ti and V-5Cr-5Ti alloys tested at room temperature

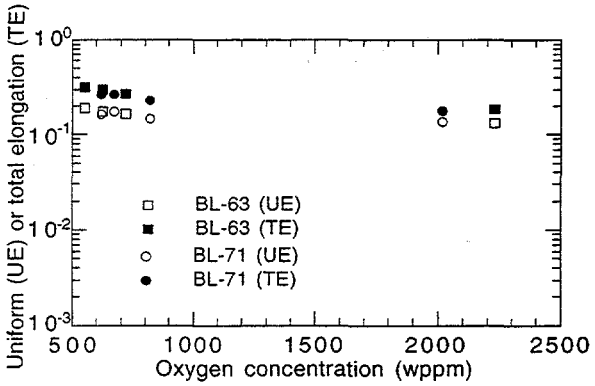

Figure 4. Uniform and total elongation as a function of O uptake during preoxidation and subsequent H_2 exposure for V-4Cr-4Ti and V-5Cr-5Ti alloys tested at room temperature

least a factor of 2 over those of alloys annealed for 1 h at 1050°C. Engineering stress/engineering strain curves for large- and small-grain materials after 100 h exposure at 500°C to a pH_2 of 0.01 torr were presented in the previous report [1]. During this period, additional tests were conducted on larger-grain-size materials after 100 h exposure in 5×10^{-2} torr of H_2 pressure. With the increased grain size, both alloys exhibited a slight increase in strength and some decrease in elongation. Decrease in uniform and total elongation was much more pronounced at the higher H_2 pressure of 5×10^{-2} torr. Examination of the fracture surfaces and specimen cross sections, and measurements of hardness profiles, are in progress and the results will be used to correlate the microstructure, H concentration, and hardness data with the tensile properties of the alloys.

REFERENCES

1. K. Natesan and W. K. Soppet, "Tensile Properties of V-Cr-Ti Alloys After Exposure in Hydrogen-Containing Environments," Fusion Reactor Materials Progress Report for the Period Ending December 31, 1997, Argonne National Laboratory, DOE/ER-0313/23, p. 127, March 1998.

2. K. Natesan and M. Uz, "Oxidation Kinetics and Microstructure of V-(4-5)wt.% Cr-(4-5)wt.% Ti Alloys Exposed to Air at 300-650°C," Fusion Reactor Materials Progress Report for the Period Ending June 30, 1996, Argonne National Laboratory, DOE/ER-0313/20, p. 105, Oct. 1996.

3. M. Uz, K. Natesan, and V. B. Hang, J. Nucl. Mater. 245 (1997) 191-200.

OXIDATION BEHAVIOR OF V-Cr-Ti ALLOYS IN LOW-PARTIAL-PRESSURE OXYGEN ENVIRONMENTS*

K. Natesan and M. Uz (Argonne National Laboratory)

OBJECTIVE

The objectives of this task are to (a) quantify the oxygen partial pressure (pO_2) in argon and helium environments of various different purity levels, (b) determine the oxygen uptake of V-Cr-Ti alloys as a function of temperature and pO_2 in the exposure environment, (c) examine the microstructural characteristics of oxide scales and oxygen trapped at the grain boundaries in the substrate alloys, and (d) establish performance relationships between exposure time, exposure temperature, and oxygen concentration in the alloy for application in fusion reactor systems.

SUMMARY

A test program is in progress at Argonne National Laboratory to evaluate the effect of pO_2 in the exposure environment on oxygen uptake, scaling kinetics, and scale microstructure in V-Cr-Ti alloys. The data indicate that the oxidation process follows parabolic kinetics in all of the environments used in the present study. From the weight change data, parabolic rate constants were evaluated as a function of temperature and exposure environment. The temperature dependence of the parabolic rate constants was described by an Arrhenius relationship. Activation energy for the oxidation process was fairly constant in the oxygen pressure range of1 x 10^{-6} to 1 x 10^{-1} torr for both the alloys. The activation energy for oxidation in air was significantly lower than in low-pO_2 environments, and for oxidation in pure O_2 at 760 torr was much lower than in low-pO_2 environments. X-ray diffraction analysis of the specimens showed that VO_2 was the dominant phase in low-pO_2 environments, while V_2O_5 was dominant in air and in pure oxygen at 760 torr.

EXPERIMENTAL PROGRAM

The heats of vanadium alloy selected for the study had nominal compositions of V-5 wt.%Cr-5 wt.%Ti (designated BL-63) and V-4 wt.%Cr-4 wt.%Ti (designated BL-71). Sheets of the alloys were annealed for 1 h at 1050°C prior to oxidation and tensile testing. Coupon specimens that measured ≈15 x 7.5 x 1 mm were used for the oxidation studies. Our earlier work on oxidation of these alloys was conducted in air in a thermogravimetric test apparatus at temperatures of 300 to 650°C [1-4]. During this period, several oxidation experiments were conducted on V-4Cr-4Ti (identified as 44) and V-5Cr-5Ti (identified as 55) alloys at oxygen partial pressures in the range 1 x 10^{-6} to 1 x 10^{-1} torr at several temperatures in the range of 400-700°C. Specimens were exposed to these environments in a reaction chamber with an O_2 bleed/feed system to maintain the desired oxygen pressure. Specimens were retrieved periodically and weighed, and dimensions were measured. The oxidation products were examined by X-ray diffraction (XRD) analysis, and the scale microstructures were evaluated by scanning electron microscopy (SEM) and energy-dispersive X-ray analysis. In addition, microhardness was measured on cross sections of exposed specimens to obtain hardness profiles and correlate them with oxygen concentration in the alloys.

RESULTS AND DISCUSSION

Extensive studies were conducted on the oxidation kinetics of 44 and 55 alloys in air over a temperature range of 300-650°C; the results were reported earlier [1-4]. The current oxidation study on the two alloys involves exposure of the alloys to low-pO_2 environments. Tables 1 and 2 list the experimental variables such as pO_2 in the exposure environment and test temperature used in several of the experiments for the 44 and 55 alloys, respectively. Figure 1 shows normalized weight changes (in mg/mm^2) for 44 and 55 alloys after exposure at 500°C in several low-pO_2 environments. Similar data were obtained at other temperatures listed in Tables 1 and 2.

Table 1. Oxidation parameters of V-4Cr-4Ti alloy at various oxygen pressures

Oxygen pressure (torr)	Temperature (°C)	k_p ($mg^2mm^{-4}h^{-1}$)	k_o ($mg^2mm^{-4}h^{-1}$)	Q (kJ/mol)
5×10^{-6}	500	1.6×10^{-7}	8.6×10^4	174
	600	3.1×10^{-6}		
	700	4.1×10^{-5}		
5×10^{-4}	500	1.3×10^{-7}	3.9×10^5	185
	600	3.2×10^{-6}		
	700	4.7×10^{-5}		
1×10^{-1}	500	4.0×10^{-8}	9.9×10^5	199
	600	1.7×10^{-6}		
	700	2.2×10^{-5}		
160 (air)	400	1.4×10^{-7}	2.2×10^2	120
	500	1.1×10^{-6}		
	575	1.2×10^{-5}		
	620	2.5×10^{-5}		
760	450	2.6 x10-8	1.5×10^9	231
	525	1.6×10^{-6}		
	600	1.9×10^{-5}		

Table 2. Oxidation parameters of V-5Cr-5Ti alloy at various oxygen pressures

Oxygen Pressure (torr)	Temperature (°C)	k_p ($mg^2mm^{-4}h^{-1}$)	k_o ($mg^2mm^{-4}h^{-1}$)	Q (kJ/mol)
5×10^{-6}	500	1.3×10^{-7}	1.4×10^4	168
	600	2.1×10^{-7}		
	700	3.4×10^{-5}		
5×10^{-4}	500	1.1×10^{-7}	8.8×10^4	177
	600	2.3×10^{-6}		
	700	3.0×10^{-5}		
1×10^{-1}	500	3.6×10^{-8}	4.8×10^5	195
	600	9.4×10^{-7}		
	700	1.8×10^{-5}		
160 (air)	400	8.9×10^{-8}	2.3×10^3	137
	500	7.1×10^{-7}		
	575	4.6×10^{-6}		
	650	9.0×10^{-5}		
760	450	1.8×10^{-8}	1.5×10^{10}	247
	525	1.7×10^{-6}		
	600	2.0×10^{-5}		

The weight change data were correlated with time by the parabolic relationship $w^2 = k_p.t$, where w is weight change, t is exposure time, and k_p is a parabolic rate constant. The k_p values calculated for various exposure conditions are also listed in Tables 1 and 2. Figure 2 shows the temperature dependence of the parabolic rate constant for the two alloys exposed to different oxygen pressures. The temperature dependence of the parabolic rate constant was described by the

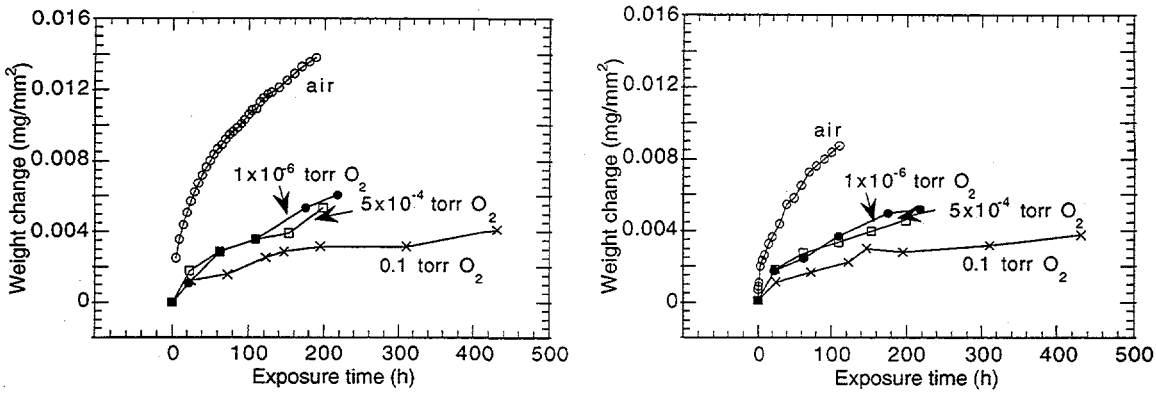

Fig. 1. Thermogravimetric weight change data for 44 (left) and 55 (right) alloys after exposure in low-pO_2 and air environments at 500°C.

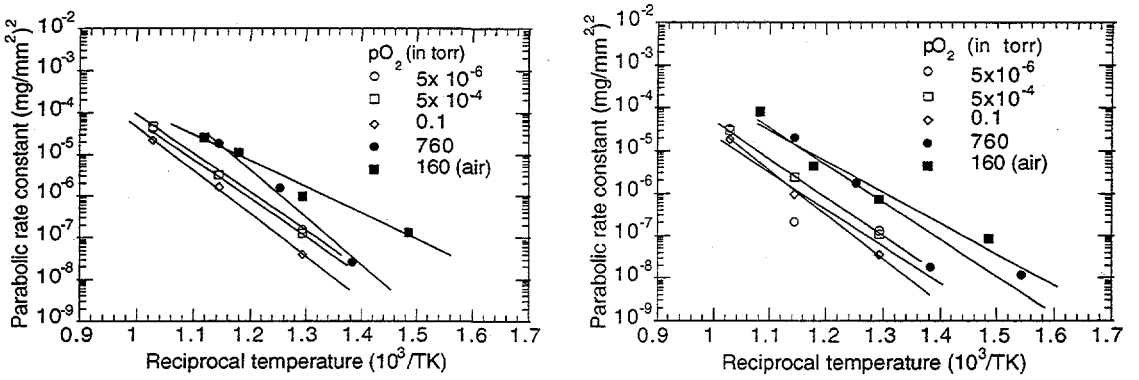

Fig. 2. Temperature dependence of parabolic rate constant for oxygen uptake of 44 (left) and 55 (right) alloys in several low-pO_2 and air environments.

relationship $k_p = k_o \exp[-Q/(RT)]$, where k_o is a preexponential term, Q is the activation energy for the oxidation process, R is a gas constant, and T is absolute temperature. The values for k_o and Q, calculated from the best fit of the experimental data at various oxygen pressures, are also listed in Tables 1 and 2. The results show that the activation energy for the oxidation process is fairly constant at oxygen pressures in the range 10^{-6} to 10^{-1} torr. The activation energy calculated from data in the air tests was significantly lower, and in pure oxygen-tests (at 760 torr) was substantially higher than the values obtained at low-pO_2 conditions. It is not clear at present whether the type of scale (predominantly V_2O_5) that forms in air and in pure O_2 is the cause for this difference.

Table 3 lists the XRD data obtained on several specimens exposed to various oxygen pressures. The oxide VO_2 was the predominant phase that formed in both alloys when exposed to oxygen pressures in the range 10^{-6} to 10^{-1} torr. V_2O_5 was the primary phase in specimens exposed to air and to pure oxygen at 760 torr. Detailed microstructural evaluation of the specimens, especially those exposed to low-pO_2 environments, is in progress to characterize the role of pO_2 variation on the morphology of the scales and substrate penetration of oxygen.

REFERENCES

[1] K. Natesan and W. K. Soppet, "Effect of Oxidation on Tensile Properties of a V-5Cr-5Ti Alloy," Proc. 2nd Intl. Conf. Heat-Resistant Materials, eds. K. Natesan, P. Ganesan, and G. Lai, ASM International, Sept. 11-14, 1995, Gatlinburg, TN, 375.

Table 3. Phases identified[a] in V-4Cr-4Ti and V-5Cr-5Ti alloys by X-ray diffraction[b] analysis

Oxygen pressure (Torr)	Temperature (°C)	Phases identified in alloy	
		V-4Cr-4Ti	V-5Cr-5Ti
5×10^{-6}	500	VO_2, TiV_4O_{10}	VO_2, V_2O_4
	700	VO2, $V_{16}O_3$, CrV_2O_6	V_2O_5, V_5O_9, $V_{16}O_3$
5×10^{-4}	600	VO_2, V_2O_4, $CrVO_4$	VO_2, V_2O_4, $CrVO_4$
	700	VO_2, V_2O_4, $CrVO_4$	VO_2, V_2O_4, $CrVO_4$
0.1	600	VO_2, V_2O_4	VO_2, V_2O_4, $CrVO_4$
	700	VO_2, V_2O_4, $CrVO_4$	VO_2, V_2O_4, $CrVO_4$
760	375	V_2O_5, V_2O_3, V_3O_7	V_2O_5, VO_2, V_2O_4
	600	V_2O_5, $V_2Ti_3O_9$, VO_2	V_2O_5, VO_2

[a]Phases identified in all samples oxidized in air (pO_2 = 160 torr) were primarily V_2O_5.

[b]X-ray diffraction unit was run at 1 degree/min.

[2] K. Natesan and W. K. Soppet, "Effect of Oxygen and Oxidation on Tensile Properties of V-5Cr-5Ti Alloy," J. Nucl. Mater., 233-237 (1996) 482-487.

[3] K. Natesan and M. Uz, "Oxidation Kinetics and Microstructure of V-(4-5) wt.%Cr-(4-5) wt.%Ti Alloys Exposed to Air at 300-650°C," Fusion Reactor Materials Semiannual Progress Report for Period Ending June 30, 1996, DOE/ER-0313/20, p. 105, Oct. 1996.

[4]. M. Uz, K. Natesan, and V. B. Hang, J. Nucl. Mater. 245 (1997) 191-200.

MICROSTRUCTURAL CHARACTERIZATION OF EXTERNAL AND INTERNAL OXIDE PRODUCTS ON V-4Cr-4Ti -- B. A. Pint, P. M. Rice, L.D. Chitwood, J. H. DeVan and J. R. DiStefano (Oak Ridge National Laboratory)

OBJECTIVE

The objective of this task is to assess the reaction product and microstructural changes in V-4Cr-4Ti after exposure to 1atm air and low oxygen pressures (10^{-6}Torr) at 500°C. In both cases, transmission electron microscopy (TEM) is required to observe the fine structure of the oxide scale and grain boundaries of the internally-oxidized vanadium alloys.

SUMMARY

Air oxidation of V-4Cr-4Ti at 500°C at 1atm resulted in the formation of a thin (100-150nm) external vanadium nitride layer which was identified beneath a thicker (1.5μm) vanadium oxide scale. This nitride layer would only be detected by high-resolution, analytical electron microscopy techniques. Subsequent tests comparing room temperature tensile properties for exposure in laboratory air, dry air and dry oxygen at 1atm showed more embrittlement in air than in O_2. Internal oxidation of coarse-grained V-4Cr-4Ti at low oxygen pressures at 500°C was followed by TEM examination. In a sample with a 1400ppmw O addition, which is sufficient to reduce the ductility to near zero, there appeared to be an oxygen denuded zone (150-250nm) near the grain boundaries with precipitates at the grain boundaries and uniform ultra-fine (<5nm) oxygen particles in the matrix. In a similar O-loaded specimen that was subsequently annealed for 4h at 950°C to restore ductility, large oxide particles were observed in the matrix and at the grain boundaries.

PROGRESS AND STATUS

Experimental Procedure

All of the experiments were conducted on V-4Cr-4Ti. Exposures at 1atm were conducted in a tube furnace at 500°C using both coupons and tensile specimens annealed at 1050°C. Experiments were conducted in both laboratory air (tube open) or in dry air or dry oxygen using endcaps on the tube and bottled gas. After exposure, samples were analyzed using scanning electron microscopy (SEM), glancing angle x-ray diffraction (GAXRD) and TEM equipped with an energy dispersive x-ray diffractometer (EDX) and an electron energy loss spectrometer (EELS).

Low pressure exposures were conducted in an ultra high vacuum system with a leak valve to achieve an oxygen partial pressure of 10^{-6}Torr. Prior to exposure the samples were annealed at 1200°C to produce a relatively large grain size. The coupons were exposed for 48h at 500°C and then annealed for 100h at 600°C to homogenize the oxygen distribution. Oxygen content was determined by weighing the samples before and after exposure. Half of the samples were then annealed for 4h at 950°C, which has been shown to restore room temperature ductility to O-loaded vanadium[1].

TEM samples were prepared in parallel (using electropolishing) near the center of the specimen and in section by a combination of mechanical thinning and precision ion milling.

Results and Discussion

Using SEM, the oxide on V-4Cr-4Ti after 200h at 500°C was observed to have blade-like grains and to be 3-4μm thick. GAXRD identified V_2O_5, V_6O_{13}, and V_4O_9 but no nitrides or Cr- or Ti-rich phases. Using cross-sectional TEM/EELS, four regions were identified in the reaction layer (Figure 1) with grain size, d:

(A) 0-150nm from metal; no visible crystal structure	d<5nm	VN_x layer
(B) 150-450nm from metal; very fine grains	d=10-15nm	VO_n
(C) 450-1μm from metal; small grains	d≈50nm	VO_y
(D) >1μm from metal; large, faulted grains	d=250-1000nm	VO_z

The inner layer (Figure 2) was analyzed by EELS in order to determine the presence of nitrogen and the absence of any Ti enrichment (Figure 3). Some particles were observed at the metal-oxide interface but also were not enriched in Ti. No segregation was observed at oxide grain boundaries. There was a slight reduction in the O/V ratio towards the gas interface which may reflect the different oxides observed by GAXRD. Previous work had suggested a titanium nitride layer formed during air oxidation[2]. The vanadium nitride layer observed in the present work is too thin to be detected by conventional microprobe, SEM/EDX analysis or GAXRD.

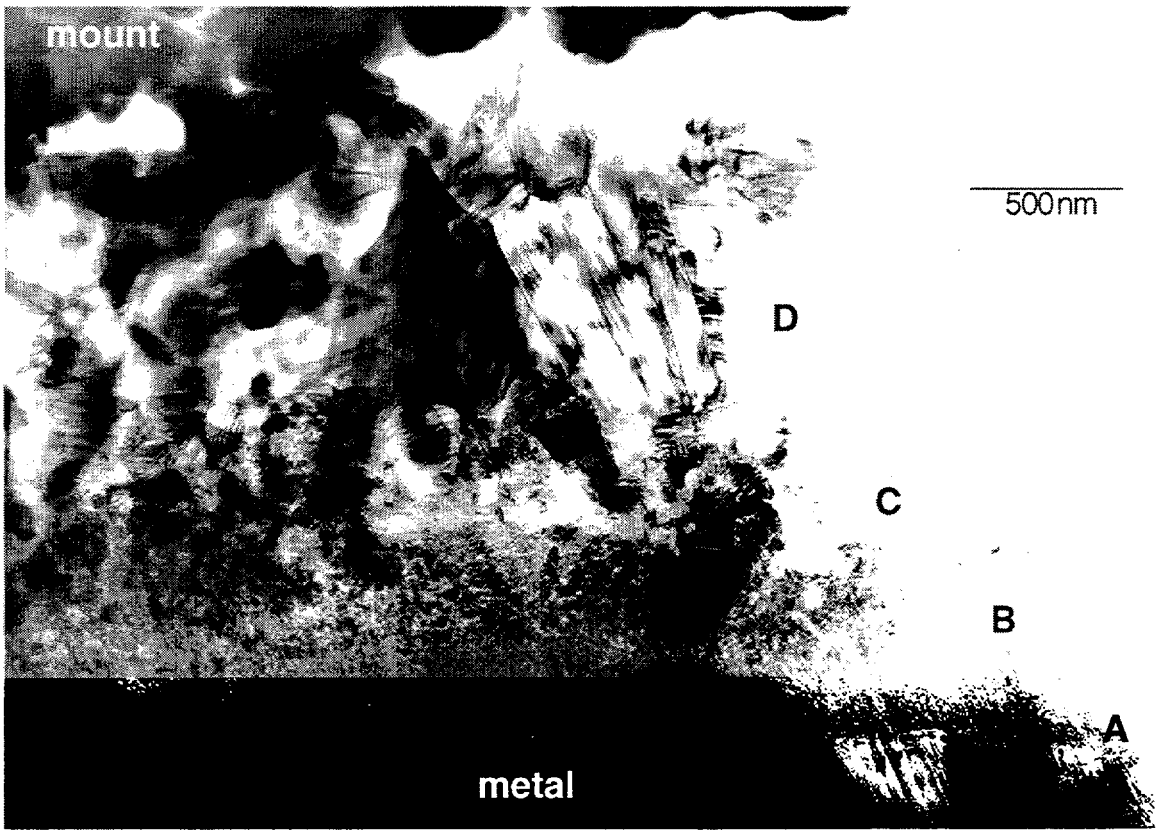

Figure 1. TEM bright field image of the external scale formed on V-4Cr-4Ti after 200h at 500°C. Four distinct layers are identified with increasing grain size. Layer A is rich in nitrogen while the others are vanadium oxide.

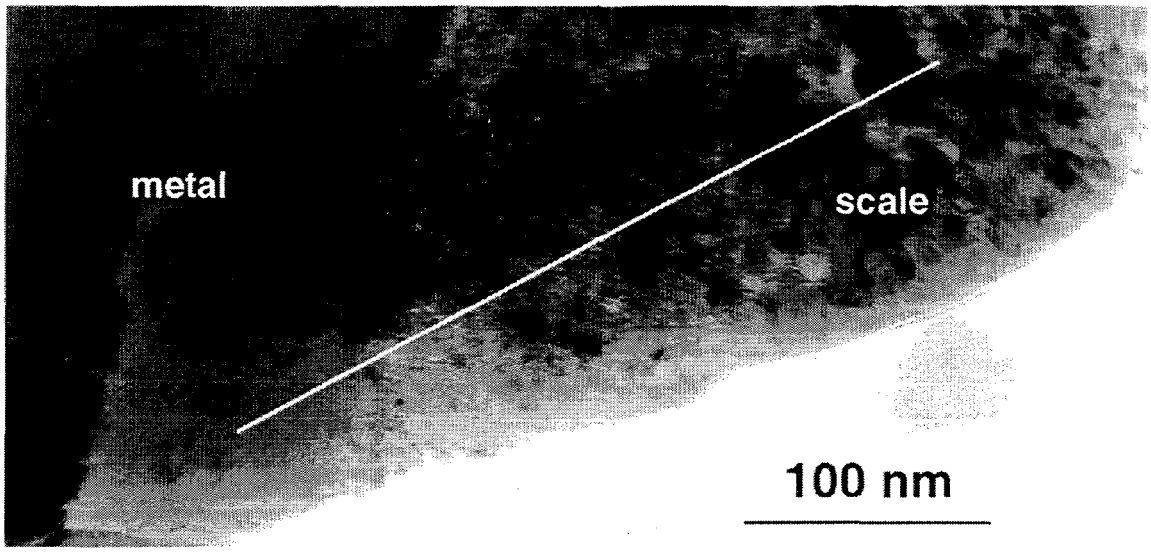

Figure 2. TEM bright field image of the external scale formed on V-4Cr-4Ti after 200h at 500°C. The line denotes where the EELS profile in Figure 3 was performed across the metal-scale interface.

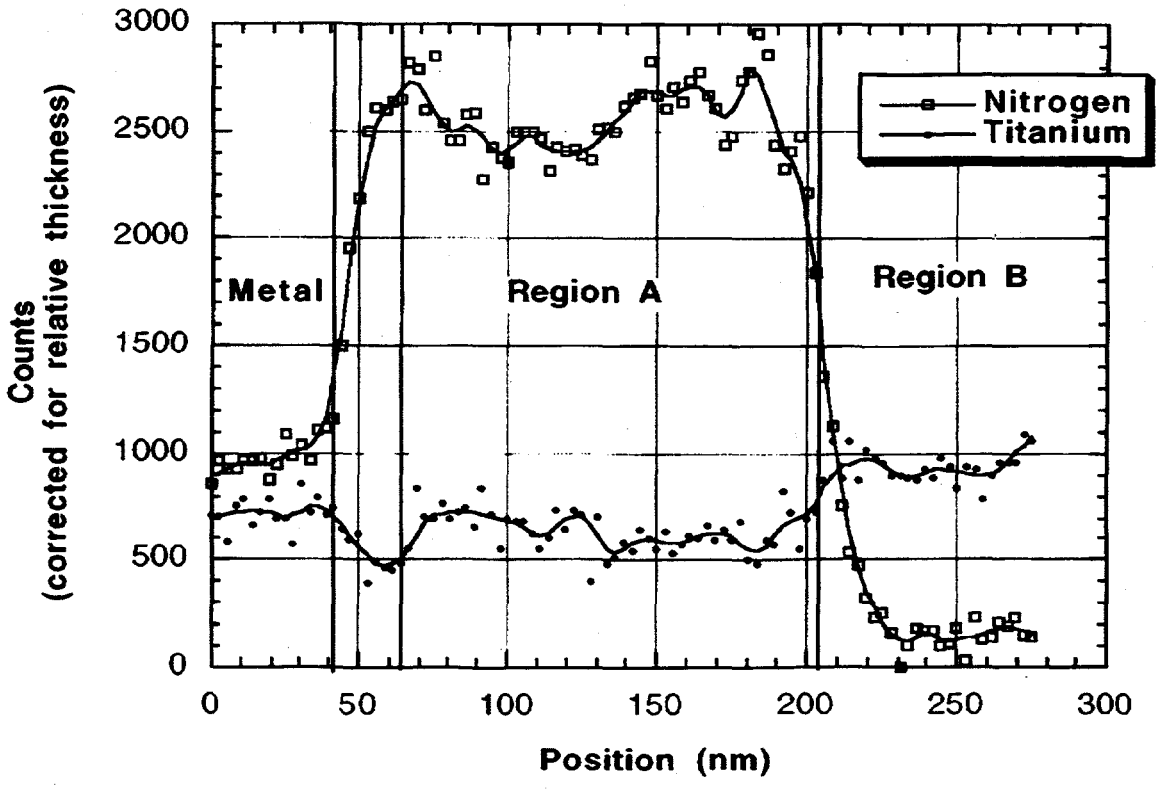

Figure 3. TEM/EELS profile along the line marked in Figure 2. The layer is clearly enriched in N but not in Ti, indicating a VN_x layer. Regions A and B correspond to the layers indicated in Figure 1.

In order to explore any possible role of this nitride layer in affecting diffusion through the external scale or changing the mechanical properties of the underlying alloy, coupons and tensile specimens were exposed in flowing dry oxygen, dry air and laboratory air. In general, there was little difference between the rate of weight gain in air and oxygen indicating that the nitride layer was neither accelerating or decelerating the rate of corrosion. Relative to changes in mechanical properties, there was slightly more embrittlement in laboratory air than in dry O_2 (Table I). Results for dry air were in between, possibly indicating a slight effect of water vapor on embrittlement.

Table I. Mechanical properties results comparing samples exposed at 500°C in 1atm of laboratory air and oxygen. The laboratory air exposure appeared to embrittle the alloy more than a comparable exposure in dry oxygen. The dry air exposure had an intermediate effect.

	Dry Oxygen		Laboratory Air		Dry Air	
Oxidation Time:	Yield Strength (MPa)	Elongation (%)	Yield Strength (MPa)	Elongation (%)	Yield Strength (MPa)	Elongation (%)
50h	338, 356	17.8, 20.3	405, 405	14.2, 14.4	355,371	17.7,18.2
200h	355, 376	11.4, 12.0	386,413	7.2, 7.7	383,395	8.3,9.5

Characterization of the vanadium alloy after exposure to a low oxygen partial pressure at 500°C (1434ppmw O addition) revealed a uniform matrix microstructure with ultra fine oxide precipitates, Figure 4. At every grain boundary there was a 100-200nm denuded zone adjacent to the boundary and precipitates along the boundary. Chemical analysis has not yet been performed on these precipitates.

After a similar oxygen addition at 10^{-6}Torr and 500°C (1160ppmw O) followed by annealing for 4h at 950°C, the microstructure was remarkably different (Figure 5). Large TiO_x precipitates were observed in the matrix and on the boundaries. The platelets followed established crytallographic patterns in the vanadium alloy. The denuded zone appeared to be retained adjacent to the grain boundaries indicating that the fine precipitates prior to annealing at 950°C grew significantly. The 950°C anneal improves the room temperature alloy ductility from near 0% to 15-20%. Without the anneal, the fracture is predominantly intergranular. Since grain boundary precipitates are observed before and after annealing, their presence does not appear to affect ductility. The denuded zone adjacent to the boundaries has been proposed to be an important factor in the failure[3] and future work will focus on characterizing the composition of this region.

REFERENCES

1. J. R. DiStefano and J. H. DeVan, J. Nucl. Mater. 249 (1997) 150.
2. K. Natesan and W. K. Soppet, in Heat Resistant Materials II, K. Natesan, P. Ganesan and G. Lai, eds. (ASM International, Materials Park, OH, 1995) p.375.
3. C. T. Liu, H. Inouye, R. W. Carpenter, Met. Trans. 4 (1973) 1839.

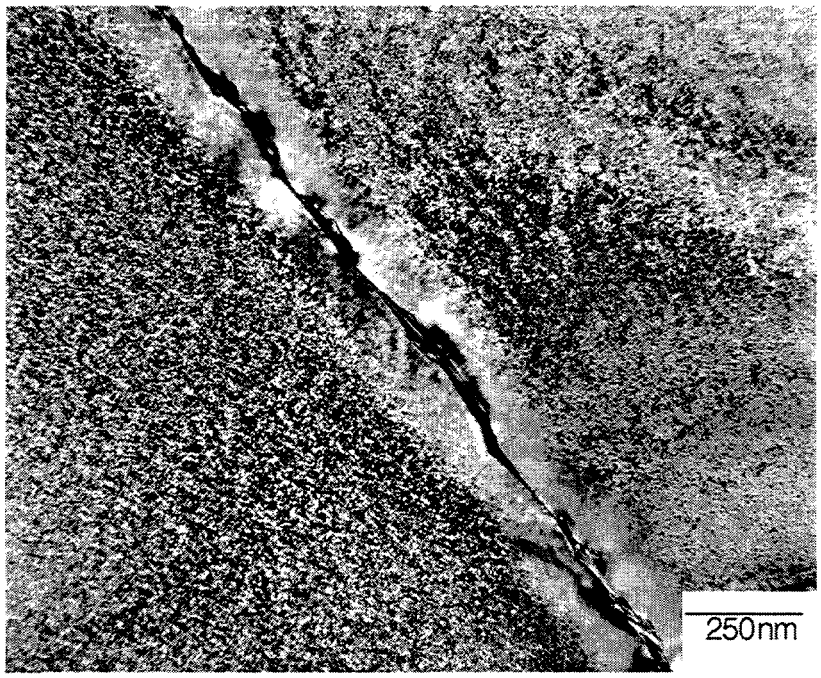

Figure 4. TEM bright field image of V-4Cr-4Ti after the addition of 1434ppmw O at 500°C and annealing for 100h at 600°C. Fine oxide precipitates are observed in the matrix and larger precipitates at the grain boundary which is surrounded by a precipitate denuded zone.

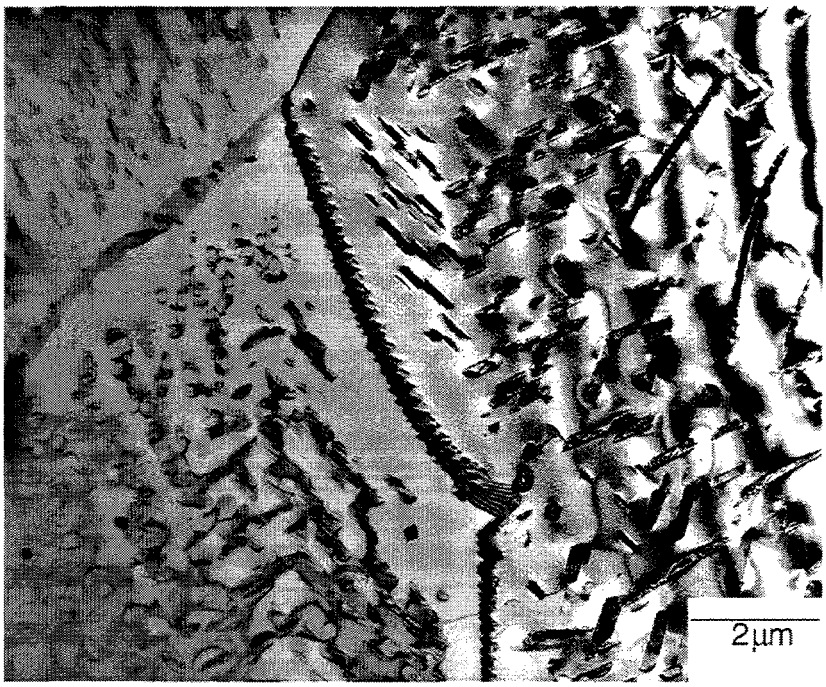

Figure 5. TEM bright field image of a similarly exposed alloy as in Figure 4 (1160ppmw O) but including a 4h at 950°C anneal. In this case, large oxide precipitates are observed.

DEVELOPMENT OF ELECTRICALLY INSULATING CaOCOATINGS*

K. Natesan, C. B. Reed, M. Uz, and D. L. Rink (Argonne National Laboratory)

OBJECTIVE

The objectives of this task are to (a) develop electrically insulating coatings with emphasis on basic understanding of the thermodynamic conditions and kinetics of coating development in lithium-calcium mixtures to achieve stable in-situ coatings of CaO in an Li/Li-Ca environment; (b) perform detailed postexposure analysis of the surface layers using several electron-optical techniques to characterize the elemental and phase compositions, quantify stratification in the layers, and establish the role of compositional changes on the coating defect and microstrucure; (c) measure the electrical resistance of the coatings, initially external to Li and eventually in situ in an Li environment; and (d) establish optimal procedures from the standpoint of sample preparation, Li chemistry, exposure time and temperature, and sequence of operations to obtain reliable and reproducible coatings with adequate electrical resistance for use in an Li environment.

SUMMARY

A systematic study has been initiated to develop electrically insulating CaO coatings by vapor phase transport and by in-situ formation in a liquid Li environment. Several experiments were conducted in vapor transport studies with variations in process temperature, time, specimen location, specimen surface preparation, and pretreatment. Several of the coatings obtained by this method exhibited Ca concentration in the range of 60-95 wt.% on the surface. However, coating thickness has not been very uniform among several samples exposed in the same run or even within the same sample. The coatings developed in these early tests degraded after 24 h exposure to Li at 500°C. Additional experiments are underway to develop better-adhering and more dense coatings by this method.

A program to develop in-situ CaO coatings in Li has been initiated, and the first set of capsule tests at 800°C in three different Li-Ca mixtures will be completed in early July. Specimens included in the run are bare V-4Cr-4Ti alloy, specimens with a grit-blasted surface and O-precharged in 99.999% Ar, polished specimens precharged in a 99.999% Ar and 5000 ppm O_2-N_2 mixture, and prealuminized V-5Cr-5Ti alloy preoxidized in a 5000 ppm O_2-N_2 mixture. Additional experiments at lower temperatures are planned.

BACKGROUND

The primary mechanism of CaO coating formation involves reactions of oxygen from the V alloy with Ca dissolved in the Li. Several variables in this reaction include temperature, time, O concentration in V alloy, and Ca concentration in Li. Scoping tests were conducted by exposing small coupons of V alloys at several temperatures to Li containing various concentrations of Ca(2-50 at %). Generally, increasing the O concentration in the surface regions of V by exposure to low-pressure O_2 environments before exposure to the Li-Ca alloy produced thicker oxide reaction products, but the results were not conclusive. A range of conditions (temperature, oxygen pressure during preexposure, and time) were investigated to determine which provided the best coating characteristics. In the initial investigations, CaO coatings were obtained by reacting V alloy coupons in Li-Ca in small capsules (<100 cm^3) at temperatures of 400-800°C. CaO coatings ≈10 mm thick were successfully formed on V alloys; however, microcracks were observed at room temperature but spallation of the coating was not observed.

Additional tests were conducted to evaluate the effects of thermal cycling/thermal shock resistance of these coatings. Results obtained by thermally cycling the Li-Ca vessel indicated that the ceramic resistivity behavior (increase in resistivity with a decrease in temperature) initially observed was followed by a sharp decrease in resistivity. This decrease was attributed to cracking of the coating. An increase in temperature was followed by an increase in resistance, with a

possibility of self-healing of the cracks. These types of tests were duplicated with similar results. Significant resistances ($R \times A > 1000\ \Omega \cdot cm^2$) were obtained from these "self-healing" experiments; however, the resistance values were typically much lower than the initial high resistance values.

Results obtained in these experiments were considered sufficiently encouraging to initiate tests on a larger scale, i.e., a static test vessel containing ≈3 L of Li-Ca alloy. These tests were conducted with rod-type (pencil) specimens with rounded ends in an attempt to minimize adherence of residual liquid metal to the end of the specimens and possible cracking at sharp corners. V-alloy specimens exposed to Li-Ca at temperatures of 400-500°C exhibited a modest increase in resistance with time, indicating formation of a very thin insulating coating.

A range of coating parameters (exposure temperatures and times, Ca content in Li, and pre-oxidation) were investigated. These tests were conducted primarily with only a few percent Ca in Li; however, the general procedure remained the same; viz., oxygenation of the V alloy surface, exposure of the specimen to the Li-Ca alloy, gas-phase oxidation of the Ca coating in most cases, and subsequent compatibility or resistance testing in the Li (usually in Li with low Ca content to ensure self-healing). These tests generally were less successful than the previous tests, typically exhibiting thinner coatings and much lower resistance values from *in-situ* measurements. Resistance measurements by probes indicated high resistance over most of the surface at room temperature, whereas many specimens exhibited very low resistance immediately upon insertion into the liquid. In several cases, relatively high resistance was observed initially, but upon exposure to Li-Ca, electrical shorting (low resistance) occurred after <1 hr exposure.

An important result obtained in the analysis of the coatings involved the composition, in particular the amount of V in the insulator coating. High resistivity was observed at Ca/V ratios above 4, whereas significantly lower resistivities were obtained when V concentration in the coatings significantly exceeded 20% of the total cation concentration.

In general, the CaO coatings developed on pencil samples exhibited several microscopic and macroscopic defects upon reexposure to Li, and in-situ resistance measurements of these specimens showed significant decreases to values corresponding to those of uncoated specimens within a few minutes of exposure. Several specimens were examined for defects by masking different regions of specimens with Ga; resistance measurements were conducted on the masked specimens. The results showed high resistance at several locations, indicating that the specimens develop some type of layer with high resistance but that this layer is neither uniform nor defect-free.

Several of these specimens were also examined by scanning electron microscopy (SEM) and energy dispersive X-ray (EDX) techniques, both radially at a given elevation of the specimen and axially at various elevations. Results indicated that the innermost region, adjacent to the V alloy, consisted of V, Ca, and O (and probably Li, which was removed during the alcohol wash). Away from this region and toward the Li side of the interface, the specimens exhibited a higher Ca content and lower V content than in the interior. It is possible that this layer consisted of Li, Ca, and O. Based on the results for the microstructures and elemental compositions of several of the pencil specimens, we concluded that the specimens develop layers that contain Ca and have high resistance at several locations within a specimen. Such a layer does not consist of CaO alone, but displays a gradation in composition with high V/low Ca at the specimen surface and high Ca/low V at the Li side of the interface. We was also concluded that the thickness of the coating is an important variable and that initially a high-V layer develops over which a high-Ca layer (which imparts high resistance) develops. It appears that coating thicknesses in excess of 5 μm may be needed to obtain high resistance values and to ensure adequate coverage in all areas.

In addition to evaluating the coatings developed on the pencil specimens, several coupon specimens of V alloy were were exposed to the same procedure as the pencil specimens, except

that the Ca-deposited specimens were oxidized at 550 or 625°C. The surface layers on these specimens (without cleaning treatment in alcohol and water) were examined by SEM/EDX and X-ray diffraction (XRD). The results showed that at both temperatures, the outer layer consisted of Li_2O, CaO, and Li_3VO_4, and the inner layer contained CaO and Li_3VO_4. Only trace amounts of Li_2O and V_4O_9 were detected in the inner layer. SEM analysis of the specimen oxidized at 550°C indicated isolated patches of Ca-rich oxide and V-rich oxide in the innerlayer. Similar analysis of the specimen oxidized at 625°C indicated predominantly a single phase consistingof Ca, V, and O. Of course, some Li might have been present in these regions (since Li could not be detected by EDX) but the amount should be small, based on the XRD results for the inner layers. The results indicate that oxidation at temperatures <550°C may be beneficial in developing Ca-rich oxides.

Several experimental and procedural variables can have a significant effect on the chemical and mechanical integrity of the coating. The key experimental variables are oxygen precharging time, temperature, and oxygen content of the gas phase; time, temperature, composition and concentration of impurities (e.g., H and N) in the Li-Ca mixture used for exposure of oxygen-precharged specimens; and time, temperature, and oxygen content of the gas phase for oxidation of the Ca-rich surface layer. In addition, the procedural variables include removal of Li after exposure to the Li-Ca mixture and before oxidation, method of Li removal (such as alcohol dissolution, vacuum distillation, etc.), time allowed to drip-clean a sample of Li by allowing the sample to remain in the cover-gas environment above the liquid Li, and removal of residual Li/Li_2O from the sample after Ca oxidation.

EXPERIMENTAL PROGRAM

In an attempt to gain further fundamental understanding, experiments were conducted to develop Ca-rich coatings by using the pack diffusion process. The experiments involved exposure of specimens of V alloy to a pack of fine pellets of Ca at temperatures of 700-800°C. The specimens were either completely enclosed within the pack or were hung above the pack material in a static Ar environment. The vapor pressure of Ca at 700-800°C is sufficient to deposit a layer of Ca on the specimens. Several geometrical arrangements were examined to obtain a uniform coating of Ca on the specimens, which were typically coupons measuring 5 to 10 x 5 x 1 mm. The alloys included V-4Cr-4Ti and V-5Cr-5Ti with and without prealuminization. In addition, specimens with various surface roughnesses (polished, grit-blasted, etc.) were included in the evaluation. Deposition of Mg at ≈600°C was also attempted.

The present work on *in-situ* development of insulator coatings emphasizes a basic understanding of the thermodynamic conditions and kinetics of coating development in Li-Ca mixtures to achieve stable coatings of CaO *in-situ* in a Li/Li-Ca environment. The effort will concentrate on detailed postexposure analysis of the surface layers by using several electron-optical techniques to characterize the elemental and phase compositions, quantify stratification in the layers, and establish the role of compositional changes on coating defects, microstructure, and resistance. Among the key variables that influence coating formation and its chemical and mechanical integrity are test temperature, test time, Li chemistry (including Ca content and trace element concentrations), and alloy chemistry and specimen surface preparation. To ensure flexibility in adjusting the Li-Ca chemistry in these experiments, capsules containing ≈50-60 mL of Li-Ca mixture are used for specimen exposure. The capsules are made of Type 300 series stainless steel with a retractable 0.25-mm-thick liner of V-alloy to avoid Li contact with the steel. The materials to be evaluated include V-4Cr-4Ti in bare and prealuminized conditions with various surface treatments in terms of roughness and precharging of in surface regions with oxygen.

Initially, four exposure temperatures of 800, 700, 600, and 500°C are used for exposure of samples in the Li-Ca mixture. Ca contents of the mixture are10-90 wt.% and exposure time will be ≈100 h. At Ca contents >30 wt.%, the $CaLi_2$ phase is expected to deposit as the specimens are cooled, while at a Ca content of 10 wt.%, β-Ca and α-Ca deposits are expected. A furnace has been set up to accommodate at least five capsules simultaneously at a given temperature. The

capsules undergo rocking action to enable mixing of the Ca-Li mixture at elevated temperature. Upon exposure, the capsules will be inverted at temperature to drain the specimens of Li and will then be cooled to room temperature. Subsequently, the capsules will be cut open, the sample holder will be retrieved, and the specimens (without removing the Li) will undergo postexposure examination. Both XRD and SEM with EDX will be the primary modes for analyzing the specimens. After the specimens are examined, they will be oxidized in either air or 99.999% Ar to oxidize the Ca into CaO. The specimens will be reexamined after oxidation to determine the thickness, composition, and morphology of the oxide layer, and its adhesion characteristics with the substrate at room temperature. The results will be correlated with the metallurgical and chemical structures of the coatings and the lithium exposure conditions. These initial capsule experiments will establish the roles of several key variables on coating development.

RESULTS AND DISCUSSION

Coating by Vapor Phase Transport

Figure 1 shows typical photomicrographs of the surface of a Ca-deposited V-4Cr-4Ti specimen and of the surface and cross section of the specimen after oxidation. The layer in the cross-section photograph is ≈8-10 μm thick. EDX analysis of the specimen showed a gradation in composition, with more V in the alloy side of the scale and more Ca in the outer region of the scale. The Ca content range was 0-70 wt.% as a function of depth.

In all, 12 runs were conducted for deposition of Ca or Ca/Mg on V alloys. After deposition, the specimens were oxidized in air at 600°C to convert the deposited metals into their respective oxides. The specimens exhibited insulating characteristics after this oxidation step. Detailed XRD studies on these specimens showed good correlation between high resistance values (at room temperature) and high Ca/Mg concentration in oxide form. Ca concentrations in the range of 60-80 wt.% were obtained in several specimens. However, coating thicknesses in a given specimen or between different specimens were not uniform; in some specimens, coating spallation was noted. Several promising coated specimens were exposed to high-purity Li at 500°C for 24-48 h to examine coating integrity. In some cases, Li-exposed specimens exhibited high resistance but only in isolated locations, indicating that the coating deteriorated during Li exposure. XRD analysis of the Li-exposed specimens showed some indication that locations with high Ca content had high resistance at room temperature. The results also showed that Ca and/or Mg deposition via vapor phase transport is possible but that the thickness of the coating and adhesive bonding of the coating with the substrate produced by this method may need further improvement. Additional experiments with several procedural modifications are currently in progress.

In-Situ Coating Development

Figure 2 shows the specimen assembly used in the capsule experiments in Li. The first capsule experiment at 800°C has been initiated. Three Li-Ca mixtures with Ca contents of 39, 59, and 85 wt.% were used in this run. Specimens included in the run are bare V-4Cr-4Ti alloy, a specimen with a grit-blasted surface and O-precharged in 99.999% Ar, polished specimens precharged in 99.999% Ar and 5000 ppm O_2-N_2 mixture, and a prealuminized V-5Cr-5Ti alloy preoxidized in 5000 ppm O_2-N_2 mixture. The first run is expected to be completed in early July.

REFERENCES

1. J. H. Park, T. Domenico, G. Dragel, and R. W. Clark, "Development of Electrical Insulator Coatings for Fusion Power Applications," Fusion Eng. Design 27 (1995) 682.

2. J. H. Park and G. Dragel, "Fabrication and Performance Testing of CaO Insulator Coatings on V-5%Cr-5%Ti in Liquid Lithium," Fusion Reactor Materials Semiannual Progress Report for the Period Ending September 30, 1994, DOE/ER-0313/17 (1994) pp. 231-244.

3. J. H. Park and T. F. Kassner, J. Nucl. Mater. 233-237 (1996) 476-481.

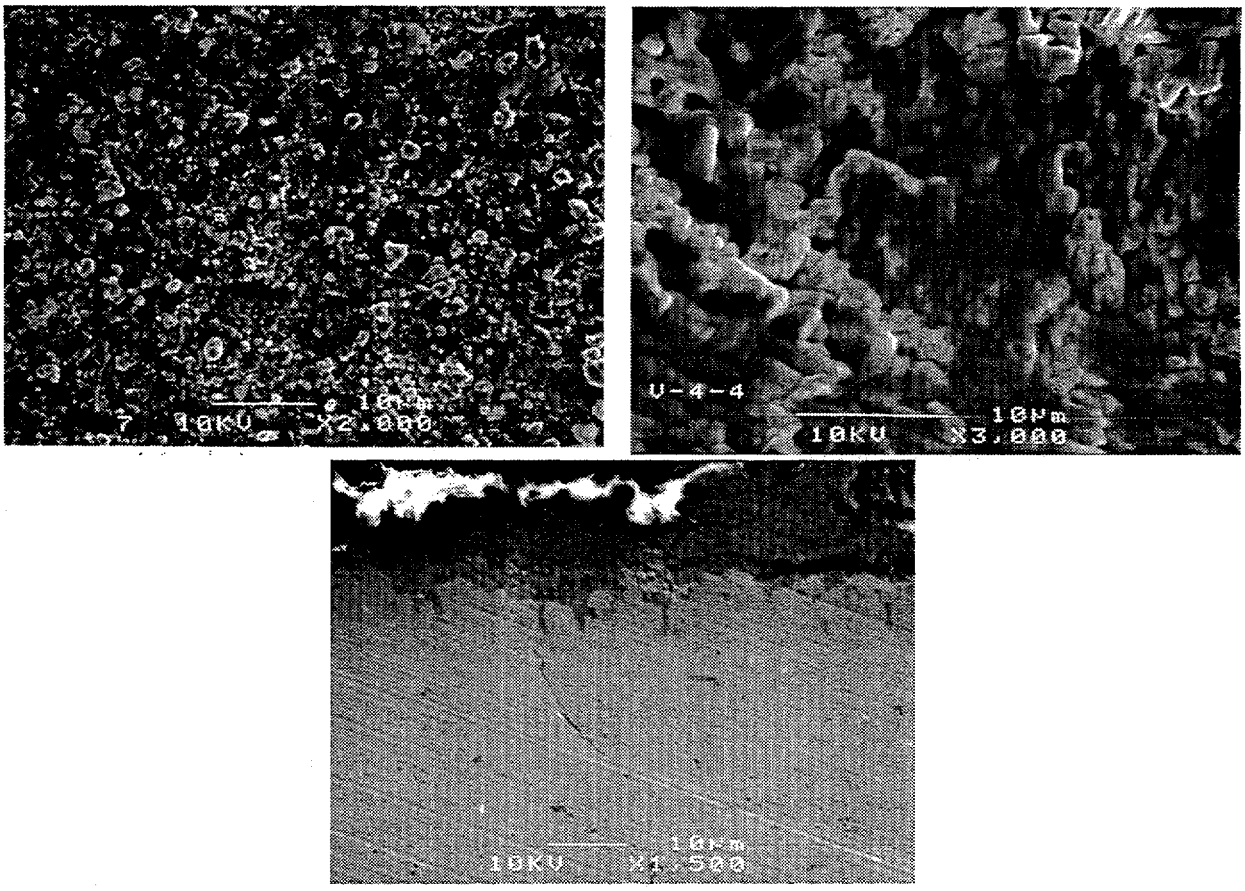

Fig.1. SEM photomicrographs of surface of V-4Cr-4Ti alloy after Ca deposition (top left), after oxidation of Ca deposited specimen (top right), and cross section of oxidized specimen (bottom).

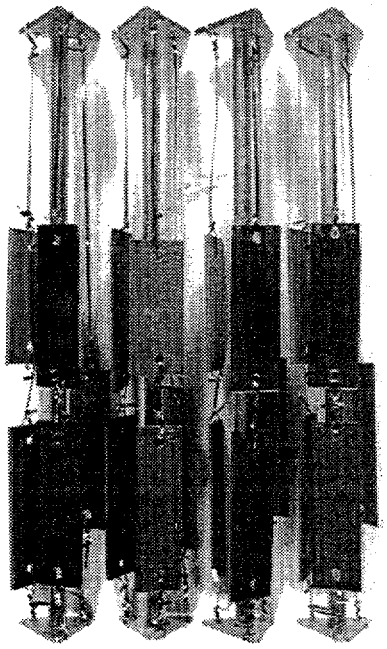

Fig. 2. Macrophotograph of specimen assembly used for in-situ coating development in liquid Li.

LASER-WELDED V-Cr-Ti ALLOYS: MICROSTRUCTURAL AND MECHANICAL PROPERTIES*

K. Natesan, D. L. Smith, Z. Xu, and K. H. Leong (Argonne National Laboratory)

OBJECTIVE

The objectives of this task are to (a) determine the optimal parameters for laser beam welding of sheets of V-Cr-Ti alloys; (b) examine the microstructural characteristics of welded sections, including base metal, heat-affected-region, and core of weld; (c) evaluate the influence of different postwelding heat treatments on microstructural characteristics; and (d) evaluate the mechanical properties, such as tensile and impact, of laser-welded materials.

SUMMARY

A systematic study has been in progress at Argonne National Laboratory to examine the use of YaG or CO_2 lasers to weld sheet materials of V-Cr-Ti alloys and to characterize the microstructural and mechanical properties of the laser-welded materials. In addition, several postwelding heat treatments are being applied to the welded samples to evaluate their benefits, if any, to the structure and properties of the weldments. Hardness measurements are made across the welded regions of different samples to evaluate differences in the characteristics of various weldments. Several weldments were used to fabricate specimens for four-point bend tests. Several additional weldments were made with a YaG laser; here, the emphasis was on determining the optimal weld parameters to achieve deep penetration in the welds. A preliminary assessment was then made of the weldments on the basis of microstructure, hardness profiles, and defects.

EXPERIMENTAL PROGRAM

The heat of vanadium alloy selected for the study had a nominal composition of V-4 wt.%Cr-4 wt.%Ti (designated as BL-71). A 4-mm-thick sheet of the alloy was used for the welding study. Earlier microstructural and hardness results were reported on several different welds made under the same welding conditions but subsequently given different postwelding heat treatments [1]. Several of these weldments were fabricated into four-point bend specimens with a cross section of 3.3 mm and a shallow notch in the base-metal side of the welded specimen. Testing of these specimens at several temperatures (such as that of liquid N_2, -100°C, -40°C, and room temperature) is in progress. During this period, welding of an additional 4-mm-thick plate was continued with a YaG laser in a pulsed mode. The purpose of this study is to increase the weld penetration from ≈1.2 mm in earlier welded samples to as deep as 3 mm or more. Welding parameters such as power, traverse speed, pulse time, overlap, etc., are being examined to obtain optimal quality in the final weld. Samples are being cut from different welds, and detailed microstructural analysis and hardness measurements are being conducted.

RESULTS AND DISCUSSION

In the last report, we presented microstructural and hardness data on laser-welded V-4Cr-4Ti alloy. The welds in that study were made with a YaG laser in a continuous mode of operation and with an spatial overlap of 90-95%. Weld depth in those specimens was ≈1.2 mm and the hardness profiles showed a substantial increase (from an initial Vickers hardness value of 170-180, upto 240-280) in the center of the weld; this value stayed high across almost the entire weld zone. The earlier effort directed at developing an acceptable postwelding heat treatment showed that five passes of diffused laser beam over the welded region softened the weld material, especially in the root region of the weld. Several of these post-welded materials have been used to fabricate four-point bend specimens and testing of these specimens, at room temperature has begun.

During this period, YaG laser welding of additional 4-mm-thick plate was continued in the pulsed mode. The purpose of this study is to increase the weld penetration from ≈1.2 mm in earlier-welded samples to as deep as 3 mm or more. In the pulsed mode, the energy of the laser beam was increased to values of 4.5-5.5 J/ms; pulse width was maintained at 3 ms. Further, workpiece traverse speed was varied between 10 and 40 mm/s.

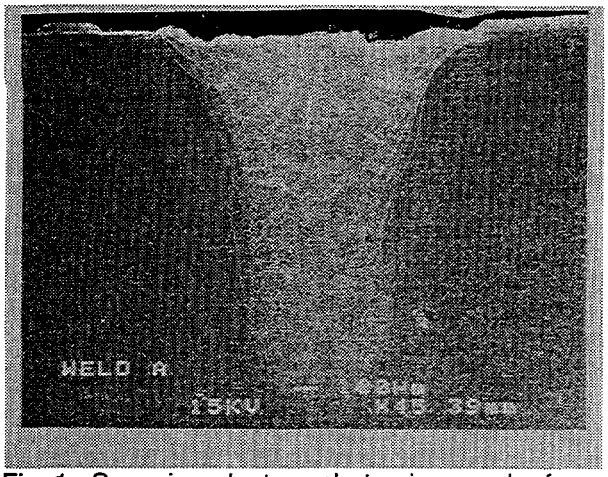

Fig. 1. Scanning electron photomicrograph of weldment A.

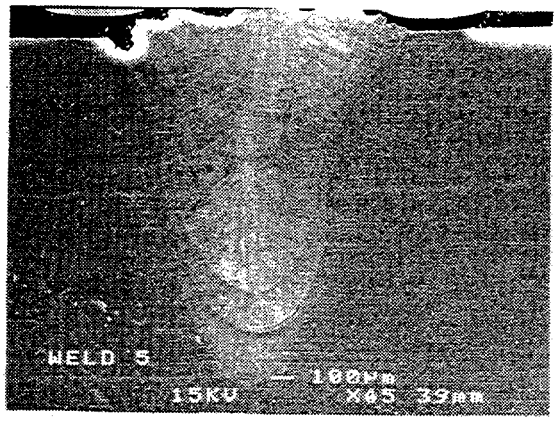

Fig. 2. Scanning electron photomicrograph of weldment 5.

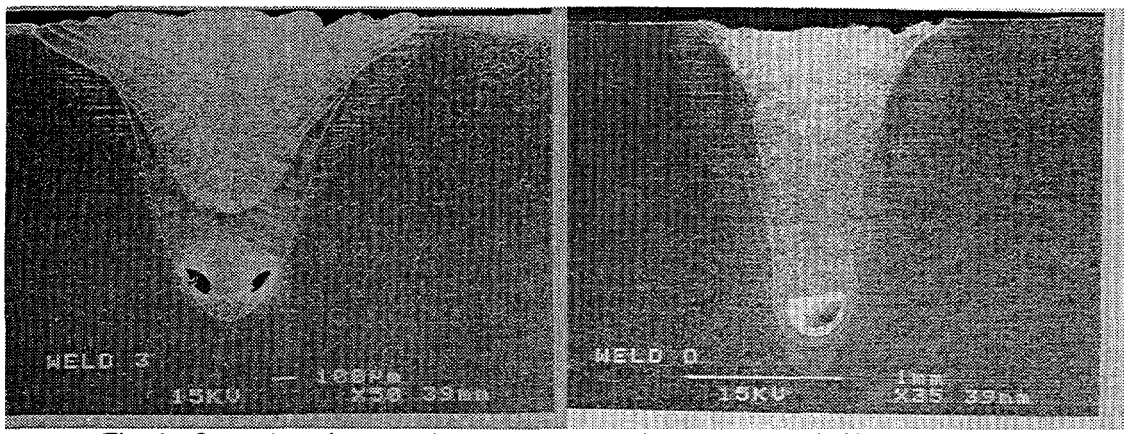

Fig. 3. Scanning electron photomicrograph of weldments 3 (left) and D (right).

Four different welds (identified as A, B, C, and D) were made with laser energy in the range of 5.2-5.5 J/ms. The work piece traversed at 30, 20, 25, and 25 mm/s for welds A, B, C, and D, respectively. Penetration depths in the four welds were 1.80, 2.46, 2.23, and 2.23 mm, respectively. Weld A, with a shallower penetration, exhibited almost no porosity, and no undue material transfer to the weld surface was noted. Figure 1 shows a low-magnification photomicrograph of weld A. Welds B, C, and D, with somewhat deeper penetration, exhibited root porosity in the weld as shown in Figure 2 for weld D, which is typical of the others. The cause of this root porosity and the adjustments to welding parameters in order to eliminate this defect are under investigation.

Six different welds (identified as 1, 2, 3, 4, 5, and 6) were made with laser energy of 4.2 J/ms; pulse width was maintained at 3 ms. The workpiece traverse speed was maintained at 40 mm/s for welds 1, 2, and 3, while for welds 4, 5, and 6 it was 30 mm/s. Depths of penetration in the six welds were 1,26, 1.37, 1.26, 1.65, 1.78, and 1.59 mm, respectively. Examination of the weld cross sections showed that 4, 5, and 6 had almost no macroporosity, but 1, 2, and 3 exhibited significant root porosity. Figure 3 shows low-magnification photomicrographs of weld 3 (typical of 1, 2, and 3) and weld 5 (typical of 4, 5, and 6). Two conclusions can be drawn from this study. First, to increase the depth of penetration of the weld, the laser energy must be higher; it is evident that the higher energy used for welds A-D resulted in deeper penetration than the lower power used for welds 1-6. Second, the traverse speed of the workpiece seems to have an effect (which may not display a 1:1 correlation) on development of root porosity in the welds. For example, welds 1-3 (made with a traverse speed of 40 mm/s) showed defects, while welds 4-6 (with a traverse speed of 30 mm/s) exhibited no defects. On the other hand, weld A (made with a laser energy of 5.2 J/ms and traverse speed of 30 mm/s) was defect-free, while welds B and C, (made with the same laser

energy and traverse speeds of 20 and 25 mm/s) exhibited defects.

In all the welds (1-6 and A-D) made in the present batch, variation in grain size from the root of the weld to the free-surface region was lower than that observed in welds reported earlier [1]. Also, in the earlier welds, the grains near the top of the weld were columnar, which is dictated by rate of cooling and solidification, but such a structure was confined to only the center region in the present welds. Further, the weld cross section shows definite contours evenly spaced in the root region, similar to those observed in earlier welds. The dark- and light-shaded grains in the weld are due to differences in grain orientation, and virtually no compositional variations were observed between these grains.

Vickers hardness measurements were made on defectless weldments in the surface-to-root direction and from the centerline of the weld toward the base metal at half-width of the weld. Measurements were on welds A, 4, 5, and 6. Figure 4 shows the hardness profiles for these welds in the two directions. The results indicate that in three of the four (specimens A, 4, and 6) weldments, the hardness value gradually decreases from ≈200-210 in the centerline of the weld to ≈160 in the base metal over a distance of 0.4-0.5 mm from the weld centerline. In these three weldments, hardness was fairly constant in the range of 200-210 from the surface-to-root direction, after which a sharp drop in hardness is noted. Weldment 5 exhibited unusually high hardness in both directions, the cause for which is not known at present. The results also indicate that substantial additional work is needed to evaluate the role of different weld parameters on the structure and property of the laser weldments.

REFERENCES

1. K. Natesan, D. L. Smith, P. G. Sanders, and K. H. Leong, "Laser-Welded V-Cr-Ti Alloys: Microstructural and Mechanical Properties," Fusion Reactor Materials Progress Report for the Period Ending December 31, 1997, Argonne National Laboratory, DOE/ER-0313/23, p. 136, March 1998.

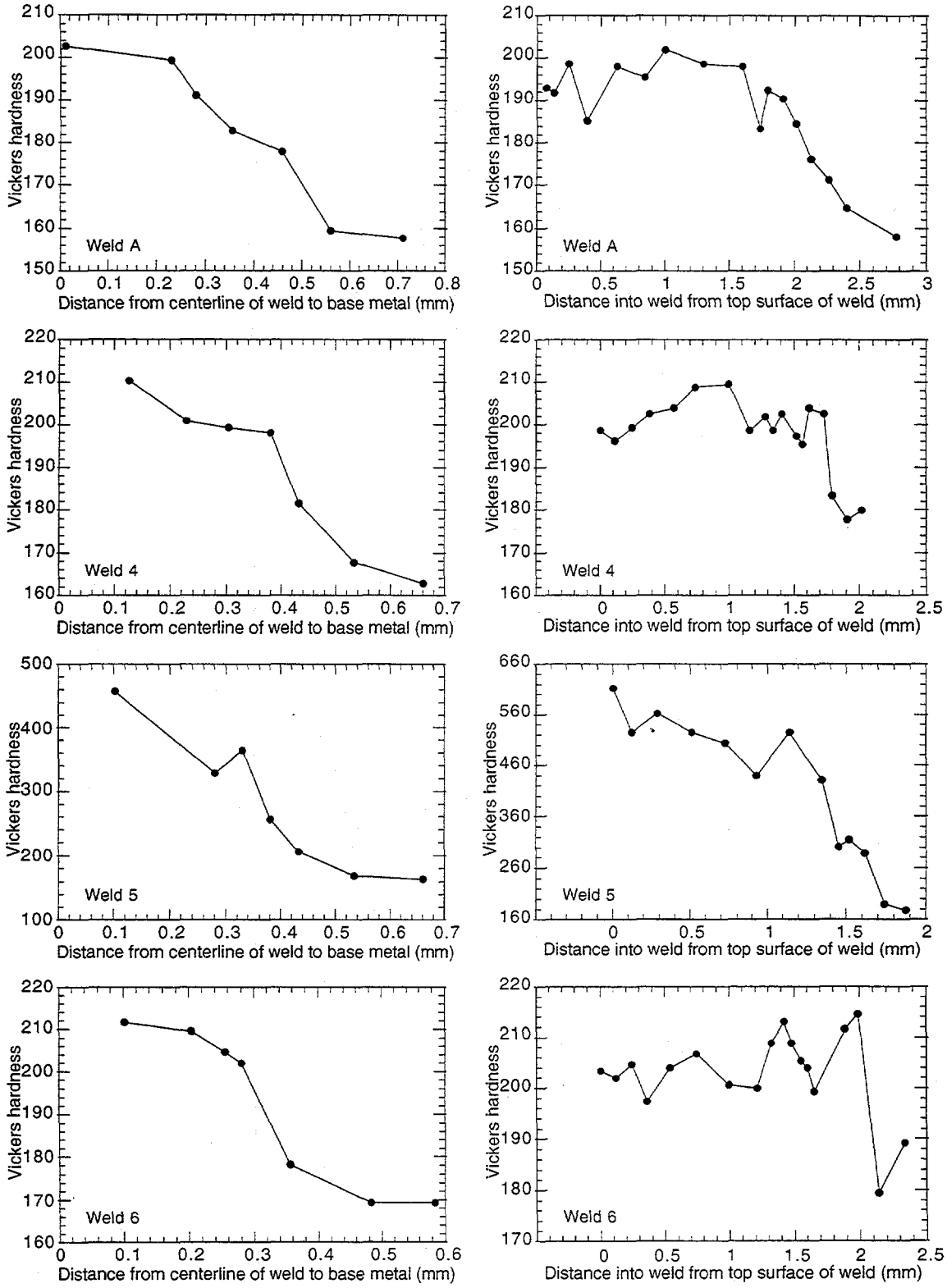

Fig. 4. Vickers hardness profiles for weldments A, 4, 5, and 6 in surface-to-root direction and from weld centerline-to-base metal at half-width of weldment.

2.0 SILICON CARBIDE COMPOSITE MATERIALS

THERMOPHYSICAL AND MECHANICAL PROPERTIES OF SiC/SiC COMPOSITES — S. J. Zinkle and L. L. Snead (Oak Ridge National Laboratory)

OBJECTIVE

The objective of this report is to summarize the thermophysical and mechanical properties of SiC/SiC composites in order to provide a reference design basis for the Advanced Power EXtraction (APEX) project.

SUMMARY

The key thermophysical and mechanical properties for SiC/SiC composites are summarized, including temperature-dependent tensile properties, elastic constants, thermal conductivity, thermal expansion, and specific heat. The effects of neutron irradiation on the thermal conductivity and dimensional stability (volumetric swelling, creep) of SiC is discussed. The estimated lower and upper temperatures limits for structural applications in high power density fusion applications are 400 and 1000°C due to thermal conductivity degradation and void swelling considerations, respectively. Further data are needed to more accurately determine these estimated temperature limits.

PROGRESS AND STATUS

Introduction

In order to provide a reference design basis for the Advanced Power EXtraction (APEX) project, published data on the thermophysical and mechanical properties of SiC/SiC composites have been compiled. Property data for SiC/SiC composites are not contained in conventional fusion materials data bases such as the ITER Materials Properties Handbook (IMPH). The IMPH should be used as the reference point for design calculations if the full property database is included in a future version of the Handbook. Several recent publications have reviewed many of the general considerations associated with fusion engineering designs that incorporate SiC/SiC composites, and can be consulted for additional information [1-6].

The engineering database for SiC/SiC composites is very limited, since large quantities of high-quality fibers such as Hi-Nicalon type S (produced by Nippon Carbon) have not been available up to the present time. Much of the published data has been generated on composites fabricated with lower-quality fibers such as ceramic grade Nicalon (cg-Nicalon). Table 1 compares some properties of several commercial SiC-based fibers and bulk SiC. The chemical composition, density, elastic constants, thermal conductivity, and neutron radiation resistance of cg-Nicalon (which contains 11.7 wt.% O and has a C/Si atomic ratio of 1.31) [7] is considerably different from that of bulk crystalline SiC which is present in the matrix. The nonstoichiometric Hi-Nicalon fibers (containing 0.5 wt.% O and a C/Si atomic ratio of 1.39) [7] are also considerably different from SiC. Recent fibers such as Hi-Nicalon Type S (0.2 wt.% O and a C/Si atomic ratio of 1.05) [7] and Dow Sylramic (0.8 wt.% O and a C/Si atomic ratio of 1.0) [8] are expected to produce improved composite properties in the unirradiated and irradiated condition compared to cg-Nicalon and Hi-Nicalon.

Table 1. Comparison of properties of commercial SiC-based fibers and bulk SiC [7-10].

	cg-Nicalon	Hi-Nicalon	Hi-Nicalon type S	Dow Sylramic	Bulk SiC
Diameter (μm)	14	12-14	12	10	—
Tensile strength (GPa)	2.0-3.0	2.8-3.4	2.6-2.7	2.8-3.4	~0.1
Elastic modulus (GPa)	170-220	270	420	390-400	460
Density (g/cm^3)	2.55	2.74	2.98-3.10	3.0-3.10	3.25
Coefficient of thermal expansion ($10^{-6}/K$)	3.2	3.5	—	5.4	4.0
Thermal conductivity at 20°C (W/m-K)	1.5	4	18	40-45	100-350
Oxygen content (wt.%)	11.7	0.5	0.2	0.8	0.0
C/Si atomic ratio	1.31	1.39	1.05	1.0	1.0

Yield and ultimate tensile strength (unirradiated)

Most of the available data on ceramic matrix composites have been generated using flexural bend strength tests (3- or 4-point bending). Although bend tests are useful for qualitative screening in order to investigate variations in processing parameters, uniaxial tensile testing is preferred for the generation of an engineering data base. Ceramic matrix composites are engineered to produce a moderate amount of fiber pullout during deformation. Extensive fiber pullout produces low ultimate tensile strengths, whereas limited fiber pullout leads to brittle failure modes similar to monolithic ceramics. The optimum tensile toughness generally occurs in ceramic composites with tensile elongations on the order of ~0.2 to 0.5%. Therefore, the 0.2% "yield" strength, which is commonly used for tensile testing in metals, is comparable to the composite ultimate tensile strength. A more appropriate "yield" strength for ceramic matrix composites is the proportional stress limit (corresponding to the onset of matrix microcracking), although the location of the proportional limit is subject to relatively large experimental uncertainty.

The ultimate tensile strength of several different grades of SiC/SiC composites containing 40 vol.% fibers (0/90 weave) have been recently measured by tensile testing [2,11]. The UTS ranged from 200 to 280 MPa at room temperature and from 228 to 254 MPa at 1000°C for two different types of SiC/SiC composites fabricated with cg-Nicalon fibers. A room temperature UTS of 217 MPa was measured for a composite fabricated using Hi-Nicalon fibers. The corresponding proportional stress limits were 55 to 70 MPa for room temperature tests of SiC/SiC composites fabricated with cg-Nicalon fibers. Tensile data are not yet available for SiC/SiC composites fabricated with Hi-Nicalon type S or comparable advanced SiC fibers, although composite strengths comparable to that of present-day SiC/SiC composites are expected from theoretical considerations. Specifically, the matrix microcracking stress would be expected to be slightly higher with Hi-Nicalon type S fibers (due to a better match with the elastic modulus of the matrix), whereas the ultimate tensile strength would be reduced due to the lower fiber strength of prototype versions of Hi-Nicalon type S (cf. Table 1).

Yield and ultimate strength (irradiated)

Neutron irradiation can produce a significant decrease in the flexural strength of SiC/SiC composites fabricated with cg-Nicalon fibers, due to neutron-induced densification of the fibers which causes debonding at the matrix/fiber interfaces [5,12]. Strength decreases up to a factor of two have been observed in some cases. Improved irradiated behavior is predicted for composites containing SiC-based fibers which have demonstrated better resistance to neutron irradiation, such as Hi-Nicalon, MER-999, and Dow Corning Sylramic fibers [6,9,13,14]. Experimental studies on composites fabricated with advanced fibers are need to determine whether there is any significant degradation of mechanical strength in these materials.

Elastic constants

The elastic constants for SiC/SiC composites depend on the details of the fabrication procedure. Fibers such as cg-Nicalon have elastic constants which are considerably different from crystalline SiC, and therefore strongly influence the measured elastic constants of the composite. In addition, matrix porosity (typically ~8 to 10%) also affects the elastic constants of the composite. The room temperature Young's moduli of SiC-based fibers range from ~200 GPa for cg-Nicalon to 270 GPa for Hi-Nicalon, and 420 GPa and 400 GPa for Hi-Nicalon Type S and Dow Sylramic [7,8,13]. The corresponding Young's modulus for bulk crystalline SiC varies from 460 GPa at room temperature to 435 GPa at 1000°C [15]. Somewhat lower values of 415 GPa (20°C) to 392 GPa (1000°C) have been reported for sintered alpha-SiC [16]. According to measurements obtained during tensile testing, the Young's modulus for a given SiC/SiC composite shows a very slight (5%) increase as the temperature is increased from 20 to 1000°C [11]. The quantitative values are strongly dependent on the fabrication process, with values for cg-Nicalon fiber-based composites (40 vol.% fibers) ranging from 141 to 215 GPa at room temperature [11]. The corresponding Young's modulus for a SiC/SiC composite fabricated with Hi-Nicalon fibers was 270 GPa. Values approaching 400 GPa would be expected for high-quality, low-porosity SiC/SiC composites fabricated with Sylramic or Hi-Nicalon type S fibers. Matrix microcracking (in composites subjected to stress above the proportional limit of ~70 MPa) will cause a reduction in the elastic modulus [17]. The shear modulus for bulk (sintered) alpha-SiC is 179 GPa at room temperature and 169 GPa at 1000°C [16]. Poisson's ratio for bulk SiC is ~0.18 between 20 and 1000°C [15,16].

Thermal expansion, specific heat and thermal conductivity

The themophysical properties of SiC/SiC composites (particularly thermal conductivity) are also dependent on the fabrication procedure. The measured instantaneous coefficient of thermal expansion (α_{th}) for SiC/SiC composites fabricated with cg-Nicalon fibers (40 vol.% fibers) are 2.5-3 ppm/°C, with no pronounced dependence on temperature between 20 and 1000°C [11,18]. The lower value refers to through-thickness measurements on 2-D composites, and the higher value refers to in-plane measurements. The bulk SiC value is 2.2 ppm/°C at room temperature and 5.0 ppm/°C at 1000°C, with an average value between 20 and 1000°C of 4.0 ppm/°C [15,16]. The specific heat at constant pressure (C_P) varies from 620-640 J/kg-K at 20°C to 1200-1250 J/kg-K at 1000°C for both monolithic SiC and SiC/SiC composites, where the higher values refer to bulk SiC [2,11,15,16,19]. The most rapid changes in the specific heat occur at temperatures below 200°C, which corresponds to about one-half of the Debye temperature for SiC (~900 K). The specific heat for bulk SiC is 1134 J/kg-K at 500°C and 1189 J/kg-K at 700°C [15,19]. A slightly less pronounced variation in the temperature-dependent specific heat has been recently presented for sintered alpha-SiC [16]. The source of the specific heat discrepancy between ref. [16] and refs. [15,19] is uncertain.

The thermal conductivity of SiC/SiC composites is strongly dependent on the processing conditions, type of fiber, and fiber architecture. The upper limit for thermal conductivity corresponds to that obtained in single crystal and high-purity CVD SiC, with maximum values of ~320 W/m-K at room temperature and 78 W/m-K at 1000°C (Fig. 1). The thermal conductivity of most of the currently-available commercial fibers is significantly lower than that of bulk high-purity SiC, and therefore the fibers typically do not make a large contribution to the conductivity of the composite. The thermal conductivity of SiC-based fibers at 20-500°C varies from ~1.5 W/m-K for cg-Nicalon and ~4 W/m-K for Hi-Nicalon to 18 W/m-K for Hi-Nicalon type S [20]. Room temperature thermal conductivities for recently developed Sylramic and Tyranno-SA fibers are ~40-45 and 64 W/m-K, respectively [8,21]. The in-plane thermal conductivity for a 2-D (0/90) plain weave SiC/SiC composite fabricated from cg-Nicalon fibers (40 vol.%) and a CVI matrix (10% porosity) varies from ~19 W/m-K at 20°C to 8 W/m-K at 1000°C [2,11]. The corresponding through-thickness conductivities are 9 and 3 W/m-K, respectively. The through-thickness thermal conductivity for a 2-D (0/90) plain weave SiC/SiC composite fabricated from Hi-Nicalon fibers (40 vol.%) and a CVI matrix (10% porosity) is ~15 W/m-K at 20°C [2,11]. SiC/SiC composites with

transverse thermal conductivities of ~75 W/m-K at room temperature and 30-35 W/m-K at 1000°C have recently been fabricated using CVR and reaction sintering techniques [22,23].

Unlike the case for metals (where the thermal conductivity is dominated by electron transport), irradiation can cause a significant reduction in the thermal conductivity of SiC/SiC composites. The degradation is particularly large at low irradiation temperatures, as shown in Fig. 2. An approach to saturation occurs at low damage levels during low temperature (<300°C) irradiation. The fluence dependence of the conductivity degradation has not yet been studied at high temperatures. The limited existing data base indicates the irradiated thermal conductivity at high irradiation temperatures (~1000°C) is about 25 to 50% of the unirradiated value for bulk SiC irradiated to damage levels greater than 20 dpa [5,24]. The largest relative degradation in thermal conductivity is observed in materials with the highest initial thermal conductivity, i.e., the irradiated thermal conductivity in bulk tends to approach a similar value irrespective of the unirradiated thermal conductivity.

The values shown in Fig. 2 represent the upper limit of expected thermal conductivities for irradiated SiC/SiC composites, since impurities and porosity introduced during fabrication of composites (as well as fiber-matrix phonon scattering and the lower conductivity of existing fibers compared to bulk SiC) would cause a degradation in the conductivity of SiC/SiC composites compared to monolithic SiC. Due to the poor radiation stability of cg-Nicalon, very low irradiated thermal conductivity data are obtained in composites fabricated with this type of fiber [24]. A more realistic estimate of the irradiated thermal conductivity of composites with advanced (radiation resistant) fibers is obtained by using data obtained on composites fabricated with SiC whiskers (SiC_w). The thermal conductivity of a SiC/SiC_w composite irradiated to 43 dpa at 1000°C ranged from ~12.5 W/m-K at 400°C to ~10 W/m-K at 1000°C [24]. The effects of fusion-relevant helium generation rates on the thermal conductivity of irradiated SiC has not been investigated.

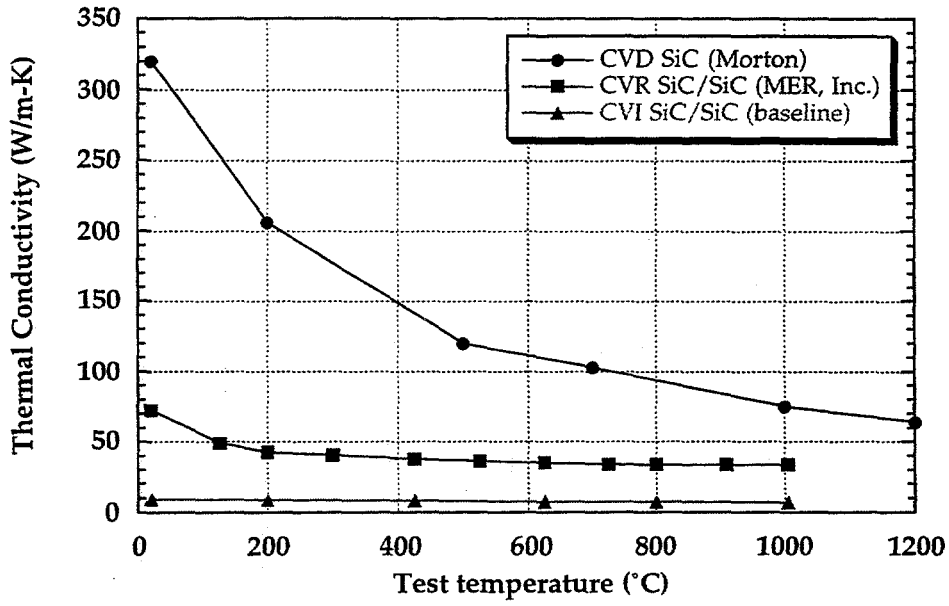

Fig. 1. Comparison of the transverse thermal conductivity of monolithic CVD SiC and two grades of SiC/SiC composites [15,23].

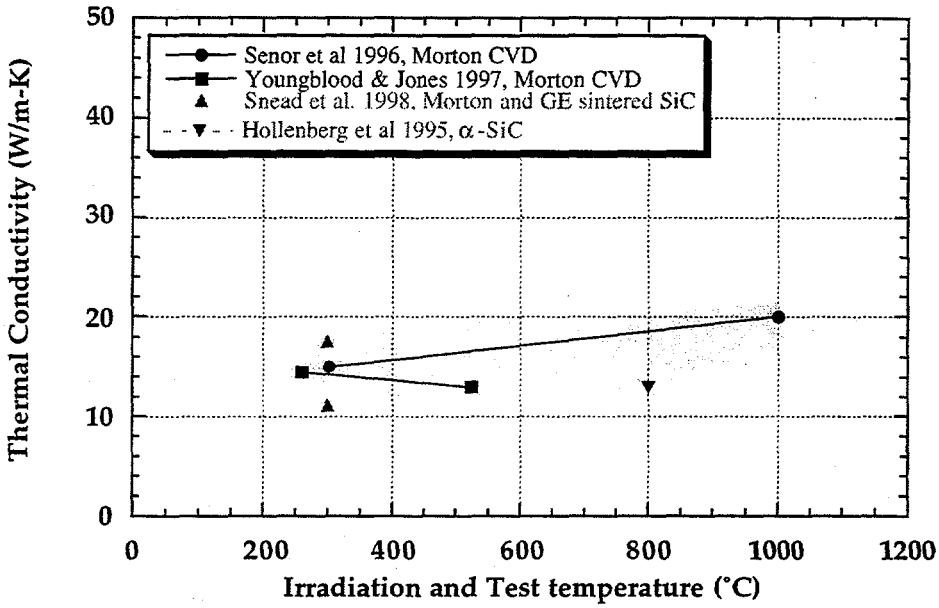

Fig. 2. Effect of neutron irradiation on the thermal conductivity of bulk SiC [6,24-26]. The studies in refs. [24-26] were performed on samples irradiated to 25-43 dpa, whereas the data by Snead et al. were obtained on samples irradiated to 0.1 dpa.

Irradiation-induced dimensional changes

A summary of the radiation-induced swelling in monolithic SiC as a function of irradiation temperature is shown in Fig. 3 [6,14,26-29]. Three distinct temperature regimes can be identified. At low temperatures (<150°C), a crystalline to amorphous phase transition is induced at relatively low doses (0.1-1 dpa). The amorphous phase has a much lower density compared to the crystalline phase, which results in ~11% swelling [29]. Bulk SiC exhibits moderate swelling due to neutron irradiation at temperatures between 150 and 900°C. The swelling in this temperature range is attributable to small point defect clusters, and is commonly referred to as "point defect swelling". The swelling decreases with increasing irradiation temperature, and reaches an apparent saturation level after relatively low doses. For example, the swelling observed at 500°C after 25 dpa [26] lies within the data scatter band obtained for ~1 dpa irradiations. At high irradiation temperatures, void swelling occurs in SiC. The minimum temperature for significant void swelling in SiC is somewhat uncertain. Early work by Price [28] indicated that significant void swelling did not occur for irradiation temperatures below ~1100°C. However, two recent studies have observed high volumetric swelling in SiC irradiated at ~1000°C [6,14]. Further work is needed to determine the minimum temperature for void swelling in SiC. The effects of fusion-relevant helium generation on the dimensional stability of SiC has not been adequately studied.

One important consequence of the large chemical differences between currently available SiC-based fibers and pure SiC (Table 1) is that the fibers and stoichiometric SiC matrix in the composite will respond differently to irradiation. Figure 4 shows the effect of neutron irradiation on the density of SiC and SiC-based fibers at 500-650°C [6,9,26,30]. A moderate amount of swelling (~1.2%) occurs in pure SiC during irradiation, with an apparent saturation in swelling observed at doses above ~0.1 displacements per atom (dpa). In contrast, both ceramic grade

Nicalon and Hi-Nicalon experience significant densification, with the largest densification observed in the lower-grade cg-Nicalon fibers. The data in Fig. 4 and other studies [9,26,31,32] indicate that amount of densification in cg-Nicalon increases with increasing irradiation temperature between 150 and 810°C. The shrinkage of the fibers during irradiation causes debonding with the matrix, and produces low strength in irradiated composites fabricated using current grades of SiC-based fibers. The typical decrease in strength observed in irradiated composites is ≥20%, depending on the irradiation conditions.[5,6,26] Smaller strength changes would be expected in irradiated composites containing advanced fibers (due to a better match with the SiC matrix behavior), but experimental data are not yet available.

Irradiation creep

The magnitude of irradiation creep has not been accurately determined for either monolithic SiC or SiC/SiC composites. Rough estimates obtained for monolithic SiC suggest that the irradiation creep constant may be $K \sim 10^{-12}$ $(Pa\text{-}dpa)^{-1}$ at 500-1100°C [33], which is lower than the value observed for some other ceramics [34].

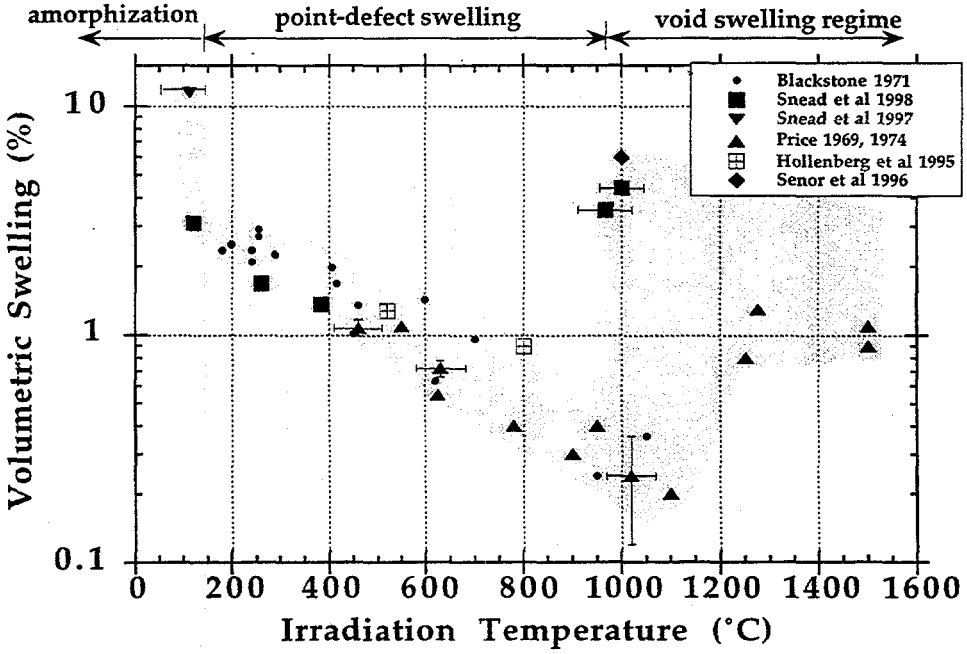

Fig. 3. Radiation induced swelling in bulk SiC as a function of irradiation temperature [6,14,26-29].

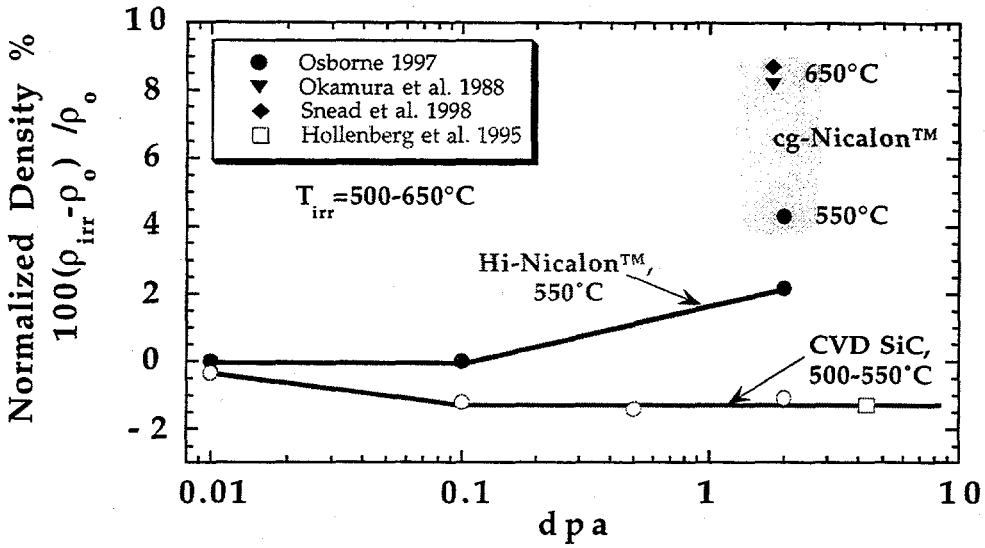

Fig. 4. Comparison of the effect of low-dose neutron irradiation at 500-650°C on the density of SiC and SiC-based fibers [6,9,26,30].

Recommended reference operating temperature limits

The minimum operating temperature limit will be determined by either the crystalline to amorphous transition temperature (~120°C for fusion reactor damage rates) [29], or else radiation-induced degradation in the thermal conductivity. The thermal conductivity degradation is very severe even at low doses for low temperature (≤300°C) irradiations (cf. Fig. 2). The thermal conductivity degradation becomes less pronounced with increasing irradiation temperature up to ~1000°C, due to a decrease in the saturation concentration of point defect clusters. Additional experimental data at temperatures between 400 and 1000°C are needed to quantify the thermal conductivity degradation as a function of dose and temperature. The maximum temperature limit will likely be determined by void swelling considerations, although there are not sufficient data at elevated temperatures (900-1400°C) to make a clear determination. The tentative reference minimum and maximum operating temperature limits for the purposes of the APEX design study are 400°C (due to thermal conductivity degradation concerns) and 1000°C (due to void swelling concerns).

References

1. R.H. Jones and C.H. Henager, Jr., J. Nucl. Mater. 219 (1995) 55.
2. R.H. Jones et al., J. Nucl. Mater. 245 (1997) 87.
3. L.L. Snead, Fusion Technology 24 (1993) 65.
4. L.L. Snead and O.J. Schwarz, J. Nucl. Mater. 219 (1995) 3.
5. L.L. Snead, R.H. Jones, A. Kohyama and P. Fenici, J. Nucl. Mater. 233-237 (1996) 26.
6. L.L. Snead et al., J. Nucl. Mater. 253 (1998) 20.
7. M. Takeda, J. Sakamoto, A. Saeki and H. Ichikawa, in Ceramic Engineering and Science Proceedings vol. 17, No. 4 (American Ceramic Society, Westerville, OH, 1996) p. 35.
8. J. Lipowitz, J.A. Rabe, A. Zangvil and Y. Xu, in Ceramic Engineering and Science Proceedings vol. 18, No. 3 (American Ceramic Society, Westerville, OH, 1997) p. 147.

9. M.C. Osborne, Ph.D Thesis (Dept. Materials Science and Engineering, Rensselaer Polytechnic Institute, 1997).
10. G.E. Youngblood, R.H. Jones, G.N. Morscher and A. Kohyama, in Fusion Materials Semiann. Prog. Report for period ending June 30 1997, DOE/ER-0313/22 (Oak Ridge National Lab, 1997) p. 81.
11. E. Lara-Curzio, in Encyclopedia of Ceramic Engineering, ed. M.N. Rahaman (Marcel Dekker, New York, 1998) in press.
12. R.H. Jones, C.H. Henager, Jr., G.E. Youngblood and H.L. Heinisch, Fusion Technology 30 (1996) 969.
13. M.C. Osborne, C.R. Hubbard, L.L. Snead and D. Steiner, J. Nucl. Mater. 253 (1998) 67.
14. D.J. Senor et al., Fusion Technology 30 (1996) 956.
15. Morton, personal communication product literature.
16. R.G. Munro, J. Phys. Chem. Ref. Data 26 (1997) 1195.
17. A.G. Evans, Acta Mater. 45 (1997) 23.
18. D.J. Senor, D.J. Trimble, G.A. Newsome and J.J. Woods, in Ceramic Engineering and Science Proceedings vol. 18, No. 3 (American Ceramic Society, Westerville, OH, 1997) p. 591.
19. W.D. Kingery, H.K. Bowen and D.R. Uhlmann, Introduction to Ceramics, 2nd Ed. (John Wiley & Sons, New York, 1976) p. 1032.
20. K. Okamura, M. Narisawa, T. Yamamura and M. Sato, 8th Int. Conf. on Fusion Reactor Materials, Sendai, J. Nucl. Mater. (1998) submitted.
21. Ceramic Engineering and Science Proceedings vol. 19 (American Ceramic Society, Westerville, OH, 1997) in press.
22. A. Sayano et al., 8th Int. Conf. on Fusion Reactor Materials, Sendai, J. Nucl. Mater. (1998) submitted.
23. W. Kowbel, K.T. Tsou, J.C. Withers and G.E. Youngblood, in Fusion Materials Semiann. Prog Rep. for period ending Dec. 31 1997, DOE/ER-0313/23 , 1997) p. 172.
24. D.J. Senor et al., Fusion Technology 30 (1996) 943.
25. G.E. Youngblood and R.H. Jones, in Fusion Materials Semiann. Prog. Report for period ending Dec. 31 1997, DOE/ER-0313/23 (Oak Ridge National Lab, 1997) p. 166.
26. G.W. Hollenberg et al., J. Nucl. Mater. 219 (1995) 70.
27. R. Blackstone and E.H. Voice, J. Nucl. Mater. 39 (1971) 319.
28. R. Price, Nucl. Tech. 35 (1977) 320.
29. L.L. Snead, S.J. Zinkle, J.C. Hay and M.C. Osborne, Nucl. Instr. Meth. B (1998) in press.
30. K. Okamura et al., J. Nucl. Mater. 155-157 (1988) 329.
31. L.L. Snead, M. Osborne and K.L. More, J. Mater. Res. 10 (1995) 736.
32. G.E. Youngblood, R.H. Jones, A. Kohyama and L.L. Snead, 8th Int. Conf. on Fusion Reactor Materials, Sendai, Japan, J. Nucl. Mater., in press; also Fusion Materials Semiann. Prog. Report for period ending Dec. 31 1997, DOE/ER-0313/23 (1997) 163.
33. C.A. Lewinsohn et al., J. Nucl. Mater. 253 (1998) 36.
34. Z. Zhu and P. Jung, J. Nucl. Mater. 212-215 (1994) 1081.

A REVIEW OF JOINING TECHNIQUES FOR SiC_F/SiC COMPOSITES FOR FIRST WALL APPLICATIONS - C.A. Lewinsohn and R.H. Jones (Pacific Northwest National Laboratory)*

OBJECTIVE

The objective of this work is to review the methods currently available for joining silicon carbide composites and to critique their suitability for structural applications in fusion energy systems.

SUMMARY

Many methods for joining monolithic and composite silicon carbide are available. Three techniques are candidates for use in fusion energy systems: in-situ displacement reactions, pre-ceramic polymer adhesives, and reaction bonding. None of the methods are currently developed enough to satisfy all of the criteria required, i.e., low temperature fabrication, high strength, and radiation stability.

PROGRESS AND STATUS

Introduction

The development of fusion energy systems places many demanding criteria on the materials to be used in this application. One criterion, is the need for a hermetic material that can chemically and mechanically withstand high-temperatures and neutron fluxes as the "first-wall" material. In addition, the radioactivation of the material to be used as the first wall should be below the limits for a safe and environmentally benign lifecycle. A candidate material for this application is silicon carbide fiber-reinforced, silicon carbide (SiC/SiC). SiC/SiC composites possess desirable thermal, mechanical, and nuclear stability. A limitation of these materials, however, is that they can only be produced in limited sizes and shapes. Therefore, to fabricate a complete fusion energy system a method of joining SiC/SiC components, without compromising the properties that are needed, is required. This report will review the methods currently available for joining monolithic and composite silicon carbide and critique their suitability for fusion energy system applications.

Since silicon carbide has many desirable properties for use as a "first-wall" in a fusion energy system, it is undesirable to use a joining technique that would expose another material at the inner face of the first wall. In addition, to avoid poisoning the plasma the first wall must be hermetic. Thus, it is highly likely that a means of joining SiC/SiC components to each other is required. In addition, the first wall material will have to be supported by another structure, that may be a metal, which means that joining of SiC/SiC to metals must also be considered.

Joining of ceramics to ceramics or to metals is an area that has been investigated for many years and, because of its complexity, remains an area of extensive research. This review will cover both ceramic to ceramic and ceramic to metal joining, since both situations may be found in fusion energy systems, but it will focus on joining of silicon carbide composites to themselves. From the limited amount of research performed on joining SiC/SiC to itself and other materials there is no reason to believe that it does not behave any differently from

---

*Pacific Northwest National Laboratory (PNNL) is operated for the U.S. Department of Energy by Battelle Memorial Institute under contract DE-AC06-76RLO-1830.

silicon carbide with respect to joining. Silicon carbide has been successfully joined to itself via direct diffusion bonding, brazing, codensification of green bodies and binders, reactive metal bonding, pressurized combustion reactions, in-situ displacement reactions, preceramic polymer adhesives, glassy interlayers, and reaction bonding. The principles of several joining techniques will be presented, and advantages and disadvantages, relative to other joining techniques, will be addressed. In addition, the suitability of each technique for fusion energy systems, according to current design criteria, will be discussed.

Certain additional issues arise due to the use of composite as opposed to monolithic silicon carbide. The first of these issues concerns the degradation of fibers at an elevated temperature determined by each type of fiber. The second issue concerns oxidation of the fiber to matrix interphase, and the subsequent removal of fiber bridging stresses, above approximately 500°C in the presence of oxygen. Another issue regards the loss in load carrying capacity of fiber-reinforced plies that are machined to obtain the desired component or joint technologies. All of these mechanisms may lead to weak regions in the proximity of the joint. To minimize composite degradation, due to joining, the joining temperature should be as low as possible and post-densification machining of the composite surfaces should be avoided.

Literature Review

A. Methods of Joining Ceramics to Ceramics

1. Mechanical Interlocking

A relatively simple means of joining components is by mechanical means. Due to the difficulty of machining dense ceramics and their brittle fracture properties, conventional fastening techniques that may be used to join metal components, such as nuts and bolts, screws, rivets, etc., are rarely successful when applied to ceramics, especially at high temperatures. Other mechanical fastening techniques, however, are feasible. These techniques include clamping, retaining brackets, and shrink-fit methods. As will be discussed later, the large mismatch in thermal expansion between metals and ceramics inhibits the use of metal fasteners.

Clamping components consists of using an intermediate component to apply pressure to the components to be joined. The current fusion energy systems designs propose toroidal reactors. To obtain a continuous toroidal shape via clamping smaller components would be extremely difficult. The first wall material is designed to be subject to a large thermal gradient, hence large thermal stresses. These stresses are the reason that SiC/SiC, as opposed to monolithic silicon carbide, is considered as a potential candidate material. Any type of clamp that is used would also have to be fabricated from SiC/SiC to retain the desirable thermomechanical and nuclear properties. Clamping, therefore, does not remove the problem of joining SiC/SiC to itself. Clamping may be a suitable mechanical joining technique, but it would have to be complemented with another joining method to obtain a hermetic seal.

In principle, clamping and the use of retaining brackets are similar. These techniques rely on using another component to apply compressive stress on the components to be joined. Retaining fasteners are similar to conventional metal nuts and bolts. The fastener passes through the components to be joined and an attachment is made at each end to hold the

components together. A disadvantage of the use of retaining fasteners is the difficulty in obtaining hermetic seals where the fastener passes through the component. If silicon carbide retainers are used, to avoid introducing another material at the first wall, the problem remains of attaching a piece larger than the hole on each end. Obtaining a strong, hermetic joint in this manner would also be difficult and would rely on some sealant material. Finding a sealant that can withstand the service conditions and can be fabricated easily may be difficult. In addition, the existence of a hole in the SiC/SiC component will likely lead to matrix cracks which could effect the hermetic properties and residual thermomechanical behavior of the component. As with clamping, the use of retaining fasteners does not eliminate the need for joining SiC/SiC to itself since fasteners can only provide mechanical attachment of components without hermetic sealing between the components.

The third method of mechanical interlocking, shrink fitting, may hold some promise for fusion applications. Shrink-fitting is a very well established method that has been used for centuries (notably in gun barrels). The technique relies on thermal expansion to temporarily increase the inner diameter (ID) of an outer component while an inner component is inserted into position. After the outer component cools, the ID is constrained by the outer diameter of the inner component. The difference between the original ID and the constrained ID of the outer piece is called the misfit strain. The misfit strain produces compressive stresses across the interface that holds the components together. Inversely, the inner component could be cooled and the same result would be obtained. Although, shrink fitting is commonly used for cylindrical components, the technique also can be applied to planar geometries.

Although mechanical interlocking methods can be used to achieve strong physical bonding between SiC/SiC components, the additional requirements of hermetic properties and use of radiation tolerant materials (i.e., SiC/SiC or silicon carbide) preclude their use as the sole means to join SiC/SiC components. Clamping or shrink-fitting methods, however, may be considered in combination with other joining techniques.

2. Brazing

Brazing of ceramics involves using a component that forms a liquid phase during joining. The process uses a braze material that is chemically compatible with both components to be joined. The braze material forms strong chemical bonds with surfaces to be joined. Since self diffusion rates in ceramics, especially in non-oxide ceramics, are relatively slow in comparison to most metals, braze materials that form strong chemical bonds with ceramics and have acceptable diffusion rates are used. Two types of brazes are commonly used: noble metal brazes and reactive metal brazes. Noble metal brazes are typically silver or platinum alloys and may include copper or nickel. The use of noble metal brazes usually requires metallization of the ceramic surfaces. Since many metal brazes do not wet ceramic surfaces, metals that are more thermodynamically reactive than the ceramic cationic species are often used. The addition of minor amounts of reactive metals (i.e., Ti, Al, etc.) allows formation of an oxide or carbide layers that are compatible with corresponding ceramic materials.

Brazing with reactive metals requires processing in vacuum or inert environments to prevent a reaction between the braze metal and the environment. If it is not possible to braze under a vacuum or in an inert atmosphere the ceramic material must be pre-metallized to enhance bonding between the braze material and the ceramic. A common metallization technique, useful for oxide ceramics or ceramics with oxide containing grain boundaries, involves

applying a slurry of molybdenum and manganese to the surface of the ceramic and firing under conditions that oxidize the manganese but not the molybdenum (1). Under the right conditions, MnO forms a glassy phase bonds with oxide ceramic phases while the molybdenum forms a porous layer that the MnO glassy phase also infiltrates. Often this layer is then electroplated with nickel to create a good surface for brazing. Another form of metallization involves coating the ceramic surface with titanium hydride. The material is fired under reduced pressure under which the hydride decomposes and titanium undergoes a redox reaction with the ceramic surface to form a strong chemical bond (2). Other metallization techniques include sputter deposition and physical vapor deposition, however metallization of SiC has had limited results (3).

Brazing has been used to join silicon nitride (Si_3N_4) and SiC to themselves using copper-titanium and nickel-titanium (4-7). A number of braze compositions based on silver-copper alloys have been found to be successful in joining ceramics to metals and ceramics to themselves (3,4). Other metals include aluminum (8), silicon (9), and tin (10,11). Since even those metals developed for brazing do not wet most ceramic surfaces completely, active metal fillers are often used to promote wetting and to improve the properties of the brazed joints. Alloys of silver, copper, and more than 10 atomic % titanium have produced extremely good joints between silicon carbide materials (4, 12-15). A variety of other metals, such as zirconia, hafnia, nickel, beryllium, chromium, vanadium, indium, and cobalt have also been used as active metal fillers in brazes for ceramics (16-21).

The low temperature strength of brazed joints between silicon carbide and itself are relatively high. Naka et al. used an alloy of copper and titanium and were able to obtain maximum values of the shear strength of 80 MPa (22) . Lemoine et al. obtained values of the shear strength of single and double lap joints between SiC/SiC and itself, brazed with silicon, of about 20 MPa, tested in flexure (9). Ferro and Derby obtained typical values of 200-250 MPa for the tensile strength of aluminum metal brazed joints between reaction-bonded silicon carbide (8). Iseki reported tensile strengths of as high as 490 MPa for silicon carbide joined to itself with a complex joint of metal interlayers (23). Nakamura and Shigematsu obtained a mean strength of 96 MPa, with a Weibull modulus of 3.2, for joints formed by an alloy of silver, copper, and titanium between silicon carbide composites consisting of hot pressed fibers (24). Since joints will generally fail under shear stresses (if the structure is designed correctly), the relevance of a tensile strength for a joint is questionable. Furthermore, it is difficult to compare strength values from one study to another due to the different test methodologies used. Nevertheless, it is apparent that a variety of brazing techniques can be used to obtain reasonably strong joints between monolithic or composite silicon carbide at room temperature.

Unfortunately, all of the brazing techniques presented so far suffer from one of two problems at elevated temperatures: the formation of brittle reaction products, or stresses due to thermal expansion mismatches. Although attempts have been made to insert diffusion barrier or compliant interlayers between the braze material and the ceramic to be joined, these approaches have met with limited success. Thus, it is doubtful that a brazing technique can be developed to satisfy the requirements of fusion energy systems.

3. Diffusion Bonding

Since there are limited metal systems that wet ceramics and due to the thermal expansion mismatch stresses present in many brazed joints, solid state diffusion is also used to join

ceramic materials to each other, or metals, when it is important to preserve the high temperature properties of the ceramics. Generally a metal that reacts forms thermodynamically stable chemical bonds with the ceramic materials to be joined is sandwiched between the surfaces to be joined. The joint forms by diffusion. Variables that effect the quality of diffusion bonded joints are temperature, metal melting temperature, applied pressure (25,26). Generally, the temperature used to form the joint affects the kinetics of the joining reaction. Since diffusion bonding is controlled by diffusion rates it can be time consuming, hence temperature becomes an important variable. Interdiffusion of the metal and ceramic will most likely occur by diffusion the metal into the ceramic. In some cases, however, the phases formed during joining will also vary with the temperature used to form the joint. It has been found, empirically, that the strength of ceramic to metal joints increases with increasing melting point of the metal (27).

Bates et al. (28) bonded silicon carbide to itself by placing a slip of SiC powder on the faying surfaces, cold isostatic pressing (CIP) the pieces together, and sintering the components (temperature, time, and environment not specified). When tested in flexure, these joints exhibited strengths of 140 MPa with a Weibull modulus of 17.0 for one composition of sintered silicon carbide; 351 MPa with a Weibull modulus of 45, for another. The strength of these joints decreased less than 10% when tested at 1530°C. An approach of this type has not been attempted for SiC/SiC composites, however the temperatures that would be required to sinter the silicon carbide slip would be excessively high for SiC/SiC materials. Silicon carbide is typically sintered at above 1500°C, depending on the amount and type of sintering aids used, which would be an unfeasible approach for assembling large scale structures in fusion energy systems. Furthermore, diffusion bonding often requires the application of external pressure during joining which would also be unfeasible for fusion energy system construction.

4. Glassy interlayers

An alternate method to join ceramics without requiring excessively high-temperatures is to use a glassy interlayer between the components to be joined. This method is used commercially to join gas-tight Al_2O_3 envelopes to niobium for sodium vapor lamps (29). Powdered glass or mixtures of glass forming powders can be applied to the surfaces to be joined and heated to obtain mechanical and chemical bonding. Glasses can be made of similar compositions to the base ceramic materials. For example, silicon-oxycarbide and silicon oxy-nitride glasses can be used to bond with silicon carbide and silicon nitride, respectively (3). The composition of glasses can be tailored, or graded near interfaces, to minimize thermal expansion mismatches. In addition, glassy materials typically have low elastic moduli that also reduce residual stresses due to thermal expansion mismatches. A major drawback of glassy materials is that they soften with increasing temperature. Certain compositions of glasses, however, can be devitrified to form crystalline materials known as glass-ceramics. Glass-ceramic materials are typically stronger and tougher, and more heat resistant, than glasses of similar compositions, but their elastic moduli are concomitantly higher.

Ferraris et al. fabricated joints between SiC/SiC composites using borosilicate, boro-aluminosilicate, and barium containing boro-aluminosilicate glasses (30-32). All of the glasses wet the composites and formed joints with minimal porosity. The borosilicate joint was very weak, but the other two glass compositions were reported to be stronger. Ferraris et al. did not report a value of the strength of the joints. Lemoine, Salvo, Ferraris, et al.

investigated other glass compositions and discovered that a zinc-borate glass, also containing MgO, SiO_2, Al_2O_3, and Na_2O, wet the surfaces of SiC/SiC readily and penetrated the intrinsic porosity of the composites (33). Unfortunately, the shear strengths of these joints, measured by flexural testing of single and double lap joints was extremely low, approximately 2 MPa. In addition to having poor mechanical properties, boron is not an attractive element in first wall components from a radiological perspective.

5. Cements

Adhesive ceramic joints are usually formed by cement-mortar materials. These materials are a mixture of materials that undergo a variety of low temperature reactions (i.e., hydration, amalgamation, etc.) to form a strongly bonded phase. The suitability of cement type jointing materials for high temperature applications is limited. Certain air-setting materials, usually composed of mixtures of magnesium-alumino-silicates, retain their useful properties up to about 1100°C. These materials are usually supplied in a solvent and cure by evaporation.

Other cement materials are cured by chemical reactions catalyzed by acids or bases. Phosphate, chloride, and sulfate cement precursors usually cure exothermically, whereas sodium and potassium silicates are non-exothermic. Cements cured by chemical reaction usually offer superior properties relative to those that set due to hydration or evaporation. Cements have been used to join non-oxide ceramics prior to nitride bonding or sinter-HIPping (3, 34).

Recently, amalgams of copper and gallium have been used to join silicon carbide ceramics (35). The base material consists of a mixture of copper and gallium powders that spontaneously alloy when mixed. During amalgamation of copper and gallium there is an increase in volume. To obtain a strong joint with these amalgams it is necessary to utilize joint geometries that have a constrained gap between the parts to be joined. If the gap is filled by the volume increase occurring during amalgamation then the joint will be under residual compression, similar to a joint made by shrink-fitting. The yield strength of the amalgam was approximately 150 MPa at 900°C. The ability to apply this joining technique without applied temperature and pressure warrants further investigation for fusion energy system applications.

6. In-situ Displacement Reactions

A displacement reaction, between a metal and a ceramic material, involves the exchange of the cation of the ceramic with the metal yielding a new ceramic compound and a metal phase of the original cation. These reactions occur when the new ceramic phase is thermodynamically more stable than the original one, although sometimes heat or energy must be supplied for the reaction to proceed. Not only can novel materials be produced via displacement reactions, but self-reinforced microstructures may also result (36). When the displacement reaction is performed in the region to be joined it is referred to as in situ. In situ displacement reactions have been used to join monolithic silicon carbide components with very good high temperature mechanical properties (37,38).

Rabin joined SiC/SiC to itself using titanium, carbon, and nickel powders applied to the faying surfaces and subsequently hot-pressing, at 1400°C under 20 to 50 MPa (37). During hot-pressing, the powders react to form TiC in a Ni matrix. There was evidence of some reaction between the phases in the joint material and the silicon carbide. Due to the large mismatch

in thermal expansion coefficient of the TiC/Ni layer and the SiC/SiC material cracks formed upon cooling. Rabin also joined sintered silicon carbide to itself using an in situ reaction method that formed SiC and $MoSi_2$ (37). This method required the formation of a porous carbon framework that obtained by pyrolysis of a furfural alcohol resin. Silicon and silicon containing 3% molybdenum were used to infiltrate the porous carbon layer created between the pieces to be joined. Infiltration was conducted at 1400-1460°C. Extremely dense joints, with little free silicon, were obtained. The strength of the joints was 251 $\pm$ 61 MPa, when tested in flexure at room temperature.

Henager and Jones have also used in situ displacement reactions to fabricate joints between silicon carbide and itself (38). Powder mixtures of TiC and Si were made into thin tapes, approximately 100 m thick, by tape casting. The tape cast layers were placed between pieces of silicon carbide and heated to either 1200°C or 1400°C under 20 MPa of compressive stress. The resulting joints consisted of a continuous Ti_3SiC_2 phase containing high aspect ratio and equiaxed SiC particles. The interlaminar shear strength was measured using a modified double edge notched sample in compression. Interlaminar shear stress values of about 35 MPa, at room temperature, were obtained.

A disadvantage of the in-situ displacement reaction technique is that the current methods require application of external heat and pressure during joining that would be unfeasible for large structures. Nevertheless, joints made from in-situ displacement reactions have exhibited equal to or higher strengths than the monolithic ceramics that they have been used to join. The possibility of obtaining tough, self-reinforced joints with similar thermomechanical properties as the materials to be joined warrants further investigation of this approach for components used in fusion energy systems.

7. Preceramic Polymers

A relatively new technique for joining ceramic material has been the use of preceramic polymers (39-47). This approach has been applied mainly to joining of non-oxide ceramics, since many of the traditional methods of ceramic-to-ceramic joining were developed for oxide ceramics. Preceramic polymers are organometallic materials consisting of polymerized hydrocarbon compounds containing various metallic elements. These materials can be readily pyrolized to form ceramic materials when heated to temperatures between 800-1400°C. Two commonly used polymers are siloxanes and carbosilanes. Both polymers convert to silicon oxycarbide materials after pyrolysis. The main advantage of using preceramic polymers is that they can be applied as liquids, slurries, and pastes, and converted to ceramic materials with similar thermomechanical properties as the materials to be joined. Furthermore, conversion of preceramic polymers to silicon carbide joints creates a joint material with the required radiation stability desired in fusion energy system applications.

Colombo obtained joints between pieces of reaction bonded silicon carbide with tensile strengths, measured in flexure at room temperature, of almost 220 MPa and interlaminar shear strengths, also measured at room temperature, of 26.6 MPa (46). These joints were obtained by pyrolysis of a silicone resin at 1200°C without applied pressure. Pyrolysis of a polycarbosilane preceramic precursor failed to create satisfactory joints. The joint formed by pyrolysis of the silicon resin did not react with the reaction bonded silicon carbide and, therefore, acted as an adhesive layer. Yajima also obtained unsatisfactory joints with polycarbosilane materials (39). An understanding of the physical mechanisms that occur

during joining with preceramic precursors may provide an explanation for these observations and lead to improvements in this method of joining.

Sherwood et al. (41) have developed a novel method for joining SiC/SiC using hydro-polycarbosilane resins mixed with chopped fibers and reactive metal filler particles (i.e., silicon). The joints were formed by heating at 1000°C for 1 hour. The method involves cutting the surfaces to be joined so that fibers extend from the surfaces to provide mechanical interlocking with the joining material. Using this technique, butt joints with flexural strengths of between 27 and 55 MPa were obtained. Modification of the joint geometry, by creating an augmented dovetail (with an additional, unimpregnated layer of Nicalon fiber cloth at each surface to be joined), and incorporation of silicon powder led to an increase in the strength value to 103-110 MPa. In addition, Sherwood et al. reported promising preliminary results using a mixture of SiC powders and HPCS to join monolithic silicon carbide (41). The results described above indicate that the use of preceramic polymers to form joints between SiC/SiC and itself is relatively poorly understood, yet exhibits promise for use in fusion energy systems.

8. Reaction Bonding

Another method for obtaining joints consisting of mostly silicon carbide is reaction bonding. Reaction bonding consists of combining silicon, carbon, and sometimes silicon carbide precursors, followed by causing a reaction at elevated temperatures, to form silicon carbide. Since the volume of the products is greater than that of the reactants, the reaction typically can not proceed to completion and residual silicon or porosity remains. Numerous investigators, however, have optimized the composition and microstructure of the reactants to obtain dense silicon carbide products with the least amount of residual silicon (3). In addition, the silicon carbide formed by reaction bonding often interpenetrates with silicon carbide components it is used to join. At elevated temperatures, near the melting point of silicon (1410°C), the silicon can deform plastically. A more severe failure mechanism due to the presence of the residual silicon is also possible. Since the silicon does not wet silicon carbide it will gradually "sweat" out of the structure to the surface and form nodules. These nodules can act as failure origins for brittle fracture. Nevertheless, reaction bonded silicon carbide is an attractive material for joining applications in fusion energy systems.

Rabin developed a technique for joining sintered silicon carbide to itself using layers of SiC and C powders applied to the surfaces to be joined (48). Powders of silicon carbide and carbon were either mixed in a slurry or tape cast. The pieces to be joined were held together and small amounts of silicon metal were placed near the joints. The specimens were heated to either 1400°C and 1460°C and the silicon was drawn into the joint by capillary forces where it reacted to form silicon carbide. The joint material reacted with the silicon carbide specimens to form continuous grains of silicon carbide across the interface. The tape casting technique allowed formation of thin joints, however it was difficult to control the amount of carbon in the tape cast layer. Joints formed from powder slurries had room temperature flexural strengths of 166 $\pm$ 30 MPa, whereas joints formed by using tape cast layers had strengths ranging from 222 to 376 MPa, at room temperature. If the tape cast layers were densified, by uniaxial pressing, prior to joining higher strength could be obtained due to the higher initial density of the carbon in the tapes. If the carbon density is too high then the volume increase associated with reaction bonding prohibits transport of silicon and porosity remains. If the carbon density is too low then the reaction will be incomplete and residual silicon will remain.

Anderson et al. modified one of the joining techniques described by Rabin involving pyrolysis of an organic resin to microporous carbon followed by infiltration of aluminum, silicon, and boron powders (42). Although this method does not technically involve preceramic polymers it could be adapted to involve infiltration of a microporous ceramic material formed by pyrolysis of a preceramic polymer. Anderson et al. fabricated joints with room temperature strengths of about 90 MPa, and shear strengths of about 50 MPa (42).

Singh has joined reaction bonded, sintered, and composite silicon carbide using a reaction bonding approach (49-51). Singh's approach consists of making a paste, slurry, or tape of a carbonaceous material and applying this to the surfaces to be joined. The carbonaceous material is cured at 100°C for 15-20 minutes. After curing, the joint is infiltrated with silicon or silicon alloys at 1425°C for 15 minutes. The tensile strength of the joints, measured in flexure, was about 190 MPa and was insensitive to temperature up to 1350°C (50, 51). There was a significant dependency of the joint strength on its thickness. Joints that were approximately 350 m thick had strength values of 44 $\pm$ 2 MPa. Joints that were 20-55 m thick had strength values of about 190 MPa. These results suggest that there are some residual thermal stresses in the thicker joints that are not present in the thinner joint.

The results described above indicate that reaction bonding is also a promising technique for joining monolithic and composite silicon carbide. The major drawback to using reaction bonding to join composites is that the specimen must be heated above the melting point of silicon (1410°C). Fortunately, other metals can be combined with silicon to form lower melting eutectic compounds. Another drawback of reaction bonding, however, is the potential for forming joints with excess silicon. Silicon may transmute to ^{26}Al that has been predicted to prohibit "hands-on" recycling of SiC/SiC (52). Since, there currently are not any techniques for recycling unirradiated SiC/SiC, nor are any likely to be developed given the nature of ceramic materials, this limitation may not be critical.

B. Special Issues Concerning Joining of Silicon Carbide for Fusion Energy Systems

Aside from producing economically viable power, fusion energy systems will be required to operate in a safe and environmentally benign manner over their lifetimes. Therefore, the materials used in these systems will be required to have a variety of unique properties. Consideration of these properties has shown that SiC/SiC composites are extremely attractive first wall materials (53-56). In addition to radiation resistance, mechanical integrity, and desirable thermal properties, SiC/SiC is the only low-activation material that has satisfied design criteria of safety during operation and maintenance, injury due to accidental release, and waste management. To preserve the suitability of SiC/SiC for use in fusion energy systems, the joining method used must also satisfy the conditions of radiation resistance, mechanical integrity, desirable thermal properties, safety during operation and maintenance, injury due to accidental release, and waste management.

The requirements of safety, injury, and waste management have been considered from the perspective of identifying elements that form transmutation products, after exposure to fusion energy system operating conditions, that exceed the accepted limits (57,58). From this point of view, several elements that may potentially be attractive for use in joining are excluded. Nickel, molybdenum, niobium, and cobalt are unacceptable. Since the SiC/SiC materials that are currently available satisfy the safety, injury, and waste management criteria as well as the structural and radiation stability criteria it is logical to conclude that the most suitable

joining material should have a composition and microstructure as close as possible to SiC/SiC. In addition, thermally-induced and elastically-induced mechanical stresses would be minimized by use of a joining material with properties similar to that of the material to be joined.

Since the current designs for fusion energy systems incorporate large SiC/SiC components the use of externally applied pressure, during joining, is unfeasible. In addition, since joining will occur at the construction site of a fusion energy system it is preferable that the joining technique be performed in the ambient environment. The mechanical properties of the currently available SiC/SiC materials degrade above 1200-1400°C due to microstructural instabilities in the fibers. Therefore, the temperature used for joining must be below that which causes degradation of the fibers. In addition, the joining technique must be compatible with the other materials and processes used during assembly of the fusion energy system.

CONCLUSIONS

Numerous methods exist for joining SiC/SiC materials, but most have drawbacks that render them unsuitable for use in fusion energy systems. Mechanical joining may be acceptable in combination with another technique that provides hermetic properties. Brazing is generally unsuitable for the proposed service temperatures, due to the formation of brittle phases and thermal expansion mismatch stresses. Direct diffusion bonding is also unsuitable since the temperatures required to obtain bonding are in excess of those that cause damage to the fibers in SiC/SiC. Glassy interlayers are in early stages of development, but the preliminary values of the strength of these joints are disconcerting. In addition, many of the components of good glass forming compositions may pose neutron activation problems. In situ displacement reactions show promise for forming mechanically reliable joints, but methods must be developed that do not require applied pressure during joining. Preceramic polymers appear very promising, but very little is known about their behavior during joining. Finally, reaction bonding is also capable of providing strong joints for SiC/SiC but has two drawbacks: the use of excessive temperatures, and the presence of residual silicon.

FUTURE WORK

Both from a mechanical and a radiological perspective it is desirable to fabricate joints of compositions as close to pure silicon carbide as possible. Aside from further investigation of joining techniques, analysis of optimum joint geometries is required. Furthermore, evaluation of valid techniques for measuring irradiated and unirradiated mechanical properties of joints is also required. Considering the detailed review presented above, polymer precursor methods are strong candidates for detailed investigation while efforts can be made to remove the limitations of in situ displacement reaction and reaction bonding joining methods.

REFERENCES

1. D.M. Mattox, and H.D. Smith, "Role of Manganese in the Metallization of High-Alumina Ceramics," Am. Ceram. Soc. Bull., **64** [10], 1363-1367 (1985).

2. R.J. Bondley, "Metal-Ceramic Brazed Seals," Electronics, **20** [7], 97-99, 1947.

3. M.M. Schwartz, Ceramic Joining, ASM International, Materials Park, Ohio, 1990.

4. O.M. Akelsen, "Review: Advances in Brazing Ceramics," J. Mat. Sci., **27** 1989-2000 (1992).

5. W. Tillmann, E. Lugscheider, R. Xu, and J.E. Indacochea, "Kinetic and Microstructural Aspects of the Reaction Layer at Ceramic/Metal Braze Joints," J. Mat. Sci., **31** 445-452 (1996).

6. A.M. Hadian, R.A.L. Drew, "Strength and Microstructure of Silicon Nitride Ceramics Brazed with Nickel-Chromium-Silicon Alloys," J. Am. Ceram. Soc., **79** [3] 659-665 (1996).

7. S.D. Peteves, and M.G. Nicholas, "Evaluation of Brazed Silicon Nitride Joints: Microstructure and Mechanical Properties," J.Am. Ceram. Soc., **79** [6] 1553-1562 (1996).

8. A.C. Ferro, and B. Derby, "Liquid Phase Bonding of Siliconized Silicon Carbide," J. Mat. Sci., **30**, 6119-6135 (1995).

9. P. Lemoine, M. Ferraris, M. Salvo, and M. Montorsi, "Fracture Characterization of Silicon-Joined Ceramic Matrix Composites," pp. 459-464, High-Temperature Ceramic -Matrix Composites I, A.G. Evans and R. Naslain (eds.), Ceram. Trans., **57**, The American Ceramic Society, Westerville, Ohio, USA, 1995.

10. R.R. Kapoor, and T.W. Eagar, Met. Trans., **20B**, 919 (1989).

11. R.R. Kapoor, and T.W. Eagar, J. Am. Ceram. Soc., **72**, 448 (1989).

12. T. Iseki, H. Matsuzaki, and J.K. Boadi, Am. Ceram. Soc. Bull., 64, 322 (1985).

13. T. Yano, H. Suematsu, and T. Iseki, J. Mat. Sci., **23**, 3362 (1988).

14. S. Kato, T. Yano, and T. Iseki, J. Ceram. Soc. Jpn., **101**, 325 (1993).

15. H. Okamura, M. Sakamoto, and T. Shida, J. Jpn. Weld. Soc., **8**, 108 (1990).

16. A.J. Moorehead, C.S. Morgan, J.J. Woodehouse, and R.W. Reed, Weld. J., **60**, 17 (1981).

17. H. Mizuhara, and E. Huebel, "Joining Ceramic to Metal with Ductile Active Filler Metal," Welding Journal, **65** [10], 43-51 (1986).

18. B. Wielage, R. Dammer, and P. Dyrda, Pract. Met., **26**, 133 (1986).

19. T. Kuzumaki, T. Ariga, Y. Miyamoto, and T. Kobayashi, ISIJ Int., **30**, 403 (1990).

20. D.A. Canonico, N.C. Cole, and G.M. Slaughter, Weld. J, **56**, 31 (1977).

21. R. Morrell, Handbook of Properties of Technical and Engineering Ceramics, Part I: An Introduction for the Engineer and Designer, HMSO, London, UK, 1985.

22. M. Naka, T. Tanaka, and I. Okamoto, J. High Temp. Soc., **11**, 218 (1985).

23. T. Iseki, K. Arakawa, and H. Suzuki, J. Mat. Sci. Lett., **15**, 1049 (1980).

24. M. Nakamura, and I. Shigematsu, J. Mat. Sci., **31**, 6099-6104 (1996).

25. O.M. Akselsen, "Review: Diffusion Bonding of Ceramics," J. Mat. Sci., **27**, 569-579 (1992).

26. T.J. Moore, "Feasibility Study of the Welding of SiC," J. Am. Ceram. Soc., **68** [6], C151-C153 (1985).

27. J.T. Klomp, Ceram. Sci., **5**, 501 (1970).

28. C.H. Bates, M.R. Foley, G.A. Rossi, G.J. Sunberg, and F.J. Wu, "Joining of Non-Oxide Ceramics for High-Temperature Applications," Am. Ceram. Soc. Bull., **69** [3], 350-356 (1990).

29. C.I. McVey, "High-Pressure Sodium Lamps Seals and Recent Improvements," J. IES, **8** [1], 72-77 (1979).

30. M. Ferraris, C. Badini, M. Montorsi, P. Appendino, H.W. Scholz, "Joining of Sic_f/SiC Composites for Thermonuclear Fusion Reactors," J. Nuclear Mat., **212-215** 1613-1616 (1994).

31. M. Salvo, M. Ferraris, P. Lemoine, M. Appendino Montorsi, M. Merola, "Joining of CMCs for Thermonuclear Fusion Applications," J. Nuclear Mat., **233-237** 949-953 (1996).

32. P. Lemoine, M. Ferraris, M. Salvo, M. Montorsi, and H. Scholz, pp. 183 in Advances in Science and Technology, vol. 9, P. Vincenzini (Ed.), Techna Srl., 1995.

33. P. Lemoine, M. Salvo, M. Ferraris, M. Montorsi, and H. Scholz, "Reaction of SiC_f/SiC Composites with a Zinc Borate Glass," J. Am. Ceram. Soc., **78** [6], 1691-1694 (1995).

34. R.J. Bratton, and A.N. Holden, "Ceramics in Gas Turbines for Electric Power Generators," in Ceramics for High Performance Applications III, J. Burke (Ed.), Proc. of Fifth Army Matls. Technology Conf., Brookhill Publishing Co., Brookhill, MA, USA (1974).

35. M. Heim, L. A. B. Tessarotto, and V.A. Greenhut, "Copper/Gallium Amalgam for Ceramic-Metal Bonds," to appear in Cer. Eng. Sci. Proc., **19** [3-4], 1998.

36. R. Radhakrishnan, C.H. Henager, Jr., J.L. Brimhall, and S.B. Bhaduri, "Synthesis of Ti_3SiC_2/SiC and $TiSi_2$/SiC Composites using Displacement Reactions in the Ti-Si-C System," Scripta Met. et Mater., **34** [12], 1809-1814 (1996).

37. B.H. Rabin, "Joining of Fiber-reinforced SiC Composites by In Situ Reaction Methods," Mat. Sci. & Eng., **A 130**, L1-L5 (1990).

38. C.H. Henager, Jr., and R.H. Jones, "Joining of SiC Ceramics Using Displacement Reactions," pp. 117-125 in Ceramic Joining, I.E. Reimanis, C.H. Henager, Jr., and A.P. Tomsia (Eds.), Ceramic Transactions, vol. 77, The American Ceramic Society, Westerville, Ohio, USA, 1997.

39. S. Yajima, K. Okamura, T. Shishido, Y. Hasegawa, and T. Matsuzawa, "Joining of SiC to SiC Using Polyborosiloxane," Am. Ceram. Soc. Bull., **60**, 253, (1981).

40. A. Donato, P. Colombo, and M.O. Abadirashid, "Joining of SiC to SiC using a preceramic Polymer," pp. 431-436 in High-Temperature Ceramic -Matrix Composites I, A.G. Evans and R. Naslain (eds.), Ceram. Trans., **57**, The American Ceramic Society, Westerville, Ohio, USA, 1995.

41. W.J. Sherwood, C.K. Whitmarsh, J.M Jacobs, and L.V. Interrante, "Joining Ceramic Composites Using Active Metal/HCPS Preceramic Polymer Slurries," Cer. Eng. Sci. Proc., **18**, 177-184 (1997).

42. I.E. Anderson, S. Ijadi-Maghsoodi, O. Unal., M. Nostrati, and W.E. Bustamante, "Development of a Compound for Low Temperature Joining of SiC Ceramics and CFCC Composites," pp. 25-40 in Ceramic Joining, I.E. Reimanis, C.H. Henager, Jr., and A.P. Tomsia (Eds.), Ceramic Transactions, vol. 77, The American Ceramic Society, Westerville, Ohio, USA, 1997.

43. O. Unal, I.E. Anderson, M. Nostrati, S. Ijadi-Maghsoodi, T.J. Barton, and F.C. Laabs, "Mechanical Properties and Microstructure of a Novel SiC/SiC Joint," pp. 185-194 in Ceramic Joining, I.E. Reimanis, C.H. Henager, Jr., and A.P. Tomsia (Eds.), Ceramic Transactions, vol. 77, The American Ceramic Society, Westerville, Ohio, USA, 1997.

44. O. Unal, I.E. Anderson, and S. Ijadi-Maghsoodi, "A Test Method to Measure Shear Strength of Ceramic Joints at High Temperatures," J. Am. Ceram. Soc., **80** [5], 1281-1284 (1997).

45. P. Colombo, "Joining Ceramics Using Preceramic Polymers," in Interfacial Science in Ceramic Joining, NATO Advanced Research Workshop, Bled, Slovenia, November 12-15, 1997.

46. P. Colombo, V. Sglavo, E. Pippel, and J. Woltersdorf, "Joining of Reaction-Bonded Silicon Carbide Using a Preceramic Polymer," J. Mat. Sci., **33**, 2409-2416 (1998).

47. E. Pippel, J. Woltersdorf, P. Colombo, and A. Donato, "Structure and Composition of Interlayers in Joints Between SiC Bodies," J. Eur. Ceram. Soc., **17**, 1259-1265 (1997).

48. B.H. Rabin, and G.A. Moore, "Joining of SiC-Based Ceramics by Reaction Bonding Methods," J. Mat. Synth. & Proc., **1** [3], 195-201 (1993).

49. M. Singh, "A Reaction Forming Method for Joining of Silicon Carbide-Based Ceramics," Scripta Mater., **37** [8], 1151-1154 (1997).

50. M. Singh, S.C. Farmer, and J.D. Kiser, "Joining of Silicon Carbide-Based Ceramics by Reaction Forming Approach," Cer. Eng. Sci. Proc. 18 [3], 161-166 (1997).

51. M. Singh, "Joining of Sintered Silicon Carbide Ceramics For High Temperature Applications," J. Mat. Sci. Lett, in press.

52. H.W. Scholz, M. Zucchetti, K. Casteleyn, and C. Adelhelm, "Purity and Radioactive Decay Behaviour of Industrial 2D-reinforced SiC_f/SiC Composites," J. Nuc. Mat., **212-215**, 655-661 (1994).

53. R.H. Jones, C.H. Henager, and G.W. Hollenberg, J. Nuc. Mat., **191-194**, 75-83 (1992).

54. P. Fenici and H.W. Scholz, J. Nuc. Mat., **212-215** (1994).

55. P. Rocco, H.W. Scholz, M. Zucchetti, "Silicon Carbide and the New Low Activation Requirements for a Fusion Reactor First Wall," J. Nuc. Mat., **191-194**, 1474-1479 (1992).

56. P. Rocco, M. Zucchetti, "The Impact of Low-activation Criteria on the Development of Novel Materials for Fusion," J. Nuc. Mat., **212-215**, 649-654 (1994).

57. L.R. Greenwood, and F.A. Garner, "Transmutation of Mo, Re, W, Hf, and V in various irradiation Test Facilities and STARFIRE," J. Nuc. Mat., **212-215**, 635-639 (1994).

58. E.T. Cheng, G. Saji, "Activation and Waste Management Considerations of Fusion Materials," J. Nuc. Mat., **212-215**, 621-627 (1994).

THE HFIR 14J SIC/SIC COMPOSITE AND SIC FIBER COLLABORATION -
G.E. Youngblood and R.H. Jones (Pacific Northwest National Laboratory)*, Akira Kohyama and Yutai Katoh (Kyoto University), Akira Hasegawa (Tohoku University), Reinhard Scholz (European Joint Research Commission), and Lance Snead (Oak Ridge National Laboratory)

OBJECTIVE

The objective of this report is to summarize the planned tests of the SiC composite and fiber specimens selected for the upcoming JUPITER 14J irradiation experiment in the HFIR reactor.

SUMMARY

A short introduction with references establishes the current status of research and development of SiC_f/SiC composites for fusion energy systems with respect to several key issues. The SiC fiber and composite specimen types selected for the JUPITER 14J irradiation experiment are presented together with the rationale for their selection.

PROGRESS AND STATUS

Introduction

The HFIR/14J neutron irradiation experiment is part of the U.S./Monbusho collaboration. This report describes the portion of the collaboration that will examine the irradiation behavior of SiC composites and SiC-based fibers. The HFIR/14J experiment will be the third in a series of such experiments [1]. The first irradiation in this series was carried out in the EBR-II reactor during 1993-94 as part of the COBRA 1A2 experiment. In COBRA 1A2, the SiC-type specimens were irradiated at 800°C to a relatively high dose of 80 dpa-SiC. The just-completed second irradiation in this series was carried out as part of the HFIR/11J-12J experiment at 300 and 500°C to a dose of ≈10 dpa-SiC. PIE tests for the 11J-12J experiment will be performed during 1999. The HFIR/14J irradiation is scheduled to commence in January, 1999 and will be carried out at 300, 500 and 800°C to a dose of ≈10 dpa-SiC, the same dose as for the HFIR/11J-12J experiment.

Results from the COBRA 1A2 SiC experiment are described in detail in previous semiannual progress reports [2-4]. At the time of this experiment, the most advanced continuous fiber-reinforced SiC composite (SiC_f/SiC) was made by Dupont using the isothermal chemical vapor infiltration (ICVI) method. This composite was made with ceramic grade (CG) Nicalon™ fiber coated with a 150 nm pyrocarbon (PyC) interface. A 3D surface showing a proposed strength-irradiation dose-temperature dependence derived from experimental data for this "reference" material is given in [2]. The topological features of the 3D surface suggested three degradation mechanisms for the composite, all of which were related to the thermochemical and structural instability of the Nicalon CG fiber in a neutron irradiation environment. The approximately 50% strength degradation of the Dupont SiC_f/SiC reference material irradiated at 800°C was related to a mass loss mechanism whereby the fiber oxygen constituent reacted with carbon, either within the fiber amorphous Si-C-O

* Pacific Northwest National Laboratory is operated for the U.S. department of Energy by Battelle Memorial Institute under Contract DE-AC06-76RLO 1830.

phase or as the PyC interface, and was exsolved as CO gas [3]. Together with the mass loss mechanism, Nicalon CG fibers irradiated at temperatures exceeding 800°C exhibited crystallization and grain growth, which were correlated to observed decreases in fiber tensile strength [5]. Thus overall, irradiated Nicalon CG fiber loses strength and shrinks, and it debonds from the CVI matrix in a composite made with this fiber. In other experiments at lower irradiation temperatures (<500°C), a relatively large differential SiC matrix swelling and fiber shrinkage also caused fiber/matrix debonding and degradation of the composite strength [6]. Composite made with Nicalon CG fiber generally is considered unacceptable for fusion applications. It was suggested that replacing the Nicalon CG with Hi Nicalon™ fiber , a fiber with much reduced oxygen content and temperature stability to about 1200°C, would alleviate these problems in the composite. In fact, a composite made with Hi Nicalon fiber irradiated at 385°C to 1.1 dpa-SiC exhibited only a 20% strength degradation [7]. This SiC$_f$/SiC composite was made with a multilayer interface which also probably had a bearing on its somewhat improved mechanical behavior.

Even better irradiation stability is expected if a composite could be fabricated using more crystalline, stoichiometric SiC fibers such as Dow Corning Sylramic™, Nippon Carbon Hi Nicalon Type S™ or Ube Tyranno SA™, in which case composite matrix and fiber properties should be closely matched so that differential swelling or shrinkage would be minimized. Preliminary fiber density [8] and length change studies [4] before and after irradiation indicated expected swelling behavior for the irradiated Sylramic fiber. Unfortunately, the Sylramic fiber tensile strength decreased 50% after irradiation at 500°C to 2 dpa-SiC. This observed decrease in strength was related to the approximately 3% TiB_2 content of the Sylramic fiber [8]. Nicalon Type S fiber does not contain boron, however at this time composites made with Type S fiber have not been available for irradiation testing.

To date, neutron irradiation experiments primarily have emphasized the examination of the stability and strength degradation of SiC$_f$/SiC composites and SiC fibers [9,10]. Other key issues and some preliminary performance requirements have been identified for further examination in reference [11] as well as in the proceedings of the 1st and 2nd IEA-sponsored SiC/SiC composite workshops for fusion applications [12,13]. Papers reporting on the key issues of design and specimen testing, component fabrication, joining, thermal conductivity, irradiation creep, impurities and activation effects also appear in these proceedings and elsewhere [14-19].

Plans

Information on the capsule design for 14J is presented in a report by Grossbeck, et al., in this issue. The actual SiC specimen matrix includes 102 bend bars (described in Tables 1A-1C), 22 fiber tubes (described in Tables 2A-2B), 20 thermal diffusivity discs (described in Table 3), 40 TEM discs (described in Table 4) and 6 fiber creep BSR fixtures (described in Table 5). Also given in these tables is the primary focus of the study for each of the selected specimen types.

The new "reference" SiC$_f$/SiC was made by Dupont Lanxide Corp. using a conventional isothermal chemical vapor infiltration (ICVI) process. The fabric preform made with Hi Nicalon fiber was CVD-coated with a 150 nm thick PyC interface. The original plate was 2.3 mm thick, contained six plies of 2D 0-90 weave fabric and had a bulk density of 2.60 ± 0.04 g/cc. The plate was cut into several flexure bars and some thermal diffusivity discs. Room

Table 1A. Bend bars* (30 x 6.0 x 2.2 mm^3) to be irradiated at 800°C

Composite Type	No	Supplier (Process)	Primary Focus
Hi Nic/150nm PyC/0-90	5	Dupont (ICVI)	"Reference" Composite
Hi Nic/porous SiC/0-90	4	ORNL (FCVI)	porous SiC interface
Hi Nic/multilayer/0-90	5	Hypertherm (ICVI)	multilayer interface
Sylramic/multilayer/0-90	5	Hypertherm (ICVI)	Stoichiometric fiber/multilayer
MER CVR/CVR/0-90	4	MER (CVR)	Improved thermal conductivity
MER CVR/Ceraset/0-90	4	MER (CVR-CVI)	Improved thermal conductivity
Nic CG/PyC/Guipex 3D	5	SEP (ICVI)	3D weave architecture
Ti_3SiC_2 (monolithic)	5	Drexel (sintered)	irradiation stability
CVD-β SiC (monolithic)	5	Mitsui (CVD)	Dense monolithic SiC reference
Nic S/PyC/0-90	5	NRIM (ICVI)	Stoichiometric SiC fiber
Nic S/PyC/0-90	5	ORNL (FCVI)	Stoichiometric SiC fiber
Nic S (chopped)/PyC	5	ORNL (FCVI)	Dense, improved T. Cond.
Nic S/PyC/0-90	5	Ube (PIP)	Stoich. fiber/ stability PIP matrix
Adv. PCS/multilayer/3D	5	? (Hot press)	Dense, improved T. Cond.
Other	5	? (?)	?

* 37/35 bend bars supplied by U.S./Japan, respectively.

Table 1B. Bend bars* (30 x 6.0 x 2.2 mm^3) to be irradiated at 500°C

Composite Type	No	Supplier/Process	Primary Focus
Hi Nic/150 PyC/0-90	3	Dupont (ICVI)	"Reference" Composite
Nic S/PyC/0-90	5	ORNL (FCVI)	Stoichiometric SiC fiber
Nic S (chopped)/PyC	5	ORNL (FCVI)	Isotropic/hermetic
Nic S/PyC/0-90	5	Ube (PIP)	Stoich. fiber/ stability PIP matrix

* 3/15 bend bars supplied by U.S./ Japan, respectively.

Table 1C. Bend bars* (30 x 6.0 x 2.2 mm^3) to be irradiated at 300°C

Composite Type	No	Supplier/Process	Primary Focus
Hi Nic/150 PyC/0-90	3	Dupont (ICVI)	"Reference" Composite
Nic S/PyC/0-90	5	ORNL (FCVI)	Stoichiometric SiC fiber
Nic S (chopped)/PyC	5	ORNL (FCVI)	Dense, improved T. Cond.
Nic S/PyC/0-90	5	Ube (PIP)	Stoich. fiber/ stability PIP matrix

* 3/9 bend bars supplied by U.S./ Japan, respectively.

Table 2A. Fiber tubes* (2.0 mm dia x 60 mm) to be irradiated at 800°C

Fiber Type	No	Supplier	Density (g/cc)	XRD-gs (nm)
Hi Nicalon	2	Nippon	2.69	4.4
Hi Nicalon (annealed at 1500°C/1hr)	2	Nippon	2.81	?
Hi Nicalon S	2	Nippon	3.08	11
Tyranno SA	2	Tyranno	?	?
Sylramic	2	Dow Corning	3.0-3.1	80
MER CVR	2	MER	2.8	<5
Other	3			

* 15 fiber tubes supplied by U.S. Each fiber bundle is 52.0 mm long.

Table 2B. Fiber tubes* (2.0 mm dia x 60 mm) to be irradiated at 500 and 300°C

Fiber Type	No	Supplier	Density (g/cc)	XRD-gs (nm)
Hi Nicalon	1	Nippon	2.69	4.4
Hi Nicalon S	1	Nippon	3.08	11
Sylramic	1	Dow Corning	3.0-3.1	80
Tyranno SA (300°C only)	1	Ube	?	?

* 7 fiber tubes supplied by U.S. Each fiber bundle is 52.0 mm long.

Table 3. Diffusivity discs* (10.0 mm dia x 2.0-2.5 mm) irradiated at 800, 500 and 300°C

Capsule /Type	Morton ß-CVD	MER/ Hybrid	MER/ CVR	Nic S-2D (FCVI)	Nic S-chopped (FCVI)	Nic S-2D (PIP)	Total
800°C	2	2	2	3	3	2	14
500°C	2			1			3
300°C	2			1			3

* 12/8 discs supplied by U.S./Japan, respectively.

Table 4. TEM discs* (3.0 mm dia x 0.20 mm) to be irradiated a 800, 500 and 300°C

Capsule	Morton ß-CVD	Primary Focus
800°C	20	Examine irradiation defect structure
500°C	10	plus effects of post-irradiation isochronal
300°C	10	annealing on this structure

* 40 discs supplied by U.S.

Table 5. Fiber Creep by BSR.* (Two tubes 44.5 mm dia x 11.5 mm) irradiated at 800°C

Fiber Type	Characteristic Temperature for Thermal Creep (1 Hr.)	Characteristic Temperature for Thermal Creep (100 Hr.)
Hi Nicalon S	1450°C	1260°C
Sylramic	1420°C	1260°C
Tyranno SA	?	?
Hi Nicalon	1230°C	1080°C
Hi Nicalon (annealed)	?	1230°C
MER CVR	1550°C	?

* 2 creep tubes each loaded with 3 different fiber types supplied by U.S.

temperature 4-pt bend strength, strain to failure and thermal conductivity values were measured to be 628 ± 22 MPa , 0.90 ± 0.03 % and ≈13 W/mK, respectively. These values represent a significant improvement over values of similarly processed unirradiated SiC_f/SiC made with Nicalon CG fiber. As part of this collaborative effort, samples of this material also will be irradiated in the JMTR reactor at 800 and 1000°C to 0.5 dpa and in the HFR/Petten reactor at 750°C to 1.2, 2.5 and 5.3 dpa. Other samples will be used in helium implantation studies [18]. Properties of this new reference SiC_f/SiC before and after irradiation will be compared to the properties of similarly fabricated SiC_f/SiC except with a thicker PyC interface (1000 nm), which currently is being irradiated in HFIR as part of the JUPITER 12J experiment.

In general, the overall dimensional and structural stability after irradiation will be examined for all the other composite variations. Four point flexure tests on the standard 30 x 6.0 x 2.2 mm^3 bars will be carried out at the irradiation temperature to characterize and compare mechanical property behaviors. Changes in the composite stability and mechanical properties then will be related to the variations of fiber type, interface, architecture and matrix fabrication among the selected composites. Two monolithic SiC-based materials are included in the bend bar matrix. The Ti_3SiC_2 material has a graphitic-like structure [20], and potentially could be used as a CVD-applied fiber coating. The monolithic CVD ß-SiC material is included to simulate the radiation performance of a composite matrix-like material.

Since the performance of the fiber has such a strong bearing on the overall radiation performance of the composite, bare fiber tows of each of the fiber types used in the composites will be irradiated and tested following procedures discussed in [21]. For irradiation, each fiber type is inserted into a separate protective tube (2.0 mm od by 1.0 mm id x 60 mm) made from Hexoloy™ sintered SiC. The fiber bundles themselves are carefully cut to a 52.0 mm length which provides sufficient material for length change, tensile strength, density and XRD analyses.

For several fusion component design options, the thermal conductvity should exceed 10-30 W/mK during irradiation. Therefore, a concerted effort has been carried out to optimize the thermal conductivity of some types of SiC composites while maintaining acceptable mechanical properties [12,13, 22]. For these specific types of materials, thermal diffusivity discs will be included in the matrix. To further analyze the fundamental behavior of phonon scattering by irradiation induced defects, several TEM discs made from Morton ß-SiC will be

inserted at all three of the irradiation temperatures. Post-irradiation annealing of the TEM discs will allow analysis of the resulting defect structures.

Finally, irradiation enhanced creep will be examined for the most advanced SiC fiber types using a bend stress relaxation (BSR) method [23]. These data will be compared to the irradiation creep data obtained by Scholz using a dynamic torsion method [11,12].

FUTURE WORK

The characterization of the properties for the unirradiated SiC composite and fiber specimens will be continued through 1999.

ACKNOWLEDGMENTS

This collaborative research program is sponsored by the Fusion Energy Sciences Program of the U.S. Department of Energy and the Monbusho Fusion Energy Program of Japan. Special acknowledgments are due to several industrial and research organizations (in the U.S.- Morton International Corp., MER Corp., Hypertherm Corp., Dow Corning Corp., Dupont Lanxide Corp., and the Oak Ridge National Laboratory, and in Japan through the CREST-ACE program - Nippon Carbon Co., Ube Industries, and the National Research Institute for Metals/NRIM) who have contributed samples and data for these irradiation effects studies.

REFERENCES

1. A.F. Rowcliffe, M.L. Grossbeck and J.P. Robertson, "Schedule and status of irradiation experiments," p. 356 in Fusion Materials Semiannual Progress Report (FMSPR),1997, DOE/ER-0313/23.

2-4. G.E. Youngblood, C.H. Henager and R.H. Jones, "Effects of neutron irradiation on the strength of continuous fiber reinforced SiC/SiC composites," p. 117 and "Thermochemical instability effects in SiC-based fibers and SiC_f/SiC composites," p. 111 in FMSPR 1996 and 1997, DOE/ER-0313/21 & 22, respectively; and G.E. Youngblood, R.H. Jones, Akira Kohyama and L.L. Snead, "Radiation response of SiC-Basedbased fibers," p. 163 in FMSPR,1997, DOE/ER-0313/23.

5. C.H. Henager, G.E. Youngblood, D.J. Senor, G.A. Newsome and J.J. Woods, "Dimensional stability and tensile strength of irradiated Nicalon CG and Hi Nicalon fibers," J Nucl. Mater. 253, 60-66 (1998).

6. Lance L. Snead, R.A. Lowden, M. Osborne and R.J. Shinavski, "Development and irradiation of SiC/SiC composites for fusion," p. 121 in Ref. 12.

7. L.L. Snead, M.C. Osborne, R.A. Lowden, J. Strizak, R. J. Shinavski, K.L. More, W.S. Eatherly, J. Bailey and A.M. Williams, "Low dose irradiation performance of SiC interphase SiC/SiC composites," J. Nucl. Mater. 253, 20-30 (1998).

8. M.C. Osborne, C.R. Hubbard, L.L. Snead and D. Steiner, "Neutron irradiation effects on the density, tensile properties and microstructural changes in Hi Nicalon™ and Sylramic™ SiC fibers," ibid. 67-77 (1998).

9. R.H. Jones, D. Steiner, H.L. Heinisch, G.A. Newsome and H.M. Kerch, "Review-Radiation resistant ceramic matrix composites," ibid. 245, 87-107 (1997).

10. Lance L. Snead, "Development of Silicon Carbide Composites for Fusion," Fusion Technology 24, 65-82 (1993).

11. R.H. Jones, C.H. Henager, G.E. Youngblood and H.L. Heinisch, "SiC/SiC composites for structural applications in fusion energy systems," ibid. 30, 969-976 (1996).

12. Proceedings of the 1st IEA International Workshop on SiC/SiC Ceramic Composites for Fusion Structural Applications, Editors: P. Fenici and A. Frias Rebelo, Oct. 28-29, 1996, Ispra (VA)-Italy.

13. Proceedings of the 2nd IEA/JUPITER Joint International Workshop on SiC/SiC Ceramic Composites for Fusion Applications, Editors A. Kohyama, R.H. Jones and P. Fenici, Oct. 23-24, 1997, Sendai, Japan.

14. Holger H. Streckert, Kirk P. Norton and Clement P.C. Wong, "Hermetic SiC composite tubes," Amer. Ceram. Soc. Bulletin 75(12), 61-64 (1996).

15. D.J. Senor, G.E. Youngblood, C.E. Moore, D.J. Trimble, G.A. Newsome and J.J. Woods, "Effects of neutron irradiation on the thermal conductivity of SiC-based composites and monolithic ceramics," Fusion Technology 30(3), 943-955 (1996).

16. G.E. Youngblood, R.H. Jones, G.N. Morscher and Akira Kohyama, "Creep behavior for advanced polycrystalline SiC fibers," p. 89 and p. 81 in FMSPR, Dec. 31, 1996 and June 30, 1997, respectively. DOE/ER-0313/21 & 22.

17. C.A. Lewinsohn, M.L. Hamilton, G.E. Youngblood, R.H. Jones, F.A. Garner, S.L. Hecht and A. Kohyama, "Irradiation-enhanced creep in SiC: data summary and planned experiments," J. Nucl. Mater. 253, 36-46 (1998).

18. A. Hasegawa, M. Saito, K. Abe and R.H. Jones, "Helium implantation effects on mechanical properties of SiC_f/SiC composites," ibid., 31-35.

19. T. Yano, H. Miyazaki, M. Akiyoshi and T. Iseki, "X-ray diffractometry and high-resolution electron microscopy of neutron-irradiated SiC to a fluence of 1.9×10^{27} n/m^2," ibid., 78.

20. Michael W. Barsoum and Tamer El-Raghy, "Synthesis and characterization of a remarkable ceramic: Ti_3SiC_2," J. Amer. Ceram. Soc. 79(7), 1953-56 (1996).

21. G.E. Youngblood and R.H. Jones, "Methods of radiation effects evaluation of SiC/SiC composite and SiC fibers," p. 37 in Ref. 13.

22. J.C. Withers, W. Kowbel, R.O. Loutfy, G.E. Youngblood and C. Wong, "High thermal conductivity SiC/SiC composites for fusion applications I and II," p. 87 and p.172 in FMSPR, Dec. 31, 1996, and Dec. 31, 1997, respectively. DOE/ER-0313/21 & 23.

23. G.E. Youngblood, M.L. Hamilton and R.H. Jones, "Technique for measuring irradiation creep in polycrystalline SiC fibers," p. 146 in FMSPR, 6/30/96, DOE/ER-0313/20.

NEUTRON IRRADIATION INDUCED AMORPHIZATION OF SILICON CARBIDE —

L. L. Snead* and J. C. Hay+ (Oak Ridge National Laboratory)

+Present address: IBM Thomas J Watson Research Center, P.O. Box 218, Room 218, Yorktown Heights, NY 10596-0218

OBJECTIVE

This paper describes the properties of neutron amorphized SiC and an estimate of the critical temperature for amorphization of SiC under neutron irradiation.

SUMMARY

This paper provides the first known observation of silicon carbide fully amorphized under neutron irradiation. Both high purity single crystal hcp and high purity, highly faulted (cubic) chemically vapor deposited (CVD) SiC were irradiated at approximately 60°C to a total fast neutron fluence of 2.6×10^{25} n/m^2. Amorphization was seen in both materials, as evidenced by TEM, electron diffraction, and x-ray diffraction techniques. Physical properties for the amorphized single crystal material are reported including large changes in density (-10.8%), elastic modulus as measured using a nanoindentation technique (-45%), hardness as measured by nanoindentation (-45%), and standard Vickers hardness (-24%). Similar property changes are observed for the amorphized CVD SiC. Using measured thermal conductivity data for the CVD SiC sample, the critical temperature for amorphization at this neutron dose and flux, above which amorphization is not possible, is estimated to be greater than 130°C.

PROGRESS AND STATUS

Introduction

Amorphization of silicon carbide has been studied in support of fundamental materials science and in application driven programs for reasons such as the use of SiC for electronic devices and in nuclear power systems. Several research groups have shown that SiC becomes amorphous during ion-beam irradiation at temperatures between 77 K and room temperature for damage levels equivalent to 0.1 to 0.5 displacements per atom (dpa) [1-9]. Most of these studies on SiC amorphization have used low-energy (<1 MeV) ion-beams [1,2,4-7], with a few researchers using high energy electrons [10-13].

Recent interest in SiC amorphization has focused on the temperature dependence of the critical dose for amorphization. In-situ TEM observation of the critical dose for amorphization as a function of irradiation temperature has been studied using 2 MeV electrons [11-13] and 360 keV Ar and 1.5 MeV xenon ions [14-17]. Zinkle and Snead have used 0.56 MeV silicon ions implanted into samples which were then prepared for TEM observation [8,9,18]. In all these studies, the threshold for amorphization of single crystal SiC was measured as a function of temperature. It was observed that there is a temperature-independent amorphization dose at low temperatures followed by a temperature above which the damage level required to amorphize SiC increases rapidly. In each case an apparent asymptotic increase in the amorphization dose occurred, yielding a "critical temperature" above which amorphization appears impossible. This critical temperature has been reported to range between 20°C to 70°C for electrons [11,12,19], ~150°C for Si ions [9,18] and ~220°C for Xe ions [15], all with similar damage rates of ~1×10^{-3} dpa/s. It is noted that both Weber [14,15] and Matsunaga's [10] work did not observe a significant difference in amorphization threshold between α and β SiC, whereas Inui reported a threshold temperature ~50°C higher for faulted β-SiC [12].

While the amorphization has been demonstrated for a number of ceramics using electron and ion irradiation, there is very little information on neutron-induced ceramic amorphization. There has been significant work on the microstructural and physical properties of neutron amorphized quartz [20-22], though the crystal to amorphous transition is due to radiolysis rather than due to displaced atoms. Other silicates, such as beryl ($3BeO\text{-}Al_2O_3\text{-}6SiO_2$), garnet ($Ca_3Al_2Si_3O_{12}$), topaz ($A_{l2}(OH)_2SiO_4$) and zircon ($ZrSiO_4$) also amorphize at neutron dose levels equivalent to ~0.6 dpa [23]. It has also been claimed that graphite amorphizes under neutron irradiation [24,25] at dose and temperatures < 1 dpa and 200°C, though, as pointed out by Kelly [26], the Raman spectra used as an indication for amorphization is consistent with the formation of in-plane edge dislocation dipoles. Another convincing piece of evidence against neutron induced amorphization of graphite, as quoted by previous authors [24,25] is that the dimensional change continues to behave anisotropically as the dose is increased above the apparent amorphization dose [26]. Diamond, however, has been shown to undergo amorphization during neutron bombardment by several researchers [27-32]. Of interest for diamond and the other amorphized ceramics is the large associated density change. Specifically, the decrease in density upon amorphization is 45% for diamond [27-31], ~15% for quartz [20,33], >6.2% for beryl [23], >5.5 for garnet [23], and >9% for zircon [34]. This swelling can be contrasted with the typical radiation-induced point defect strain in crystalline ceramics of less than a few percent [20].

Experimental

Samples of Cree Systems, Inc., 6H alpha single crystal SiC and Morton Advanced Materials CVD SiC were used in this study. The single crystal SiC wafer was purchased with an aluminum doping level of ~5 wppm. All other impurities for the single crystal material were in the wppb range. The CVD SiC is characterized as a highly faulted 3C structure with all impurities, as measured by the manufacturer, in the ppb range with the exception of titanium which is listed as 1.4 wppm. These materials were irradiated in the HT-3 hydraulic rabbit position of the High Flux Isotope Reactor at ORNL in perforated aluminum capsules. The samples were irradiated in contact with ~53°C flowing coolant water at a fast neutron flux of 7.8×10^{18} n/m^2-s (E>0.1 MeV) to a total fluence of 2.6×10^{25} n/m^2 (E>0.1 MeV). This fluence level is equal to a damage level of ~2.6 dpa, assuming a displacement energy of 40 eV for both the Si and C sublattices. The single crystal material was irradiated as wafer fragments of 0.34 mm thickness. The CVD SiC was irradiated as a 6 mm diameter, 10 mm long cylinder.

Specimen densities were obtained with density gradient columns using mixtures of tetrabromoethane-methylene iodide or ethylene bromide-bromoform for the unirradiated and irradiated samples, respectively. The accuracy of the measurement was better than 0.001 g/cc and was found to be reproducible in repeated measurements and consistent for duplicate samples. All samples were immersed in hydrofluoric acid for a period greater than 24 hr to remove any surface silica prior to measurement. Microindentation hardness and elastic modulus were determined using a Nanoindentor™-II with a peak loading of 30 mN and a constant loading rate of 1.5 mN/sec. The CVD SiC sample was polished with 1 mm diamond paste before indentation. A Buehler Micromet 3 microhardness testing machine was used at 500 g and 1 kg loads to measure the Vickers hardness. The two loads gave essentially the same hardness values. Only the 1 kg load hardness data is reported here. Indentation fracture toughness was found using cracks produced with the Vickers indentor. TEM microscopy was performed using a Philips CM-12 microscope on samples which were mechanically thinned and ion-milled with argon ions at 6 keV and an incident angle of 15° using a liquid-nitrogen-cooled stage during milling. After foil perforation, the specimens were milled at 3 keV and 9° for 10 minutes at ambient temperature to reduce surface amorphization associated with argon implantation. This procedure has been used extensively on ion-implanted SiC and causes minimal surface amorphization.

RESULTS AND DISCUSSION

Amorphization of Neutron Irradiated SiC

As stated in the introduction, there has been no demonstration of neutron-induced amorphization of SiC. There has been substantial work on the swelling, microstructure and mechanical properties of neutron irradiated SiC, though the majority of this work has been at elevated temperatures or at fluences apparently too low to induce amorphization. Primak et al. [35] reported irradiating single crystal 6H silicon carbide to 3×10^{24} n/m^2 (fast) at ~30°C in the MTR. The maximum swelling measured using macroscopic means was reported at 1.24%. Pravdyuk et al [36] measured macroscopic swelling and microscopic lattice expansion of 1.03% following irradiation to 7.2×10^{24} n/m^2 at ~120°C for an unspecified neutron energy spectrum. Other data have been generated at 140°C by Corelli et al. [37] to 7.2×10^{24} n/m^2 (E>1 MeV) which showed approximately 0.5% swelling. It should be noted that Corelli's materials were hot pressed and contained boron and free silicon which affected the rate of swelling as a function of neutron fluence. Above 200°C there are significant data [35,38-44] to high doses in single crystal and stoichiometric polycrystal forms of SiC which exhibit two general trends. First, the swelling of SiC in the 200-1000°C range saturates at a fast neutron fluence of approximately 1×10^{25} n/m^2 (E>0.1 MeV). Second, the amount of swelling appears to linearly decrease with increasing irradiation temperature and approaches zero at 1000°C.

The materials in this study were taken to approximately an order of magnitude higher dose than the 30°C irradiated materials of Primak [35]. A volumetric change of 10.8% was found for the single crystal material, which is substantially higher than expected due to point defect accumulation. Both single crystal and CVD SiC samples were examined by TEM. The diffraction patterns of these materials show diffuse rings typical of an amorphous material. There was no indication of diffraction spots anywhere in the sample and no contrast was found during dark field imaging. X-ray analysis (performed on the sample prior to sample thinning for TEM) also showed no evidence of crystallinity. A separate paper analyzes the microstructure of this material and the recrystallization kinetics determined by in-situ TEM annealing [45].

A substantial radial temperature gradient occurred during irradiation of the 6 mm diameter CVD SiC cylinder due to the constraint that the nuclear heat generated in the sample was removed through the sample periphery. The periphery of the sample was in contact with the ~53°C coolant water. The effect of this temperature gradient, which will be discussed in some detail in Section 3.3, was to create an amorphous periphery around a crystalline core. TEM examination near the center of the irradiated CVD sample showed a combination of diffuse rings and weak spots in the diffraction pattern. Dark field imaging in this area yielded spot-reflections on the order of 10 nm in size. Near the center of the sample both bright field images and diffraction patterns were indistinguishable from those of unirradiated material. While this is proof that the sample center remained crystalline, it is not sufficient evidence to rule out the presence of small amorphous islands within a crystalline matrix.

Physical Properties of Neutron Amorphized SiC

Physical properties such as density, hardness and elastic modulus of amorphized single and polycrystalline SiC have been previously estimated from measurements of surface or buried amorphous layers produced by ion beam irradiation. Specifically, the density has been inferred by surface step height measurements [46-48], by observing the increase in total range with TEM [8,9,17,49], or by x-ray techniques [50,51], yielding a density decrease ranging from about -22% to -15%. The normalized hardness, defined as the ratio of the as-irradiated to unirradiated hardness, (H_i/H_u), [17,47,48,52] and the normalized modulus (E_i/E_u) [17,52] for ion irradiated (amorphous) SiC have likewise ranged in the literature from 45%-70% and 70-76%, respectively.

(A) Swelling

Property measurement of the bulk amorphous samples in this study offers several advantages over measurement on the surface or buried layers associated with ion beam amorphized SiC. For example, the density (swelling) can be measured with an uncertainty of ±0.001 g/cc using the density gradient column technique. For the 2.6 dpa irradiated 6H single crystal SiC the density was found to be 2.857 g/cc, corresponding to a 10.8% reduction in density from the 3.204 g/cc unirradiated value. It is interesting to note that Snead [9] previously reported a similar decrease in density for hot pressed β-SiC (-10.1% or 2.84 g/cc) and sintered α-SiC (-11.8% or 2.79 g/cc) which were neutron irradiated to a fluence of ~1.5×10^{26} m^{-2} (E>0.1 MeV) at approximately 70°C. However, since the volumetric swelling from ion beam studies was reported to be 15-20%, it was incorrectly assumed that these neutron irradiated samples were only discontinuously amorphous. The difference in amorphous density of hot pressed β-SiC and sintered α-SiC materials and the amorphous density found in this paper for amorphized single crystal α-SiC (2.857 g/cc) is thought to be due to the presence of sintering aids (Si and B) in the hot pressed and sintered materials.

The density of the CVD SiC sample was measured to be 2.895 g/cc yielding a density decrease of 9.62% from the unirradiated value (3.203 g/cc.) As discussed in the previous section, the periphery of this 6 mm sample was amorphous while the center appeared crystalline by TEM. The measured density is therefore an averaged density of a heterogeneous (crystalline plus amorphous) sample.

(B) Mechanical Properties

The bulk nature of these specimens also allows measurement of elastic modulus and hardness without concern for underlying crystalline material influencing the results (i.e. substrate effects). These substrate effects are a common problem for the measurement of hardness and elastic modulus from ion beam modified surface or buried layers. While sensitive volume associated with hardness is defined by the material plastically deformed by the indentor, the elastic modulus as calculated from a microindentation unloading curve [53] is an average modulus integrated over a volume much larger than the plastically deformed volume. For a semi-infinite medium Samuels and Mulhearn [54] have shown that the elastic-plastic boundary extends hemispherically approximately ten times the indent depth. For the 30 mN load used in this study, this gives a plastically deformed radius for the amorphous SiC (~170 nm contact depth) of approximately 1.7 microns.

The mechanical properties of both unirradiated and irradiated materials are summarized in Table 1. Using a Nanoindentor-II, as was used in some of the previous ion beam studies [9,17,46], the measured hardness of the neutron amorphized 6H-SiC decreased from 38.7±2 to 21.0±1 GPa, while the elastic modulus decreased from 528±14 to 292±5 GPa. The errors quoted correspond to ± one standard deviation. The normalized hardness (H_{irr}/H_{unirr}) is measured to be 54±4% which is in approximate agreement with previous estimates [17,47,48,52]. However, the 55±2% normalized modulus is significantly lower than previous estimates obtained on ion-irradiated specimens with the exception of one study which used nanoindentation on a 3 MeV carbon ion irradiated specimen prepared in cross section [55]. This would suggest that substrate effects, which would be minimized for cross sectional indentation, and eliminated for the bulk amorphous materials of this study, were affecting previously reported elastic modulus measurements.

At a 1 kg load the Vickers hardness for the unirradiated single crystal and CVD SiC was measured to be 2245±107 and 2330±80 kg/mm^2, respectively. The hardness of the Morton CVD SiC at 500g loading was 2339 ±100 kg/mm^2 which agrees well with the manufacturer's 500g quoted hardness of 2500 kg/mm^2. For the single crystal and CVD SiC amorphized samples the (1 kg) Vickers hardness was measured to be 1708±35 and 1797± 75 kg/mm^2, respectively. This yields a normalized residual Vickers hardness of 76±3.8% for the single crystal material and 77±4.2% for the CVD SiC. The indentation fracture toughness was calculated for the unirradiated and

Table 1. Summary of measured properties for unirradiated and 2.6 dpa SiC irradiated at ~70°C

		Single Crystal SiC	CVD SiC
H (GPa); Nanoindentor	Unirradiated	38.7 ± 2	36.2 ± 1.3
	2.6 dpa	21.0 ± 1	23.4 ± 0.6
	H_i/H_{unirr}	54 ± 4%	64.6 ± 3.8%
E (GPa); Nanoindentor	Unirradiated	528 ± 14	500 ± 11
	2.6 dpa	292 ± 45	291 ± 7.5
	H_i/H_{unirr}	55 ± 2%	58.2 ± 1.9
H (Kg/mm^2); Vickers	Unirradiated	2245 ± 107	2330 ± 80
	2.6 dpa	1708 ± 35	1797 ± 75
	H_i/H_{unirr}	76 ± 4%	77 ± 4%
Density (g/cm^3)	Unirradiated	3.204	3.203
	2.6 dpa	2.857	2.895
	H_i/H_{unirr}	10.8%	

Only sample periphery amorphized. Data is not a bulk measurement.

amorphized single crystal SiC sample using the Evans-Davis model [56] at a Vicker's load of 500g. The average crack length from a series of ten indents was used along with the Vicker's hardness data and the elastic modulus measured by microindentation (using the Nanoindentor-II). The indentation fracture toughness, K_c, was calculated to increase from 2.5 MPa/m$^{1/2}$ for the unirradiated material to 3.2 MPa/m$^{1/2}$ for the amorphized SiC.

Figures 1 and 2 give the hardness and modulus as measured with the Nanoindentor-II along the radius of the 6 mm diameter CVD SiC sample. From Fig. 1 it is seen that the hardness at the center of the sample (radial distance of zero in Fig.) is somewhat scattered with mean of 36.2±1.2 GPa which is in agreement with measurements taken on unirradiated material. As the indents move outward radially the hardness falls off rapidly reaching a minimum of 23.4±0.6 GPa, or a normalized hardness of approximately 64.6±3.8%. The elastic modulus shows a similar trend decreasing from 375 ± 10.6 GPa to 291±7.5 GPa. The errors in these cases refer to ± 1 standard deviation at radii of 0-0.25 mm and 2.5-3.0 mm, respectively.

The modulus measured at the center of the sample (Fig. 2) is substantially lower than the 500 GPa modulus measured on an unirradiated sample. Such a decrease in elastic modulus is expected for neutron irradiated ceramics [20]. Specifically, for the same Morton CVD SiC material and measurement technique used in this study, Osborne [57] reported an elastic modulus of ~420 GPa for a 2×20^{25} n/m^2 (E>0.1 MeV) irradiation at ~150°C. It would be expected that for the higher dose material in this study the point defect concentration would be increased and the elastic modulus would be lower. The normalized modulus for the amorphized SiC using the 500±11 GPa unirradiated value is 58.2±1.9%. The scatter associated with the nanoindentation measurement in Figs. 1 and 2 is due in part to the intrinsic machine error and to sample surface roughness. The larger scatter towards the center of the specimen may be attributed to either indent position with respect to crystal grain boundaries or the effect of these grains on the surface finish. As the plastic depth of the indentor was on the order of 200 nm, the small crystallites as discussed in Section 3.1 should not have contributed to the scatter.

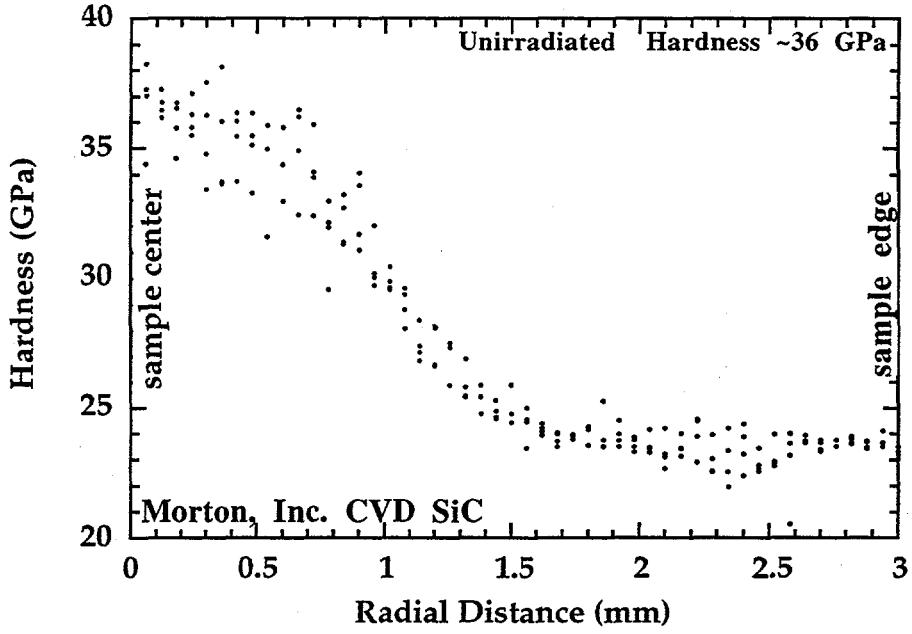

Fig. 1. Hardness as a function of radius for the 2.6 dpa neutron irradiated CVD sample.

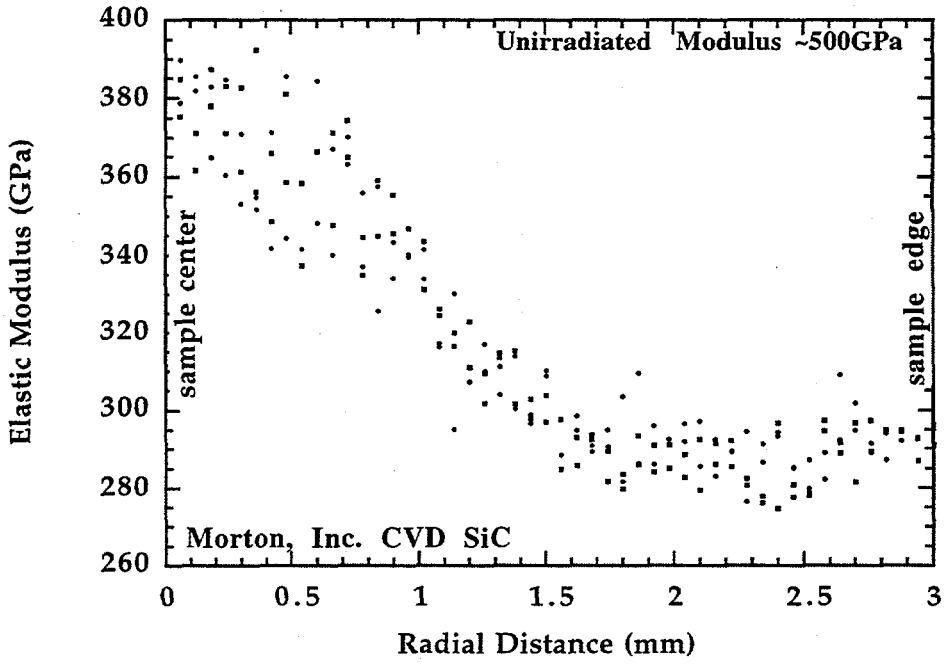

Fig. 2. Elastic modulus as a function of radius for the 2.6 dpa neutron irradiated CVD SiC sample.

(C) Estimated Critical Amorphization Temperature

As discussed in the introduction the critical temperature above which amorphization does not occur has been reported to range between 20 and 220°C [9,11,12,15,18,19] for a damage rate of ~1 ×1 0^{-3} dpa/s. Below this temperature, the dose required to amorphize SiC appears to approach a constant, although the amorphization dose may be a function of the PKA energy transferred. For example Inui [11,12] reported a threshold dose of 0.5-1.0 dpa for 2 MeV electron irradiation whereas Weber [15] reported a threshold dose of 0.2 dpa for 1.5 MeV Xe^{+} ion irradiation. This can be qualitatively explained if one considers that the amorphization in SiC is due to free energy increases associated with point defect accumulation and chemical disordering [58]. Since the amount of chemical disordering per dpa increases with increasing PKA energy, less displacement damage is required to produce amorphization with heavy ions as compared to electrons at all temperatures.

An estimate of the critical temperature for amorphization for fission neutrons can be found using Figs. 1 and 2. From these plots the point at which the material transforms from crystalline to discontinuously amorphous is at a radius of approximately 1 mm. At 2.6 dpa, for the fast neutron dose rate of ~ 8×10^{-7} dpa/s, this measured transition point defines the threshold amorphization temperature.

The effect of neutron collisions in ceramics is, among other things, to create lattice vacancies that serve as phonon scattering centers which significantly reduce thermal conductivity [8,9,18,59-61]. From a companion irradiation experiment under identical conditions [62], it is known that a damage level of 0.01 dpa at ~70°C does not cause amorphization. However, it reduces the room temperature thermal conductivity from 2.56 to 0.31 W/cm-K. Irradiation to 0.1 dpa at ~300°C reduces the thermal conductivity to 0.11 W/cm-K [62]. Knowing the thermal conductivity as a function of fluence, a simple 1-D thermal transport equation can be used with the measured thermal conductivity data to determine the sample internal temperature as a function of neutron dose. Measured thermal conductivity data [62] are used to generate the curves of Fig. 3. The temperature of the periphery of the sample is taken to be 60°C, to account for the 7°C calculated film temperature drop between the sample edge and the ~53°C coolant. At the beginning of irradiation the room temperature thermal conductivity (2.56 W/cm-K) is quite high, resulting in a negligible sample internal temperature gradient as seen in the lower curve of Fig. 3. The remaining inset thermal conductivity data are calculated from measured thermal diffusivities [62]. Note that at 0.1 dpa the conductivity is assumed to be 0.1 W/cm-K through comparison with a 0.1 dpa irradiation at 300°C which yielded 0.11 W/cm-K. Also note that room temperature thermal conductivity values are used in Fig. 3. Using these room temperature thermal conductivity values, which are slightly greater than the thermal conductivities at temperature, will yield slightly lower internal temperatures (~4%). Accurate data on thermal conductivity as a function of both dose and temperature for SiC is not yet available.

As the thermal conductivity of the silicon carbide degrades during the irradiation the sample internal temperature increases. At some damage level the periphery of the sample becomes amorphous and the thermal conductivity further decreases to ~0.04 W/cm-K [62]. This measurement was on the discontinuously amorphized CVD SiC sample and most likely gave a somewhat higher thermal conductivity than if the sample had been fully amorphous. A future measurement of a fully amorphous sample would therefore be desirable. Assuming concentric cylinders with distinct thermal conductivity for the crystalline and amorphous regions, the upper curve of Fig. 3 defines the temperature profile for the sample at 2.6 dpa. The assumed transition point from crystalline to discontinuously amorphous material gives an estimate for the temperature threshold for this 2.6 dpa and ~ 8×10^{-7} dpa/s irradiation. This estimate is considered a lower limit for the threshold amorphization temperature and is somewhat greater than 130°C.

This value for the critical amorphization temperature is in reasonable agreement with the ~150°C critical amorphization temperature found by Zinkle [9,18] and Snead [9,18] who used energetic

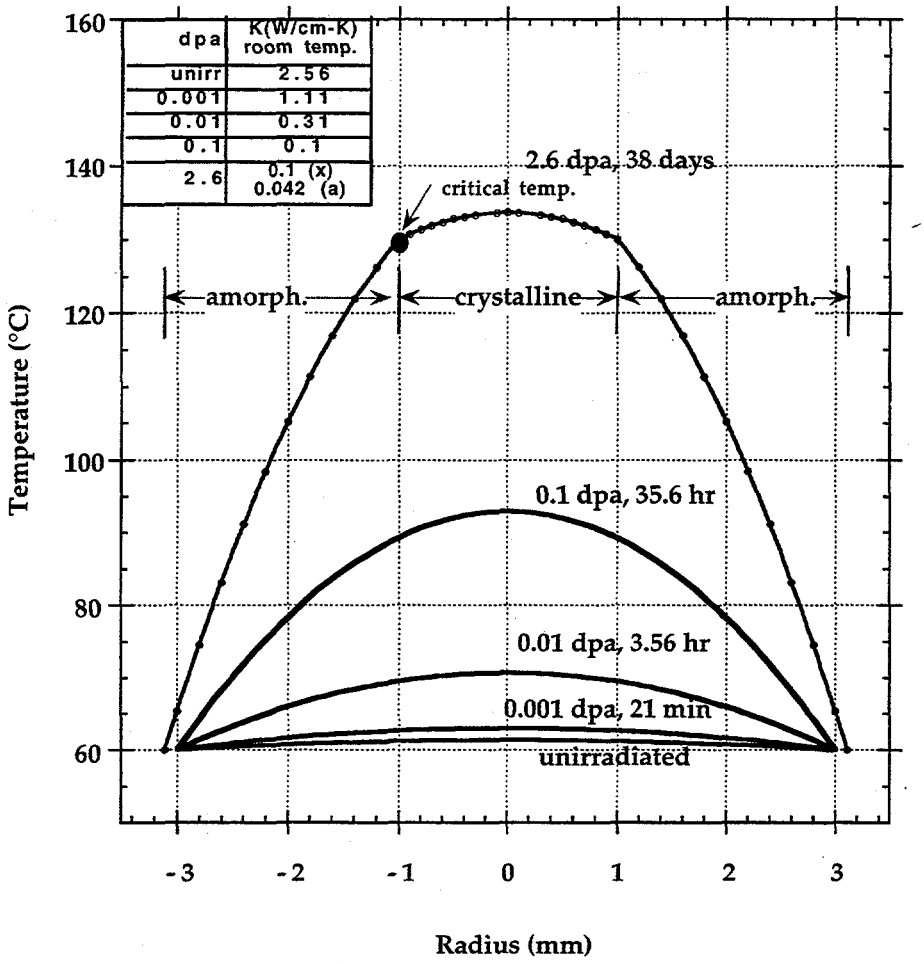

Fig. 3. Internal temperature as a function of dose for the neutron irradiated CVD SiC samples.

silicon ions at 1×10^{-3} dpa/s and is intermediate between the 20-70°C critical temperature found using 2 MeV electrons [11,12,19] and ~220°C for 1.5 MeV Xe ions [15] which also used a displacement rate of 1×10^{-3} dpa/s. The similarity with the silicon ion and the dissimilarity with the electron and xenon ion irradiations can be qualitatively explained considering the nature of the cascades for the various ions. The silicon ion PKA energy is roughly similar with that imparted by an energetic neutron while the average PKA energies for the xenon ion irradiations is substantially greater. Conversely, the electron can only impart enough energy in an elastic collision with the Si or C atoms to create simple Frenkel pairs. However, other explanations exist for the difference in measured amorphization temperature thresholds. As discussed elsewhere [8], the Xenon and electron irradiation used the "in-situ" method where the amorphizing sample was imaged on a thin TEM foil during irradiation. The silicon ion implantations were "ex-situ" measurements where TEM samples were prepared following irradiation. For both of these techniques the potential exists for stress fields altering the results, while the in-situ measurement has the added potential complication of the surface acting as a sink for migrating defects.

CONCLUSIONS

A clear demonstration of the amorphization of silicon carbide caused by the elastic collisions with fast neutrons has been made. Due to the bulk nature of the amorphized material accurate data can be obtained on certain mechanical properties and compared with data from previous ion beam irradiations. While the hardness data generated in this study falls within the somewhat wide range in hardness values previously reported, both the previously reported density and elastic modulus of amorphized SiC appear to be substantially different from the actual values. High purity single crystal alpha SiC and high purity polycrystalline beta SiC irradiated to 2.6 dpa at ~60°C have transformed from the crystalline state with a density of 3.203±0.001 to an amorphous state with 10.8% lower density. Using a nanoindentation technique the normalized hardness for the single crystal and polycrystalline material is about 54% and 65% of the unirradiated values, respectively, while the normalized elastic modulus is about 55% and 58%, respectively. Vickers normalized hardness was ~76% for amorphous single and polycrystal material. An increase in the indentation fracture toughness from 2.5 to 3.2 $MPa/m^{1/2}$ is also observed upon SiC amorphization. Using measured values of thermal conductivity for irradiated crystalline SiC and the amorphized SiC the lower limit for the threshold temperature for amorphization of SiC by fission neutrons at 2.6 dpa and $\sim 8 \times 10^{-7}$ dpa/s was estimated to be 130°C. This estimate is in reasonable agreement with previous silicon ion irradiations.

ACKNOWLEDGMENTS

*Research sponsored by the Office of Fusion Energy Sciences, U.S. Department of Energy, under contract DE-AC05-96OR22464 with Lockheed Martin Energy Research Corp.

REFERENCES

[1] R.R. Hart, H.L. Dunlap, and O.J. Marsh, Radiat. Eff. 9 (1971) 261.
[2] J.A. Edmond, R.F. Davis, S.P. Withrow, and K.L. More, J. Mater. Res. 3 (1988) 321.
[3] C.W. White et al., Mater. Sci. Reports 4 (1989) 41.
[4] J.M. Williams, C.J. McHargue, and B.R. Appleton, Nucl. Instrum and Meth. 209/210 (1983) 317.
[5] J.A. Spitznagel et al., Nucl. Instrum. Meth. in Phys. Res. B16 (1986) 237.
[6] N.G. Chechenin et al., Nucl. Instrum. and Meth. in Phys. Res. B65 (1992) 341.
[7] L.L. Horton et al., Nucl. instrum. meth. in Phys. Res. B65 (1992) 345.
[8] L.L. Snead and S.J. Zinkle, MRS Symposium on Microstructure of Irradiated Materials, Boston, Ma., 373, eds. I.M. Robertson et al. (Materials Research Society, Inc., 1995) p. 377.
[9] L.L. Snead and S.J. Zinkle, in Microstructure Evolution During Irradiation, MRS Symposium Proceedings vol. 439, eds. I.M. Robertson et al. (Materials Research Society, Pittsburgh, 1997) p. 595.
[10] A. Matsunaga, C. Kinoshita, K. Nakai, and Y. Tomokiyo, J. Nucl. Mater. 179-181 (1991) 457.
[11] H. Inui, H. Mori, and T. Sakata, Phil. Mag. B 66 (1992) 737.
[12] H. Inui, H. Mori, and H. Fujita, Phil. Mag. B 61 (1990) 107.
[13] C. Kinoshita et al., Proceedings of the 11th International Conference on Electron Microscopy (Japanese Society of Electron Microscopy, 1986).
[14] W.J. Weber and L.M. Wang, Nucl. Instrum. Meth. Phys. Res. B 106 (1995) 298.
[15] W.J. Weber, L.M. Wang, and N. Yu, Nucl. Instrum. Meth. Phys. Res. B 116 (1996) 322.
[16] W.J. Weber and N. Yu, Proceedings of the International Conference on Defects in Insulating Materials (1997) in press.
[17] W.J. Weber, N. Yu, L.M. Wang, and N.J. Hess, J. Nucl. Mat. 244 (1997) 258.
[18] S.J. Zinkle and L.L. Snead, Nucl. Instr. Meth. B 116 (1996) 92.
[19] H. Inui, H. Mori, and H. Fujita, Acta Metall. 37 (1989) 1337.
[20] R.A. Wullaert, in Effects of Radiation on Materials and Components, eds. J.F. Kircher and R.E. Bowman (Reinhold Publishing Corp., London, 1964) p. 277.

[21] E. Lell, N.J. Kreidl, and J.R. Hensler, in Progress in Ceramic Science vol. 4, ed. J.E. Burke (Pergamon Press, 1966) p. 1.
[22] F.W. Clinard, Jr. and L.W. Hobbs, in Physics of Radiation Effects in Crystals, eds. R.A. Johnson and A.N. Orlov (Elsevier, Amsterdam, 1986) p. 387.
[23] M.C. Wittels and F.A. Sherrill, ORNL Solid State Division Annual Progress Report for Period Ending August 31, 1959 Report ORNL-2829 (1959).
[24] T. Tanabe, S. Muto, Y. Gotoh, and K. Niwase, J. Nucl. Mat. 175 (1989) 258.
[25] K. Niwase, K. Nakamura, T. Shikama, and T. Tanabe, J. Nucl. Mater. 170 (1990) 106.
[26] B.T. Kelly, J. Nucl. Mater. 172 (1990) 237.
[27] E.R. Vance, H.J. Milledge, and A.T. Collins, J. Phys. D: Appl. Phys. 5 (1972) L40.
[28] V.Y. Karasov et al., Sov. Phys. Solid State 26 (1984) 1739.
[29] E.R. Vance, J. Phys. C : Solid St. Phys. 4 (1971) 257.
[30] D.T. Keating, Acta Crystallogr. 16 (1963) A113.
[31] D.T. Keating, J. Phys. Chem. Solids 29 (1968) 771.
[32] V.A. Nikolaenko and V.G. Gordeev, Radiat. Eff. Def. Solids 139 (1996) 183.
[33] J.R. Gilbreath and O.C. Simpson, Argonne National Laboratory Report ANL-4888 (1953).
[34] J.H. Crawford and M.C. Wittels, Second International Conference on Peaceful Uses of Atomic Energy, Geneva, Switzerland , 1958) p. 300.
[35] W. Primak, L.H. Fuchs and P.P. Day, Phys. Rev. 103 (1956) 1184.
[36] N.F. Pravdyuk, V.A. Nikolaenko, V.I. Kapuchin, and V.N. Kusnetsov, Properties of Reactor Materials and the Effects of Radiation Damage Proceedings, ed. D.J. Littler (Butterworths, 1962) p. 57.
[37] J.C. Corelli, J. Hoole, J. Lazzaro, and C.W. Lee, J. Amer. Ceram. Soc. 66 (1983) 529.
[38] R. Blackstone and E.H. Voice, J. Nucl. Mater. 39 (1971) 319.
[39] G.W. Hollenberg et al., J. Nucl. Mat. 219 (1995) 70.
[40] R.J. Price, J. Nucl. Mat. 46 (1973) 268.
[41] R.J. Price, J. Nucl. Mat. 48 (1973) 47.
[42] R.J. Price, J. Nucl. Mat. 33 (1969) 17.
[43] R.P. Thorne and V.C. Howard, Proc. Brit. Ceram. Soc. 7 (1967) 439.
[44] R. Mathews, J. Nucl. Mater. 51 (1974) 203.
[45] L.L. Snead, S.J. Zinkle, J.C. Hay, and M.C. Osborne, accepted Nucl. Instrum. Meth. B (1997).
[46] C.J. McHargue and J.M. Williams, Nucl. Instrum. Meth. in Phys. B80/81 (1993) 889.
[47] C.J. McHargue et al., Mat. Sci. Eng. 69 (1985) 123.
[48] C.J. McHargue and C.S. Yust, J. Amer. Ceram. Soc. 67 (1984) 117.
[49] J. Bentley, L.J. Romana, L.L. Horton, and C.J. McHargue, Phase Formation and Modification by Beam-Solid Interactions, eds. G.S. Was, L.E. Rehn and D.M. Follstaedt (Materials Research Soc., 1992) p. 363.
[50] W. Bolse, J. Conrad, T. Rodle, and T. Weber, Surf. Coat. Techn. 74-75 (1995) 927.
[51] V. Heera, J. Stoemenos, R. Kogler, and W. Skorupa, J. Appl. Phys. 77 (1995) 2999.
[52] C.J. McHargue, D.L. Joslin, and J.M. Williams, Nucl. Instrum. Meth. B 46 (1990) 185.
[53] W.C. Oliver and G.M. Pharr, J. Mater. Res. 7 (1992) 1564.
[54] L.E. Samuels and T.O. Mulhearn, J. Mech. and Phys. of Solids 5 (1957) 125.
[55] L.L. Snead, S.J. Zinkle, and D. Steiner, J. Nucl. Mat. 191-194 (1992) 560.
[56] A.G. Evans, Proceedings of the Eleventh National Symposium on Fracture Mecahnics Part II., ed. S.W. Frieman (ASTM, Philadelphia, 1979) p. 112.
[57] M.C. Osborne, L.L. Snead, and J.C. Hay, J. Mater. Res. submitted (1998).
[58] A.T. Motta and D.R. Olander, Acta Metall. Mater. 38 (1990) 2175.
[59] P.G. Klemens, in Solid State Physics, Vol. 7, eds. F. Seitz and D. Turnbull (Academic Press, New York, 1958) p. 1.
[60] P.G. Klemens, in Thermal Conductivity, Vol. 1, ed. R.P. Tye (Academic Press, New York, 1969) p. 1.
[61] P.G. Klemens, G.F. Hurley, and F.W. Clinard, Jr., in Proc. 2nd Topical Meeting on the Technology of Controlled Nuclear Fusion, CONF-760935, eds. G.L. Kulcinski and N.M. Burleigh (National Tech. Inform. Service, Springfield, VA, 1976) p. 957.
[62] L.L. Snead, S.J. Zinkle, and D.P. White, to be published (1998).

3.0 FERRITIC/MARTENSITIC STEELS

THERMOPHYSICAL AND MECHANICAL PROPERTIES OF Fe-(8-9)%Cr REDUCED ACTIVATION STEELS — S. J. Zinkle, J. P. Robertson and R. L. Klueh (Oak Ridge National Laboratory)

OBJECTIVE

The objective of this report is to summarize the thermophysical and mechanical properties of 8-9%Cr reduced activation ferritic/ martensitic steels in order to provide a reference design basis for the Advanced Power EXtraction (APEX) project.

SUMMARY

The key thermophysical and mechanical properties for 8-9%Cr reduced activation ferritic/ martensitic steels are summarized, including temperature-dependent tensile properties in the unirradiated and irradiated conditions, stress-rupture behavior, elastic constants, thermal conductivity, thermal expansion, specific heat, and ductile-to-brittle transition temperature. The estimated lower and upper temperatures limits for structural applications are 250 and 550°C due to radiation hardening/embrittlement and thermal creep considerations, respectively.

PROGRESS AND STATUS

Introduction

In order to provide a reference design basis for the Advanced Power EXtraction (APEX) project, published data on the thermophysical and mechanical properties for 8-9%Cr reduced activation ferritic/ martensitic steels have been compiled. Due to the large existing data base on these steels, a comprehensive evaluation of all published data was not attempted. Only a limited amount of property data for these steels is contained in the most recent version (Pub. 5) of the ITER Materials Properties Handbook (IMPH). The IMPH should be used as the reference point for design calculations if the full property database is included in a future version of the Handbook.

1. Ultimate tensile strength (unirradiated)

The ultimate tensile strength for several heats of Fe-(8-9)%Cr reduced activation steels has been measured by numerous researchers. The tensile properties have been found to be comparable to those of conventional Fe-(8-9)%Cr steels. Figure 1 summarizes some of the ultimate tensile strength (UTS) data obtained in tensile tests on F82H (Fe-8%Cr-2%WVTa) and other heats of 8-9Cr (conventional and reduced activation) ferritic/martensitic steels [1-6]. The least squares fitted equation for the ultimate tensile strength over the temperature range of 20-700°C is

$$\sigma_{UTS}(MPa)= 682.8 -1.1617*T +0.005472*T^2 -1.1166e\text{-}05*T^3 +6.2357e\text{-}09*T^4$$

where the temperature (T) is in °C. The correlation coefficient for the plotted data using this equation is R=0.8955.

2. Yield strength (unirradiated)

Figure 2 summarizes the yield strength data obtained on several heats of Fe-(8-9)%Cr conventional and reduced activation steels. The least squares fitted equation for the yield strength over the temperature range of 20-700°C is

$$\sigma_Y(MPa)= 531.4 -0.38794*T +0.001482*T^2 -2.3965e\text{-}06*T^3 -1.4506e\text{-}10*T^4$$

where the temperature (T) is in °C. The correlation coefficient for the plotted data using this equation is R=0.8835. The corresponding least squares equation fitted only to the yield strength data of F82H reduced activation Fe-8Cr steel is

$$\sigma_Y(MPa)= 544.2 -0.18491*T -0.0003603*T^2 +2.2141e\text{-}06*T^3 -3.5596e\text{-}09*T^4$$

R=0.96242

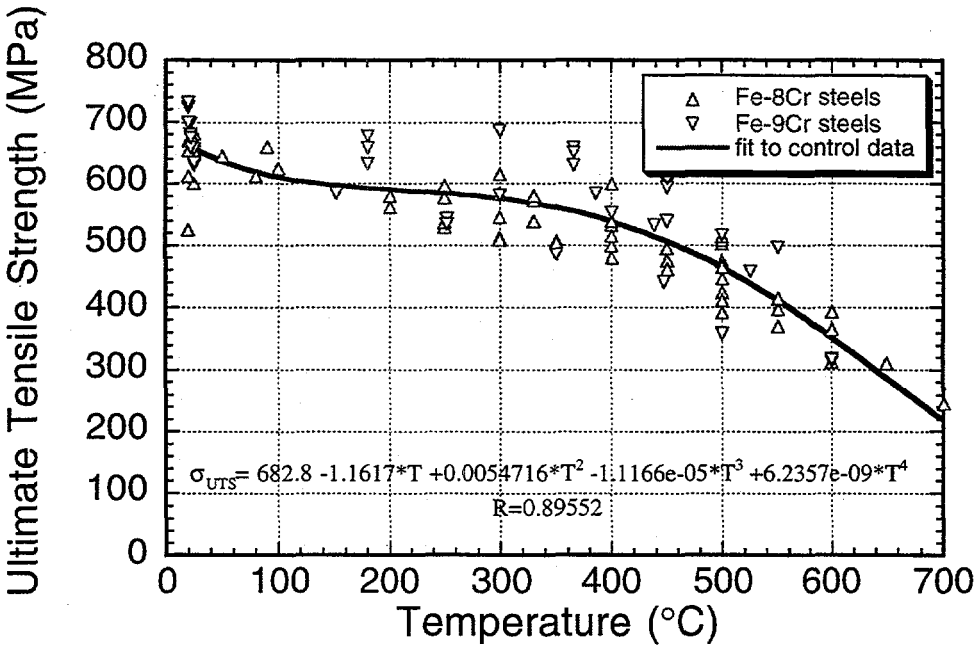

Fig. 1. Ultimate tensile strength of unirradiated 8-9%Cr steels [1-6].

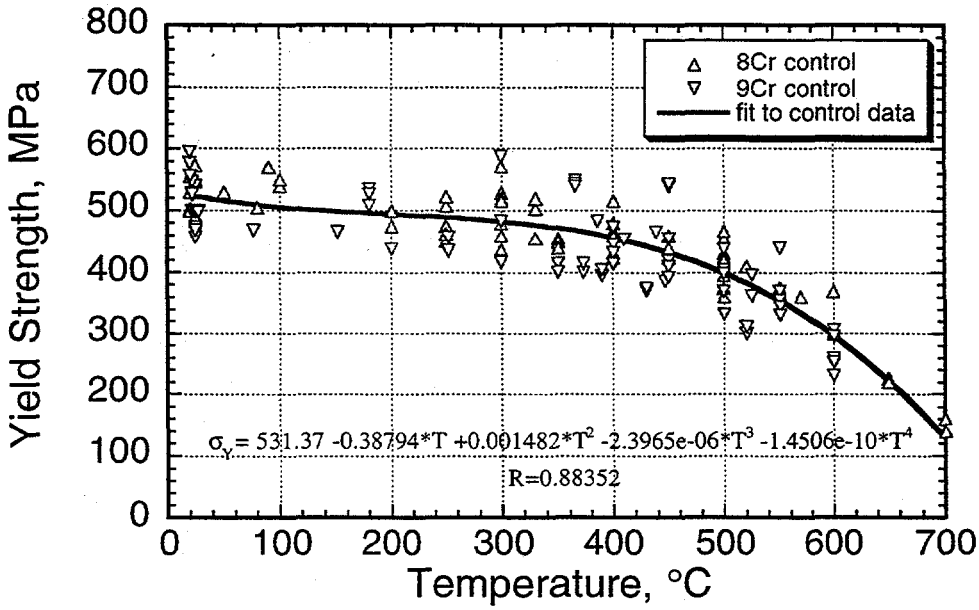

Fig. 2. Yield strength of unirradiated 8-9%Cr steels [1-4,6].

3. Yield and ultimate strength (irradiated)

Neutron irradiation causes a pronounced increase in the yield and ultimate tensile strength of 8-9%Cr conventional and reduced activation steels at temperatures below ~400°C, but has little effect on the strength at higher temperatures. Figure 3 shows a comparison of the unirradiated and irradiated yield strength for irradiation temperatures between 50 and 600°C. The effects of fusion-relevant helium generation on the yield and ultimate strength have not been adequately studied, although only minor changes have been observed in studies performed to date [7-9].

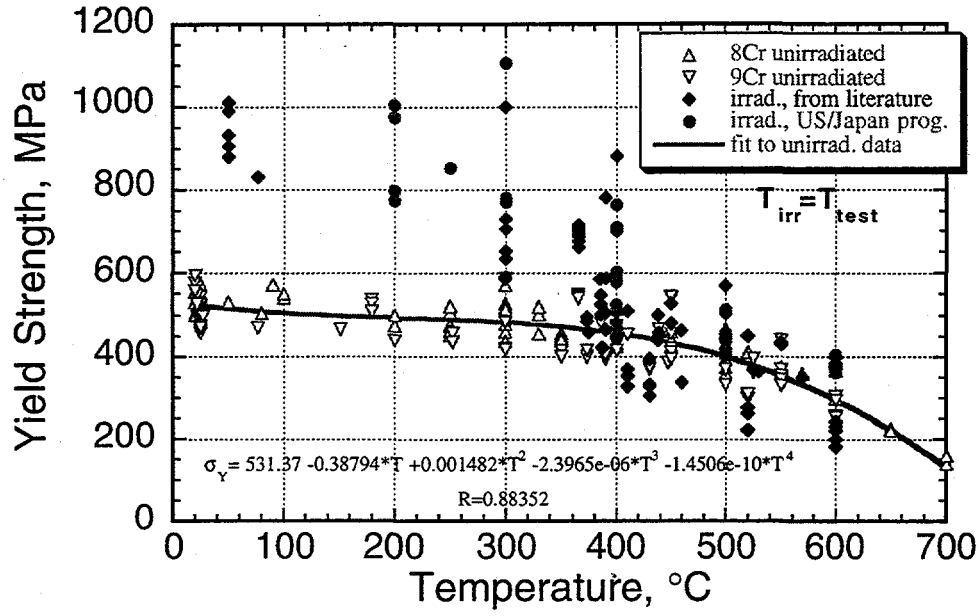

Fig. 3. Comparison of the yield strength of unirradiated and irradiated 8-9%Cr steels [6].

4. Uniform and Total Elongation (unirradiated and irradiated)

The uniform elongations of unirradiated 8-9%Cr conventional and reduced activation steels exhibit relatively low values (≤5%) at all temperatures from 20 to 700°C [6]. As shown in Fig. 4, the unirradiated uniform elongation decreases slowly from ~5% to ~1% over this temperature range. The corresponding total elongations range from ~10 to 30%. The low uniform elongation is a typical feature associated with the martensitic structure. Uniform elongations of >5% at temperatures from 20 to 650°C have been observed in oxide dispersion strengthened ferritic steel [10,11], which is a promising alternative to ferritic/martensitic steel (see section 8). As shown in Fig. 5, irradiation causes a decrease in the uniform and total elongations, particularly for irradiation temperatures below 400°C [1-3,6,9,12]. Data for both reduced-activation and conventional Fe-(8-9)%Cr steels are plotted in this figure. The uniform elongation is very low (<3%) at all investigated irradiation temperatures. The total elongation remains above ~7% for all irradiation conditions investigated to date, and it increases with increasing irradiation temperature (Fig. 5). The effects of fusion-relevant helium generation on tensile elongation have not been adequately studied.

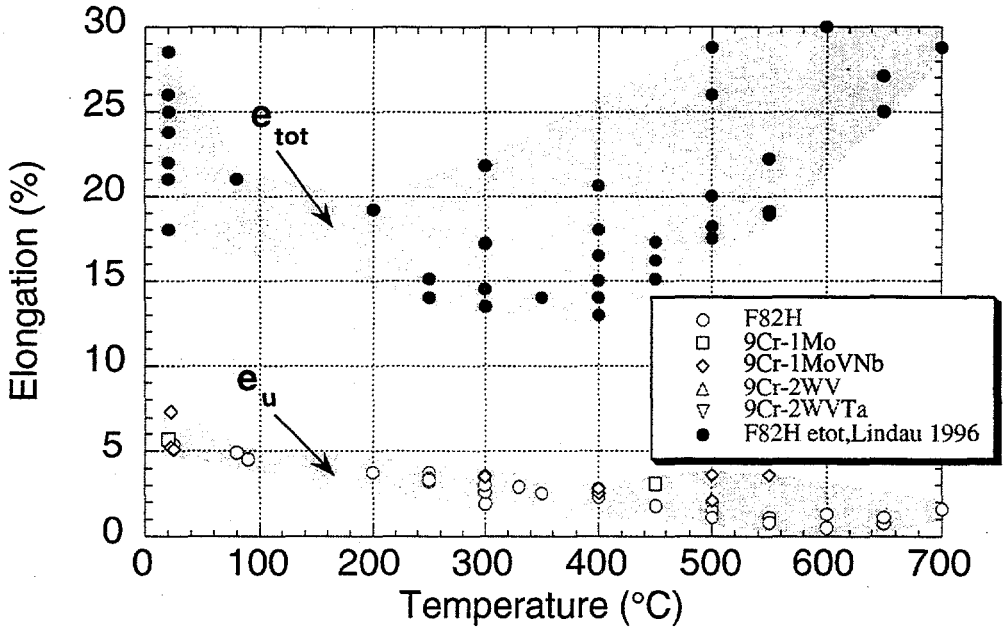

Fig. 4. Uniform and total elongation of unirradiated 8-9%Cr steels [1-3,6].

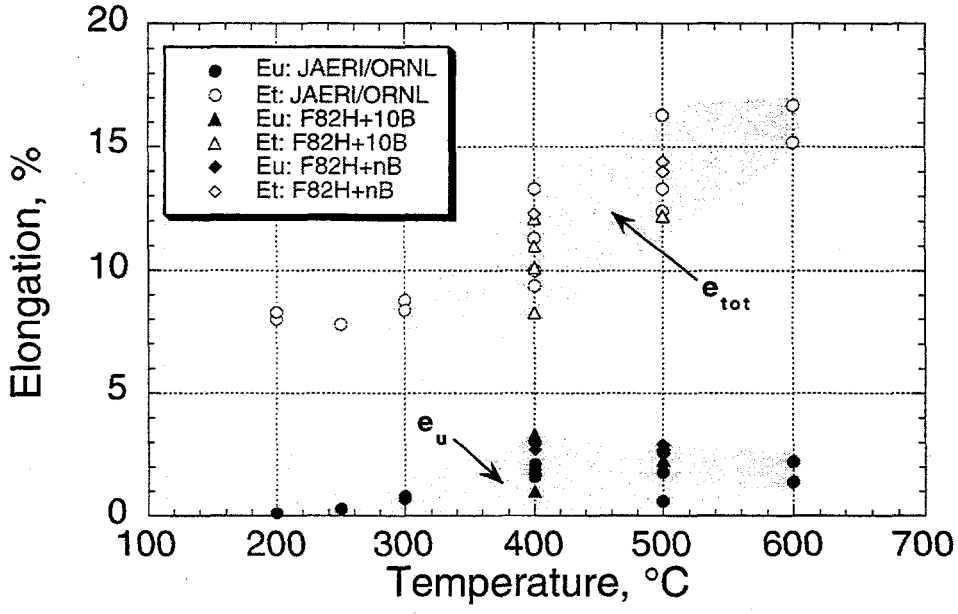

Fig. 5. Uniform and total elongation of irradiated 8-9%Cr steels [1-3,6]. The test temperature equals the irradiation temperature.

5. Reduction in area

The reduction in area (RA) as measured on unirradiated and irradiated 8-9%Cr steel tensile specimens is shown in Fig. 6 [1,3,5,6]. The unirradiated reduction in area is high (>80%) at all test temperatures between 20 and 700°C. Irradiation causes a decrease in the RA (particularly at low irradiation and test temperatures), but the reduction in area remains acceptably high in the limited number of tensile specimens examined to date. Helium effects have not been adequately studied.

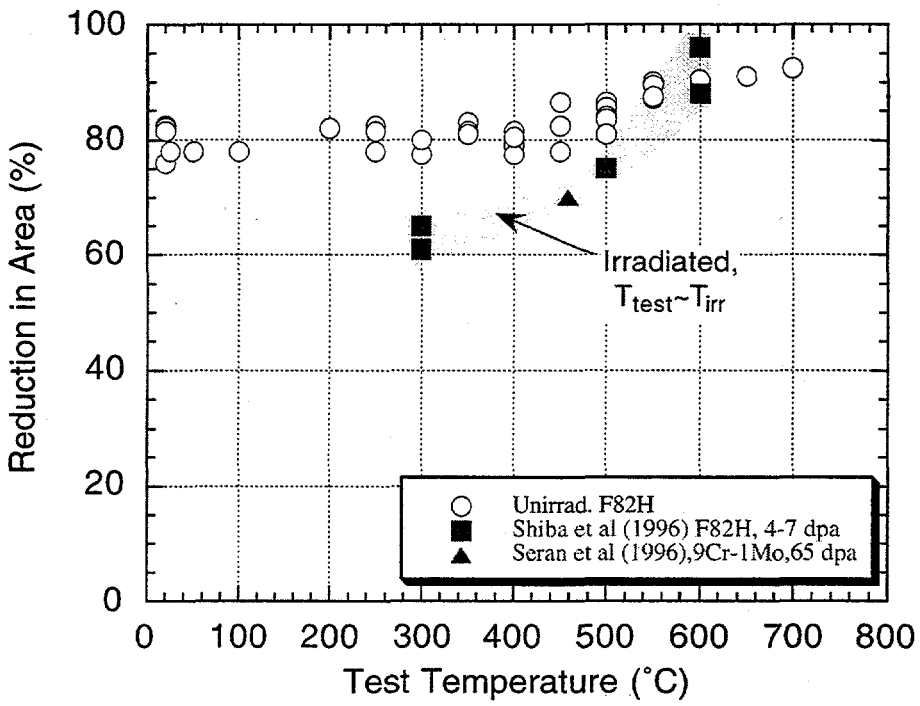

Fig. 6. Reduction in area of unirradiated and irradiated 8-9%Cr steels [1,3,5,6].

6. Stress-strain curves

Figure 7 shows representative stress-strain curves obtained on miniature "type SS-3" sheet tensile specimens (0.76 × 1.52 × 7.6 mm gage dimensions) for F82H steel tensile tested at a strain rate of 1.1×10^{-3} s^{-1} following neutron irradiation at 200-600°C [6,9,12]. Pronounced flow localization is observed for irradiation temperatures below ~400°C, whereas adequate strain hardening capacity occurs at temperatures ≥400°C.

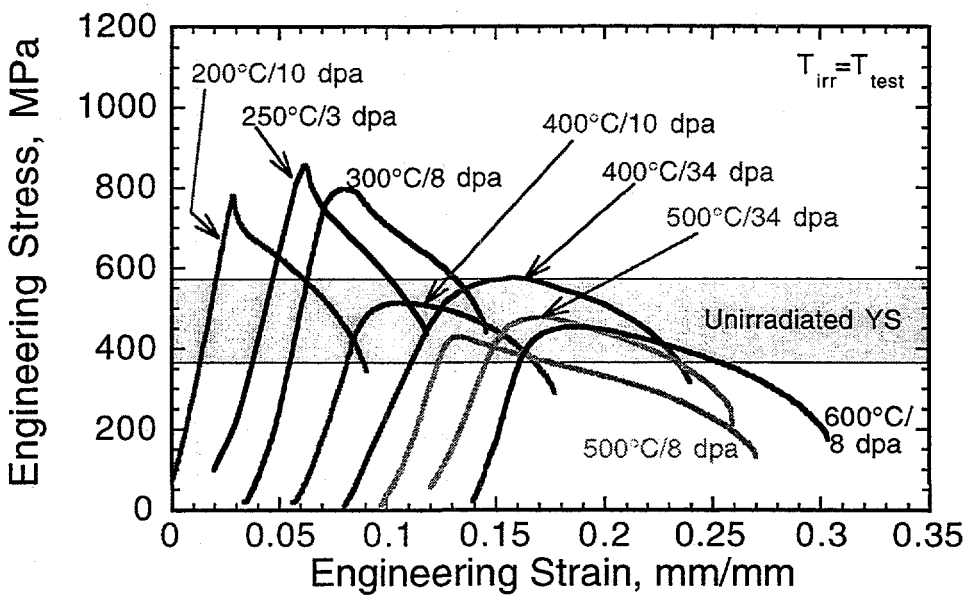

Fig. 7. Load vs. normalized crosshead displacement tensile curves for F82H irradiated to 3-34 dpa at 200-600°C [6,9,12].

7. Elastic constants

The elastic constants for F82H (8Cr-2WVTa) have been measured between 20 and 700°C [3,5], and Young's modulus has been measured from -150 to 350°C for several other reduced-activation steels including Fe-9Cr alloys [13]. The temperature-dependent elastic constants for F82H exhibit approximately bilinear behavior, which a slope change occurring near 450-500°C. The change in the temperature dependence of the elastic constants at 450-500°C was attributed to annealing effects on the martensitic structure at the higher temperatures [3,5]. The following equations for Young's modulus (E_Y) and the shear modulus (G) are obtained from the F82H experimental data [3,5] in the temperature interval between 20 and 450°C:

$$E_Y \text{ (GPa)} = 233 - 0.0558*T \qquad \text{(T in Kelvin)}$$

$$G \text{ (GPa)} = 90.1 - 0.0209*T \qquad \text{(T in Kelvin)}$$

At temperatures above 450°C, Young's modulus for F82H decreases approximately linearly from E_Y=193 to 160 GPa as the temperature is increased from 450 to 700°C. The shear modulus similarly decreases from G= 75 to 60.5 GPa as the temperature is increased from 450 to 700°C. Poisson's ratio ($\nu=(E_Y/2G) - 1$) is constant up to 500°C with a value of 0.29, and then slowly increases to 0.31 at 700°C.

8. Stress-rupture

There have been numerous studies of the creep and stress-rupture behavior of unirradiated and irradiated 8-9%Cr steels at temperatures up to 650°C (0.5 T_M) [1,2,5,14]. Good creep resistance exists for temperatures up to ~550°C (0.45 T_M), but poor creep resistance occurs at 600°C and above. For example, the 10,000 h creep rupture strength of F82H is 200 MPa at 550°C, 120 MPa at 600°C and 50 MPa at 650°C [1,5]. Improvements in the thermal creep resistance of reduced-activation ferritic steels can be achieved with oxide dispersion strengthened (ODS) alloys

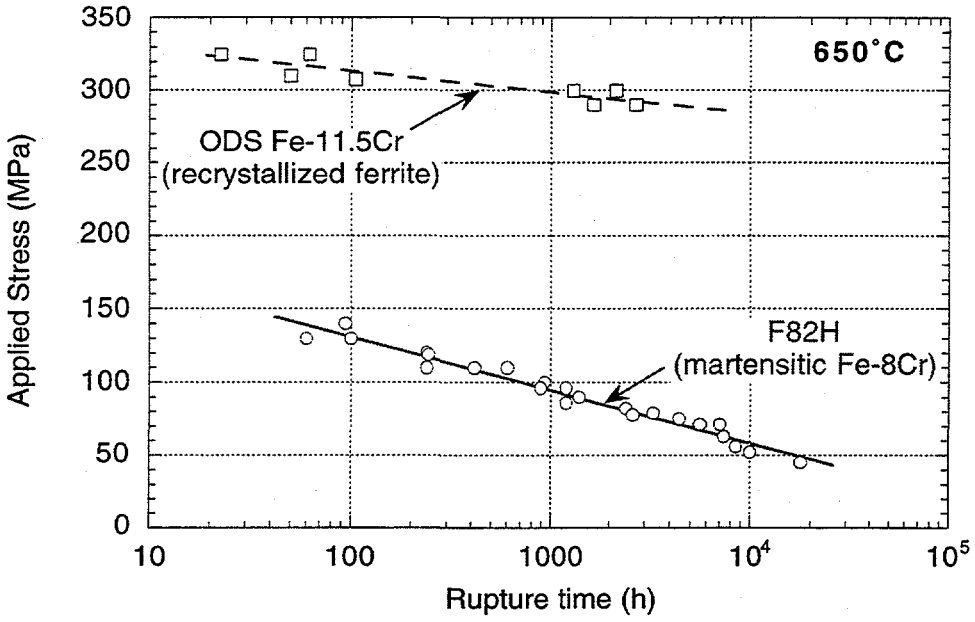

Fig. 8. Creep rupture strength of F82H martensitic steel and ODS ferritic steel [1,5,10,15].

[10,11,15,16]. Figure 8 compares the creep rupture strength at 650°C of F82H ferritic/martensitic steel and a recently developed ODS ferritic steel (Fe-11.5Cr-2.2W-0.23Ti-0.015C-0.2Y_2O_3) which has uniform creep rupture properties in the longitudinal and transverse direction [1,5,10,15].

9. Thermal expansion, specific heat and thermal conductivity

The thermophysical properties for several different heats of F82H (8Cr-2WVTa) have been measured from room temperature to 700°C [1,3,5]. The mean coefficient of thermal expansion (α_{th}) varied from 10.4 ppm/°C at room temperature to 12.4 ppm/°C at 700°C. The specific heat at constant pressure (C_P) varied from 470 J/kg-K at 20°C to 810 J/kg-K at 700°C. The specific heat increase was approximately linear with temperature between 20 and 500°C, and was strongly nonlinear above 500°C. The thermal conductivity at 20-800°C was determined from thermal diffusivity measurements using laser flash techniques and was found to be nearly independent of temperature, with an average value of 33 W/m-K between 20 and 700°C for two different heats of F82H.

10. Ductile to brittle transition temperature (unirradiated and irradiated)

The measured value of the ductile to brittle transition temperature (DBTT) in body-centered cubic materials depends on numerous experimental parameters, including the specimen geometry, strain rate, and the sharpness of the notch where the crack is initiated (notch acuity) [17]. The measured DBTT in miniature unirradiated F82H machined Charpy vee-notch (MCVN) specimens ranges from about -60°C to -110°C, where the lower DBTT was obtained using 1.5 mm thick Charpy impact specimens [2,9,18]. The DBTT for unirradiated F82H measured on precracked compact tension specimens is near -50°C [19]. Low temperature irradiation causes a moderate increase in the DBTT (ΔDBTT~20 to 100°C) of advanced reduced activation 8-9Cr steels for the damage levels investigated to date [2,9,12,18,20,21]. Very small changes in the DBTT (ΔDBTT <50°C) have been observed in 8-9%Cr steels irradiated at temperatures above 400°C. The effect

of fusion-relevant helium generation rates on the DBTT in irradiated specimens has not been adequately studied.

11. Magnetic properties

Ferritic steels are ferromagnetic, and could affect the plasma operation by introducing perturbations in the local magnetic field, depending on the details of the reactor design. The saturation magnetic flux density (B_s) of unirradiated F82H varies from 1.95 T at room temperature to 1.75 T at 400°C [5]. The magnetic field strength required to produce complete saturation is approximately 3000 Oersted (2.4×10^5 A/m) for temperatures between 20 and 400°C [5]. The remanent magnetic flux density (B_r) decrease from 0.21 T to 0.17 T over this temperature range. Changes in coercive force, B_r, and permeability may occur under irradiation, whereas changes in B_s are not expected to occur during irradiation unless there is a phase transformation [22]. Ferromagnetic properties of ferritic steels have not been measured following high-dose irradiation. No measurable radiation-induced changes have been observed at low doses (<<1 dpa) [22].

12. Recommended reference operating temperature limits

The maximum operating temperature limit for 8-9%Cr reduced activation ferritic/martensitic steels is ~550°C, due to thermal creep considerations. Somewhat higher temperatures could be tolerated for components exposed to low mechanical stresses. Oxide dispersion strengthened ferritic alloys under development may be capable of operation up to temperatures of 650°C or higher [10,11,15,16]. Additional work on irradiated specimens is needed before the minimum operating temperature limit can be established. The reference minimum operating temperature limit will be controlled by radiation hardening, which causes loss of ductility and an increase in the ductile to brittle transition temperature. According to the available irradiation data, the DBTT of 8-9%Cr steels remains near or below room temperature following neutron irradiation at temperatures between 200 and 550°C [2,9,12,18,20,21]. There is some limited evidence that fusion-relevant helium generation rates may cause a further increase in the DBTT beyond that attributable to matrix hardening (defect cluster) effects [8,9,20]. Further work is needed to determine the effect of helium on fracture properties. For the purposes of the APEX design study, the proposed reference minimum operating temperature for 8-9%Cr steels is 250°C.

References

[1] N. Yamamouchi, M. Tamura, H. Hayakawa, A. Hishinuma, T. Kondo, J. Nucl. Mater. 191-194 (1992) 822.

[2] K. Ehrlich, in: Proc. IEA Working Group Meeting on Ferritic/Martensitic Steels, Culham, UK, October 1996, ORNL/M-5674, ed. R.L. Klueh, (Oak Ridge National Lab, 1996).

[3] K. Shiba, N. Yamanouchi, A. Tohyama, in: Fusion Materials Semiann. Progress Report for Period ending June 30, 1996, DOE/ER-0313/20 (Oak Ridge National Lab, 1996) p. 190.

[4] K. Shiba, M. Suzuki, A. Hishinuma, J. Nucl. Mater. 233-237 (1996) 309.

[5] K. Shiba, A. Hishinuma, A. Tohyama, K. Masamura, Japan Atomic Energy Research Institute Report JAERI-Tech 97-038 (1997).

[6] J.P. Robertson, R.L. Klueh, K. Shiba, A.F. Rowcliffe, Fusion Materials Semiann. Prog Rep. for period ending Dec. 31 1997, DOE/ER-0313/23 (Oak Ridge National Lab, 1997) 179.

[7] R.L. Klueh, P.J. Maziasz, J. Nucl. Mater. 187 (1992) 43.

[8] R.L. Klueh, D.J. Alexander, J. Nucl. Mater. 230 (1996) 191.

[9] A. Hishinuma, A. Kohyama, R.L. Klueh, D.S. Gelles, W. Dietz, K. Ehrlich, 8th Int. Conf. on Fusion Reactor Materials, Sendai, J. Nucl. Mater. (1998) submitted.

[10] S. Ukai et al., in: Intern. Symp. on Material Chemistry in Nuclear Environment (National Research Institute of Metals, Tsukuba, Ibaraki, Japan, 1996) p. 891.

[11] S. Ukai, T. Nishida, H. Okada, T. Okuda, M. Fujiwara, J. Nucl. Sci. Technol. 34 (1997) 256.

[12] A.F. Rowcliffe, J.P. Robertson, E. Wakai, K. Shiba, D.J. Alexander, S. Jitsukawa, 8th Int. Conf. on Fusion Reactor Materials, Sendai, J. Nucl. Mater. (1998) submitted.

[13] H.T. Lin, B.A. Chin, in: Fusion Reactor Materials Semiann. Progress Report for Period ending September 30, 1987, DOE/ER-0313/3, 1987) p. 43.

[14] A. Kohyama, A. Hishinuma, Y. Kohno, K. Shiba, A. Sagara, in: Proc. ISFNT-4, Tokyo, Japan, 1997) in press.
[15] S. Ukai, T. Nishida, T. Okuda, T. Yoshitake, 8th Int. Conf. on Fusion Reactor Materials, Sendai, J. Nucl. Mater. (1998) submitted.
[16] D.K. Mukhopadhyay, F.H. Froes, D.S. Gelles, presented at 8th Int. Conf. on Fusion Reactor Materials, Sendai (1997).
[17] G.E. Lucas, G.R. Odette, J.W. Sheckherd, K. Edsinger, B. Wirth, in: Fusion Materials Semiann. Progress Report for Period ending March 31, 1995, DOE/ER-0313/18 (Oak Ridge National Lab, 1995) p. 147.
[18] A. Kohyama, in: Proc. IEA Working Group Meeting on Ferritic/Martensitic Steels, Culham, UK, October 1996, ORNL/M-5674, ed. R.L. Klueh, (Oak Ridge National Lab, 1996.
[19] H.-X. Li, R.H. Jones, J.P. Hirth, D.S. Gelles, J. Nucl. Mater. 233-237 (1996) 258.
[20] R.L. Klueh, D.J. Alexander, J. Nucl. Mater. 218 (1995) 151.
[21] L.E. Schubert, M.L. Hamilton, D.S. Gelles, in: Fusion Materials Semiann. Progress Report for Period ending June 30, 1996, DOE/ER-0313/20 (Oak Ridge National Lab, 1996) p. 171.
[22] D.S. Billington, J.H. Crawford, Jr., Radiation Damage in Solids, Princeton University Press, Princeton, NJ, 1961.

ANALYSIS OF STRESS-INDUCED BURGERS VECTOR ANISOTROPY IN PRESSURIZED TUBE SPECIMENS OF IRRADIATED FERRITIC-MARTENSITIC STEEL: JLF-1 - D. S. Gelles (Pacific Northwest National Laboratory)* and T. Shibayama (University of Hokkaido, Japan)

OBJECTIVE

The objective of this effort is to provide understanding of microstructural evolution in irradiated ferritic/martensitic steels for first wall applications in a fusion reactor.

SUMMARY

A procedure for determining the Burgers vector anisotropy in irradiated ferritic steels allowing identification of all a<100> and all $\frac{a}{2}$<111> dislocations in a region of interest is applied to a pressurized tube specimen of JLF-1 irradiated at 430°C to 14.3 x 10^{22} n/cm^2 (E > 0.1 MeV) or 61 dpa. Analysis of micrographs indicates large anisotropy in Burgers vector populations develop during irradiation creep.

PROGRESS AND STATUS

Introduction

In a previous report,[1] it was shown that irradiation creep induced Burgers vector anisotropy for perfect dislocations could be determined in pressurized creep tubes of the Japanese duplex ferritic steel JFMS irradiated in the FFTF/MOTA. The procedure used a process of ellimination to identify each of the a<100> and $\frac{a}{2}$<111> Burgers vector in a field of view.

More recently, pressurized tube specimens of JLF-1 were made available for microstructural examination and it was possible to again examine Burgers vector anisotropy.[2] JLF-1 is the first of a series of low activation Fe-9Cr-2W-0.2V steels which were prepared to exclude nickel and molybdenum additions. Three sets of up to four tubes were irradiated, three tubes at 430°C, four tubes at 460°C and four tubes at 520°C. All sets contained unstressed conditions. Microstructural examination of these pressurized tubes was a part of the Monbusho experimental objectives.

Experimental Procedure

Pressurized tubes of JLF-1 steel were made from tubing fabricated from rod stock. The chemical composition of the rod stock is given in Table 1. Tube segments had dimensions of 0.57 mm outside diameter, 0.20 mm wall thickness, and were 19.8 mm in length. Endcaps of the same material were electron beam welded to both ends of the tubing segments. One endcap had a small (0.13 mm diameter) hole for pressurization to obtain the desired hoop stress at the design irradiation temperature. The pressurization gas was helium. Diameter measurements were made using a non-contacting laser measurement system before and after irradiation. Three specimens were irradiated in level 2 of FFTF/MOTA 2A in canister 4D-2 and 2B in canister 4D-1 at 430°C for an accumulated exposure time of 503.4 equivalent full power

---

*Pacific Northwest National Laboratory (PNNL) is operated for the U.S. Department of Energy by Battelle Memorial Institute under contract DE-AC06-76RLO-1830.

days, over 12082 h. The estimated accumulated damage in these creep specimens during irradiation was 14.3 x 10^{22} n/cm^2 (E > 0.1 MeV) or 61 dpa.[2]

Table 1. Nominal Composition of JLF-1 (wt%) with balance Fe

Cr	C	Mo	W	Mn	Nb	V
9.04	.097	>.01	1.97	0.46	na	0.19
Si	P	S	Ni	N	Ta	Ti
>0.1	na	na	na	na	0.07	.001

na - not available

Following irradiation and diametral measurement, one JLF-1 specimen, comprising the maximum stress condition following irradiation at the lowest temperature of 430°C (VA08), was selected for microstructural examination and Burgers vector anisotropy measurement.

The specimen was sectioned with a slow speed saw by first removing the end caps and then splitting the tube longitudinally. Curved disks 3 mm in diameter were then punched from the central region of the split tube using a punch designed for tubing specimens. The disks were mechanically ground flat and then thinned for transmission electron microscopy using standard procedures. Examinations were performed using a JEOL 1200EX transmission electron microscope with a double tilting goniometer stage. Column realignment was found to be necessary after each change in specimen tilt.

Results

Diameter change and swelling measurements

Diameter change measures for the pressurized tube specimens of JLF-1 from the FFTF/MOTA are given in Table 2, and the diametral creep strains are plotted using closed diamonds, as a function of hoop stress in Figure 1, with measurements for HT-9 and JFMS, a duplex steel, for comparison.[3]

Table 2. Creep Data on JLF-1 Pressurized Tubes Irradiated in FFTF

ID	VA02	VA05	VA08	VA01	VA04	VA07	VA10
Temperature (°C)	430			459			
Hoop Stress (MPa)	0	30	60	0	30	60	100
Diametral Strain (%)	0.04	0.13	0.27	0.03	0.08	0.16	0.23

ID	VA00	VA03	VA06	VA09
Temperature (°C)	519			
Hoop Stress (MPa)	0	30	60	100
Diametral Strain (%)	na	0.23	0.61	0.60

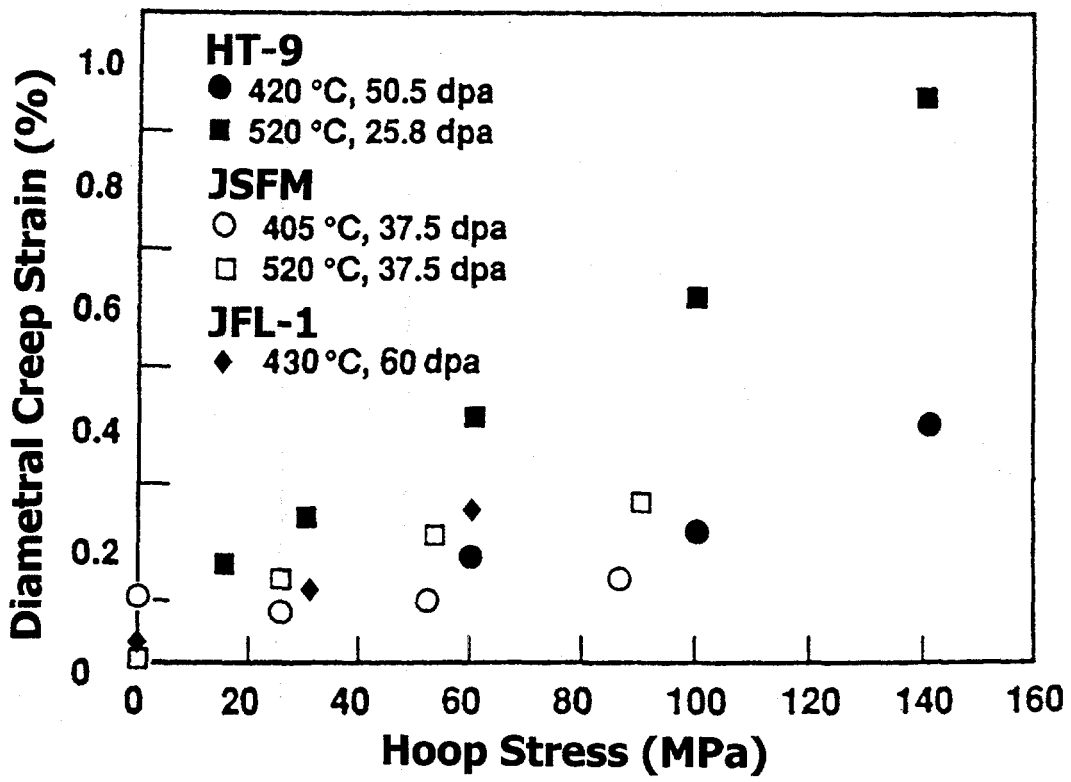

Figure 1. Irradiation Creep Response of JFMS and JLF-1 in Comparison with HT-9 as a Function of Hoop Stress.

From Figure 1, it can be shown that allowing for differences in dose, JLF-1 has creep strengths similar to HT-9 and JFMS. JLF-1 shows non-linear behavior with greater curvature than that for HT-9 indicative of complex behavior such as precipitation. A more detailed description of creep response in ferritic steels has recently been published by Toloczko et al.[4]

Swelling as determined from density change was measured only for specimens VA02 and VA08 of JLF-1. Results are provided in Table 3. Table 3 indicates that swelling was 0.658% for unstressed JLF-1 irradiated at 430°C to 61 dpa whereas under a hoop stress of 60 MPA the swelling increased to 0.885%.

Table 3. Swelling in JLF-1 specimens irradiated at 430°C as a function of stress

Specimen ID	Stress	Swelling
VA02	0 MPa	0.658
VA08	60 MPa	0.886

Microstructural examination

Microstructural examination of JLF1 was limited to specimen VA08 which had been pressurized to the largest hoop stress of 60 MPa. Furthermore, only dislocation anisotropy was studied in

detail. However, irradiated was found to have caused no major changes in microstructure; no void swelling was found and no evidence for further precipitation could be identified. These findings appear contradictory to swelling measurements given in Table 3. A possible explanation lies in the anticipated precipitation of tungsten in the form of $M_{23}C_6$.

An area was selected for analysis of dislocation anisotropy with orientation near (013) and with the tube length effectively parallel to $[01\bar{1}]$. A sequence of six micrographs was taken using $\vec{g}$ = [200], [011] and $[\bar{1}10]$. Three of the images are provided in Figure 2 to show the dislocation structure found within a region bounded by subgrain boundaries. The area shown in Figure 2 has also been analyzed to provide a quantitative estimate for Burgers vector anisotropy. The foil is again approximately 67 nm thick, but the field of view for measurement is similar to that shown in order to avoid subgrain boundary effects. From Table 4, it can be shown that dislocation densities vary between 0.9 and 9.5×10^9 cm^{-2}, corresponding to a factor of about ten variation. Anisotropy develops in both the $\frac{a}{2}$<111> and a<100> populations.

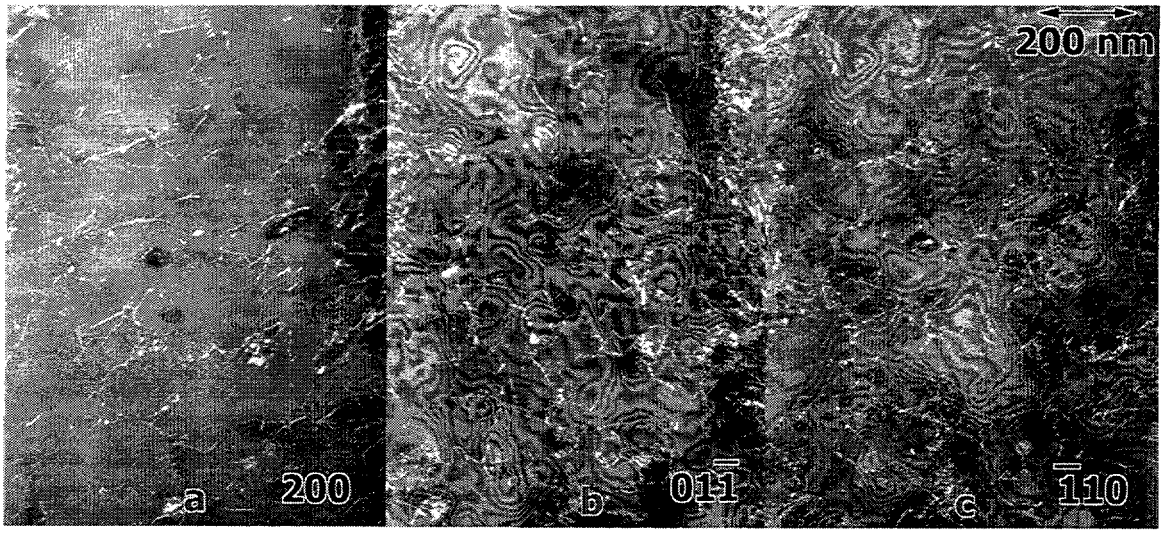

Figure 2. Weak Beam Dark Field Micrographs of an Area in Specimen VA08 Arranged for Comparison of Dislocations using 200 contrast in a), $01\bar{1}$ contrast in b), $\bar{1}10$ contrast in c).

Table 4. Dislocation Density Measurements, Showing Burgers Vector Anisotropy as a function of Burgers vector for specimen VA08 of JLF-1 irradiated at 430°C with a hoop stress of 60 MPa and compared to Specimen RR03 of JFMS Irradiated at 407°C with a Hoop Stress of 86 MPa.[1]

Burgers vector		$\frac{a}{2}[111]$	$\frac{a}{2}[\bar{1}11]$	$\frac{a}{2}[1\bar{1}1]$	$\frac{a}{2}[11\bar{1}]$	a[100]	a[010]	a[001]
$10^9 cm^{-2}$	VA08	9.47	1.38	3.03	2.65	0.89	2.27	4.17
	RR03	1.94	1.02	0.62	4.50	1.77	4.28	4.72

Discussion

This work has provided an opportunity to extend Burgers vector anisotropy determination in the ferritic alloy class. Procedures have been tested, and results have been generated showing that a significant anisotropy can be generated in ferritic/martensitic steels at 400-430°C for stress levels of 60-86 MPa. This discussion section is intended to cover two topics: limitations of the procedure and significance of the results.

The analysis given in Table 4 is based on measurements that may not be statistically significant. The specimen thicknesses were only 67 nm, and only about 40 dislocations were analyzed in the field of view. Dislocation motion may have occurred in such thin foils, although evidence for such motion was not observed. Few dislocation nodes could be found in the analyzed regions to show that the Burgers vector identification did not violated energy balances. Also, dislocation density measurements have not yet been completed on an unstressed specimen.

The results that anisotropy as large as a factor of 8 in JFMS and 10 in JLF-1 between different Burgers vector populations is surprising, given the limited amount of total strain found in the specimens. The strain measured in specimen RR03 was 0.15% and in VA08, it was 0.27%, whereas the unstressed specimen RR00 deformed 0.11% presumably due to precipitation and VA02 deformed 0.04 despite swelling of 0.658%. Therefore, the strain due to irradiation creep may have been as low as 0.04% in RR03 but 0.24% possibly influenced by precipitation in VA08. In comparison, results on austenitic steels provided similar levels of anisotropy in irradiated pressurized tubes, with deformations ranging between -0.02 and 1.255%.[5] The lower value corresponded to a situation where the perfect dislocation population had only just been generated, and therefore the average dislocation velocity was very low. Therefore, it appears that the present results indicate that dislocation motion may have been very limited in the JFMS specimen for the dose level achieved, about 40 dpa possibly caused by the high precipitate density found in the specimen.

CONCLUSIONS

Procedures have been developed to determine Burgers vector anisotropy in ferritic/martensitic steels containing both $\frac{a}{2}$<111> and a<100> Burgers vectors. The procedures have been tried on two irradiated pressurized tube specimens of JFMS steel irradiated in the FFTF/MOTA. Analysis of results for the specimens irradiated at stresses of 60 to 86 MPa indicates differences in Burgers vector anisotropy as large as a factor of 10.

AKNOWLEDGEMENT

This work was supported by JUPITER and the FFTF/MOTA on the US/Japan collaboration program.

REFERENCES

1. D. S. Gelles, A. Kimura, and R. J. Puigh, DOE/ER-0313/12, 123.

2. A. Kohyama, Y. Kohno, K. Asakura, M. Yoshino, C. Namba and C. R. Eiholzer, J. Nucl. Mater., V212-215 (1994) 751.

3. A. Kohyama and R. J. Puigh, "Irradiation Creep Behavior of a Japanese Ferritic Steel," FFTF/MOTA Annual Progress Report, Fusion Year 1988 (National Institute for Fusion Research, Nagoya, June 1989) 180.

4. M. B. Toloczko, F. A. Garner and C. R. Eiholzer, J. Nucl. Mater., (1998) to be published.

5. D. S. Gelles in Effects of Radiation on Materials: Twelfth International Symposium, ASTM STP 870, Vol. I, F. A. Garner and J. S. Perrin, Eds. (ASTM, Philadelphia, 1985) 98.

Mechanical Properties of Irradiated 9Cr-2WVTa Steel, R. L. Klueh, D. J. Alexander (Oak Ridge National Laboratory) and M. Rieth (Forschungszentrum Karlsruhe Institut für Materialforschung II)

Objective

The goal of this study is to evaluate the impact behavior of irradiated ferritic steels and relate the changes in properties to the heat treatment of the steel.

SUMMARY

An Fe-9Cr-2W-0.25V-0.07Ta-0.1C (9Cr-2WVTa) steel has excellent strength and impact toughness before and after irradiation in the Fast Flux Test Facility and the High Flux Reactor (HFR). The ductile-brittle transition temperature (DBTT) increased only 32°C after 28 dpa at 365°C in FFTF, compared to a shift of ≈60°C for a 9Cr-2WV steel—the same as the 9Cr-2WVTa steel but without tantalum. This difference occurred despite the two steels having similar tensile properties before and after irradiation. The 9Cr-2WVTa steel has a smaller prior-austenite grain size, but otherwise microstructures are similar before irradiation and show similar changes during irradiation. The irradiation behavior of the 9Cr-2WVTa steel differs from the 9Cr-2WV steel and other similar steels in two ways: (1) the shift in DBTT of the 9Cr-2WVTa steel irradiated in FFTF does not saturate with fluence by ≈28 dpa, whereas for the 9Cr-2WV steel and most similar steels, saturation occurs at <10 dpa, and (2) the shift in DBTT for 9Cr-2WVTa steel irradiated in FFTF and HFR increased with irradiation temperature, whereas it decreased for the 9Cr-2WV steel, as it does for most similar steels. The improved properties of the 9Cr-2WVTa steel and the differences with other steels were attributed to tantalum in solution.

PROGRESS AND STATUS

Introduction

A nominally Fe-9Cr-2W-0.25V-0.07Ta-0.1C (9Cr-2WVTa) steel (composition in wt %) has been developed for possible use in fusion power plants [*1*]. A major problem of ferritic/martensitic steels for fusion applications involves the embrittlement caused by irradiation hardening. This embrittlement is measured in a Charpy impact test as a shift in ductile-brittle transition temperature (DBTT) caused by the irradiation. The 9Cr-2WVTa steel has shown excellent resistance to such embrittlement after irradiation at 365°C in the Fast Flux Test Facility (FFTF) [*2-5*] and the High Flux Reactor (HFR) [*6,7*].

Several irradiation experiments have been conducted that compared the behavior of the 9Cr-2WVTa steel with a 9Cr-2WV steel, which is the same as the 9Cr-2WVTa but without tantalum [*2-5,8*]. The steels show similar hardening when irradiated at 365°C, but the 9Cr-2WVTa shows considerably less embrittlement. There are also other differences in the behavior of this steel relative to the 9Cr-2WV steel and steels such as 9Cr-1MoVNb (modified 9Cr-1Mo) and 12Cr-1MoVW (Sandvik HT9).

In this report, observations from irradiation experiments in FFTF and HFR that contained the 9Cr-2WVTa steel will be reviewed, and the combined results will be analyzed to try to understand the behavior of the steel during irradiation and how the properties of this type of steel might be improved.

Experimental Procedure

The 9Cr-2WV and 9Cr-2WVTa steels are nominally Fe-9Cr-2W-0.25V-0.1C (in wt. %) without and with 0.07% Ta, respectively. They were prepared as 18 kg ESR heats by Combustion

Engineering, Inc, Chattanooga, TN. In addition to the nominal compositions of Cr, W, V, C, and Ta, elements normally found in such steels (e.g., Mn, Si, etc.,) were adjusted to levels typical of commercial steel processing practice. Melt compositions have been published [3].

The steels were normalized and tempered prior to irradiation. Normalization involved an austenitization treatment of 0.5 h at 1050°C in a helium atmosphere, followed by cooling in flowing helium gas. The steels were tempered 1 h at 750°C.

Tensile specimens were machined from 0.76-mm sheet. The tensile specimens were 25.4 mm long and had a reduced gage section 7.62 mm long by 1.52 mm wide by 0.76 mm thick. Tensile tests were at 365°C in vacuum on a 120-kN Instron universal test machine at a nominal strain rate of $\approx 1 \times 10^{-3}$ s^{-1}.

Charpy specimens for the FFTF irradiations were one-third size V-notch specimens measuring 3.3 x 3.3 x 25.4 mm with a 0.51-mm-deep 30° V-notch and a 0.05- to 0.08-mm-root radius were machined from normalized-and-tempered 15.9-mm plates. Impact specimens for the HFR irradiations were European subsize standard specimens, 3 x 4 x 27 mm with a notch depth of 1 mm. Specimens were machined along the rolling direction with the notch transverse to the rolling direction (L-T orientation). The DBTT was determined at an energy level midway between the upper and lower shelf energies. Details on the test procedure for the subsize impact specimens have been published [6,8].

Two tensile specimens and six Charpy specimens of each heat were irradiated in the Materials Open Test Assembly of FFTF over the range 7-28 dpa at 365°C [2-5] and Charpy specimens were irradiated to ≈14 dpa at 393°C [8]. Charpy specimens of the 9Cr-2WVTa steel were also irradiated in the High Flux Reactor (HFR) in the Netherlands to 0.8 and 2.5 dpa at 250, 300, 350, 400, and 450°C [6,7]. Details on the irradiation conditions were given in the previous publications [2-8].

Results

Three irradiation experiments will be discussed: (1) irradiation of the 9Cr-2WV and 9Cr-2WVTa steels in FFTF at 365°C to ≈7, 14, 21, and 28 dpa [2-5], (2) irradiation of 9Cr-2WV and 9Cr-2WVTa steels in FFTF at 393°C to ≈14 dpa [8], and (3) irradiation of 9Cr-2WVTa steel in HFR to 0.2, 0.8, and 2.5 dpa at 250, 300, 350, 400, and 450°C [6,7].

Irradiation in FFTF at 365 °C

Tensile tests were conducted on the 9Cr-2WV and 9Cr-2WVTa steels irradiated to three fluences in FFTF at 365°C (Table 1). There was little difference in the strength of the two steels, either before or after irradiation [Fig. 1(a)]. The strength increase saturated with fluence. Likewise, there was little difference in the uniform and total elongation out to ≈15 dpa, although there appeared to be a slight divergence at the highest fluence, especially for the total elongation [Fig. 1(b)].

Charpy specimens were irradiated in FFTF to four fluences at ≈365°C (Table 2). The 9Cr-2WVTa steel has a lower transition temperature prior to irradiation, and it improves that superiority during irradiation by developing a smaller shift in DBTT (ΔDBTT) (Table 2 and Fig. 2). For the 9Cr-2WV steel, the DBTT appears to increase to a fairly constant value—it saturates with fluence. In Fig. 2, the DBTT value for 9Cr-2WV at 16.7 dpa appears spurious, and the other three values indicate that saturation occurred around 0°C after a ΔDBTT of ≈60°C (Table 1). In contrast to that behavior, the DBTT for 9Cr-2WVTa steel does not appear to saturate (Fig. 2), but rather, it appears to increase continuously with fluence up to 27.6 dpa. However, even without saturation, the DBTT after 27.6 dpa for the 9Cr-2WVTa is still only -56°C with a ΔDBTT of only 32°C.

TABLE 1. Tensile properties of Cr-W steels irradiated in FFTF at 365°C[a]

Steel	Fluence (dpa)	Strength (MPA) Yield	Ultimate	Elongation (%) Uniform	Total
9Cr-2WV	0	549	659	4.7	12.3
	7.7	710	764	3.5	10.2
	16.7	697	745	2.3	9.0
	27.6	705	756	2.3	8.7
9Cr-2WVTa	0	544	652	4.3	12.3
	6.4	669	734	3.9	11.1
	15.4	699	765	2.9	9.7
	27.2	710	769	3.5	12.0

[a] Values are the average of two tests.

Irradiation in FFTF at 393 °C

Two sets of Charpy specimens of 9Cr-2WV and 9Cr-2WVTa steels were irradiated to 14 dpa at 393°C in FFTF (Table 2) [8]. For the 9Cr-2WV steel, the DBTT values (-14 and -28°C) at 393°C were lower than the saturation value at 365°C (about 0°C). The saturation at 365°C was chosen for comparison rather than the value at 16.7 dpa (closer to 14 dpa), because, as discussed above, the 16.7 dpa level appears to be in error relative to the other three values, which were similar and indicative of a saturation with fluence.

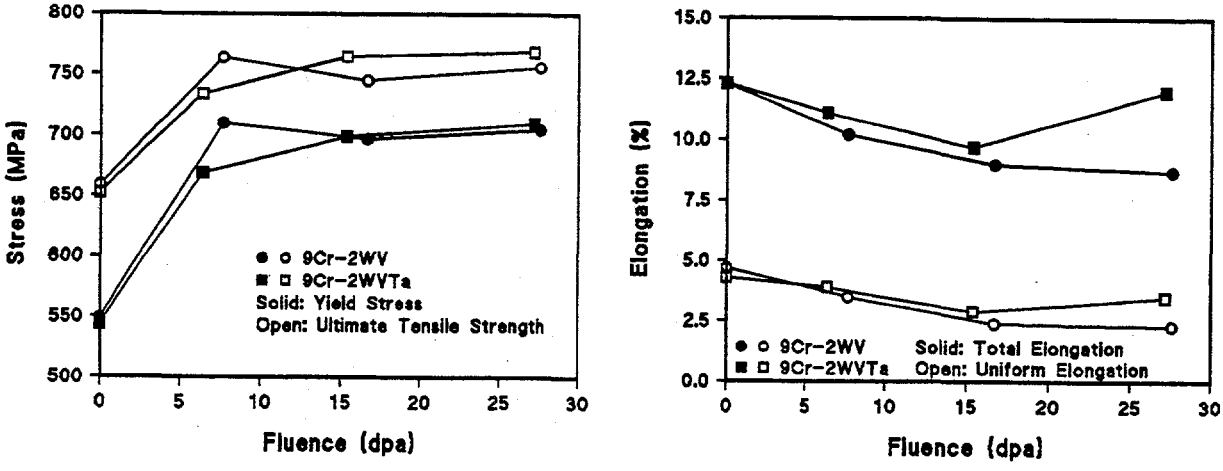

Figure 1. The (a) yield stress and ultimate tensile strength and (b) the uniform and total elongation for 9Cr-2WV and 9Cr-2WVTa steels irradiated at 365°C in FFTF.

Table 2. Charpy impact properties of Cr-W steels irradiated in FFTF at 365°C[a]

Steel	Temp (°C)	Fluence (dpa)	DBTT (°C)	ΔDBTT (°C)	USE (J)
9Cr-2WV	Unirr	0	-60		8.4
	365	7.7	8	68	6.4
	365	16.7	-32	28	6.3
	365	23.9	-8	52	6.3
	365	27.6	1	61	6.6
	393	14	-14	46	8.1
	393	14	-28	32	8.0
9Cr-2WVTa	Unirr	0	-88		11.2
	365	6.4	-84	4	8.6
	365	15.4	-74	14	8.5
	365	22.5	-67	21	9.6
	365	27.6	-56	32	8.1
	393	14	-53	34	8.4
	393	14	-45	43	8.9

[a] Evaluated at an energy level halfway between the upper and lower shelves.

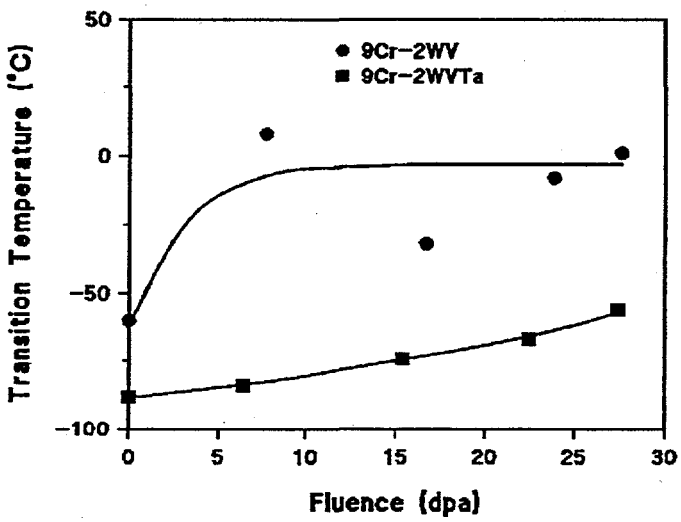

Figure 2. The transition temperature as a function of fluence for 9Cr-2WV and 9Cr-2WVTa steels irradiated at 365°C in the FFTF.

Contrary to the observation on the 9Cr-2WV steel, the DBTT values for the 9Cr-2WVTa steel after irradiation to 14 dpa at 393°C (-53 and -45°C) were higher than the DBTT observed after irradiation at 365°C to 15.4 dpa (-74°C). Although the DBTTs for the 9Cr-2WVTa steel were below those for the 9Cr-2WV steel after irradiation at 393°C, the ΔDBTTs for the 9Cr-2WVTa steel and the 9Cr-2WV steel were quite similar (46 and 32°C for the 9Cr-2WV and 34 and 43°C for the 9Cr-2WVTa steel) (Table 2) [8].

Irradiation in the HFR

Rieth et al. irradiated six steels, including the 9Cr-2WVTa steel, in the HFR at 250, 300, 350, 400, and 450°C to 0.2, 0.8, and 2.4 dpa [*6,7*]. The steels included two conventional Cr-Mo steels, MANET-I (nominally Fe-11Cr-0.8Mo-0.2V-0.9Ni-0.16Nb-0.06Zr-0.14C) and MANET-II (Fe-10Cr-0.6Mo-0.2V-0.7Ni-0.14Nb-0.4Zr-0.1C), and four low-activation steels, OPTIFER-Ia (Fe-9.3Cr-1W-0.25V-0.07Ta-0.1C), OPTIFER-II (Fe-9.4Cr-1.1Ge-0.3V-0.13C), F82H (Fe-8Cr-2W-0.2V-0.02Ta-0.1C), and 9Cr-2WVTa. Melt compositions have been published [*6*].

Figure 3 from Rieth et al. shows the DBTT for the different steels after irradiation to 0.8 dpa [*6*]. Of interest for this discussion is the superior behavior of the 9Cr-2WVTa steel (labeled ORNL) between 250 and 400°C. However, between 350 and 450°C, the DBTT of the 9Cr-2WVTa increases, which is contrary to the of the other five steels.

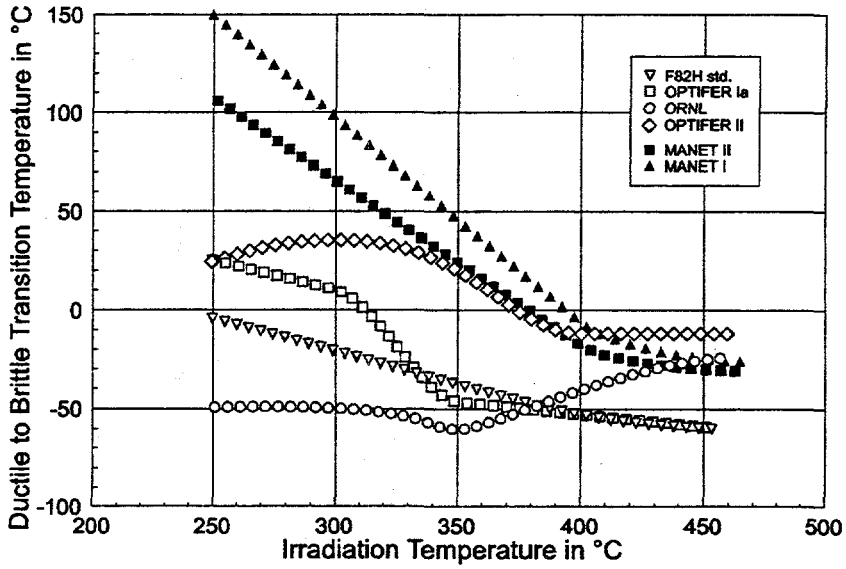

Figure 3. Transition temperature as a function of irradiation temperature for six steels irradiated in the HFR.

Microstructures of 9Cr-2WV and 9Cr-2WVTa Steels

A detailed TEM examination indicated that the microstructures of the 9Cr-2WV and 9Cr-2WVTa steels were quite similar both before and after irradiation in FFTF at 420°C to ≈36 dpa [*10*]. Microstructures were typical for tempered martensite. Lath size (width) was estimated to be ≈0.3 μm for both steels before irradiation, and it increased during irradiation to 0.4 and 0.45 μm for the 9Cr-2WV and 9Cr-2WVTa, respectively. The major microstructural difference in the two steels was the smaller prior-austenite grain size of the 9Cr-2WVTa steel (22 μm) compared to the 9Cr-2WV steel (32 μm) [*2*].

Although the size and density of the precipitates differed slightly in the two steels, the amounts were similar before and after irradiation. Most of the precipitate was $M_{23}C_6$ with lesser amounts of MC (Table 3) [*10*]. Analysis of the MC by X-ray energy dispersive spectroscopy indicated it was mainly vanadium rich, but in the 9Cr-2WVTa steel, some of it was tantalum rich. It was estimated that less than half of the tantalum was present in the MC [*10*]. Subsequent atom

probe analysis of the 9Cr-2WVTa indicated that over 90% of the tantalum remained in solution in the normalized-and-tempered steel [*11*]. No atom probe studies were conducted on irradiated specimens. There were only slight differences in the size and number density of precipitates for 9Cr-2WV and 9Cr-2WVTa (Table 3), but the amounts were similar. A slight increase in precipitate size and a corresponding reduction in number density occurred for both steels during irradiation [*10*].

Table 3. Precipitates in 9Cr-2WV and 9Cr-2WVTa steels before and after irradiation

Steel	Before Irradiation			After Irradiation		
	Ppt	Density (m^{-3})	Avg Diam (nm)	Ppt	Density (m^{-3})	Avg Diam (nm)
9Cr-2WV	$M_{23}C_6$	$5.9x10^{19}$	125	$M_{23}C_6$	$3.2x10^{19}$	160
	MC	$1.2x10^{18}$	54	MC	$1.1x10^{18}$	60
9Cr-2WVTa	$M_{23}C_6$	$4.5x10^{19}$	136	$M_{23}C_6$	$4.1x10^{19}$	143
	MC	$7.5x10^{18}$	29	MC	$5.6x10^{18}$	36

The major microstructural change that occurred during irradiation of the 9Cr-2WV and 9Cr-2WVTa steels was the formation of dislocation loops. Again there was no difference in the loop number density and size of the loops for the two steels [*10*]; loops were estimated to have an average size of ≈50 nm and a number density of $\approx 3x10^{21}$ m^{-3} for both steels. Total dislocation line density was estimated at $\approx 5x10^{14}$ m^{-2} for both steels [*10*].

Discussion

The 9Cr-2WVTa steel has excellent impact toughness, as measured by a low DBTT before irradiation. It also has excellent resistance to irradiation embrittlement, as demonstrated by a small shift in DBTT after irradiation at 250-450°C [*2-8*]. To try to understand the origin of the irradiation resistance of the 9Cr-2WVTa steel and the difference in properties with other similar steels, the properties of the steel will first be compared with those of the 9Cr-2WV, which differs from the 9Cr-2WVTa by not containing 0.07% Ta.

Irradiation hardening, as measured by an increase in yield stress, occurs for martensitic steels, such as the conventional 9Cr-1MoVNb and 12Cr-1MoVW steels, when irradiated at ≤425°C [*12,13*]. Hardening generally saturates with fluence [*12,13*], and the tensile properties of the 9Cr-2WV and 9Cr-2WVTa saturated by 7-10 dpa when irradiated at 365°C in FFTF (Fig. 1) [*5*]. Irradiation hardening causes the increase in DBTT, and just as hardening saturates with fluence, the DBTT and ΔDBTT also saturate for the 9Cr-1MoVNb and 12Cr-1MoVW steels [*12,14*]. Saturation in ΔDBTT occurred for the 9Cr-2WV steel but not for the 9Cr-2WVTa steel when irradiated at 365°C in FFTF (Fig. 2) [*5*].

The observation of similar tensile properties for 9Cr-2WV and 9Cr-2WVTa steels is not unexpected based on the similar microstructures [*10*], although in some previous tests, the 9Cr-2WVTa steel was 4-10% stronger than the 9Cr-2WV steel over the range 25 to 600°C (the smallest difference occurred at the highest test temperatures) [*1*]. The major microstructural difference in the two steels appears to be the prior-austenite grain size, which could account for part or all of the difference in Charpy impact transition temperature in the normalized-and-tempered condition. Tantalum, like niobium, is known to inhibit austenite grain growth, although the effect is usually concluded to be caused by carbides [*15*]. For 9Cr-2WVTa steel, tantalum in solution or a very small amount of TaC must cause the smaller grain size, because

most of the tantalum was in solution after the normalizing-and-tempering treatment [*11*]. Grain size can affect tensile behavior, but it did not appear to do so in this case [Fig. 1(a)].

Aside from some relatively minor changes in the precipitate size and precipitate number density, which were similar for the 9Cr-2WV and 9Cr-2WVTa steels (Table 3), the major effect of irradiation on microstructure was the formation of dislocation loops; the number and size of loops formed and the final dislocation density in the two steels was the same after irradiation [*10*]. Similar microstructural changes resulted in similar changes in tensile properties, as might be expected (Fig. 1). Thus, the only significant difference in the 9Cr-2WV and 9Cr-2WVTa steels before and after irradiation was the prior-austenite grain size and the tantalum in solution.

Prior-austenite grain size could explain the difference in the Charpy impact properties of the normalized-and-tempered steels. However, the 9Cr-2WVTa showed two types of behavior that differed from what was observed for similar steels—either conventional Cr-Mo steels (e.g., 9Cr-1MoVNb and 12Cr-1MoVW) or Cr-W steels (e.g., 9Cr-2WV, F82H, etc.). These differences were: (1) a continuous, albeit slow, increase in DBTT with increasing fluence (out to ≈28 dpa at 365°C) for the 9Cr-2WVTa, compared with a saturation in DBTT with fluence for other steels and (2) an increase in DBTT with increasing irradiation temperature for the 9Cr-2WVTa compared with a decrease with irradiation temperature for most other steels [*12,14*].

The increase in DBTT with fluence for 9Cr-2WVTa was not large, but it was continuous from ≈7 to 28 dpa (Fig. 2) (ΔDBTT increased from 4 to 32°C). This was different from the behavior of 9Cr-2WV steel (Fig. 2). With the exception of the scatter in the 9Cr-2WV steel data due to the result at 16.7 dpa, the data gave a clear indication of a saturation of ΔDBTT with fluence. This difference in the two steels cannot be explained by the difference in prior-austenite grain size, because prior-austenite grain size does not change during irradiation [*8*]. The lath size changes, but the change for the two steels was similar (the lath size of 9Cr-2WVTa was even estimated to be slightly larger than that of the 9Cr-2WV after irradiation) [*10*]. A possible explanation is that tantalum in solution causes the superior impact properties of the 9Cr-2WVTa, and tantalum is removed from solution during irradiation by precipitation to cause the deterioration in properties.

Irradiation hardening decreases with increasing temperature, and therefore, the ΔDBTT should decrease with increasing irradiation temperature. This is what is observed for most steels [*6,8,12*]. At 400-425°C, hardening generally ceases [*12,13*], and ΔDBTT decreases to a small value or zero [*12*]. This has been observed for 9Cr-1MoVNb and 12Cr-1MoVW [*12,13*] and MANET [*16*] steels and, as seen in Fig. 3 for the 7-10% Cr steels irradiated to 0.8 dpa in HFR, the DBTT decreased with increasing irradiation temperature for all but the 9Cr-2WVTa steel [*6*]. Above ≈400°C where hardening ceases, the DBTT for all but the 9Cr-2WVTa steel appeared to approach a constant low value, and the ΔDBTT approached a small value. In contrast to these observations, the DBTT of the 9Cr-2WVTa at 450°C was larger than at 350 and 450°C.

Contrary to the 9Cr-2WVTa steel, the DBTT of the 9Cr-2WV steel decreased with increasing temperature for irradiations at 365 and 393°C (Table 2). A similar observation was made for the following steels irradiated in the same experiment [*8*]: Fe-2.25Cr-0.25V-0.1C, Fe-2.25Cr-1W-0.25V-0.1C, Fe-2.25Cr-2W-0.1C, Fe-2.25Cr-2W-0.25V-0.1C, and Fe-12Cr-2W-0.25V-0.1C.

The difference in the effect of temperature on the 9Cr-2WVTa steel and the other steels in HFR and FFTF, especially the 9Cr-2WV, must again be sought in the tantalum in solution, since this is the major difference between 9Cr-2WV and 9Cr-2WVTa. The increase in DBTT with increasing irradiation temperature follows if tantalum is precipitating during irradiation. Diffusion increases with irradiation temperature, and at the higher temperature, diffusion accelerates the precipitation of tantalum over precipitation at lower temperatures. Likewise, an increase in fluence (dpa) will allow more irradiation-accelerated diffusion and more tantalum precipitation.

The ductile-brittle transition is explained by the variation in flow stress with temperature and the fracture stress for cleavage (Fig. 4) [17]. Flow stress increases with decreasing temperature, and as temperature decreases, it eventually exceeds the cleavage fracture stress, at which

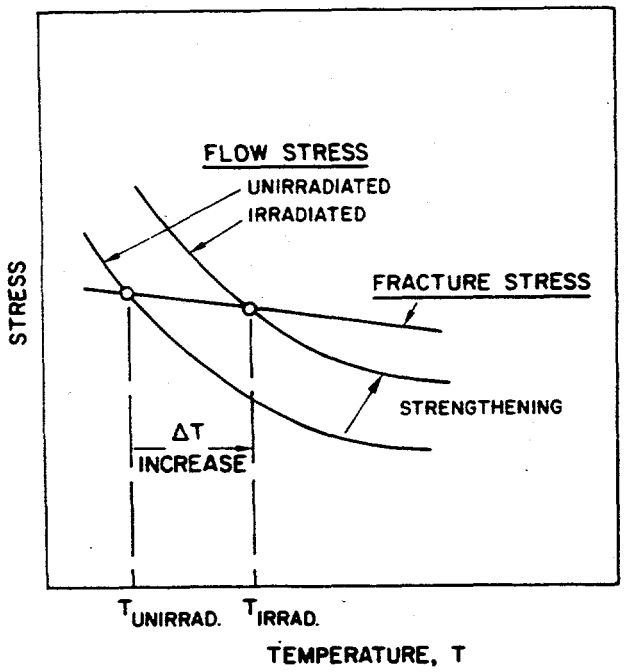

Figure 4. Schematic illustration of effect of irradiation on the transition temperature.

temperature a brittle cleavage fracture occurs (the DBTT). Irradiation causes an increase in flow stress, which causes an increase in DBTT, assuming fracture stress is unchanged (Fig. 4).

No detailed measurements of the flow stress with temperature exist for the unirradiated and irradiated 9Cr-2WV and 9Cr-2WVTa steels. At 365°C, there was little difference in the tensile properties of the two steels as normalized and tempered, after thermal aging for up to 20000 h at 365°C, and after ≈28 dpa at 365°C in FFTF (Fig. 1) [5]. That means the observed differences in transition temperature for the two steels cannot be explained by irradiation hardening. One explanation is that tantalum in solution increases the fracture stress, and then during irradiation, precipitation of the tantalum causes the fracture stress to decrease [8].

Assuming the above hypothesis is correct, tantalum should precipitate in the 9Cr-2WVTa until equilibrium is achieved, after which the change in DBTT should saturate with fluence. This should also occur for the other tantalum-containing steels shown in Fig.3, namely, F82H (0.02% Ta) and OPTIFER Ia (0.07% Ta). Figure 3 shows data after 0.8 dpa, and no increase in DBTT at the highest irradiation temperature is observed for these two steels. Rieth et al. [7] recently published the combined data for the steels irradiated to 0.2, 0.8, and 2.5 dpa in HFR, and Fig. 5 shows the results for F82H [Fig. 5(a)], OPTIFER Ia [Fig. 5(b)] and 9Cr-2WVTa [Fig. 5(c)]—the tantalum-containing steels. After 2.5 dpa, the DBTT at 450°C for all three steels is higher than it is at 350 and 400°C. The behavior of the three tantalum-containing steels contrasted with MANET-I [Fig. 6(a)], MANET-II [Fig. 6(b)], and OPTIFER-II [Fig. 6(c)]—steels with no tantalum. With one exception, the steels without tantalum additions do not show a DBTT after 2.5 dpa at 450°C that is above that at 350 and 400°C. The only exception is MANET-II, where the DBTT at 450°C is slightly higher than at 400°C, but it is well below that at 350°C.

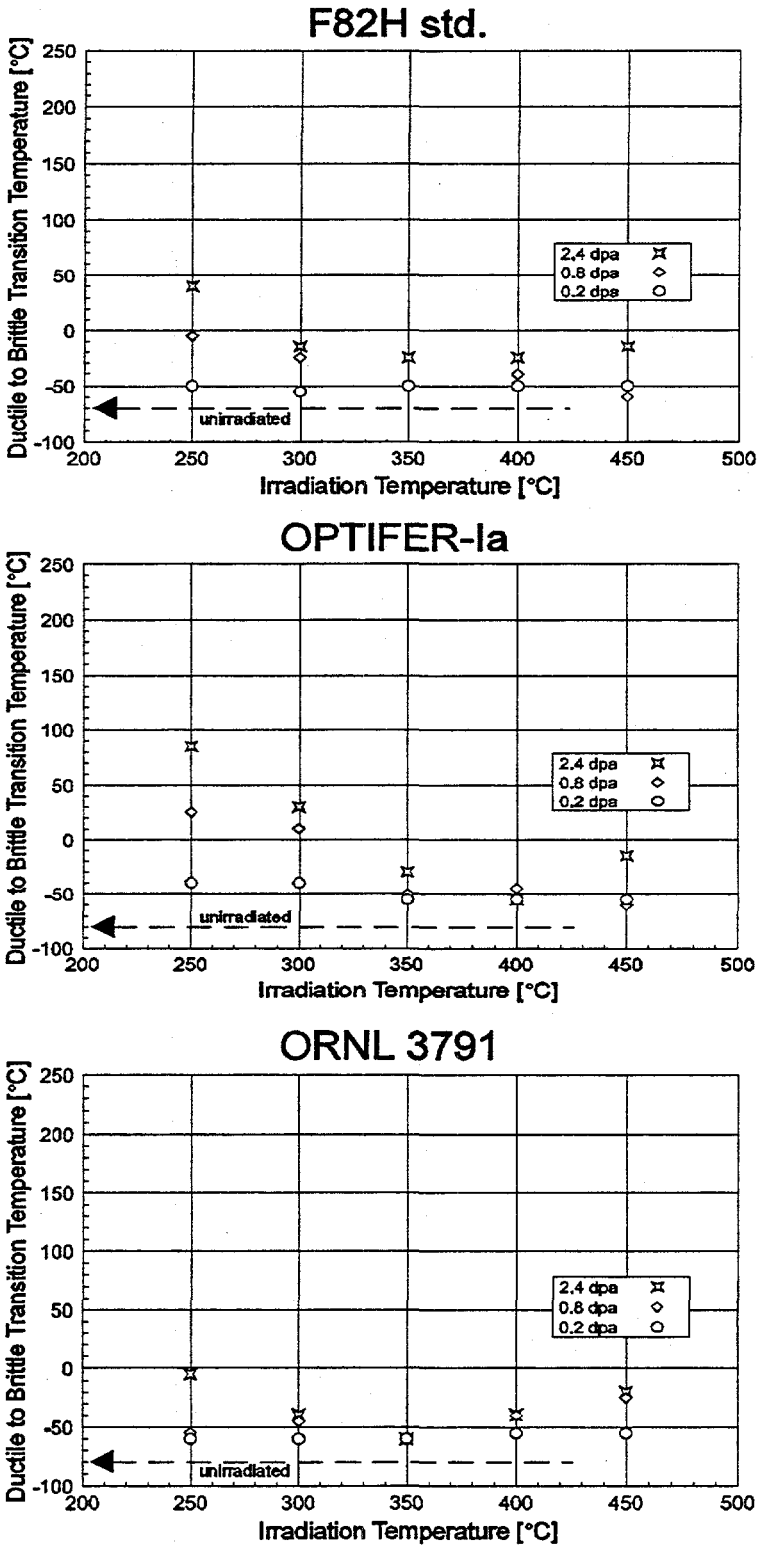

Figure 5. Ductile-brittle transition temperature as a function of irradiation temperature for the (a) F82H (b) OPTIFER-Ia, and (c) 9Cr-2WVTa steels.

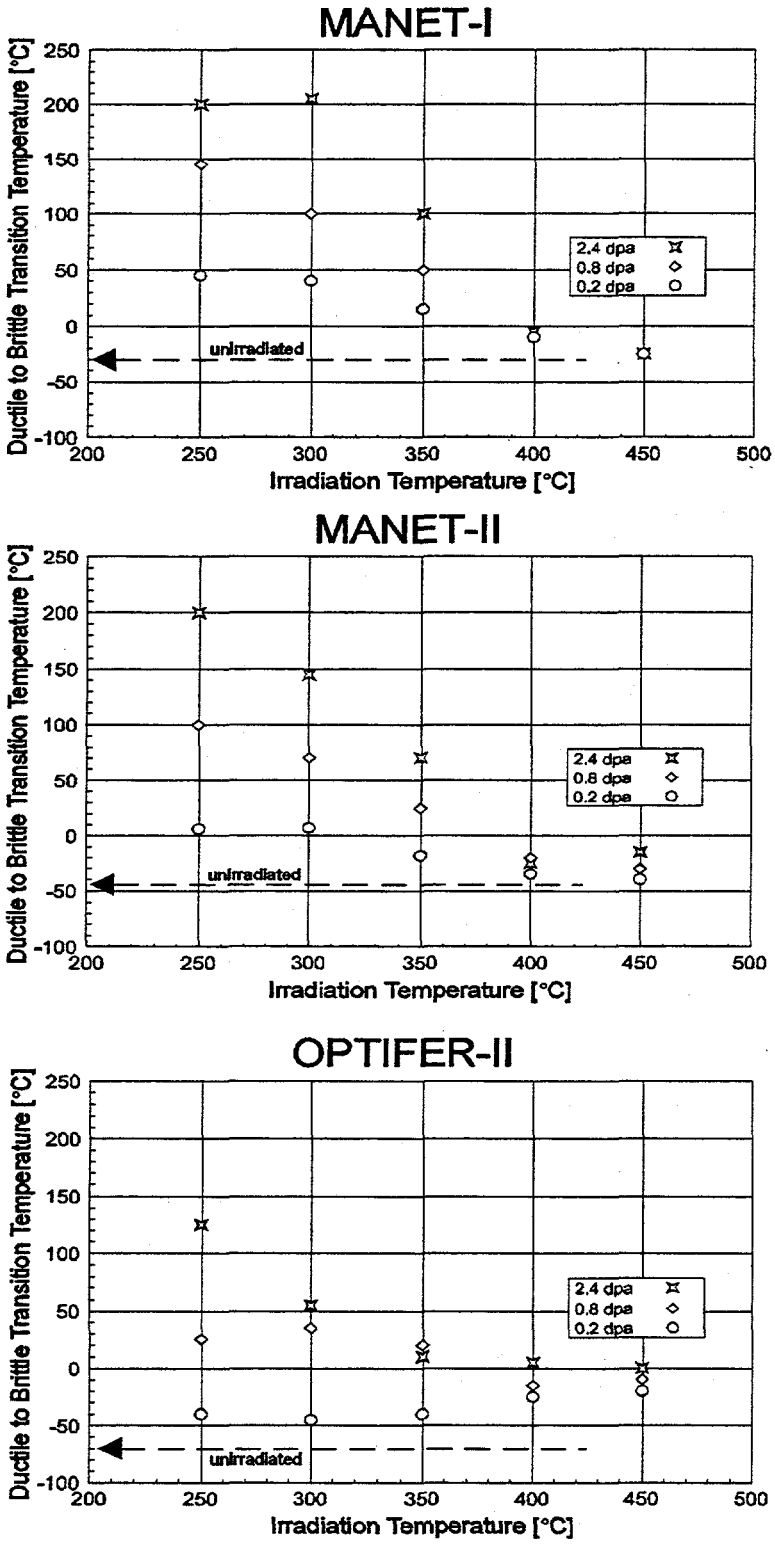

Figure 6. Ductile-brittle transition temperature as a function of irradiation temperature for the (a) MANET-I, (b) MANET-II, and (c) OPTIFER-II steels.

It is recognized that Charpy data can contain considerable scatter. Nevertheless, the trend of these data for the tantalum-containing F82H and OPTIFER-Ia appear to agree with the suggestion that tantalum causes the inverse temperature effect for the DBTT of the 9Cr-2WVTa steel. A loss of tantalum from solution during the irradiation can explain these results, although the actual loss of tantalum needs to be confirmed. Atom probe analysis is probably the best method to study this given the small amount of tantalum in the steels.

Figures 5 and 6 show some other interesting effects relative to the above discussion. First, equilibrium was not established for any of the steels at the lowest temperature by 0.8 dpa (the DBTT subsequently increased during the 2.5 dpa irradiation). Whether saturation was achieved by 2.5 dpa can only be determined by higher dose experiments. Several of the steels give an indication of saturation at 300°C, and at 350°C, saturation appears to have been reached for most of the steels by 0.8 dpa. This should be a metastable saturation for tantalum-containing steels, since with time (fluence), tantalum should precipitate at temperatures below 450°C (based on the FFTF results) and have the same effect at the lower temperatures as at 450°C.

These results raise the question about the usefulness of tantalum in the 9Cr-2WVTa steel. The increase in DBTT with fluence should continue until tantalum equilibrium is reached. If it is assumed that at equilibrium essentially all of the tantalum is removed from solution, the matrix of the 9Cr-2WVTa will be similar to that of the 9Cr-2WV (the only difference will be the few tantalum-rich precipitates in the 9Cr-2WVTa, which do not appear to affect the strength). Similar microstructures imply similar ΔDBTTs. This would seem to indicate that, although the ΔDBTT of the 9Cr-2WVTa increases with dose, it should be similar to that of the 9Cr-2WV when the tantalum in solution reaches equilibrium. This means the 9Cr-2WVTa will still have an advantage over the 9Cr-2WV, because it had the lowest DBTT in the normalized-and-tempered condition. That initial advantage could be due to the smaller prior-austenite grain size of the 9Cr-2WVTa steel.

That this conclusion might be correct is seen from the observations on the 9Cr-2WV and 9Cr-2WVTa steels after irradiation in FFTF at 393°C (Table 2). At this temperature, the ΔDBTT values for the two tests for each steel were respectively 34 and 43°C for 9Cr-2WVTa compared to 46 and 34°C for 9Cr-2WV; thus, the large advantage for the 9Cr-2WVTa steel at 365°C is no longer there at 393°C. With allowances for data scatter, the shifts can be concluded to be similar. Because of the lower DBTT of the 9Cr-2WVTa before irradiation, this steel still has a lower DBTT than the 9Cr-2WV after the 393°C irradiation.

If the above analysis is correct, the advantage for the 9Cr-2WVTa steel after precipitation of the tantalum is attributed to the smaller prior-austenite grain size in the tantalum-containing steel. Therefore the tantalum addition is beneficial. However, if this analysis is correct, it should be possible to get similar results in the absence of tantalum if the grain size of the 9Cr-2WV steel could be reduced, say by an appropriate heat treatment.

Summary and Conclusions

An Fe-9Cr-2W-0.25V-0.07Ta-0.1C (9Cr-2WVTa) steel shows excellent resistance to irradiation embrittlement as manifested by the small shift in DBTT after irradiation to ≈7-28 dpa at 365°C in FFTF. Tantalum plays an important role in the exceptional irradiation resistance of the 9Cr-2WVTa, because the ΔDBTT for the 9Cr-2WVTa steel after ≈28 dpa at 365°C (32°C) is considerably smaller than for a 9Cr-2WV steel—the same steel but without tantalum—also irradiated to ≈28 dpa at 365°C (ΔDBTT≈60 °C). The 9Cr-2WVTa steel also had excellent irradiation resistance relative to other steels when irradiated in HFR at 250-450°C.

The 9Cr-2WVTa steel displayed differences in behavior from other steels. First, the DBTT of the 9Cr-2WVTa steel increased continuously with fluence when irradiated at 365°C in FFTF,

compared to the 9Cr-2WV steel that showed a saturation in ΔDBTT with fluence. Contrary to most other steels of this type, the 9Cr-2WVTa steel also showed a larger DBTT and increase in DBTT at 400-450°C than at the lower irradiation temperatures (250-350°C) in the HFR and higher values at 393°C than 365°C in FFTF.

The increased resistance to irradiation-induced embrittlement of the 9Cr-2WVTa steel was attributed to tantalum in solution causing in increase in the fracture stress. A precipitation of tantalum from solution during irradiation was hypothesized to cause the difference in behavior of a tantalum-containing steel compared to one without tantalum when fluence or temperature is increased.

References

[1] Klueh, R. L., "Heat Treatment Behavior and Tensile Behavior of Cr-W Steels," Metallurgical Transactions, Vol. 20A, 1989, pp. 463-470.
[2] Klueh, R. L., Alexander, D. J., and Maziasz, P. J., "Impact Behavior of Reduced-Activation Ferritic Steels Irradiated in the Fast Flux Test Facility,", Journal of Nuclear Materials, Vol. 186, 1992, pp. 185-195.
[3] Klueh, R. L. and Alexander, D. J., "Impact Toughness of Irradiated Reduced-Activation Ferritic Steels," Journal of Nuclear Materials, Vol. 212-215,1994, pp. 736-740.
[4] Klueh, R. L. and Alexander, D. J., "Impact Behavior of Reduced-Activation Steels Irradiated to 24 dpa," Journal of Nuclear Materials, Vol. 233-237, 1996, pp. 336-341.
[5] Klueh, R. L. and Alexander, D. J., "Tensile and Charpy Impact Properties of Irradiated Reduced-Activation Ferritic Steels," Effects of Radiation on Materials: 18th International Symposium, ASTM STP 1325, R. K. Nanstad, M. L. Hamilton, F.A. Garner, and A.S. Kumar, Eds., American Society for Testing and Materials, 1998, to be published.
[6] Rieth, M., Dafferner, B., and Röhrig, H. D., Journal of Nuclear Materials, Vol. 233-237, 1996, pp. 351-355.
[7] Rieth, M., Dafferner, B., and Röhrig, H. D., "Embrittlement Behaviour of Different International Low Activation Alloys after Neutron Irradiation," Journal of Nuclear Materials, to be published.
[8] Klueh, R. L. and Alexander, D. J., "Effect of Heat Treatment and Irradiation Temperature on Impact Behavior of Irradiated Reduced-Activation Ferritic Steels," Journal of Nuclear Materials, to be published.
[9] Alexander, D. J., Nanstad, R. K., Corwin, W. R., and Hutton, J. T., "A Semiautomated Computer-Interactive Dynamic Impact Testing System," Applications of Automation Technology to Fatigue and Fracture Testing, ASTM STP 1092, Braun, A. A., Ashbaugh, N. E., and Smith, F. M., Eds., American Society for Testing and Materials, Philadelphia, 1990, pp. 83-94.
[10] Kai, J. J. and Klueh, R. L. R. L., "Microstructural Analysis of Neutron Irradiated Martensitic Steels," Journal of Nuclear Materials, Vol. 230, 1996, pp. 116-123.
[11] Jayaram, R. and Klueh, R. L., "Microstructural Characterization of 5-9% Cr-2%W-V-Ta Martensitic Steels," Metallurgical and Materials Transactions, to be published.
[12] Hu, W. and Gelles, D. S., "The Ductile-to-Brittle Transition Behavior of Martensitic Steels Neutron Irradiated to 26 dpa," Influence of Radiation on Material Properties: 13th International Symposium (Part II) ASTM STP 956, F. A. Garner, C. H. Henager, Jr., and N. Igata, Eds., American Society for Testing and Materials, Philadelphia, 1987, pp. 83-97.
[13] Klueh, R. L. and Vitek, J. M., "Tensile Properties of 9Cr-1MoVNb and 12Cr-1MoVW Steels Irradiated to 23 dpa at 390 to 550°C," Journal of Nuclear Materials, Vol. 182, 1991, pp. 230-239.
[14] Klueh, R. L. and Alexander, D. J., "Heat Treatment Effects on Impact Toughness of 9Cr-1MoVNb and 12Cr-1MoVW Steels Irradiated to 100 dpa," Journal of Nuclear Materials, to be published.
[15] Krauss, G., Steels: Heat Treatment and Processing Principles, ASM International, Materials Park, OH, 1990, pp. 199-201.
[16] Rieth, M., Dafferner, B., Röhrig, H. D., and Wassilew, C. "Charpy Impact Properties of Martensitic

10.6% Cr Steel (MANET-I) Before and After Neutron Exposure," Fusion Engineering and Design, Vol. 29, 1995, pp. 365-370.
[17] Hawthorne, J. R., "Irradiation Embrittlement," Treatise on Materials Science and Technology, Vol. 25, 1983, pp. 461-524.

MICROSTRUCTURAL ANALYSIS OF FERRITIC-MARTENSITIC STEELS IRRADIATED AT LOW TEMPERATURE IN HFIR - N. Hashimoto (Oak Ridge National Laboratory), E. Wakai (Japan Atomic Energy Research Institute), J. P. Robertson (ORNL), and A. F. Rowcliffe (ORNL)

OBJECTIVE

The purpose of this work is to investigate the microstructural evolution of ferritic/martensitic steel irradiated at low temperatures to damage levels of about 3 dpa in order to relate the microstructure to the mechanical properties, in particular the fracture toughness and the yield strength.

SUMMARY

Disk specimens of ferritic-martensitic steel, HT9 and F82H, irradiated to damage levels of ~3 dpa at irradiation temperatures of either ~90°C or ~250°C have been investigated by using transmission electron microscopy. Before irradiation, tempered HT9 contained only $M_{23}C_6$ carbide. Irradiation at 90°C and 250°C induced a dislocation loop density of $1x10^{22}$ m^{-3} and $8x10^{21}$ m^{-3}, respectively. In the HT9 irradiated at 250°C, a radiation-induced phase, tentatively identified as α', was observed with a number density of less than $1x10^{20}$ m^{-3}. On the other hand, the tempered F82H contained $M_{23}C_6$ and a few MC carbides; irradiation at 250°C to 3 dpa caused minor changes in these precipitates and induced a dislocation loop density of $2x10^{22}$ m^{-3}. Difference in the radiation-induced phase and the loop microstructure may be related to differences in the post-yield deformation behavior of the two steels.

PROGRESS AND STATUS

1. Introduction

Ferritic/martensitic steels are attractive candidate structural first wall materials for fusion reactors [1]. Neutron irradiation at low temperature can cause an increase in the yield stress and a decrease in the uniform elongation, as determined by tensile test. Additionally the ductile-brittle transition temperature (DBTT) may increase and the upper shelf energy may decrease,, as determined by a Charpy impact test. It was previously reported [2] that irradiation of HT9 to ~3 dpa in HFIR at 250 °C resulted in an increase in yield stress of about 450 MPa accompanied by a reduction in uniform elongation from 12% to 6% when tested at the irradiation temperature. Although the F82H underwent somewhat less hardening (ΔYS=350 MPa) at 250°C, the uniform elongation was reduced to less than 0.5%. In spite of the loss of strain hardening capacity observed for the F82H, the fracture toughness values of both alloys were similar at 250°C. In addition, the F82H maintained good toughness at room temperature; on the other hand, the HT9 exhibited lower-shelf brittle behavior at room temperature.

The objective of the this study is to investigate microstructure of ferritic/martensitic steels, HT9 and F82H, irradiated at low temperatures and to damage levels of about 3 dpa in order to relate the microstructure to the mechanical properties, in particular the fracture toughness and the yield strength.

2. Experimental Procedure

HT9 and F82H were included in this experiment; the compositions are given in Table 1. Standard 3-mm diameter transmission electron microscopy (TEM) disks were punched from 0.25-mm thick sheet stock, and then these disk were normalized and tempered as indicated in Table 2.

Table 1. Chemical compositions of F82H and HT9 (wt%). (Balance Fe)

Steel	Cr	Ni	Mo	Mn	Si	C	N	V	W	Ta	P	S
HT9	12.1	0.51	1.04	0.57	0.17	0.20	0.027	0.28	0.45	-	.016	.003
F82H	7.65	0.05	-	0.49	0.09	0.093	0.002	0.18	1.98	0.038	.001	.001

Table 2. Normalizing and tempering conditions for F82H and HT9.

Steel	Normalizing	Tempering
HT9	1.0 h at 1050°C / AC	2.5 h at 780°C / AC
F82H	0.5 h at 1040°C / AC	1.5 h at 740°C / AC

The disks were irradiated in HFIR in the capsules of HFIR-MFE-JP-17 and JP-18 at nominal irradiation temperatures of either 90°C or 250°C to neutron fluences producing ~3 dpa. The helium concentration was about 2 and 30 appm in F82H and HT9, respectively.

TEM specimens were thinned using an automatic Tenupol electropolishing unit located in a hot cell. TEM disks were examined using a JEM-2000FX (LaB_6) transmission electron microscope equipped with a special objective lens polepiece that lowers the magnetic field at the ferro-magnetic specimen. The foil thicknesses were measured by thickness fringes in order to evaluate quantitative defect density values.

3. Results

3.1 Microstructure of tempered HT9 and F82H

Figure 1 shows the microstructure of tempered HT9 and F82H. In both of them, dislocations were observed with a density of about $1x10^{14}$ m^{-2}. The tempered F82H contained $M_{23}C_6$ and a few MC carbide, while tempered HT9 contained only $M_{23}C_6$ carbides. The summary of the microstructure, dislocation and precipitates, in HT9 and F82H are given in Table 3. The tempered HT9 contains $M_{23}C_6$ carbides with a number density of $7.0x10^{18}$ m^{-3} and mean diameter of 310 nm. In F82H, the number density and mean diameter of $M_{23}C_6$ carbides are higher and smaller than that of tempered HT9, as shown in table 3.

Table 3. The summary of microstructure in HT9 and F82H before irradiation.

Steel	Dislocation	Precipitates		
	Density (m^{-2})	ppt.	Mean diameter (nm)	Number density (m^{-3})
HT9	$1x10^{14}$	$M_{23}C_6$	310	$7.0x10^{18}$
F82H	$1x10^{14}$	$M_{23}C_6$	73	$6.0x10^{19}$
		MC	14	$<1x10^{20}$

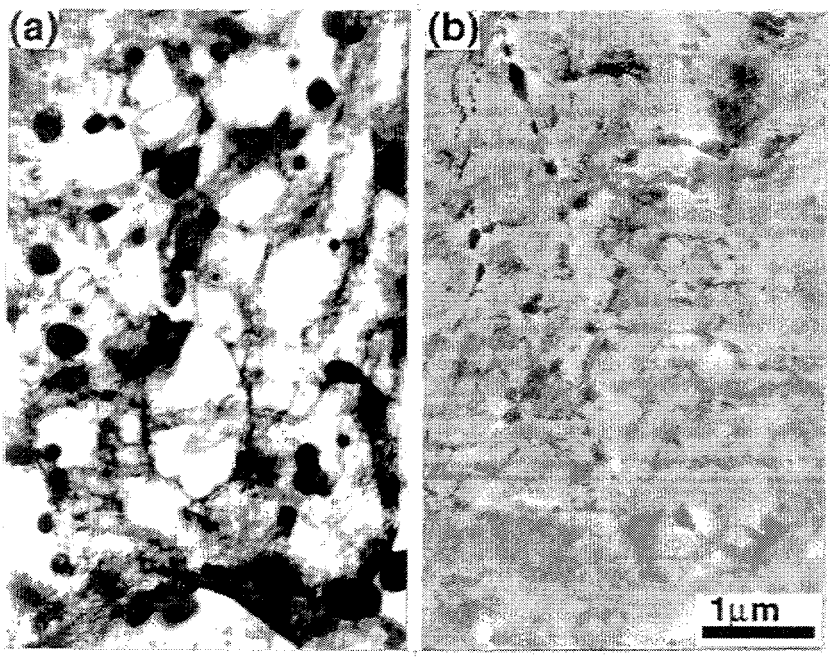

Fig. 1 Microstructures of HT9 (a) and F82H (b) before irradiation.

3.2. Microstructural evolution of HT9 irradiated to ~3 dpa

Figure 2 shows the dislocation segments and loops, which were obtained in HT9 after irradiation at 90°C and 250°C to 3 dpa using the diffraction conditions: **B**=[001], **g**= (011), (**g**, 5**g**). For HT9, the irradiation induced dislocation loop densities of $2.5x10^{21}$ m^{-3} and $1.7x10^{22}$ m^{-3} with mean diameters of 5 nm and 5 nm, respectively. The dislocation loops in the specimen irradiated at 90°C were perfect types of $\mathbf{b} = \mathbf{a}_0\langle 100\rangle$ on {100} , while irradiation at 250°C induced loops of perfect types of not only $\mathbf{b} = \mathbf{a}_0\langle 100\rangle$ on {100} but also $\mathbf{b} = (\mathbf{a}_0/2)\langle 111\rangle$ on {111}. The total dislocation density, which means the total line length of the dislocation loops, irradiated at 250°C is larger than that at 90°C. Table 4 summarizes the quantitative results for dislocation loops and total dislocation density.

Table 4. The dislocation density of HT9 before and after irradiation at 90°C and 250°C to 3 dpa.

Condition	Dislocation loop		Total
	Number density (m^{-3})	Mean diameter (nm)	Dislocation density (m^{-2})
Before irradiation	-	-	$<1x10^{14}$
Irr. at 90°C	$2.5x10^{21}$	5	$4.0x10^{13}$
Irr. at 250°C	$1.7x10^{22}$	5	$2.6x10^{14}$

HT9 contained $M_{23}C_6$ carbide before irradiation, the irradiation at 90°C caused minor changes in these precipitates, but induced no other carbides. In the HT9 irradiated at 250°C, a radiation-induced phase, tentatively identified as α', was observed with a number density of $1x10^{20}$ m^{-3}. Fig. 3 shows a micrograph of α' precipitates, which was taken by using the 2.5 dimension method on weak beam dark-field conditions: **B**=[133], **g**= (110), (**g**, 5**g**). The summary of precipitates before and after irradiation at 90°C and 250°C to 3 dpa is given in Table 5.

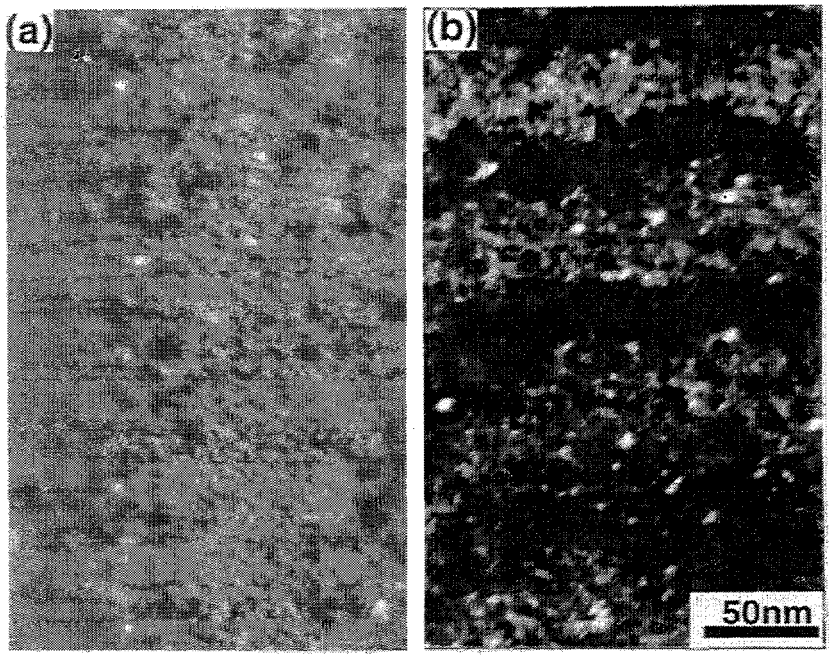

Fig. 2 Microstructures of the dislocation segments and loops in HT9 after irradiation at 90°C (a) and 250°C (b), the diffraction conditions: **B**=[001], **g**= (011), (**g**, 5**g**).

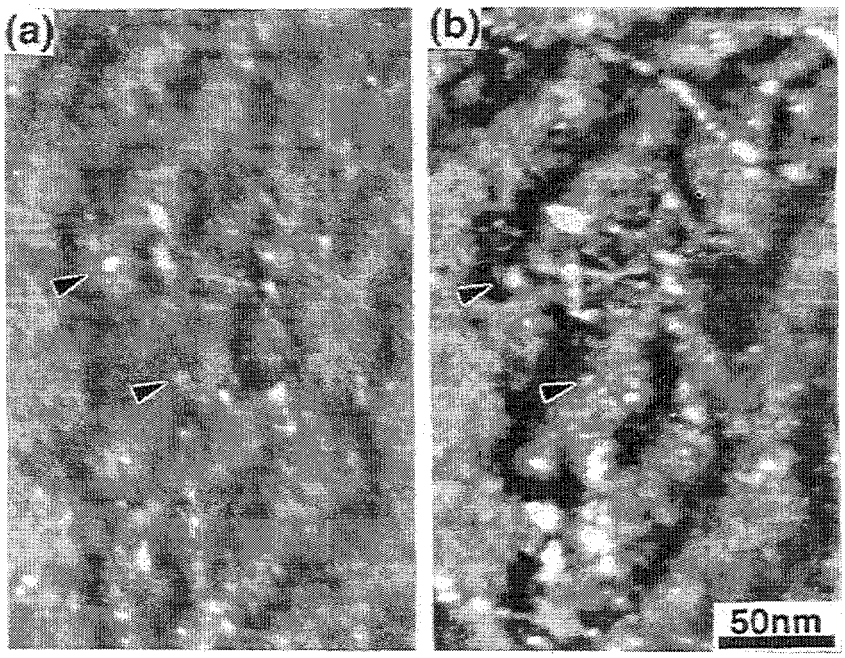

Fig. 3 A stereo-pair of α' precipitates in HT9 irradiated at 250°C to 3 dpa. (a) and (b) are taken with overfocus and underfocus conditions, respectively, on weak beam dark-field conditions: **B**=[133], **g**= (110), (**g**, 5**g**).

Table 5. Precipitate statistics in HT9 before and after irradiation at 90°C and 250°C to 3 dpa.

Steel	ppt.	Before irradiation		After irradiation (90°C)		After irradiation (250°C)	
		Mean diameter (nm)	Number density (m^{-3})	Mean diameter (nm)	Number density (m^{-3})	Mean diameter (nm)	Number density (m^{-3})
HT9	$M_{23}C_6$	310	$7.0x10^{18}$	310	$6.8x10^{18}$	313	$6.4x10^{18}$
	α'	-	-	-	-	<4	$<1x10^{20}$

3.3. Microstructure of F82H irradiated to ~3 dpa

Figure 4 shows the dislocation segments and loops, which formed on {111} planes with (**a**/2)<111> Burgers vectors, in F82H after irradiation at 250°C to 3 dpa. The irradiation at 250°C induced a higher dislocation loop density of $2x10^{22}$ m^{-3} with a larger mean diameter of 8 nm in F82H than that in HT-9 ($5x10^{21}$ m^{-3} with 5 nm). Table 6 summarizes the quantitative results of dislocation loops and total dislocation density.

Table 6. The dislocation density of F82H before and after irradiation at 250°C.

Condition	Dislocation loop		Total
	Number density (m^{-3})	Mean diameter (nm)	Dislocation density (m^{-2})
Before irradiation			$1x10^{14}$
Irr. at 250°C	$2x10^{22}$	8	$5x10^{14}$

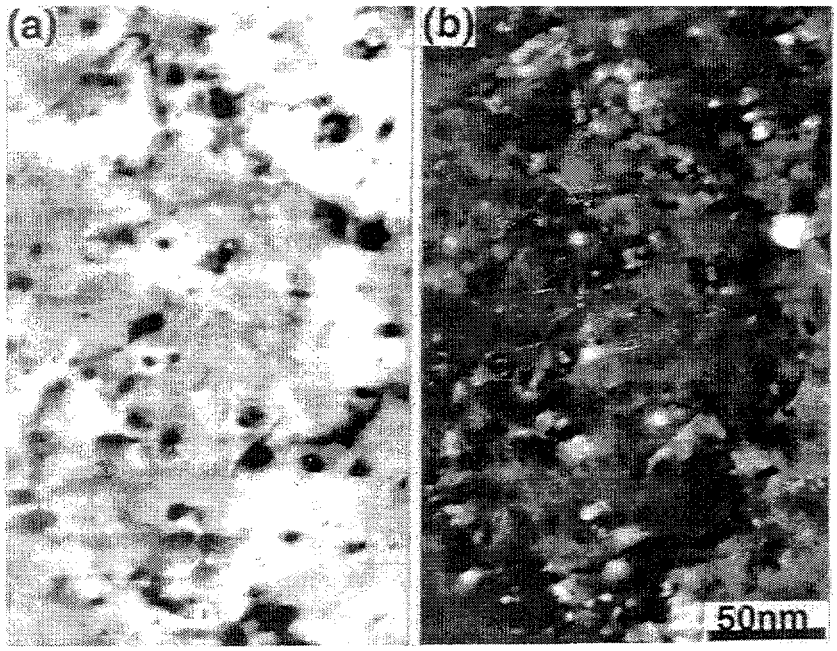

Fig. 4 Microsgraphs of the dislocation segments and loops in F82H after irradiation at 250°C to 3 dpa. (a) is a bright-field image and (b) is a dark-field image on weak beam dark-field conditions: **B**=[133], **g**= (110), (**g**, 3**g**).

Before irradiation, the tempered F82H contained $M_{23}C_6$ and a few MC carbides. The irradiation at 250°C to 3 dpa caused minor changes in these precipitates. Table 7 shows summary of precipitates in F82H before and after irradiation at 250°C to 3 dpa. Irradiation at 250°C to 3 dpa caused only minor changes in these precipitates.

Table 7. Precipitate statistics in F82H before and after irradiation at 250°C up to 3 dpa.

Before irradiation			After irradiation (250°C, 3 dpa)		
ppt.	Mean diameter (nm)	Number density (m^{-3})	ppt.	Mean diameter (nm)	Number density (m^{-3})
$M_{23}C_6$	73	$6.0x10^{19}$	$M_{23}C_6$	73	$5.8x10^{19}$
MC	14	$<1x10^{20}$	MC	13	$1x10^{20}$

4. Discussion

It is well known that ferritic steels have excellent swelling resistance among the alloys considered for fusion structural applications. In this study, the neutron irradiation induced no cavities in both the HT9 and the F82H because of the low irradiation temperatures and low dose.
Before irradiation, there was a significant difference in the distribution of precipitates between the HT9 and the F82H. The HT9 contained a larger amount of $M_{23}C_6$ carbides than the F82H, which is attributed to the HT9 having twice as much carbon. There were no MC carbides in the HT9. The irradiation caused little change in the $M_{23}C_6$ and the MC carbides in both alloys, while, in the HT9 irradiated at 250°C, a low density of precipitates, tentatively identified α', formed in the matrix. These small particles were detected by using the 2.5 dimension method on weak beam dark-field conditions. It is generally believed that in high-chromium ferritic steels, there is a possibility to form aging emblittlement due to the formation of α'-phase through either spinodal decomposition or nucleation and growth, depending on the aging temperature [3]. Under irradiation, however, the critical content of chromium necessary to form α'-phase may be lower than that during thermal aging. Previous studies of irradiated 12Cr steel [4-6] also reported the particles and identified them as chromium-enriched α'-phase. Mechanical property studies indicate that the HT9 showed a large shift in ductile-brittle transition temperature (DBTT) and a reductions of fracture toughness after irradiation to 3 dpa at 250°C. On the other hand, in the F82H irradiated at 250°C to 3 dpa, the shift of DBTT and the decrease in fracture toughness were less than that in HT9. As discussed in a previous paper [7], it is believed that this phase formed in HT9 may contribute to the decrease in toughness.

The irradiation of HT9 at 90°C and 250°C induced dislocation loops which were perfect types of $\mathbf{b}= \mathbf{a}_0\langle 100\rangle$ on {100} and/or $\mathbf{b} = (\mathbf{a}_0/2)\langle 111\rangle$ on {111}. Total dislocation density irradiated at 250°C is larger than that at 90°C because of the higher number density. On the other hand, irradiation of F82H at 250°C induced dislocation loops on {111} planes with $(\mathbf{a}_0/2)\langle 111\rangle$ Burgers vectors. In Fe-Cr binary alloys, with respect to dislocation evolution in an initially almost dislocation-free condition, interstitial type dislocation loops with an $\mathbf{a}_0\langle 100\rangle$ and/or $(\mathbf{a}_0/2)\langle 111\rangle$ Burgers vector develop during irradiation [8,9]. According to an investigation of dislocation loop evolution in ferritic alloys irradiated to high fluence [10,11], the $\mathbf{a}_0\langle 100\rangle$ type dislocation loops were sensitive to chromium content and a number of $\mathbf{a}_0\langle 100\rangle$ type dislocation loops were present in Fe-12Cr alloy irradiated at 420°C to 140 dpa, while in the Fe-6Cr and Fe-9Cr alloys, their number density was extremely low. This difference of the nucleation of interstitial loops could be explained by chromium stabilization of interstitial clusters, and/or α' precipitation promotes the loop nucleation in Fe-12Cr alloy. On the other hand, according to previous paper which

investigated a relationship between type of dislocation loop and content of interstitial impurities, there is a tendency for $\mathbf{a}_0$<100> type loop to form in low-purity alloys [12]. The HT9 used in this study has twice as much carbon and ten times as much nitrogen as the F82H, and there is a possibility that the difference in impurity content affects loop formation. The growth rate of loops should be controlled by not only dislocation bias for interstitials and vacancies but also the stability, i.e., the strain energy, of loops [12], the differences of the growth rate and the number density between $\mathbf{a}_0$<100> and ($\mathbf{a}_0$/2)<111> type loops at lower temperature should be investigated. It is possible that these differences in evolution of dislocation loops and radiation-induced phases during irradiation could be related to the different post-yield deformation behavior observed in the two alloys.

FUTURE WORK

Further analysis will be carried out of the relationships between the microstructural parameters and the measured flow and fracture properties.

ACKNOWLEDGMENTS

The authors are grateful to Dr. M.L. Grossbeck for providing valuable irradiated samples. They also would like to thank Drs. R.L. Klueh and S.J. Zinkle for their helpful discussions. This research was supported in part by an appointment to the Oak Ridge National Laboratory Postdoctoral Research Associates Program administered jointly by the Oak Ridge Institute for Science and Education and Oak Ridge National Laboratory, and sponsored by the Office of Fusion Energy Sciences, U.S. Department of Energy, under contact DE-AC05-96 OR22464 with Lockheed Martin Energy Research Corp., and the Japan Atomic Energy Research Institute.

REFERENCES

1) R.L. Klueh, K. Ehrlich, and F Abe, J. Nucl. Mater.**191-194** (1992) 116.
2) D.J. Alexander, J.E. Powel, M.L. Grossbeck, A.F. Rowcliffe, and K. Shiba, *Effects of Radiation on Materials*: 17th International Symposium, ASTM STP 1270, D.S. Gelles, R.K. Nanstad, A.S. Kumar, and E.A. Little, Eds., American Society for Testing and Materials, Philadelphia, PA (1996) p. 945
3) Metals Handbooks, 10th Ed., Vol. 1 (American Society for Metals, Metals Park, PA, 1992)
4) J.J. Kai and R.D. Lee, J. Nucl. Mater. **175** (1990) 227.
5) P. Dubuisson, D. Gibson, and J.L. Seran, J. Nucl. Mater. **205** (1993) 178.
6) D.S. Gelles, *Effects of Radiation on Materials*: 14th International Symposium, ASTM STP 1046, N.H. Packan, R.E. Stoller, and A.S. Kumar, Eds., American Society for Testing and Materials, Philadelphia, PA (1990) p. 73.
7) R.L. Klueh, J.J. Kai, and D.J. Alexander, J. Nucl. Mater. **225** (1995) 175.
8) N. Yoshida, et al., J. Nucl. Mater., **155-157** (1988), 1232.
9) D.S. Gelles, Annual Progress Report for Fusion Year, (1991), 348.
10) Y. Katoh, A. Kohyama and D.S. Gelles, J. Nucl. Mater., **225** (1996) 154.
11) D.S. Gelles, J. Nucl. Mater., **225** (1995) 163.
12) E. Wakai et al., Proceeding of Ultra High Purity Base metals, UHPM-94, 488.

4.0 COPPER ALLOYS AND HIGH HEAT FLUX MATERIALS

PROGRESS REPORT ON THE INFLUENCE OF TEST TEMPERATURE AND GRAIN BOUNDARY CHEMISTRY ON THE FRACTURE BEHAVIOR OF ITER COPPER ALLOYS

– M. Li, J. F. Stubbins (University of Illinois), D. J. Edwards (Pacific Northwest National Laboratory)

OBJECTIVE

The objective of this study is to determine the effects of temperature, changes in grain boundary chemistry and changes in other microstructural features on the tensile and fracture behavior of GlidCop™ CuAl25, Hycon 3HP CuNiBe, and Elbrodur CuCrZr at elevated temperatures.

SUMMARY

This collaborative study was initiated to determine mechanical properties at elevated temperatures of various copper alloys by University of Illinois and Pacific Northwestern National Lab (PNNL) with support of OMG Americas, Inc. and Brush Wellman, Inc. This report includes current experimental results on notch tensile tests and pre-cracked bend bar tests on these materials at room temperature, 200 and 300°C. The elevated temperature tests were performed in vacuum and indicate that a decrease in fracture resistance with increasing temperature, as seen in previous investigations. While the causes for the decreases in fracture resistance are still not clear, the current results indicate that environmental effects are likely less important in the process than formerly assumed.

PROGRESS AND STATUS

1. Introduction

High strength, high conductivity copper alloys have been considered as candidate materials for first wall and divertor heat sink applications in the proposed International Thermonuclear Experimental Reactor (ITER) [1]. Three different copper alloys are under consideration, namely dispersion-strengthened CuAl25 alloy, and precipitation-hardened CuNiBe and CuCrZr alloys. This study focuses on the following copper alloys: GlidCop™ CuAl25, Hycon 3HP CuNiBe, and Elbrodur CuCrZr. Although the processing and microstructures of these three alloys are quite different, the general trend for each alloy is that the tensile properties and fracture toughness decrease as temperature increases, and in the case of the CuAl25 and CuNiBe, the fracture toughness drops very rapidly at T $\geq$200°C [2]. The toughness degradation with increasing temperature has been presumed to be related to an environmental effect and/or an impurity effect. However, no evidence supports the idea that the environmental effect is the only factor responsible for the poor toughness. Vacuum tests still showed that the fracture toughness of CuAl25, CuNiBe decreases with increasing temperature. This study focused on the effects of temperature and grain boundary chemistry change on fracture behaviors of three copper alloys.

2. Experimental Procedures

Three copper alloys, GlidCop™ CuAl25, Hycon 3HP CuNiBe, and Elbrodur CuCrZr were tested at room temperature, 200 and 300°C, and analyzed by optical microscopy, scanning electron microscopy, and Auger electron microscopy.

The GlidCop™ CuAl25 (Heat #C-8064, ITER grade 0) was supplied by OMG Americas, Inc. in the form of 1 inch thick plate with a pure copper cladding. It was in the cross-rolled and annealed condition, and boron deoxidized. The grain size is about 4 μm in width and 15 μm in length [3]. The Hycon 3HP CuNiBe (Heat #46546) was supplied by Brush Wellman, Inc. in the form of 1.25 inch thick plate. The plates were in the HT temper condition (cold worked and aged), and then heat-treated again to produce an AT tempered condition (solutionized, quenched, and aged). It has equiaxed grains of about 40 μm [3]. The Elbrodur CuCrZr (Heat # AN4946) was supplied by S. J. Zinkle in the cold worked and aged condition (F37 temper). This copper alloy has grains 25 μm in width and 48 μm in length [3]. The chemical compositions of the three copper alloys are listed in Table 1.

Table 1 Chemical Composition (wt%) of three copper alloys

Materials	Chemical Composition (wt%)				
GlidCop™ CuAl25	0.25 Al	23ppm Fe	6ppm Pb	~250ppm B	10ppm S
Hycon 3HP CuNiBe	0.35 Be	1.92 Ni	<0.01 Co	<0.01 Fe	<0.03 Cr
Elbrodur CuCrZr	0.65 Cr	0.10 Zr	/	/	/

Fracture toughness tests were performed on an MTS closed-loop servohydraulic test frame with the test furnace system (Model FR210), which allow elevated temperature fracture testing in vacuum. The nominal oxygen partial pressure was 2.57×10^{-10} Torr and the nominal water partial pressure was 1.23×10^{-9} Torr. Tungsten mesh heating element and molybdenum heat shields for operation to 1700°C in vacuum provide the usable work zone of 89mm in diameter and 127mm in height. Specimen temperatures were monitored and controlled by two Type K thermocouples attached to the specimen surface. Extensometry was achieved with a capacitive displacement device (Capacitec, Model 3201-SP amplifier and Model HPT-150 probe) which produces a voltage proportional to the gap spacing between the probe and the grounded plate. MTS 0.2" extensometer was used to calibrate the Capacitec probe at room temperature for each alloy. Fracture toughness tests over three temperatures, RT, 200, and 300°C, were conducted with notched tensile specimens and four-point bending bar specimens. Room temperature tests were performed in air, and high temperature tests were performed in vacuum. The heating rate was approximately 3.5°C/min for the elevated temperature tests. After reaching the desired temperature, the specimen was held in vacuum at temperature for approximately 0.5 hour to stabilize the temperature before loading. All fracture toughness tests were controlled with specialized LABVIEW software. For both notched tensile fracture tests and four-point bend tests, the same strain rates were chosen for each alloy considering the strain rate sensitivity of three copper alloys[1]. The geometry of notched tensile specimens and four-point bending specimens is shown in figure 1. The notched tensile specimens were oriented in the L-S orientation with the notches perpendicular to the rolling direction. These specimens could not be fatigue-precracked because of relatively small diameter of notched section. A cross-head speed of 0.006 mm/sec was chosen consistent with ASTM E399. This cross-head speed corresponds to the strain rate of order of 10^{-4} s^{-1}, which is typically used in static fracture toughness tests. The four-point bend specimens were oriented in the L-S orientation

also with the notches perpendicular to the rolling direction. Dimensions of the as-received materials and the limitation of the vacuum chamber size prevent the use of ASTM standard size specimens. Efforts were made to satisfy ASTM standard in testing practice as closely as possible. The fatigue precracking from the notches was performed at room temperature in air prior to testing. Cyclical loading with the ratio of minimum to maximum load of 0.1 was chosen for cycles between 10^5 and 10^6 depending on the alloy. Sine waveform was used with the frequency of 3 Hz. In order to monitor the crack growth with microscope, the specimens were polished with 6 micron diamond polish before precracking. The nominal crack length (total length of the notch plus the fatigue crack) was about 0.3 to 0.4 of width. According to ASTM E399, the crosshead speed for fracture testing was chosen as 0.013mm/sec. The crack length measurements were confirmed with traveling microscopes.

A Perkin Elmer Phi 660 Auger microprobe was used to examine the fracture surface chemistry of the notched tensile specimens. To minimize oxidation of the fracture surfaces, failed specimens were unloaded and cut into Auger specimens in about half an hour. They were then kept under vacuum. Fractographic observations were made with a Hitachi S-800 SEM operated at 10 kV. Typical fracture surfaces are examined to identify the features relating to the fracture micromechanisms. Optical microscopy was used to examine the macroscopic characteristics of plastic zones and fracture surfaces of the specimens.

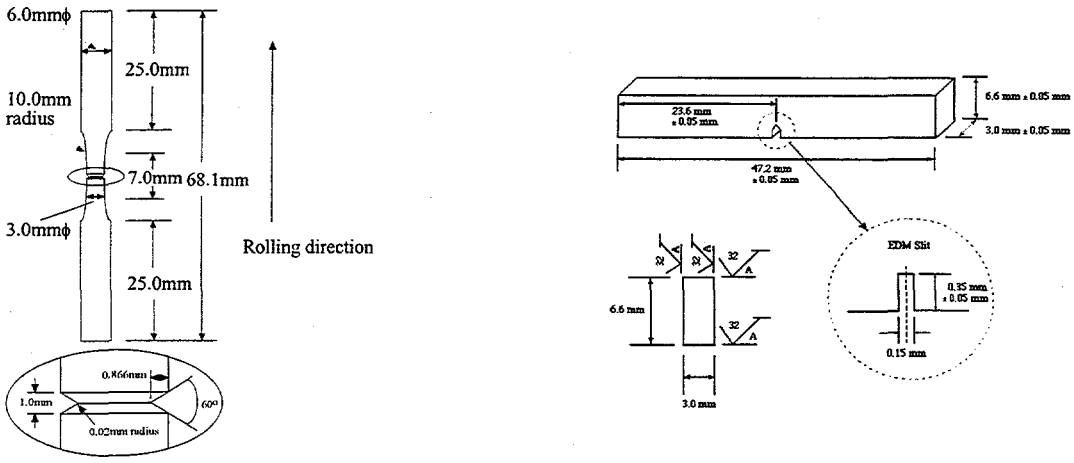

Figure 1. Geometry and size of notched tensile specimen and four-point bending specimen

3. Results

3.1 Fracture behavior of copper alloys

The plastic deformation and fracture behavior were found to be quite different among three copper alloys. Figure 2 shows load-displacement curves of notched tensile specimens for the three copper alloys at each of three test temperatures. Displacements were converted from Capacitec extension data by the calibration of extensometer at room temperature. GlidCop^{TM} CuAl25 shows significant plastic deformation over three temperatures. The fracture loads decrease as temperature increases. Elbrodur CuCrZr shows larger plastic deformation compared with GlidCop^{TM} CuAl25. Hycon 3HP CuNiBe shows relatively brittle behavior at all three temperatures compared with GlidCop^{TM} CuAl25 and Elbrodur CuCrZr. Moreover, as temperature increases, brittle fracture in CuNiBe alloy is more evident, and the fracture loads decrease significantly. In order to compare the fracture behavior of each

copper alloy, fracture energy was obtained by integrating the area under each load-displacement curve. Figure 3 shows fracture energy versus temperatures of notched tensile specimens for three copper alloys. Fracture energy of GlidCop™ CuAl25 and Hycon 3HP CuNiBe decreases rapidly as the test temperature increases. For Elbrodur CuCrZr, the fracture energy does not show much change at 200°C, but decrease at 300°C. The fracture energy was also quite different at each test temperature depending on the material. Comparing these three alloys, fracture energy of CuCrZr is highest, and fracture energy of CuNiBe is lowest over the three temperatures. Figure 4 shows comparison of fracture energy with fracture toughness in the range of temperature 20°C to 300°C. The fracture toughness data were reported by D. J. Alexander [4]. All of these three copper alloys show similar trends of fracture energy decreases to fracture toughness decreases with increasing temperature. This comparison suggests that the relative fracture behavior of these copper alloys can be evaluated by simple tension tests. This is very useful for study of fracture micromechanism analysis where the exact values of fracture toughness are not critical.

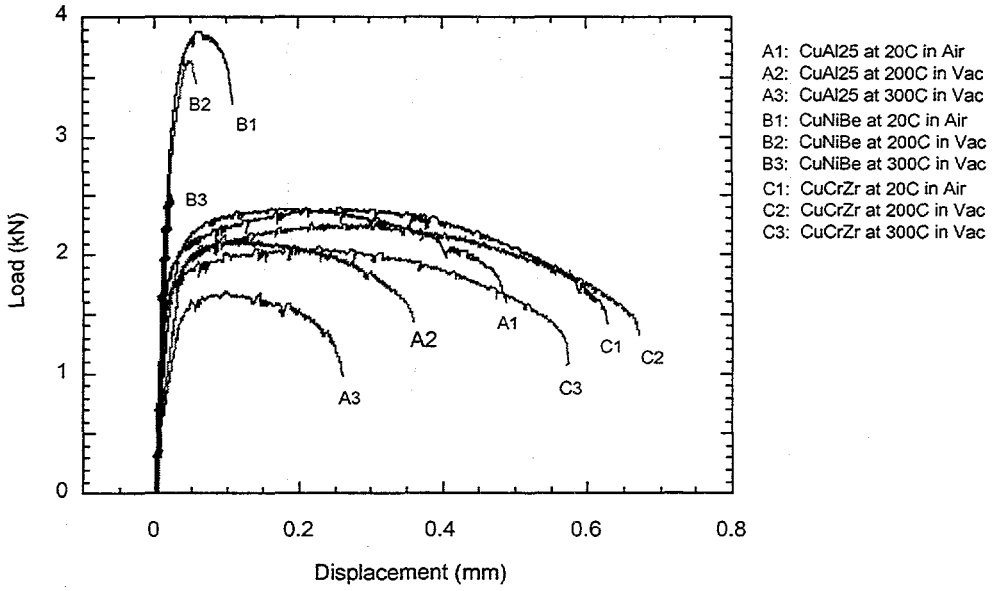

Figure 2. Load vs. displacement of notched tensile specimens for three copper alloys

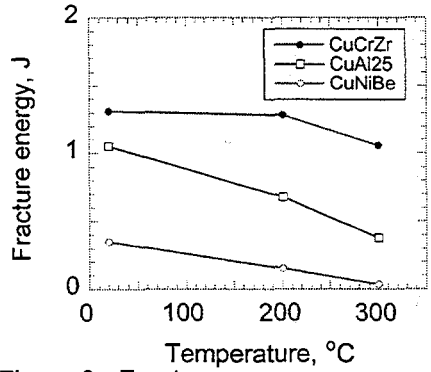

Figure 3. Fracture energy versus temperature of notched tensile specimens for three copper alloys

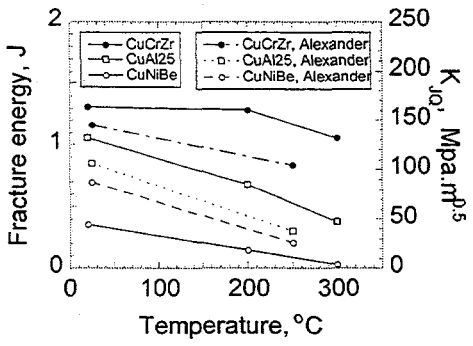

Figure 4. Comparison of fracture energy with fracture toughness of notched tensile specimens for three copper alloys

3.2 Fracture surface analysis

The fracture surfaces of the notched tensile specimens were examined by SEM to identify the significant features relating to the fracture performance. A macroscopic comparison of room temperature and 200°C conditions on the fracture surfaces for CuAl25 indicates that the fracture surfaces of both specimens are reasonably flat. A close examination of failure surfaces shows that at 20 and 200°C, both specimens have a large amount of plasticity-induced microvoid formation, which can be seen in figure 5. Figure 6 shows the failure surfaces of CuNiBe tested at 20, 200, and 300°C. All specimens show mixed modes of transgranular fracture and intergranular fracture; the percentage of intergranular fracture increases as the test temperature increases. This percentage increase of intergranular fracture corresponds to the fracture energy change at the different temperatures. Fractographic examinations of CuCrZr alloy over three temperatures are shown in figure 7. Microvoid coalescence is the main fracture mechanism for CuCrZr alloy at all test temperatures. The depth and width of the observed dimples are very similar at all three temperatures. Compared to CuAl25, the dimple size of CuCrZr alloy is larger than that of CuAl25 alloy. At higher magnification, cracking second-phase particles are visible inside dimples.

The fracture surface chemistry was thoroughly analyzed by Auger Electron Spectroscopy. Auger spectra were taken from fracture surfaces of CuAl25 tested at room temperature and 200°C temperature. Significant oxygen, carbon and chlorine are presented on fracture surfaces. Chlorine was probably from lab water vaporization. No aluminum was observed. Chemical mapping of chlorine and copper on CuAl25 failure surface at 200°C does not provide much information. Auger spectra were also taken on fracture surfaces on CuNiBe at 300°C temperature. Both area-analysis and point-analysis show significant amount of oxygen, carbon, silicon and chlorine. No beryllium segregation near grain boundaries can be detected. Composition-depth profiles on and adjacent to grain boundaries on the fracture surface of CuNiBe at 300°C do not show much difference in the distribution of beryllium and nickel. Auger analysis on the fracture surfaces of CuCrZr alloy tested at 300°C shows similar results. These results are clouded by the formation of oxides at the free fracture surfaces. Continuing work aimed at addressing this problem.

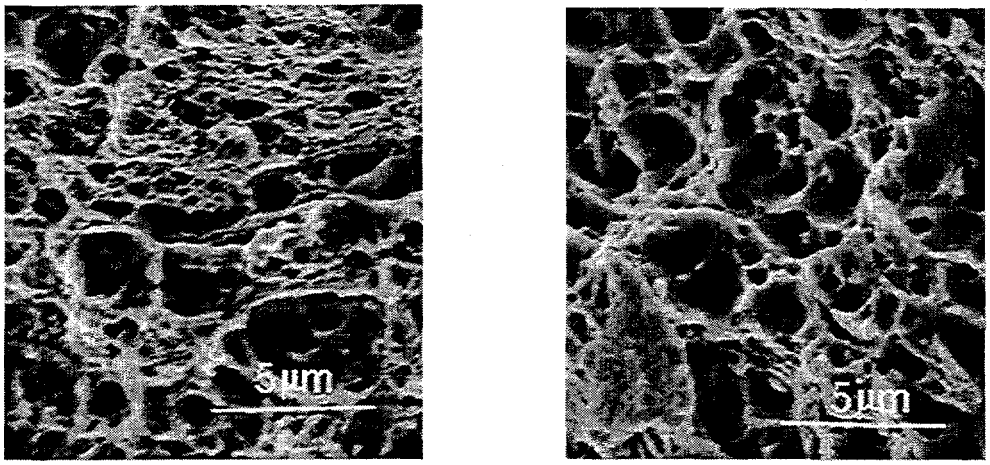

20°C 200°C

Figure 5. SEM fractographs of the fracture surfaces of notched tensile specimens for CuAl25

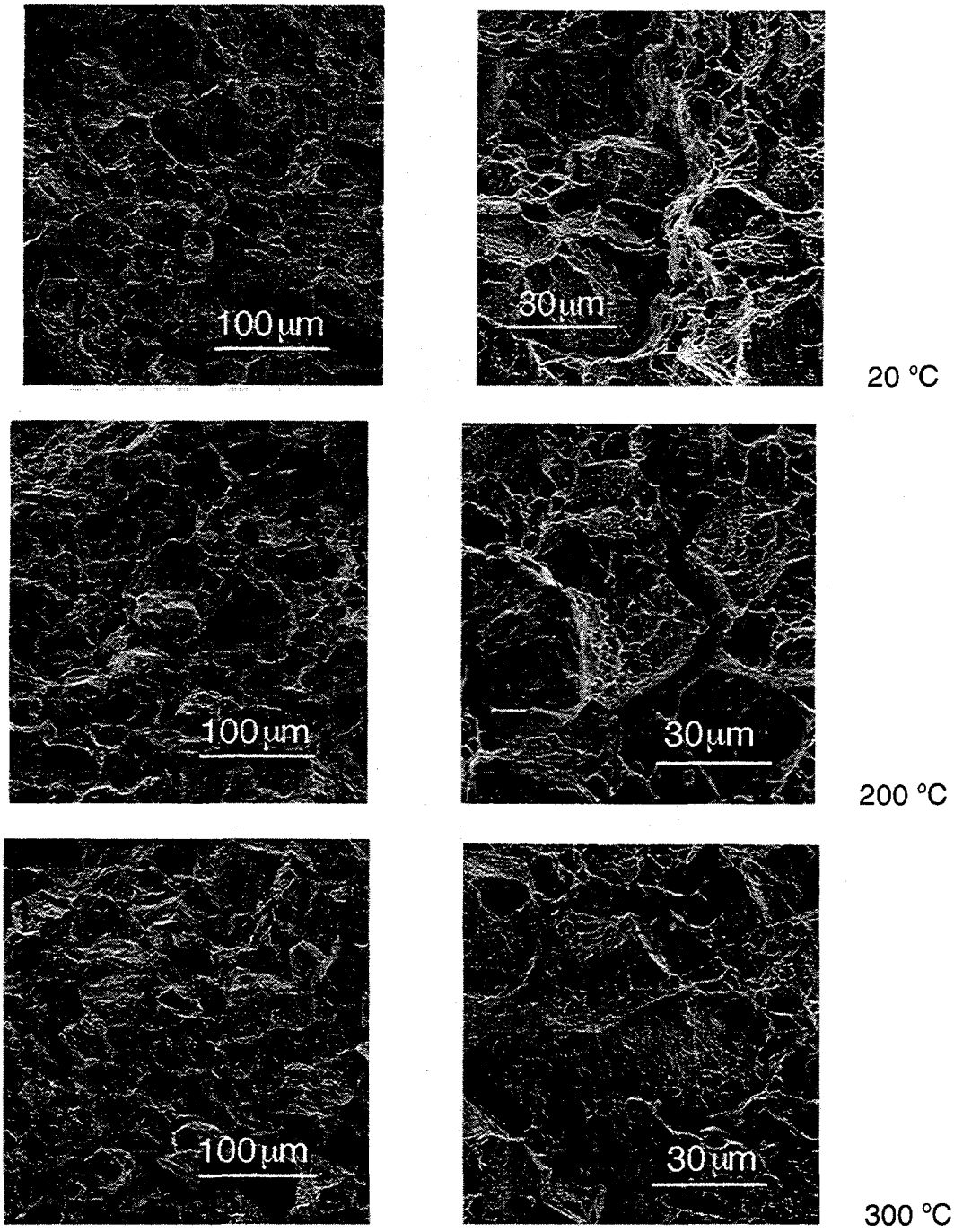

Figure 6. SEM fractographs of the fracture surfaces of notched tensile specimens for CuNiBe

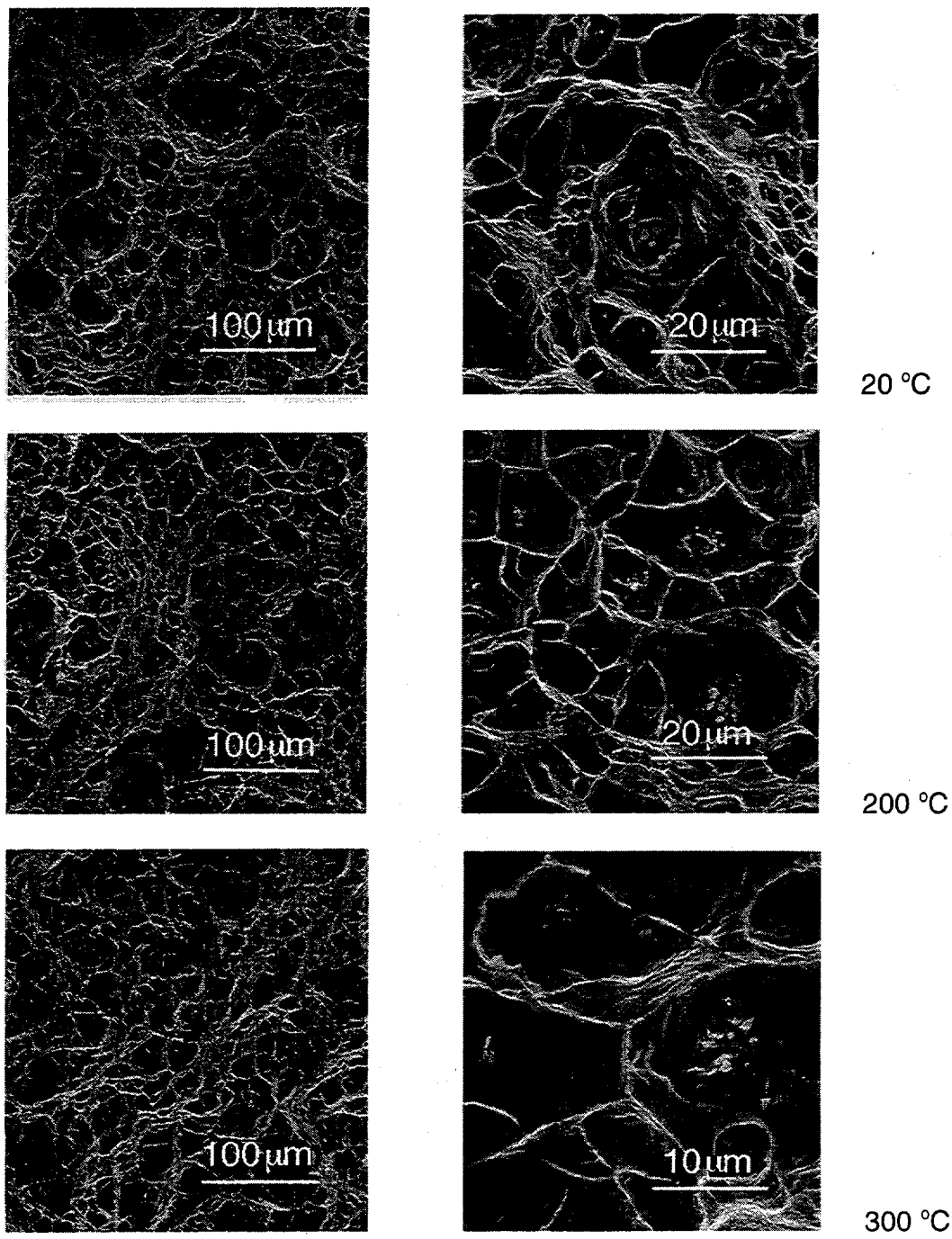

Figure 7. SEM fractographs of the fracture surfaces of notched tensile specimens for CuCrZr

3.3 Fracture behavior analysis on four-point bending specimens

The precracked four-point bend specimens were used for fracture toughness tests to determine temperature effects. Subsize specimens were intended for J-integral fracture toughness tests. Limitation in the specimen dimension and the testing machine prevented valid J-integral fracture tests. Measurements of fracture toughness, K_Q, succeeded on CuNiBe alloy, but failed on CuAl25 and CuCrZr alloys due to rather ductile behavior in these cases. The K_Q measurements for CuNiBe alloy are shown in figure 8. The plot shows that fracture toughness decreases rapidly as the temperature increases. Compared to the data from Alexander [4], significant differences exit for the room temperature value (figure 9), most likely due to constraint considerations at the most ductile condition.

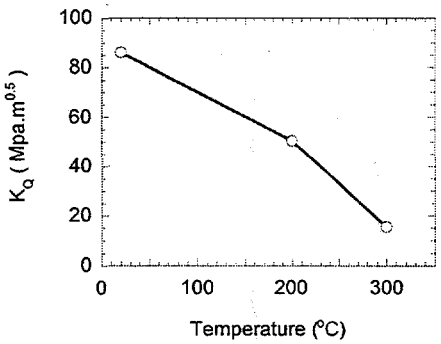

Figure 8. Fracture toughness vs. temperature of four-point bending tests for CuNiBe

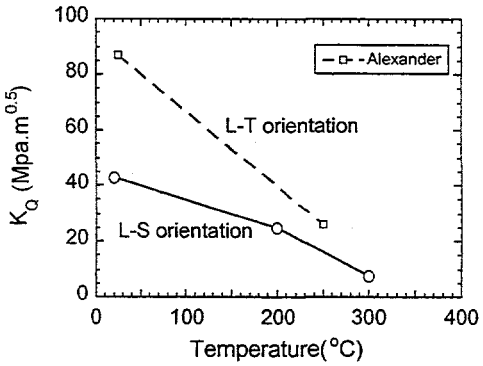

Figure 9. Comparison of fracture toughness of CuNiBe with data after Alexander

Although no valid fracture toughness values were obtained on CuAl25 and CuCrZr alloys, the macroscopic observations of failed specimens of three copper alloys by optical microscopy show quite different fracture features, see figure 10. The CuCrZr alloy shows significant plastic zones at both room temperature and 300°C. There is no visible crack growth. CuAl25 alloy shows similar plastic zone characteristic to the CuCrZr alloy at room temperature test. However, the fracture features at markedly different at 300°C.

It is interesting to note that not only a relatively large plastic zone is formed around the initial crack, but also two cracks extend in opposite directions perpendicular to the initial crack direction. This indicates the strong preference for crack growth along the rolling directions instead of the initial crack direction. The CuNiBe specimen shows an initial shear crack growth mode at room temperature. At 300°C, the crack extends straight along the initial crack direction.

Discussion

The main purpose of this study was to investigate the effect of temperature on the fracture behavior and the fracture mechanisms of copper alloys at high temperatures. While it is most convenient to evaluate the fracture toughness by standard procedures, the limitation in the dimension of the material and other factors necessitates the development of a non-standard method, mostly the design of a non-standard specimen geometry. Notch tension testing is an attractive method for obtaining a fast inexpensive estimate of a material's toughness with reasonable accuracy. Fracture energy of notched tensile specimens for copper alloys gives the relative accurate evaluation of fracture toughness of materials. Notch tension testing provides a useful estimation of fracture behavior in case that focus is

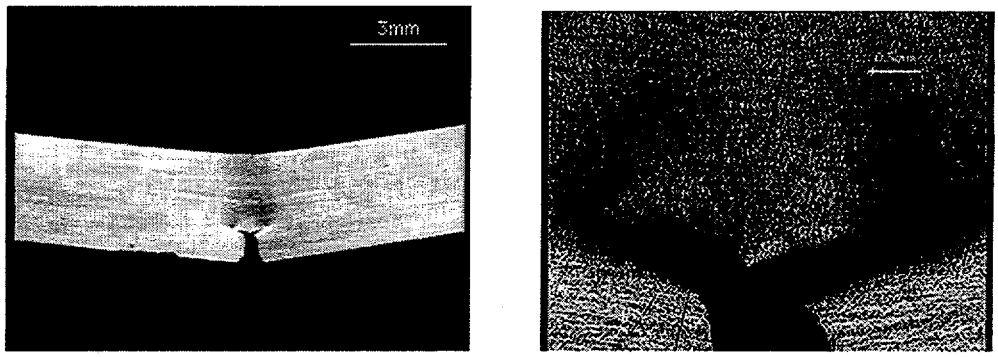

(a) Fracture feature of four-point bending specimen for CuAl25 at 300°C test at low magnification and high magnification

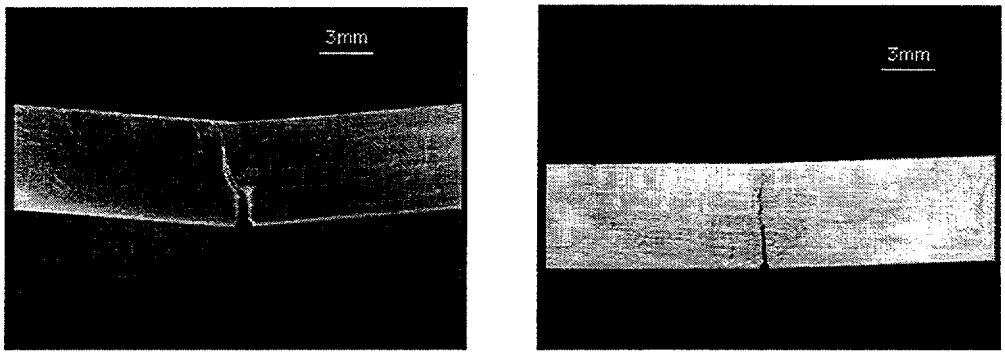

20°C 300°C

(b) Fracture features of four-point bending specimen for CuNiBe at 20 and 300°C tests

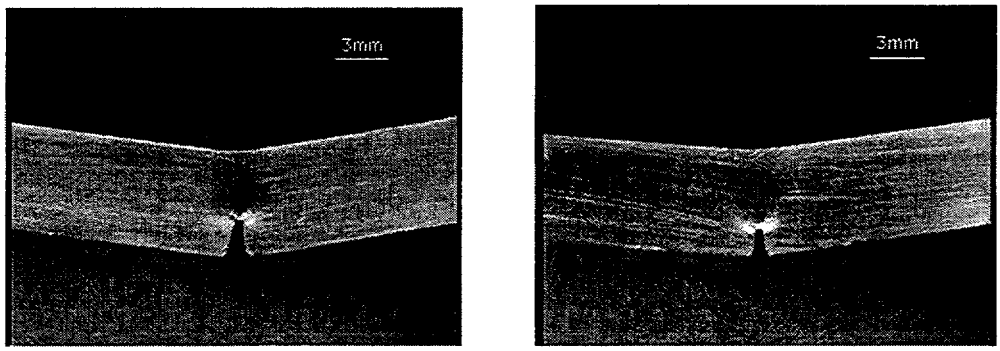

20°C 300°C

(c) Fracture features of four-point bending specimen for CuCrZr at 20 and at 300°C tests

Figure 10. Fracture features of four-point bending specimens of three copper alloys

on the fracture mechanism analysis. Due to the small diameter of notched section, it was not possible to fatigue-precrack the notched tensile specimens. This might be one of reasons that fracture testing at elevated temperature results in transgranular fracture mode instead of expected intergranular fracture mode. Most of the fracture energy was likely consumed in the crack initiation processes.

All elevated temperature fracture tests were performed in vacuum. Both notched tensile fracture tests and four-point bending fracture tests indicate that the fracture behaviors of three copper alloys degraded as temperature increased, however, CuCrZr shows less degradation compared to CuAl25 and CuNiBe alloys. The literature suggests that environmental effects could be a factor responsible for the poor fracture toughness of copper alloys [4]. This study provides the evidence that an environmental effect can not be the predominant cause of poor fracture toughness.

The SEM fracture surface morphology reveals that CuNiBe shows mixed intergranular and transgranular fracture modes. This intergranular fracture can result from a number of processes. Microvoid nucleation and coalescence at inclusions or second-phase particles located along grain boundaries, grain boundary crack and cavity formation associated with elevated temperature stress rupture, decohesion between contiguous grains due to the presence of brittle elements at grain boundaries, and insufficient number of independent slip systems to accommodate plastic deformation between contiguous grains could be the cause of grain boundary separation [3]. Be is believed to be the most critical element concerning intergranular fracture of CuNiBe. For CuCrZr alloy, tests at all three temperatures show similar microvoid coalescence fracture mechanism. Second-phase particle cracking provided the nucleation sites of microvoids. Compared to CuNiBe and CuCrZr alloys, it is more complicated to identify the fracture mechanism of CuAl25 alloy. Both notched tensile tests and four-point bending fracture tests show that fracture behavior degrades relatively rapidly with increasing temperature.

ACKNOWLEDGEMENTS

This work was supported by the Associated Western Universities (AWU) through a grant from the Pacific Northwest National Laboratory (PNNL) under the US DOE Fusion Materials Program, as well as by OMG Americas, Inc. and Brush Wellman, Inc.. We would like to express our appreciation to D. J. Edwards, PNNL, and the US DOE Fusion Materials Program for supplying the GlidCop and Hycon materials, produced by OMG Americas, Inc. and Brush Wellman, Inc. respectively. We would also like to thank S. J. Zinkle, ORNL, for supplying the CuCrZr alloy. The Advanced Materials Testing and Evaluation Laboratory (AMTEL), UIUC and the Center for Microanalysis of Materials in Seitz Materials Research Laboratory, UIUC provided the mechanical testing facilities and microanalysis facilities.

REFERENCES

1. S. J. Zinkle and W. S. Eatherly, Fusion materials Semiannual progress Report, DOE/ER-0313/21 (1996) 165
2. K. D. Leedy, J. F. Stubbins, D. J. Edwards, and R. R. Solomon, Fusion Materials Semiannual progress Report, DOE/ER-0313/22 (1997) 149.
3. K. D. Leedy, Ph.D. Thesis, University of Illinois at Urbana-Champaign, 1997
4. D. J. Alexander, S. J. Zinkle, and A. F. Rowcliffe, Fusion Materials Semiannual Progress Report, DOE/ER-0313/21 (1996) 175.
5. R. W. Hertzberg, Deformation and Fracture Mechanics of Engineering Materials, 1983

COMPARISON OF PROPERTIES AND MICROSTRUCTURES OF TRÉFIMÉTAUX AND HYCON 3HP™ AFTER NEUTON IRRADIATION - D.J. Edwards (Pacific Northwest National Laboratory)*, B.N. Singh, P. Toft and M. Eldrup (Risø National Laboratory)

(Summary of a presentation at the 19th International Symposium on the Effects of Radiation on Materials in Seattle, WA, June. 1998)

EXTENDED ABSTRACT

The precipitation strengthened CuNiBe alloys are among three candidate copper alloys being evaluated for application in the first wall, divertor, and limiter components of ITER. Generally, CuNiBe alloys have higher strength but poorer conductivity compared to CuCrZr and Cu-Al_2O_3 alloys. Brush-Wellman Inc. has manufactured an improved version of their Hycon CuNiBe alloy that has higher conductivity while maintaining a reasonable level strength [1,2]. It is of interest, therefore, to investigate the effect of irradiation on the physical and mechanical properties of this alloy.

In the present work we have investigated the physical and mechanical properties of the Hycon 3HP™ alloy both before and after neutron irradiation and have compared its microstructure and properties with the European CuNiBe candidate alloy manufactured by Tréfimétaux. Tensile specimens of both alloys were irradiated in the DR-3 reactor at Risø to displacement dose levels up to 0.3 dpa at 100, 250 and 350°C. Both alloys were tensile tested in the unirradiated and irradiated conditions at 100, 250 and 350°C. Both pre- and post-irradiation microstructures of the alloys were investigated in detail using transmission electron microscopy. Fracture surfaces were examined under a scanning electron microscope. Electrical resistivity measurements were made on tensile specimens before and after irradiation; all measurements were made at 23°C.

In the unirradiated condition the Tréfimétaux alloy possesses a higher density of smaller precipitates, producing a lower yield strength and much lower electrical conductivity than in the case of the Hycon alloy. Both alloys proved to be susceptible to embrittlement when the test temperature exceeded 250°C, exhibiting a transition from a ductile transgranular failure mode to a combination of ductile/brittle intergranular failure.

Irradiation clearly alters the microstructure and solute distribution within both alloys. Changes in the electrical conductivity (Table 1) and the size distributions of the precipitates (Fig. 1), evolution of the precipitate reflections in the diffraction patterns, as well as precipitation within the prior denuded zones, indicate that dissolution and reprecipitation occur at all irradiation temperatures to some extent depending on the irradiation conditions. The effect of irradiation is also seen in the mechanical properties (Table 2, Figure 2). Irradiation increases the susceptibility to embrittlement when tested above 250°C, while the large increases in strength that occur when irradiated and tested at 100°C suggest that radiation-induced redistribution of the solute is occurring, possibly forming small nanoscale precipitates that have not yet been observed. Various researchers [3-8] and the evidence provided in this report suggest that more than one mechanism may be responsible for the embrittlement that occurs at temperatures > 200°C, mechanisms such as solute segregation to the grain boundaries and oxygen adsorption. The effect of oxygen and possibly other

---

* Pacific Northwest National Laboratory (PNNL) is operated for the U.S. Department of Energy by Battelle Memorial Institute under contract DE-AC06-76RLO-1830.

is needs to be investigated more thoroughly through controlled experiments that the effects of temperature and strength as well as irradiation.

he Tréfimétaux alloy may simply require different thermomechanical processing to e its overall behavior, at present the Hycon alloy appears to be the best alloy for lower rature applications, especially considering its higher electrical conductivity and higher th. Careful evaluation of this material to determine the fracture toughness and crack gation characteristics at lower irradiation temperatures over a range of doses would useful.

At this point it seems unlikely that CuNiBe alloys can be recommended for applications in neutron environments where the irradiation temperature exceeds 200°C. Applications at temperatures below 200°C might be plausible, but only after careful experiments have determined the dose dependence of the mechanical properties and the effect of sudden temperature excursions on the material to establish the limits on the use of the alloy.

ACKNOWLEDGEMENTS

The present work was partly funded by the European Fusion Technology Programme. The authors wish to thank B. F. Olsen, N.J. Pederson and J.L. Lindbo. DJ Edwards would like to thank Risø National Laboratory for the support and assistance during his visit. His work was also partly supported by the U.S. Department of Energy under contract DE-AC06-76RLO 1830 with the Battelle Memorial Institute at the Pacific Northwest National Laboratory.

REFERENCES

1. J.C. Harkness, W. D. Spiegelberg, and W. Raymond, "Beryllium-Copper and Other Beryllium-Containing Alloys", Metals Handbook, Vol. 2, 10th Edition, ASM International, Philadelphia, (1990), p. 403

2. H.A. Murray, I.J. Zatz, and J.O. Ratka, Cyclic Deformation, Fracture, and Nondestructive Evaluation or Advanced Materials: Second Volume, ASTM STP 1184, M.R. Mitchell and O. Buck, Eds., ASTM, Philadelphia, (1994), p. 109

3. R. Muthiah, A. Guha and C.J. McMahon, Jr., Materials Science Forum, 207-209, (1996) p. 585.

4. R. Misra, C.J. McMahon, Jr. and A. Guha, Scripta Metall. et. Mater. 31, (1995), p. 1471.

5. M. Kanno, Z. Metallkde, Bd. 79, March 1988, p. 684.

6. S.J. Zinkle and W.S. Eatherly, Fusion Materials Semiannual Progress Report for the Period Ending Dec. 31, 1996, DOE/ER-0313/21, p. 165.

7. S.J. Zinkle and W.S. Eatherly, Fusion Materials Semiannual Progress Report for the Period Ending June. 30, 1996, DOE/ER-0313/20, p. 207.

8. D.J Edwards, submitted for publication in the Proceedings of the 19th International Symposium on the Effects of Irradiation on Materials, held June 16-18, 1998 in Seattle, Washington, ASTM STP 1366.

Table 1. Electrical Conductivity of Unirradiated CuNiBe Alloys and Irradiated to 0.1 and 0.3 dpa at Various Temperatures.

Alloy	Irradiation Temperature (°C)	Relative Conductivity (%)
Tréfimétaux CuNiBe	Unirradiated	42.6
	100	41.4
	250	43
	350	50.1
Hycon 3HP™	Unirradiated	64.6
	100	54.9
	250, 0.1 dpa	59.9
	250, 0.3 dpa	53.9
	350	65.7

Table 2. Tensile Results on Unirradiated CuNiBe Alloys and Irradiated to 0.1 and 0.3 dpa at Various Temperatures.

Alloy	Irradiation Temperature (°C)	$\sigma_{0.2}$ (MPa)	σ_{max} (MPa)	ε_u (%)	ε_{total} (%)
Tréfimétaux CuNiBe	Unirradiated 22°C	585	826	23.8	28.3
	Unirradiated 100°C	590	824	21.4	28.8
	Unirradiated 250°C	630	825	15.0	19.0
	Unirradiated 350°C	Not specimens tested			
	100	885	940	3.3	5.9
	250	690	705	0.3	1.5
	350	Specimen broke in mount			
Hycon 3HP™	Unirradiated 22°C	720	800	7.2	10.2
	Unirradiated 100°C	720	780	7.2	11.4
	Unirradiated 250°C	690	730	3.0	5.1
	Unirradiated 350°C	640	680	0.9	2.7
	100	810	840	0.8	4.5
	250, 0.1 dpa	670	705	1.0	3.4
	250, 0.3 dpa	620	660	1.0	3.1
	350	405	Broke prematurely		

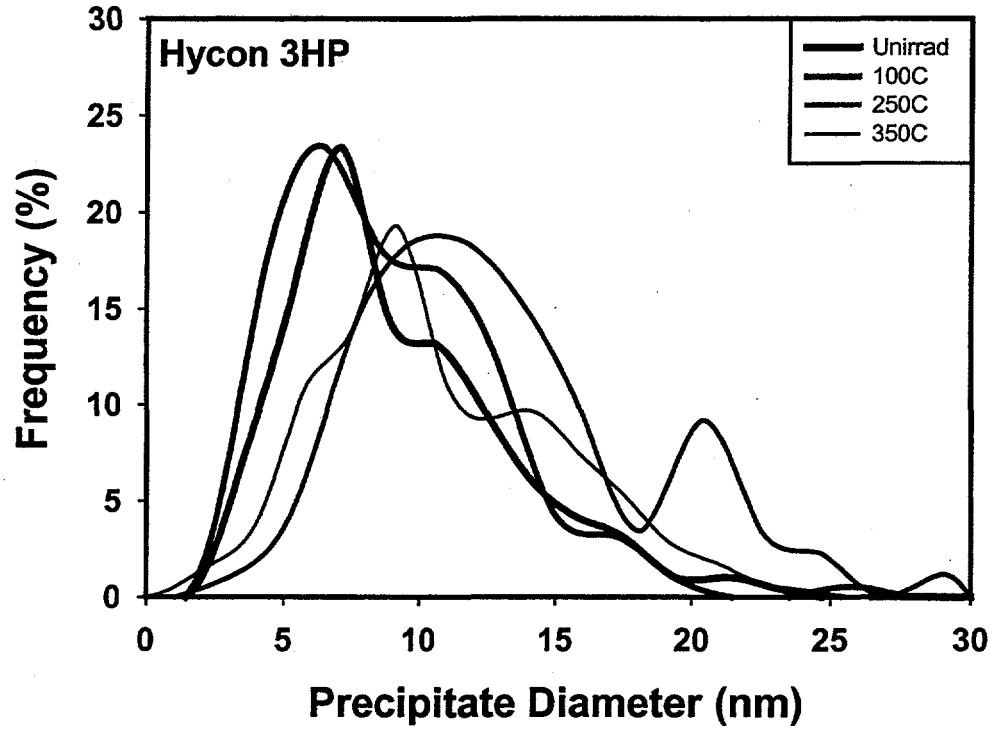

Figure 1. Size distribution of the γ″ precipitates in the unirradiated and irradiated Hycon alloy after irradiation to 0.3 dpa. Note that the size distribution broadens as the irradiation temperature is increased.

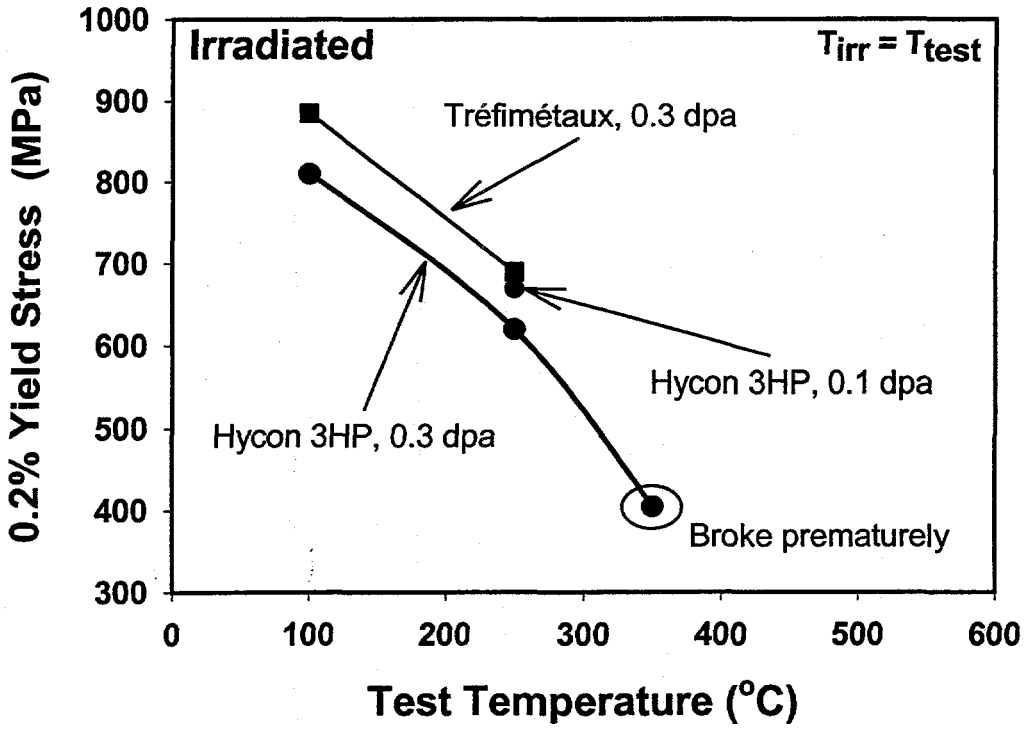

Figure 2. Yield strength of the irradiated CuNiBe alloys as a function of test temperature. Note that at $T_{test} \geq 350°C$ both alloys failed prematurely or during specimen mounting for testing, evidence of the extreme embrittlement caused by irradiation.

TENSILE AND ELECTRICAL PROPERTIES OF HIGH-STRENGTH HIGH-CONDUCTIVITY COPPER ALLOYS — S.J. Zinkle and W.S. Eatherly (Oak Ridge National Laboratory)

OBJECTIVE

The objective of this report is to summarize recent data on the electrical conductivity and tensile properties of CuCrNb and low-temperature diffusion bonded CuCrZr alloys

SUMMARY

Electrical conductivity and tensile properties have been measured on an extruded and annealed CuCrNb dispersion strengthened copper alloy which has been developed for demanding aerospace high heat flux applications. The properties of this alloy are somewhat inferior to GlidCop dispersion strengthened copper and prime-aged CuCrZr over the temperature range of 20-500°C. However, if the property degradation in CuCrZr due to joining operations and the anisotropic properties of GlidCop in the short transverse direction are taken into consideration, CuCrNb may be a suitable alternative material for high heat flux structural applications in fusion energy devices. The electrical conductivity and tensile properties of CuCrZr that was solution annealed and then simultaneously aged and diffusion bonded are also summarized. A severe reduction in tensile elongation is observed in the diffusion bonded joint, particularly if a thin copper shim is not placed in the diffusion bondline.

PROGRESS AND STATUS

Introduction

High-strength copper alloys are being considered for the divertor structure and first wall heat sink of the proposed International Thermonuclear Experimental Reactor, as well as the centerpost magnet in low aspect ratio tokamaks. The unirradiated electrical conductivity and mechanical properties of several candidate high-strength, high-conductivity copper alloys have been recently measured, including GlidCop Al25 (IG0) dispersion strengthened copper produced by OMG Americas, Hycon 3HP CuNiBe produced by Brush-Wellman, and CuCrZr produced by Kabelmetal and Zollern [1-4]. The effect of various heat treatment cycles including simulation hot isostatic pressure (HIP) and diffusion bonding treatments with fast or slow cooling have been investigated to a limited degree [3,4].

In order to provide additional data on high strength, high conductivity copper alloys, electrical conductivity and tensile measurements were initiated on an alternative dispersion strengthened copper alloy that is being considered for aerospace applications (Cu-8at.%Cr -4at.%Nb). The CuCrNb alloy contains a moderate density of refractory Cr_2Nb precipitates which are resistant to particle coarsening for heat treatment temperatures approaching the melting point of copper [5-7]. This alloy has been reported to exhibit superior tensile strengths compared to conventional copper alloys such as precipitation hardened NARloy Z, Cu-3%Ag-0.5%Zr [6]. However, there is very little published information on the electrical or thermal conductivity of CuCrNb, and also there is no known published information on the effect of specimen orientation (longitudinal vs. transverse).

The results of tensile tests on CuCrZr which had been solution quenched and simultaneously aged and HIP diffusion bonded are also reported in this contribution.

Experimental Procedure

The CuCrNb was extruded at NASA-Lewis and then exposed to a simulated brazing cycle of 925°C for 1 h. Type SS3 sheet tensile specimens and miniature disk compact tension specimens in both longitudinal and transverse orientations were machined from the 0.71 × 2.8 × 10.7 cm strip. The 2 cm thick plate of Cu-0.65%Cr-0.10%Zr (Elbrodur G) obtained by Boeing was fabricated by KM-Kabelmetal, Osnabrück, Germany as an F37 (solution quenched, cold-worked and aged) temper, heat #AN4946. According to the vendor's specifications, the F37 temper produced a room temperature yield strength of 363 MPa and an electrical conductivity of 90% IACS. The CuCrZr plate was subsequently solution annealed for 1 h at 980°C and water quenched at Boeing, machined, and then HIP diffusion bonded at 500°C for 3 h at a pressure of 207 MPa. The diffusion bonded components were then shipped to ORNL, and miniature type SS-3 sheet tensile specimens (gage dimensions 7.6 x 1.5 × 0.76 mm) were machined such that the diffusion bondline was contained in the central portion of the gage region. Since the height of the diffusion bonded component was approximately 2 cm, the 2.54 cm long SS-3 specimens were machined at an inclined angle of ~35 degrees.

Four-point probe electrical resistivity measurements were performed at room temperature on a total of 4 to 6 different SS-3 sheet tensile specimens for each of the thermomechanical conditions, using procedures summarized elsewhere [1]. The temperature was recorded for each measurement and the resistivity data were corrected to a reference temperature of 20°C using the copper resistivity temperature coefficient of $d\rho/dT = 6.7 \times 10^{-11}$ Ω-m/K. Nonuniformities in the width and thickness in the specimen gage region caused the typical experimental uncertainty of individual resistivity measurements to be ±0.5%. The relation 17.241 nΩ-m=100% IACS (international annealed copper standard) was used to convert the resistivity measurements to electrical conductivity values.

The tensile properties of the SS-3 sheet tensile specimens were measured at crosshead speeds of 0.0016 to 0.42 mm/s, which corresponds to initial strain rates of 2.1×10^{-4} to 0.056 s^{-1} in the gage region, respectively. The room temperature tests were performed in air, and the elevated temperature tests were performed in vacuum (10^{-6} to 10^{-5} torr). One specimen was tested in an Instron servohydraulic machine for each experimental condition. The tensile properties were determined from graphical analysis of the chart recorder curves. A plastic deformation offset of 0.2% was used for measuring the yield strength.

Results and Discussion

The room temperature electrical conductivities of the Cu-8Cr-4Nb and diffusion bonded CuCrZr specimens are listed in Table 1. The CuCrZr specimens exhibited high conductivity values. The CuCrNb specimens had conductivities comparable to that measured in the higher conductivity heats of Hycon 3HP CuNiBe [1].

Table 1. Room temperature electrical properties measured in the present study.

Alloy and heat treatment	Meas. resistivity at 20°C	Electrical conductivity
Cu-8Cr-4Nb, extruded & annealed		
longitudinal	23.50 nΩ-m	73.4±0.8% IACS
transverse	23.61 nΩ-m	73.0±1.0% IACS
Kabelmetal CuCrZr, diffusion bonded		
with 0.13 mm Cu shim	19.12 nΩ-m	90.1±0.7% IACS
without Cu shim	19.50 nΩ-m	88.4±0.3% IACS

The tensile properties of the Cu-8Cr-4Nb specimens tested at different strain rates are listed in Table 2. The ultimate strength decreases by about a factor of two between room temperature and 500°C , with no significant difference between longitudinal and transverse orientations. The uniform and total elongations were high at all test temperatures up to 500°C. The strength and elongation generally increased with increasing strain rate, in agreement with previous studies on copper alloys [2,4]. The measured tensile strengths are rather impressive, considering that the material was annealed at 925°C for 1 h prior to testing. Such a high temperature annealing would produce dramatic softening in CuCrZr or CuNiBe precipitation hardened alloys. The yield and ultimate strengths of the annealed CuCrNb at test temperatures of 20-500°C are about 10 to 20% lower than that of CuCrZr in the ITER solutionized and aged condition. The yield and ultimate strength of the annealed CuCrNb is about 10% larger than for CuCrZr that was given a simulated diffusion bond heat treatment at ~950°C with a moderate gas quench (~2°C/s) followed by thermal aging at 475 for 2 h [3].

Table 2. Summary of extruded and high temperature annealed Cu-8Cr-4Nb tensile test results.

Orientation, ID number	Temperature (°C)	strain rate (s^{-1})	Yield Strength (MPa)	Ultimate Strength (MPa)	Uniform Elongation (%)	Total Elongation (%)
longitudinal						
CN02	20	1.1×10^{-3}	219	397	16.4	22.6
CN03	200	1.1×10^{-3}	201	308	12.8	22.0
CN01	300	2.1×10^{-4}	170	238	10.7	18.6
CN04	300	1.1×10^{-3}	155	253	12.9	23.0
CN06	300	0.056	247	280	10.7	22.3
CN05	500	1.1×10^{-3}	147	203	9.5	17.6
transverse						
CN07	20	2.1×10^{-4}	213	370	16.1	21.7
CN08	20	1.1×10^{-3}	274	387	16.1	21.9
CN09	200	1.1×10^{-3}	189	306	14.9	25.0
CN10	300	1.1×10^{-3}	159	248	12.4	21.4
CN12	300	0.056	199	279	14.3	21.0
CN11	500	1.1×10^{-3}	146	196	10.4	17.5

The fracture toughness measurements on CuCrNb [8] indicated values of about 55 MPa-$m^{1/2}$ for the T-L orientation and ~65 MPa-$m^{1/2}$ for the L-T orientation over the temperature range of 20-250°C. These values are much lower than the fracture toughness measured for CuCrZr in both the ITER heat treatment condition (210 MPa-$m^{1/2}$ at 20°C and ~145 MPa-$m^{1/2}$ at 250 C for both orientations) and for a simulated gas quench (~2°C/s) and aged condition that is representative of a divertor module diffusion bond thermal cycle (219 MPa-$m^{1/2}$ at 20°C and 152 MPa-$m^{1/2}$ at 250°C) [8]. Therefore, the extruded and annealed CuCrNb base metal does not appear to offer any clear advantages over the CuCrZr alloy for ITER applications since the tensile properties and the electrical conductivity are comparable whereas the fracture toughness is much lower than CuCrZr. The effects of irradiation on the mechanical properties of CuCrNb are not known.

Table 3 summarizes the tensile property measurements performed on the diffusion bonded CuCrZr specimens. The tensile strength was considerably lower than that of CuCrZr base metal in the optimized solution quenched and aged condition [2,3]. This may be due to precipitate overaging associated with the long aging time and high aging temperature compared to the strength- and conductivity-optimized condition of 460-480°C for 2 h. Of greater significance is the low tensile ductility observed at all test conditions. From the near equivalence of the uniform and total elongations, it can be concluded that the reduction in area is very low (reduction in area measurements have not yet been performed on these specimens). The specimens which contained a 0.13 mm pure copper shim in the diffusion bondline exhibited higher ductility compared to specimens which did not contain a copper shim.

Table 3. Summary of diffusion bonded Cu-Cr-Zr tensile test results.

Orientation, ID number	Temperature (°C)	strain rate (s^{-1})	Yield Strength (MPa)	Ultimate Strength (MPa)	Uniform Elongation (%)	Total Elongation (%)
with Cu shim						
67-1	20	1.1×10^{-3}	213	298	5.5	5.7
67-3	20	1.1×10^{-3}	225	311	6.9	7.0
67-2	200	1.1×10^{-3}	196	257	4.2	4.5
67-4	200	1.1×10^{-3}	198	255	4.2	4.4
w/o Cu shim						
77-3	20	1.1×10^{-3}	209	209	~0.1	~0.1
77-1	200	1.1×10^{-3}	229	235	0.3	0.3
77-2	200	1.1×10^{-3}	210	210	0.2	0.2
77-4	200	1.1×10^{-3}	199	199	~0.1	~0.1

ACKNOWLEDGEMENTS

The CuCrNb and diffusion bonded CuCrZr materials were supplied by Kevin Slattery, Boeing (St. Louis).

REFERENCES

[1] S.J. Zinkle, W.S. Eatherly, in: Fusion Materials Semiannual Progress Report for Period ending June 30, 1996, DOE/ER-0313/20 (Oak Ridge National Lab, 1996) p. 207.
[2] S.J. Zinkle, W.S. Eatherly, in: Fusion Materials Semiannual Progress Report for Period ending Dec. 31, 1996, DOE/ER-0313/21 (Oak Ridge National Lab, 1996) p. 165.
[3] S.J. Zinkle, W.S. Eatherly, in: Fusion Materials Semiannual Progress Report for Period ending June 30, 1997, DOE/ER-0313/22 (Oak Ridge National Lab, 1997) p. 143.
[4] D.J. Edwards, in: Fusion Materials Semiannual Progress Report for Period ending Dec. 31, 1997, DOE/ER-0313/23 (Oak Ridge National Lab, 1997) p. 213.
[5] K.R. Anderson, J.R. Groza, R.L. Dreshfield, D. Ellis, Mater. Sci. Eng. A 169 (1993) 167.
[6] K.R. Anderson, J.R. Groza, R.L. Dreshfield, D. Ellis, Metall. Mater. Trans. A 26 (1995) 2197.
[7] M.M. Dadras, D.G. Morris, Scripta Mater. 38 (1998) 199.
[8] D.J. Alexander, S.J. Zinkle, A.F. Rowcliffe, presented at the 19th ASTM Symposium on Effects of Radiation on Materials, Seattle, WA, June, 1998.

Round Robin Comparison of Tensile Results on GlidCop Al25 — D. J. Edwards (Pacific Northwest National Laboratory), S. J. Zinkle (Oak Ridge National Laboratory), S. A. Fabritsiev (DV Efremov Institute), and A. S. Pokrovsky (Research Institute of Atomic Reactors)

SUMMARY

A round robin comparison of the tensile properties of GlidCop™ Al25 oxide dispersion strengthened copper was initiated between collaborating laboratories to evaluate the test and analysis procedures used in the irradiation experiments in SRIAR in Dimitrovgrad. The tests were conducted using the same tensile specimen geometry as used in previous irradiation experiments, with tests at each laboratory being conducted in air or vacuum at 25, 150, and 300°C at a strain rate of 3×10^{-4} s^{-1}. The strength of the GlidCop™ Al25 decreased as a the test temperature increased, with no observable effect of testing in air versus vacuum on the yield and ultimate strengths. The uniform elongation decreased by almost a factor of 3 when the test temperature was raised from room temperature to 300°C, but the total elongation remained roughly constant over the range of test temperatures. Any effect of testing in air on the ductility may have been masked by the scatter introduced into the results because each laboratory tested the specimens in a different grip setup. In light of this, the results of the round robin tests demonstrated that the test and analysis procedures produced essentially the same values for tensile yield and ultimate, but significant variability was present in both the uniform and total elongation measurements due to the gripping technique.

Introduction

A series of irradiation experiments on copper alloys has been conducted in the SM 2-3 reactor in Dimitrovgrad, Russia [1-5]. These experiments have provided considerable data on the tensile properties of the various candidate alloys being considered for use in the ITER device. However, difficulties arose in the testing and analysis that raised questions concerning the accuracy of the data obtained from the tensile tests. Variables such as microstructural variations within the alloy plate, dimensional variations introduced during specimen fabrication, and temperature control during irradiation and testing have all been considered as possible explanations for the apparent differences. Although some of these concerns have been explained by subsequent testing, a series of round robin tests using specimens from one source were initiated to ensure that all of the laboratories involved in the irradiation experiments test the specimens and analyze the data in a consistent manner. It is hoped that these tests will allay any doubts about using the data generated in the SM2-3 irradiation experiments.

Experimental Procedure

The material used in this comparison was GlidCop™ Al25 (ITER Grade 0) supplied to the Efremov Institute by OMG Americas. Type STS tensile specimens were machined from the 20 mm plate and sent to each of the following four laboratories: Pacific Northwest National Laboratory, Oak Ridge National Laboratory, DV Efremov Institute, St. Petersburg, Russia, and the Scientific Research Institute of Atomic Reactors (SRIAR) in Dimitrovgrad, Russia, where the irradiation experiments were conducted. A schematic of the STS tensile geometry is provided in Figure 1. This geometry was also used in the SM2.1 and SM2.3 irradiation experiments on copper alloys.

The tensile tests were conducted in vacuum at ORNL and SRIAR and in open air at PNNL and Efremov. The room temperature tensile tests at ORNL were conducted in either vacuum or open air for purposes of comparison, but all tests at 150 and 300°C were conducted under a vacuum of less than ~10^{-6} torr. A strain rate of ~3×10^{-4} s^{-1} was used for the tests at PNNL, ORNL, and the Efremov Institute, but for the screw driven machines located in the hot cells at SRIAR a slightly higher strain rate of 4.2×10^{-4} s^{-1} was used. This slight difference in strain rate is known from previous work [6,7] to not have any discernible effect on the tensile properties of the Al25. In the testing performed at PNNL the specimens were held using specially designed grips that used small pins to align the specimens. The 3.2 mm diameter pinholes were machined into the

specimens after being shipped to PNNL. A face plate screwed onto the front surface of the specimens provided the clamping force necessary to hold the specimens with some support from the pins. Because of alignment difficulties it was determined that the screws needed to be tightened while the entire assembly was under a preload of ~50 lbs. (well below the yield), otherwise a slight misorientation of the specimen or grips would alter the slope of the tensile curve as the specimen and grips realigned themselves at higher loads. Temperature control during the testing was accomplished using a thermocouple attached directly to the exposed grip or gage. Since the tests were conducted in open air, the hold time to equalize the temperature throughout the specimen was only 5 minutes, which also served to minimize the oxidation that occurred at the higher test temperatures.

The tests at ORNL were performed using a modified type SS3 tensile specimen grip system that relied on pins to support the entire specimen load during testing. The 2.4 mm diameter pinholes were machined in the specimens after they were shipped to ORNL. Thermocouples were placed in contact with the gage surface during the testing, and a hold time of approximately 15 to 30 minutes was used to equilibrate the temperature. Some of the initial ORNL tests were conducted at slightly lower temperatures than desired due to a unforeseen problem when the temperature was measured by a single thermocouple placed on the specimen gage region. The grips were colder than the center of the gage section and completely shielded the shoulder and end tab regions of the specimen from the clam-shell furnace. This caused the specimen temperature to be considerably lower than the surrounding furnace temperature even for hold times of more than 30 minutes. Measurements with a second thermocouple placed on the gage section indicated that the actual specimen temperature was about ~30°C lower than measured by the original thermocouple (the original thermocouple was sensing an average of the "colder" specimen and surrounding "hotter" furnace environment temperature). After the discrepancy was found, all subsequent tests were conducted using the temperature reading from the second thermocouple located on the gage section. The tests at the lower temperatures are also included in this report.

The testing conducted in the two Russian laboratories used a "shoulder-loaded" gripping system were 4 pins make contact with the shoulders of the tab end of the specimens, thereby providing the support during testing. The temperature was controlled by thermocouples placed on the gage section of the specimens. The tests were performed in vacuum at SRIAR and in open air at Efremov.

All four laboratories used either a graphical analysis of chart recorder data or data acquired on a computerized data acquisition system to determine the tensile properties. The crosshead displacement was used to measure the actual elongations, not extensometers. The 0.2% yield strength, ultimate strength, uniform and total elongation are all summarized in this report.

Results and Discussion

The yield strengths as measured at all four laboratories as a function of temperature are presented in Figure 2. The yield strength of the GlidCop™ Al25 clearly decreases as the test temperature is increased from 25 to 300°C. The ultimate tensile strength presented in Figure 3 shows basically the same trend, with a scatter band similar to that of the yield strength. The UTS data from U.S. laboratories was systematically higher than the corresponding UTS data from the Efremov Institute and SRIAR, but still within an acceptable error of ±20 MPa. In general each set of strength data is indistinguishable from each other within the scatter of the data, indicating that the yield and ultimate strengths are being consistently and accurately measured in an identical manner across the different laboratories. The influence of test environment (air vs. vacuum) is not evident in the strength data, which is in reasonable agreement with earlier results on the strain rate and temperature dependence of the GlidCop™ alloys [6,7]. The grip system also does not appear to cause any noticeable discrepancies in the measured strength of the specimens. The measurement of the elongation proved to be a different matter however, as can be seen in Figures 4 and 5. Both the uniform and total elongation measured at PNNL and ORNL are consistently higher than that measured by the Efremov Institute, and the uniform elongation is

typically higher than that measured at SRIAR. Despite this all of the data sets exhibit the same basic trend for the uniform and total elongation. The uniform elongation monotonically decreased with increased with increasing test temperature to a level of ~4% at 300°C. The total elongation was observed to be essentially independent of test temperature, although considerable scatter was present between the data sets from the four laboratories.

Some variability in the uniform elongation may be expected since the relatively low strain hardening capacity of the extruded GlidCop™ plate produces a rather wide plateau in the tensile curve neat the ultimate stress. Therefore, it is somewhat subjective to determine the precise location of where the specimen begins to neck. The differences in the total elongation are harder to explain, even taking into account the large degree of scatter. A pin-loaded grip system might produce higher elongations than either the clamped or shoulder-loaded grip systems since shear stresses associated with misalignment are minimized. However, at present the authors have no explanation for why the Efremov data is consistently lower than that measured at the other three laboratories. The large scatter in the total elongation indicates that the final failure of the specimens is subject to some variability, and may in fact be due to some local inhomogeneity in the microstructure that influences the failure of the specimens. It is interesting to note that the scatter band for the uniform elongation is only ±2%, whereas the data for the total elongation can vary by as much as a factor of two when comparing the data from different laboratories at the same test temperature.

Conclusions

Overall the round robin results show that the tensile strength is reliable and consistently measured by each laboratory. Unforeseen problems with the temperature control and other external variables can of course affect the final results, but if one assumes that those problems do not exist, then the strength data is consistent between the four laboratories. The differences in uniform elongation are minor and don't necessarily change the conclusions that would be drawn from the data, but the large scatter in the total elongation is certainly an issue that needs to be investigated further.

Acknowledgments

D. J. Edwards would like to thank D. Criswell for performing all of the tensile tests. D. J. Edwards participation in this experiment was funded by the U.S. Department of Energy under contract DE-AC06-76RLO 1830 with the Battelle Memorial Institute at the Pacific Northwest National Laboratory.

References

1. S.J. Zinkle and S.A. Fabritsiev (Nuclear Fusion supplement), 5 (1994) 163-192.
2. D.J. Edwards, S.A. Fabritsiev, A.S. Pokrovsky, S.J. Zinkle, R.F. Mattas, and R.D. Watson, Fusion Materials Semiannual Progress Report for the Period ending December 31, 1995, DOE/ER-0313/19, (Oak Ridge National Laboratory), p. 165.
3. S.A. Fabritsiev, A.S. Pokrovsky, S.J. Zinkle, and D.J. Edwards, J. Nucl. Mater. 233-237 (1996) 513-518.
4. S.A. Fabritsiev, A. S. Pokrovsky, S.J. Zinkle, A.F. Rowcliffe, D.J. Edwards, F.A. Garner, V.A.Sandakov, B.N Singh, and V.R. Barabash, J. Nucl. Mater. 233-237 (1996) 526-533.
5. S.A. Fabritsiev, A.S. Pokrovsky, D.J. Edwards, S.J. Zinkle , and A.F. Rowcliffe, The Effect of Neutron Irradiation on Mechanical Properties of Cu/SS Joints for ITER Applications, presented at ICFRM-8, Sendai, October 1997.
6. S.J. Zinkle and W.S. Eatherly, in Fusion Materials Semiannual Progress Report for Period ending December 31, 1996, DOE/ER-0313/21 (Oak Ridge National Laboratory) p. 165.
7. D.J Edwards, submitted for publication in the Proceedings of the 19th International Symposium on the Effects of Irradiation on Materials, held June 16-18, 1998, in Seattle, Washington, ASTM STP 1366.

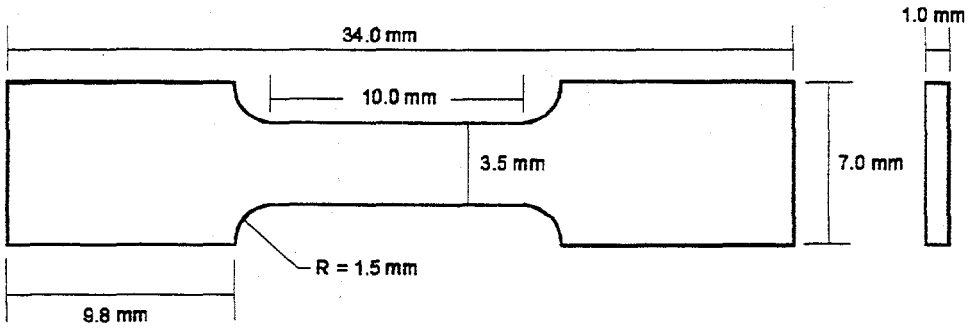

Figure 1 STS tensile geometry used in the round robin comparison. This same geometry was used in the first two series of irradiation experiments (SM2.1 and SM2.3).

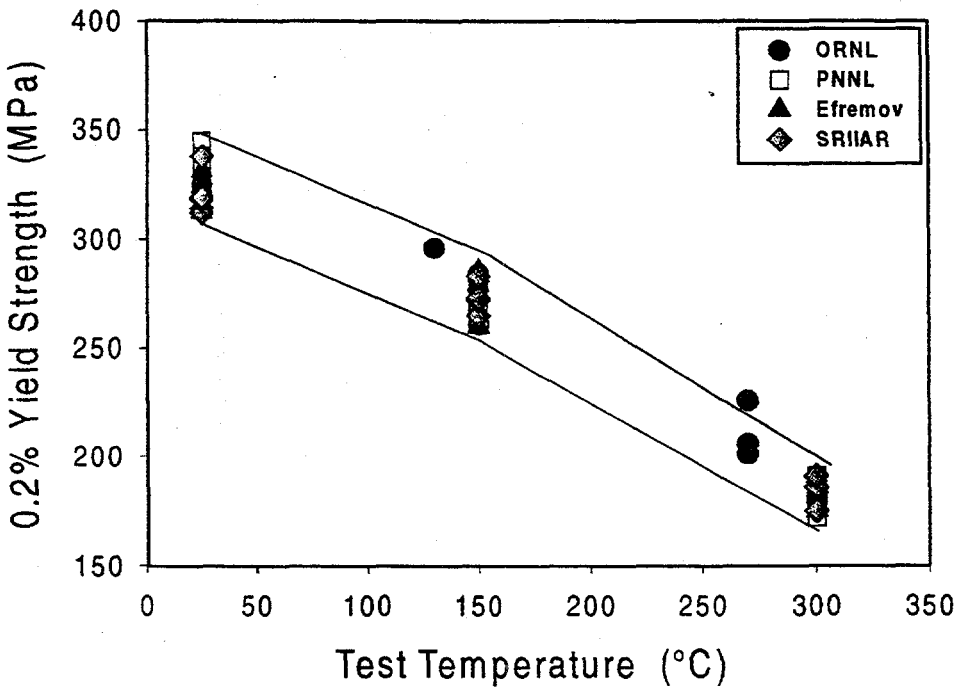

Figure 2 The 0.2% yield strength data from each of the four laboratories is plotted as a function of temperature. The data are all in agreement and demonstrate that the yield strength can be determined consistently.

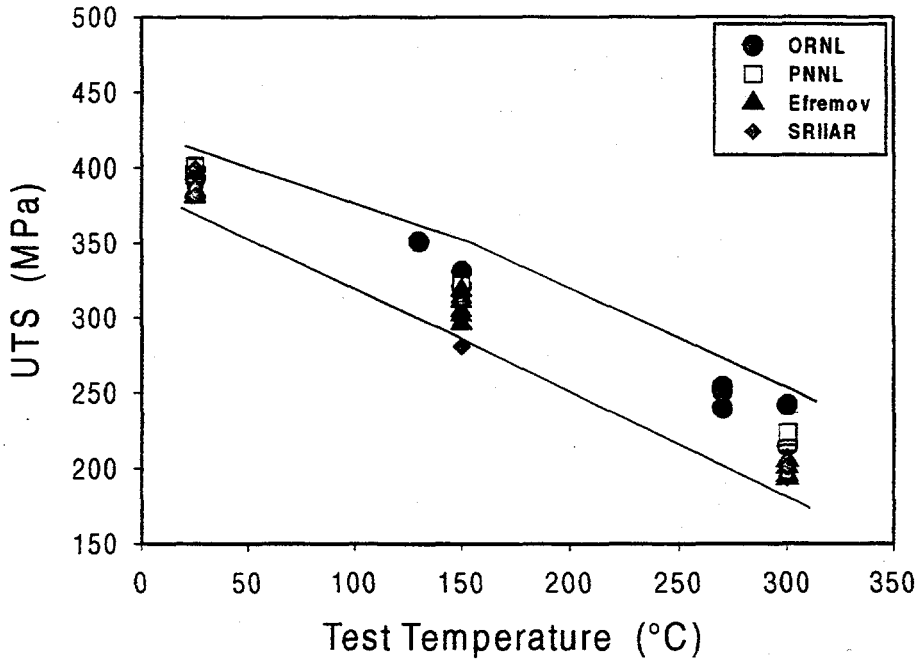

Figure 3 The ultimate strength exhibits more scatter between the four laboratories compared to the yield strength. The data from PNNL and ORNL appear to be systematically higher, but within the overall error of the measurements.

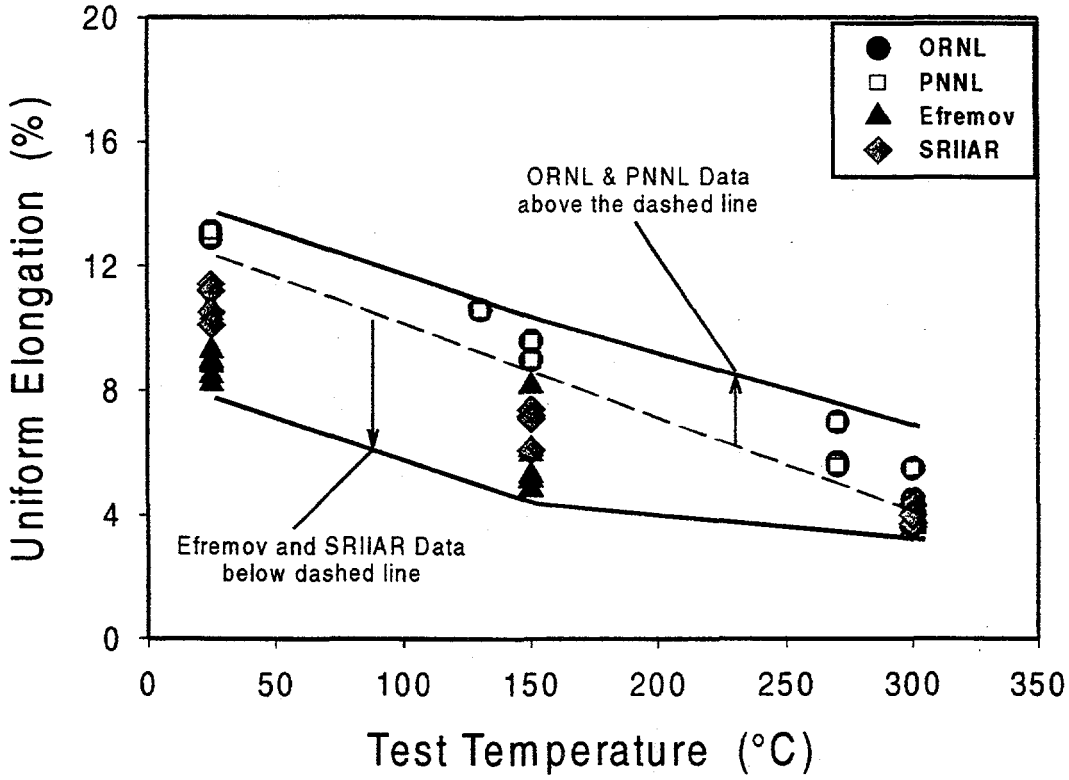

Figure 4 The uniform elongation results from Efremov and SRIAR are both lower on average than the corresponding PNNL and ORNL, but all the data show the same behavior. The manner in which the uniform elongation is chosen off the tensile curve could account for the differences, as well as possible differences introduced by the different gripping systems used. The scatter in the data are about 4-5% at room temperature and 150ºC, with the scatter lower at 300ºC.

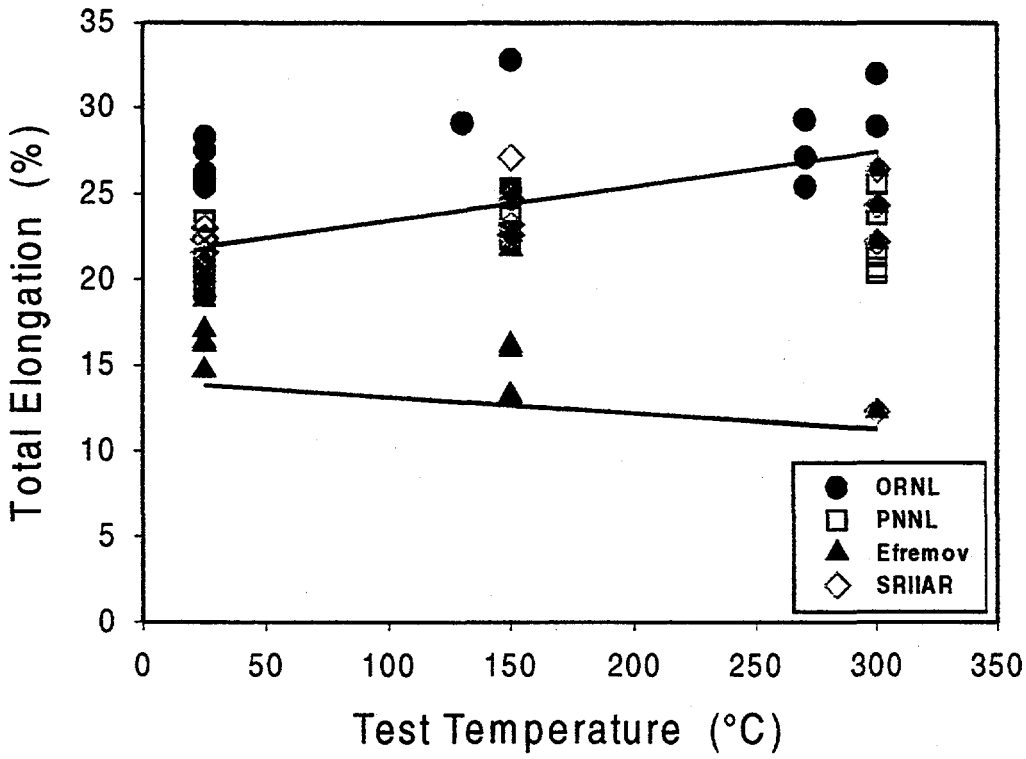

Figure 5 The total elongation data proved to exhibit the most scatter of any of the data sets between the four laboratories. The trend lines are drawn to reflect the Efremov data set only. It remains uncertain as to why the total elongation measured by the Efremov Institute exhibits greater scatter and lower values on average than that measured by the other three laboratories.

PROGRESS REPORT ON THE BEHAVIOR AND MODELING OF COPPER ALLOY TO STAINLESS STEEL JOINTS FOR ITER FIRST WALL APPLICATIONS — J. Min, J. Stubbins, J. Collins (University of Illinois), and A. F. Rowcliffe (Oak Ridge National Laboratory)

OBJECTIVE

The objective of this study is to understand the stress states that lead to failure of copper alloy to stainless steel joints for ITER first wall, limiter, and divertor applications. Of particular interest is the behavior of joints between GlidCop™ CuAl25 and 316L SS when loaded such that the joint is inclined at 45° with respect to the loading direction.

SUMMARY

The stress states that lead to failure of joints between GlidCop™ CuAl25 and 316L SS were examined using finite element modeling techniques to explain experimental observations of behavior of those joints. The joints were formed by hot isostatic pressing (HIP) and bend bar specimens were fabricated with the joint inclined 45° to the major axis of the specimen. The lower surface of the bend bar was notched in order to help induce a precrack for subsequent loading in bending. The precrack was intended to localize a high stress concentration in close proximity to the interface so that its behavior could be examined without complicating factors from the bulk materials and the specimen configuration. Preparatory work to grow acceptable precracks caused the specimen to fail prematurely while the precrack was still progressing into the specimen toward the interface. This prompted the finite element model calculations to help understand the reasons for this behavior from examination of the stress states throughout the specimen. An additional benefit sought from the finite element modeling effort was to understand if the stress states in this non-conventional specimen were representative of those that might be experienced during operation in ITER.

PROGRESS AND STATUS

1. Background

Specimens of GlidCop™ CuAl25 and 316L SS were taken from hot isostatically pressed (HIP) plates for testing in the unirradiated and the irradiated states. The HIP conditions were 982°C at 101 MPa for 2 hr. The material compositions and the results of mechanical testing and microstructural analysis of this and other HIP bonded plates in the unirradiated conditions were reported previously [1]. For the purposes of developing a miniature specimen configuration for irradiation testing that would provide a reasonably severe loading condition for the joint, bend bar specimens with the joint inclined 45° to the major axis were fabricated. The specimen configuration and dimensions are shown in Fig. 1.

The specimen design was selected for its ability to provide a complex state of stress at the interface. The local stress-state was to be intensified by the presence of a crack tip very close to the interface. This necessitated the growth of a precrack from the starter notch to a length nearly half way through the specimen. This was to be accomplished by fatigue loading at moderate load levels. Specimens with such precracks were to be tested to failure by loading in three point bending in both the unirradiated and the irradiated state. The bending loads were to be applied so that the lower side was supported at each end, and the upper side was loaded just opposite the starter notch in the middle of the upper surface.

Specimens with a sufficiently long pre-crack were to be loaded monotonically to note their load-deflection response and to provide information about the failure mode (e.g. delamination, plastic bending or brittle failure through the base materials).

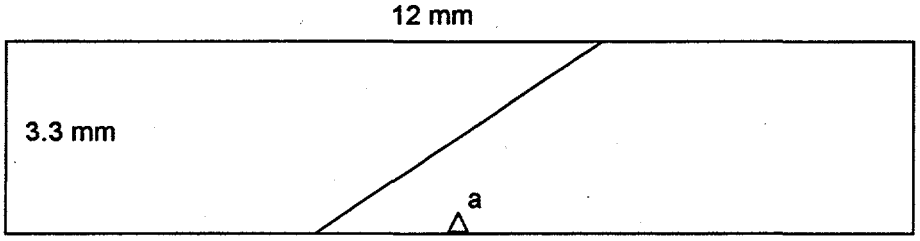

Figure 1. Bend bar configuration showing the 45° inclination of the HIP joint to the major axis of the specimen and the position of the starter notch at the center of the lower surface of the specimen.

When attempts were made to initiate and grow the precracks, it was found that specimens either bent prematurely when CuAl25 side was down (i.e. on the right side of the specimen as shown in figure 1) or specimens delaminated prematurely when the SS side was down. This frustrated the development of a useful miniature specimen configuration since it was not possible to grow precracks of appropriate length. It also brought the strength of the joint into question since it was not anticipated that the joint would fail in such a manner, particularly in the unirradiated, as-fabricated state. This led to a further analysis of the stress states induced by loading of this specimen configuration.

2. Modeling Approach

To better understand the nature of the stress states and the failure modes, finite element analysis was performed on the specimen configuration shown in figure 1. Most of the analysis was done with the commercial FEM software package ANSYS. The model employed 6-node triangular elements (plane strain), 549 total elements. Loads were applied in 3-point bending. For consistency, of results were compared for an applied load of 30 MN. Calculations were carried out for a number of precrack lengths, from 0.3 to 1.3 mm. The effect of material orientation was also considered such that calculations were performed for bend specimens with either the CuAl25 on the upper side and 316L SS on the lower side, or vice versa.

The materials properties for CuAl-25 and 316L SS were taken from those developed to model the initial plate materials where good agreement was found between experimental results and other FEM modeling efforts [1]. The tensile behavior was modeled using a bilinear hardening model where the elastic loading portion is represented by the Young's modulus. The initial plastic, strain hardening behavior was modeled with a yield strength and a plastic modulus. The values for the two respective materials are shown in table 1.

3. Results and Discussion

The results of the FEM analysis for several loading conditions and crack lengths were compared. For the purposes of discussion, the von Mises stresses for CuAl25 on 316L SS and for 316LSS on CuAl25 are shown in figures 2 and 4 for notch lengths of 0.3 and 1.3 mm, respectively. The shear stress distributions are shown in figures 3 and 5, for notch lengths of 0.3 and 1.3 mm, respectively, from the same calculations. All plots are for a load of 30MN. Several points of comparison are noteworthy in these plots.

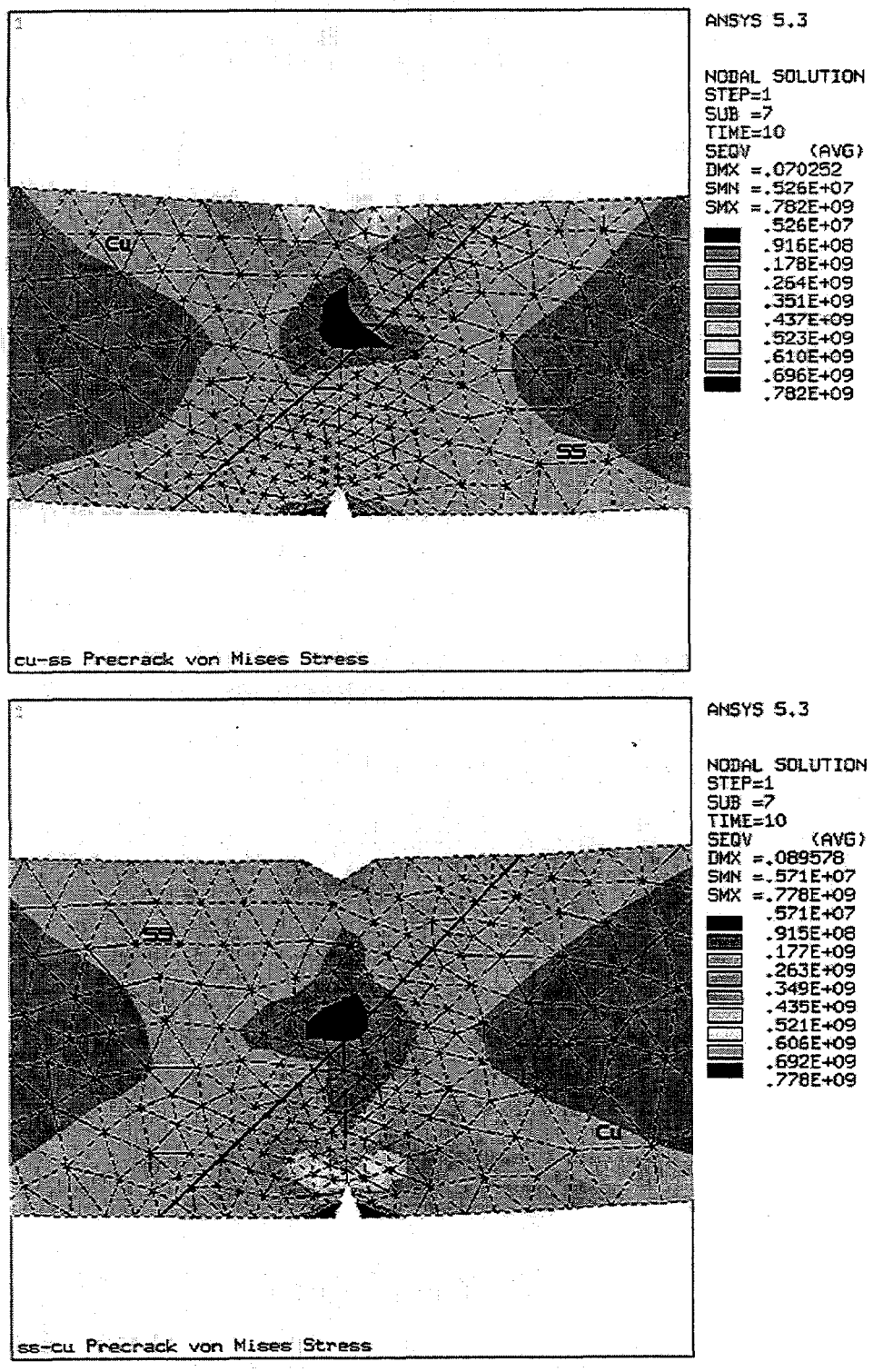

Figure 2 : von Mises Stresses with a 0.3mm notch

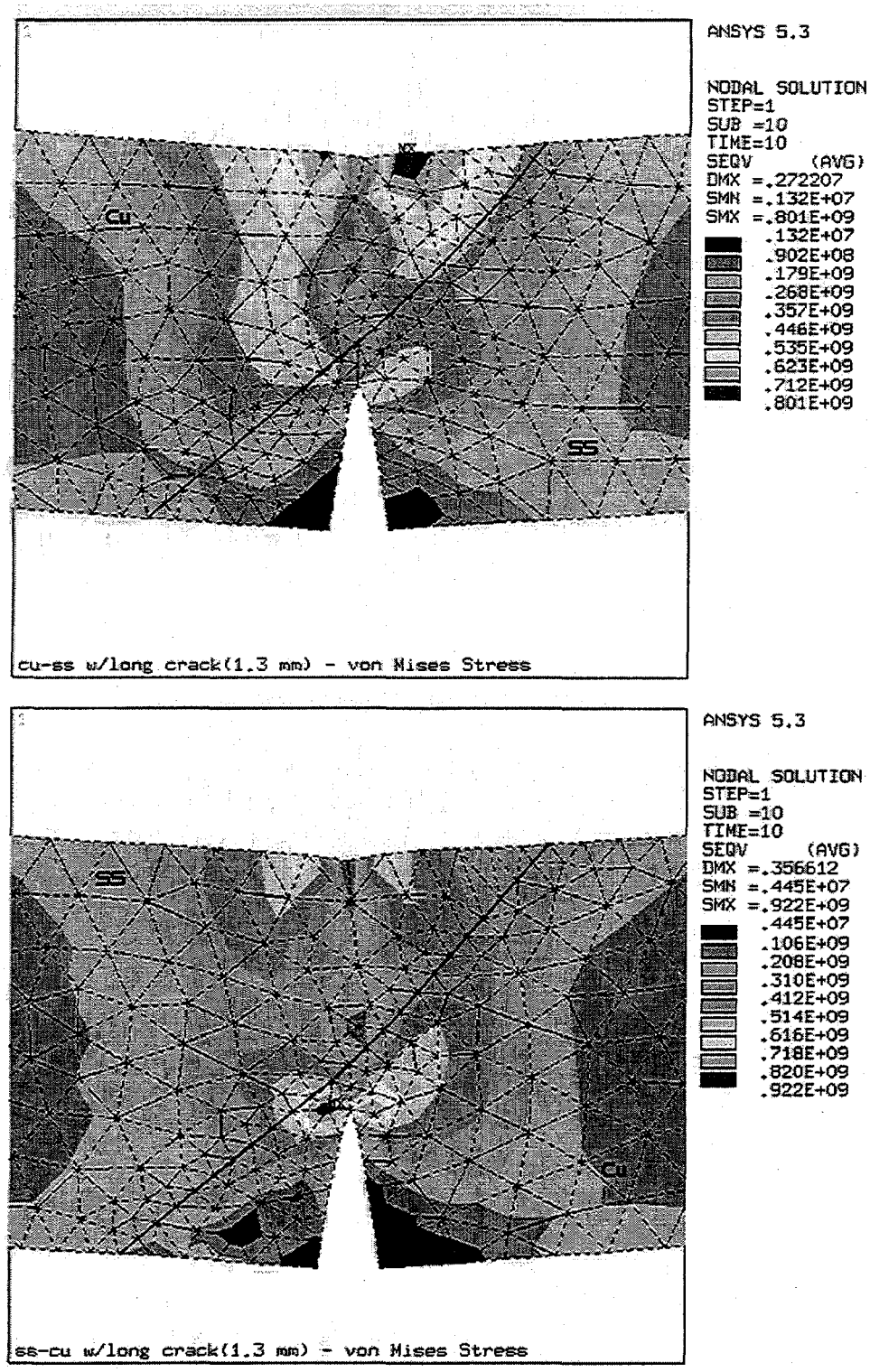

Figure 3 : von Mises Stresses with a 1.3mm notch

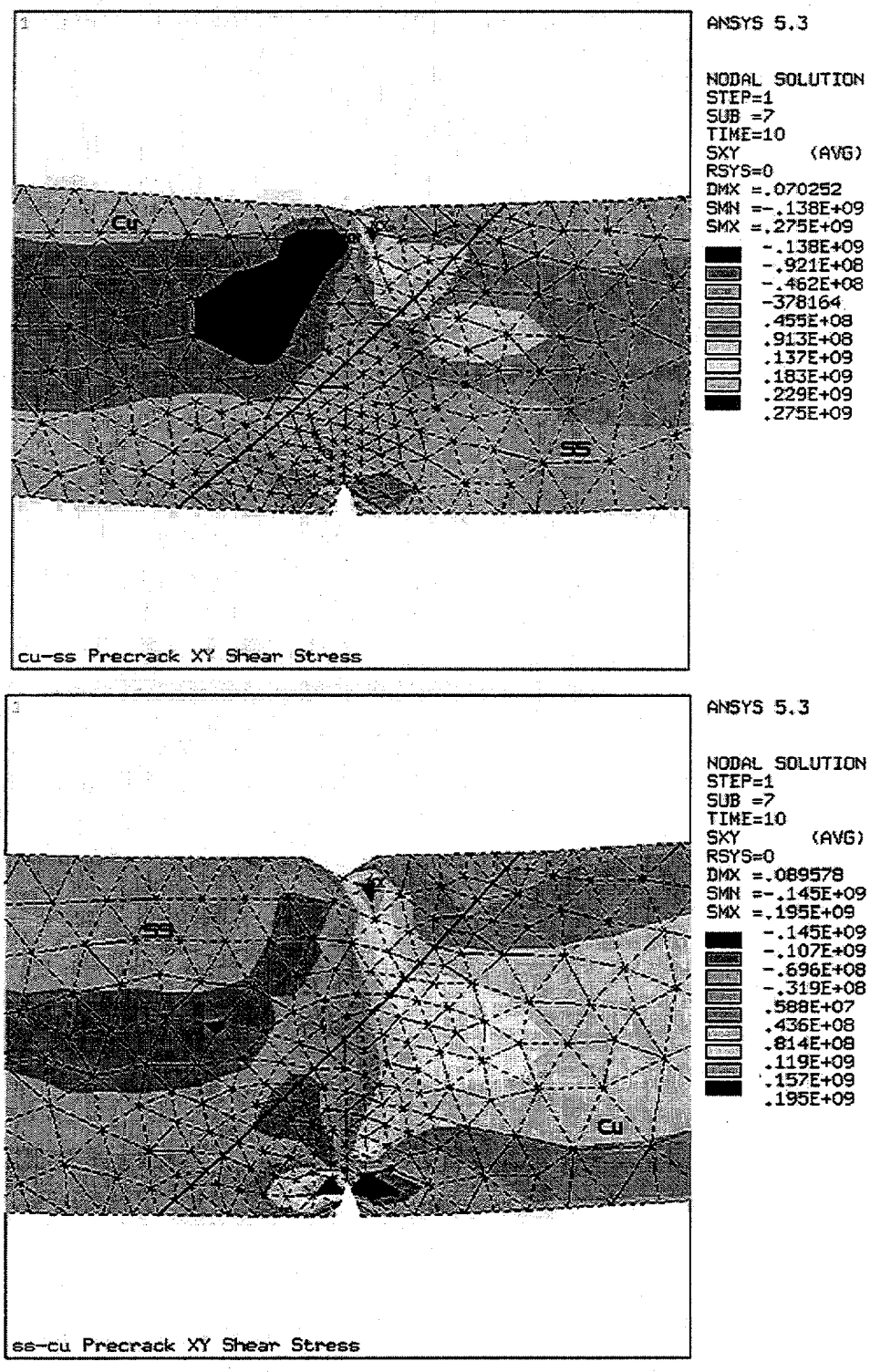

Figure 4 : Shear Stresses with a 0.3mm notch

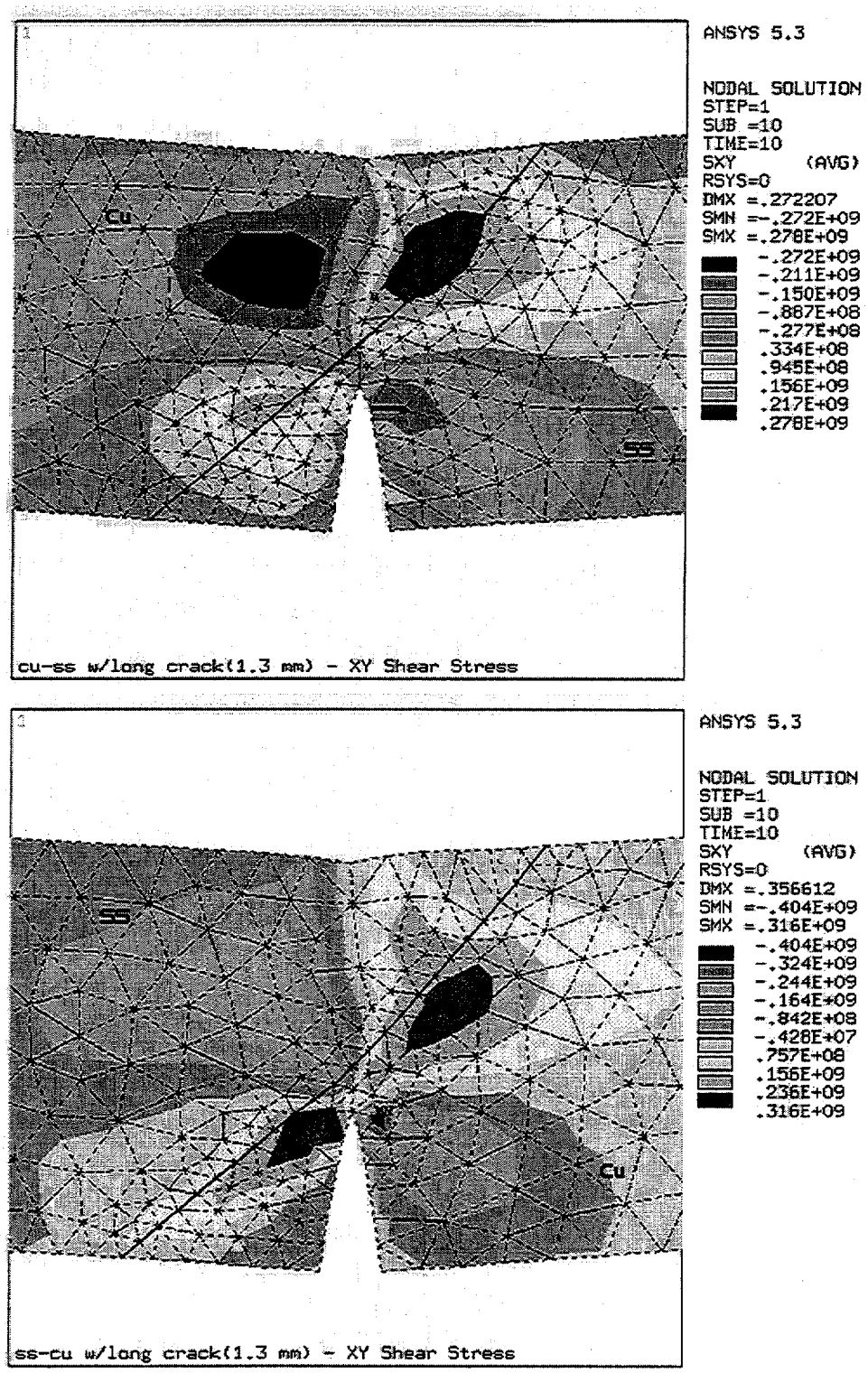

Figure 5 : Shear Stresses with a 1.3mm notch

Table 1. Materials Properties for CuAl25 and 316L SS Used in the FEM Analysis

Material	Elastic Modulus (GPa)	Yield Strength (MPa)	Plastic Modulus (GPa)	Density (kg/m^3)	Poisson's Ratio
316L SS	200	207	8.0	7860	0.283
CuAl-25	130	400	11.0	8940	0.343

The first major point of comparison is the relative distribution of stresses around the notch tip with the notch either in the CuAl25 compared to the notch in 316L SS. The broader stress distribution in the CuAl25 indicates that the strain hardening behavior of the 316L SS is more severe than in CuAl25 despite the high yield strength of the latter material used for modeling. This results in a more localized crack tip stress field for the 316L SS compared to the CuAl25 and is consistent with the experimental observation that under fatigue loading a starter crack could be initiated in the 316L SS when it was on the lower, notched side. Under similar loading conditions, the bend specimens merely deformed without the initiation of a starter crack when the CuAl25 side was down.

A broad comparison of the stress states shown in figures 2 through 5 indicates that the initial concept that the major stress concentrations would occur in the vicinity of the interface at the center of the specimens is not borne out by the FEM calculations. In fact, the major stress concentrations are off-center, but do develop along the interface as well as at the notch tip and the load points. The shear stress values are high along the interface for both specimen orientations, and are likely the major cause of the delamination as observed during precracking with the 316L SS on the bottom. The precise nature of the initiating conditions for failure by delamination is not known. Lap shear measurements on these joints indicated that they should posses a shear strength in excess of 100 MPa [1]; the calculated values here are in excess of that level. Nevertheless, some local or microscopic process for initiating a crack along the interface is required. A mechanism for the development of a starter crack has not yet been identified. It is also useful to note that the calculated stress concentrations at the points of intersection of the interface with the upper and lower surfaces are not especially large. From the calculations, it would appear unlikely that a crack would first initiate at the intersection with the surface. A second point to note is that the highest resolved stresses along the interface are in shear. Studies of interfaces in brittle materials indicate that tensile stresses may dominate the failure process [2]. The stress states leading to delamination in ductile materials is still not well clarified.

The deformation behavior of the CuAl25, as modeled here, is also important in assessing the potential modes of failure. Because of its lower plastic modulus, it tends to deform over larger specimen volumes than does the 316L SS. This tends to cause the shorter wedge of CuAl25 in the central section of the specimen to deform readily in comparison to the 316L SS. This leads to the formation of a plastic hinge through the CuAl25 resulting in an overall deformation of the specimen. While the conditions for delamination are likely useful as a guide for limiting stresses for ITER design considerations, the likelihood of plastic hinges forming through thin sections of CuAl25 is small I practice. Thus the usefulness the information regarding the bending of the specimen during precracking with the CuAl25 on the lower, notched side is of questionable value for design purposes.

The current study was limited to modeling behavior of specimens at room temperature, taken to be the stress free state. In actuality, residual stresses due to fabrication or due to exposure at other temperatures should be considered. Mismatches in thermal expansion

coefficients between the two materials would result in interfacial stresses that are not considered here. The magnitudes of residual stresses are likely much smaller than those imposed by the notch and loading conditions considered in these FEM calculations. In fact, the intended use of a sharp crack tip to concentrate the stresses at the interface in the current specimen design was to elevate local stresses at the interface. Available elastic analysis of a crack tip near an interface between dissimilar materials indicates that the dissimilar metals can either accelerate or retard crack propagation based on the relative values of the Young's moduli [3]. In the current cases, it was not possible to bring the crack tip near enough to the interface to examine this possibility.

Further examination of the stress states and failure process in this specimen configuration should also account for the unique material properties of the interfacial zone. It was found in this and other experimental work [1] that the interfacial fracture takes place next to the interface in the diffusion zone of the CuAl25. Because the inter-diffusion zone has a microstructure that differs from either base material, it is appropriate to consider it as a separate material. Further modeling should take into account the nature of the precipitate structure, and possible porosity, in the zone as likely sites for ductile tearing or other crack initiation processes.

4. Conclusions

Finite element analysis was performed on a miniature bend bar specimen comprised of a bilayer of CuAl25 and 316L SS. The specimen was designed such that the interface was inclined at 45° through the specimen. The lower section contained a notch or precrack that was intended to concentrate a load on the portion of the interface at the center of the specimen in order to test its mechanical properties. The FEM analysis indicated that the copper alloy tended to deform more readily than the stainless steel. This results in the spreading of the strain over a larger portion of the specimen when the copper alloy is on the bottom. This leads to the formation of a plastic hinge and the specimen fails by excess ductile deformation, an unlikely event in component applications. When the stainless steel is place on the bottom during loading, the stresses are concentrated more locally and this permits the development of a crack. In both cases, however, the maximum stress concentrations on the interface are not at the center of the specimen, rather they are shifted off-center. In addition, the major stress concentrations appear to be dominated by the shear components and this likely supports the initiation of delamination, as noted in precracking specimens with 316L SS on the bottom. The precise mechanism for delamination of the interface cannot be resolved from the current analysis, but is important for design considerations.

REFERENCES

1. J. F. Stubbins, et al., Cu/SS Joining Techniques; Development and Testing: Final Report for U.S. ITER Task T212 (CY1996), ITER/US/97/IV-BL-1 (February 1997)

2. J. W. Hutchinson and Z. Suo, "Mixed Mode Cracking in Layered Materials," Advances in Applied Mechanics, 39 (1992) 63-191.

3. Y. Sugimura, P. G. Lim, C. F. Shih, and S. Suresh, "Fracture Normal to a Bimaterial Interface of Plasticity on Crack Tip Shielding and Amplification," Acta metall. mater., 41, 3 (1995) 1157-1169.

5.0 AUSTENITIC STAINLESS STEELS

No contributions.

6.0 INSULATING CERAMICS AND OPTICAL MATERIALS

No contributions.

7.0 SOLID BREEDING MATERIALS

LOW-TEMPERATURE LOW-DOSE NEUTRON IRRADIATION EFFECTS ON BRUSH WELLMAN S65-C AND KAWECKI BERYLCO P0 BERYLLIUM —

L. L. Snead (Oak Ridge National Laboratory)

OBJECTIVE

This paper presents a summary of the results studying the effects of neutron irradiation to ITER-grade Brush Wellman S65-C beryllium and Kawecki Berylco P0 beryllium.

SUMMARY

The mechanical property results for two high quality beryllium materials subjected to low temperature, low dose neutron irradiation in water moderated reactors are presented. Materials chosen were the S65-C ITER candidate material produced by Brush Wellman, and Kawecki Berylco Industries P0 beryllium. Both materials were processed by vacuum hot pressing. Mini sheet tensile and thermal diffusivity specimens were irradiated in the temperature range of ~100-275°C from a fast (E>0.1 MeV) neutron dose of 0.05 to 1.0 x 10^{25} n/m^2 in the High Flux Isotope Reactor (HFIR) at the Oak Ridge National Laboratory and the High Flux Beam Reactor (HFBR) at the Brookhaven National Laboratory. As expected from earlier work on beryllium, both materials underwent significant embrittlement with corresponding reduction in ductility and increased strength. Both thermal diffusivity and volumetric expansion were measured and found to be negligible in this temperature and fluence range. Of significance from this work is that while both materials rapidly embrittle at these ITER relevant irradiation conditions, some ductility (>1-2%) remains, which contrasts with a body of earlier work including recent work on the Brush-Wellman S65-C material irradiated to slightly higher neutron fluence.

PROGRESS AND STATUS

Introduction

Beryllium has been considered for nuclear fuel cladding, nuclear fuel compacts and as a neutron moderator for fission power plants dating back to the early 1950's. Other than the non-structural application as a core moderator/reflector, this material has found little use in nuclear applications due to its low ductility.

The limited ductility of the various types of beryllium is a function of many factors including temperature, chemical purity, grain size and to some extent the rate at which the material is strained. Moreover, the hexagonally close packed beryllium crystal itself is resistant to slip severely limiting ductility potential of the material. The beryllium hcp crystal has only two operating slip modes (at least at low temperatures) being basal slip (0001) and prismatic slip ($10\underline{1}0$). For a high quality, high purity material, the ductility can be categorized into three temperature dependent regimes. In the low temperature regime (T<200°C) the shear stress required to activate prismatic slip is quite high and failure typically occurs by cleavage of the basal plane. Total elongation in this temperature range for a high quality, vacuum hot pressed material (specifically Brush Wellman S65-C at 150°C) is ~5% in the direction parallel to the pressing direction and ~20% in the transverse direction. As the temperature is increased above this lower temperature regime the critical stress for prismatic slip decreases and both slip modes combine to yield peak total elongations of about 50% both parallel and transverse to the forming direction. In this intermediate temperature regime (~200-500) the failure is primarily ductile/fibrous tearing. As the temperature is further increased intergranular failure begins to occur returning the total elongation to below 20%.

Irradiation of beryllium with high energy neutrons has the effect of producing small loops or "black spots" at low temperatures (<400°C)[1-5] with helium, formed by beryllium interaction with fast neutrons, forming bubbles from 325-400°C[6,7] and higher. The helium tends to form at grain boundaries from 325-600°C[7-15] and is also reported to be on dislocations within grains in the temperature range of 450-550°C.[7,8] Because the upper temperature of this study is ~50°C less than the lowest temperature at which helium bubbles have been observed, the helium is thought to be in solid solution, though it is conceivable that bubbles too small to be easily resolved using transmission electron microscopy are present.

Both point defect clusters and helium bubbles adversely effect the mechanical properties of beryllium, regardless of its metallurgical form. Point defect clusters and bubbles tend to block dislocation motion resulting in a severe reduction in elongation and increased strength [1-3,10-13,16-21] and hardness [8,9,14,17,20,22]. The irradiation effects database has been reviewed in the past [7,17] mainly including work conducted prior to 1970.

Materials, Irradiation and Experimental Techniques

Materials

Table 1 lists the mechanical properties and impurity levels in the two materials chosen for this study. The first materials listed is an ITER first wall candidate beryllium, Brush Wellman S65-C. This material is vacuum hot pressed from impact ground Be powder (11-45 μm) at ~1050-1150°C followed by a 870°C heat treatment to remove aluminum from solution by forming $AlFeBe_2$ precipitates. The S65-C beryllium was provided by Brush Wellman (BW) and designated as process Lot 4880 and is a commercially available, high quality structural beryllium. The grain size of the final product was ~9 μm. The second material chosen for this study was manufactured by the now defunct Kawecki Berylco Industries (KBI) and is designated as P0 (P-zero) taken from a billet No. 040. This material was manufactured (circa 1975) by vacuum hot pressing impact ground powder (~9 μm) at a temperature of 1065°C. The grain size of the final product was ~2.9 μm. This was a research grade material processed for reduced impurity content by doubly electrolytically refining the beryllium powder.

From Table 1 significant difference are seen in both mechanical properties and chemical composition for the two materials chosen. The strength (at least in the longitudinal direction) is greater for the KBI-P0 material as compared with the BW S65-C, while the fracture elongation is somewhat higher for the BW-S65-C. It is interesting to note that, while the KBI-P0 billets of material had very good ductility at the time of their manufacture, the elevated amount of BeO as compared with the BW S65-C (3.36 -vs.- 0.64 w/%), and possible other metallurgical improvements, yields lower elongation than the present day commercial BW S65-C beryllium.

Samples were machined of each material by Speedring, Inc. (Cullman, AL) to Brush Wellman specifications. Two sample geometries were fabricated: (1) SS-3 mini-sheet tensile specimens which are pin loaded sheet tensiles, and (2) 6 mm diameter, 4 mm thick cylinders.

Irradiation Exposures

Two water moderated fission reactors were used for the specimen irradiation. The Hydraulic Tube facility at the High Flux Isotope Reactor (HFIR) at the Oak Ridge National Laboratory was used to study the effect of fluence range at a constant irradiation temperature. Mini-sheet tensile specimens and thermal diffusivity (6 mm) discs were loaded inside an aluminum holder which was welded inside a "rabbit" capsule. The capsules were then baked at 200°C and stored in the presence of hygroscopic media. The rabbit was welded shut in an ultra high purity (UHP) helium environment. Each rabbit was radiographed and underwent a QA procedure to ensure air or water was unable to penetrate the capsule. Sample temperature was achieved by gas-gap

Table 1. Properties of Beryllium Materials Provided by Manufacturer

	Brush Wellman S-65C	Kawecki Berylco P0
Yield Stress (MPa) - Long.	257	
-Trans.	265	530
Ultimate Stress (MPa) - Long.	381	
-Trans.	414	655
Fracture Elongation (%)- Long	3.5	
-Trans.	6.6	4.9
Density		
Impurities : (wt %) BeO	0.64	3.36
(wt %) C	0.038	0.173
(appm) Fe	670	1000
Al	230	120
Si	255	70
Mg	30	40
Zn	<10	NA
Ni	<20	95
Mn	<20	30
Cu	25	15
Ti	65	NA
Co	8	<5
N	120	NA
Cr	50	90

conduction of the nuclear heating between the sample holder and the rabbit body, both made of Type 6061-T6 aluminum. Rabbits were irradiated in the HT-3 position with a thermal and fast (E>0.1 MeV) neutron flux of 2.2×10^{19} and 7.8×10^{18} n/m^2, respectively.[23] Fluences of irradiation were 0.05, 0.2 and 1.0×10^{25} n/m^2 (E>0.1 MeV) at a calculated irradiation temperature of 300°C.

The High Flux Beam Reactor (HFBR) at the Brookhaven National Laboratory was used to study the effects of varied irradiation temperature at a constant fluence. Two irradiation capsules were designed for insertion into the V-15 core thimble position. Each capsule consisted of separate gas-gapped subcapsules containing the samples. Variations in the sample temperature in the different subcapsules was achieved by varying the gas gap between the subcapsules and the inside of the external capsule, which was in contact with the core coolant water. The subcapsule bodies were electro-discharge machined from Type 6061-T6 aluminum. Each subcapsule typically contained 4 SS-3 tensile specimens. After the samples were loaded, a Type 304 stainless steel roll pin (a spring) was lightly hammered into place to ensure that the specimens were in good thermal contact with the subcapsule wall. Each subcapsule used one type-K thermocouple which monitored temperature throughout the irradiation.

All samples and capsule components (for both reactor irradiations) were ultrasonically cleaned in isopropyl alcohol and acetone prior to capsule assembly. After the HFBR capsule was assembled and the ~33 meter umbilical Type 8000 aluminum tubing was welded in place, the capsule was helium leak checked using a helium mass spectrometer. The capsule was then evacuated using an oil-free turbomolecular pump and back-filled with UHP helium to 15 psig. This procedure was repeated three times. Between the first and second evacuation cycles the capsule was baked out to 400°C under vacuum. After the final backfill to 15 psig the pressure was monitored continuously from time of assembly until the end of the irradiation. At no time did the capsule pressure reach atmospheric pressure before or during the irradiation. However, a small helium leak caused the capsule pressure to decrease during irradiation. This was corrected during irradiation by valving off the irradiation capsules, and then evacuating and back-filling the gas

handling manifolds with helium (which were not removed after capsule construction.) Once the manifold was purged and backfilled with UHP helium, the capsule was repressurized with helium to 15 psig.

At the time of these irradiations the HFBR was operating at 30 MW_{th} power. Recently, Greenwood [24] has conducted a calculation on a single dosimetry sample near the center of the V-15 thimble. The fast neutron fluence in this case was approximately half the value which he previously measured. For this paper, the recent flux measurements are used. Also, based on Monte Carlo calculations it is assumed that the center 40 cm of 55 cm core is flux-invariant, therefore no flux gradient along the capsule (hence the samples) is expected. Each of the capsules were irradiated for an estimated fast (E>0.1 MeV) and thermal fluences of $\sim 5 \pm 0.2 \times 10^{24}$ n/m^2 and 2.3×10^{24} n/m^2, respectively. During irradiation, the temperature of the samples were recorded continuously. The temperature variation for two HFBR irradiations were always less than 12°C, most of which is accounted for by movement of the capsule to the center of the core during irradiation. Data presented in the results section represents the mean value with the error bars representing the range.

Based on calculations made (Gabriel [25]) and the revised spectra of the HFBR provided by Greenwood [24] the helium concentration and displacements per atom (dpa) for the various irradiations are listed in Table 2. Note that due to the relatively higher flux at the extreme end of the neutron spectrum, the HFBR V-15 spectrum produces a slightly higher He/dpa ratio than the HFIR HT position.

Table 2. Irradiation Conditions

	Thermal Fluence $\times 10^{25}$ n/m^2	Fast Fluence $\times 10^{25}$ n/m^2 (E>0.1MeV)*	Fast Fluence $\times 10^{25}$ n/m^2 (E>1.0MeV)	dpa	He conc. (appm)	He/dpa
HFIR	0.14	0.05	0.026	0.04	10	
	0.6	0.20	0.11	0.15	37	250
	2.8	1.0	0.53	0.74	190	
HFBR	2.3	5 ± 0.5	2.1 ± 0.2	0.34	250	824

* energy cut-off is listed as E>0.11 MeV for HFBR results[24]

Experimental Techniques

The thermal diffusivity of the samples was measured by a custom built thermal flash (xenon laser) apparatus. Following the thermal flash on the front surface, the rear surface temperature was measured by the infrared signal and the diffusivity calculated following Clark and Taylor's analysis.[26] Density and thickness values corresponding to the unirradiated or irradiated condition were used for the unirradiated and irradiated measurements, respectively. For the thermal diffusivity calculations the density was calculated by dry weight and physical dimensions. The thermal diffusivity of every specimen was measured before and after irradiation.

The room temperature thermal conductivity (K) was calculated using the measured thermal diffusivity (α), measured density (ρ), and the assumed specific heat (C_p) as follows:

$$K = \alpha \rho C_p$$

The conversion from thermal diffusivity to thermal conductivity used the assumption that the specific heat remained unchanged with irradiation.

Density was determined for calculation of swelling by using a density gradient column according to ASTM D1505-85 utilizing chemical mixtures of trichloroethane and ethylene bromide and calibrated glass floats [27]. The linear density gradient of the column was 0.35 $(mg/cm^3)/cm$

yielding an accuracy of relative density change of approximately 0.005%. Prior to dropping the samples in the density gradient column all specimens were etched in a mixture of hydrofluoric acid and ethyl alcohol and then dried. Visible etching and etch pits were observed.

Tensile testing was performed in load control digitally recording the cross head displacement. Elevated temperature testing was performed in static argon with the thermocouple in contact with the sample grips. Room temperature testing was in air. A temperature saturation of at least 15 minutes was used prior to applying tensile load. In both the unirradiated and irradiated condition the S65-C specimens were pin-loaded while the irradiated P0 specimens had to be shoulder loaded due to failure at the pin-holes. A cross head displacement rate 0.001 s^{-1} was applied for the SS-3 mini-sheet tensile specimens which have a ~0.76 cm gage section. This displacement rate is approximately the same as that used in the recent European ITER beryllium irradiation program [28] though is about an order of magnitude higher than the value recommended by the Materials Advisory Board [29]. The effect of increasing strain rate in beryllium is to reduce the temperature at which beryllium moves from brittle to ductile failure. However, this temperature shift is expected to be small for the strain rate differences noted here [30,31], though the general effect of strain rate on failure mode does need to be further studied, especially for irradiated material.

A Buehler Micromet 3 microhardness testing machine was used at 500 g and 1 kg loads to measure the Vickers hardness. The two loads gave essentially the same hardness values and the 500 g loads are reported here. Specimens were prepared for hardness testing by wet sanding the surface (in oil) to a polished finish. Any potential effects of the surface polish affecting the hardness were dismissed by indenting unprepared and prepared surfaces of unirradiated material and noting that no difference in hardness was seen over a wide range of applied load.

Results

Swelling and Thermal Conductivity

The effect of irradiation to these doses and temperatures had essentially no effect on the thermal conductivity or density of the materials selected. The density of the S65-C beryllium was measured to be 1.844 g/cc, or 99.82 percent theoretical density (%td) while the density of the P0 beryllium was 1.849, or 100.05 %td. The higher than theoretical density of the P0 material can be explained by the elevated level of BeO (3.36 w/% at ~3.0 g/cc density) in this material, as seen in Table 1. Upon irradiation, swelling occurred in all materials, though the amount of swelling was very small. The largest swelling occurred for the HFIR material irradiated to 1×10^{25} n/m^2 at approximately 300°C yielding +0.027±0.005% for the S65-C material and 0.038±0.005% for the P0 material. The swelling of the HFBR materials was less than this (~0.02 %) and no difference with respect to the irradiation temperature was observed. These swelling levels are consistent with the work of Gol'tsev and coworkers [7,32]. It is noted that the temperatures at which the materials were irradiated in this study were substantially below the lowest temperature at which helium bubbles have been observed [6,7] and is therefore in a region where point defect mobility and clustering is responsible for swelling.

The thermal conductivity of unirradiated S65-C beryllium was measured to be 190 ±~5 W/m-K. This was found using the measured thermal diffusivity and assumed unirradiated density of 1.844 g/cc and specific heat of 1.825 J/g-K. In the case of the material irradiated to 1×10^{25} n/m^2 (E>0.1 MeV) at ~300°C, the thermal conductivity was within the experimental error of the unirradiated value. A significant reduction in thermal conductivity is not expected unless the material is irradiated in the temperature and flux range where helium bubble formation and swelling becomes pronounced.

Hardness

The embrittlement of these beryllium materials as a function of dose and temperature is given in Figs. 1 and 2, respectively. The elevated level of BeO in the KBI-P0 material results in a higher initial hardness for this material as compared to the S65-C material. Specifically, the room temperature unirradiated Vickers hardness was measured to be 228±3 Kg/mm^2 as compared to 181±2 Kg/mm^2 for S65-C. Essentially no increase in hardness was observed a dose of 0.05×10^{25} n/m^2 (E>0.1 MeV) for the P0 material while a marked increase was seen for both materials following 0.2×10^{25} n/m^2 (E>0.1 MeV) . As the fluence was further increased to 1.0×10^{25} n/m^2 (E>0.1 MeV) the hardness of both materials substantially increased. As seen in Fig. 2, the dependence of hardness on irradiation temperature is significantly different for the two materials. The higher BeO content P0 material appears to have a weak dependence on irradiation temperature while the increased hardness (DH) for the S65-C appears to drop off with irradiation temperature from a DH~44 Kg/mm^2 following the 110°C irradiation to ~25 Kg/mm^2 for the 237°C irradiated material.

Tensile Properties

The effects of the neutron irradiation induced embrittlement on the tensile properties of both types of beryllium are given in Figs. 3-8. These figures plot the tensile data as a function of irradiation temperature for a constant HFBR dose and as a function of HFIR dose at a constant irradiation temperature. The elongation specified is the total (fracture) elongation while the yield strength is defined at the 0.2% offset yield. Specific dpa and helium concentration limits are found in Table 2.

As seen in Figs. 3 and 4, the effect of the neutron induced embrittlement of the S65-C to a dose of 0.2×10^{25} n/m^2 is to increase the tensile strength and reduce the total elongation. In the irradiated condition both room temperature and 300°C tensile curves exhibited ductile failure with ~2% and ~5% total elongation at failure (compliance corrected), respectively. For the irradiation temperature range shown in Fig. 5, the yield strength at room temperature decreases with increasing irradiation temperature, while the total elongation increases slightly. Figure 6 shows the same samples as plotted in Fig. 5, though for irradiation temperature tests. The trend toward increasing total elongation is still apparent, though the tensile strength appears to increase between the 106°C and 202°C irradiations, and then to fall off slightly. It is noted that the data points in figs.3-8 represent single sample tests and as seen from the 202°C irradiation of Fig. 6 (and in Figs. 3 and 7), there is a fair scatter in the tensile data (in contrast with the hardness data (Figs. 1 and 2.) It is clear the significant increase in hardness from the 0.2 to 1.0×10^{25} n/m^2 level, as well as recent tensile and fracture toughness data on S65-C material irradiated to higher doses[28] that the S65-C material will continue to embrittle as dose is increased and will eventually become completely brittle.

Figures 7 and 8 gives the tensile properties for the KBI P0 material irradiated as a function of dose in the HFIR. At equivalent doses of 0.2×10^{25} n/m^2, the P0 and S65-C both undergo approximately 50 MPa increase in room temperature yield strength, though the P0 material appears to lose substantially more ductility to become near completely brittle by a dose of 1.0×10^{25} n/m^2 for both room temperature and irradiation temperature tests. It is noted that the S65-C material, both at room temperature and 300°C, has substantially higher unirradiated fracture elongation (Table 1.)

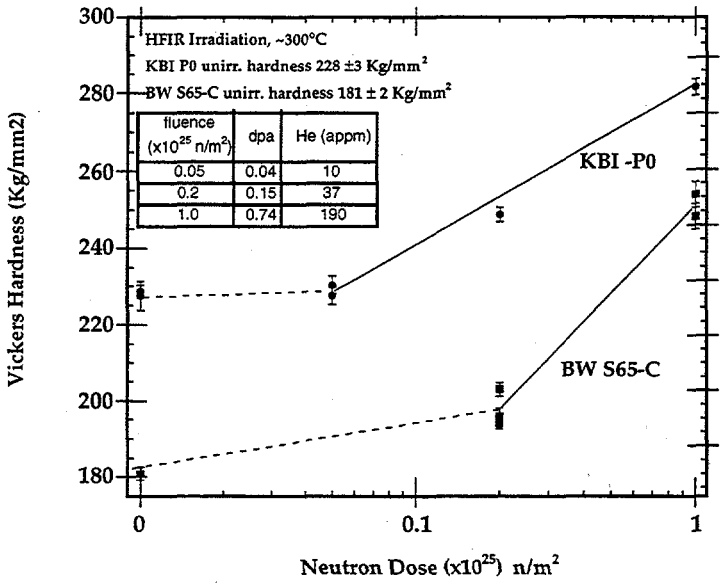

Figure 1. Hardness of BW S65-C and KBI P0 beryllium as a function of neutron dose.

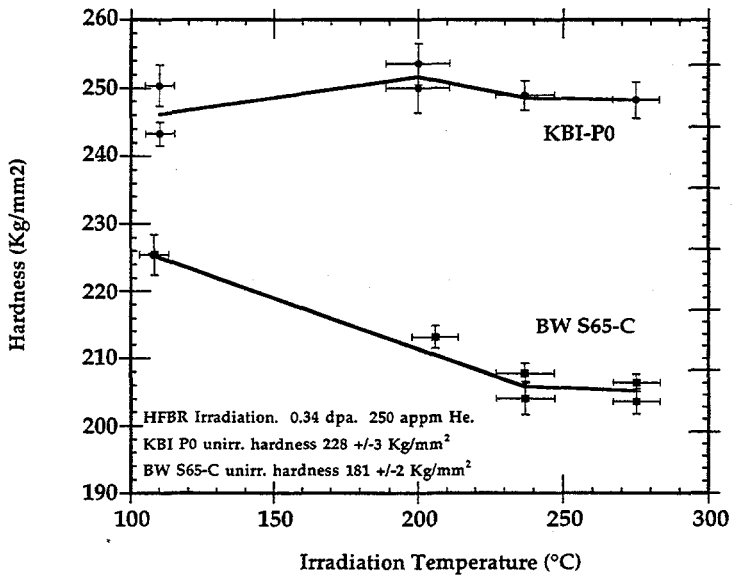

Figure 2 : Hardness of BW S65-C and KBI P0 beryllium as a function of irradiation temperature.

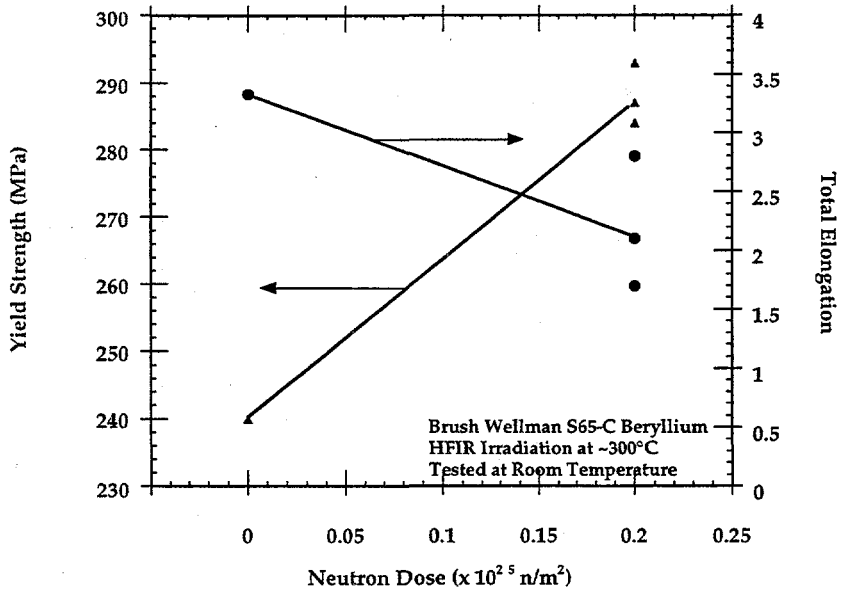

Figure 3 : Room temperature yield strength and elongation of BW S65-C beryllium as a function of neutron dose.

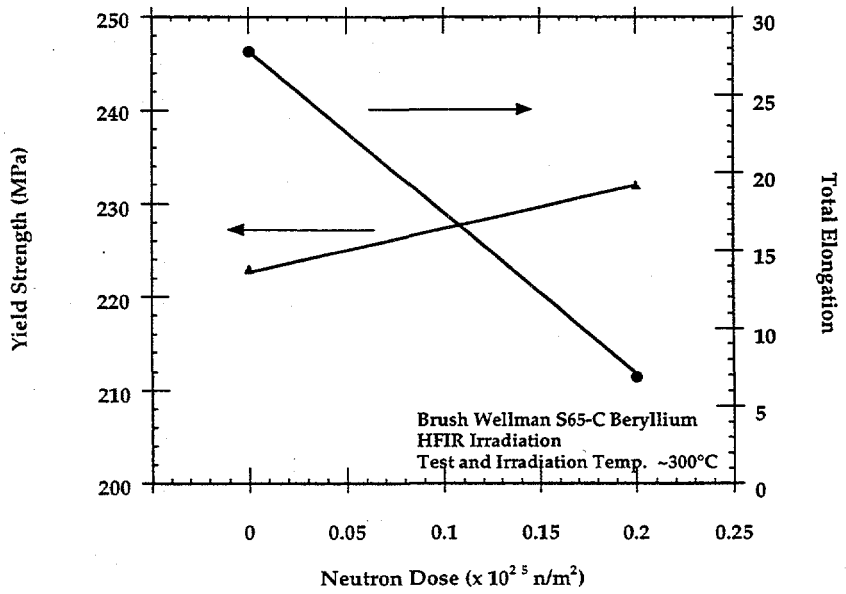

Figure 4 : Yield strength and elongation of BW S65-C beryllium as a function of neutron dose measured at the irradiation temperature.

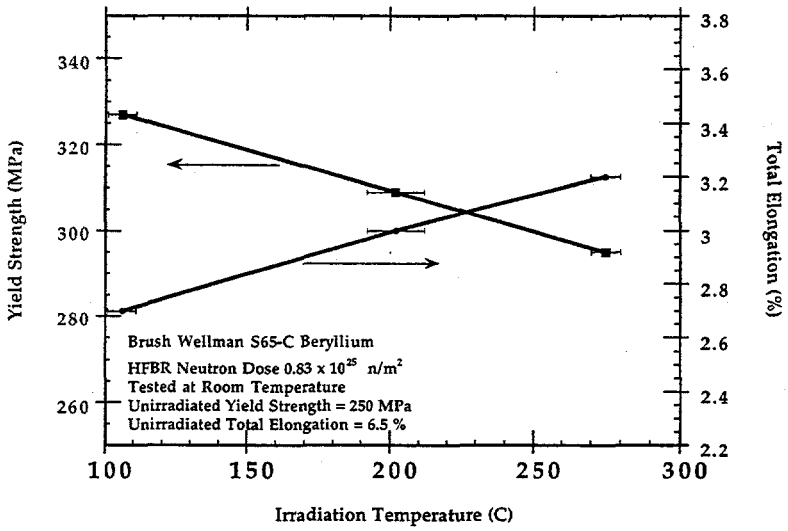

Figure 5 : Room temperature yield strength and elongation of neutron irradiated BW S65-C beryllium as a function of irradiation temperature.

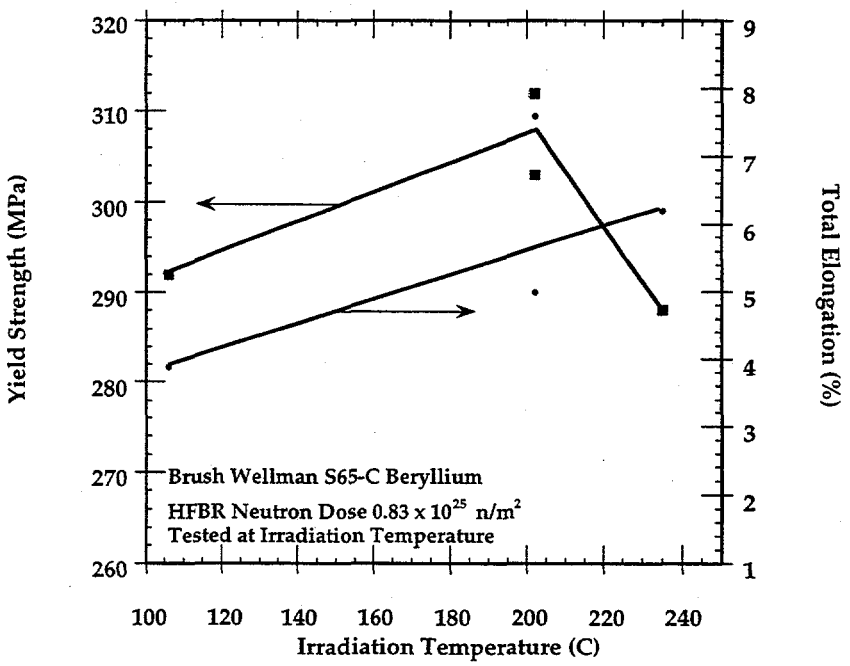

Figure 6 : Yield strength and elongation of neutron irradiated BW S65-C beryllium as a function of irradiation temperature measured at the irradiation temperature.

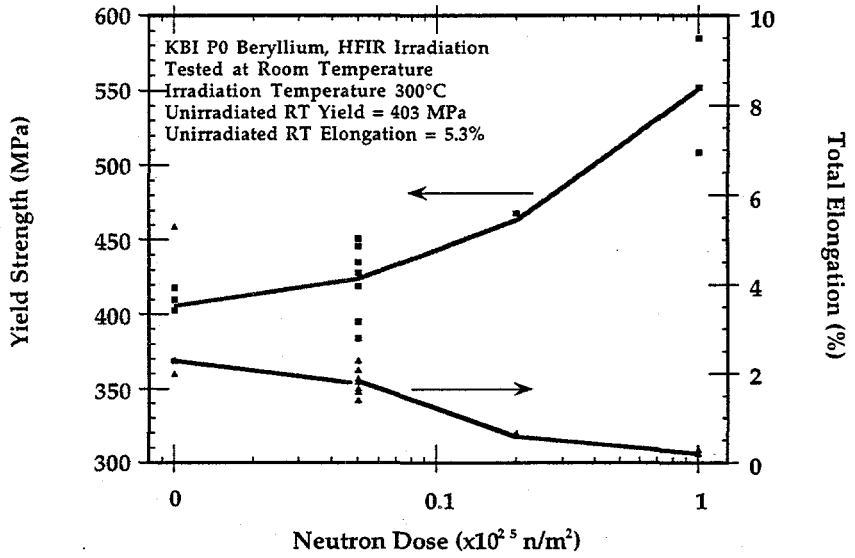

Figure 7 : Room temperature yield strength and elongation of KBI-P0 beryllium as a function of neutron dose.

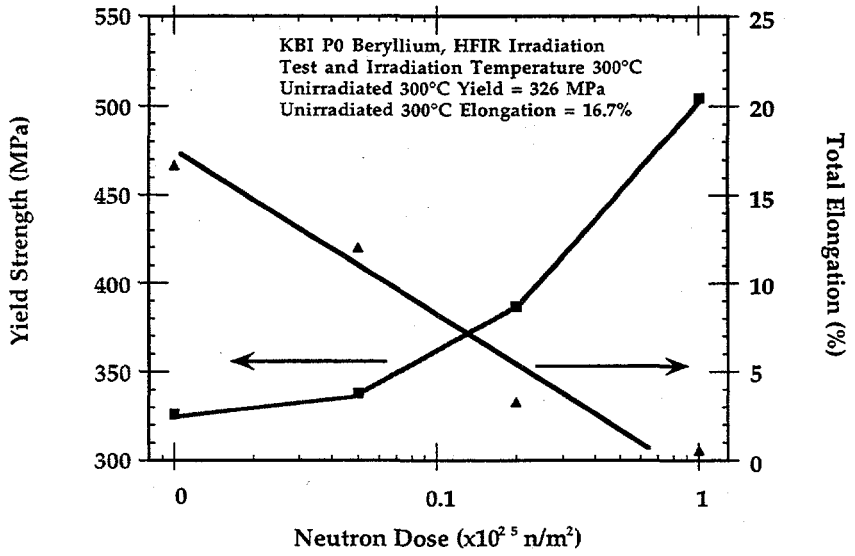

Figure 8 : Yield strength and elongation of KBI-P0 beryllium as a function of neutron dose measured at the irradiation temperature.

ACKNOWLEDGMENTS

The author would like to thank Dave Dombrowski and the Brush Wellman company for provision of the S65-C material as well as for valuable technical assistance. I would also like to thank Ben Odegard of the Sandia National Laboratory for providing the materials and pertinent information regarding the Kawecki Berylco Industries P0 material. Technical help was also provided by J. P. Strizak, J. L. Bailey, and A. M. Williams for which I am grateful. Research sponsored by the Office of Fusion Energy Sciences, U.S. Department of Energy, under contract DE-AC05-96OR22464 with Lockheed Martin Energy Research Corp.

REFERENCES

[1] J.B. Rich and G.P. Walters, in The Metallurgy of Beryllium : Institute for Metals Monograph No. 28 (Chapman and Hall Ltd., London, 1961) p. 362.
[2] J.M. Beeston et al., Proc. Symp. on Materials Performance in Operating Nuclear Systems, CONF-730801 , 1973) p. 59.
[3] G.P. Walters, J. Less Common Metals 11 (1966) 77.
[4] D.S. Gelles and H.L. Heinisch, J. Nucl. Mater. 191-194 (1992) 194.
[5] R.S. Barnes, in The Mettalurgy of Beryllium: Institutte of Metals Monograph and Report Series No. 28 (Chapman and Hall, Ltd, London, 1961) p. 372.
[6] J.M. Beeston, L.G. Miller, E.L. Wood-Jr and R.W. Moir, J. Nucl. Mater. 122-123 (1984) 802.
[7] D.S. Gelles, G.A. Sernyaev, M.D. Donne and H. Kawamura, J. Nucl. Mater. 212-215 (1994) 29.
[8] J.B. Rich, G.P. Walters and R.S. Barnes, The Metallurgy of Beryllium 4 (1961) 287.
[9] B.S. Hickman et al., Report UKAEA TRG Report 540 (1963).
[10] B.S. Hickman and G. Bannister, Report Part 2, AAEC/E-115 (also TRG Report 540 UKAEA) (1963).
[11] G.T. Stevens and B.S. Hickman, Report AAEC/E-133 (1965).
[12] J.M. Beeston, in Effects of Radiation on Structural Materials vol. ASTM-STP 426 ((ASTM, Philidelphia, PA), 1967) p. 135.
[13] E.D. Hyam and G. Sumner, Radiation Damage in Solids, vol. 1 (IAEA, Vienna, 1962) p. 323.
[14] J.R. Weir, in The Mettalurgy of Beryllium : Institute of Metals Monograph and Report Series No. 28 (Chapman and Hall, Ltd, London, 1961) p. 395.
[15] R. Sumerling and E.D. Hyam, in The Mettalurgy of Beryllium : Institute of Metals Monograph and Report Series No. 28 (Chapman and Hall, Ltd, London, 1961) p. 381.
[16] E.H. Smith et al., Proc. Symp. on the Physical Metallurgy of Beryllium, Gatlinburg, CONF-730801 , 1973) p. 41.
[17] J.M. Beeston, Nucl. Eng. Des. 14 (1970) 445.
[18] J.M. Beeston, G.R. Longhurst, R.S. Wallace and A.P. Abeln, J Nucl. Mater. 195 (1992) 102.
[19] M.H. Bartz, in Properties of Reactor Materials, Second United Nations Conf. on the Peaceful Uses of Atomic Energy vol. 5 (United Nations, Geneva, 1958) p. 466.
[20] B.S. Hickman, in The Mettalurgy of Beryllium : Institute of Metals Monograph and Report Series No. 28 (Chapman and Hall, Ltd, London, 1961) p. 410.
[21] S. Morozumi, S. Goto and M. Kinno, J. Nucl. Mater. (1977) 82.
[22] J.B. Rich, G.B. Redding and R.S. Barnes, J. Nucl. Mater. 1 (1961) 96.
[23] S.T. Mahmood, S. Mirzadeh, K. Farrel and J.F. Pace, Oak Ridge National Laboratory, Oak Ridge Report ORNL/TM--12831 (1995).
[24] L.R. Greenwood and R.T. Ratner, in Fusion Materials Semiannual Progress Report for Period Ending Dec 31, 1997. vol. DOE/ER-0313/23 , 1998) p. 309.
[25] T.A. Gabriel, B.L. Bishop and F.W. Wiffen, Oak Ridge National Laboratory, Oak Ridge Report ORNL/TM-6361 (1979).
[26] L.M. Clark and R.E. Taylor, J. Appl. Phys 46 (1975) 114.
[27] ASTM, D1505-85, Standard Test Method for Density of Plastics by Density Gradient Technique, 1985.

[28] R. Chaouadi, F. Moons and J.L. Puzzolante, SCK.CEN, Mol, Belgium Report TEC97/51/F040010/15/RC (1997).
[29] Tests Methods Subcommittee Committee on Beryllium Metallurgy. National Academy of Sciences-National Research Council, Washington Report Publication MAB-205-M.
[30] A.J. Martin and G.C. Ellis, in The Mettalurgy of Beryllium : Institute of Metals Monograph and Report Series No. 28 (Chapman and Hall, Ltd, London, 1961) p. 3.
[31] G.L. Turner, in Beryllium Science and Technology vol. 1, eds. D. Webster and G.J. London (Plenum Press, 1979) p. 145.
[32] V.P. Gol'tsev, G.A. Sernyaev and Z.I. Chechetkina, Nauka i Teknika, Minsk (1977).

8.0 RADIATION EFFECTS, MECHANISTIC STUDIES, AND EXPERIMENTAL METHODS

No contributions.

9.0 DOSIMETRY, DAMAGE PARAMETERS, AND ACTIVATION CALCULATIONS

NEUTRON DOSIMETRY AND DAMAGE CALCULATIONS FOR THE ATR-A1 IRRADIATION

- L. R. Greenwood and R. T. Ratner (Pacific Northwest National Laboratory)*

OBJECTIVE

To provide dosimetry and damage analysis for fusion materials irradiation experiments.

SUMMARY

Neutron fluence measurements and radiation damage calculations are reported for the collaborative U.S./Japan ATR-A1 irradiation in the Advanced Test Reactor (ATR) at Idaho National Engineering Laboratory (INEL). The maximum total neutron fluence at midplane was 9.4×10^{21} n/cm^2 (5.5×10^{21} n/cm^2 above 0.1 MeV), resulting in about 4.6 dpa in vanadium.

PROGRESS AND STATUS

The ATR-A1 experiment was designed to obtain mechanical property data, including in-reactor creep, on vanadium alloys irradiated at about 200 and 300 °C.[1] The drop-in type capsule was irradiated from December 2, 1995 to May 5, 1996 for a total of 135.95 effective full power days at an average power of 25 MW. Each subcapsule contained a gadolinium filter measuring 1.7 mm in thickness to reduce the thermal neutron flux in order to mitigate transmutation effects.

Neutron dosimetry capsules were inserted at five different elevations in the assembly. At two positions (-2.4 cm and –57.1 cm), six different dosimetry monitors consisting of Fe, Ti, Nb, Cu, 80.2%Mn-Cu, and 0.1%Co-Al were used to determine the neutron energy spectrum. The other three dosimetry capsules only contained Fe and 0.1% Co-Al to determine the flux gradients.

After irradiation, the gamma activities in each monitor wire were measured and then converted to activation rates, as listed in Table 1, by correcting for nuclear burnup, gamma self-absorption, decay during and after irradiation, isotopic abundance, and atomic weight. Burnup corrections are based on an iterative procedure for the thermal/epithermal monitor reactions. The resulting estimates of the thermal/epithermal neutron fluences were then used to calculate burnup corrections for the threshold fast neutron monitor reactions. Thanks to the gadolinium filter, burnup corrections were quite small averaging 1-3% for the thermal/epithermal reactions and < 1% for the threshold reaction rates. The activation rates listed in Table 1 are normalized to a reactor power of 25 MW and have a net absolute uncertainty of about 3%. Upon analysis, the copper dosimeter irradiated at –2.4 cm was found to be an empty capsule so that we could not obtain data for this flux monitor.

The activation rates in Table 1 were fit to a polynomial function of form $f(x) = f(0) [1 - a x - b x^2]$, where x is the vertical height from reactor centerline in cm, as shown in Figure 1. All of the data are reasonably well fit by the average polynomial coefficients $a = 1.39 \times 10^{-3}$ and $b = 2.16 \times 10^{-4}$. The ratio of activation rates for the thermal and fast neutron reactions does not change appreciably over the height of the irradiation assembly. This suggests that the neutron energy spectrum remains relatively constant while the absolute flux values decrease about a factor of

---

* Pacific Northwest National Laboratory (PNNL) is operated for the U.S. Department of Energy by Battelle memorial Institute under contract DE-AC06-76RLO-1830.

two from midplane to the top or bottom of the assembly. Midplane activation rates were thus used in the STAY'SL[2] computer code to adjust the neutron flux spectrum. STAY'SL performs a generalized least-squares adjustment of all measured and calculated values including the measured activities, calculated spectra, and neutron cross sections. Neutron cross sections and their uncertainties were generally taken from the ENDF/B-V[3] evaluation. The starting neutron spectrum was determined from an unfiltered spectrum calculated by B. Schnitzler[4], using a simple approximation to determine the effect of the gadolinium filter. The adjusted neutron fluence values are listed in Table 2 and the spectra are shown in Figure 2. As can be seen in the figure, the shape of the neutron spectrum remains about the same from midplane to the end of the assembly, except for the very low energy neutrons.

Neutron damage calculations were performed using the SPECTER computer code[5] at the midplane position of ATR. Midplane dpa and helium (appm) values are listed in Table 2. The measured value of 4.6 dpa for vanadium is very close to the planned exposure of 4.7 dpa. The fluence and damage values at other experimental positions can be calculated by the gradient equation given above. Damage parameters for other elements or compounds have been calculated and are readily available on request.

Due to the presence of the gadolinium filter, the transmutation of vanadium to chromium is only 0.046% at midplane.

FUTURE WORK

Additional experiments are being planned for the ATR.

REFERENCES

1. H. Tsai, R. V. Strain, I. Gomes, D. L. Smith, L. R. Greenwood, and H. Matsui, Status of ATR-A1 Irradiation Experiment on Vanadium Alloys and Low-Activation Steels, Fusion Reactor Materials Semiannual Progress Report, DOE/ER-0313/22, pp. 303-326 (1997).

2. F. G. Perey, Least Squares Dosimetry Unfolding: The Program STAY'SL, ORNL/TM-6062 (1977).

3. Evaluated Nuclear Data File, Part B, Version V, National Nuclear Data Center, Brookhaven National Laboratory.

4. B. Schnitzler, Idaho National Engineering Laboratory, private communication, 1998.

5. L. R. Greenwood and R. K. Smither, SPECTER: Neutron Damage Calculations for Materials Irradiations, ANL/FPP-TM-197, January 1985.

Table 1. Activation Rates (at/at-s) – ATR-A1 – 25 MW

Position/Monitor	Ht,cm	$^{54}Fe(n,p)^{54}Mn$ (E-11)	$^{59}Co(n,\gamma)^{60}Co$ (E-9)	$^{46}Ti(n,p)^{46}Sc$ (E-12)
AS-1	57.3	0.463	0.375	
AS-10	-2.4	2.17	2.08	2.86
AS-12	-18.2	2.03	1.85	
AS-16	-36.8	1.72	1.44	
AS-17	-57.1	0.789	0.662	1.01
Position/Monitor	**Ht,cm**	$^{55}Mn(n,2n)^{54}Mn$ (E-14)	$^{93}Nb(n,\gamma)^{94}Nb$ (E-10)	$^{63}Cu(n,\alpha)^{60}Co$ (E-14)
AS-1	57.3			
AS-10	-2.4			
AS-12	-18.2	6.05	2.94	
AS-16	-36.8			
AS-17	-57.1	2.28	0.975	4.94

Table 2. Midplane Fluence and Damage Values for ATR-A1

Neutron Fluence, $\times 10^{21}$ n/cm^2	
Total	9.41
Thermal (<.5 eV)	0.012
0.5 eV - 0.11 MeV	3.93
> 0.11 MeV	5.46
> 1 MeV	2.55

Element	dpa	He,appm
C	3.9	5.0
Al	7.1	2.0
V	4.6	0.068
Cr	4.2	0.53
Fe	3.8	0.93
Ni Fast	3.9	14.6
^{59}Ni	0.0	0.6
Total	3.9	15.2
Cu	4.8	0.77
316SS	3.9	2.7

Note: 316SS = Fe(0.645), Ni(0.13), Cr(0.18), Mn(0.019), Mo(0.026)

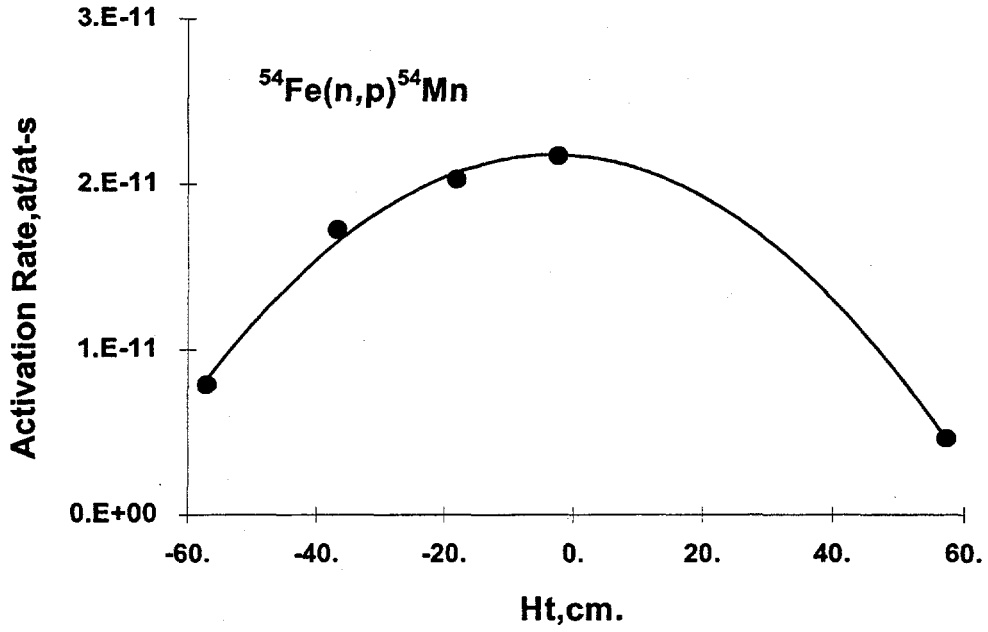

Figure 1. Activation rate of ^{54}Mn from the $^{54}Fe(n,p)$ reaction vs. elevation in the ATR-A1 assembly. The trendline is a polynomial, as described in the text.

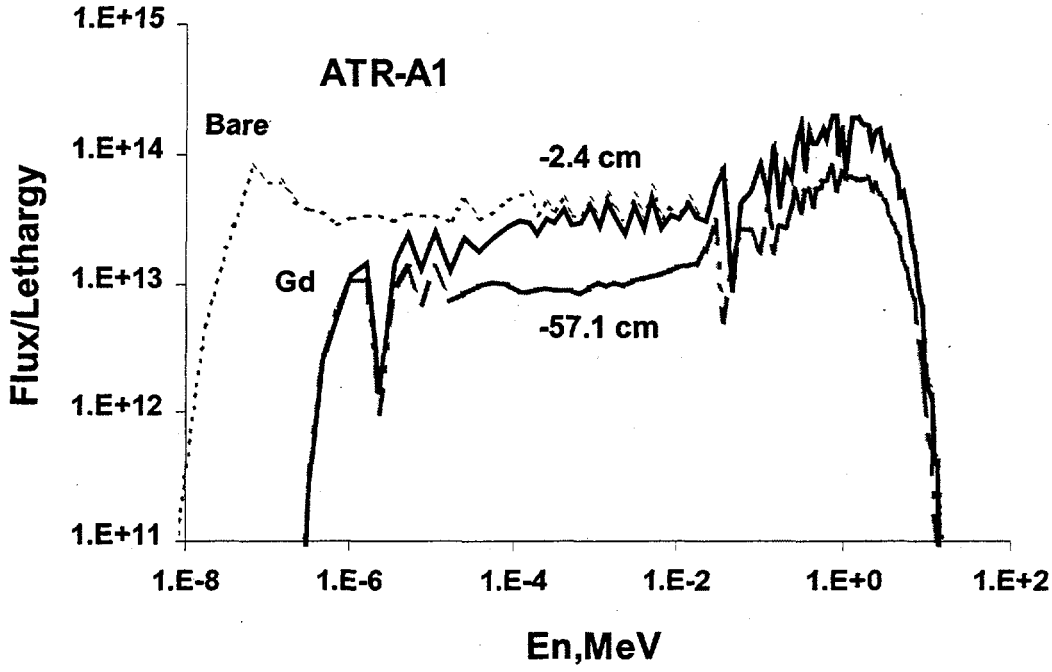

Figure 2. Neutron energy spectra adjusted by STAY'SL at –2.4 (solid line) and –57.1 cm (dashed line) below midplane in the ATR-A1 assembly. Note the effects of the Gd filter at low neutron energies. The bare, unfiltered neutron spectrum at –2.4 cm is shown as a dotted line.

ANALYSIS AND RECOMMENDATIONS FOR DPA CALCULATIONS IN SiC - H.L. Heinisch (Pacific Northwest National Laboratory)*

OBJECTIVE

The objective of this work is to recommend a procedure for calculating the radiation dose parameter displacements per atom (DPA) for SiC that will be accepted for use throughout the international fusion materials community.

SUMMARY

Recent modeling results, coupled with the implications of available experimental results, provide sufficient information to achieve consensus on the values of threshold displacement energies to use in DPA calculations. The values recommended here, 20 eV for C and 35 eV for Si, will be presented for adoption by the international fusion materials community at the next IEA SiC/SiC workshop.

PROGRESS AND STATUS

Displacements per atom(DPA) has become the standard unit for irradiation doses in structural materials, especially under neutron irradiation, because DPA represents, in a simple way, not only the amount of radiation received, but also the response of the material to the irradiation. Damage-based dose parameters are required because radiation damage in structural materials is studied using a variety of irradiation sources, which differ in their ability to produce damage depending on the mass and energy of the irradiating particles. Furthermore, results of these studies must be extrapolated to fusion irradiation environments that do not yet exist. DPA is a calculated dose parameter that takes into account the energy lost to the material by the irradiating particles in the form of energy that is available to cause displacement damage. The "damage energy" is converted into "displacements" in terms of the threshold displacement energy for the material.

DPA is not generally a measure of the number of stable defects created or remaining in the material at any time. This is especially true in the case of cascade-producing irradiation, where a high percentage of displaced atoms recombine immediately within the cascade volume. The calculated DPA value has, however, become a standard against which to compare the numbers of stable defects actually produced in cascade-producing irradiations. Thus, the concept of DPA is important not only as a measure of radiation dose received, but also in assessing the efficiency of defect production as a function of cascade energy and irradiating particle type.

DPA is calculated using the measured fluence of irradiating particles, the energy spectrum of the irradiating particles, the recoil atom energy spectrum for each irradiating particle, the damage energy of each recoil (the kinetic energy of the recoil less the energy lost to electronic stopping), and the model for displacements as a function of recoil damage energy. The displacement model is usually taken to be the NRT model [1], in which the number of displacements produced by a recoil atom with energy E_r having damage energy T_{dam} is

---

* Pacific Northwest National Laboratory (PNNL) is operated for the U.S. Department of Energy by Battelle Memorial Institute under contract DE-AC06-76RLO-1830.

$$n(E_r) = \frac{0.8T_{dam}}{2E_d},$$

where E_d is the threshold displacement energy, and $T_{dam} > 2\ E_d$.

The concept of DPA was first developed for metals, and originally formulated within the context of pure metals. In alloys, DPA values are commonly determined as the compositionally weighted sum of DPA calculated for the individual elements in their pure metals. In SiC and other non-metallically bonded compounds, the separate elements have displacement energies unique to the compound and often significantly different from each other. Calculation of DPA for SiC is straightforward once the threshold displacement energies are known for Si and C in SiC.

The threshold displacement energy is an experimentally measurable quantity (usually by determining the threshold electron energy for measurable displacements), but in multicomponent systems it is often difficult to measure the displacement energy of each component separately, except for the component with the lowest displacement threshold. Such is the case with SiC, where the reported measurements of especially the Si displacement threshold vary widely [2]. Computer simulations indicate that the displacement energy varies significantly with crystallographic direction, which may account for some of the variation in measured values. (The two-step electron-C-Si collision process can also lead to erroneously small electron energy thresholds for Si displacements [2].)

Since E_d is essentially a scaling parameter in the DPA calculation, why is it important to use the correct, measured displacement threshold energies, as long as everyone agrees to use the same values? For simply the purpose of damage correlation, it probably does not matter what values are used as long as they are used universally. On the other hand, our understanding of the radiation-induced defect structure and microstructural changes will be greatly enhanced if we use as a reference the DPA values that correctly reflect the relative numbers of each type of displacement. Furthermore, the displacement energies will eventually be measured precisely, so it is important for any values chosen as standards for DPA calculations to be as realistic as possible to avoid significant reevaluation or possible confusion in the future.

A comprehensive review of experimental measurements and results of molecular dynamics (MD) simulations of displacement energies in SiC is given in Ref. 2. Since the publication of Ref. 2, more MD simulations were done in a few selected directions by R. Devanathan, T. Diaz de la Rubia and W.J. Weber (under DOE/OBES and DOE/OFES sponsorship) using an improved interatomic potential, as reported in Ref. 3. Even more recently, Devanathan and Weber (under DOE/OBES) have extended their MD calculations to include many more directions. Also, MD simulations of the threshold displacement energies in alpha-SiC have been initiated by H. Serizawa, R. Devanathan, W.J. Weber and H.L. Heinisch. Publications on the most recent simulations in both alpha- and beta-SiC are under preparation. Based on these additional MD simulations, it now appears that sufficient information exists for promoting a consensus on the values of threshold displacement energies to use in DPA calculations. The values recommended here are 20 eV for C and 35 eV for Si, Pending publication of the most

recent MD results, a recommendation will be circulated within the fusion SiC community that these threshold displacement energy values be adopted for DPA calculations.

REFERENCES

1. M.J. Norgett, M.T. Robinson and I.M. Torrens, *Nucl. Eng. Design 33* (1975) 50.
2. S.J. Zinkle and C. Kinoshita, *J. Nucl. Mater.* 251 (1997) 200.
3. R. Devanathan, T. Diaz de la Rubia and W.J. Weber, *J. Nucl. Mater.*, 253 (1998) 47.

10.0 MATERIALS ENGINEERING AND DESIGN REQUIREMENTS

IMPACT OF STRUCTURAL DESIGN CRITERIA ON FIRST WALL SURFACE HEAT FLUX LIMIT* - S. Majumdar (Argonne National Laboratory)

SUMMARY

The irradiation environment experienced by the in-vessel components of fusion reactors presents structural design challenges not envisioned in the development of existing structural design criteria such as the ASME Code or RCC-MR. From the standpoint of design criteria, the most significant issues stem from the irradiation-induced changes in material properties, specifically the reduction of ductility, strain hardening capability, and fracture toughness with neutron irradiation. Recently, Draft 7 of the ITER structural design criteria (ISDC), which provide new rules for guarding against such problems, was released for trial use by the ITER designers.[1] The new rules, which were derived from a simple model based on the concept of elastic follow up factor, provide primary and secondary stress limits as functions of uniform elongation and ductility. The implication of these rules on the allowable surface heat flux on typical first walls made of type 316 stainless steel and vanadium alloys are discussed.

PROGRESS AND STATUS

Introduction

Austenitic stainless steels have long been known to be embrittled by fission neutron environment.[2-4] Such effects may be further exacerbated by significant generation of transmutation products like He under fusion neutron environment. Typical stress-strain curves for type 316 stainless steel fission reactor irradiated and tested at 250°-270°C are shown in Fig. 1.[5] Note the significant hardening accompanied by losses of strain hardening capability, uniform elongation, and total elongation with fluence. Vanadium alloys (e.g., V-4Cr-4Ti) show similar embrittlement behavior when irradiated and tested at temperatures < 400°C.[6] Traditional design codes are not intended to be applicable to materials with such tensile properties.

Structural design criteria

The basic structural damages (excluding buckling) have been broadly categorized in the ISDC as belonging to either M-type (monotonic) damage, .e.g., necking, gross yielding and fast (brittle) fracture or C-type (cyclic) damage, e.g., ratcheting, fatigue and creep-fatigue, depending on whether they can potentially cause structural failure during the first application of the loading or by repeated application of the loading, respectively. In the traditional design codes as well as ISDC, M-type damage is guarded against by limiting the primary membrane stress intensity to S_m (an allowable stress based on yield and ultimate tensile strengths) and the primary membrane plus bending stress intensity to kS_m, where k is a bending shape factor (k =1.5 for solid rectangular section). However, ISDC considers three additional M-type damages that are generally not considered in the traditional design codes. They are (1) plastic flow localization, (2) local fracture due to exhaustion of ductility and (3) fast (brittle) fracture, all of which are attributable to irradiation effects. To provide safety factors against the first two type of damages, the ISDC includes two new elastic analysis stress limits - S_e limit for primary plus secondary membrane stress intensity and S_d limits for primary plus secondary membrane plus bending stress intensities, with and without peak stress (stress concentration) effects. Note that in the traditional design codes, there is generally no limit on the secondary or peak stress due to M-

---

* Work supported by U.S. Department of Energy, Office of Fusion Energy Research, under Contract W31-109-Eng-38.

type loading, the assumption being that the material is sufficiently ductile to accommodate these deformation-controlled stresses by local yielding. For unirradiated annealed austenitic stainless steels and vanadium alloys, the numerical values of S_e and S_d are orders of magnitude higher than typical maximum stresses expected in practice and are never controlling. They may become controlling only when the material is sufficiently embrittled by irradiation so that the uniform elongation drops below 2%.

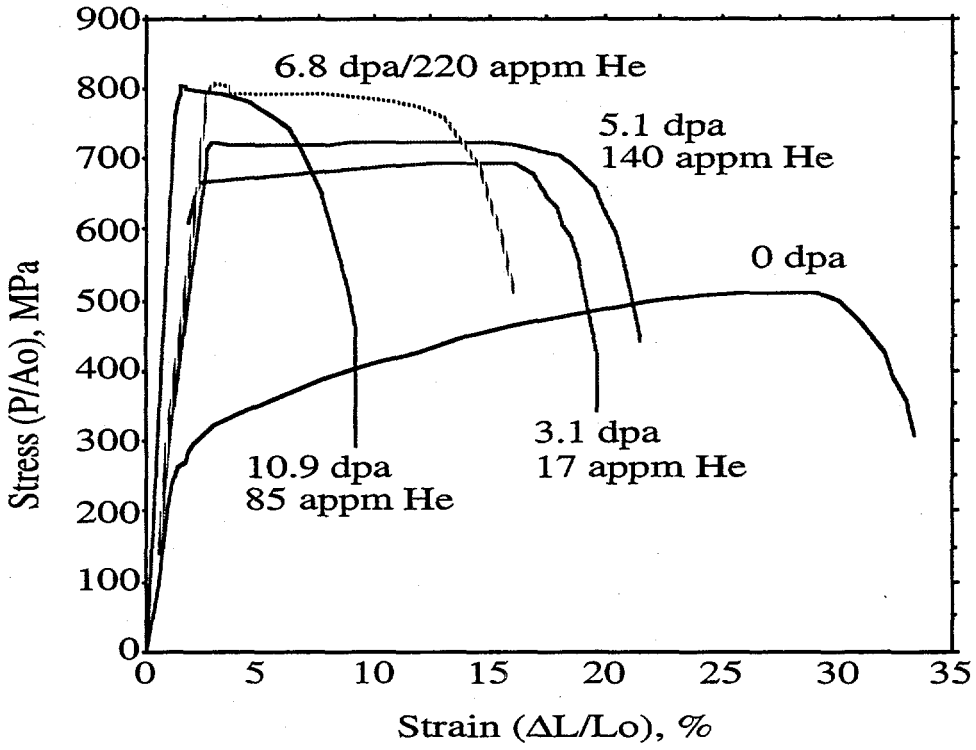

Fig. 1 Typical variation of the uniaxial stress-strain curve of Type 316 LN-IG stainless steel with fluence at 250°-270°C.

In the traditional design codes as well as ISDC, one option for guarding against ratcheting due to C-type loading is the $3S_m$ limit for primary plus secondary stress intensity. However, the $3S_m$ limit is often unduly conservative, particularly for designs with low primary stress. An alternative rule that is usually less conservative than the $3S_m$ rule, is based on the Bree diagram and has been adopted in the ISDC.

Implication of ISDC on allowable surface heat flux

To illustrate the implication of the design rules of ISDC on the surface heat flux capability of irradiated fusion reactor blanket/first wall, we consider a typical first wall geometry, shown in Fig. 2, subjected to a surface heat flux (Q) and coolant pressure (p). Thus, the temperature distribution through the structure is bilinear, being constant in the back wall. In most cases, the boundary condition considered is one of generalized plane strain, i.e., the structure can expand freely in-plane without bending out-of-plane. In one case, we considered the effects of complete constraint to expansion and bending. The design rules considered for setting the surface heat flux limits are (1) the $3S_m$ rule for primary plus secondary stresses, (2) the S_e limit for

primary plus secondary membrane stress, (3) the S_d limit for primary plus secondary stress without peak stress, and (4) ratcheting limit based on Bree diagram rule.[1] In addition, we also indicate the limits implied by various maximum material temperature limits. Note that the $3S_m$ limits can be exceeded provided the Bree diagram rule is satisfied. We have not included limits based on fast fracture, creep, fatigue or those due to stress concentration effects at the coolant hole corners. For the design configuration and coolant pressures considered, the primary and secondary membrane stresses are very low and the permissible surface heat fluxes as determined by the S_e limit are never controlling and therefore not reported except in the case of a fully constrained blanket/first wall. Because of the simplicity of the stress analysis model, the surface heat flux limits reported here should be considered for comparison purposes only and should not be viewed as absolute limits.

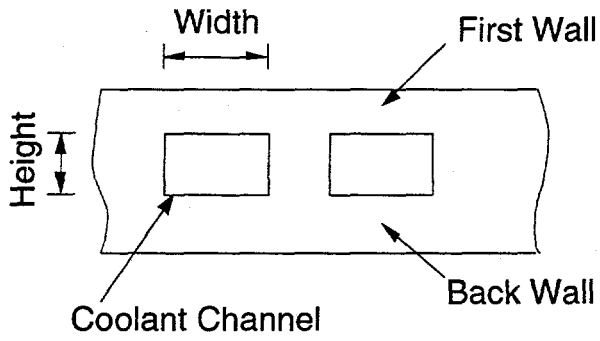

Fig. 2 Typical first-wall/coolant-channel/back-wall geometry considered.

Type 316 stainless steel

The surface heat flux limits for a low-temperature/low-pressure and high-temperature/high-pressure designs are shown in Figs. 3a and 3b, respectively. Since the Bree diagram ratcheting limit falls above the maximum ordinate value shown, the $3S_m$ limits for the low temperature design (Fig. 3a) can be exceeded up to the T_{max}=425°C limits. Even in the irradiation embrittled condition ($\varepsilon_u < 2\%$), the $3S_m$ limits can be exceeded significantly. In the high-temperature/high-pressure design (Fig. 3b), the various allowable surface heat flux curves are shifted differently and the irradiation embrittlement (S_d) limit is never controlling unless the T_{max} = 550°C limit can be exceeded significantly. At small first wall thicknesses, the $3S_m$ limit is above the Bree limit because a small but finite ratcheting strain will occur only during the first cycle. The $3S_m$ limit can be exceeded up to the Bree limit beyond a first wall thickness of 3.5 mm; however, the T_{max} = 550°C limit is violated above a thickness of 4 mm.

Vanadium alloy

The surface heat flux limits for a V-4Cr-4Ti blanket/first wall design are shown for generalized plane strain and fully constrained conditions in Figs. 4a and 4b, respectively. In both cases, the allowable surface heat flux can exceed the $3S_m$ limit up to the Bree limit or the T_{max} limit, whichever is less. For the generalized plane strain case (Fig. 4a), the surface heat flux limits by irradiation embrittlement (S_d) rule fall below the Bree limits but can exceed the $3S_m$ limits without violating the T_{max} = 700°C limits up to a first wall thickness of 4 mm. For first wall thicknesses $\geq$ 5 mm, T_{max} = 700°C limit is below even the $3S_m$ limit. For the fully constrained

case (Fig. 4b), the $3S_m$ limits, the S_d limits, and the Bree limits are all shifted downwards by about 0.5 MW/m^2. Although the surface heat flux limits due to primary plus secondary membrane stress limits (S_e) fall within the range of the ordinates plotted, they are still much higher than the S_d limits or the $T_{max} = 750°C$ limits.

Conclusions

New rules using the concept of elastic follow up factor (r-factor) have been included in the ISDC to account for the loss of uniform elongation (strain hardening) and true strain at rupture due to irradiation. For designs with low primary stress, the primary plus secondary membrane stress limit (S_e) may never be controlling.

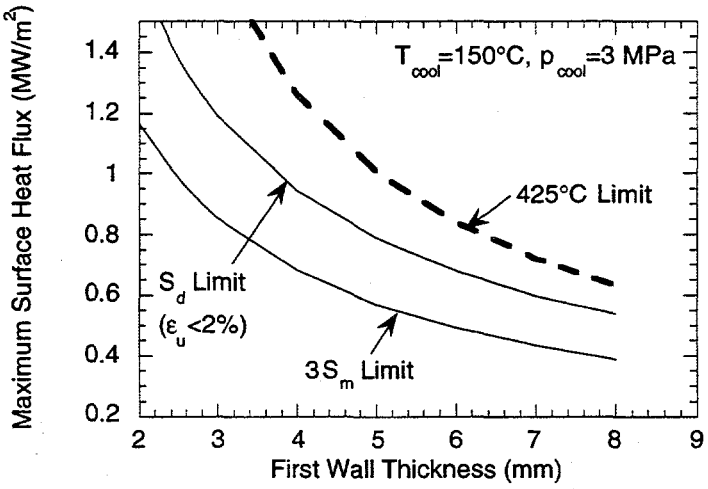

(a)

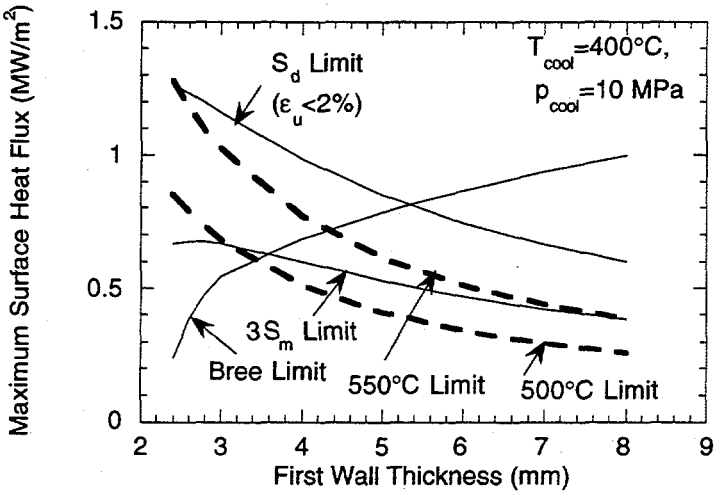

(b)

Fig. 3 Surface heat flux limits as functions of first wall thickness on type 316 stainless steel blankets with a 5 mm thick back wall for a (a) low temperature, low pressure design with 8 mm wide 4 mm high coolant channels and (b) high temperature, high pressure design with 10 mm wide and 20 mm high coolant channels.

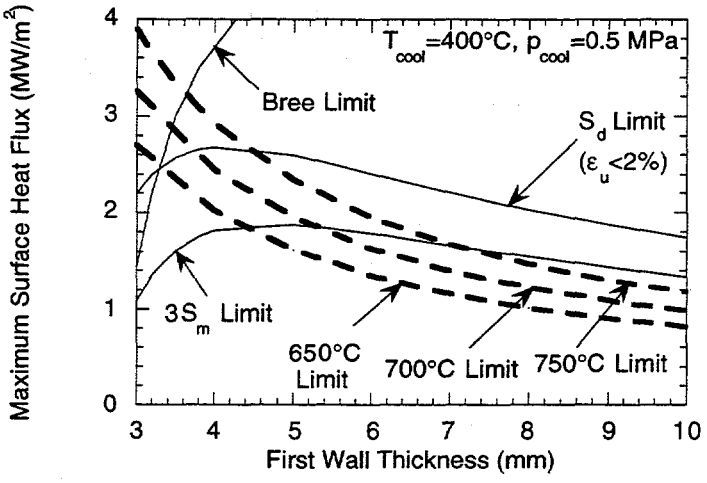

(a)

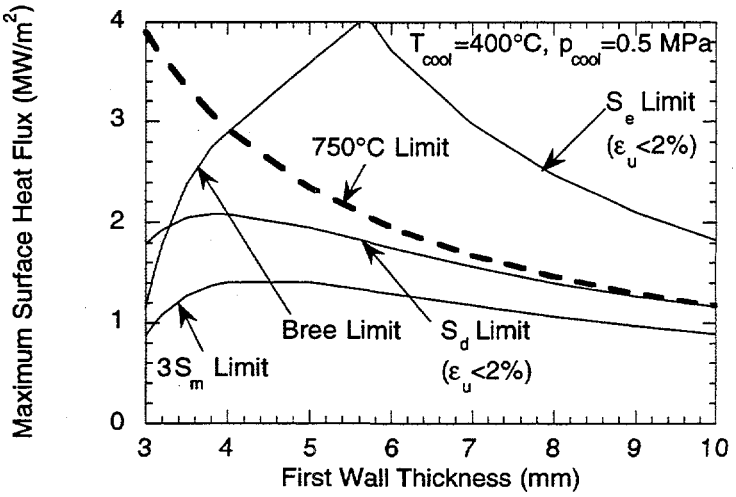

(b)

Figure 4 Surface heat flux limits as functions of first wall thickness on V-4Cr-4Ti blankets with a 5 mm thick back wall, 100 mm wide and 50 mm high coolant channels for (a) generalized plane strain condition and (b) fully constrained condition.

The maximum surface heat flux limits by the various design rules considered here for first wall designs with drilled rectangular coolant channels depend on design variables such as coolant temperature, coolant pressure, material, first wall thickness, degree and type of constraint to deformation. In most cases, the $3S_m$ rule provides the most conservative values of permissible surface heat flux. These limits can be exceeded up to the Bree limits provided the maximum metal temperature limits are not exceeded. For the vanadium alloy blanket, the maximum metal temperature limits can be the controlling criterion for maximum surface heat flux, particularly for first wall thickness > 4 - 5 mm and if a conservative criterion such as T_{max} = 650°C is imposed. Thus, the maximum heat flux capability of vanadium alloy blankets may be significantly increased if the maximum temperature criterion can be relaxed. To emphasize, the surface heat flux limits presented here are not absolute limits, but are used only for comparison purposes.

REFERENCES

1. S. Majumdar and P. Smith, "Treatment of Irradiation Effects in Structural Design Criteria for Fusion Reactors," Proc. 4th Intl. Symp. on Fusion Nucl. Tech. (ISFNT-4), April 6-11, 1997, Tokyo.

2. M. G. Horsten and M. I. deVries, "Irradiation Hardening and Loss of Ductility of Type 316 L(N) Stainless Steel Plate Material due to Neutron Irradiation", ASTM-STP-1270, Amer. Soc. for Testing and Mat., (1996), pp. 919-932.

3. J. E. Pawel, A. F. Rowcliffe, D. J. Alexander, M. L. Grossbeck, and K. Shibata, "Effects of Low Temperature Neutron Irradiation on Deformation Behavior of Austenitic Stainless Steels", J. Nucl. Mat., Vol. 233-237 (1996), pp. 202-206.

4. G. E. Lucas, M. Billone, J. E. Pawel, and M. L. Hamilton, "Implications of Radiation-Induced Reductions in Ductility to the Design of Austenitic Stainless Steel Structures, J. Nucl. Mat., Vol. 233-237 (1996), pp. 207-212.

5. A. A. Tavassoli, Assessment of austenitic stainless steels, ITER Task BL-URD3 Report F. A. 3591-ITER, June 1994.

6. L. L. Snead, S. J. Zinkle, D. J. Alexander, A. F. Rowcliffe, J. P. Roberson, and W. S. Eatherly, "Summary of the Investigation of Low Temperature, Low Dose Radiation Effects on the V-4Cr-4Ti Alloy", Fusion Reactor Materials Semiannual Progress Report for the Period Ending December 31, 1997, DOE/ER-0313/23.

ELASTIC-PLASTIC ANALYSIS OF THE SS-3 TENSILE SPECIMEN*

S. Majumdar (Argonne National Laboratory)

SUMMARY

Tensile tests of most irradiated specimens of vanadium alloys are conducted using the miniature SS-3 specimen which is not ASTM approved. Detailed elastic-plastic finite element analysis of the specimen was conducted to show that, as long as the ultimate to yield strength ratio is less than or equal to 1.25 (which is satisfied by many irradiated materials), the stress-plastic strain curve obtained by using such a specimen is representative of the true material behavior.

PROGRESS AND STATUS

Introduction

The SS-3 specimen has a much shorter gage length than typical ASTM-standard tensile specimens. More importantly, the solid area ratio between a section at the hole and that at the gage center is only 1.9 for the SS-3 specimen compared to 3 for typical ASTM standard specimens. This large area ratio in the ASTM standard specimen guarantees that there is little or no yielding in the grip section of the specimen during a tensile test. This is an important consideration for tests in which strain is not measured directly by an extensometer because errors will be introduced in the stress-strain curve as obtained from the measured load-displacement curve if large plastic strains occur outside the gage in the grip section. For this reason, if the ultimate to yield strength ratio of the test material is ≥ 1.9, the SS-3 specimen cannot be used to obtain the stress-strain curve. Even for materials with the ultimate to yield strength ratio < 1.9 (e.g., irradiated materials), there is a greater chance for yielding in the grip section of the SS-3 specimen than in an ASTM standard specimen, principally due to stress concentration effects. Elastic-plastic finite element analyses were conducted to estimate the effect of plastic yielding outside the gage section on the measured load-displacement (thus the stress-strain) curve.

Model for analysis

One quarter of the SS-3 (Fig. 1) specimen was analyzed using the finite element (4100 nodes and 3900 elements) program ANSYS with elastic-plastic material properties of irradiated (0.4 dpa) V-4Cr-4Ti at 420°C as reported in reference 1 (yield = 340 MPa, ultimate = 430 MPa and uniform elongation = 8%). The loading pin was assumed to be perfectly rigid and an initial radial clearance of 0.025 mm was assumed between the hole and the loading pin. Contact elements were used for modeling the transmission of load from the pin to the specimen. Thus, initially there was a line contact and the area of contact increased with increased loading. The analysis was carried out till 5% plastic strain (420 MPa) at the gage section.

---

* Work supported by U.S. Department of Energy, Office of Fusion Energy Research, under Contract W31-109-Eng-38.

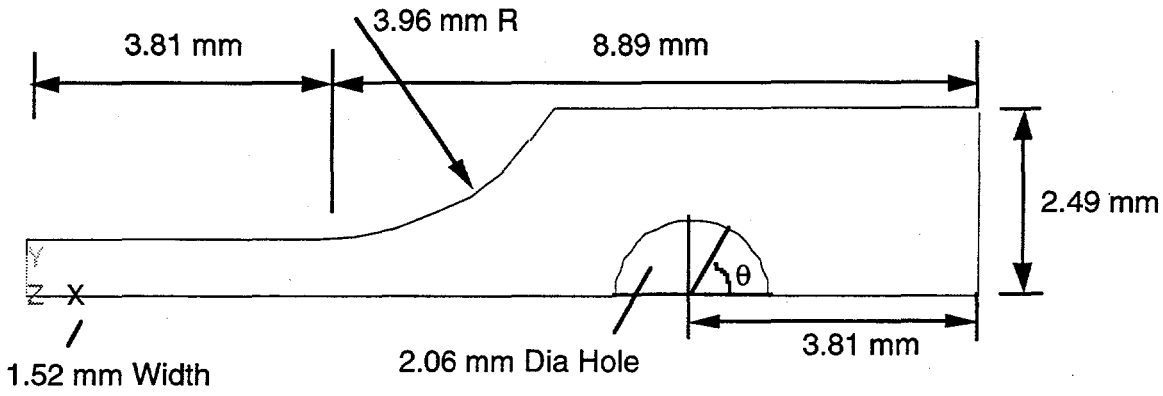

Fig.1 Geometry of specimen SS-3 (1/4 of specimen shown) with a thickness of 0.76 mm.

Results

A contour plot of tangential plastic strain near the hole at the final loading is shown in Fig. 2. There is about a 0.5% maximum plastic strain at the edge of the hole at the minimum cross-section of the specimen and a 1% plastic strain at the point of contact. However, note that the zones of tensile plastic strain are fully contained within elastic enclaves. The fact that the tensile plastic zone does not spread to the lateral free surface of the specimen is not surprising because the ultimate to yield ratio for this material is about 1.25 which is less than the area ratio 1.9.

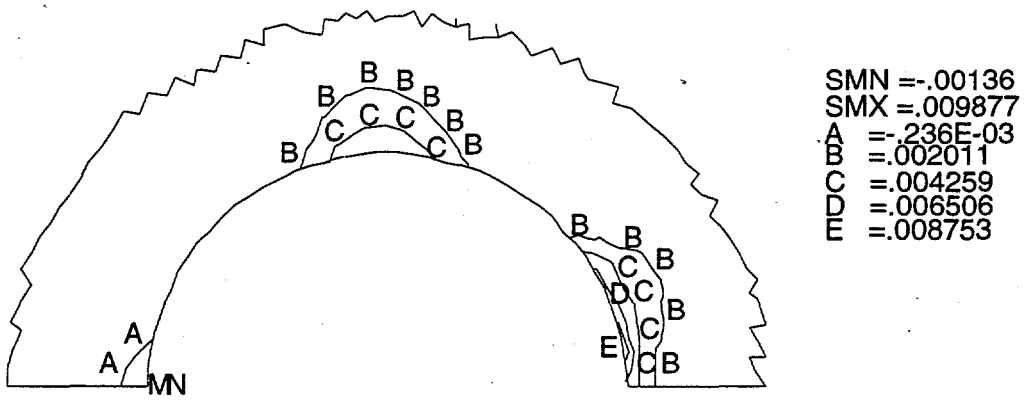

Fig. 2 Contours of constant hoop plastic strain near the hole for a gage section plastic strain of 0.05 (stress = 420 MPa).

Angular variations (angle θ defined in Fig. 1) of the radial contact stress and radial plastic strain at the periphery of the hole at various gage section stress levels are shown in Figs. 3a and 3b, respectively. Compressive plastic yielding starts at the contact point from the very beginning and spreads with increased loading up to θ=40° at the final load level. Significant yielding occurs near the hole before there is any yielding at the gage section.

Significant yielding in the grip area could introduce nonlinearity in the load-displacement curve before the onset of yielding in the gage section and thus make the usefulness of the load-displacement curve questionable. To check this out, the load-displacement curve from the finite element analysis was used to derive the stress strain curve assuming that the displacements in

the finite element analysis was used to derive the stress strain curve assuming that the displacements in the grip sections were negligible, i.e., the strain was obtained by dividing the total displacement at the loading pin by the gage length (7.62 mm.). A comparison between the derived and the input stress-strain curves, shown in Fig. 4a, shows that this assumption is incorrect because a significant component of the displacement comes from the grip section outside the gage.

Next, in accordance with usual experimental procedure, the stress-plastic strain curve was derived from the computed load displacement curve by first subtracting the elastic (initial linear part) displacement from the total displacement to obtain the plastic displacement and then attributing the plastic displacement to the uniform gage section only. The resulting stress-plastic strain curve is compared with the input stress-plastic strain curve in Fig. 4b. The good agreement between the two shows that in spite of significant yielding in the grip section, the stress-plastic strain curve for this material can be obtained from the load-displacement curve with good accuracy.

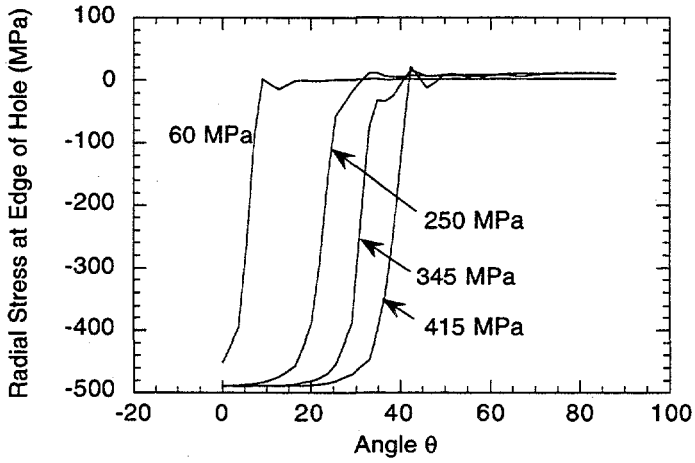

(a)

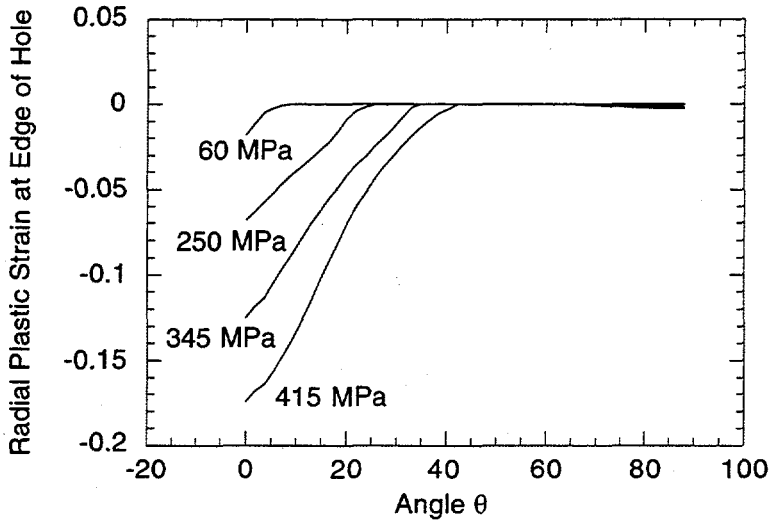

(b)

Fig. 3 Angular variations of radial (a) contact stress and (b) plastic strain at the edge of the hole for various values of gage section stress.

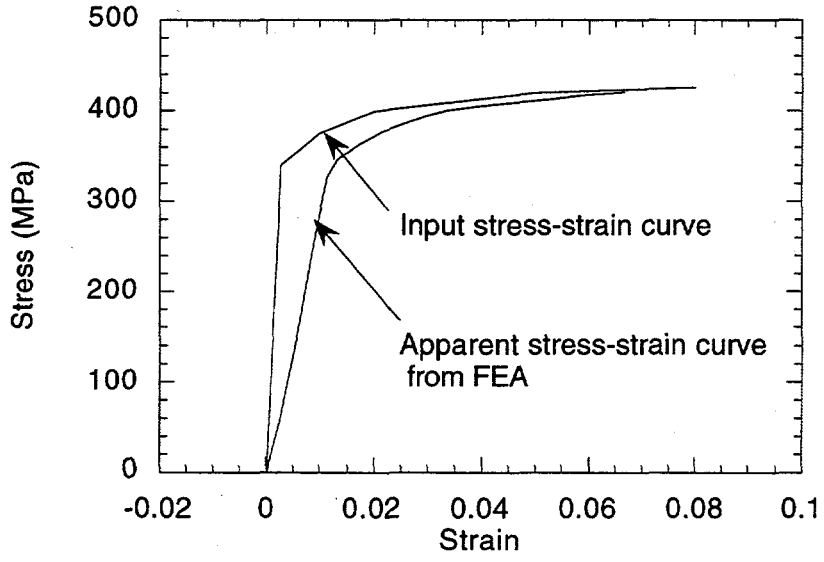

(a)

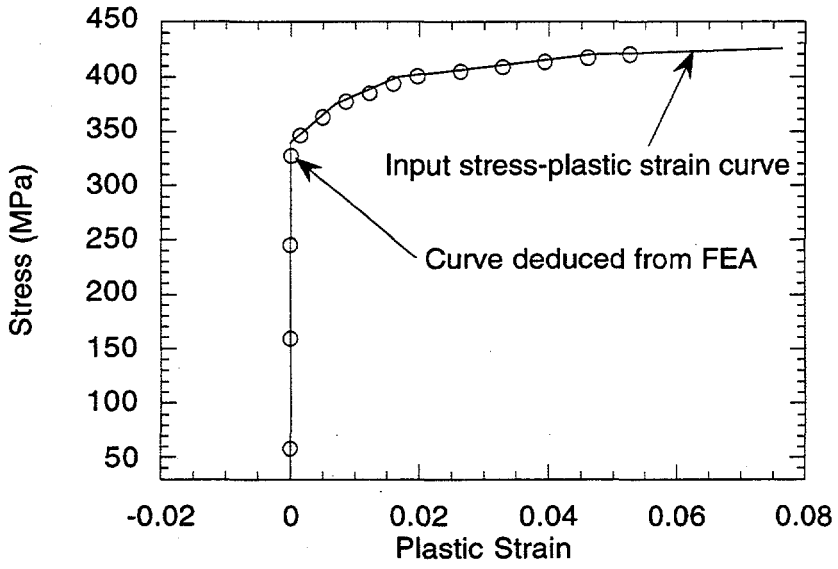

(b)

Fig. 4 Comparisons of (a) input stress-strain curve and apparent stress-strain curve derived from load-displacement curve by FEA and (b) input stress-plastic strain curve and stress-plastic strain curve derived from computed load-displacement curve by FEA.

Discussions and Conclusions

A detailed elastic-plastic finite element analysis of the SS-3 specimen using stress-strain curve for irradiated V-4Cr-4Ti at 420°C showed that large compressive plastic strains occurred at the contact area between the loading pin and the specimen. Significant tensile yielding also occurred at the periphery of the hole 90° away from the contact zone due to stress concentration effects. However for materials with ultimate to yield ratio of 1.25, this plastic zone was fully contained within an elastic enclave. As a result, the contributions of these plastic strains to the plastic displacement of the loading pin were small compared to those from the gage section. Thus, the stress-plastic strain curve for this material can be derived from the load-displacement curve with good accuracy. However, note that it was assumed that the material at the contact area continued to carry high compressive stress (ultimate stress) with high accumulated compressive plastic strain (much greater than uniform elongation) without cracking. If the compressive ductility (or the crushing strength) of the material is reduced by irradiation significantly and the contact area experiences cracking, non-linearity in the load-displacement curve may occur before the gage section reaches yield, thus introducing some uncertainty in the determination of the yield stress.

The SS-3 specimen is acceptable for irradiated materials for which the ultimate to yield strength ratio is low (≤1.25). However, unless an extensometer is used to measure the gage section strain directly, only the stress-plastic strain curve can be obtained - the full stress-strain curve cannot be obtained.

REFERENCE

1. Thermophysical and mechanical properties for V-(4-5%)Cr-(4-5%)Ti Alloys, draft report by S. J. Zinkle, Oak Ridge National Laboratory, May 1, 1998.

11.0 IRRADIATION FACILITIES, TEST MATRICES, AND EXPERIMENTAL METHODS

STATUS OF LITHIUM-FILLED SPECIMEN SUBCAPSULES FOR THE HFIR-MFE-RB-10J EXPERIMENT — J. P. Robertson, M. Howell, and K. E. Lenox (Oak Ridge National Laboratory)

OBJECTIVES

The objective of this research is to irradiate a sufficient variety and number of mechanical properties specimens of V-4Cr-4Ti at 420 and 480°C in order to study the flow and fracture behavior and to establish a mechanism-based approach to modeling the effects of external parameters on fracture.

SUMMARY

The HFIR-MFE-RB-10J experiment will be irradiated in a Removable Beryllium position in the HFIR for 10 reactor cycles, accumulating approximately 5 dpa in steel. The upper region of the capsule contains two lithium-filled subcapsules containing vanadium specimens. This report describes the techniques developed to achieve a satisfactory lithium fill with a specimen occupancy of 26% in each subcapsule.

PROGRESS AND STATUS

The HFIR-MFE-RB-10J experiment, conducted under the U. S. DOE/Japan Atomic Energy Research Institute Collaborative Testing Program, will be irradiated in a Removable Beryllium position in the HFIR for 10 reactor cycles, accumulating approximately 5 dpa in steel. The upper region of the capsule contains two lithium-filled subcapsules containing vanadium specimens. One subcapsule will operate at 420°C and one will operate at 480°C. The lower region of the capsule contains austenitic and ferritic steel specimens operating at 250°C. The capsule will be surrounded by a Eu_2O_3 shield in order to harden the spectrum and prevent unwanted transmutations.

The vanadium specimens in this experiment were encapsulated in lithium-filled subcapsules to control the vanadium absorption of the interstitial impurities carbon, nitrogen, and oxygen, and to provide temperature uniformity between specimens.

There were five major issues to be resolved prior to filling the subcapsules with lithium and each of these is briefly discussed here. A complete report is in progress.

Specimen loading: Each subcapsule was made out of type 316 stainless steel. The interior diameter was 2.62 cm and the interior height was 9.75 cm. Fifty-one SS-3 type flat tensile specimens, 23 one-third size pre-cracked Charpy V-notch specimens, six creep tubes, one DC(T) fracture toughness specimen, and one 1.52 cm-long tube containing 25 TEM disks were put into each subcapsule. A loading arrangement had to be devised such that all the specimens fit and were surrounded by lithium, and that they stayed in place during the various welding and inspection procedures. The specimens were arranged into three layers such that the top of the upper layer was 5.59 cm high in the capsule, leaving a gas gap at the top of the capsule of 4.17 cm. This gas gap was required to be at least 1.45 cm in order to accommodate all of the gas contained in the pressurized tubes, should they burst. A sleeve of high purity vanadium sheet metal was fit inside the capsule to minimize the exposure of the lithium to the steel wall and to serve as a getter material during irradiation. Of the total internal subcapsule volume, including the necessary gas gap, vanadium specimens occupy 26%. For comparison, the specimen packing fraction in the EBR-II X530 experiment ranged from about 11 (for a mixture of SS-3 tensile and TEM disk specimens) to 33% (for a mixture of DCT-B specimens and 1/3-size Charpy specimens) for the various subcapsules [1].

handled in a flowing argon glovebox and specimens taken for analyses were triply contained in glass bottles, plastic zipper bags, and mason jars. After purification, samples were taken by forcing a small amount of the Li into a "dead-end" tube that was then welded closed. The metals analyses were performed in the Chemical and Analytical Sciences Division of ORNL. The oxygen content was analyzed by neutron activation analysis in the Analytical Services Organization (ASO) at Y-12. The ASO also performed nitrogen analyses using a modified Kjeldahl procedure. Twin samples were also sent to the Analytical Chemistry Laboratory of Argonne National Laboratory for analysis via the modified Kjeldahl procedure. In each instance, the receiving laboratory was notified of the sample shipment and was prepared to take the appropriate actions to maintain the cleanliness of the sample. The on-site sample shipments were made by special courier and the shipments to ANL were by overnight express mail.

Lithium source and purification: "High purity" Li-7 was obtained from the Y-12 Plant in Oak Ridge. This isotope of lithium was chosen in order to reduce the production of tritium by transmutation reactions in the HFIR. The lithium was 99.99% Li-7. Because of its cost and rarity, extreme care was used to minimize the volumes left behind as "scrap" in the processing steps. The Li-7 was provided in the form of irregular chunks, approximately 125 cm^3 each. The chunks were melted, slagged, and then gettered with chromium chips and then zirconium chips and titanium foil. The as-melted material had a nitrogen content of 540 μg/g (540 wt ppm), an oxygen content of 0.17%, and only trace amounts of metallic impurities. The lithium was pushed through a 40 μm filter to remove any remaining slag material and the larger oxide particles but no attempt was made to getter for oxygen. The as-gettered material that went into the experimental capsules had a nitrogen content of 26 μg/g (26 wt ppm) and an oxygen content of 0.16 wt%.

Capsule filling: The capsules were filled using a technique known as the "blowback" method. In this technique, the specimens are placed inside the capsule and the capsule head is welded in place. This head has two penetrating tubes: lithium flows in one, fills the capsule, and overflows out the exit tube. After the capsule is completely full, high purity helium is blown back through the exit tube and the excess Li is blown back through the fill tube to the reservoir. Once the Li level recedes down to the height of the fill tube, only helium gas flows back up the fill tube and the Li level is set. For the fill process, the Li was pushed under high purity He gas pressure through clean stainless steel tubing. All connections were made with stainless steel swagelock fittings. In preparation for capsule filling, the lithium temperature was raised to 400°C. This temperature was a compromise based on two factors: as the temperature increases, lithium is more likely to wet the steel capsule and the vanadium specimens and the lithium flows easier in the transfer tubes. Above 500°C, however, the lithium begins to leach nickel from the stainless steel. Prior to filling, the capsule was evacuated to a vacuum on the order of 10^{-1} torr. A valve on the exit tube was closed and the Li was forced in from the reservoir; the pressure was gradually increased to 69 kPa. The lithium was then blown back with both minimum pressure and flow rate. The capsule was then left to soak at temperature (400°C) and a vibration applied. After a soak/vibration of about 45 minutes, the fill and blowback processes were repeated. After the capsule was filled, the fill and exit tubes were crimped closed using a specially designed tool to ensure a good seal. The exterior portion of these tubes were then cut to the design length and welded.

Detection of fill level: The nature of this fill process required the establishment of a non-destructive technique to measure the lithium fill level. A number of techniques were attempted but only two proved very useful. Both were performed on the capsules while they were still attached to the fill system so that, if the fill was not adequate, the capsules could be filled again. Once the fill tubes are crimped and the capsule removed from the fill system, no more lithium can be added. Standard x-ray radiographs using a portable x-ray source were taken of the capsules while they were still attached to the system. The lithium level showed up as a faint contrast change against the black of the gas gap at the top of the capsule. The steel wall, the steel fill tubes, and the vanadium specimens appeared very bright and the lithium contrast was not visible in these regions. The second useful technique was a variation on ultrasonics. Through experimentation, it was determined that a relationship existed between the presence of Li and the wall ringing induced by an ultrasonic transducer. Even though several interfaces existed because

of the capsule liner, the lithium dampened the ringing significantly. This damping was used to estimate the fill level to within about 0.3 cm. This same method could was also used to locate and size any significant (greater than 1.3 cm diameter) internal voids within the capsule.

CONCLUSIONS

The techniques outlined above resulted in the successful filling of the two subcapsules required for the HFIR-MFE-RB-10J experiment. The fill level was confirmed by x-ray and by ultrasound and the fill uniformity was confirmed by ultrasound and by a post-weld weight measurement. The shape of the lithium meniscus seen in the x-ray implies that the lithium is wetting the vanadium liner and therefore is also wetting the vanadium specimens .

FUTURE WORK

A complete report detailing all aspects of this project is in progress.

REFERENCES

1. H. Tsai, R. V. Strain, A. G. Hins, H. M. Chung, L. J. Nowicki, and D. L. Smith, in Fusion Materials Semiannual Progress Report (March 31, 1995), DOE/ER-0313/18, U.S. DOE Office of Fusion Energy, July 1995, p. 85.

SPECIMEN LOADING LIST FOR THE VARYING TEMPERATURE EXPERIMENT —

A. L. Qualls and R. G. Sitterson (Oak Ridge National Laboratory)

OBJECTIVE

The objective of this report is to present a detailed summary of the specimen loading for the DOE/MONBUSHO varying temperature irradiation experiment HFIR-RB-13J.

SUMMARY

The varying temperature experiment HFIR-RB-13J has been assembled and inserted in the reactor. Approximately 5300 specimens were cleaned, inspected, matched, and loaded into four specimen holders. A listing of each specimen loaded into the steady temperature holder, its position in the capsule, and the identification of the corresponding specimen loaded into the varying temperature holder is presented in this report.

PROGRESS AND STATUS

Introduction

The varying temperature experiment [1,2] was assembled during the last reporting period. Approximately 5300 specimens were cleaned, inspected, matched, and loaded into four specimen holders. The purpose of this experiment is to investigate the effects of neutron fluence on the microstructure and mechanical properties of candidate fusion reactor structural materials to the effects of receiving 10% of the fluence at reduced temperature.

The specimens were loaded into holders, which were then pumped under high vacuum, backfilled to a pressure of 1 atmosphere with clean, dry helium (water content < 1 ppm, oxygen content < 2 ppm) and sealed. The sealed holders were assembled into the experimental region of the capsule. This loading report documents specimen location within the capsule along with some details concerning final assembly. Specimen locations are denoted in terms of 1) holder (350°C or 500°C), 2) hole (B1, B2,...,T4, T5), 3) axial position within hole and, 4) location within axial position (where applicable). Locations within axial positions are listed differently for different specimen types. Tensile specimens are listed in order of their position in a stack of 13 to 17. TEMs are listed in order of their insertion into the tube. Bend bar specimens (Bend Bar #7) are listed according to their position within a stack of 10 specimens placed in the square channel of a sleeve (top row, side, or bottom). CVN specimens are also listed according to their location in a stack of 4 specimens placed in an identical sleeve (top, or bottom).

A listing of each specimen loaded into a steady temperature holder, its position (holder, hole, position in hole, position within position) in the capsule, and the number of the corresponding specimen loaded into a varying temperature holder is provided in Appendix A of this report. A "b" or "nm" in the match column indicates that the specimen does not have a match. Some expected specimens were missing and were not loaded, however the match may be loaded and is listed if so. Experimenters were notified individually about missing specimens.

Specimen Loading

Loading of the four holders is rather complicated. Matched specimens are located an equal distance above (steady temperature zones) and below (varying temperature zones) the reactor mid-plane in order to receive similar neutron fluences. Holders located opposite the reactor mid-plane see inverted flux gradients, therefore specimens loaded in the top of an upper holder must have their match located in the bottom of a lower holder to properly match fluences.

Generally, specimens of a single type supplied by the an experimenter are located at or about the same elevation within a holder. For example, Dr. Kimura has tensile specimens in three of the four tensile holes of each holder. His specimens are irradiated at the top of the steady temperature holders (upper holders) and at the bottom of the varying temperature holders (lower holders) in order to put them into similar flux regions. Two of the tensile holes load from the top of the holder and two from the bottom. Therefore Dr. Kimura's tensiles are loaded as the last group of the stack into the holes open at the top of the upper holders, as the first group of the stack into the holes at the bottom of the upper holders, as the first group of the stack into the holes at the top of the lower holders, and as the last group of the stack into the holes at the bottom of the lower holders.

The holes are numbered from a Top Dead Center (TDC) mark on the top of the holders counting in the clockwise direction. T2 and T5 are tensile holes. The holes on the bottom of the holders are numbered from this same TDC mark as projected onto the bottom surface, counting in the clockwise direction from the projected mark as you look directly at the bottom surface. The projected mark passes through a tensile hole numbered B1.

The numbering of positions within specimen stacks is counted from the top of the holders. There are 5 tensile positions, 4 CVN positions, 8 bar positions, and 2 TEM positions. Again, as an example, Dr. Kimura's tensile specimens loaded at the top of the upper holders are in position 1, whether the hole was loaded from the bottom or top. The matching specimens are loaded into position 5 of the tensile holes in the lower holders.

When loading the specimens, the following steps were taken:

(1) Specimens were formed into two matching groups.
(2) The groups were formed into stacks and loaded into sleeves.
(3) One end of each sleeve was marked with the desired holder and hole number such that the orientation of the sleeve could be verified as it was inserted.

As a sleeve was inserted, the hole number was checked against the sleeve number, and photographs were taken of the identifying marks.

Loading of the Tensile Specimens
(T2,T5,B1,B4)

The tensile specimens were arranged into groups of approximately 15. The groups are held together using pure tungsten wire shaped in the form of a cotter pin with the bent end twisted 90 degree from the legs. The tensile specimens were stacked face to face and the pins were inserted through the end tab holes. The looped end of the wire constrains one end specimen and the two legs are bent to constrain the other end specimen. This was done to assist with loading and to hold specimens in the proper orientation for heat transfer.

Loading of the CVN specimens
(B3, B5, T3)

The CVN specimens are arranged into groups of 4 and stacked into 4 axial positions within a sleeve. The sleeve is a cylindrical bar with a machined square channel along its axis and a cap that covers the specimens in the channel and completes the cylinder. The cap has end tabs which prevent specimens from sliding out the end of the channel.

Loading of the TEM specimens
(T1, B4, B6)

The TEMs are loaded into tubes. Two of these tubes are inserted into three holes in each holder. The tubes are labeled as either "holder-hole-A" or "holder-hole-B", and are marked at the end

into which the specimens were inserted. In other words, the last specimen loaded is directly under the marked end of the tube. The first specimen loaded into a tube is numbered 1, and the successive specimens are numbered accordingly. In the top holes of the upper holders, tube B is inserted first and tube A is loaded on top of it. The marked end of the tube B is near the middle of the holder and the marked end of tube A is near the top of the holder. For the holes on the bottom of the upper holders, tube A was inserted in the inverted position (the mark could not be seen) and then B was inverted and inserted after A. Again, the marked end of the A tubes are at the top of the upper holders and the marked end of the B tubes are near the middle of the holders. Therefore, specimen 1 in tube A is near the center of the holder in all holes. Specimen 1 of tube B is always near the bottom of the steady temperature holders.

The tubes in the lower holders are loaded inverted with respect to those in the upper holders. For the top holes of the lower holder, tube A was inverted (marks could not be seen) and inserted and then tube B was inverted and inserted on top of A. The marked end of A was near the bottom of the lower holders and the marked end of B was near the middle of the lower holders. Specimen 1 of tube A is near the middle of the holder. Specimen 1 of tube B is near the top of the lower holders. For the bottom holes of the lower holders, B was inserted first (marked end near the middle) and A was placed on top of it (marked end near the bottom). Again, specimen 1 of tube A is near the middle of the holder. Specimen 1 of tube B is near the top of the lower holders. When looking into the holes before sealing them, the marks of the A tubes could be seen in the top holes of the upper holders and in the bottom holes of the lower holders.

The order in which TEMs were loaded in the tube are included in the final loading list. This is indicative of the numbered location of the specimen in the tube. It does not provide the actual location of the specimen, because of variations in the thickness of specimens. Tubes that are not completely filled by the specimens have Dispal spacers to fill the remainder of the tube. The lengths of the spacers are recorded, and an estimated location of each specimen will be provided along with an estimated fluence after irradiation has been completed and the dosimetry analyzed.

Loading of the Bar-7 specimens
(B2)

The Bar-7 specimens are loaded into a sleeve and capped, similar to what was done for the CVN specimens. There are 10 specimens to a group and eight groups to a stack. There is only one stack per holder. A Dispal filler piece is inserted into the middle of the groups to complete the square. All of the specimens are located on the outside layer of the grouping, and at least one surface of each specimen is in contact with the either the sleeve or the sleeve cap.

Thermometry and Dosimetry

The majority of the thermometry in the holders are included in three Thermocouple Array Tubes (TCATS) that extend the entire length of the four stacked holders. The TCATs are located at different angular locations at the same radial position within the holders. Each contain seven thermocouple junctions which are displaced over the length of the four holders so that each holder has 5 thermocouple junctions, equally spaced in the axial direction, within it.

Each holder contains a hole filled with dosimetry and dummy specimens. The dummy specimens are intended to provide a measured indication of the temperature difference from the centerline of specimens to the thermocouple junctions in the TCATS. Initially, two dummy specimen groups were to be measured in each holder, however, all of the intended measurements are not included in the final assembly.

A reduced sized tensile specimen sleeve was designed to fit into the smaller dummy specimen hole, however it could not be inserted unless the number of specimens in it was reduced to the point that the measurement was no longer valid. Instead of inserting tensile specimens, a solid cylinder of Dispal was fabricated and inserted in the two locations originally designated for the

dummy tensile specimens. The outer diameter of the sleeve is identical to that of the sleeves containing the CVN and BAR7 specimens and the TEM housing tubes. This measurement will provide an indication of the temperature difference from the holder to a specimen sleeve.

Several thermocouples installed into the upper holders were damaged by the insertion and pulling of the electric resistance heaters into position. Therefore, some of the dummy specimens inserted do not have working thermocouples installed and the data is simply lost. The loading of the dummy specimens is as follows:

Holder	Location
LTST	Dispal Blank in top dummy specimen location
HTST	Tungsten Bar 7 specimens in bottom specimen location
HTST	Stainless Steel TEM specimens in top specimen location
HTST	CVN specimens in bottom specimen location
HTVT	CVN specimens in bottom specimen location

The capsule contains neutron dosimetry near the top and bottom of the four holders. The dosimetry capsules were provided by L. R. Greenwood of PNNL and are numbered as follows:

53	Top of LTST holder
56	Bottom of LTST holder
59	Top of HTST holder
61	Bottom of HTST holder
62	Top of HTVT holder
63	Bottom of HTVT holder
70	Top of LTVT holder
71	Bottom of LTVT holder

The dosimetry will be retrieved and analyzed after irradiation.

REFERENCES:

1. A. L. Qualls and T. Muroga, "Progress on the Design of a Varying Temperature Irradiation Experiment for Operation in HFIR," Fusion Materials Semiannual Progress Report for period ending December 31, 1996, p. 255.

2. A. L. Qualls, M. T. Hurst, D. L. Raby, D. W. Sparks, and T. Muroga, "Progress Report on the Varying Temperature Experiment," Fusion Materials Semiannual Progress Report for period ending June 30, 1997, p. 243.

Appendix A -

Listing of the Specimens Loaded into the Varying Temperature Experiment

1. Low Temperature Steady Temperature and Low Temperature Variable Temperature Holder

2. High Temperature Steady Temperature and High Temperature Variable Temperature Holder

specimen	experimenter	type	irr. temp.	hole	position	position(2)	affiliation	match
k331	Kimura	tensile	350	b1	1	1	Japan	k231
k332	Kimura	tensile	350	b1	1	2	Japan	k232
k333	Kimura	tensile	350	b1	1	3	Japan	k233
k341	Kimura	tensile	350	b1	1	4	Japan	k241
k342	Kimura	tensile	350	b1	1	5	Japan	k242
k343	Kimura	tensile	350	b1	1	6	Japan	k243
k344	Kimura	tensile	350	b1	1	7	Japan	k244
k345	Kimura	tensile	350	b1	1	8	Japan	k245
k3s1	Kimura	tensile	350	b1	1	9	Japan	k2s1
k3s2	Kimura	tensile	350	b1	1	10	Japan	k2s2
k3s3	Kimura	tensile	350	b1	1	11	Japan	k2s3
k3s4	Kimura	tensile	350	b1	1	12	Japan	k2s4
k3t1	Kimura	tensile	350	b1	1	13	Japan	k2t1
k3t2	Kimura	tensile	350	b1	1	14	Japan	k2t2
k3t3	Kimura	tensile	350	b1	1	15	Japan	k2t3
vc01	US	tensile	350	b1	1	16	US	b
vc02	US	tensile	350	b1	1	17	US	b
lff1	Kohno	tensile	350	b1	2	1	Japan	lfd1
lff2	Kohno	tensile	350	b1	2	2	Japan	lfd2
lff3	Kohno	tensile	350	b1	2	3	Japan	lfd3
lff4	Kohno	tensile	350	b1	2	4	Japan	lfd4
lff5	Kohno	tensile	350	b1	2	5	Japan	lfd5
lff6	Kohno	tensile	350	b1	2	6	Japan	lfd6
lff7	Kohno	tensile	350	b1	2	7	Japan	lfd7
lff8	Kohno	tensile	350	b1	2	8	Japan	lfd8
lbf1	Kohno	tensile	350	b1	2	9	Japan	lbd1
lbf2	Kohno	tensile	350	b1	2	10	Japan	lbd2
lbf3	Kohno	tensile	350	b1	2	11	Japan	lbd3
lbf4	Kohno	tensile	350	b1	2	12	Japan	lbd4
lbf5	Kohno	tensile	350	b1	2	13	Japan	lbd5
l1f1	Kohno	tensile	350	b1	2	14	Japan	l1d1
l1f2	Kohno	tensile	350	b1	2	15	Japan	l1d2
l1f3	Kohno	tensile	350	b1	2	16	Japan	l1d3
f4h7	Satou	tensile	350	B1	3	1	Japan	f4h0
f4h8	Satou	tensile	350	B1	3	2	Japan	f4h1
f4h9	Satou	tensile	350	B1	3	3	Japan	f4h2
f4ha	Satou	tensile	350	B1	3	4	Japan	f4h3
f4hb	Satou	tensile	350	B1	3	5	Japan	f4h4
f4ic2	Satou	tensile	350	B1	3	6	Japan	f4h5
f5k0	Satou	tensile	350	B1	3	7	Japan	f5h0
f5h7	Satou	tensile	350	B1	3	8	Japan	f5h1
f5h8	Satou	tensile	350	B1	3	9	Japan	f5h2
f5h9	Satou	tensile	350	B1	3	10	Japan	f5h3
f5ha	Satou	tensile	350	B1	3	11	Japan	f5h4
f5hb	Satou	tensile	350	B1	3	12	Japan	f5h5
f6h6	Satou	tensile	350	B1	3	13	Japan	f6h0
f6ht	Satou	tensile	350	B1	3	14	Japan	f6h1
f6h8	Satou	tensile	350	b1	3	15	Japan	f6h2
va01	US	tensile	350	b1	3	16	US	b
va02	US	tensile	350	b1	3	17	US	b
t604	Matsui	tensile	350	B1	4	1	Japan	t601
t605	Matsui	tensile	350	B1	4	2	Japan	t602
t606	Matsui	tensile	350	B1	4	3	Japan	t603
t704	Matsui	tensile	350	B1	4	4	Japan	t701
t705	Matsui	tensile	350	B1	4	5	Japan	t702
t706	Matsui	tensile	350	B1	4	6	Japan	t703
t804	Matsui	tensile	350	B1	4	7	Japan	t801
t805	Matsui	tensile	350	B1	4	8	Japan	t802
t806	Matsui	tensile	350	B1	4	9	Japan	t803
ty24	Matsui	tensile	350	B1	4	10	Japan	ty21
ty25	Matsui	tensile	350	B1	4	11	Japan	ty22
ty26	Matsui	tensile	350	B1	4	12	Japan	ty23
tj24	Matsui	tensile	350	B1	4	13	Japan	tj21
tj25	Matsui	tensile	350	B1	4	14	Japan	tj22
tj26	Matsui	tensile	350	B1	4	15	Japan	tj23
t204	Matsui	tensile	350	b1	4	16	Japan	t201
tb01	Kkueh	tensile	350	b1	5	1	US	tb05
tb02	Kkueh	tensile	350	b1	5	2	US	tb06
tb03	Kkueh	tensile	350	b1	5	3	US	tb07
tb04	Kkueh	tensile	350	b1	5	4	US	tb08
xe01	Kkueh	tensile	350	b1	5	5	US	xe05
xe02	Kkueh	tensile	350	b1	5	6	US	xe06
xe03	Kkueh	tensile	350	b1	5	7	US	xe07
xe04	Kkueh	tensile	350	b1	5	8	US	xe08
fp01	Kkueh	tensile	350	b1	5	9	US	fp05
fp02	Kkueh	tensile	350	b1	5	10	US	fp06
fp03	Kkueh	tensile	350	b1	5	11	US	fp07
fp04	Kkueh	tensile	350	b1	5	12	US	fp08
fq01	Kkueh	tensile	350	b1	5	13	US	fq05
fq02	Kkueh	tensile	350	b1	5	14	US	fq06
fq03	Kkueh	tensile	350	b1	5	15	US	fq07
fq04	Kkueh	tensile	350	b1	5	16	US	fq08
gkc1	Kurishita	bar7	350	b2	1	b	Japan	gkc6
gkc2	Kurishita	bar7	350	b2	1	b	Japan	gkc7
gkc3	Kurishita	bar7	350	b2	1	b	Japan	gkc8
gkc4	Kurishita	bar7	350	b2	1	s	Japan	gkc9
gkc5	Kurishita	bar7	350	b2	1	s	Japan	gkca
gkd1	Kurishita	bar7	350	b2	1	s	Japan	gkd6
gkd2	Kurishita	bar7	350	b2	1	s	Japan	gkd7
gkd3	Kurishita	bar7	350	b2	1	t	Japan	gkd8
gkd4	Kurishita	bar7	350	b2	1	t	Japan	gkd9
gkd5	Kurishita	bar7	350	b2	1	t	Japan	gkda
k3t1	Kimura	bar7	350	b2	2	b	Japan	k2t1
k3t2	Kimura	bar7	350	b2	2	b	Japan	k2t2
k3t3	Kimura	bar7	350	b2	2	b	Japan	k2t3
k3t4	Kimura	bar7	350	b2	2	s	Japan	k2t4
k3t5	Kimura	bar7	350	b2	2	s	Japan	k2t5
gkb1	Kurishita	bar7	350	b2	2	s	Japan	gkb6
gkb2	Kurishita	bar7	350	b2	2	s	Japan	gkb7
gkb3	Kurishita	bar7	350	b2	2	t	Japan	gkb8
gkb4	Kurishita	bar7	350	b2	2	t	Japan	gkb9
gkb5	Kurishita	bar7	350	b2	2	t	Japan	gkba
k3r1	kimura	bar7	350	b2	3	b	Japan	k2r1
k3r2	kimura	bar7	350	b2	3	b	Japan	k2r2
k3r3	kimura	bar7	350	b2	3	b	Japan	k2r3
k3r4	kimura	bar7	350	b2	3	s	Japan	k2r4
k3r5	kimura	bar7	350	b2	3	s	Japan	k2r5
k3s1	kimura	bar7	350	b2	3	s	Japan	k2s1
k3s2	kimura	bar7	350	b2	3	s	Japan	k2s2
k3s3	kimura	bar7	350	b2	3	t	Japan	k2s3
k3s4	kimura	bar7	350	b2	3	t	Japan	k2s4
k3s5	kimura	bar7	350	b2	3	t	Japan	k2s5
gka1	Kurishita	bar7	350	b2	4	b	Japan	gka6
gka2	Kurishita	bar7	350	b2	4	b	Japan	gka7
gka3	Kurishita	bar7	350	b2	4	b	Japan	gka8
gka4	Kurishita	bar7	350	b2	4	s	Japan	gka9
gka5	Kurishita	bar7	350	b2	4	s	Japan	gkaa
gk36	Kurishita	bar7	350	b2	4	s	Japan	gk56
gk37	Kurishita	bar7	350	b2	4	s	Japan	gk57
gk38	Kurishita	bar7	350	b2	4	t	Japan	gk58
gk39	Kurishita	bar7	350	b2	4	t	Japan	gk5a
gk3a	Kurishita	bar7	350	b2	4	t	Japan	gk5a
gk81	Kurishita	bar7	350	b2	5	b	Japan	gk86
gk82	Kurishita	bar7	350	b2	5	b	Japan	gk87
gk83	Kurishita	bar7	350	b2	5	b	Japan	gk88
gk84	Kurishita	bar7	350	b2	5	s	Japan	gk89
gk85	Kurishita	bar7	350	b2	5	s	Japan	gk8a
gk91	Kurishita	bar7	350	b2	5	s	Japan	gk96
gk92	Kurishita	bar7	350	b2	5	s	Japan	gk97
gk93	Kurishita	bar7	350	b2	5	t	Japan	gk98
gk94	Kurishita	bar7	350	b2	5	t	Japan	gk99
gk95	Kurishita	bar7	350	b2	5	t	Japan	gk9a
gk61	Kurishita	bar7	350	b2	6	b	Japan	gk66
gk62	Kurishita	bar7	350	b2	6	b	Japan	gk67
gk63	Kurishita	bar7	350	b2	6	b	Japan	gk68
gk64	Kurishita	bar7	350	b2	6	s	Japan	gk69
gk65	Kurishita	bar7	350	b2	6	s	Japan	gk6a
gk71	Kurishita	bar7	350	b2	6	s	Japan	gk76
gk72	Kurishita	bar7	350	b2	6	s	Japan	gk77
gk73	Kurishita	bar7	350	b2	6	t	Japan	gk78
gk74	Kurishita	bar7	350	b2	6	t	Japan	gk79
gk75	Kurishita	bar7	350	b2	6	t	Japan	gk7a
gk21	Kurishita	bar7	350	b2	7	b	Japan	gk26
gk22	Kurishita	bar7	350	b2	7	b	Japan	gk27
gk23	Kurishita	bar7	350	b2	7	b	Japan	gk28
gk24	Kurishita	bar7	350	b2	7	s	Japan	gk29
gk25	Kurishita	bar7	350	b2	7	s	Japan	gk2a
gk41	Kurishita	bar7	350	b2	7	s	Japan	gk46
gk42	Kurishita	bar7	350	b2	7	s	Japan	gk47
gk43	Kurishita	bar7	350	b2	7	t	Japan	gk48
gk44	Kurishita	bar7	350	b2	7	t	Japan	gk49
gk45	Kurishita	bar7	350	b2	7	t	Japan	gk4a
gk01	Kurishita	bar7	350	b2	8	b	Japan	gk06
gk02	Kurishita	bar7	350	b2	8	b	Japan	gk07
gk03	Kurishita	bar7	350	b2	8	b	Japan	gk08
gk04	Kurishita	bar7	350	b2	8	s	Japan	gk09
gk05	Kurishita	bar7	350	b2	8	s	Japan	gk0a
gk11	Kurishita	bar7	350	b2	8	s	Japan	gk16
gk12	Kurishita	bar7	350	b2	8	s	Japan	gk17
gk13	Kurishita	bar7	350	b2	8	t	Japan	gk18
gk14	Kurishita	bar7	350	b2	8	t	Japan	gk19
gk15	Kurishita	bar7	350	b2	8	t	Japan	gk1a
lhd9	Kohno	cvn	350	b3	1	b	Japan	lhb7
lhf1	Kohno	cvn	350	b3	1	b	Japan	lhd8
SiC7	Kohno	cvn	350	b3	1	t	Japan	SiC5
SiC8	Kohno	cvn	350	b3	1	t	Japan	SiC6
lhb9	Kohno	cvn	350	b3	2	b	Japan	lhb3
lhd1	Kohno	cvn	350	b3	2	b	Japan	lhb4
lhd2	Kohno	cvn	350	b3	2	t	Japan	lhb5
lhd3	Kohno	cvn	350	b3	2	t	Japan	lhb6
l2f5	Kohno	cvn	350	b3	3	b	Japan	l2d5
l2f6	Kohno	cvn	350	b3	3	b	Japan	l2d6
l2f7	Kohno	cvn	350	b3	3	t	Japan	l2d7
lhb8	Kohno	cvn	350	b3	3	t	Japan	lhb2
l2f1	Kohno	cvn	350	b3	4	b	Japan	l2d1
l2f2	Kohno	cvn	350	b3	4	b	Japan	l2d2
l2f3	Kohno	cvn	350	b3	4	t	Japan	l2d3
l2f4	Kohno	cvn	350	b3	4	t	Japan	l2d4
k3t4	Kimura	tensile	350	b4	1	1	Japan	k2t
k3p1	Kimura	tensile	350	b4	1	2	Japan	k2p
k3p2	Kimura	tensile	350	b4	1	3	Japan	k2p
k3p3	Kimura	tensile	350	b4	1	4	Japan	k2p
k3p4	Kimura	tensile	350	b4	1	5	Japan	k2p
k3n1	Kimura	tensile	350	b4	1	6	Japan	k2n
k3n2	Kimura	tensile	350	b4	1	7	Japan	k2n
k3n3	Kimura	tensile	350	b4	1	8	Japan	k2n
k3n4	Kimura	tensile	350	b4	1	9	Japan	k2n
k3n5	Kimura	tensile	350	b4	1	10	Japan	k2n
k3n6	Kimura	tensile	350	b4	1	11	Japan	k2n
k3n7	Kimura	tensile	350	b4	1	12	Japan	k2n
k3n8	Kimura	tensile	350	b4	1	13	Japan	k2n

k321	Kimura	tensile	350	b4	1	14	Japan	k22
k322	Kimura	tensile	350	b4	1	15	Japan	k22
l1f4	Kohno	tensile	350	b4	2	1	Japan	l1d
l1f5	Kohno	tensile	350	b4	2	2	Japan	l1d
l2f1	Kohno	tensile	350	b4	2	3	Japan	l2d
l2f2	Kohno	tensile	350	b4	2	4	Japan	l2d
l2f3	Kohno	tensile	350	b4	2	5	Japan	l2d
l2f4	Kohno	tensile	350	b4	2	6	Japan	l2d
l2f5	Kohno	tensile	350	b4	2	7	Japan	l2d
lhf1	Kohno	tensile	350	b4	2	8	Japan	lhd
lhf2	Kohno	tensile	350	b4	2	9	Japan	lhd
lhf3	Kohno	tensile	350	b4	2	10	Japan	lhd
lhf4	Kohno	tensile	350	b4	2	11	Japan	lhd
lhf5	Kohno	tensile	350	b4	2	12	Japan	lhd
lhf6	Kohno	tensile	350	b4	2	13	Japan	lhd
lhf7	Kohno	tensile	350	b4	2	14	Japan	lhd
t716	Matsui	tensile	350	b4	2	15	Japan	T713
t717	Matsui	tensile	350	b4	2	16	Japan	T714
T718	Matsui	tensile	350	b4	2	16	Japan	T715
f6ha	Satou	tensile	350	b4	3	1	Japan	f6h3
f6k3	Satou	tensile	350	b4	3	2	Japan	f6h4
f7h6	Satou	tensile	350	b4	3	3	Japan	f7h0
f7h7	Satou	tensile	350	b4	3	4	Japan	f7h1
f7h8	Satou	tensile	350	b4	3	5	Japan	f7h2
f8h9	Satou	tensile	350	b4	3	6	Japan	f8h0
f8ha	Satou	tensile	350	b4	3	7	Japan	f8h1
f8hb	Satou	tensile	350	b4	3	8	Japan	f8h3
f3h3	Satou	tensile	350	b4	3	9	Japan	f3h0
f3h4	Satou	tensile	350	b4	3	10	Japan	f3h1
f3h5	Satou	tensile	350	b4	3	11	Japan	f3h2
f3hl	Satou	tensile	350	b4	3	12	Japan	f3hg
f2h3	Satou	tensile	350	b4	3	13	Japan	f2h1
f2h4	Satou	tensile	350	b4	3	14	Japan	f2h2
foh3	Satou	tensile	350	b4	3	15	Japan	foh1
t205	Matsui	tensile	350	b4	4	2	Japan	t202
t206	Matsui	tensile	350	b4	4	3	Japan	t203
t304	Matsui	tensile	350	b4	4	4	Japan	t301
t305	Matsui	tensile	350	b4	4	5	Japan	t302
t306	Matsui	tensile	350	b4	4	6	Japan	t303
t404	Matsui	tensile	350	b4	4	7	Japan	t401
t405	Matsui	tensile	350	b4	4	8	Japan	t402
t406	Matsui	tensile	350	b4	4	9	Japan	t403
t504	Matsui	tensile	350	b4	4	10	Japan	t501
t505	Matsui	tensile	350	b4	4	11	Japan	t502
t506	Matsui	tensile	350	b4	4	12	Japan	t503
a703	ohnuki	tensile	350	b4	4	13	Japan	a701
a704	ohnuki	tensile	350	b4	4	14	Japan	a702
a713	ohnuki	tensile	350	b4	4	15	Japan	a711
a714	ohnuki	tensile	350	b4	4	16	Japan	a712
a723	ohnuki	tensile	350	b4	4	17	Japan	a721
xh01	Kiueh	tensile	350	b4	5	1	US	xh05
xh02	Kiueh	tensile	350	b4	5	2	US	xh06
xh03	Kiueh	tensile	350	b4	5	3	US	xh07
xh04	Kiueh	tensile	350	b4	5	4	US	xh08
xi01	Kiueh	tensile	350	b4	5	5	US	xi05
xi02	Kiueh	tensile	350	b4	5	6	US	xi06
xi03	Kiueh	tensile	350	b4	5	7	US	xi07
xi04	Kiueh	tensile	350	b4	5	8	US	xi08
ta01	Kiueh	tensile	350	b4	5	9	US	ta05
ta02	Kiueh	tensile	350	b4	5	10	US	ta06
ta03	Kiueh	tensile	350	b4	5	11	US	ta07
ta04	Kiueh	tensile	350	b4	5	12	US	ta08
ts24	Matsui	tensile	350	b4	5	14	Japan	ts21
ts25	Matsui	tensile	350	b4	5	15	Japan	ts22
ts26	Matsui	tensile	350	b4	5	16	Japan	ts23
lbf7	Kohno	cvn	350	b5	1	b	Japan	lbd7
l1f1	Kohno	cvn	350	b5	1	b	Japan	l1d1
l1f2	Kohno	cvn	350	b5	1	t	Japan	l1d2
l1f3	Kohno	cvn	350	b5	1	t	Japan	l1d3
lbf3	Kohno	cvn	350	b5	2	b	Japan	lbd3
lbf4	Kohno	cvn	350	b5	2	b	Japan	lbd4
lbf5	Kohno	cvn	350	b5	2	t	Japan	lbd5
lbf6	Kohno	cvn	350	b5	2	t	Japan	lbd6
k339	Kimura	cvn	350	b5	3	b	Japan	k239
lff1	Kohno	cvn	350	b5	3	b	Japan	lfd1
lff2	Kohno	cvn	350	b5	3	t	Japan	lfd2
lff3	Kohno	cvn	350	b5	3	t	Japan	lfd3
k331	Kimura	cvn	350	b5	4	b	Japan	k231
k332	Kimura	cvn	350	b5	4	b	Japan	k232
k333	Kimura	cvn	350	b5	4	t	Japan	k233
k334	Kimura	cvn	350	b5	4	t	Japan	k234
k3n1	Kimura	tem	350	b6	1	1	Japan	k2n1
k3n2	Kimura	tem	350	b6	1	2	Japan	k2n2
k3n3	Kimura	tem	350	b6	1	3	Japan	k2n3
k3n4	Kimura	tem	350	b6	1	4	Japan	k2n4
k3n5	Kimura	tem	350	b6	1	5	Japan	k2n5
k3n6	Kimura	tem	350	b6	1	6	Japan	k2n6
k3n7	Kimura	tem	350	b6	1	7	Japan	k2n7
k321	Kimura	tem	350	b6	1	8	Japan	k221
k322	Kimura	tem	350	b6	1	9	Japan	k222
k323	Kimura	tem	350	b6	1	10	Japan	k223
k324	Kimura	tem	350	b6	1	11	Japan	k224
k331	Kimura	tem	350	b6	1	12	Japan	k231
k332	Kimura	tem	350	b6	1	13	Japan	k232
k333	Kimura	tem	350	b6	1	14	Japan	k233

k334	Kimura	tem	350	b6	1	15	Japan	k234
k341	Kimura	tem	350	b6	1	16	Japan	k241
k342	Kimura	tem	350	b6	1	17	Japan	k242
k343	Kimura	tem	350	b6	1	18	Japan	k243
k344	Kimura	tem	350	b6	1	19	Japan	k244
k351	Kimura	tem	350	b6	1	20	Japan	k251
k352	Kimura	tem	350	b6	1	21	Japan	k252
k353	Kimura	tem	350	b6	1	22	Japan	k253
k354	Kimura	tem	350	b6	1	23	Japan	k254
k361	Kimura	tem	350	b6	1	25	Japan	k261
k362	Kimura	tem	350	b6	1	26	Japan	k262
k363	Kimura	tem	350	b6	1	27	Japan	k263
k364	Kimura	tem	350	b6	1	28	Japan	k264
k371	Kimura	tem	350	b6	1	29	Japan	k271
k372	Kimura	tem	350	b6	1	30	Japan	k272
k373	Kimura	tem	350	b6	1	31	Japan	k273
k374	Kimura	tem	350	b6	1	32	Japan	k274
k381	Kimura	tem	350	b6	1	33	Japan	k281
k382	Kimura	tem	350	b6	1	34	Japan	k282
k383	Kimura	tem	350	b6	1	35	Japan	k283
k384	Kimura	tem	350	b6	1	36	Japan	k284
k391	Kimura	tem	350	b6	1	37	Japan	k291
k392	Kimura	tem	350	b6	1	38	Japan	k292
k393	Kimura	tem	350	b6	1	39	Japan	k293
k394	Kimura	tem	350	b6	1	40	Japan	k294
k3s1	Kimura	tem	350	b6	1	41	Japan	k2s1
k3s2	Kimura	tem	350	b6	1	42	Japan	k2s2
k3s3	Kimura	tem	350	b6	1	43	Japan	k2s3
k3s4	Kimura	tem	350	b6	1	44	Japan	k2s4
k3s5	Kimura	tem	350	b6	1	45	Japan	k2s5
k3s6	Kimura	tem	350	b6	1	46	Japan	k2s6
k3s7	Kimura	tem	350	b6	1	47	Japan	k2s7
k3t1	Kimura	tem	350	b6	1	48	Japan	k211
k3t2	Kimura	tem	350	b6	1	49	Japan	k212
k3t3	Kimura	tem	350	b6	1	50	Japan	k213
k3t4	Kimura	tem	350	b6	1	51	Japan	k214
k3t5	Kimura	tem	350	b6	1	52	Japan	k215
k3t6	Kimura	tem	350	b6	1	53	Japan	k216
k3t7	Kimura	tem	350	b6	1	54	Japan	k217
k3p1	Kimura	tem	350	b6	1	55	Japan	k2p1
k3p2	Kimura	tem	350	b6	1	56	Japan	k2p2
k3p3	Kimura	tem	350	b6	1	57	Japan	k2p3
k3p4	Kimura	tem	350	b6	1	58	Japan	k2p4
k3p5	Kimura	tem	350	b6	1	59	Japan	k2p5
k3p6	Kimura	tem	350	b6	1	60	Japan	k2p6
k3p7	Kimura	tem	350	b6	1	61	Japan	k2p7
k3k1	Kimura	tem	350	b6	1	62	Japan	k2k1
k3k2	Kimura	tem	350	b6	1	63	Japan	k2k2
k3k3	Kimura	tem	350	b6	1	64	Japan	k2k3
k3k4	Kimura	tem	350	b6	1	65	Japan	k2k4
k3k5	Kimura	tem	350	b6	1	66	Japan	k2k5
k3l1	Kimura	tem	350	b6	1	67	Japan	k2l1
k3l2	Kimura	tem	350	b6	1	68	Japan	k2l2
k3l3	Kimura	tem	350	b6	1	69	Japan	k2l3
k3l4	Kimura	tem	350	b6	1	70	Japan	k2l4
k3l5	Kimura	tem	350	b6	1	71	Japan	k2l5
k3m1	Kimura	tem	350	b6	1	72	Japan	k2m1
k3m2	Kimura	tem	350	b6	1	73	Japan	k2m2
k3m3	Kimura	tem	350	b6	1	74	Japan	k2m3
k3m4	Kimura	tem	350	b6	1	75	Japan	k2m4
k3m5	Kimura	tem	350	b6	1	76	Japan	k2m5
k3n1	Kimura	tem	350	b6	1	77	Japan	k2n1
k3n2	Kimura	tem	350	b6	1	78	Japan	k2n2
k3n3	Kimura	tem	350	b6	1	79	Japan	k2n3
k3n4	Kimura	tem	350	b6	1	80	Japan	k2n4
k3n5	Kimura	tem	350	b6	1	81	Japan	k2n5
k3r1	Kimura	tem	350	b6	1	82	Japan	k2r1
k3r2	Kimura	tem	350	b6	1	83	Japan	k2r2
k3r3	Kimura	tem	350	b6	1	84	Japan	k2r3
k3r4	Kimura	tem	350	b6	1	85	Japan	k2r4
k3r5	Kimura	tem	350	b6	1	86	Japan	k2r5
k3r6	Kimura	tem	350	b6	1	87	Japan	k2r6
k3r7	Kimura	tem	350	b6	1	88	Japan	k2r7
k3r8	Kimura	tem	350	b6	1	89	Japan	k2r8
k3t1	Kimura	tem	350	b6	1	90	Japan	k211
k3t2	Kimura	tem	350	b6	1	91	Japan	k212
k3t3	Kimura	tem	350	b6	1	92	Japan	k213
k3t4	Kimura	tem	350	b6	1	93	Japan	k214
k3t5	Kimura	tem	350	b6	1	94	Japan	k215
k3t6	Kimura	tem	350	b6	1	95	Japan	k216
k3t7	Kimura	tem	350	b6	1	96	Japan	k217
k3t8	Kimura	tem	350	b6	1	97	Japan	k218
k3s1	Kimura	tem	350	b6	1	98	Japan	k2s1
k3s2	Kimura	tem	350	b6	1	99	Japan	k2s2
k3s3	Kimura	tem	350	b6	1	100	Japan	k2s3
k3s4	Kimura	tem	350	b6	1	101	Japan	k2s4
k3s5	Kimura	tem	350	b6	1	102	Japan	k2s5
k3s6	Kimura	tem	350	b6	1	103	Japan	k2s6
k3s7	Kimura	tem	350	b6	1	104	Japan	k2s7
k3s8	Kimura	tem	350	b6	1	105	Japan	k2s8
g751	Shibayama	tem	350	B6	1	106	Japan	g851
g752	Shibayama	tem	350	B6	1	107	Japan	g852
g701	Shibayama	tem	350	B6	1	108	Japan	g801
g702	Shibayama	tem	350	B6	1	109	Japan	g802
g711	Shibayama	tem	350	B6	1	110	Japan	g811
g712	Shibayama	tem	350	B6	1	111	Japan	g812
g721	Shibayama	tem	350	B6	1	112	Japan	g821
g722	Shibayama	tem	350	B6	1	113	Japan	g822
g731	Shibayama	tem	350	B6	1	114	Japan	g831

g732	Shibayama	tem	350	B6	1	116	Japan	g832
g741	Shibayama	tem	350	B6	1	117	Japan	g841
g742	Shibayama	tem	350	B6	1	118	Japan	g842
g7d1	Shibayama	tem	350	B6	1	119	Japan	g8d1
g7d2	Shibayama	tem	350	B6	1	120	Japan	g8d2
t%06	Shibayama	tem	350	B6	1	121	Japan	t%01
t%07	Shibayama	tem	350	B6	1	122	Japan	t%02
t%08	Shibayama	tem	350	B6	1	123	Japan	t%03
ta06	Shibayama	tem	350	B6	1	124	Japan	ta01
ta07	Shibayama	tem	350	B6	1	125	Japan	ta02
t#06	Shibayama	tem	350	B6	1	126	Japan	t#01
t#07	Shibayama	tem	350	B6	1	127	Japan	t#02
t#08	Shibayama	tem	350	B6	1	128	Japan	t#03
av32	Kinoshita	tem	350	B6	1	129	Japan	av30
av33	Kinoshita	tem	350	B6	1	130	Japan	av31
av83	Kinoshita	tem	350	B6	1	131	Japan	av80
av8f	Kinoshita	tem	350	B6	1	132	Japan	av81
av92	Kinoshita	tem	350	B6	1	133	Japan	av91
av93	Kinoshita	tem	350	B6	1	134	Japan	av9a
al02	Kinoshita	tem	350	B6	1	135	Japan	al00
al03	Kinoshita	tem	350	B6	1	136	Japan	al01
ah82	Kinoshita	tem	350	B6	1	137	Japan	ah80
ah83	Kinoshita	tem	350	B6	1	138	Japan	ah81
aa00	Kinoshita	tem	350	b6	1	139	Japan	aa03
aa01	Kinoshita	tem	350	b6	1	140	Japan	aa05
aa02	Kinoshita	tem	350	b6	1	141	Japan	aa08
aa0g	Kinoshita	tem	350	b6	1	142	Japan	aa09
an54	Kinoshita	tem	350	b6	1	144	Japan	an50
an55	Kinoshita	tem	350	b6	1	145	Japan	an51
an56	Kinoshita	tem	350	b6	1	146	Japan	an52
an57	Kinoshita	tem	350	b6	1	147	Japan	an53
ac14	Kinoshita	tem	350	b6	1	148	Japan	ac10
ac15	Kinoshita	tem	350	b6	1	149	Japan	ac11
ac16	Kinoshita	tem	350	b6	1	150	Japan	ac12
ac17	Kinoshita	tem	350	b6	1	151	Japan	ac13
am35	Kinoshita	tem	350	b6	1	152	Japan	am30
am36	Kinoshita	tem	350	b6	1	153	Japan	am31
am37	Kinoshita	tem	350	b6	1	154	Japan	am32
am38	Kinoshita	tem	350	b6	1	155	Japan	am34
ffh0	Hasegawa	tem	350	b6	2	1	Japan	ffg0
ffh1	Hasegawa	tem	350	b6	2	2	Japan	ffg2
ffh3	Hasegawa	tem	350	b6	2	3	Japan	ffg3
ffh4	Hasegawa	tem	350	b6	2	4	Japan	ffg4
ffh5	Hasegawa	tem	350	b6	2	5	Japan	ffg5
ffh6	Hasegawa	tem	350	b6	2	6	Japan	ffg6
ffh7	Hasegawa	tem	350	b6	2	7	Japan	ffg7
ffh8	Hasegawa	tem	350	b6	2	8	Japan	ffg8
ffi0	Hasegawa	tem	350	b6	2	9	Japan	ffk0
ffi2	Hasegawa	tem	350	b6	2	10	Japan	ffk1
ffi3	Hasegawa	tem	350	b6	2	11	Japan	ffk2
ffi4	Hasegawa	tem	350	b6	2	12	Japan	ffk3
ffi5	Hasegawa	tem	350	b6	2	13	Japan	ffk5
ffi6	Hasegawa	tem	350	b6	2	14	Japan	ffk6
ffi7	Hasegawa	tem	350	b6	2	15	Japan	ffk7
ffi9	Hasegawa	tem	350	b6	2	16	Japan	ffk8
ffb0	Hasegawa	tem	350	b6	2	18	Japan	ffa0
ffb1	Hasegawa	tem	350	b6	2	19	Japan	ffa1
ffb2	Hasegawa	tem	350	b6	2	20	Japan	ffa2
ffb3	Hasegawa	tem	350	b6	2	21	Japan	ffa3
ffb5	Hasegawa	tem	350	b6	2	22	Japan	ffa5
ffb6	Hasegawa	tem	350	b6	2	23	Japan	ffa6
ffb7	Hasegawa	tem	350	b6	2	24	Japan	ffa7
ffb8	Hasegawa	tem	350	b6	2	25	Japan	ffa8
ffd0	Hasegawa	tem	350	b6	2	26	Japan	ffd0
ffd2	Hasegawa	tem	350	b6	2	27	Japan	ffd2
ffd3	Hasegawa	tem	350	b6	2	28	Japan	ffd3
ffd4	Hasegawa	tem	350	b6	2	29	Japan	ffd4
ffd5	Hasegawa	tem	350	b6	2	30	Japan	ffd5
ffd6	Hasegawa	tem	350	b6	2	31	Japan	ffd6
ffd7	Hasegawa	tem	350	b6	2	32	Japan	ffd7
fr20	Hasegawa	tem	350	b6	2	33	Japan	fr10
fr21	Hasegawa	tem	350	b6	2	34	Japan	fr11
fr24	Hasegawa	tem	350	b6	2	35	Japan	fr12
fr25	Hasegawa	tem	350	b6	2	36	Japan	fr14
fr26	Hasegawa	tem	350	b6	2	37	Japan	fr15
fr27	Hasegawa	tem	350	b6	2	38	Japan	fr16
fr28	Hasegawa	tem	350	b6	2	39	Japan	fr17
fr29	Hasegawa	tem	350	b6	2	40	Japan	fr18
gke1	Kurishita	tem	350	b6	2	41	Japan	gke6
gke2	Kurishita	tem	350	b6	2	42	Japan	gke7
gkf1	Kurishita	tem	350	b6	2	43	Japan	gkf6
gkf2	Kurishita	tem	350	b6	2	44	Japan	gkf7
gkg1	Kurishita	tem	350	b6	2	45	Japan	gkg6
gkg2	Kurishita	tem	350	b6	2	46	Japan	gkg7
gkh1	Kurishita	tem	350	b6	2	47	Japan	gkh6
gkh2	Kurishita	tem	350	b6	2	48	Japan	gkh7
gkh3	Kurishita	tem	350	b6	2	49	Japan	gkh8
gkj1	Kurishita	tem	350	b6	2	50	Japan	gkj6
gkj2	Kurishita	tem	350	b6	2	51	Japan	gkj7
gkk1	Kurishita	tem	350	b6	2	52	Japan	gkk6
gkk2	Kurishita	tem	350	b6	2	53	Japan	gkk7
gkk3	Kurishita	tem	350	b6	2	54	Japan	gkk8
gkk4	Kurishita	tem	350	b6	2	55	Japan	gkk9
gkl1	Kurishita	tem	350	b6	2	56	Japan	gkl6
gkl2	Kurishita	tem	350	b6	2	57	Japan	gkl7
gkl3	Kurishita	tem	350	b6	2	58	Japan	gkl8
gkm1	Kurishita	tem	350	b6	2	59	Japan	gkm6
gkm2	Kurishita	tem	350	b6	2	60	Japan	gkm7
gkm3	Kurishita	tem	350	b6	2	61	Japan	gkm8

gkm4	Kurishita	tem	350	b6	2	62	Japan	gkm9
gkn1	Kurishita	tem	350	b6	2	63	Japan	gkn6
gkn2	Kurishita	tem	350	b6	2	64	Japan	gkn7
gkn3	Kurishita	tem	350	b6	2	65	Japan	gkn8
gkn4	Kurishita	tem	350	b6	2	66	Japan	gkn9
gkp1	Kurishita	tem	350	b6	2	67	Japan	gkp6
gkp2	Kurishita	tem	350	b6	2	68	Japan	gkp7
gkp3	Kurishita	tem	350	b6	2	69	Japan	gkp8
gkp4	Kurishita	tem	350	b6	2	70	Japan	gkp9
gkq1	Kurishita	tem	350	b6	2	71	Japan	gkq6
gkq2	Kurishita	tem	350	b6	2	72	Japan	gkq7
gkq3	Kurishita	tem	350	b6	2	73	Japan	gkq8
gkq4	Kurishita	tem	350	b6	2	74	Japan	gkq9
gkr1	Kurishita	tem	350	b6	2	75	Japan	gkr6
gkr2	Kurishita	tem	350	b6	2	76	Japan	gkr7
gkr3	Kurishita	tem	350	b6	2	77	Japan	gkr8
gks1	Kurishita	tem	350	b6	2	78	Japan	gks6
gks2	Kurishita	tem	350	b6	2	79	Japan	gks7
gks3	Kurishita	tem	350	b6	2	80	Japan	gks8
gkt1	Kurishita	tem	350	b6	2	81	Japan	gkt6
gkt2	Kurishita	tem	350	b6	2	82	Japan	gkt7
gkt3	Kurishita	tem	350	b6	2	83	Japan	gkt8
gkt4	Kurishita	tem	350	b6	2	84	Japan	gkt9
gku1	Kurishita	tem	350	b6	2	85	Japan	gku6
gku2	Kurishita	tem	350	b6	2	86	Japan	gku7
gku3	Kurishita	tem	350	b6	2	87	Japan	gku8
gku4	Kurishita	tem	350	b6	2	88	Japan	gku9
gkv1	Kurishita	tem	350	b6	2	89	Japan	gkv6
gkv2	Kurishita	tem	350	b6	2	90	Japan	gkv7
gkw1	Kurishita	tem	350	b6	2	91	Japan	gkw6
gkw2	Kurishita	tem	350	b6	2	92	Japan	gkw7
gkw3	Kurishita	tem	350	b6	2	93	Japan	gkw8
gkw4	Kurishita	tem	350	b6	2	94	Japan	gkw9
gkx1	Kurishita	tem	350	b6	2	95	Japan	gkx6
gkx2	Kurishita	tem	350	b6	2	96	Japan	gkx7
gkx3	Kurishita	tem	350	b6	2	97	Japan	gkx8
a603	Ohnuki	tem	350	B6	2	98	Japan	a601
a604	Ohnuki	tem	350	b6	2	99	Japan	a602
a613	Ohnuki	tem	350	b6	2	100	Japan	a611
a614	Ohnuki	tem	350	b6	2	101	Japan	a612
a624	Ohnuki	tem	350	b6	2	103	Japan	a622
a633	Ohnuki	tem	350	b6	2	104	Japan	a631
a634	Ohnuki	tem	350	b6	2	105	Japan	a632
a643	Ohnuki	tem	350	b6	2	106	Japan	a641
a644	Ohnuki	tem	350	b6	2	107	Japan	a642
a803	Ohnuki	tem	350	b6	2	108	Japan	a801
a804	Ohnuki	tem	350	b6	2	109	Japan	a802
a623	Ohnuki	tem	350	b6	2	110	Japan	a621
a813	Ohnuki	tem	350	b6	2	110	Japan	a811
a814	Ohnuki	tem	350	b6	2	111	Japan	a812
a824	Ohnuki	tem	350	b6	2	112	Japan	a822
a834	Ohnuki	tem	350	b6	2	113	Japan	a832
a003	Ohnuki	tem	350	B6	2	114	Japan	a001
a004	Ohnuki	tem	350	B6	2	115	Japan	a002
a013	Ohnuki	tem	350	B6	2	116	Japan	a011
a014	Ohnuki	tem	350	B6	2	117	Japan	a012
a023	Ohnuki	tem	350	B6	2	118	Japan	a021
a024	Ohnuki	tem	350	B6	2	119	Japan	a022
a033	Ohnuki	tem	350	B6	2	120	Japan	a031
a034	Ohnuki	tem	350	B6	2	121	Japan	a032
a823	Ohnuki	tem	350	b6	2	121	Japan	a821
a043	Ohnuki	tem	350	B6	2	122	Japan	a041
a044	Ohnuki	tem	350	B6	2	123	Japan	a042
a833	Ohnuki	tem	350	b6	2	123	Japan	a831
a053	Ohnuki	tem	350	B6	2	124	Japan	a051
a054	Ohnuki	tem	350	B6	2	125	Japan	a052
a063	Ohnuki	tem	350	B6	2	126	Japan	a061
a064	Ohnuki	tem	350	B6	2	127	Japan	a062
a073	Ohnuki	tem	350	B6	2	128	Japan	a071
a074	Ohnuki	tem	350	B6	2	129	Japan	a072
a084	Ohnuki	tem	350	B6	2	130	Japan	a083
a093	Ohnuki	tem	350	B6	2	131	Japan	a091
a094	Ohnuki	tem	350	B6	2	132	Japan	a092
a104	Ohnuki	tem	350	B6	2	133	Japan	a103
ye01	Watanabe	tem	350	T1	1	1	Japan	yg01
ye02	Watanabe	tem	350	T1	1	2	Japan	yg02
ye03	Watanabe	tem	350	T1	1	3	Japan	yg03
ye04	Watanabe	tem	350	T1	1	4	Japan	yg04
ye05	Watanabe	tem	350	T1	1	5	Japan	yg05
ye06	Watanabe	tem	350	T1	1	6	Japan	yg06
ye07	Watanabe	tem	350	T1	1	7	Japan	yg07
ye08	Watanabe	tem	350	T1	1	8	Japan	yg08
ye09	Watanabe	tem	350	T1	1	9	Japan	yg09
ye10	Watanabe	tem	350	T1	1	10	Japan	yg10
ye11	Watanabe	tem	350	T1	1	11	Japan	yg11
ye12	Watanabe	tem	350	T1	1	12	Japan	yg12
ye13	Watanabe	tem	350	T1	1	13	Japan	yg13
ye14	Watanabe	tem	350	T1	1	14	Japan	yg14
ye15	Watanabe	tem	350	T1	1	15	Japan	yg15
ye16	Watanabe	tem	350	T1	1	16	Japan	yg16
ye17	Watanabe	tem	350	T1	1	17	Japan	yg17
ye18	Watanabe	tem	350	T1	1	18	Japan	yg18
ye19	Watanabe	tem	350	T1	1	19	Japan	yg19
ye20	Watanabe	tem	350	T1	1	20	Japan	yg20
ye21	Watanabe	tem	350	T1	1	21	Japan	yg21
ye22	Watanabe	tem	350	T1	1	22	Japan	yg22
ye23	Watanabe	tem	350	T1	1	23	Japan	yg23

ye24	Watanabe	tem	350	T1	1	24	Japan	yg24
ye25	Watanabe	tem	350	T1	1	25	Japan	yg25
ye26	Watanabe	tem	350	T1	1	26	Japan	yg26
ye27	Watanabe	tem	350	T1	1	27	Japan	yg27
ye28	Watanabe	tem	350	T1	1	28	Japan	yg28
ye29	Watanabe	tem	350	T1	1	29	Japan	yg29
ye30	Watanabe	tem	350	T1	1	30	Japan	yg30
ye31	Watanabe	tem	350	T1	1	31	Japan	yg31
ye32	Watanabe	tem	350	T1	1	32	Japan	yg32
ye33	Watanabe	tem	350	T1	1	33	Japan	yg33
ye34	Watanabe	tem	350	T1	1	34	Japan	yg34
ye35	Watanabe	tem	350	T1	1	35	Japan	yg35
ye36	Watanabe	tem	350	T1	1	36	Japan	yg36
ye37	Watanabe	tem	350	T1	1	37	Japan	yg37
ye38	Watanabe	tem	350	T1	1	38	Japan	yg38
ye39	Watanabe	tem	350	T1	1	39	Japan	yg39
ye40	Watanabe	tem	350	T1	1	40	Japan	yg40
ye41	Watanabe	tem	350	T1	1	41	Japan	yg41
ye42	Watanabe	tem	350	T1	1	42	Japan	yg42
ye43	Watanabe	tem	350	T1	1	43	Japan	yg43
ye44	Watanabe	tem	350	T1	1	44	Japan	yg44
ye45	Watanabe	tem	350	T1	1	45	Japan	yg45
ye46	Watanabe	tem	350	T1	1	46	Japan	yg46
ye47	Watanabe	tem	350	T1	1	47	Japan	yg47
ye48	Watanabe	tem	350	T1	1	48	Japan	yg48
ye49	Watanabe	tem	350	T1	1	49	Japan	yg49
ye50	Watanabe	tem	350	T1	1	50	Japan	yg50
ye51	Watanabe	tem	350	T1	1	51	Japan	yg51
ye52	Watanabe	tem	350	T1	1	52	Japan	yg52
ye53	Watanabe	tem	350	T1	1	53	Japan	yg53
ye54	Watanabe	tem	350	T1	1	54	Japan	yg54
ye55	Watanabe	tem	350	T1	1	55	Japan	yg55
ye56	Watanabe	tem	350	T1	1	56	Japan	yg56
ye57	Watanabe	tem	350	T1	1	57	Japan	yg57
ye58	Watanabe	tem	350	T1	1	58	Japan	yg58
ye59	Watanabe	tem	350	T1	1	59	Japan	yg59
ye60	Watanabe	tem	350	T1	1	60	Japan	yg60
ye61	Watanabe	tem	350	T1	1	61	Japan	yg61
ye62	Watanabe	tem	350	T1	1	62	Japan	yg62
ye63	Watanabe	tem	350	T1	1	63	Japan	yg63
ye64	Watanabe	tem	350	T1	1	64	Japan	yg64
ye65	Watanabe	tem	350	T1	1	65	Japan	yg65
ye66	Watanabe	tem	350	T1	1	66	Japan	yg66
ye67	Watanabe	tem	350	T1	1	67	Japan	yg67
ye68	Watanabe	tem	350	T1	1	68	Japan	yg68
ye69	Watanabe	tem	350	T1	1	69	Japan	yg69
ye70	Watanabe	tem	350	T1	1	70	Japan	yg70
ye71	Watanabe	tem	350	T1	1	71	Japan	yg71
ye72	Watanabe	tem	350	T1	1	72	Japan	yg72
ye73	Watanabe	tem	350	T1	1	73	Japan	yg73
ye74	Watanabe	tem	350	T1	1	74	Japan	yg74
ye75	Watanabe	tem	350	T1	1	75	Japan	yg75
ye76	Watanabe	tem	350	T1	1	76	Japan	yg76
ye77	Watanabe	tem	350	T1	1	77	Japan	yg77
ye78	Watanabe	tem	350	T1	1	78	Japan	yg78
ye79	Watanabe	tem	350	T1	1	79	Japan	yg79
ye80	Watanabe	tem	350	T1	1	80	Japan	yg80
ye81	Watanabe	tem	350	T1	1	81	Japan	yg81
ye82	Watanabe	tem	350	T1	1	82	Japan	yg82
ye83	Watanabe	tem	350	T1	1	83	Japan	yg83
ye84	Watanabe	tem	350	T1	1	84	Japan	yg84
ye85	Watanabe	tem	350	T1	1	85	Japan	yg85
ye86	Watanabe	tem	350	T1	1	86	Japan	yg86
ye87	Watanabe	tem	350	T1	1	87	Japan	yg87
ye88	Watanabe	tem	350	T1	1	88	Japan	yg88
ye89	Watanabe	tem	350	T1	1	89	Japan	yg89
ye90	Watanabe	tem	350	T1	1	90	Japan	yg90
ye91	Watanabe	tem	350	T1	1	91	Japan	yg91
ye92	Watanabe	tem	350	T1	1	92	Japan	yg92
ye93	Watanabe	tem	350	T1	1	93	Japan	yg93
ye94	Watanabe	tem	350	T1	1	94	Japan	yg94
ye95	Watanabe	tem	350	T1	1	95	Japan	yg95
ye96	Watanabe	tem	350	T1	1	96	Japan	yg96
ye97	Watanabe	tem	350	T1	1	97	Japan	yg97
ye98	Watanabe	tem	350	T1	1	98	Japan	yg98
ye99	Watanabe	tem	350	T1	1	99	Japan	yg99
yf01	Watanabe	tem	350	T1	1	100	Japan	yh01
yf02	Watanabe	tem	350	T1	1	101	Japan	yh02
yf03	Watanabe	tem	350	T1	1	102	Japan	yh03
yf04	Watanabe	tem	350	T1	1	103	Japan	yh04
yf05	Watanabe	tem	350	T1	1	104	Japan	yh05
yf06	Watanabe	tem	350	T1	1	105	Japan	yh06
yf07	Watanabe	tem	350	T1	1	106	Japan	yh07
yf08	Watanabe	tem	350	T1	1	107	Japan	yh08
yf09	Watanabe	tem	350	T1	1	108	Japan	yh09
yf10	Watanabe	tem	350	T1	1	109	Japan	yh10
yf11	Watanabe	tem	350	T1	1	110	Japan	yh11
yf12	Watanabe	tem	350	T1	1	111	Japan	yh12
yf13	Watanabe	tem	350	T1	1	112	Japan	yh13
yf14	Watanabe	tem	350	T1	1	113	Japan	yh14
yf15	Watanabe	tem	350	T1	1	114	Japan	yh15
yf16	Watanabe	tem	350	T1	1	115	Japan	yh16
yf17	Watanabe	tem	350	T1	1	116	Japan	yh17
yf18	Watanabe	tem	350	T1	1	117	Japan	yh18
yf19	Watanabe	tem	350	T1	1	118	Japan	yh19
yf20	Watanabe	tem	350	T1	1	119	Japan	yh20
yf21	Watanabe	tem	350	T1	1	120	Japan	yh21
yf22	Watanabe	tem	350	T1	1	121	Japan	yh22
yf23	Watanabe	tem	350	T1	1	122	Japan	yh23

yf24	Watanabe	tem	350	T1	1	123	Japan	yh24
yf25	Watanabe	tem	350	T1	1	124	Japan	yh25
yf26	Watanabe	tem	350	T1	1	125	Japan	yh26
yf27	Watanabe	tem	350	T1	1	126	Japan	yh27
yf28	Watanabe	tem	350	T1	1	127	Japan	yh28
yf29	Watanabe	tem	350	T1	1	128	Japan	yh29
yf30	Watanabe	tem	350	T1	1	129	Japan	yh30
yf31	Watanabe	tem	350	T1	1	130	Japan	yh31
yf32	Watanabe	tem	350	T1	1	131	Japan	yh32
yf33	Watanabe	tem	350	T1	1	132	Japan	yh33
yf34	Watanabe	tem	350	T1	2	1	Japan	yh34
yf35	Watanabe	tem	350	T1	2	2	Japan	yh35
yf36	Watanabe	tem	350	T1	2	3	Japan	yh36
yf37	Watanabe	tem	350	T1	2	4	Japan	yh37
yf38	Watanabe	tem	350	T1	2	5	Japan	yh38
yf39	Watanabe	tem	350	T1	2	6	Japan	yh39
yf40	Watanabe	tem	350	T1	2	7	Japan	yh40
yf41	Watanabe	tem	350	T1	2	8	Japan	yh41
yf42	Watanabe	tem	350	T1	2	9	Japan	yh41
ffn1	Iseki	tem	350	T1	2	10	Japan	ffn3
ffn2	Iseki	tem	350	T1	2	11	Japan	ffn4
jpc1	Iseki	tem	350	T1	2	12	Japan	jpc3
jpc2	Iseki	tem	350	T1	2	13	Japan	jpc4
f2c1	Iseki	tem	350	T1	2	14	Japan	f2c3
f2c2	Iseki	tem	350	T1	2	15	Japan	f2c4
f9c1	Iseki	tem	350	T1	2	16	Japan	f9c3
f9c2	Iseki	tem	350	T1	2	17	Japan	f9c4
f0c1	Iseki	tem	350	T1	2	18	Japan	f0c3
foc2	Iseki	tem	350	T1	2	19	Japan	foc4
fon1	Iseki	tem	350	T1	2	20	Japan	fon3
fon2	Iseki	tem	350	T1	2	21	Japan	fon4
f2n1	Iseki	tem	350	T1	2	22	Japan	f2n3
f2n2	Iseki	tem	350	T1	2	23	Japan	f2n4
f5n1	Iseki	tem	350	T1	2	24	Japan	f5n3
f5n2	Iseki	tem	350	T1	2	25	Japan	f5n4
f1m1	Iseki	tem	350	T1	2	26	Japan	f1m3
f1m2	Iseki	tem	350	T1	2	27	Japan	f1m4
f3m1	Iseki	tem	350	T1	2	28	Japan	f3m3
f3m2	Iseki	tem	350	T1	2	29	Japan	f3m4
f1v1	Iseki	tem	350	T1	2	30	Japan	f1v3
f1v2	Iseki	tem	350	T1	2	31	Japan	f1v4
f3v1	Iseki	tem	350	T1	2	32	Japan	f3v3
f3v2	Iseki	tem	350	T1	2	33	Japan	f3v4
vvn1	Iseki	tem	350	T1	2	34	Japan	vvn3
vvn2	Iseki	tem	350	T1	2	35	Japan	vvn4
v5n1	Iseki	tem	350	T1	2	36	Japan	v5n3
v5n2	Iseki	tem	350	T1	2	37	Japan	v5n4
v1n1	Iseki	tem	350	T1	2	38	Japan	v1n3
v1n2	Iseki	tem	350	T1	2	39	Japan	v1n4
v2n1	Iseki	tem	350	T1	2	40	Japan	v2n3
v2n2	Iseki	tem	350	T1	2	41	Japan	v2n4
ffl1	Kohno	tem	350	T1	2	42	Japan	ffd1
ffl2	Kohno	tem	350	T1	2	43	Japan	ffd2
ffl3	Kohno	tem	350	T1	2	44	Japan	ffd3
ffl4	Kohno	tem	350	T1	2	45	Japan	ffd4
ffl5	Kohno	tem	350	T1	2	46	Japan	ffd5
ffl6	Kohno	tem	350	T1	2	47	Japan	ffd6
ffl7	Kohno	tem	350	T1	2	48	Japan	ffd7
ffl8	Kohno	tem	350	T1	2	49	Japan	ffd8
ffl9	Kohno	tem	350	T1	2	50	Japan	ffd9
fffa	Kohno	tem	350	T1	2	51	Japan	ffda
fffb	Kohno	tem	350	T1	2	52	Japan	ffdb
fffd	Kohno	tem	350	T1	2	53	Japan	ffdd
ffff	Kohno	tem	350	T1	2	54	Japan	ffdf
fffg	Kohno	tem	350	T1	2	55	Japan	ffdg
fffh	Kohno	tem	350	T1	2	56	Japan	ffdh
lbf1	Kohno	tem	350	T1	2	57	Japan	lbd1
lbf2	Kohno	tem	350	T1	2	58	Japan	lbd2
lbf3	Kohno	tem	350	T1	2	59	Japan	lbd3
lbf4	Kohno	tem	350	T1	2	60	Japan	lbd4
lbf5	Kohno	tem	350	T1	2	61	Japan	lbd5
lbf6	Kohno	tem	350	T1	2	62	Japan	lbd6
lbf7	Kohno	tem	350	T1	2	63	Japan	lbd7
l1f1	Kohno	tem	350	T1	2	64	Japan	l1d1
l1f2	Kohno	tem	350	T1	2	65	Japan	l1d2
l1f3	Kohno	tem	350	T1	2	66	Japan	l1d3
l1f4	Kohno	tem	350	T1	2	67	Japan	l1d4
l1f5	Kohno	tem	350	T1	2	68	Japan	l1d5
l1f6	Kohno	tem	350	T1	2	69	Japan	l1d6
l1f7	Kohno	tem	350	T1	2	70	Japan	l1d7
l2f1	Kohno	tem	350	T1	2	71	Japan	l2d1
l2f2	Kohno	tem	350	T1	2	72	Japan	l2d2
l2f3	Kohno	tem	350	T1	2	73	Japan	l2d3
l2f4	Kohno	tem	350	T1	2	74	Japan	l2d4
l2f5	Kohno	tem	350	T1	2	75	Japan	l2d5
l2f6	Kohno	tem	350	T1	2	76	Japan	l2d6
l2f7	Kohno	tem	350	T1	2	77	Japan	l2d7
lhf1	Kohno	tem	350	T1	2	78	Japan	lhd1
lhf2	Kohno	tem	350	T1	2	79	Japan	lhd2
lhf3	Kohno	tem	350	T1	2	80	Japan	lhd3
lhf4	Kohno	tem	350	T1	2	81	Japan	lhd4
lhf5	Kohno	tem	350	T1	2	82	Japan	lhd5
lhf6	Kohno	tem	350	T1	2	83	Japan	lhd6
lhf7	Kohno	tem	350	T1	2	84	Japan	lhd7
lhf8	Kohno	tem	350	T1	2	85	Japan	lhd8
lhf9	Kohno	tem	350	T1	2	86	Japan	lhd9
lhfa	Kohno	tem	350	T1	2	87	Japan	lhda
lhfb	Kohno	tem	350	T1	2	88	Japan	lhdb
lhfd	Kohno	tem	350	T1	2	89	Japan	lhdd

b2m7	Yoshie	tem	350	T1	2	90	Japan	b2m9
b2m8	Yoshie	tem	350	T1	2	91	Japan	b2ma
bk9l	Yoshie	tem	350	T1	2	92	Japan	bk9r
bk9m	Yoshie	tem	350	T1	2	93	Japan	bk9s
b03y	Yoshie	tem	350	T1	2	94	Japan	b040
b03z	Yoshie	tem	350	T1	2	95	Japan	b041
b15y	Yoshie	tem	350	T1	2	96	Japan	b160
b15z	Yoshie	tem	350	T1	2	97	Japan	b161
b6ly	Yoshie	tem	350	T1	2	98	Japan	b6m1
b6lz	Yoshie	tem	350	T1	2	99	Japan	b6m2
b65y	Yoshie	tem	350	T1	2	100	Japan	b660
b65z	Yoshie	tem	350	T1	2	101	Japan	b661
b55y	Yoshie	tem	350	T1	2	102	Japan	b560
b55z	Yoshie	tem	350	T1	2	103	Japan	b562
bze1	Yoshie	tem	350	T1	2	104	Japan	bze3
bze2	Yoshie	tem	350	T1	2	105	Japan	bze4
bze9	Yoshie	tem	350	T1	2	106	Japan	bzf1
bzf0	Yoshie	tem	350	T1	2	107	Japan	bzf2
bzf7	Yoshie	tem	350	T1	2	108	Japan	bzf9
bzf8	Yoshie	tem	350	T1	2	109	Japan	bzg0
b5ly	Yoshie	tem	350	T1	2	110	Japan	b5m0
b5lz	Yoshie	tem	350	T1	2	111	Japan	b5m1
b1ly	Yoshie	tem	350	T1	2	112	Japan	b1m0
b1lz	Yoshie	tem	350	T1	2	113	Japan	b1m1
b75y	Yoshie	tem	350	T1	2	114	Japan	b760
b75z	Yoshie	tem	350	T1	2	115	Japan	b761
b7ly	Yoshie	tem	350	T1	2	116	Japan	b7m0
b7lz	Yoshie	tem	350	T1	2	117	Japan	b7m1
b85y	Yoshie	tem	350	T1	2	118	Japan	b880
b85z	Yoshie	tem	350	T1	2	119	Japan	b861
b8ly	Yoshie	tem	350	T1	2	120	Japan	b8m0
b8lz	Yoshie	tem	350	T1	2	121	Japan	b8m1
bz11	Yoshie	tem	350	T1	2	122	Japan	bz13
bz12	Yoshie	tem	350	T1	2	123	Japan	bz14
bz17	Yoshie	tem	350	T1	2	124	Japan	bz19
bz18	Yoshie	tem	350	T1	2	125	Japan	bz21
bz24	Yoshie	tem	350	T1	2	126	Japan	bz26
bz25	Yoshie	tem	350	T1	2	127	Japan	bz27
bz29	Yoshie	tem	350	T1	2	128	Japan	bz32
bz31	Yoshie	tem	350	T1	2	129	Japan	bz33
bz36	Yoshie	tem	350	T1	2	130	Japan	bz38
bz37	Yoshie	tem	350	T1	2	131	Japan	bz39
bz43	Yoshie	tem	350	T1	2	132	Japan	bz45
bz44	Yoshie	tem	350	T1	2	133	Japan	bz46
bz49	Yoshie	tem	350	T1	2	134	Japan	bz52
bz51	Yoshie	tem	350	T1	2	135	Japan	bz53
bz56	Yoshie	tem	350	T1	2	136	Japan	bz58
bz57	Yoshie	tem	350	T1	2	137	Japan	bz59
bz63	Yoshie	tem	350	T1	2	138	Japan	bz65
bz64	Yoshie	tem	350	T1	2	139	Japan	bz66
bz69	Yoshie	tem	350	T1	2	140	Japan	bz72
bz71	Yoshie	tem	350	T1	2	141	Japan	bz73
bz76	Yoshie	tem	350	T1	2	142	Japan	bz78
bz77	Yoshie	tem	350	T1	2	143	Japan	bz79
bz83	Yoshie	tem	350	T1	2	144	Japan	bz85
bz84	Yoshie	tem	350	T1	2	145	Japan	bz86
bz89	Yoshie	tem	350	T1	2	146	Japan	bz92
bz91	Yoshie	tem	350	T1	2	147	Japan	bz93
xr48	Mukouda	tem	350	T1	2	148	Japan	xr62
xr49	Mukouda	tem	350	T1	2	149	Japan	xr63
xr4a	Mukouda	tem	350	T1	2	150	Japan	xr64
xr4b	Mukouda	tem	350	T1	2	151	Japan	xr65
xr4d	Mukouda	tem	350	T1	2	152	Japan	xr66
xr4f	Mukouda	tem	350	T1	2	153	Japan	xr67
xr4g	Mukouda	tem	350	T1	2	154	Japan	xr68
xr4h	Mukouda	tem	350	T1	2	155	Japan	xr69
xr4k	Mukouda	tem	350	T1	2	156	Japan	xr6a
xr4l	Mukouda	tem	350	T1	2	157	Japan	xr6b
xr4m	Mukouda	tem	350	T1	2	158	Japan	xr6d
xr4r	Mukouda	tem	350	T1	2	159	Japan	xr6f
xr4s	Mukouda	tem	350	T1	2	160	Japan	xr6g
xr4t	Mukouda	tem	350	T1	2	161	Japan	xr6h
xr4x	Mukouda	tem	350	T1	2	162	Japan	xr6k
xr4y	Mukouda	tem	350	T1	2	163	Japan	xr6l
xr51	Mukouda	tem	350	T1	2	164	Japan	xr6m
xr52	Mukouda	tem	350	T1	2	165	Japan	xr6r
xr53	Mukouda	tem	350	T1	2	166	Japan	xr6s
xr54	Mukouda	tem	350	T1	2	167	Japan	xr6t
xr3b	Mukouda	tem	350	T1	2	168	Japan	xr55
xr3d	Mukouda	tem	350	T1	2	169	Japan	xr56
xr3f	Mukouda	tem	350	T1	2	170	Japan	xr57
xr3g	Mukouda	tem	350	T1	2	171	Japan	xr58
xr3h	Mukouda	tem	350	T1	2	172	Japan	xr59
xr3k	Mukouda	tem	350	T1	2	173	Japan	xr5a
xr3l	Mukouda	tem	350	T1	2	174	Japan	xr5b
xr3m	Mukouda	tem	350	T1	2	176	Japan	xr5d
xr3r	Mukouda	tem	350	T1	2	176	Japan	xr5f
xr3s	Mukouda	tem	350	T1	2	177	Japan	xr5g
xr3t	Mukouda	tem	350	T1	2	178	Japan	xr5h
xr3x	Mukouda	tem	350	T1	2	179	Japan	xr5k
xr3y	Mukouda	tem	350	T1	2	180	Japan	xr5l
xr41	Mukouda	tem	350	T1	2	181	Japan	xr5m
xr42	Mukouda	tem	350	T1	2	182	Japan	xr5r
xr43	Mukouda	tem	350	T1	2	183	Japan	xr5s
xr44	Mukouda	tem	350	T1	2	184	Japan	xr5t
xr45	Mukouda	tem	350	T1	2	185	Japan	xr5x
xr46	Mukouda	tem	350	T1	2	186	Japan	xr5y
xr47	Mukouda	tem	350	T1	2	187	Japan	xr61

k321	Kimura	tensile	350	t2	1	1	Japan	k22
k322	Kimura	tensile	350	t2	1	2	Japan	k22
k323	Kimura	tensile	350	t2	1	3	Japan	k22
k331	Kimura	tensile	350	t2	1	4	Japan	k23
k332	Kimura	tensile	350	t2	1	5	Japan	k23
g701	Shibayama	tensile	350	t2	1	6	Japan	g801
g702	Shibayama	tensile	350	t2	1	7	Japan	g802
g703	Shibayama	tensile	350	t2	1	8	Japan	g803
g704	Shibayama	tensile	350	t2	1	9	Japan	g804
g711	Shibayama	tensile	350	t2	1	10	Japan	g811
g712	Shibayama	tensile	350	t2	1	11	Japan	g812
g713	Shibayama	tensile	350	t2	1	12	Japan	g813
g714	Shibayama	tensile	350	t2	1	13	Japan	g814
g721	Shibayama	tensile	350	t2	1	14	Japan	g821
g722	Shibayama	tensile	350	t2	1	15	Japan	g822
vb02	US	tensile	350	t2	1	16	US	nm
vb03	US	tensile	350	t2	1	17	US	nm
yf51	Watanabe	tensile	350	t2	2	1	Japan	yh51
yf52	Watanabe	tensile	350	t2	2	2	Japan	yh52
yf53	Watanabe	tensile	350	t2	2	3	Japan	yh53
yf54	Watanabe	tensile	350	t2	2	4	Japan	yh54
yf55	Watanabe	tensile	350	t2	2	5	Japan	yh55
yf56	Watanabe	tensile	350	t2	2	6	Japan	yh56
yf57	Watanabe	tensile	350	t2	2	7	Japan	yh57
yf58	Watanabe	tensile	350	t2	2	8	Japan	yh58
yf59	Watanabe	tensile	350	t2	2	9	Japan	yh59
yf60	Watanabe	tensile	350	t2	2	10	Japan	yh60
yf61	Watanabe	tensile	350	t2	2	11	Japan	yh61
yf62	Watanabe	tensile	350	t2	2	12	Japan	yh62
yf63	Watanabe	tensile	350	t2	2	13	Japan	yh63
yf64	Watanabe	tensile	350	t2	2	14	Japan	yh64
yf65	Watanabe	tensile	350	t2	2	15	Japan	yh65
yf80	Watanabe	tensile	350	t2	3	1	Japan	yh80
yf81	Watanabe	tensile	350	t2	3	2	Japan	yh81
yf82	Watanabe	tensile	350	t2	3	3	Japan	yh82
yf83	Watanabe	tensile	350	t2	3	4	Japan	yh83
yf84	Watanabe	tensile	350	t2	3	5	Japan	yh84
yf85	Watanabe	tensile	350	t2	3	6	Japan	yh85
yf86	Watanabe	tensile	350	t2	3	7	Japan	yh86
yf87	Watanabe	tensile	350	t2	3	8	Japan	yh87
yf88	Watanabe	tensile	350	t2	3	9	Japan	yh88
yf89	Watanabe	tensile	350	t2	3	10	Japan	yh89
yf90	Watanabe	tensile	350	t2	3	11	Japan	yh90
yf91	Watanabe	tensile	350	t2	3	12	Japan	yh91
yf92	Watanabe	tensile	350	t2	3	13	Japan	yh92
d001	Zinkle	tensile	350	t2	3	14	US	d004
d002	Zinkle	tensile	350	t2	3	15	US	d005
d003	Zinkle	tensile	350	t2	3	16	US	d006
a724	ohnuki	tensile	350	t2	4	1	Japan	a722
a733	ohnuki	tensile	350	t2	4	2	Japan	a731
a734	ohnuki	tensile	350	t2	4	3	Japan	a732
a743	ohnuki	tensile	350	t2	4	4	Japan	a741
a744	ohnuki	tensile	350	t2	4	5	Japan	a742
a205	Ohnuki	tensile	350	t2	4	6	Japan	a201
a206	Ohnuki	tensile	350	t2	4	7	Japan	a202
a207	Ohnuki	tensile	350	t2	4	8	Japan	a203
a208	Ohnuki	tensile	350	t2	4	9	Japan	a204
a224	Ohnuki	tensile	350	t2	4	10	Japan	a221
a225	Ohnuki	tensile	350	t2	4	11	Japan	a222
a226	Ohnuki	tensile	350	t2	4	12	Japan	a223
a243	Ohnuki	tensile	350	t2	4	13	Japan	a240
a244	Ohnuki	tensile	350	t2	4	14	Japan	a241
a245	Ohnuki	tensile	350	t2	4	15	Japan	a242
rv37	Zinkle	tensile	350	t2	5	1	US	nm
rv38	Zinkle	tensile	350	t2	5	2	US	nm
rv01	Zinkle	tensile	350	t2	5	3	US	rv39
rv02	Zinkle	tensile	350	t2	5	4	US	rv40
rv03	Zinkle	tensile	350	t2	5	5	US	rv07
rv04	Zinkle	tensile	350	t2	5	6	US	rv08
rv05	Zinkle	tensile	350	t2	5	7	US	rv09
rv06	Zinkle	tensile	350	t2	5	8	US	rv10
dc01	Zinkle	tensile	350	t2	5	9	US	rv11
dc02	Zinkle	tensile	350	t2	5	10	US	rv12
dc03	Zinkle	tensile	350	t2	5	11	US	dc09
dc04	Zinkle	tensile	350	t2	5	12	US	dc10
dc05	Zinkle	tensile	350	t2	5	13	US	dc11
dc06	Zinkle	tensile	350	t2	5	14	US	dc12
t516	Matsui	tensile	350	t2	5	15	Japan	t513
t517	Matsui	tensile	350	t2	5	16	Japan	t514
t518	Matsui	tensile	350	t2	5	17	Japan	t515
l1f4	Kohno	cvn	350	T3	1	b	Japan	l1d4
l1f5	Kohno	cvn	350	T3	1	b	Japan	l1d5
l1f6	Kohno	cvn	350	T3	1	t	Japan	l1d6
l1f7	Kohno	cvn	350	T3	1	t	Japan	l1d7
lff8	Kohno	cvn	350	T3	2	b	Japan	lfd8
lff9	Kohno	cvn	350	T3	2	b	Japan	lfd9
lbf1	Kohno	cvn	350	T3	2	t	Japan	lbd1
lbf2	Kohno	cvn	350	T3	2	t	Japan	lbd2
lff4	Kohno	cvn	350	T3	3	b	Japan	lfd4
lff5	Kohno	cvn	350	T3	3	b	Japan	lfd5
lff6	Kohno	cvn	350	T3	3	t	Japan	lfd6
lff7	Kohno	cvn	350	T3	3	t	Japan	lfd7
k335	Kimura	cvn	350	T3	4	b	Japan	k235
k336	Kimura	cvn	350	T3	4	b	Japan	k236
k337	Kimura	cvn	350	T3	4	t	Japan	k237
k338	Kimura	cvn	350	T3	4	t	Japan	k238

f4g3	Satou	tem	350	T4	1	1	Japan	f4g0
f4g4	Satou	tem	350	T4	1	2	Japan	f4g1
f4g5	Satou	tem	350	T4	1	3	Japan	f4g2
f4gl	Satou	tem	350	T4	1	4	Japan	f4gg
f4gm	Satou	tem	350	T4	1	5	Japan	f4gh
f4gr	Satou	tem	350	T4	1	6	Japan	f4gk
f4h3	Satou	tem	350	T4	1	7	Japan	f4h0
f4h4	Satou	tem	350	T4	1	8	Japan	f4h1
f4h5	Satou	tem	350	T4	1	9	Japan	f4h2
f5g4	Satou	tem	350	T4	1	10	Japan	f5g1
f5g5	Satou	tem	350	T4	1	11	Japan	f5g2
f5g6	Satou	tem	350	T4	1	12	Japan	f5g3
f5gl	Satou	tem	350	T4	1	13	Japan	f5gg
f5gm	Satou	tem	350	T4	1	14	Japan	f5gh
f5gr	Satou	tem	350	T4	1	15	Japan	f5gk
f5h3	Satou	tem	350	T4	1	16	Japan	f5h0
f5h5	Satou	tem	350	T4	1	17	Japan	f5h1
f5h6	Satou	tem	350	T4	1	18	Japan	f5h2
f6g4	Satou	tem	350	T4	1	19	Japan	f6g1
f6g5	Satou	tem	350	T4	1	20	Japan	f6g2
f6g6	Satou	tem	350	T4	1	21	Japan	f6g3
f6gl	Satou	tem	350	T4	1	22	Japan	f6gg
f6gm	Satou	tem	350	T4	1	23	Japan	f6gh
f6gr	Satou	tem	350	T4	1	24	Japan	f6gk
f6h2	Satou	tem	350	T4	1	25	Japan	f6h0
f6h3	Satou	tem	350	T4	1	26	Japan	f6h1
f7g4	Satou	tem	350	T4	1	27	Japan	f7g0
f7g5	Satou	tem	350	T4	1	28	Japan	f7g1
f7g6	Satou	tem	350	T4	1	29	Japan	f7g3
f7gm	Satou	tem	350	T4	1	30	Japan	f7gg
f7gr	Satou	tem	350	T4	1	31	Japan	f7gh
f7gs	Satou	tem	350	T4	1	32	Japan	f7gk
f7h4	Satou	tem	350	T4	1	33	Japan	f7h1
f7h5	Satou	tem	350	T4	1	34	Japan	f7h2
f7h6	Satou	tem	350	T4	1	35	Japan	f7h3
f8g3	Satou	tem	350	T4	1	36	Japan	f8g0
f8g4	Satou	tem	350	T4	1	37	Japan	f8g1
f8g5	Satou	tem	350	T4	1	38	Japan	f8g2
f8gl	Satou	tem	350	T4	1	39	Japan	f8gg
f8gm	Satou	tem	350	T4	1	40	Japan	f8gh
f8gr	Satou	tem	350	T4	1	41	Japan	f8gk
f8h4	Satou	tem	350	T4	1	42	Japan	f8h0
f8h5	Satou	tem	350	T4	1	43	Japan	f8h1
f8h6	Satou	tem	350	T4	1	44	Japan	f8h2
f3g2	Satou	tem	350	T4	1	45	Japan	f3g0
f3g3	Satou	tem	350	T4	1	46	Japan	f3g1
f2g4	Satou	tem	350	T4	1	47	Japan	f2g0
f2g5	Satou	tem	350	T4	1	48	Japan	f2g2
f2g7	Satou	tem	350	T4	1	49	Japan	f2g3
f2d5	Satou	tem	350	T4	1	50	Japan	f2d4
f304	Satou	tem	350	T4	1	51	Japan	f302
f305	Satou	tem	350	T4	1	52	Japan	f303
f404	Satou	tem	350	T4	1	53	Japan	f402
f405	Satou	tem	350	T4	1	54	Japan	f403
f504	Satou	tem	350	T4	1	55	Japan	f502
f505	Satou	tem	350	T4	1	56	Japan	f503
f3gk	Satou	tem	350	T4	1	57	Japan	f3gg
f3gl	Satou	tem	350	T4	1	58	Japan	f3gh
f0g3	Satou	tem	350	T4	1	59	Japan	f0g0
f0g4	Satou	tem	350	T4	1	60	Japan	f0g2
xh01	US	tem	350	T4	1	61	US	xh03
xh02	US	tem	350	T4	1	62	US	xh04
xi71	US	tem	350	T4	1	63	US	xi73
xi72	US	tem	350	T4	1	64	US	xi74
ta32	US	tem	350	T4	1	65	US	ta34
ta33	US	tem	350	T4	1	66	US	ta35
tb32	US	tem	350	T4	1	67	US	tb34
tb33	US	tem	350	T4	1	68	US	tb35
xe81	US	tem	350	T4	1	69	US	xe83
xe82	US	tem	350	T4	1	70	US	xe84
fp01	US	tem	350	T4	1	71	US	fp03
fp02	US	tem	350	T4	1	72	US	fp04
fq01	US	tem	350	T4	1	73	US	fq03
fq02	US	tem	350	T4	1	74	US	fq04
ay1	US	tem	350	T4	1	75	US	cy1
ay2	US	tem	350	T4	1	76	US	cy2
az1	US	tem	350	T4	1	77	US	cz1
az2	US	tem	350	T4	1	78	US	cz2
dp01	US	tem	350	T4	1	79	US	dp02
bn01	US	tem	350	T4	1	80	US	bn07
bn02	US	tem	350	T4	1	81	US	bn08
bn03	US	tem	350	T4	1	82	US	bn09
nf01	US	tem	350	T4	1	83	US	nf04
nf02	US	tem	350	T4	1	84	US	nf05
nf03	US	tem	350	T4	1	85	US	nf06
MgTiO3-1	US	tem	350	T4	1	86	US	MgTiO3-3
MgTi2O5-1	US	tem	350	T4	1	87	US	nm
tz06	Matsui	tem	350	T4	2	1	Japan	tz01
tz07	Matsui	tem	350	T4	2	2	Japan	tz02
tz08	Matsui	tem	350	T4	2	3	Japan	tz03
tz09	Matsui	tem	350	T4	2	4	Japan	tz04
tz10	Matsui	tem	350	T4	2	5	Japan	tz05
ty06	Matsui	tem	350	T4	2	6	Japan	ty01
ty07	Matsui	tem	350	T4	2	7	Japan	ty02
ty08	Matsui	tem	350	T4	2	8	Japan	ty03
ty09	Matsui	tem	350	T4	2	9	Japan	ty04
ty10	Matsui	tem	350	T4	2	10	Japan	ty05
tx06	Matsui	tem	350	T4	2	11	Japan	tx01
tx07	Matsui	tem	350	T4	2	12	Japan	tx02

tx08	Matsui	tem	350	T4	2	13	Japan	tx03
tx09	Matsui	tem	350	T4	2	14	Japan	tx04
tx10	Matsui	tem	350	T4	2	15	Japan	tx05
tv06	Matsui	tem	350	T4	2	16	Japan	tv01
tr06	Matsui	tem	350	T4	2	17	Japan	tr01
tr07	Matsui	tem	350	T4	2	18	Japan	tr02
tv07	Matsui	tem	350	T4	2	19	Japan	tv02
tr08	Matsui	tem	350	T4	2	20	Japan	tr03
tr09	Matsui	tem	350	T4	2	21	Japan	tr04
tv08	Matsui	tem	350	T4	2	23	Japan	tv03
tr10	Matsui	tem	350	T4	2	23	Japan	tr05
tp06	Matsui	tem	350	T4	2	24	Japan	tp01
tv09	Matsui	tem	350	T4	2	26	Japan	tv04
tp07	Matsui	tem	350	T4	2	26	Japan	tp02
tp08	Matsui	tem	350	T4	2	27	Japan	tp03
tv10	Matsui	tem	350	T4	2	29	Japan	tv05
tp09	Matsui	tem	350	T4	2	29	Japan	tp04
tp10	Matsui	tem	350	T4	2	30	Japan	tp05
tt06	Matsui	tem	350	T4	2	31	Japan	tt01
to06	Matsui	tem	350	T4	2	32	Japan	to01
to07	Matsui	tem	350	T4	2	33	Japan	to02
tt07	Matsui	tem	350	T4	2	34	Japan	tt02
to08	Matsui	tem	350	T4	2	35	Japan	to03
to09	Matsui	tem	350	T4	2	36	Japan	to04
tt08	Matsui	tem	350	T4	2	37	Japan	tt03
to10	Matsui	tem	350	T4	2	38	Japan	to05
tn06	Matsui	tem	350	T4	2	39	Japan	tn01
tt09	Matsui	tem	350	T4	2	40	Japan	tt04
tn07	Matsui	tem	350	T4	2	41	Japan	tn02
tn08	Matsui	tem	350	T4	2	42	Japan	tn03
tt10	Matsui	tem	350	T4	2	43	Japan	tt05
tn09	Matsui	tem	350	T4	2	44	Japan	tn04
tn10	Matsui	tem	350	T4	2	45	Japan	tn05
ts06	Matsui	tem	350	T4	2	46	Japan	ts01
tm06	Matsui	tem	350	T4	2	47	Japan	tm01
tm07	Matsui	tem	350	T4	2	48	Japan	tm02
ts07	Matsui	tem	350	T4	2	49	Japan	ts02
tm08	Matsui	tem	350	T4	2	50	Japan	tm03
tm09	Matsui	tem	350	T4	2	51	Japan	tm04
ts08	Matsui	tem	350	T4	2	52	Japan	ts03
tm10	Matsui	tem	350	T4	2	53	Japan	tm05
tl06	Matsui	tem	350	T4	2	54	Japan	tl01
ts09	Matsui	tem	350	T4	2	55	Japan	ts04
tl07	Matsui	tem	350	T4	2	56	Japan	tl02
tl08	Matsui	tem	350	T4	2	57	Japan	tl03
ts10	Matsui	tem	350	T4	2	58	Japan	ts05
tl09	Matsui	tem	350	T4	2	59	Japan	tl04
tl10	Matsui	tem	350	T4	2	60	Japan	tl05
tk06	Matsui	tem	350	T4	2	61	Japan	tk01
tk07	Matsui	tem	350	T4	2	62	Japan	tk02
tk08	Matsui	tem	350	T4	2	63	Japan	tk03
tk09	Matsui	tem	350	T4	2	64	Japan	tk04
tk10	Matsui	tem	350	T4	2	65	Japan	tk05
tj06	Matsui	tem	350	T4	2	66	Japan	tj01
tj07	Matsui	tem	350	T4	2	67	Japan	tj02
tj08	Matsui	tem	350	T4	2	68	Japan	tj03
tj09	Matsui	tem	350	T4	2	69	Japan	tj04
tj10	Matsui	tem	350	T4	2	70	Japan	tj05
ti06	Matsui	tem	350	T4	2	71	Japan	ti01
ti07	Matsui	tem	350	T4	2	72	Japan	ti02
ti08	Matsui	tem	350	T4	2	73	Japan	ti03
ti09	Matsui	tem	350	T4	2	74	Japan	ti04
ti10	Matsui	tem	350	T4	2	75	Japan	ti05
tg06	Matsui	tem	350	T4	2	76	Japan	tg01
tg07	Matsui	tem	350	T4	2	77	Japan	tg02
tg08	Matsui	tem	350	T4	2	78	Japan	tg03
tg09	Matsui	tem	350	T4	2	79	Japan	tg04
tg10	Matsui	tem	350	T4	2	80	Japan	tg05
tf06	Matsui	tem	350	T4	2	81	Japan	tf01
tf07	Matsui	tem	350	T4	2	82	Japan	tf02
tf08	Matsui	tem	350	T4	2	83	Japan	tf03
tf09	Matsui	tem	350	T4	2	84	Japan	tf04
tf10	Matsui	tem	350	T4	2	85	Japan	tf05
tc06	Matsui	tem	350	T4	2	86	Japan	tc01
tc07	Matsui	tem	350	T4	2	87	Japan	tc02
tc08	Matsui	tem	350	T4	2	88	Japan	tc03
tc09	Matsui	tem	350	T4	2	89	Japan	tc04
tc10	Matsui	tem	350	T4	2	90	Japan	tc05
t206	Matsui	tem	350	T4	2	91	Japan	t201
t207	Matsui	tem	350	T4	2	92	Japan	t202
t208	Matsui	tem	350	T4	2	93	Japan	t203
t209	Matsui	tem	350	T4	2	94	Japan	t204
t210	Matsui	tem	350	T4	2	95	Japan	t205
t306	Matsui	tem	350	T4	2	96	Japan	t301
t307	Matsui	tem	350	T4	2	97	Japan	t302
t308	Matsui	tem	350	T4	2	98	Japan	t303
t309	Matsui	tem	350	T4	2	99	Japan	t304
t310	Matsui	tem	350	T4	2	100	Japan	t305
t406	Matsui	tem	350	T4	2	101	Japan	t401
t407	Matsui	tem	350	T4	2	102	Japan	t402
t408	Matsui	tem	350	T4	2	103	Japan	t403
t409	Matsui	tem	350	T4	2	104	Japan	t404
t410	Matsui	tem	350	T4	2	105	Japan	t405
t506	Matsui	tem	350	T4	2	106	Japan	t501
t507	Matsui	tem	350	T4	2	107	Japan	t502
t508	Matsui	tem	350	T4	2	108	Japan	t503
t509	Matsui	tem	350	T4	2	109	Japan	t504
t510	Matsui	tem	350	T4	2	110	Japan	t505
t606	Matsui	tem	350	T4	2	111	Japan	t601

t607	Matsui	tem	350	T4	2	112	Japan	t602
t608	Matsui	tem	350	T4	2	113	Japan	t603
t609	Matsui	tem	350	T4	2	114	Japan	t604
t610	Matsui	tem	350	T4	2	115	Japan	t605
t706	Matsui	tem	350	T4	2	116	Japan	t701
t707	Matsui	tem	350	T4	2	117	Japan	t702
t708	Matsui	tem	350	T4	2	118	Japan	t703
t709	Matsui	tem	350	T4	2	119	Japan	t704
t710	Matsui	tem	350	T4	2	120	Japan	t705
t806	Matsui	tem	350	T4	2	121	Japan	t801
t807	Matsui	tem	350	T4	2	122	Japan	t802
t808	Matsui	tem	350	T4	2	123	Japan	t803
t809	Matsui	tem	350	T4	2	124	Japan	t804
t810	Matsui	tem	350	T4	2	125	Japan	t805
cj01	Robertson	tensile	350	t5	1	1	US	cj04
cj02	Robertson	tensile	350	t5	1	2	US	cj05
cj03	Robertson	tensile	350	t5	1	3	US	cj06
sj01	Robertson	tensile	350	t5	1	4	US	sj04
sj02	Robertson	tensile	350	t5	1	5	US	sj05
sj03	Robertson	tensile	350	t5	1	6	US	sj06
g723	Shibayama	tensile	350	t5	1	7	Japan	g823
g724	Shibayama	tensile	350	t5	1	8	Japan	g824
g731	Shibayama	tensile	350	t5	1	9	Japan	g831
g732	Shibayama	tensile	350	t5	1	10	Japan	g832
g733	Shibayama	tensile	350	t5	1	11	Japan	g833
g734	Shibayama	tensile	350	t5	1	12	Japan	g834
g741	Shibayama	tensile	350	t5	1	13	Japan	g841
g742	Shibayama	tensile	350	t5	1	14	Japan	g842
g743	Shibayama	tensile	350	t5	1	15	Japan	g843
g744	Shibayama	tensile	350	t5	1	16	Japan	g844
yf66	Watanabe	tensile	350	t5	2	1	Japan	yh66
yf67	Watanabe	tensile	350	t5	2	2	Japan	yh67
yf68	Watanabe	tensile	350	t5	2	3	Japan	yh68
yf69	Watanabe	tensile	350	t5	2	4	Japan	yh69
yf70	Watanabe	tensile	350	t5	2	5	Japan	yh70
yf71	Watanabe	tensile	350	t5	2	6	Japan	yh71
yf72	Watanabe	tensile	350	t5	2	7	Japan	yh72
yf73	Watanabe	tensile	350	t5	2	8	Japan	yh73
yf74	Watanabe	tensile	350	t5	2	9	Japan	yh74
yf75	Watanabe	tensile	350	t5	2	10	Japan	yh75
yf76	Watanabe	tensile	350	t5	2	11	Japan	yh76
yf77	Watanabe	tensile	350	t5	2	12	Japan	yh77
yf78	Watanabe	tensile	350	t5	2	13	Japan	yh78
yf79	Watanabe	tensile	350	t5	2	14	Japan	yh79
dm01	US	tensile	350	t5	2	15	US	dm04
dm02	US	tensile	350	t5	2	16	US	dm05
dm03	US	tensile	350	t5	2	17	US	dm06
g7t0	Shibayama	tensile	350	t5	3	1	Japan	g810
g7t1	Shibayama	tensile	350	t5	3	2	Japan	g811
g7t2	Shibayama	tensile	350	t5	3	3	Japan	g812
g7t3	Shibayama	tensile	350	t5	3	4	Japan	g813
g7t4	Shibayama	tensile	350	t5	3	5	Japan	g814
g7t5	Shibayama	tensile	350	t5	3	6	Japan	g815
g7t6	Shibayama	tensile	350	t5	3	7	Japan	g816
g707	Shibayama	tensile	350	t5	3	8	Japan	g817
g7t8	Shibayama	tensile	350	t5	3	9	Japan	g818
g7t9	Shibayama	tensile	350	t5	3	10	Japan	g819
gc01	US	tensile	350	t5	3	11	US	gc07
gc02	US	tensile	350	t5	3	12	US	gc08
gc03	US	tensile	350	t5	3	13	US	gc09
gc04	US	tensile	350	t5	3	14	US	gc10
gc05	US	tensile	350	t5	3	15	US	gc11
gc06	US	tensile	350	t5	3	16	US	gc12
dq01	Singh	tensile	350	t5	4	1	US	dq04
dq02	Singh	tensile	350	t5	4	2	US	dq05
dq03	Singh	tensile	350	t5	4	3	US	dq06
yc01	Singh	tensile	350	t5	4	4	US	yc04
yc02	Singh	tensile	350	t5	4	5	US	yc05
yc03	Singh	tensile	350	t5	4	6	US	yc06
aj01	Singh	tensile	350	t5	4	7	US	aj04
aj02	Singh	tensile	350	t5	4	8	US	aj05
aj03	Singh	tensile	350	t5	4	9	US	aj06
dl01	Singh	tensile	350	t5	4	10	US	dl04
dl02	Singh	tensile	350	t5	4	11	US	dl05
dl03	Singh	tensile	350	t5	4	12	US	dl06
dp01	Singh	tensile	350	t5	4	13	US	dp05
dp02	Singh	tensile	350	t5	4	14	US	dp06
dp03	Zinkle	tensile	350	T5	4	15	US	dp07
dp04	Zinkle	tensile	350	T5	4	16	US	nm
rc01	Zinkle	tensile	350	T5	5	1	US	rc07
rc02	Zinkle	tensile	350	T5	5	2	US	rc08
rc03	Zinkle	tensile	350	T5	5	3	US	rc09
rc04	Zinkle	tensile	350	T5	5	4	US	rc10
rc05	Zinkle	tensile	350	T5	5	5	US	rc11
rc06	Zinkle	tensile	350	T5	5	6	US	rc12
fc01	Zinkle	tensile	350	T5	5	7	US	fc08
fc02	Zinkle	tensile	350	T5	5	8	US	fc09
fc03	Zinkle	tensile	350	T5	5	9	US	fc09
fc04	Zinkle	tensile	350	T5	5	10	US	fc10
fc05	Zinkle	tensile	350	T5	5	11	US	fc11
fc08	Zinkle	tensile	350	T5	5	12	US	fc12
t316	Matsui	tensile	350	t5	5	13	Japan	T313
t317	Matsui	tensile	350	t5	5	14	Japan	T314
t318	Matsui	tensile	350	t5	5	15	Japan	T315

High Temperature..... follows

specimen	experimenter	type	fr. temp.	hole	position	position(2)	affiliation	match
k5n1	Kimura	tensile	500	B1	1	1	Japan	k4n1
k5n2	Kimura	tensile	500	B1	1	2	Japan	k4n2
k5n3	Kimura	tensile	500	B1	1	3	Japan	k4n3
k5n4	Kimura	tensile	500	B1	1	4	Japan	k4n4
k5n5	Kimura	tensile	500	B1	1	5	Japan	k4n5
k5n6	Kimura	tensile	500	B1	1	6	Japan	k4n6
k5n7	Kimura	tensile	500	B1	1	7	Japan	k4n7
k5n8	Kimura	tensile	500	B1	1	8	Japan	k4n8
k521	Kimura	tensile	500	B1	1	9	Japan	k421
k522	Kimura	tensile	500	B1	1	10	Japan	k422
k523	Kimura	tensile	500	B1	1	11	Japan	k423
k524	Kimura	tensile	500	B1	1	12	Japan	k424
k525	Kimura	tensile	500	B1	1	13	Japan	k425
k5l1	Kimura	tensile	500	B1	1	14	Japan	k4l1
k5l2	Kimura	tensile	500	B1	1	15	Japan	k4l2
k5l3	Kimura	tensile	500	b1	1	16	Japan	k4l3
k5l4	Kimura	tensile	500	b1	1	17	Japan	k4l4
l1b1	Kohno	tensile	500	B1	2	1	Japan	l1a1
l1b2	Kohno	tensile	500	B1	2	2	Japan	l1a2
l1b3	Kohno	tensile	500	B1	2	3	Japan	l1a3
l1b4	Kohno	tensile	500	B1	2	4	Japan	l1a4
l1b5	Kohno	tensile	500	B1	2	5	Japan	l1a5
l2b1	Kohno	tensile	500	B1	2	6	Japan	l2a1
l2b2	Kohno	tensile	500	B1	2	7	Japan	l2a2
l2b3	Kohno	tensile	500	B1	2	8	Japan	l2a3
l2b4	Kohno	tensile	500	B1	2	9	Japan	l2a4
l2b5	Kohno	tensile	500	B1	2	10	Japan	l2a5
lhb1	Kohno	tensile	500	B1	2	11	Japan	lha1
lhb2	Kohno	tensile	500	B1	2	12	Japan	lha2
lhb3	Kohno	tensile	500	B1	2	13	Japan	lha3
lhb4	Kohno	tensile	500	B1	2	14	Japan	lha4
lhb5	Kohno	tensile	500	B1	2	15	Japan	lha5
lhb6	Kohno	tensile	500	b1	2	16	Japan	lha6
lhb7	Kohno	tensile	500	b1	2	17	Japan	lha7
f5hs	Satou	tensile	500	b1	3	1	Japan	f5hd
f5hl	Satou	tensile	500	b1	3	2	Japan	f5hf
f5hm	Satou	tensile	500	B1	3	3	Japan	f5hg
f5hx	Satou	tensile	500	B1	3	4	Japan	f5hk
f5hy	Satou	tensile	500	B1	3	5	Japan	f5hr
f5k1	Satou	tensile	500	B1	3	6	Japan	f5hh
f5k2	Satou	tensile	500	B1	3	7	Japan	f5id
f5k3	Satou	tensile	500	B1	3	8	Japan	f5k5
f5k9	Satou	tensile	500	B1	3	9	Japan	f5k6
f5kb	Satou	tensile	500	B1	3	10	Japan	f5k7
f5ks	Satou	tensile	500	B1	3	11	Japan	f5kk
f5kv	Satou	tensile	500	B1	3	12	Japan	f5km
f6hm	Satou	tensile	500	B1	3	13	Japan	f6hd
f6hr	Satou	tensile	500	B1	3	14	Japan	f6hf
f6hs	Satou	tensile	500	B1	3	15	Japan	f6hk
f6hv	Satou	tensile	500	B1	3	16	Japan	f6hl
f6hx	Satou	tensile	500	B1	3	17	Japan	f6hy
t510	Matsui	tensile	500	B1	4	1	Japan	t507
t511	Matsui	tensile	500	B1	4	2	Japan	t506
t512	Matsui	tensile	500	B1	4	3	Japan	t509
t710	Matsui	tensile	500	B1	4	4	Japan	t707
t711	Matsui	tensile	500	B1	4	5	Japan	t706
t712	Matsui	tensile	500	B1	4	6	Japan	t709
t810	Matsui	tensile	500	B1	4	7	Japan	t807
t811	Matsui	tensile	500	B1	4	8	Japan	t808
t812	Matsui	tensile	500	B1	4	9	Japan	t809
ty30	Matsui	tensile	500	B1	4	10	Japan	ty27
ty31	Matsui	tensile	500	B1	4	11	Japan	ty28
ty32	Matsui	tensile	500	B1	4	12	Japan	ty29
tz24	Matsui	tensile	500	B1	4	13	Japan	tz21
tz25	Matsui	tensile	500	B1	4	14	Japan	tz22
tz26	Matsui	tensile	500	B1	4	15	Japan	tz23
t612	Matsui	tensile	500	B1	4	16	Japan	t609
gc13	Klueh	tensile	500	B1	5	1	US	gc19
gc14	Klueh	tensile	500	B1	5	2	US	gc20
gc15	Klueh	tensile	500	B1	5	3	US	gc21
gc16	Klueh	tensile	500	B1	5	4	US	gc22
gc17	Klueh	tensile	500	B1	5	5	US	gc23
gc18	Klueh	tensile	500	B1	5	6	US	gc24
vb04	Klueh	tensile	500	B1	5	7	US	vb08
vb05	Klueh	tensile	500	B1	5	8	US	vb06
vb06	Klueh	tensile	500	B1	5	9	US	vc08
vb07	Klueh	tensile	500	B1	5	10	US	vc09
vc04	Klueh	tensile	500	B1	5	11	US	b
vc05	Klueh	tensile	500	B1	5	12	US	b
vc06	Klueh	tensile	500	B1	5	13	US	b
vc07	Klueh	tensile	500	B1	5	14	US	b
gkcb	Kurishita	bar7	500	b2	1	b	Japan	gkcg
gkcc	Kurishita	bar7	500	b2	1	b	Japan	gkch
gkcd	Kurishita	bar7	500	b2	1	b	Japan	gkci
gkce	Kurishita	bar7	500	b2	1	s	Japan	gkck
gkcf	Kurishita	bar7	500	b2	1	s	Japan	gkcg
gkdb	Kurishita	bar7	500	b2	1	s	Japan	gkdg
gkdc	Kurishita	bar7	500	b2	1	s	Japan	gkdh
gkdd	Kurishita	bar7	500	b2	1	t	Japan	gkdl
gkde	Kurishita	bar7	500	b2	1	t	Japan	gkdk
gkdf	Kurishita	bar7	500	b2	1	t	Japan	gkdl
k5l1	kimura	bar7	500	b2	2	b	Japan	k4t1
k5l2	kimura	bar7	500	b2	2	b	Japan	k4t2
k5l3	kimura	bar7	500	b2	2	b	Japan	k4t3
k5l4	kimura	bar7	500	b2	2	s	Japan	k4t4
k5l5	kimura	bar7	500	b2	2	s	Japan	k4t5
gkbb	Kurishita	bar7	500	b2	2	s	Japan	gkbg
gkbc	Kurishita	bar7	500	b2	2	s	Japan	gkbh
gkbd	Kurishita	bar7	500	b2	2	t	Japan	gkbl
gkbe	Kurishita	bar7	500	b2	2	t	Japan	gkbk
gkbf	Kurishita	bar7	500	b2	2	t	Japan	gkbl
k5r1	kimura	bar7	500	b2	3	b	Japan	k4r1
k5r2	kimura	bar7	500	b2	3	b	Japan	k4r2
k5r3	kimura	bar7	500	b2	3	b	Japan	k4r3
k5r4	kimura	bar7	500	b2	3	s	Japan	k4r4
k5r5	kimura	bar7	500	b2	3	s	Japan	k4r5
k5s1	kimura	bar7	500	b2	3	s	Japan	k4s1
k5s2	kimura	bar7	500	b2	3	s	Japan	k4s2
k5s3	kimura	bar7	500	b2	3	t	Japan	k4s3

k5s4	kimura	bar7	500	b2	3	t	Japan	k4s4
k5s5	kimura	bar7	500	b2	3	t	Japan	k4s5
gkab	Kurishita	bar7	500	b2	4	b	Japan	gkag
gkac	Kurishita	bar7	500	b2	4	b	Japan	gkah
gkad	Kurishita	bar7	500	b2	4	b	Japan	gkai
gkae	Kurishita	bar7	500	b2	4	s	Japan	gkak
gkaf	Kurishita	bar7	500	b2	4	s	Japan	gkal
gk3g	Kurishita	bar7	500	b2	4	s	Japan	gk5g
gk3h	Kurishita	bar7	500	b2	4	s	Japan	gk5h
gk3i	Kurishita	bar7	500	b2	4	t	Japan	gk5i
gk3k	Kurishita	bar7	500	b2	4	t	Japan	gk5k
gk3l	Kurishita	bar7	500	b2	4	t	Japan	gk5l
gk8b	Kurishita	bar7	500	b2	5	b	Japan	gk8g
gk8c	Kurishita	bar7	500	b2	5	b	Japan	gk8h
gk8d	Kurishita	bar7	500	b2	5	b	Japan	gk8i
gk8e	Kurishita	bar7	500	b2	5	s	Japan	gk8k
gk8f	Kurishita	bar7	500	b2	5	s	Japan	gk8l
gk9b	Kurishita	bar7	500	b2	5	s	Japan	gk9g
gk9c	Kurishita	bar7	500	b2	5	s	Japan	gk9h
gk9d	Kurishita	bar7	500	b2	5	t	Japan	gk9i
gk9e	Kurishita	bar7	500	b2	5	t	Japan	gk9k
gk9f	Kurishita	bar7	500	b2	5	t	Japan	gk9l
gk6b	Kurishita	bar7	500	b2	6	b	Japan	gk6g
gk6c	Kurishita	bar7	500	b2	6	b	Japan	gk6h
gk6d	Kurishita	bar7	500	b2	6	b	Japan	gk6i
gk6e	Kurishita	bar7	500	b2	6	s	Japan	gk6k
gk6f	Kurishita	bar7	500	b2	6	s	Japan	gk6l
gk7b	Kurishita	bar7	500	b2	6	s	Japan	gk7g
gk7c	Kurishita	bar7	500	b2	6	s	Japan	gk7h
gk7d	Kurishita	bar7	500	b2	6	t	Japan	gk7i
gk7e	Kurishita	bar7	500	b2	6	t	Japan	gk7k
gk7f	Kurishita	bar7	500	b2	6	t	Japan	gk7l
gk2b	Kurishita	bar7	500	b2	7	b	Japan	gk2g
gk2c	Kurishita	bar7	500	b2	7	b	Japan	gk2h
gk2d	Kurishita	bar7	500	b2	7	b	Japan	gk2i
gk2e	Kurishita	bar7	500	b2	7	s	Japan	gk2k
gk2f	Kurishita	bar7	500	b2	7	s	Japan	gk2l
gk4b	Kurishita	bar7	500	b2	7	s	Japan	gk4g
gk4c	Kurishita	bar7	500	b2	7	s	Japan	gk4h
gk4d	Kurishita	bar7	500	b2	7	t	Japan	gk4i
gk4e	Kurishita	bar7	500	b2	7	t	Japan	gk4k
gk4f	Kurishita	bar7	500	b2	7	t	Japan	gk4l
gk0b	Kurishita	bar7	500	b2	8	b	Japan	gk0g
gk0c	Kurishita	bar7	500	b2	8	b	Japan	gk0h
gk0d	Kurishita	bar7	500	b2	8	b	Japan	gk0i
gk0e	Kurishita	bar7	500	b2	8	s	Japan	gk0k
gk0f	Kurishita	bar7	500	b2	8	s	Japan	gk0l
gk1b	Kurishita	bar7	500	b2	8	s	Japan	gk1g
gk1c	Kurishita	bar7	500	b2	8	s	Japan	gk1h
gk1d	Kurishita	bar7	500	b2	8	t	Japan	gk1i
gk1e	Kurishita	bar7	500	b2	8	t	Japan	gk1k
gk1f	Kurishita	bar7	500	b2	8	t	Japan	gk1l
lhd6	Kohno	cvn	500	b3	1	b	Japan	lhd4
lhd7	Kohno	cvn	500	b3	1	b	Japan	lhd5
SiC3	Kohno	cvn	500	b3	1	t	Japan	SiC1
SiC4	Kohno	cvn	500	b3	1	t	Japan	SiC2
lha7	Kohno	cvn	500	b3	2	b	Japan	lha2
lha8	Kohno	cvn	500	b3	2	b	Japan	lha3
lha9	Kohno	cvn	500	b3	2	t	Japan	lha4
lhb1	Kohno	cvn	500	b3	2	t	Japan	lha5
l2b5	Kohno	cvn	500	b3	3	b	Japan	l2a5
l2b6	Kohno	cvn	500	b3	3	b	Japan	l2a6
l2b7	Kohno	cvn	500	b3	3	t	Japan	l2a7
lha6	Kohno	cvn	500	b3	3	t	Japan	lha1
l2b1	Kohno	cvn	500	b3	4	b	Japan	l2a1
l2b2	Kohno	cvn	500	b3	4	b	Japan	l2a2
l2b3	Kohno	cvn	500	b3	4	t	Japan	l2a3
l2b4	Kohno	cvn	500	b3	4	t	Japan	l2a4
k5p1	Kimura	tensile	500	b4	1	1	Japan	k4p1
k5p2	Kimura	tensile	500	b4	1	2	Japan	k4p2
k5p3	Kimura	tensile	500	b4	1	3	Japan	k4p3
k5p4	Kimura	tensile	500	b4	1	4	Japan	k4p4
k531	Kimura	tensile	500	B4	1	5	Japan	k431
k532	Kimura	tensile	500	B4	1	6	Japan	k432
k533	Kimura	tensile	500	B4	1	7	Japan	k433
k534	Kimura	tensile	500	B4	1	8	Japan	k434
k535	Kimura	tensile	500	B4	1	9	Japan	k435
k541	Kimura	tensile	500	B4	1	10	Japan	k441
k542	Kimura	tensile	500	B4	1	11	Japan	k442
k543	Kimura	tensile	500	B4	1	12	Japan	k443
k544	Kimura	tensile	500	B4	1	13	Japan	k444
k545	Kimura	tensile	500	b4	1	14	Japan	k445
t322	matsui	tensile	500	b4	1	15	Japan	t319
t323	Matsui	tensile	500	b4	1	16	Japan	t320
t324	Matsui	tensile	500	b4	1	17	Japan	t321
lfb1	Kohno	tensile	500	B4	2	1	Japan	lfa1
lfb2	Kohno	tensile	500	B4	2	2	Japan	lfa2
lfb3	Kohno	tensile	500	B4	2	3	Japan	lfa3
lfb4	Kohno	tensile	500	B4	2	4	Japan	lfa4
lfb5	Kohno	tensile	500	B4	2	5	Japan	lfa5
lfb6	Kohno	tensile	500	B4	2	6	Japan	lfa6
lfb7	Kohno	tensile	500	B4	2	7	Japan	lfa7
lfb8	Kohno	tensile	500	B4	2	8	Japan	lfa8
lbb1	Kohno	tensile	500	B4	2	9	Japan	lba1
lbb2	Kohno	tensile	500	B4	2	10	Japan	lba2
lbb3	Kohno	tensile	500	B4	2	11	Japan	lba3
lbb4	Kohno	tensile	500	B4	2	12	Japan	lba4
lbb5	Kohno	tensile	500	B4	2	13	Japan	lba5
t522	matsui	tensile	500	b4	2	14	Japan	t519
t523	Matsui	tensile	500	b4	2	15	Japan	t520
t524	Matsui	tensile	500	b4	2	16	Japan	t521
f8hm	Satou	tensile	500	b4	3	1	Japan	f8hd
f8hr	Satou	tensile	500	b4	3	2	Japan	f8hf
f8hs	Satou	tensile	500	b4	3	3	Japan	f8hg
f8ht	Satou	tensile	500	b4	3	4	Japan	f8hh
f8hv	Satou	tensile	500	b4	3	5	Japan	f8hk
f8hx	Satou	tensile	500	b4	3	6	Japan	f8hl
fohb	Satou	tensile	500	b4	3	7	Japan	fohf5

f3ha	Satou	tensile	500	b4	3	8	Japan	f3h6
f3hb	Satou	tensile	500	b4	3	9	Japan	f3h7
f3hd	Satou	tensile	500	b4	3	10	Japan	f3h9
f3h8	Satou	tensile	500	b4	3	11	Japan	f3hf
f2h0	Satou	tensile	500	b4	3	12	Japan	f2h5
f2h8	Satou	tensile	500	b4	3	13	Japan	f2h6
t722	matsui	tensile	500	b4	3	16	Japan	t718
t723	Matsui	tensile	500	b4	3	17	Japan	t720
t724	Matsui	tensile	500	b4	3	18	Japan	t721
to24	Matsui	tensile	500	b4	4	1	Japan	to21
to25	Matsui	tensile	500	B4	4	2	Japan	to22
to26	Matsui	tensile	500	B4	4	3	Japan	to23
tl24	Matsui	tensile	500	b4	4	4	Japan	tl21
tl25	Matsui	tensile	500	b4	4	5	Japan	tl22
tl26	Matsui	tensile	500	b4	4	6	Japan	tl23
t310	Matsui	tensile	500	B4	4	7	Japan	t307
t311	Matsui	tensile	500	B4	4	8	Japan	t308
t312	Matsui	tensile	500	B4	4	9	Japan	t309
t410	Matsui	tensile	500	B4	4	10	Japan	t407
t411	Matsui	tensile	500	B4	4	11	Japan	t408
t412	Matsui	tensile	500	B4	4	12	Japan	t409
t610	Matsui	tensile	500	b4	4	13	Japan	t607
t611	Matsui	tensile	500	b4	4	14	Japan	t608
t612	Matsui	tensile	500	B4	4	15	Japan	t609
xh09	Kiueh	tensile	500	B4	5	1	US	xh13
xh10	Kiueh	tensile	500	B4	5	2	US	xh14
xh11	Kiueh	tensile	500	B4	5	3	US	xh15
xh12	Kiueh	tensile	500	B4	5	4	US	xh16
ts30	Matsui	tensile(s)	500	b4	5	5	Japan	ts27
ts31	Matsui	tensile(s)	500	b4	5	6	Japan	ts28
ts32	Matsui	tensile(s)	500	b4	5	7	Japan	ts29
tr24	Matsui	tensile(s)	500	b4	5	8	Japan	tr21
tr25	Matsui	tensile(s)	500	b4	5	9	Japan	tr22
tr26	Matsui	tensile(s)	500	b4	5	10	Japan	tr23
tp24	Matsui	tensile(s)	500	b4	5	11	Japan	tp21
tp25	Matsui	tensile(s)	500	b4	5	12	Japan	tp22
tp26	Matsui	tensile(s)	500	b4	5	13	Japan	tp23
xi09	Kiueh	tensile	500	B4	5	14	US	xi13
xi10	Kiueh	tensile	500	B4	5	15	US	xi14
xi11	Kiueh	tensile	500	B4	5	16	US	xi15
xi12	Kiueh	tensile	500	B4	5	17	US	xi16
ltb07	Kohno	cvn	500	b5	1	B	Japan	lba7
ltb1	Kohno	cvn	500	b5	1	B	Japan	lta1
ltb2	Kohno	cvn	500	b5	1	T	Japan	lta2
ltb3	Kohno	cvn	500	b5	1	T	Japan	lta3
ltb03	Kohno	cvn	500	b5	2	B	Japan	lba3
ltb04	Kohno	cvn	500	b5	2	B	Japan	lba4
ltb05	Kohno	cvn	500	b5	2	T	Japan	lba5
ltb06	Kohno	cvn	500	b5	2	T	Japan	lba6
k539	Kimura	cvn	500	b5	3	B	Japan	k439
lfb1	Kohno	cvn	500	b5	3	B	Japan	lfa1
lfb2	Kohno	cvn	500	b5	3	T	Japan	lfa2
lfb3	Kohno	cvn	500	b5	3	T	Japan	lfa3
k531	Kimura	cvn	500	b5	4	B	Japan	k431
k532	Kimura	cvn	500	b5	4	B	Japan	k432
k533	Kimura	cvn	500	b5	4	T	Japan	k433
k534	Kimura	cvn	500	b5	4	T	Japan	k434
k5n1	Kimura	tem	500	b6	1	1	Japan	k4n1
k5n2	Kimura	tem	500	b6	1	2	Japan	k4n2
k5n3	Kimura	tem	500	b6	1	3	Japan	k4n3
k5n4	Kimura	tem	500	b6	1	4	Japan	k4n4
k5n5	Kimura	tem	500	b6	1	5	Japan	k4n5
k5n6	Kimura	tem	500	b6	1	6	Japan	k4n6
k5n7	Kimura	tem	500	b6	1	7	Japan	k4n7
k521	Kimura	tem	500	b6	1	8	Japan	k421
k522	Kimura	tem	500	b6	1	9	Japan	k422
k523	Kimura	tem	500	b6	1	10	Japan	k423
k524	Kimura	tem	500	b6	1	11	Japan	k424
k531	Kimura	tem	500	b6	1	12	Japan	k431
k532	Kimura	tem	500	b6	1	13	Japan	k432
k533	Kimura	tem	500	b6	1	14	Japan	k433
k534	Kimura	tem	500	b6	1	15	Japan	k434
k541	Kimura	tem	500	b6	1	16	Japan	k441
k542	Kimura	tem	500	b6	1	17	Japan	k442
k543	Kimura	tem	500	b6	1	18	Japan	k443
k544	Kimura	tem	500	b6	1	19	Japan	k444
k551	Kimura	tem	500	b6	1	20	Japan	k451
k552	Kimura	tem	500	b6	1	21	Japan	k452
k553	Kimura	tem	500	b6	1	22	Japan	k453
k554	Kimura	tem	500	b6	1	23	Japan	k454
k555	Kimura	tem	500	b6	1	24	Japan	k455
k561	Kimura	tem	500	b6	1	25	Japan	k461
k562	Kimura	tem	500	b6	1	26	Japan	k462
k563	Kimura	tem	500	b6	1	27	Japan	k463
k564	Kimura	tem	500	b6	1	28	Japan	k464
k571	Kimura	tem	500	b6	1	29	Japan	k471
k572	Kimura	tem	500	b6	1	30	Japan	k472
k573	Kimura	tem	500	b6	1	31	Japan	k473
k574	Kimura	tem	500	b6	1	32	Japan	k474
k581	Kimura	tem	500	b6	1	33	Japan	k481
k582	Kimura	tem	500	b6	1	34	Japan	k482
k583	Kimura	tem	500	b6	1	35	Japan	k483
k584	Kimura	tem	500	b6	1	36	Japan	k484
k591	Kimura	tem	500	b6	1	37	Japan	k491
k592	Kimura	tem	500	b6	1	38	Japan	k492
k593	Kimura	tem	500	b6	1	39	Japan	k493
k594	Kimura	tem	500	b6	1	40	Japan	k494
k5a1	Kimura	tem	500	b6	1	40	Japan	k4a1
k5a2	Kimura	tem	500	b6	1	41	Japan	k4a2
k5a3	Kimura	tem	500	b6	1	42	Japan	k4a3
k5a4	Kimura	tem	500	b6	1	43	Japan	k4a4
k5a5	Kimura	tem	500	b6	1	44	Japan	k4a5
k5a6	Kimura	tem	500	b6	1	45	Japan	k4a6
k5a7	Kimura	tem	500	b6	1	46	Japan	k4a7
k5a8	Kimura	tem	500	b6	1	47	Japan	k4a8
k911	Kimura	tem	500	b6	1	48	Japan	k411
k912	Kimura	tem	500	b6	1	49	Japan	k412
k913	Kimura	tem	500	b6	1	50	Japan	k413

k5l4	Kimura	tem	500	b6	1	51	Japan	k4l4
k5l5	Kimura	tem	500	b6	1	52	Japan	k4l5
k5l6	Kimura	tem	500	b6	1	53	Japan	k4l6
k5l7	Kimura	tem	500	b6	1	54	Japan	k4l7
k5p1	Kimura	tem	500	B6	1	55	Japan	k4p1
k5p2	Kimura	tem	500	B6	1	56	Japan	k4p2
k5p3	Kimura	tem	500	B6	1	57	Japan	k4p3
k5p4	Kimura	tem	500	B6	1	58	Japan	k4p4
k5p5	Kimura	tem	500	B6	1	59	Japan	k4p5
k5p6	Kimura	tem	500	B6	1	60	Japan	k4p6
k5p7	Kimura	tem	500	B6	1	61	Japan	k4p7
k5k1	Kimura	tem	500	B6	1	63	Japan	k4k1
k5k2	Kimura	tem	500	B6	1	64	Japan	k4k2
k5k3	Kimura	tem	500	B6	1	65	Japan	k4k3
k5k4	Kimura	tem	500	B6	1	66	Japan	k4k4
k5k5	Kimura	tem	500	B6	1	67	Japan	k4k5
k5l1	Kimura	tem	500	b6	1	68	Japan	k4l1
k5l2	Kimura	tem	500	b6	1	69	Japan	k4l2
k5l3	Kimura	tem	500	b6	1	70	Japan	k4l3
k5l4	Kimura	tem	500	b6	1	71	Japan	k4l4
k5l5	Kimura	tem	500	b6	1	72	Japan	k4l5
k5m1	Kimura	tem	500	b6	1	73	Japan	k4m1
k5m2	Kimura	tem	500	b6	1	74	Japan	k4m2
k5m3	Kimura	tem	500	b6	1	75	Japan	k4m3
k5m4	Kimura	tem	500	b6	1	76	Japan	k4m4
k5m5	Kimura	tem	500	b6	1	77	Japan	k4m5
k5n1	Kimura	tem	500	b6	1	78	Japan	k4n1
k5n2	Kimura	tem	500	b6	1	79	Japan	k4n2
k5n3	Kimura	tem	500	b6	1	80	Japan	k4n3
k5n4	Kimura	tem	500	b6	1	81	Japan	k4n4
k5n5	Kimura	tem	500	b6	1	82	Japan	k4n5
k5r1	Kimura	tem	500	b6	1	83	Japan	k4r1
k5r2	Kimura	tem	500	b6	1	84	Japan	k4r2
k5r3	Kimura	tem	500	b6	1	85	Japan	k4r3
k5r4	Kimura	tem	500	b6	1	86	Japan	k4r4
k5r5	Kimura	tem	500	b6	1	87	Japan	k4r5
k5r6	Kimura	tem	500	b6	1	88	Japan	k4r6
k5r7	Kimura	tem	500	b6	1	89	Japan	k4r7
k5r8	Kimura	tem	500	b6	1	90	Japan	k4r8
k5s1	Kimura	tem	500	b6	1	91	Japan	k4s1
k5s2	Kimura	tem	500	b6	1	92	Japan	k4s2
k5s3	Kimura	tem	500	b6	1	93	Japan	k4s3
k5s4	Kimura	tem	500	b6	1	94	Japan	k4s4
k5s5	Kimura	tem	500	b6	1	95	Japan	k4s5
k5s6	Kimura	tem	500	b6	1	96	Japan	k4s6
k5s7	Kimura	tem	500	b6	1	97	Japan	k4s7
k5s8	Kimura	tem	500	b6	1	98	Japan	k4s8
k911	Kimura	tem	500	b6	1	99	Japan	k411
k912	Kimura	tem	500	b6	1	100	Japan	k412
k913	Kimura	tem	500	b6	1	101	Japan	k413
k914	Kimura	tem	500	b6	1	102	Japan	k414
k915	Kimura	tem	500	b6	1	103	Japan	k415
k916	Kimura	tem	500	b6	1	104	Japan	k416
k917	Kimura	tem	500	b6	1	105	Japan	k417
k918	Kimura	tem	500	b6	1	106	Japan	k418
a607	Ohnuki	tem	500	b6	1	107	Japan	a838
a608	Ohnuki	tem	500	b6	1	108	Japan	a606
a617	Ohnuki	tem	500	b6	1	109	Japan	a815
a618	Ohnuki	tem	500	b6	1	110	Japan	a616
a627	Ohnuki	tem	500	b6	1	111	Japan	a625
a628	Ohnuki	tem	500	b6	1	112	Japan	a626
a637	Ohnuki	tem	500	B6	1	113	Japan	a835
a638	Ohnuki	tem	500	B6	1	114	Japan	a636
a647	Ohnuki	tem	500	B6	1	115	Japan	a645
a648	Ohnuki	tem	500	B6	1	116	Japan	a646
a807	Ohnuki	tem	500	B6	1	117	Japan	a805
a808	Ohnuki	tem	500	B6	1	118	Japan	a806
a817	Ohnuki	tem	500	B6	1	119	Japan	a815
a818	Ohnuki	tem	500	B6	1	120	Japan	a816
a827	Ohnuki	tem	500	B6	1	121	Japan	a825
a828	Ohnuki	tem	500	B6	1	122	Japan	a826
a837	Ohnuki	tem	500	B6	1	123	Japan	a835
a838	Ohnuki	tem	500	B6	1	124	Japan	a836
a007	Ohnuki	tem	500	B6	1	125	Japan	a005
a008	Ohnuki	tem	500	B6	1	126	Japan	a006
a017	Ohnuki	tem	500	B6	1	127	Japan	a015
a018	Ohnuki	tem	500	B6	1	128	Japan	a016
a027	Ohnuki	tem	500	B6	1	129	Japan	a025
a028	Ohnuki	tem	500	B6	1	130	Japan	a026
a037	Ohnuki	tem	500	B6	1	131	Japan	a035
a038	Ohnuki	tem	500	B6	1	132	Japan	a036
a047	Ohnuki	tem	500	B6	1	133	Japan	a045
a048	Ohnuki	tem	500	B6	1	134	Japan	a046
a057	Ohnuki	tem	500	B6	1	135	Japan	a055
a058	Ohnuki	tem	500	B6	1	136	Japan	a056
a067	Ohnuki	tem	500	B6	1	137	Japan	a065
a068	Ohnuki	tem	500	B6	1	138	Japan	a066
a077	Ohnuki	tem	500	B6	1	139	Japan	a075
a078	Ohnuki	tem	500	B6	1	140	Japan	a076
a087	Ohnuki	tem	500	B6	1	141	Japan	a085
a088	Ohnuki	tem	500	B6	1	142	Japan	a086
a097	Ohnuki	tem	500	B6	1	143	Japan	a095
a098	Ohnuki	tem	500	B6	1	144	Japan	a096
a107	Ohnuki	tem	500	B6	1	145	Japan	a105
a108	Ohnuki	tem	500	B6	1	146	Japan	a106
flha	Hasegawa	tem	500	b6	2	1	Japan	flqa
flhb	Hasegawa	tem	500	b6	2	2	Japan	flqb
flhd	Hasegawa	tem	500	b6	2	3	Japan	flqd
flhf	Hasegawa	tem	500	b6	2	4	Japan	flqf
flhr	Hasegawa	tem	500	b6	2	5	Japan	flqr
flhs	Hasegawa	tem	500	b6	2	6	Japan	flqs
flhv	Hasegawa	tem	500	b6	2	7	Japan	flqv
flhx	Hasegawa	tem	500	b6	2	8	Japan	flqx
flla	Hasegawa	tem	500	b6	2	9	Japan	flka
fllb	Hasegawa	tem	500	b6	2	10	Japan	flkb
flld	Hasegawa	tem	500	b6	2	11	Japan	flkd
fllf	Hasegawa	tem	500	b6	2	12	Japan	flkf
fllm	Hasegawa	tem	500	b6	2	13	Japan	flkm
fllr	Hasegawa	tem	500	b6	2	14	Japan	flkr
flls	Hasegawa	tem	500	b6	2	15	Japan	flks
fllx	Hasegawa	tem	500	b6	2	16	Japan	flkx
flbb	Hasegawa	tem	500	b6	2	17	Japan	flab

flbd	Hasegawa	tem	500	b6	2	18	Japan	flad
flbg	Hasegawa	tem	500	b6	2	19	Japan	flag
flbh	Hasegawa	tem	500	b6	2	20	Japan	flah
flbm	Hasegawa	tem	500	b6	2	21	Japan	flam
flbr	Hasegawa	tem	500	b6	2	22	Japan	flar
flbs	Hasegawa	tem	500	b6	2	23	Japan	flas
flbt	Hasegawa	tem	500	b6	2	24	Japan	flat
flfa	Hasegawa	tem	500	b6	2	25	Japan	flda
flfb	Hasegawa	tem	500	b6	2	26	Japan	fldb
flfd	Hasegawa	tem	500	b6	2	27	Japan	fldd
flff	Hasegawa	tem	500	b6	2	28	Japan	fldf
flfh	Hasegawa	tem	500	b6	2	29	Japan	fldh
flfk	Hasegawa	tem	500	b6	2	30	Japan	fldk
flfl	Hasegawa	tem	500	b6	2	31	Japan	fldl
flfm	Hasegawa	tem	500	b6	2	32	Japan	fldm
fr2a	Hasegawa	tem	500	b6	2	33	Japan	fr1a
fr2b	Hasegawa	tem	500	b6	2	34	Japan	fr1b
fr2f	Hasegawa	tem	500	b6	2	35	Japan	fr1f
fr2g	Hasegawa	tem	500	b6	2	36	Japan	fr1g
fr2h	Hasegawa	tem	500	b6	2	37	Japan	fr1h
fr2k	Hasegawa	tem	500	b6	2	38	Japan	fr1k
fr2l	Hasegawa	tem	500	b6	2	39	Japan	fr1l
fr2m	Hasegawa	tem	500	b6	2	40	Japan	fr1m
av37	Kinoshita	tem	500	B6	2	41	Japan	av34
av38	Kinoshita	tem	500	B6	2	42	Japan	av35
av39	Kinoshita	tem	500	B6	2	43	Japan	av36
av87	Kinoshita	tem	500	B6	2	44	Japan	av8g
av88	Kinoshita	tem	500	B6	2	45	Japan	av84
av89	Kinoshita	tem	500	B6	2	46	Japan	av86
av97	Kinoshita	tem	500	B6	2	47	Japan	av94
av98	Kinoshita	tem	500	B6	2	48	Japan	av95
av99	Kinoshita	tem	500	B6	2	49	Japan	av96
al07	Kinoshita	tem	500	B6	2	50	Japan	al04
al09	Kinoshita	tem	500	B6	2	51	Japan	al05
al0h	Kinoshita	tem	500	B6	2	52	Japan	al06
al33	Kinoshita	tem	500	B6	2	53	Japan	al30
al34	Kinoshita	tem	500	B6	2	54	Japan	al31
al38	Kinoshita	tem	500	B6	2	55	Japan	al32
ar53	Kinoshita	tem	500	B6	2	56	Japan	ar50
ar54	Kinoshita	tem	500	B6	2	57	Japan	ar51
ar55	Kinoshita	tem	500	B6	2	58	Japan	ar52
ah87	Kinoshita	tem	500	B6	2	59	Japan	ah84
ah88	Kinoshita	tem	500	B6	2	60	Japan	ah85
ah89	Kinoshita	tem	500	B6	2	61	Japan	ah86
gkeb	Kurishita	tem	500	b6	2	62	Japan	gkeg
gkeo	Kurishita	tem	500	b6	2	63	Japan	gkeh
gkfb	Kurishita	tem	500	b6	2	64	Japan	gkfg
gkfo	Kurishita	tem	500	b6	2	65	Japan	gkfh
gkgb	Kurishita	tem	500	b6	2	66	Japan	gkgg
gkgo	Kurishita	tem	500	b6	2	67	Japan	gkgh
gkhb	Kurishita	tem	500	b6	2	68	Japan	gkhg
gkho	Kurishita	tem	500	b6	2	69	Japan	gkhh
gkhd	Kurishita	tem	500	b6	2	70	Japan	gkhj
gkjb	Kurishita	tem	500	b6	2	71	Japan	gkjg
gkjo	Kurishita	tem	500	b6	2	72	Japan	gkjh
gkkb	Kurishita	tem	500	b6	2	73	Japan	gkkg
gkko	Kurishita	tem	500	b6	2	74	Japan	gkkh
gkkd	Kurishita	tem	500	b6	2	75	Japan	gkkj
gkke	Kurishita	tem	500	b6	2	76	Japan	gkkek
gkkb	Kurishita	tem	500	b6	2	77	Japan	gkkbg
gkko	Kurishita	tem	500	b6	2	78	Japan	gkkh
gkkd	Kurishita	tem	500	b6	2	79	Japan	gkkj
gkmb	Kurishita	tem	500	b6	2	80	Japan	gkmg
gkmo	Kurishita	tem	500	b6	2	81	Japan	gkmh
gkmd	Kurishita	tem	500	b6	2	82	Japan	gkmj
gkme	Kurishita	tem	500	b6	2	83	Japan	gkmk
gknb	Kurishita	tem	500	b6	2	84	Japan	gkng
gkno	Kurishita	tem	500	b6	2	85	Japan	gknh
gknd	Kurishita	tem	500	b6	2	86	Japan	gknj
gkne	Kurishita	tem	500	b6	2	87	Japan	gknk
gkpb	Kurishita	tem	500	b6	2	88	Japan	gkpg
gkpo	Kurishita	tem	500	b6	2	89	Japan	gkph
gkpd	Kurishita	tem	500	b6	2	90	Japan	gkpj
gkpe	Kurishita	tem	500	b6	2	91	Japan	gkpk
gkqb	Kurishita	tem	500	b6	2	92	Japan	gkqg
gkqo	Kurishita	tem	500	b6	2	93	Japan	gkqh
gkqd	Kurishita	tem	500	b6	2	94	Japan	gkqj
gkqe	Kurishita	tem	500	b6	2	95	Japan	gkqk
gkrb	Kurishita	tem	500	b6	2	96	Japan	gkrg
gkro	Kurishita	tem	500	b6	2	97	Japan	gkrh
gkrd	Kurishita	tem	500	b6	2	98	Japan	gkrj
gksb	Kurishita	tem	500	b6	2	99	Japan	gksg
gkso	Kurishita	tem	500	b6	2	100	Japan	gksh
gksd	Kurishita	tem	500	b6	2	101	Japan	gksj
gktb	Kurishita	tem	500	b6	2	102	Japan	gktg
gkto	Kurishita	tem	500	b6	2	103	Japan	gkth
gktd	Kurishita	tem	500	b6	2	104	Japan	gktj
gkte	Kurishita	tem	500	b6	2	105	Japan	gktk
gkub	Kurishita	tem	500	b6	2	106	Japan	gkug
gkuo	Kurishita	tem	500	b6	2	107	Japan	gkuh
gkud	Kurishita	tem	500	b6	2	108	Japan	gkuj
gkue	Kurishita	tem	500	b6	2	109	Japan	gkuk
gkvb	Kurishita	tem	500	b6	2	110	Japan	gkvg
gkvo	Kurishita	tem	500	b6	2	111	Japan	gkvh
gkwb	Kurishita	tem	500	b6	2	112	Japan	gkwg
gkwo	Kurishita	tem	500	b6	2	113	Japan	gkwh
gkwd	Kurishita	tem	500	b6	2	114	Japan	gkwj
gkwe	Kurishita	tem	500	b6	2	115	Japan	gkwk
gkxb	Kurishita	tem	500	b6	2	116	Japan	gkxg
gkxo	Kurishita	tem	500	b6	2	117	Japan	gkxh
gkxd	Kurishita	tem	500	b6	2	118	Japan	gkxj
b2mb	Yoshiie	tem	500	B6	2	119	Japan	b2mf
b2md	Yoshiie	tem	500	B6	2	120	Japan	b2mg
bk9t	Yoshiie	tem	500	b6	2	121	Japan	bk9x
bk9v	Yoshiie	tem	500	b6	2	122	Japan	bk9y
b042	Yoshiie	tem	500	b6	2	123	Japan	b044
b043	Yoshiie	tem	500	b6	2	124	Japan	b045
b162	Yoshiie	tem	500	b6	2	125	Japan	b164
b163	Yoshiie	tem	500	b6	2	126	Japan	b165
b6m3	Yoshiie	tem	500	b6	2	127	Japan	b6m6
b6m4	Yoshiie	tem	500	b6	2	128	Japan	b6m7
b662	Yoshiie	tem	500	b6	2	129	Japan	b664

b663	Yoshiie	tem	500	b6	2	130	Japan	b665
b563	Yoshiie	tem	500	b6	2	131	Japan	b566
b565	Yoshiie	tem	500	b6	2	132	Japan	b567
bze5	Yoshiie	tem	500	b6	2	133	Japan	bze7
bze6	Yoshiie	tem	500	b6	2	134	Japan	bze8
bzf6	Yoshiie	tem	500	b6	2	135	Japan	bzf5
bzf4	Yoshiie	tem	500	b6	2	136	Japan	bzf6
bzg1	Yoshiie	tem	500	b6	2	137	Japan	bzg3
bzg2	Yoshiie	tem	500	b6	2	138	Japan	bzg4
b5m2	Yoshiie	tem	500	b6	2	139	Japan	b5m4
b5m3	Yoshiie	tem	500	b6	2	140	Japan	b5m5
b1m2	Yoshiie	tem	500	b6	2	141	Japan	b1m4
b1m3	Yoshiie	tem	500	b6	2	142	Japan	b1m5
b762	Yoshiie	tem	500	b6	2	143	Japan	b764
b763	Yoshiie	tem	500	b6	2	144	Japan	b765
b7m2	Yoshiie	tem	500	b6	2	145	Japan	b7m4
b7m3	Yoshiie	tem	500	b6	2	146	Japan	b7m5
b862	Yoshiie	tem	500	b6	2	147	Japan	b864
b863	Yoshiie	tem	500	b6	2	148	Japan	b865
b8m2	Yoshiie	tem	500	b6	2	149	Japan	b8m4
b8m3	Yoshiie	tem	500	b6	2	150	Japan	b8m5
bz15	Yoshiie	tem	500	b6	2	151	Japan	bza1
bz16	Yoshiie	tem	500	b6	2	152	Japan	bza2
bz22	Yoshiie	tem	500	b6	2	153	Japan	bza3
bz23	Yoshiie	tem	500	b6	2	154	Japan	bza4
bz28	Yoshiie	tem	500	b6	2	155	Japan	bza5
bz29	Yoshiie	tem	500	b6	2	156	Japan	bza6
bz34	Yoshiie	tem	500	b6	2	157	Japan	bza7
bz35	Yoshiie	tem	500	b6	2	158	Japan	bza8
bz41	Yoshiie	tem	500	b6	2	159	Japan	bza9
bz42	Yoshiie	tem	500	b6	2	160	Japan	bzb1
bz47	Yoshiie	tem	500	b6	2	161	Japan	bzb2
bz48	Yoshiie	tem	500	b6	2	162	Japan	bzb3
bz54	Yoshiie	tem	500	b6	2	163	Japan	bzb4
bz55	Yoshiie	tem	500	b6	2	164	Japan	bzb5
bz61	Yoshiie	tem	500	b6	2	165	Japan	bzb6
bz62	Yoshiie	tem	500	b6	2	166	Japan	bzb7
bz67	Yoshiie	tem	500	b6	2	167	Japan	bzb8
bz68	Yoshiie	tem	500	b6	2	168	Japan	bzb9
bz74	Yoshiie	tem	500	b6	2	169	Japan	bzc1
bz75	Yoshiie	tem	500	b6	2	170	Japan	bzc2
bz81	Yoshiie	tem	500	b6	2	171	Japan	bzc3
bz82	Yoshiie	tem	500	b6	2	172	Japan	bzc4
bz87	Yoshiie	tem	500	b6	2	173	Japan	bzc5
bz88	Yoshiie	tem	500	b6	2	174	Japan	bzc6
bz94	Yoshiie	tem	500	b6	2	175	Japan	bzc7
bz95	Yoshiie	tem	500	b6	2	176	Japan	bzc8
yi01	Watanabe	tem	500	T1	1	1	Japan	yi01
yi52	Watanabe	tem	500	T1	1	2	Japan	yi52
yi02	Watanabe	tem	500	T1	1	3	Japan	yi02
yi53	Watanabe	tem	500	T1	1	4	Japan	yi53
yi03	Watanabe	tem	500	T1	1	5	Japan	yi03
yi54	Watanabe	tem	500	T1	1	6	Japan	yi54
yi04	Watanabe	tem	500	T1	1	7	Japan	yi04
yi55	Watanabe	tem	500	T1	1	8	Japan	yi55
yi05	Watanabe	tem	500	T1	1	9	Japan	yi05
yi56	Watanabe	tem	500	T1	1	10	Japan	yi56
yi06	Watanabe	tem	500	T1	1	11	Japan	yi06
yi57	Watanabe	tem	500	T1	1	12	Japan	yi57
yi07	Watanabe	tem	500	T1	1	13	Japan	yi07
yi58	Watanabe	tem	500	T1	1	14	Japan	yi58
yi08	Watanabe	tem	500	T1	1	15	Japan	yi08
yi59	Watanabe	tem	500	T1	1	16	Japan	yi59
yi09	Watanabe	tem	500	T1	1	17	Japan	yi09
yi60	Watanabe	tem	500	T1	1	18	Japan	yi60
yi10	Watanabe	tem	500	T1	1	19	Japan	yi10
yi61	Watanabe	tem	500	T1	1	20	Japan	yi61
yi11	Watanabe	tem	500	T1	1	21	Japan	yi11
yi62	Watanabe	tem	500	T1	1	22	Japan	yi62
yi12	Watanabe	tem	500	T1	1	23	Japan	yi12
yi63	Watanabe	tem	500	T1	1	24	Japan	yi63
yi13	Watanabe	tem	500	T1	1	25	Japan	yi13
yi64	Watanabe	tem	500	T1	1	26	Japan	yi64
yi14	Watanabe	tem	500	T1	1	27	Japan	yi14
yi65	Watanabe	tem	500	T1	1	28	Japan	yi65
yi15	Watanabe	tem	500	T1	1	29	Japan	yi15
yi66	Watanabe	tem	500	T1	1	30	Japan	yi66
yi16	Watanabe	tem	500	T1	1	31	Japan	yi16
yi67	Watanabe	tem	500	T1	1	32	Japan	yi67
yi17	Watanabe	tem	500	T1	1	33	Japan	yi17
yi68	Watanabe	tem	500	T1	1	34	Japan	yi68
yi18	Watanabe	tem	500	T1	1	35	Japan	yi18
yi69	Watanabe	tem	500	T1	1	36	Japan	yi69
yi19	Watanabe	tem	500	T1	1	37	Japan	yi19
yi70	Watanabe	tem	500	T1	1	38	Japan	yi70
yi20	Watanabe	tem	500	T1	1	39	Japan	yi20
yi71	Watanabe	tem	500	T1	1	40	Japan	yi71
yi21	Watanabe	tem	500	T1	1	41	Japan	yi21
yi72	Watanabe	tem	500	T1	1	42	Japan	yi72
yi22	Watanabe	tem	500	T1	1	43	Japan	yi22
yi73	Watanabe	tem	500	T1	1	44	Japan	yi73
yi23	Watanabe	tem	500	T1	1	45	Japan	yi23
yi74	Watanabe	tem	500	T1	1	46	Japan	yi74
yi24	Watanabe	tem	500	T1	1	47	Japan	yi24
yi75	Watanabe	tem	500	T1	1	48	Japan	yi75
yi25	Watanabe	tem	500	T1	1	49	Japan	yi25
yi76	Watanabe	tem	500	T1	1	50	Japan	yi76
yi26	Watanabe	tem	500	T1	1	51	Japan	yi26
yi77	Watanabe	tem	500	T1	1	52	Japan	yi77
yi27	Watanabe	tem	500	T1	1	53	Japan	yi27
yi78	Watanabe	tem	500	T1	1	54	Japan	yi78
yi28	Watanabe	tem	500	T1	1	55	Japan	yi28
yi79	Watanabe	tem	500	T1	1	56	Japan	yi79
yi29	Watanabe	tem	500	T1	1	57	Japan	yi29
yi80	Watanabe	tem	500	T1	1	58	Japan	yi80
yi30	Watanabe	tem	500	T1	1	59	Japan	yi30
yi81	Watanabe	tem	500	T1	1	60	Japan	yi81
yi31	Watanabe	tem	500	T1	1	61	Japan	yi31
yi82	Watanabe	tem	500	T1	1	62	Japan	yi82
yi32	Watanabe	tem	500	T1	1	63	Japan	yi32

yji83	Watanabe	tem	500	T1	1	64	Japan	yti83
yji33	Watanabe	tem	500	T1	1	65	Japan	yti33
yji84	Watanabe	tem	500	T1	1	67	Japan	yti84
yji34	Watanabe	tem	500	T1	1	68	Japan	yti34
yji85	Watanabe	tem	500	T1	1	69	Japan	yti85
yji35	Watanabe	tem	500	T1	1	70	Japan	yti35
yji86	Watanabe	tem	500	T1	1	71	Japan	yti86
yji36	Watanabe	tem	500	T1	1	72	Japan	yti36
yji87	Watanabe	tem	500	T1	1	73	Japan	yti87
yji37	Watanabe	tem	500	T1	1	74	Japan	yti37
yji88	Watanabe	tem	500	T1	1	75	Japan	yti88
yji38	Watanabe	tem	500	T1	1	76	Japan	yti38
yji89	Watanabe	tem	500	T1	1	77	Japan	yti89
yji39	Watanabe	tem	500	T1	1	78	Japan	yti39
yji40	Watanabe	tem	500	T1	1	79	Japan	yti40
yji41	Watanabe	tem	500	T1	1	80	Japan	yti41
yji42	Watanabe	tem	500	T1	1	81	Japan	yti42
yji43	Watanabe	tem	500	T1	1	82	Japan	yti43
yji44	Watanabe	tem	500	T1	1	83	Japan	yti44
yji45	Watanabe	tem	500	T1	1	84	Japan	yti45
yji46	Watanabe	tem	500	T1	1	85	Japan	yti46
yji47	Watanabe	tem	500	T1	1	86	Japan	yti47
yji48	Watanabe	tem	500	T1	1	87	Japan	yti48
yji49	Watanabe	tem	500	T1	1	88	Japan	yti49
yji50	Watanabe	tem	500	T1	1	89	Japan	yti50
yji51	Watanabe	tem	500	T1	1	90	Japan	yti51
yji90	Watanabe	tem	500	T1	1	91	Japan	yti90
yji91	Watanabe	tem	500	T1	1	92	Japan	yti91
yji92	Watanabe	tem	500	T1	1	93	Japan	yti92
yji93	Watanabe	tem	500	T1	1	94	Japan	yti93
yji94	Watanabe	tem	500	T1	1	95	Japan	yti94
yji95	Watanabe	tem	500	T1	1	96	Japan	yti95
yji96	Watanabe	tem	500	T1	1	97	Japan	yti96
yji97	Watanabe	tem	500	T1	1	98	Japan	yti97
yji98	Watanabe	tem	500	T1	1	99	Japan	yti98
yji99	Watanabe	tem	500	T1	1	100	Japan	yti99
yki01	Watanabe	tem	500	T1	1	101	Japan	ym01
yki02	Watanabe	tem	500	T1	1	102	Japan	ym02
yki03	Watanabe	tem	500	T1	1	103	Japan	ym03
yki04	Watanabe	tem	500	T1	1	104	Japan	ym04
yki05	Watanabe	tem	500	T1	1	105	Japan	ym05
yki06	Watanabe	tem	500	T1	1	106	Japan	ym06
yki07	Watanabe	tem	500	T1	1	107	Japan	ym07
yki08	Watanabe	tem	500	T1	1	108	Japan	ym08
yki09	Watanabe	tem	500	T1	1	109	Japan	ym09
yki10	Watanabe	tem	500	T1	1	110	Japan	ym10
yki11	Watanabe	tem	500	T1	1	111	Japan	ym11
yki12	Watanabe	tem	500	T1	1	112	Japan	ym12
yki13	Watanabe	tem	500	T1	1	113	Japan	ym13
yki14	Watanabe	tem	500	T1	1	114	Japan	ym14
yki15	Watanabe	tem	500	T1	1	115	Japan	ym15
yki16	Watanabe	tem	500	T1	1	116	Japan	ym16
yki17	Watanabe	tem	500	T1	1	117	Japan	ym17
yki18	Watanabe	tem	500	T1	1	118	Japan	ym18
yki19	Watanabe	tem	500	T1	1	119	Japan	ym19
yki20	Watanabe	tem	500	T1	1	120	Japan	ym20
yki21	Watanabe	tem	500	T1	1	121	Japan	ym21
yki22	Watanabe	tem	500	T1	1	122	Japan	ym22
yki23	Watanabe	tem	500	T1	1	123	Japan	ym23
yki24	Watanabe	tem	500	T1	1	124	Japan	ym24
yki25	Watanabe	tem	500	T1	1	125	Japan	ym25
yki34	Watanabe	tem	500	T1	1	127	Japan	ym34
yki26	Watanabe	tem	500	T1	1	129	Japan	ym26
yki35	Watanabe	tem	500	T1	1	131	Japan	ym35
yki27	Watanabe	tem	500	T1	1	133	Japan	ym27
yki36	Watanabe	tem	500	T1	1	134	Japan	ym36
yki30	Watanabe	tem	500	T1	2	1	Japan	ym30
yki39	Watanabe	tem	500	T1	2	2	Japan	ym39
yki31	Watanabe	tem	500	T1	2	3	Japan	ym31
yki40	Watanabe	tem	500	T1	2	4	Japan	ym40
yki32	Watanabe	tem	500	T1	2	5	Japan	ym32
yki41	Watanabe	tem	500	T1	2	6	Japan	ym41
yki33	Watanabe	tem	500	T1	2	7	Japan	ym33
yki42	Watanabe	tem	500	T1	2	8	Japan	ym42
ffn5	Iseki	tem	500	T1	2	9	Japan	ffn7
ffn6	Iseki	tem	500	T1	2	10	Japan	ffn8
fpc5	Iseki	tem	500	T1	2	11	Japan	fpc7
fpc6	Iseki	tem	500	T1	2	12	Japan	fpc8
f2c5	Iseki	tem	500	T1	2	13	Japan	f2o7
f2c6	Iseki	tem	500	T1	2	14	Japan	f2c8
f9c5	Iseki	tem	500	T1	2	15	Japan	f9o7
f9c6	Iseki	tem	500	T1	2	16	Japan	f9c8
f0c5	Iseki	tem	500	T1	2	17	Japan	f0o7
foc6	Iseki	tem	500	T1	2	18	Japan	foc8
fon5	Iseki	tem	500	T1	2	19	Japan	fon7
fon6	Iseki	tem	500	T1	2	20	Japan	fon8
f2n5	Iseki	tem	500	T1	2	21	Japan	f2n7
f2n6	Iseki	tem	500	T1	2	22	Japan	f2n8
f5n5	Iseki	tem	500	T1	2	23	Japan	f5n7
f5n6	Iseki	tem	500	T1	2	24	Japan	f5n8
f1m5	Iseki	tem	500	T1	2	25	Japan	f1m7
f1m6	Iseki	tem	500	T1	2	26	Japan	f1m8
f3m5	Iseki	tem	500	T1	2	27	Japan	f3m7
f3m6	Iseki	tem	500	T1	2	28	Japan	f3m8
f1v5	Iseki	tem	500	T1	2	29	Japan	f1v7
f1v6	Iseki	tem	500	T1	2	30	Japan	f1v8
f3v5	Iseki	tem	500	T1	2	31	Japan	f3v7
f3v6	Iseki	tem	500	T1	2	32	Japan	f3v8
vvn5	Iseki	tem	500	T1	2	33	Japan	vvn7
vvn6	Iseki	tem	500	T1	2	34	Japan	vvn8
v5n5	Iseki	tem	500	T1	2	35	Japan	v5n7
v5n6	Iseki	tem	500	T1	2	36	Japan	v5n8
v1n5	Iseki	tem	500	T1	2	37	Japan	v1n7
v1n6	Iseki	tem	500	T1	2	38	Japan	v1n8
v2n5	Iseki	tem	500	T1	2	39	Japan	v2n7
v2n6	Iseki	tem	500	T1	2	40	Japan	v2n8
lfb1	Kohno	tem	500	T1	2	41	Japan	lfa1
lfb2	Kohno	tem	500	T1	2	42	Japan	lfa2
lfb3	Kohno	tem	500	T1	2	43	Japan	lfa3
lfb4	Kohno	tem	500	T1	2	44	Japan	lfa4
lfb5	Kohno	tem	500	T1	2	45	Japan	lfa5
lfb6	Kohno	tem	500	T1	2	46	Japan	lfa6

lfb7	Kohno	tem	500	T1	2	47	Japan	lfa7
lfb8	Kohno	tem	500	T1	2	48	Japan	lfa8
lfb9	Kohno	tem	500	T1	2	49	Japan	lfa9
lfba	Kohno	tem	500	T1	2	50	Japan	lfaa
lfbb	Kohno	tem	500	T1	2	51	Japan	lfab
lfbd	Kohno	tem	500	T1	2	52	Japan	lfad
lfbf	Kohno	tem	500	T1	2	53	Japan	lfaf
lfbg	Kohno	tem	500	T1	2	54	Japan	lfag
lfbh	Kohno	tem	500	T1	2	55	Japan	lfah
lbb1	Kohno	tem	500	T1	2	56	Japan	lba1
lbb2	Kohno	tem	500	T1	2	57	Japan	lba2
lbb3	Kohno	tem	500	T1	2	58	Japan	lba3
lbb4	Kohno	tem	500	T1	2	59	Japan	lba4
lbb5	Kohno	tem	500	T1	2	60	Japan	lba5
lbb6	Kohno	tem	500	T1	2	61	Japan	lba6
lbb7	Kohno	tem	500	T1	2	62	Japan	lba7
l1b1	Kohno	tem	500	T1	2	63	Japan	l1a1
l1b2	Kohno	tem	500	T1	2	64	Japan	l1a2
l1b3	Kohno	tem	500	T1	2	65	Japan	l1a3
l1b4	Kohno	tem	500	T1	2	66	Japan	l1a4
l1b5	Kohno	tem	500	T1	2	67	Japan	l1a5
l1b6	Kohno	tem	500	T1	2	68	Japan	l1a6
l1b7	Kohno	tem	500	T1	2	69	Japan	l1a7
l2b1	Kohno	tem	500	T1	2	70	Japan	l2a1
l2b2	Kohno	tem	500	T1	2	71	Japan	l2a2
l2b3	Kohno	tem	500	T1	2	72	Japan	l2a3
l2b4	Kohno	tem	500	T1	2	73	Japan	l2a4
l2b5	Kohno	tem	500	T1	2	74	Japan	l2a5
l2b6	Kohno	tem	500	T1	2	75	Japan	l2a6
l2b7	Kohno	tem	500	T1	2	76	Japan	l2a7
lhb1	Kohno	tem	500	T1	2	77	Japan	lha1
lhb2	Kohno	tem	500	T1	2	78	Japan	lha2
lhb3	Kohno	tem	500	T1	2	79	Japan	lha3
lhb4	Kohno	tem	500	T1	2	80	Japan	lha4
lhb5	Kohno	tem	500	T1	2	81	Japan	lha5
lhb6	Kohno	tem	500	T1	2	82	Japan	lha6
lhb7	Kohno	tem	500	T1	2	83	Japan	lha7
lhb8	Kohno	tem	500	T1	2	84	Japan	lha8
lhb9	Kohno	tem	500	T1	2	85	Japan	lha9
lhba	Kohno	tem	500	T1	2	86	Japan	lhaa
lhbb	Kohno	tem	500	T1	2	87	Japan	lhab
lhbd	Kohno	tem	500	T1	2	88	Japan	lhad
xr7r	Mukouda	tem	500	T1	2	89	Japan	xr9f
xr7s	Mukouda	tem	500	T1	2	90	Japan	xr9g
xr7t	Mukouda	tem	500	T1	2	91	Japan	xr9h
xr7x	Mukouda	tem	500	T1	2	92	Japan	xr9k
xr7y	Mukouda	tem	500	T1	2	93	Japan	xr9l
xr81	Mukouda	tem	500	T1	2	94	Japan	xr9m
xr82	Mukouda	tem	500	T1	2	95	Japan	xr9r
xr83	Mukouda	tem	500	T1	2	96	Japan	xr9s
xr84	Mukouda	tem	500	T1	2	97	Japan	xr9t
xr85	Mukouda	tem	500	T1	2	98	Japan	xr9x
xr86	Mukouda	tem	500	T1	2	99	Japan	xr9y
xr87	Mukouda	tem	500	T1	2	100	Japan	xra1
xr88	Mukouda	tem	500	T1	2	101	Japan	xra2
xr89	Mukouda	tem	500	T1	2	102	Japan	xra3
xr8a	Mukouda	tem	500	T1	2	103	Japan	xra4
xr8b	Mukouda	tem	500	T1	2	104	Japan	xra5
xr8d	Mukouda	tem	500	T1	2	105	Japan	xra6
xr8f	Mukouda	tem	500	T1	2	106	Japan	xra7
xr8g	Mukouda	tem	500	T1	2	107	Japan	xra8
xr8h	Mukouda	tem	500	T1	2	108	Japan	xra9
g901	Shibayama	tem	500	T1	2	109	Japan	g001
g902	Shibayama	tem	500	T1	2	110	Japan	g002
g911	Shibayama	tem	500	T1	2	110	Japan	g011
g912	Shibayama	tem	500	T1	2	111	Japan	g012
g921	Shibayama	tem	500	T1	2	112	Japan	g021
g922	Shibayama	tem	500	T1	2	113	Japan	go22
g831	Shibayama	tem	500	T1	2	114	Japan	g031
g832	Shibayama	tem	500	T1	2	115	Japan	g032
g841	Shibayama	tem	500	T1	2	116	Japan	g041
g842	Shibayama	tem	500	T1	2	117	Japan	g042
g8d1	Shibayama	tem	500	t1	2	120	Japan	g0d1
g8d2	Shibayama	tem	500	t1	2	121	Japan	g0d2
t%16	Shibayama	tem	500	t1	2	122	Japan	t%11
t%17	Shibayama	tem	500	t1	2	123	Japan	t%12
t%18	Shibayama	tem	500	t1	2	124	Japan	t%13
ta16	Shibayama	tem	500	t1	2	125	Japan	ta11
ta17	Shibayama	tem	500	t1	2	126	Japan	ta12
t#16	Shibayama	tem	500	t1	2	127	Japan	t#11
t#17	Shibayama	tem	500	t1	2	128	Japan	t#12
t#18	Shibayama	tem	500	t1	2	129	Japan	t#13
bx1	US	tem	500	t1	2	130	US	dx1
bx2	US	tem	500	t1	2	131	US	dx2
bx3	US	tem	500	t1	2	132	US	dx1
bw1	US	tem	500	t1	2	133	US	dw1
bw2	US	tem	500	t1	2	134	US	dw2
bw3	US	tem	500	t1	2	135	US	dw3
sj07	US	tem	500	t1	2	136	US	sj10
sj08	US	tem	500	t1	2	137	US	sj11
sj09	US	tem	500	t1	2	138	US	sj12
cj07	US	tem	500	t1	2	139	US	cj10
cj08	US	tem	500	t1	2	140	US	cj11
cj09	US	tem	500	t1	2	141	US	cj12
nf07	US	tem	500	t1	2	142	US	nf10
nf08	US	tem	500	t1	2	143	US	nf11
nf09	US	tem	500	t1	2	144	US	nf12
bn08	US	tem	500	t1	2	145	US	dq03
bn09	US	tem	500	t1	2	146	US	bn13
bn10	US	tem	500	t1	2	147	US	d03
bn11	US	tem	500	t1	2	148	US	bn14
bn12	US	tem	500	t1	2	149	US	dm03
b	US	tem	500	t1	2	150	US	bn15
b	US	tem	500	t1	2	151	US	d003
t%19	US	tem	500	t1	2	152	US	t%14
t%20	US	tem	500	t1	2	153	US	t%15
ta18	US	tem	500	t1	2	154	US	ta13
ta19	US	tem	500	t1	2	155	US	ta14
ta20	US	tem	500	t1	2	156	US	ta15
t#19	US	tem	500	t1	2	157	US	t#14
t#20	US	tem	500	t1	2	158	US	t#15

MgTiOs-2	US	tem	500	t1	2	158	US	b
MgTiOs-2	US	tem	500	t1	2	158	US	b
tk5a1	Kimura	tensile	500	T2	1	1	Japan	tk4s1
tk5a2	Kimura	tensile	500	T2	1	2	Japan	tk4s2
tk5a3	Kimura	tensile	500	T2	1	3	Japan	tk4s3
tk5a4	Kimura	tensile	500	T2	1	4	Japan	tk4s4
g901	Shibayama	tensile	500	T2	1	5	Japan	g001
g902	Shibayama	tensile	500	T2	1	6	Japan	g002
g903	Shibayama	tensile	500	t2	1	7	Japan	g003
g904	Shibayama	tensile	500	t2	1	8	Japan	g004
fp09	US	tensile	500	t2	1	9	US	fp13
fp10	US	tensile	500	t2	1	10	US	fp14
fp11	US	tensile	500	t2	1	11	US	fp15
fp12	US	tensile	500	t2	1	12	US	fp16
fq09	US	tensile	500	t2	1	13	US	fq13
fq10	US	tensile	500	t2	1	14	US	fq14
fq11	US	tensile	500	t2	1	15	US	fq15
fq12	US	tensile	500	t2	1	16	US	fq16
ytk51	Watanabe	tensile	500	T2	2	1	Japan	tt802
ytk52	Watanabe	tensile	500	T2	2	2	Japan	tt803
ytk53	Watanabe	tensile	500	T2	2	3	Japan	tt810
ytk54	Watanabe	tensile	500	T2	2	4	Japan	tt811
ytk55	Watanabe	tensile	500	T2	2	5	Japan	tt812
ytk56	Watanabe	tensile	500	T2	2	6	Japan	tt807
ytk58	Watanabe	tensile	500	T2	2	7	Japan	ytk58
ytk57	Watanabe	tensile	500	T2	2	7	Japan	tt808
ytk59	Watanabe	tensile	500	T2	2	8	Japan	ytk59
ytk58	Watanabe	tensile	500	T2	2	8	Japan	tt809
ytk59	Watanabe	tensile	500	T2	2	9	Japan	ytk59
ytk60	Watanabe	tensile	500	t2	2	10	Japan	ytk60
ytk61	Watanabe	tensile	500	T2	2	11	Japan	ytk61
ytk62	Watanabe	tensile	500	t2	2	12	Japan	ytk62
ytk63	Watanabe	tensile	500	t2	2	13	Japan	ytk63
ytk64	Watanabe	tensile	500	t2	2	14	Japan	ytk64
ytk65	Watanabe	tensile	500	t2	2	15	Japan	ytk65
ytk67	Watanabe	tensile	500	T2	2	16	Japan	ytk67
f7hm	Satou	tensile	500	t2	3	1	Japan	f7hd
f7hr	Satou	tensile	500	T2	3	2	Japan	f7hf
f7hs	Satou	tensile	500	T2	3	3	Japan	f7hg
f7ht	Satou	tensile	500	T2	3	4	Japan	f7hh
f7hv	Satou	tensile	500	T2	3	5	Japan	f7hk
f7hx	Satou	tensile	500	T2	3	6	Japan	f7hl
f4hs	Satou	tensile	500	T2	3	7	Japan	f4hd
f4hv	Satou	tensile	500	T2	3	8	Japan	f4hf
f4hx	Satou	tensile	500	T2	3	9	Japan	f4hg
f4hy	Satou	tensile	500	T2	3	10	Japan	f4hh
f4k0	Satou	tensile	500	T2	3	11	Japan	f4hk
f4k1	Satou	tensile	500	T2	3	12	Japan	f4hm
f4k3	Satou	tensile	500	T2	3	13	Japan	f4hr
f4k7	Satou	tensile	500	T2	3	14	Japan	f4k4
f4k9	Satou	tensile	500	T2	3	16	Japan	f4k5
f4ka	Satou	tensile	500	T2	3	17	Japan	f4k6
tj30	Matsui	tensile	500	T2	4	1	Japan	tj27
tj31	Matsui	tensile	500	T2	4	2	Japan	tj28
tj32	Matsui	tensile	500	T2	4	3	Japan	tj29
tt24	Matsui	tensile	500	t2	4	4	Japan	tt21
tt25	Matsui	tensile	500	t2	4	5	Japan	tt22
tt26	Matsui	tensile	500	t2	4	6	Japan	tt23
a738	Ohnuki	tensile	500	t2	4	7	Japan	a736
a737	Ohnuki	tensile	500	t2	4	8	Japan	a735
a747	Ohnuki	tensile	500	t2	4	9	Japan	a745
a748	Ohnuki	tensile	500	t2	4	10	Japan	a746
cj07	Robertson	tensile	500	t2	4	11	US	cj10
cj08	Robertson	tensile	500	t2	4	12	US	cj11
cj09	Robertson	tensile	500	t2	4	13	US	cj12
sj07	Robertson	tensile	500	t2	4	14	US	sj10
sj08	Robertson	tensile	500	t2	4	15	US	sj11
sj09	Robertson	tensile	500	t2	4	16	US	sj12
rc13	Zinkle	tensile	500	t2	5	1	US	rc19
rc14	Zinkle	tensile	500	t2	5	2	US	rc20
rc15	Zinkle	tensile	500	t2	5	3	US	rc21
rc16	Zinkle	tensile	500	t2	5	4	US	rc22
rc17	Zinkle	tensile	500	t2	5	5	US	rc23
rc18	Zinkle	tensile	500	t2	5	6	US	rc24
rv13	Zinkle	tensile	500	t2	5	7	US	rv19
rv14	Zinkle	tensile	500	t2	5	8	US	rv20
rv15	Zinkle	tensile	500	t2	5	10	US	rv21
rv16	Zinkle	tensile	500	t2	5	11	US	rv22
rv17	Zinkle	tensile	500	t2	5	12	US	rv23
rv18	Zinkle	tensile	500	t2	5	13	US	rv24
dp08	US	tensile	500	t2	5	14	US	dp11
dp09	US	tensile	500	t2	5	15	US	dp12
dp10	US	tensile	500	t2	5	16	US	dp13
rv41	Zinkle	tensile	500	t2	5	17	US	rv43
rv42	Zinkle	tensile	500	t2	5	18	US	rv44
t1b4	Kohno	cvn	500	T3	1	b	Japan	t1a4
t1b5	Kohno	cvn	500	T3	1	b	Japan	t1a5
t1b6	Kohno	cvn	500	T3	1	l	Japan	t1a6
t1b7	Kohno	cvn	500	T3	1	l	Japan	t1a7
tfb8	Kohno	cvn	500	T3	2	b	Japan	tfa8
tfb9	Kohno	cvn	500	T3	2	b	Japan	tfa9
tbb1	Kohno	cvn	500	T3	2	l	Japan	tba1
tbb2	Kohno	cvn	500	T3	2	l	Japan	tba2
tfb4	Kohno	cvn	500	T3	3	b	Japan	tfa4
tfb5	Kohno	cvn	500	T3	3	b	Japan	tfa5
tfb6	Kohno	cvn	500	T3	3	l	Japan	tfa6
tfb7	Kohno	cvn	500	T3	3	l	Japan	tfa7
tk535	Kimura	cvn	500	T3	4	b	Japan	tk435
tk536	Kimura	cvn	500	T3	4	b	Japan	tk436
tk537	Kimura	cvn	500	T3	4	t	Japan	tk437
tk538	Kimura	cvn	500	T3	4	t	Japan	tk438
a3200	Robertson	tem	500	T4	1	1	US	b
a3206	Robertson	tem	500	T4	1	2	US	b
a3212	Robertson	tem	500	T4	1	3	US	b
f4g9	Satou	tem	500	T4	1	4	Japan	f4g6
xr6x	Mukouda	tem	500	t4	1	5	Japan	xr6k

f4gd	Satou	tem	500	T4	1	6	Japan	f4g7
xr6y	Mukouda	tem	500	t4	1	7	Japan	xr6l
f4gf	Satou	tem	500	T4	1	8	Japan	f4g8
xr71	Mukouda	tem	500	t4	1	9	Japan	xr8m
f4gx	Satou	tem	500	T4	1	10	Japan	f4gs
xr72	Mukouda	tem	500	t4	1	11	Japan	xr8r
f4gy	Satou	tem	500	T4	1	12	Japan	f4gv
xr73	Mukouda	tem	500	t4	1	13	Japan	xr8s
f4gz	Satou	tem	500	T4	1	14	Japan	f4gw
xr74	Mukouda	tem	500	t4	1	15	Japan	xr8t
f4h9	Satou	tem	500	T4	1	16	Japan	f4h6
xr75	Mukouda	tem	500	t4	1	17	Japan	xr8x
f4hb	Satou	tem	500	T4	1	18	Japan	f4h7
xr76	Mukouda	tem	500	t4	1	19	Japan	xr8y
f4hd	Satou	tem	500	T4	1	20	Japan	f4h8
xr77	Mukouda	tem	500	t4	1	21	Japan	xr91
f5ga	Satou	tem	500	T4	1	22	Japan	f5q7
xr78	Mukouda	tem	500	t4	1	23	Japan	xr92
f5gd	Satou	tem	500	T4	1	24	Japan	f5q8
xr79	Mukouda	tem	500	t4	1	25	Japan	xr93
f5gf	Satou	tem	500	T4	1	26	Japan	f5q9
xr7a	Mukouda	tem	500	t4	1	27	Japan	xr94
f5gx	Satou	tem	500	T4	1	28	Japan	f5qs
xr7b	Mukouda	tem	500	t4	1	29	Japan	xr95
f5gy	Satou	tem	500	T4	1	30	Japan	f5qt
xr7d	Mukouda	tem	500	t4	1	31	Japan	xr96
f5gz	Satou	tem	500	T4	1	32	Japan	f5qv
xr7f	Mukouda	tem	500	t4	1	33	Japan	xr97
f5ha	Satou	tem	500	T4	1	34	Japan	f5h7
xr7g	Mukouda	tem	500	t4	1	35	Japan	xr98
f5hb	Satou	tem	500	T4	1	36	Japan	f5h8
xr7h	Mukouda	tem	500	t4	1	37	Japan	xr99
f5hd	Satou	tem	500	T4	1	38	Japan	f5h9
xr7k	Mukouda	tem	500	t4	1	39	Japan	xr9a
f6ga	Satou	tem	500	T4	1	40	Japan	f6q7
xr7l	Mukouda	tem	500	t4	1	41	Japan	xr9b
f6gb	Satou	tem	500	T4	1	42	Japan	f6q8
xr7m	Mukouda	tem	500	t4	1	43	Japan	xr9d
f6gd	Satou	tem	500	T4	1	44	Japan	f6q9
f6gx	Satou	tem	500	T4	1	45	Japan	f6qs
f6gy	Satou	tem	500	T4	1	46	Japan	f6qt
f6gz	Satou	tem	500	T4	1	47	Japan	f6qv
f6h6	Satou	tem	500	T4	1	48	Japan	f6h4
f6h8	Satou	tem	500	T4	1	49	Japan	f6h5
f7ga	Satou	tem	500	T4	1	50	Japan	f7g7
f7gb	Satou	tem	500	T4	1	51	Japan	f7g8
f7gd	Satou	tem	500	T4	1	52	Japan	f7g9
f7gx	Satou	tem	500	T4	1	53	Japan	f7qt
f7gz	Satou	tem	500	T4	1	54	Japan	f7qv
f3gx	Satou	tem	500	T4	1	55	Japan	f7qw
f7ha	Satou	tem	500	T4	1	56	Japan	f7h7
f7hb	Satou	tem	500	T4	1	57	Japan	f7h8
f7hd	Satou	tem	500	T4	1	58	Japan	f7h9
f8ga	Satou	tem	500	T4	1	59	Japan	f8q6
f8gb	Satou	tem	500	T4	1	60	Japan	f8q7
f8gd	Satou	tem	500	T4	1	61	Japan	f8q8
f8gx	Satou	tem	500	T4	1	62	Japan	f8qs
f8gy	Satou	tem	500	T4	1	63	Japan	f8qt
f8gz	Satou	tem	500	T4	1	64	Japan	f8qv
f8ha	Satou	tem	500	T4	1	65	Japan	f8h7
f8hb	Satou	tem	500	T4	1	66	Japan	f8h8
f8hd	Satou	tem	500	T4	1	67	Japan	f8h9
f3q6	Satou	tem	500	T4	1	68	Japan	f3q4
f3q7	Satou	tem	500	T4	1	69	Japan	f3q5
f2gb	Satou	tem	500	T4	1	70	Japan	f2g8
f2gb	Satou	tem	500	T4	1	71	Japan	f2g9
f2gf	Satou	tem	500	T4	1	72	Japan	f2qs
f2d6	Satou	tem	500	T4	1	73	Japan	f2da
f30a	Satou	tem	500	T4	1	74	Japan	f308
f30b	Satou	tem	500	T4	1	75	Japan	f309
f40a	Satou	tem	500	T4	1	76	Japan	f408
a3221	Robertson	tem	500	T4	1	77	US	b
a3222	Robertson	tem	500	T4	1	78	US	b
a3217	Robertson	tem	500	T4	1	79	US	b
f40b	Satou	tem	500	T4	1	80	Japan	f409
f50a	Satou	tem	500	T4	1	81	Japan	f508
f50b	Satou	tem	500	T4	1	82	Japan	f509
f3qs	Satou	tem	500	T4	1	83	Japan	f3qm
f3qt	Satou	tem	500	T4	1	84	Japan	f3qr
f0qd	Satou	tem	500	T4	1	85	Japan	f0q5
f0qf	Satou	tem	500	T4	1	86	Japan	f0q7
fc37	Sickafus	tem	500	T4	1	87	US	rc40
fc38	Sickafus	tem	500	T4	1	88	US	rc41
rc39	Sickafus	tem	500	T4	1	89	US	rc42
rv07	Sickafus	tem	500	T4	1	90	US	rv20
rv08	Sickafus	tem	500	T4	1	91	US	rv11
rv09	Sickafus	tem	500	T4	1	92	US	rv12
rv20	Sickafus	tem	500	T4	1	93	US	rv22
rv21	Sickafus	tem	500	T4	1	94	US	rv23
dc08	Sickafus	tem	500	T4	1	95	US	dc11
dc09	Sickafus	tem	500	T4	1	96	US	dc12
dc10	Singh	tem	500	T4	1	97	US	dc13
ud57	Singh	tem	500	T4	1	98	US	ud60
ud58	Singh	tem	500	T4	1	99	US	ud61
ud59	Singh	tem	500	T4	1	100	US	ud62
qc07	Singh	tem	500	T4	1	101	US	qc10
qc08	Singh	tem	500	T4	1	102	US	qc11
qc09	Singh	tem	500	T4	1	103	US	qc12
va05	Singh	tem	500	T4	1	104	US	va08
va06	Singh	tem	500	T4	1	105	US	b
va07	Singh	tem	500	T4	1	106	US	b
va14	Singh	tem	500	T4	1	107	US	b
va15	Singh	tem	500	T4	1	108	US	b
va16	Singh	tem	500	T4	1	109	US	va17
va24	Singh	tem	500	T4	1	110	US	va27
va25	Singh	tem	500	T4	1	111	US	b
va26	Stoller	tem	500	T4	1	112	US	b
xh05	Stoller	tem	500	T4	1	113	US	xh07
xh06	Stoller	tem	500	T4	1	114	US	xh08
xi75	Stoller	tem	500	T4	1	115	US	xi79
xi76	Stoller	tem	500	T4	1	116	US	xi78
ta36	Stoller	tem	500	T4	1	117	US	ta38

ta37	Stoller	tem	500	T4	1	118	US	ta39
tb36	Stoller	tem	500	T4	1	119	US	tb39
tb37	Stoller	tem	500	T4	1	120	US	tb38
xe86	Stoller	tem	500	T4	1	121	US	xe87
xe85	Zinkle	tem	500	T4	1	122	US	xe86
fp05	Zinkle	tem	500	T4	1	123	US	fp07
fp06	Zinkle	tem	500	T4	1	124	US	fp08
fq05	Zinkle	tem	500	T4	1	125	US	fq07
fq06	Zinkle	tem	500	T4	1	126	US	fq08
by1	Zinkle	tem	500	T4	1	127	US	dy2
by2	Zinkle	tem	500	T4	1	128	US	dy1
bz1	Zinkle	tem	500	T4	1	129	US	dz3
bz2	Zinkle	tem	500	T4	1	130	US	dz2
b	Zinkle	tem	500	T4	1	131	US	dp03
a321s	Robertson	tem	500	T4	1	132	US	b
a3236	Robertson	tem	500	T4	1	133	US	b
a3237	Robertson	tem	500	T4	1	134	US	b
tz16	Matsui	tem	500	T4	2	1	Japan	tz11
tz17	Matsui	tem	500	T4	2	2	Japan	tz12
tz18	Matsui	tem	500	T4	2	3	Japan	tz13
tz19	Matsui	tem	500	T4	2	4	Japan	tz14
tz20	Matsui	tem	500	T4	2	5	Japan	tz15
ty16	Matsui	tem	500	T4	2	6	Japan	ty11
ty17	Matsui	tem	500	T4	2	7	Japan	ty12
ty18	Matsui	tem	500	T4	2	8	Japan	ty13
ty19	Matsui	tem	500	T4	2	9	Japan	ty14
ty20	Matsui	tem	500	T4	2	10	Japan	ty15
tx16	Matsui	tem	500	T4	2	11	Japan	tx11
tx17	Matsui	tem	500	T4	2	12	Japan	tx12
tx18	Matsui	tem	500	T4	2	13	Japan	tx13
tx19	Matsui	tem	500	T4	2	14	Japan	tx14
tx20	Matsui	tem	500	T4	2	15	Japan	tx15
tv16	Matsui	tem	500	T4	2	16	Japan	tv11
tr16	Matsui	tem	500	T4	2	17	Japan	tr11
tr17	Matsui	tem	500	T4	2	18	Japan	tr12
tv17	Matsui	tem	500	T4	2	19	Japan	tv12
tr18	Matsui	tem	500	T4	2	20	Japan	tr13
tr19	Matsui	tem	500	T4	2	21	Japan	tr14
tv18	Matsui	tem	500	T4	2	22	Japan	tv13
tr20	Matsui	tem	500	T4	2	23	Japan	tr15
tp16	Matsui	tem	500	T4	2	24	Japan	tp11
tv19	Matsui	tem	500	T4	2	25	Japan	tv14
tp17	Matsui	tem	500	T4	2	26	Japan	tp12
tp18	Matsui	tem	500	T4	2	27	Japan	tp13
tv20	Matsui	tem	500	T4	2	28	Japan	tv15
tp19	Matsui	tem	500	T4	2	29	Japan	tp14
tp20	Matsui	tem	500	T4	2	30	Japan	tp15
tt16	Matsui	tem	500	T4	2	31	Japan	tt11
to16	Matsui	tem	500	T4	2	32	Japan	to11
to17	Matsui	tem	500	T4	2	33	Japan	to12
tt17	Matsui	tem	500	T4	2	34	Japan	tt12
to18	Matsui	tem	500	T4	2	35	Japan	to13
to19	Matsui	tem	500	T4	2	36	Japan	to14
tt18	Matsui	tem	500	T4	2	37	Japan	tt13
to20	Matsui	tem	500	T4	2	38	Japan	to15
tn16	Matsui	tem	500	T4	2	39	Japan	tn11
tt19	Matsui	tem	500	T4	2	40	Japan	tt14
tn17	Matsui	tem	500	T4	2	41	Japan	tn12
tn18	Matsui	tem	500	T4	2	42	Japan	tn13
tt20	Matsui	tem	500	T4	2	43	Japan	tt15
tn19	Matsui	tem	500	T4	2	44	Japan	tn14
tn20	Matsui	tem	500	T4	2	45	Japan	tn15
ts16	Matsui	tem	500	T4	2	46	Japan	ts11
tm16	Matsui	tem	500	T4	2	47	Japan	tm11
tm17	Matsui	tem	500	T4	2	48	Japan	tm12
ts17	Matsui	tem	500	T4	2	49	Japan	ts12
tm18	Matsui	tem	500	T4	2	50	Japan	tm13
tm19	Matsui	tem	500	T4	2	51	Japan	tm14
ts18	Matsui	tem	500	T4	2	52	Japan	ts13
tm20	Matsui	tem	500	T4	2	53	Japan	tm15
tl16	Matsui	tem	500	T4	2	54	Japan	tl11
ts19	Matsui	tem	500	T4	2	55	Japan	ts14
tl17	Matsui	tem	500	T4	2	56	Japan	tl12
tl18	Matsui	tem	500	T4	2	57	Japan	tl13
ts20	Matsui	tem	500	T4	2	58	Japan	ts15
tl19	Matsui	tem	500	T4	2	59	Japan	tl14
tl20	Matsui	tem	500	T4	2	60	Japan	tl15
tk16	Matsui	tem	500	T4	2	61	Japan	tk11
tk17	Matsui	tem	500	T4	2	62	Japan	tk12
tk18	Matsui	tem	500	T4	2	63	Japan	tk13
tk19	Matsui	tem	500	T4	2	64	Japan	tk14
tk20	Matsui	tem	500	T4	2	65	Japan	tk15
tj16	Matsui	tem	500	T4	2	66	Japan	tj11
tj17	Matsui	tem	500	T4	2	67	Japan	tj12
tj18	Matsui	tem	500	T4	2	68	Japan	tj13
tj19	Matsui	tem	500	T4	2	69	Japan	tj14
tj20	Matsui	tem	500	T4	2	70	Japan	tj15
ti16	Matsui	tem	500	T4	2	71	Japan	ti11
ti17	Matsui	tem	500	T4	2	72	Japan	ti12
ti18	Matsui	tem	500	T4	2	73	Japan	ti13
ti19	Matsui	tem	500	T4	2	74	Japan	ti14
ti20	Matsui	tem	500	T4	2	75	Japan	ti15
tg16	Matsui	tem	500	T4	2	76	Japan	tg11
tg17	Matsui	tem	500	T4	2	77	Japan	tg12
tg18	Matsui	tem	500	T4	2	78	Japan	tg13
tg19	Matsui	tem	500	T4	2	79	Japan	tg14
tg20	Matsui	tem	500	T4	2	80	Japan	tg15
tf16	Matsui	tem	500	T4	2	81	Japan	tf11
tf17	Matsui	tem	500	T4	2	82	Japan	tf12
tf18	Matsui	tem	500	T4	2	83	Japan	tf13
tf19	Matsui	tem	500	T4	2	84	Japan	tf14
tf20	Matsui	tem	500	T4	2	85	Japan	tf15
tc16	Matsui	tem	500	T4	2	86	Japan	tc11
tc17	Matsui	tem	500	T4	2	87	Japan	tc12
tc18	Matsui	tem	500	T4	2	88	Japan	tc13
tc19	Matsui	tem	500	T4	2	89	Japan	tc14
tc20	Matsui	tem	500	T4	2	90	Japan	tc15
t216	Matsui	tem	500	T4	2	91	Japan	t211
t217	Matsui	tem	500	T4	2	92	Japan	t212
t218	Matsui	tem	500	T4	2	93	Japan	t213
t219	Matsui	tem	500	T4	2	94	Japan	t214
t220	Matsui	tem	500	T4	2	95	Japan	t215

t316	Matsui	tem	500	T4	2	96	Japan	t311
t317	Matsui	tem	500	T4	2	97	Japan	t312
t318	Matsui	tem	500	T4	2	98	Japan	t313
t319	Matsui	tem	500	T4	2	99	Japan	t314
t320	Matsui	tem	500	T4	2	100	Japan	t315
t416	Matsui	tem	500	T4	2	101	Japan	t411
t417	Matsui	tem	500	T4	2	102	Japan	t412
t418	Matsui	tem	500	T4	2	103	Japan	t413
t419	Matsui	tem	500	T4	2	104	Japan	t414
t420	Matsui	tem	500	T4	2	105	Japan	t415
t516	Matsui	tem	500	T4	2	106	Japan	t511
t517	Matsui	tem	500	T4	2	107	Japan	t512
t518	Matsui	tem	500	T4	2	108	Japan	t513
t519	Matsui	tem	500	T4	2	109	Japan	t514
t520	Matsui	tem	500	T4	2	110	Japan	t515
t616	Matsui	tem	500	T4	2	111	Japan	t611
t617	Matsui	tem	500	T4	2	112	Japan	t612
t618	Matsui	tem	500	T4	2	113	Japan	t613
t619	Matsui	tem	500	T4	2	114	Japan	t614
t620	Matsui	tem	500	T4	2	115	Japan	t615
t716	Matsui	tem	500	T4	2	116	Japan	t711
t717	Matsui	tem	500	T4	2	117	Japan	t712
t718	Matsui	tem	500	T4	2	118	Japan	t713
t719	Matsui	tem	500	T4	2	119	Japan	t714
t720	Matsui	tem	500	T4	2	120	Japan	t715
t816	Matsui	tem	500	T4	2	121	Japan	t811
t817	Matsui	tem	500	T4	2	122	Japan	t812
t818	Matsui	tem	500	T4	2	123	Japan	t813
t819	Matsui	tem	500	T4	2	124	Japan	t814
t820	Matsui	tem	500	T4	2	125	Japan	t815
g911	Shibayama	tensile	500	T5	1	1	Japan	g011
g912	Shibayama	tensile	500	T5	1	2	Japan	g012
g913	Shibayama	tensile	500	T5	1	3	Japan	g013
g914	Shibayama	tensile	500	T5	1	4	Japan	g014
g921	Shibayama	tensile	500	T5	1	5	Japan	g021
g922	Shibayama	tensile	500	T5	1	6	Japan	g022
g923	Shibayama	tensile	500	T5	1	7	Japan	g023
g924	Shibayama	tensile	500	T5	1	8	Japan	g024
g931	Shibayama	tensile	500	T5	1	9	Japan	g031
g932	Shibayama	tensile	500	T5	1	10	Japan	g032
g933	Shibayama	tensile	500	T5	1	11	Japan	g033
g934	Shibayama	tensile	500	T5	1	12	Japan	g034
g941	Shibayama	tensile	500	T5	1	13	Japan	g041
g942	Shibayama	tensile	500	T5	1	14	Japan	g042
g943	Shibayama	tensile	500	T5	1	15	Japan	g043
g944	Shibayama	tensile	500	T5	1	16	Japan	g044
yk70	Watanabe	tensile	500	t5	2	1	Japan	yk70
yk66	Watanabe	tensile	500	t5	2	1	Japan	yk66
yk70	Watanabe	tensile	500	t5	2	2	Japan	ym70
ta09	US	tensile	500	t5	2	3	US	ta13
ta10	US	tensile	500	t5	2	4	US	ta14
ta11	US	tensile	500	t5	2	5	US	ta15
ta12	US	tensile	500	t5	2	6	US	ta16
tb09	US	tensile	500	t5	2	7	US	tb13
tb10	US	tensile	500	t5	2	8	US	tb14
tb11	US	tensile	500	t5	2	9	US	tb15
tb12	US	tensile	500	t5	2	10	US	tb16
xe09	US	tensile	500	t5	2	11	us	xe13
xe10	US	tensile	500	t5	2	12	US	xe14
xe11	US	tensile	500	t5	2	13	US	xe15
xe12	US	tensile	500	t5	2	14	US	xe16
g910	Shibayama	tensile	500	T5	3	1	Japan	g010
g911	Shibayama	tensile	500	T5	3	2	Japan	g011
g912	Shibayama	tensile	500	T5	3	3	Japan	g012
g913	Shibayama	tensile	500	T5	3	4	Japan	g013
g914	Shibayama	tensile	500	T5	3	5	Japan	g044
g915	Shibayama	tensile	500	T5	3	6	Japan	g015
g916	Shibayama	tensile	500	T5	3	7	Japan	g016
g917	Shibayama	tensile	500	T5	3	8	Japan	g017
g918	Shibayama	tensile	500	T5	3	9	Japan	g018
g919	Shibayama	tensile	500	T5	3	10	Japan	g019
f4kg	Satou	tensile	500	T5	3	11	Japan	f4kh
f4km	Satou	tensile	500	T5	3	12	Japan	f4kk
f5kl	Satou	tensile	500	T5	3	13	Japan	f4kl
f6hz	Satou	tensile	500	t5	3	14	Japan	f6k1
a707	Ohnuki	tensile	500	t5	4	1	Japan	a705
a708	Ohnuki	tensile	500	T5	4	2	Japan	a706
a717	Ohnuki	tensile	500	T5	4	3	Japan	a715
a718	Ohnuki	tensile	500	T5	4	4	Japan	a716
a727	Ohnuki	tensile	500	T5	4	5	Japan	a725
a728	Ohnuki	tensile	500	T5	4	6	Japan	a726
a213	Ohnuki	tensile	500	T5	4	7	Japan	a208
a214	Ohnuki	tensile	500	T5	4	8	Japan	a210
a215	Ohnuki	tensile	500	T5	4	9	Japan	a211
a216	Ohnuki	tensile	500	T5	4	10	Japan	a212
a230	Ohnuki	tensile	500	T5	4	11	Japan	a227
a231	Ohnuki	tensile	500	T5	4	12	Japan	a228
a232	Ohnuki	tensile	500	T5	4	13	Japan	a229
a249	Ohnuki	tensile	500	T5	4	14	Japan	a246
a250	Ohnuki	tensile	500	T5	4	15	Japan	a247
a251	Ohnuki	tensile	500	T5	4	16	Japan	a248
dc13	Zinkle	tensile	500	T5	5	1	US	dc19
dc14	Zinkle	tensile	500	T5	5	2	US	dc20
dc15	Zinkle	tensile	500	T5	5	3	US	dc21
dc16	Zinkle	tensile	500	T5	5	4	US	dc22
dc17	Zinkle	tensile	500	T5	5	5	US	dc23
dc18	Zinkle	tensile	500	T5	5	6	US	dc24
fc13	Zinkle	tensile	500	T5	5	7	US	fc19
fc14	Zinkle	tensile	500	T5	5	8	US	fc20
fc15	Zinkle	tensile	500	T5	5	9	US	fc21
fc16	Zinkle	tensile	500	T5	5	10	US	fc22
fc17	Zinkle	tensile	500	T5	5	11	US	fc23
fc18	Zinkle	tensile	500	T5	5	12	US	fc24
va04	Zinkle	tensile	500	T5	5	13	US	va08
va05	Zinkle	tensile	500	T5	5	14	US	va09
va06	Zinkle	tensile	500	T5	5	15	US	b
va07	Zinkle	tensile	500	T5	5	16	US	b

STATUS OF THE IRRADIATION TEST VEHICLE FOR TESTING FUSION MATERIALS IN THE ADVANCED TEST REACTOR - H. Tsai, I. C. Gomes, and D. L. Smith (Argonne National Laboratory), A. J. Palmer, and F. W. Ingram (Lockheed Martin Idaho Technologies Company), F. W. Wiffen (U.S. Department of Energy)

SUMMARY

The design of the irradiation test vehicle (ITV) for the Advanced Test Reactor (ATR) has been completed. The main application for the ITV is irradiation testing of candidate fusion structural materials, including vanadium-base alloys, silicon carbide composites, and low-activation steels. Construction of the vehicle is underway at the Lockheed Martin Idaho Technology Company (LMITCO). Dummy test trains are being built for system checkout and fine-tuning. Reactor insertion of the ITV with the dummy test trains is scheduled for fall 1998. Barring unexpected difficulties, the ITV will be available for experiments in early 1999.

OBJECTIVE

With the demise of fast reactors in the U.S., water-cooled mixed-spectrum reactors such as the High Flux Isotope Reactor and the ATR are increasingly being relied upon for irradiation testing of fusion structural materials. Because thermal neutrons are largely absent in the first-wall and blanket regions of a fusion reactor, the challenge in using a mixed-spectrum reactor for testing fusion materials lies mainly in curtailing the undesirable side effects of thermal neutrons, e.g., atypical transmutations. The ATR-ITV project is an effort to create an instrumented, versatile test vehicle that would be suitable for a wide range of neutron damage studies on various candidate fusion materials.

ITV FUNCTIONAL REQUIREMENTS

The following functional requirements were specified by the fusion materials community and used by the LMITCO for the vehicle design.

1. Thermal Neutron Filtering

   The neutron flux in the test volume shall be hardened to limit the thermally dominant V(n,γ)Cr transmutation in vanadium-base alloys to <0.5 wt.% Cr during the irradiation. In addition, the filtered neutron spectrum shall permit the conduct of dynamic helium charging experiments (DHCEs)[1] for vanadium alloys. The thermal neutron filter shall be external and replaceable in order to maintain a high-quality neutron environment throughout the irradiation.

2. Multiple Test Temperatures and Active Temperature Control

   The vehicle shall have multiple specimen capsules, each capable of operating at different temperatures. The range of test temperatures shall be ≈250-750°C, depending on test materials requirements. The temperature for each capsule shall be monitored on a real-time basis; it should be controllable by the blending of two gases (of different thermal conductivities) in a radial gap that governs the dissipation of heat from the capsule.

---

*Work supported by U.S. Department of Energy, Office of Fusion Energy Research, under Contract W-31-109-Eng-38.

[1]The purpose of the DHCE is to study the concurrent effects of neutron damage and helium generation as they would occur in a fusion reactor. In a DHCE, tritium would be precharged in the lithium bond of the specimen capsules. During the irradiation, the tritium would diffuse from the lithium into the specimens and some would decay in-situ into ^{3}He. The challenge for DHCE in a mixed-spectrum reactor lies in preventing the back conversion of ^{3}He into ^{3}H through the (n,p) reactions, which have a high reaction cross section for thermal neutrons.

3. High Neutron Damage Rate

   The ITV shall be located in a high-fast-flux region of the ATR so that a high damage rate (≈10 dpa in vanadium per calendar year) can be attained.

4. Irradiation Duration

   Except for possible interruption to replace the thermal neutron filter, the ITV shall be capable of continuous operation for up to ≈30 dpa. (The fluence requirement for the first test train may be only ≈10 dpa.)

5. Accommodation of Liquid Metal Specimen Bond

   Capsules containing vanadium alloy specimens may require lithium or sodium bonding for reasons of heat transfer, impurity control, and DHCE. Capsules containing other types of test materials may require helium bonding.

FINAL ITV DESIGN

Through close interactions between the LMITCO designers and the fusion materials community, a design of the ITV that meets all of the above functional requirements has been achieved [1]. This finalized design is described below.

The ITV will occupy the ATR's central flux trap, which has a diameter of 81.5 mm and a length of 1219 mm (i.e., the core height). The vehicle will have three side-by-side, 31-mm-OD stainless steel in-pile tubes within the flux trap baffle. Up to nine thermocouples and 12 gas lines (for temperature control or purging) are feasible in each in-pile tube. Figure 1 is a core-region cross section of the central flux trap when it is occupied by the three ITV in-pile tubes and associated components. The instrumentation and control for each in-pile tube will be independent, i.e., each can be inserted and removed without affecting the other two. Each tube will form its own pressure boundary.

Each in-pile tube can accommodate up to five axially stacked specimen capsules. A thermocouple sleeve and a gas channel tube will separate the specimen capsules from the in-pile tube. Holes in this sleeve will accommodate the thermocouples extending from the top of the vehicle to each capsule. The thermocouples will be 1.6-mm-diameter sheathed Type K (chromel-alumel) with either single or multiple hot junctions in the sheath. The outside wall of the thermocouple sleeve and the inside wall of the gas channel tube form a gas gap. Through active regulation of the blending of the gas mixture in this gap, the temperature of each specimen capsule can be individually controlled. Helium and neon are the two blending gases chosen; other gases may also be used. The gas blending capability permits a blend range of 98% of one gas to 2% of the other to allow a broad range of control. In the unlikely event that the ability to measure or control the temperature is lost, the gas gap of the affected capsule will be automatically purged with helium to prevent overtemperature.

The ITV will have an automated digital control system. The purpose of the control system will be to monitor, control, archive data, and generate reports without the attention of operators during reactor operations. The system will provide normal onsite experiment monitoring as well as offsite real-time data transmittal via fiber-optic links and an Ethernet data bus.

A single, replaceable thermal neutron filter will encompass all three in-pile tubes. The filter will be a 2.5-mm-thick sleeve made of an Al-B alloy with 4.3 wt.% of ^{10}B. An aluminum filler block, to minimize water inside the filtered volume, will occupy the interstitial space between the three in-pile tubes. The

calculated neutron fluxes in the in-pile tubes at the core midplane are shown in Table 1. With an estimated fast flux of ≈4.5 x 10^{14} n/cm^2/s (E>0.1 MeV), the target dose rate of ≈10 dpa/y (vanadium) will be attainable at the anticipated central lobe power of 26 MW. If the sleeve is replaced every ≈5-10 dpa, the V-to-Cr transmutation would be insignificant and a DHCE would be feasible, based on the results of preliminary physics analyses [2].

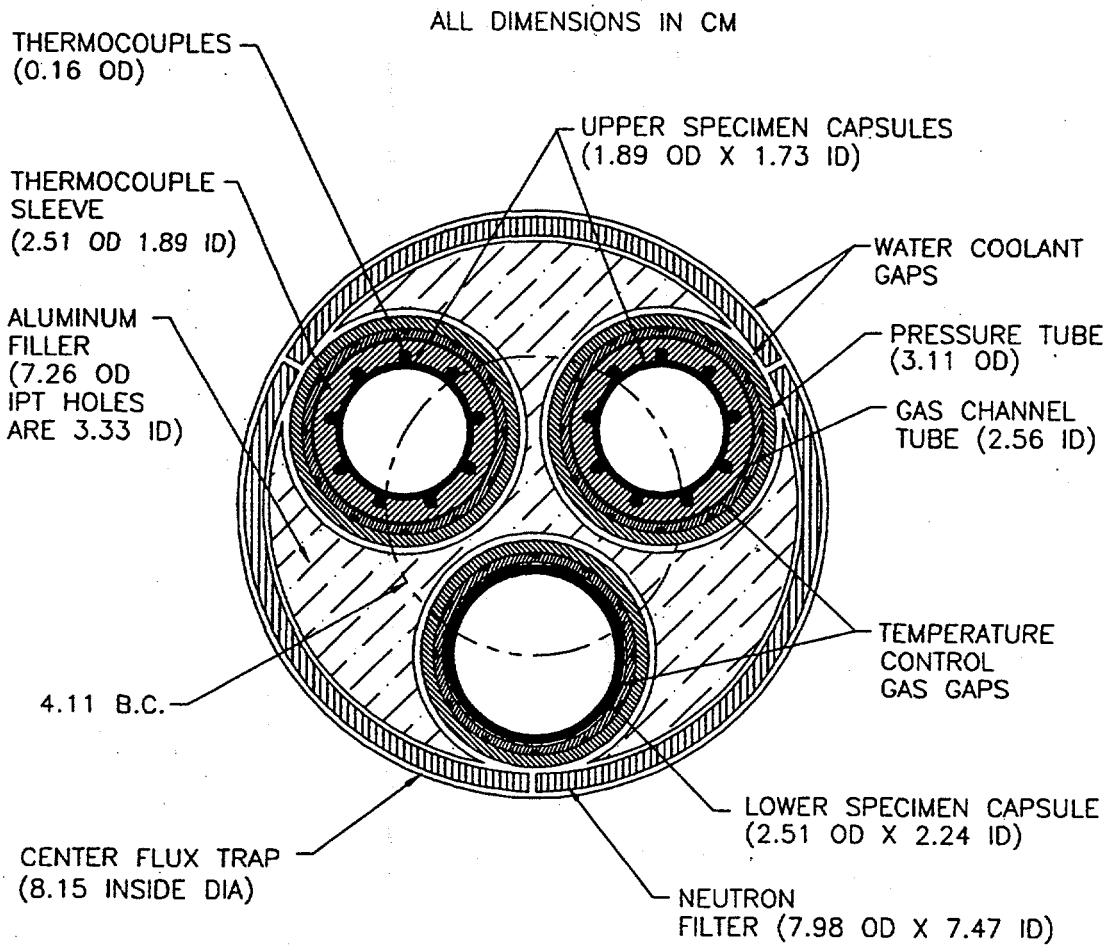

Fig. 1. Core region ITV cross section without specimens

Table 1. Calculated neutron fluxes in in-pile tubes at the core midplane at 26 MW center lobe power

	Neutron Flux (n/cm^2/s)	
	Unfiltered	Filtered
Thermal (E < 1.0eV)	1.13 x 10^{14}	1.76 x 10^{13}
Fast (E > 0.1MeV)	4.55 x 10^{14}	4.54 x 10^{14}
Total	1.02 x 10^{15}	8.63 x 10^{14}

A conceptual test train design has been generated for the initial fusion materials test in the ITV. To maximize the utilization of the high-value space near the core midplane, the in-pile tube would have five capsules of two diameters, as shown schematically in Fig. 2. The thermocouple sleeve would terminate at the top of capsule No. 2, just below the core midplane, thereby giving capsule No. 2 the largest possible diameter or volume. A trade-off of this configuration is that capsule No. 1, at the bottom, would have no instrumentation. The available test volume and instrumentation in each capsule with this conceptual test train design is shown in Table 2.

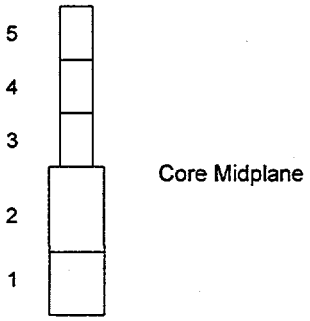

Fig. 2. Schematic diagram of five-capsule configuration for initial fusion materials experiment in ITV.

Table 2 Conceptual test train design for initial fusion materials test in ITV (see Fig. 2)

Capsule No.	Inside Ht. (mm)	Inside Dia. (mm)	Volume (cm^3)	No. of TCs[a]	No. of TC Junctions[a]	Normalized Neutron Flux[b]
5	178	16.5	38	2	4	0.42
4	178	16.5	38	2	4	0.78
3	178	16.5	38	2	2	0.97
2	320	21.3	114	3	5	0.91
1	206	21.3	73	0	0	0.44

[a]TCs: thermocouples. One each of the thermocouples in capsules 5, 4, and 2 would be a multi-junction design with three hot junctions.
[b]At axial midplane of each capsule.

STATUS OF ITV FABRICATION

The upper and lower reactor enclosures have been completed. The in-pile tubes are ≈33% complete and the dummy test trains are ≈75% complete. Essentially all ex-reactor auxiliary handling equipment is complete. Overall, about 60% of the ITV hardware has been fabricated.

FUTURE ACTIVITIES

The remaining ≈40% of the hardware is expected to be completed before mid-September 1998. During the next 49-day reactor outage, scheduled to begin on September 15, 1998, the ITV with the dummy test trains will be installed in the reactor. After the reactor start-up, the system will be checked out for one or two reactor cycles (2-3 months). Barring unexpected difficulties, the ITV would then be available for experiments in early 1999.

Discussion is ongoing between the U.S. DOE and the Japanese Monbusho in regard to using the ITV for the post-Jupiter phase of the U.S.-Japan (Monbusho) collaboration.

REFERENCES

1. F. W. Ingram, A. J. Palmer, and D. J. Stites, "Temperature Controlled Material Irradiation in the Advanced Test Reactor," 8th Int. Conf. on Fusion Reactor Materials, Sendai, Japan, Oct. 26-31, 1998 (Proc. to be published).

2. I. C. Gomes, H. Tsai, and D. L. Smith, "Neutronic Analysis of the DHCE Experiment in ATR-ITV," Fusion Materials Semiannual Progress Report for period ending June 30, 1997, DOE/ER-0313/22, pp. 232-237.

LE AND STATUS OF IRRADIATION EXPERIMENTS – A. F. Rowcliffe, ssbeck, and J. P. Robertson (Oak Ridge National Laboratory)

ΓIVE

e an updated summary of the status of irradiation experiments for the neutron- ; materials program.

RY

The current status of reactor irradiation experiments is presented in tables summarizing the experimental objectives, conditions, and schedule.

PROGRESS AND STATUS

Currently, the program has one irradiation experiment in reactor and five experiments in the design or construction stages. Postirradiation examination and testing is in progress on ten experiments.

Summary of Reactor Irradiation Experiments

Experiment	Lead Lab	Collaborators	Responsible Person	Major Objectives	Materials	Temperature °C	Dose (dpa) or fluence	Irrad. Start	Irrad. Finish	Status
EBR-II, Reactor, ANL, Idaho Falls, ID										
COBRA 1A1	PNL	ORNL, ANL, MONBUSHO	M.L. Hamilton	Tensile and fatigue prop., Charpy impact, fracture toughness, TEM	Austenitic and ferritic steels, Fe-alloys, V, Be, low act. materials, Cu alloys, Ti-Al, SiC, C-C comp.	370, 500, 600	9	Nov-92	Apr-93	
COBRA 1A2	PNL	ORNL, ANL, MONBUSHO	M.L. Hamilton	Tensile and fatigue prop., Charpy impact, fracture toughness, TEM	Austenitic and ferritic steels, Fe-alloys, V, Be, low act. materials, Cu alloys, Ti-Al, SiC, C-C comp.	370, 400, 800	33	Nov-92	Sep-94	
X530	ANL		H. Tsai, H.M. Chung	He-effects, swelling, Charpy impact, fracture toughness, tensile prop.	V alloys	370	5	Aug-94	Sep-94	
High Flux Isotope Reactor, ORNL, Oak Ridge, TN										
HFIR-CTR-60	ORNL		S.J. Zinkle	Flexure bars, TEM, indentation disks	Isotopically tailored ceramics	100-600	2.4E+26 n/m2	Dec-94	Aug-95	
HFIR-CTR-61	ORNL		S.J. Zinkle	Similar to HFIR-CTR-60			7.20E+26	Dec-94	Aug-98	
HFIR-JP-9	ORNL	JAERI	P.J. Maziasz/ J.E. Pawel	He effects by isotopic tailoring, tensile prop., TEM	Austenitic and ferritic steels	300-600	57	Jul-90	Apr-94	
HFIR-JP-10	ORNL	JAERI	P.J. Maziasz/ J.E. Pawel	He effects by isotopic tailoring, tensile prop., TEM	Austenitic and ferritic steels	300-600	17	Jul-90	Sep-91	
HFIR-JP-11	ORNL	JAERI	P.J. Maziasz/ J.E. Pawel	Similar to HFIR-JP-10			17	Jul-90	Sep-91	
HFIR-JP-12	ORNL	JAERI	P.J. Maziasz/ J.E. Pawel	Similar to HFIR-JP-9			57	Jul-90	Apr-94	
HFIR-JP-13	ORNL	JAERI	P.J. Maziasz/ J.E. Pawel	Similar to HFIR-JP-10			17	Jul-90	Sep-91	
HFIR-JP-14	ORNL	JAERI	P.J. Maziasz/ J.E. Pawel	He effects by isotopic tailoring, tensile prop., TEM	Austenitic and ferritic steels	300-600	34	Jul-90	Sep-92	

Summary of Reactor Irradiation Experiments

Experiment	Lead Lab	Collaborators	Responsible Person	Major Objectives	Materials	Temperature °C	Dose (dpa) or fluence	Irrad. Start	Irrad. Finish	Status
HFIR-JP-15	ORNL	JAERI	P.J. Maziasz/ J.E. Pawel	Similar to HFIR-JP-9			57	Jul-90	Apr-94	
HFIR-JP-16	ORNL	JAERI	P.J. Maziasz/ J.E. Pawel	Similar to HFIR-JP-10			17	Jul-90	Sep-91	
HFIR-JP-17	ORNL	JAERI	M.L. Grossbeck/ J.E. Pawel	Fracture toughness, tensile prop. TEM	Austenitic and ferritic steels	250-300	3	Dec-91	Feb-92	
HFIR-JP-18	ORNL	JAERI	M.L. Grossbeck/ J.E. Pawel	Fracture toughness, tensile prop. TEM	Austenitic and ferritic steels	60-125	3	Aug-91	Oct-91	
HFIR-JP-19	ORNL	JAERI	M.L. Grossbeck/ J.E. Pawel	Similar to HFIR-JP-18		60-125	3	Aug-91	Oct-91	
HFIR-JP-20	ORNL	JAERI	J.E. Pawel	Tensile Prop., TEM, He effects by isotopic tailoring	Austenitic and ferritic steels	300-600	8	Dec-93	Jun-94	
HFIR-JP-21	ORNL	JAERI	J.E. Pawel	Similar to HFIR-JP-20			18	Dec-93	Apr-95	
HFIR-JP-22	ORNL	JAERI	J.E. Pawel	Similar to HFIR -JP-20			34	Dec-93	Jan-96	
HFIR-JP-23	PNL	MONBUSHO	D.S. Gelles	TEM	Austenitic and ferritic steels, Cu, Mo, V alloys, TiAl	300-600	8	Dec-93	Jun-94	
HFIR-MFE-60J	ORNL	JAERI	J.L. Scott/ M.L. Grossbeck	Spectrally tailored for fusion He prod. Began in ORR as ORR-MFE-6J (6.9 dpa). TEM, Charpy, irrad. creep, tensile and crack growth prop.	Austenitic and ferritic steels, and Ni alloys	60	19 (total)	Jul-90	Nov-92	
HFIR-MFE-330J	ORNL	JAERI	J.L. Scott/ M.L. Grossbeck	Similar to HFIR-MFE-60J. Began in ORR as ORR-MFE-7J (7.4 dpa)		330	19 (total)	Jul-90	Nov-92	
HFIR-MFE-200J	ORNL	JAERI	M.L. Grossbeck/ J.E. Pawel	Similar to HFIR-MFE-60J. Began in ORR as ORR-MFE-6J (6.9 dpa)		200	17 (total)	Nov-92	Jan-95	
HFIR-MFE-400J	ORNL	JAERI	M.L. Grossbeck/ J.E. Pawel	Similar to HFIR-MFE-60J. Began as ORR-MFE-7J (7.4 dpa)		400	17 (total)	Nov-92	Jan-95	
HFIR-HT-S1, -S7	ORNL		L.L. Snead	Thermal conductivity	Various insulators	80-350	0.01-1.0	Jun-95	Aug-95	
HFIR-HT-F Series	ORNL		L. L. Snead	Fiber tensile	SiC	80-800	0.001-1.0	Jan-95	Mar-96	

Summary of Reactor Irradiation Experiments

Experiment	Lead Lab	Collaborators	Responsible Person	Major Objectives	Materials	Temperature °C	Dose (dpa) or fluence	Irrad. Start	Irrad. Finish	Status
HFIR-TRIST-ER1	ORNL	MONBUSHO/ JAERI	S.J. Zinkle	In-situ electrical conductivity	Al2O3	450	3E+25 n/m2	Apr-96	Jun-96	
HFIR-RB-10J	ORNL	JAERI	J.E. Pawel	Tensile, fracture	Vanadium, 316LN-1G, J316	200, 500	5	Oct-98	Oct-99	
HFIR-RB-11J	ORNL	MONBUSHO/ JAERI	M. L. Grossbeck	Tensile, fracture, TEM	Low activation ferritics, V alloys, SiC	300	5	Feb-97	May-98	
HFIR-RB-12J	ORNL	MONBUSHO/ JAERI	M. L. Grossbeck	Tensile, fracture, TEM	Low activation ferritics, V alloys, SiC	500	5	Feb-97	May-98	
HFIR-RB-13J	ORNL	MONBUSHO/ JAERI	S. J. Zinkle	Varying temp. experiment	Ceramics, Fe-Cr-Ni, V alloys, ferritics, copper	200, 350, 500	5	Jul-98	Jul-99	
HFIR-RB-14J	ORNL	MONBUSHO	L. L. Snead	Strength, fracture, dim. stability, diffusivity	2nd generation SiC/SiC	300, 500, 800	5	Feb-99	Feb-00	
HFIR-TRIST-TC1	ORNL	MONBUSHO/ JAERI	L. L. Snead	In-situ thermal conductivity	SiC/SiC, SiC	150-700	3	Jan-99	Dec-99	
HFIR-CTR-62	ORNL	JAERI	R.L. Klueh	Charpy impact and He effects	Reduced act. and conventional ferritic steels	300, 400	13	Apr-95	Dec-95	
HFIR-CTR-63	ORNL	JAERI	R.L. Klueh	Charpy impact and tensile, TEM, He effects	Reduced act. and conventional ferritic steels	300, 400	13	Apr-95	Dec-95	
HFIR-JP25	ORNL	JAERI	R.L. Klueh	Tensile, fracture, TEM	Low activation ferritics	300, 500	20	Feb-99	Jan-00	
High Flux Beam Reactor, Brookhaven National Laboratory										
HFBR-ISEC-3	ORNL		L.L. Snead	In-situ electrical	WESGO Al2O3	450	1.5	Jul-95	Sep-95	
HFBR-V1	ORNL		L.L. Snead	Tensile, fracture	V-4Cr-4Ti	75, 150, 225	0.4	May-95	Jun-95	
HFBR-V2	ORNL		L.L. Snead	Tensile, fracture	V-4Cr-4Ti	75, 225, 300, 375	0.4	Jul-95	Aug-95	

Summary of Reactor Irradiation Experiments

Experiment	Lead Lab	Collaborators	Responsible Person	Major Objectives	Materials	Temperature °C	Dose (dpa) or fluence	Irrad. Start	Irrad. Finish	Status
HFBR-V3	ORNL		L.L. Snead	Tensile, fracture	V-4Cr-4Ti	160, 265, 315, 420	0.4	Aug-96	Sep-96	
HFBR-V4	ORNL		L.L. Snead	Tensile, fracture	V-4Cr-4Ti	105-505	0.1	Aug-96	Sep-96	
Advanced Test Reactor, Idaho Falls										
ATR-A1	ANL	MONBUSHO	D.L. Smith	Tensile, fracture toughness, TEM, creep	Vanadium alloys	200, 300	5	Dec-95	May-96	
BOR-60 Reactor, RIAR, Dimitrovgrad, Russia										
BOR-60-Fusion-1	ORNL, ANL	RDIPE, RIAR	A.F. Rowcliffe, D.L. Smith	Mechanical and microstructural properties	V alloys	350-380	10	Jul-95	Mar-96	
SM-2 Reactor, RIAR, Dimitrovgrad, Russia										
SM-2.1	ORNL, PNL	RIAR	S.J. Zinkle	Tensile, electrical, microstructural, and creep properties	Cu alloys	100, 200, 330	1, 5	Dec-93	Feb-94	
SM-2.2	PNL	SRIAR	D.J. Edwards	Mechanical behavior of bonded materials	Cu alloys/SS, Cu/Be	120, 300	0.2	Mar-96	May-96	
SM-2.3	PNL	SRIAR	D.J. Edwards	Mechanical behavior of bonded materials	Cu alloys/SS, Cu/Be	100, 250	0.2	Dec-97	Jun-98	

Irradiation complete

Irradiation in progress

Irradiation planned

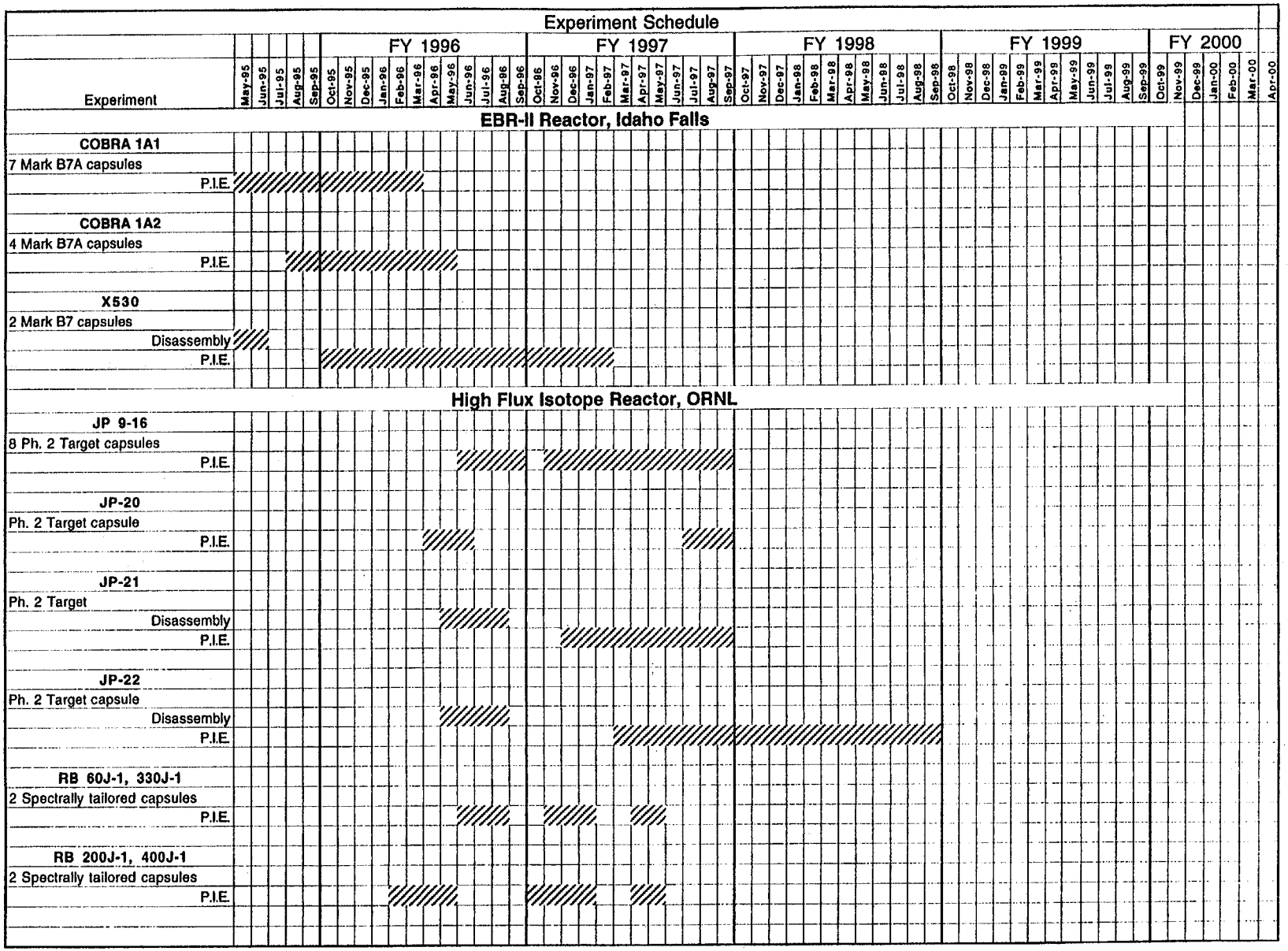
Experiment Schedule
FY 1996
FY 1997
FY 1998
FY 1999
FY 2000
Experiment
May-95 Jun-95 Jul-95 Aug-95 Sep-95 Oct-95 Nov-95 Dec-95 Jan-96 Feb-96 Mar-96 Apr-96 May-96 Jun-96 Jul-96 Aug-96 Sep-96 Oct-96 Nov-96 Dec-96 Jan-97 Feb-97 Mar-97 Apr-97 May-97 Jun-97 Jul-97 Aug-97 Sep-97 Oct-97 Nov-97 Dec-97 Jan-98 Feb-98 Mar-98 Apr-98 May-98 Jun-98 Jul-98 Aug-98 Sep-98 Oct-98 Nov-98 Dec-98 Jan-99 Feb-99 Mar-99 Apr-99 May-99 Jun-99 Jul-99 Aug-99 Sep-99 Oct-99 Nov-99 Dec-99 Jan-00 Feb-00 Mar-00 Apr-00
EBR-II Reactor, Idaho Falls
COBRA 1A1
7 Mark B7A capsules
P.I.E.
COBRA 1A2
4 Mark B7A capsules
P.I.E.
X530
2 Mark B7 capsules
Disassembly
P.I.E.
High Flux Isotope Reactor, ORNL
JP 9-16
8 Ph. 2 Target capsules
P.I.E.
JP-20
Ph. 2 Target capsule
P.I.E.
JP-21
Ph. 2 Target
Disassembly
P.I.E.
JP-22
Ph. 2 Target capsule
Disassembly
P.I.E.
RB 60J-1, 330J-1
2 Spectrally tailored capsules
P.I.E.
RB 200J-1, 400J-1
2 Spectrally tailored capsules
P.I.E.

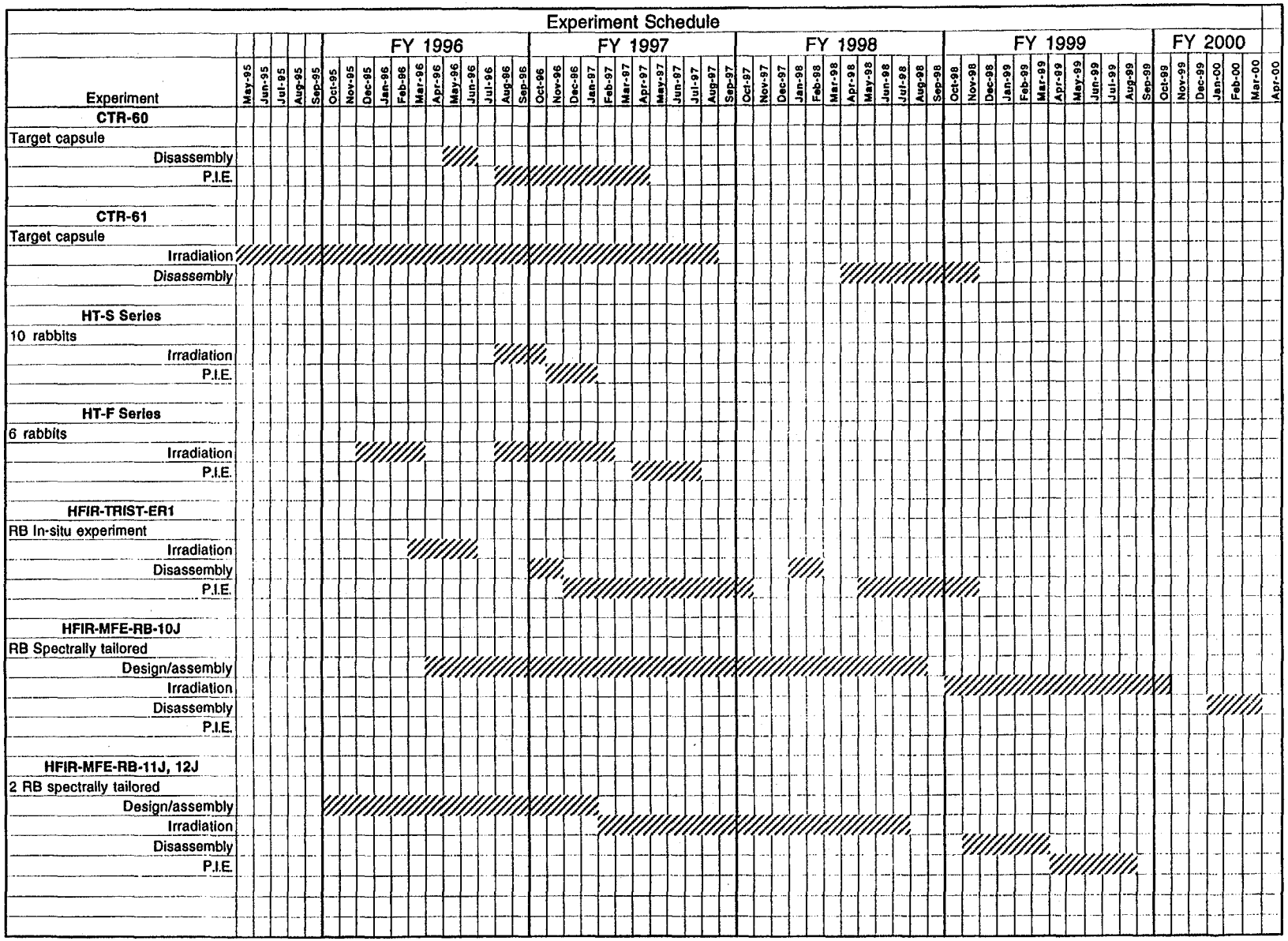
Experiment Schedule
FY 1996
FY 1997
FY 1998
FY 1999
FY 2000
Experiment
May-95
Jun-95
Jul-95
Aug-95
Sep-95
Oct-95
Nov-95
Dec-95
Jan-96
Feb-96
Mar-96
Apr-96
May-96
Jun-96
Jul-96
Aug-96
Sep-96
Oct-96
Nov-96
Dec-96
Jan-97
Feb-97
Mar-97
Apr-97
May-97
Jun-97
Jul-97
Aug-97
Sep-97
Oct-97
Nov-97
Dec-97
Jan-98
Feb-98
Mar-98
Apr-98
May-98
Jun-98
Jul-98
Aug-98
Sep-98
Oct-98
Nov-98
Dec-98
Jan-99
Feb-99
Mar-99
Apr-99
May-99
Jun-99
Jul-99
Aug-99
Sep-99
Oct-99
Nov-99
Dec-99
Jan-00
Feb-00
Mar-00
Apr-00
CTR-60
Target capsule
Disassembly
P.I.E.
CTR-61
Target capsule
Irradiation
Disassembly
HT-S Series
10 rabbits
Irradiation
P.I.E.
HT-F Series
6 rabbits
Irradiation
P.I.E.
HFIR-TRIST-ER1
RB In-situ experiment
Irradiation
Disassembly
P.I.E.
HFIR-MFE-RB-10J
RB Spectrally tailored
Design/assembly
Irradiation
Disassembly
P.I.E.
HFIR-MFE-RB-11J, 12J
2 RB spectrally tailored
Design/assembly
Irradiation
Disassembly
P.I.E.

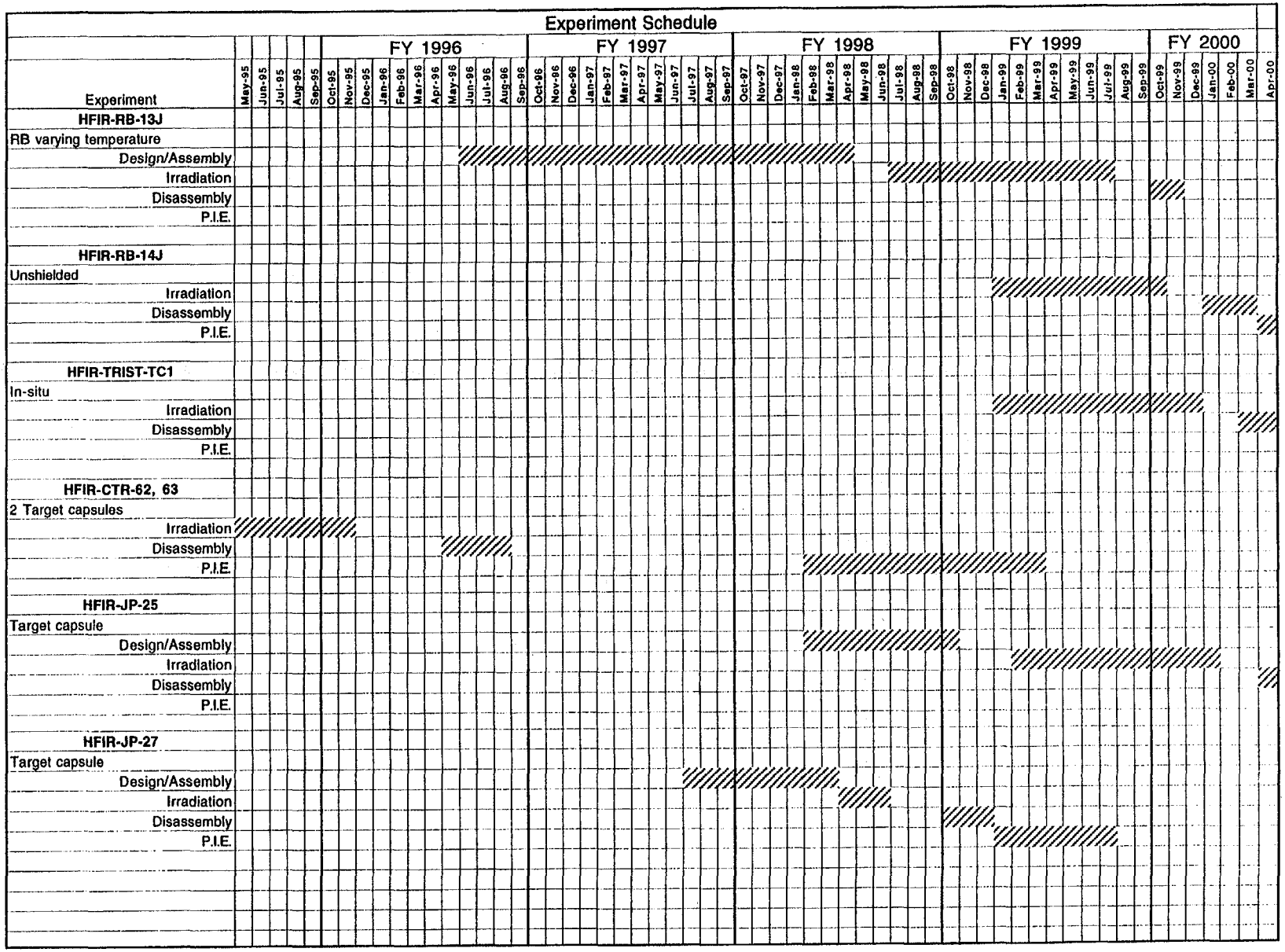
Experiment Schedule
FY 1996
FY 1997
FY 1998
FY 1999
FY 2000
Experiment
May-95
Jun-95
Jul-95
Aug-95
Sep-95
Oct-95
Nov-95
Dec-95
Jan-96
Feb-96
Mar-96
Apr-96
May-96
Jun-96
Jul-96
Aug-96
Sep-96
Oct-96
Nov-96
Dec-96
Jan-97
Feb-97
Mar-97
Apr-97
May-97
Jun-97
Jul-97
Aug-97
Sep-97
Oct-97
Nov-97
Dec-97
Jan-98
Feb-98
Mar-98
Apr-98
May-98
Jun-98
Jul-98
Aug-98
Sep-98
Oct-98
Nov-98
Dec-98
Jan-99
Feb-99
Mar-99
Apr-99
May-99
Jun-99
Jul-99
Aug-99
Sep-99
Oct-99
Nov-99
Dec-99
Jan-00
Feb-00
Mar-00
Apr-00
HFIR-RB-13J
RB varying temperature
Design/Assembly
Irradiation
Disassembly
P.I.E.
HFIR-RB-14J
Unshielded
Irradiation
Disassembly
P.I.E.
HFIR-TRIST-TC1
In-situ
Irradiation
Disassembly
P.I.E.
HFIR-CTR-62, 63
2 Target capsules
Irradiation
Disassembly
P.I.E.
HFIR-JP-25
Target capsule
Design/Assembly
Irradiation
Disassembly
P.I.E.
HFIR-JP-27
Target capsule
Design/Assembly
Irradiation
Disassembly
P.I.E.

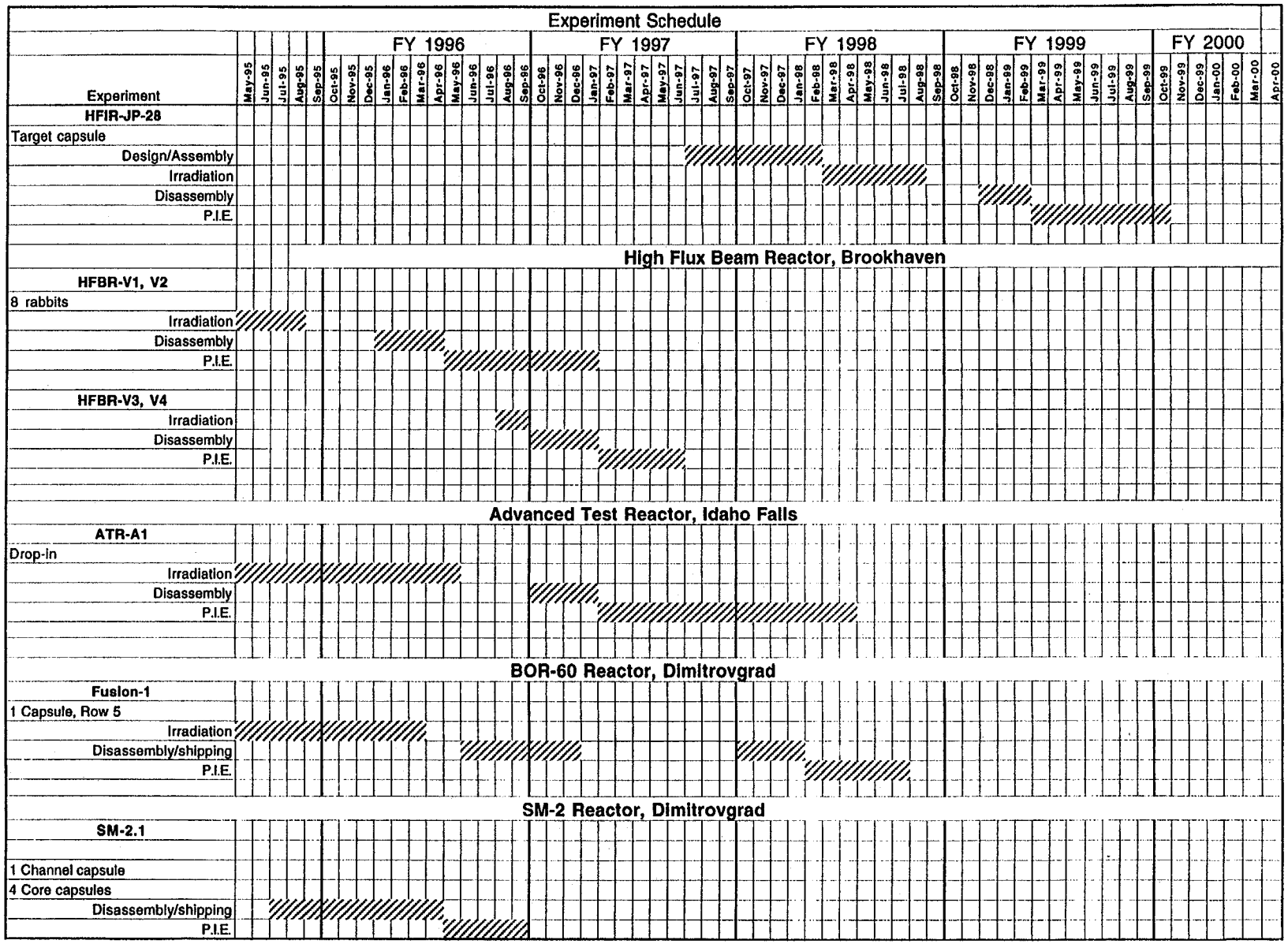
Experiment Schedule
FY 1996
FY 1997
FY 1998
FY 1999
FY 2000
Experiment
HFIR-JP-28
Target capsule
Design/Assembly
Irradiation
Disassembly
P.I.E.
High Flux Beam Reactor, Brookhaven
HFBR-V1, V2
8 rabbits
Irradiation
Disassembly
P.I.E.
HFBR-V3, V4
Irradiation
Disassembly
P.I.E.
Advanced Test Reactor, Idaho Falls
ATR-A1
Drop-in
Irradiation
Disassembly
P.I.E.
BOR-60 Reactor, Dimitrovgrad
Fusion-1
1 Capsule, Row 5
Irradiation
Disassembly/shipping
P.I.E.
SM-2 Reactor, Dimitrovgrad
SM-2.1
1 Channel capsule
4 Core capsules
Disassembly/shipping
P.I.E.

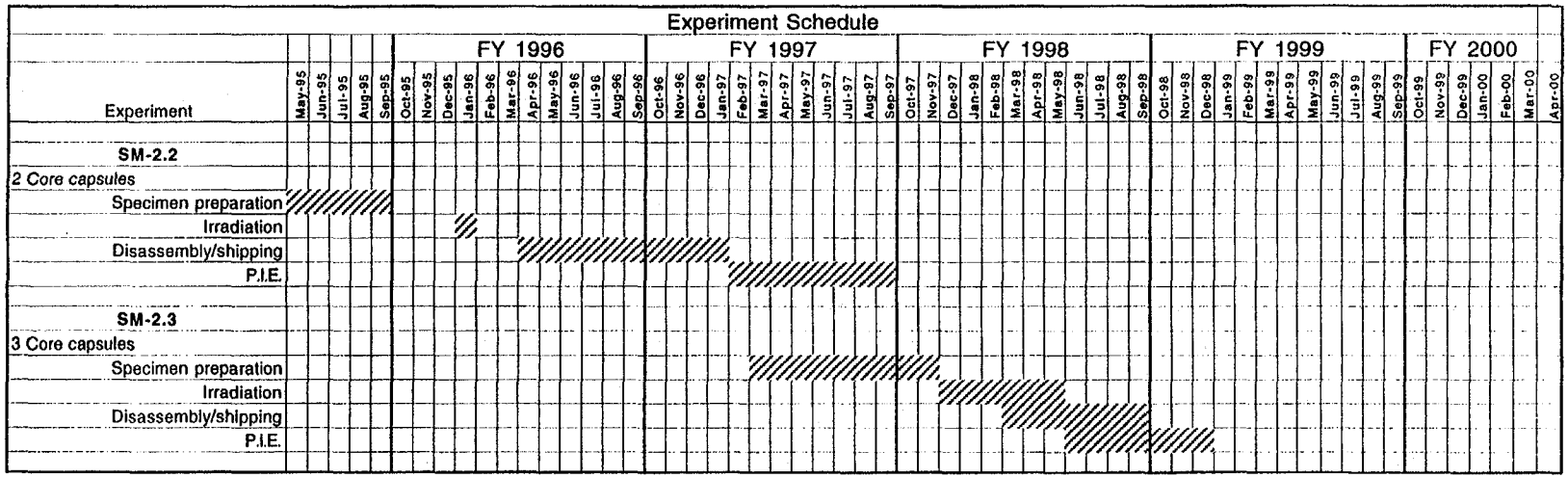
Experiment Schedule
FY 1996
FY 1997
FY 1998
FY 1999
FY 2000
Experiment
May-95
Jun-95
Jul-95
Aug-95
Sep-95
Oct-95
Nov-95
Dec-95
Jan-96
Feb-96
Mar-96
Apr-96
May-96
Jun-96
Jul-96
Aug-96
Sep-96
Oct-96
Nov-96
Dec-96
Jan-97
Feb-97
Mar-97
Apr-97
May-97
Jun-97
Jul-97
Aug-97
Sep-97
Oct-97
Nov-97
Dec-97
Jan-98
Feb-98
Mar-98
Apr-98
May-98
Jun-98
Jul-98
Aug-98
Sep-98
Oct-98
Nov-98
Dec-98
Jan-99
Feb-99
Mar-99
Apr-99
May-99
Jun-99
Jul-99
Aug-99
Sep-99
Oct-99
Nov-99
Dec-99
Jan-00
Feb-00
Mar-00
Apr-00
SM-2.2
2 Core capsules
Specimen preparation
Irradiation
Disassembly/shipping
P.I.E.
SM-2.3
3 Core capsules
Specimen preparation
Irradiation
Disassembly/shipping
P.I.E.

Distribution

1-16. Argonne National Laboratory, 9700 South Cass Avenue, Argonne, IL 60439

M. C. Billone	C. E. Johnson	J. H. Park
O. K. Chopra	F. Kassner	D. L. Smith
H. M. Chung	J. P. Kopasz	W. Tam
D. R. Diercks	R. F. Mattas	H. C. Tsai
J. Gazda	K. Nateson	
A. B. Hull	L. A. Niemark	

17-18. Argonne National Laboratory, EBR-II Division, P.O. Box 2528, Idaho Falls, ID 83403-2528

H. P. Planchon D. L. Porter

19. Auburn University, Department of Mechanical Engineering, 201 Ross Hall, Auburn, AL 36849

B. A. Chin

20-33. Pacific Northwest National Laboratory, P.O. Box 999, Richland, WA 99352

D. J. Edwards	M. L. Hamilton	R. H. Jones
F. A. Garner (5)	H. L. Heinisch	R. J. Kurtz
D. S. Gelles	G. W. Hollenberg	J. Youngblood
L. R. Greenwood		

34. Carnegie Institute of Technology, Carnegie-Mellon University, Schenley Park, Pittsburgh, PA 15213

W. M. Garrison, Jr.

35. Commissariat à l'Energie Atomique, Direction des Technologies Advancées, M2R1/DECM Cen-Saclay, Gif Sur Yvette, Cedex, France

F. Tavassoli

36. Dow Corning Corporation, 3901 S. Saginaw Rd., MS-500, Midland, MI 48686-0995

R. E. Jones

37-39. General Atomics, P.O. Box 85608, San Diego, CA 92138

W. R. Johnson K. R. Schultz C. Wong

40. Georgia Institute of Technology, Fusion Research Center, 0225, Atlanta, GA 30332

W. M. Stacey

41. Grand Canyon University, Department of Natural Science, 3300 W. Camelback Rd., Phoenix, AZ 85017

W. A. Coghlan

42-44. Idaho National Engineering Laboratory, Fusion Safety Program, P.O. Box 1625, Idaho Falls, ID 83415-3523

G. Longhurst K. McCarthy D. Petti

45. Knolls Atomic Power Laboratory, P.O. Box 1072, Schenectady, NY 12301

G. Newsome

46-47. Lawrence Livermore National Laboratory, P.O. Box 808, Livermore, CA 94550

E.C.N. Dalder J. Perkins

48-54. Los Alamos National Laboratory, Los Alamos, NM 87545
J. L. Anderson, R. G. Castro, D. W. Cooke, E. H. Farnum, R. E. Siemon, W. F. Sommer, K. E. Sickafus

55-57. Massachusetts Institute of Technology, Department of Metallurgy and Materials Science, Cambridge, MA 02139
L. W. Hobbs, N. J. Grant, K. C. Russell

58. Massachusette Institute of Technology, Plasma Fusion Center Headquarters, Cambridge, MA 02139
D. B. Montgomery

59-60. McDonnell-Douglas Corporation, Mail Code 1067220, P.O. Box 516, St. Louis, MO 63166-0516
J. W. Davis, G. W. Wille

61. MER Corp., 7960 South Kolb Rd., Tucson, AZ 85706
W. Kowbel

62. Merrimack College, Dept. of Physics, 315 Turnpike Street, North Andover, MA 01845
D. P. White

63. M. J. Schiff & Associates, 1291 N. Indian Hill Blvd., Claremont, CA 91711-3897
G.E.C. Bell

64. NASA Lewis Research Center, MS-106-5, Cleveland, OH 44135
G. Morscher

65-67. National Institute of Standards and Technology, Boulder, CO 80302
F. R. Fickett, H. I. McHenry, R. P. Reed

68-69. Naval Research Laboratory, Code 6506, Washington, DC 20375
D. L. Gibson, J. A. Sprague

70-112. Oak Ridge National Laboratory, P.O. Box 2008, Oak Ridge, TN 37831
Central Research Library
Document Reference Section
Laboratory Records Department (2)
Laboratory Records-RC
Patent Section
J. Bentley
E. E. Bloom
T. D. Burchell
S. D. Connery
J. R. DiStefano
G. M. Goodwin
R. H. Goulding
M. L. Grossbeck
N. Hashimoto
J. F. King
E. A. Kenik
R. L. Klueh
E. H. Lee
L. K. Mansur
P. J. Maziasz
Y. Miwa
B. A. Pint
L. Qualls
T. C. Reuther
J. P. Robertson
A. F. Rowcliffe (10)
M. J. Saltmarsh
J. Sheffield
L. L. Snead
R. E. Stoller
K. R. Thoms
R. L. Wallace
S. J. Zinkle

113. Oregon Graduate Institute, Dept. of Materials Science & Engineering, 19600 N.W. Von Neumann Drive, Beaverton, OR 97006
J. M. McCarthy

114-116. Princeton University, Princeton Plasma Physics Laboratory, P.O. Box 451, Princeton, NJ 08540
R. C. Davidson, Long-Poe Ku, D. M. Meade

117-118. Rensselaer Polytechnic Institute, Troy, NY 12181
D. Duquette D. Steiner

119. Rockwell International Corporation, NA02, Rocketdyne Division, 6633 Canoga Avenue,Canoga Park, CA 91304
D. W. Kneff

120-122. Sandia National Laboratories, Fusion Technology Dept., Dept. No 6531, P.O. Box 5800, Albuquerque, NM 87185-5800
M. J. Davis M. Ulrickson R. D. Watson

123-125. Sandia National Laboratories, Livermore Division 8316, Livermore, CA 94550
W. Bauer K. Wilson W. G. Wolfer

126. San Diego State University, Mechanical Engineering Dept., San Diego, CA 92182-0191
L. D. Thompson

127. Texas A&M University, Box 397, Prairie View, TX 77446
D. Baker

128. TSI Research, 225 Stevens Ave., #110, Solana Beach, CA 92075
E. T. Cheng

129-130. University of California at San Diego, U.S. ITER Project Office, 9500 Gilman Drive, Bldg. 302, La Jolla, CA 92093-0035
C. C. Baker T. R. James

131. University of California at San Diego, Fusion Energy Research Program, 9500 Gilman Drive, MC0417, La Jolla, CA 92093-0417
M. Tillack

132-133. University of California, Dept. of Mechanical and Environmental Engineering, Engineering II, Room 2355, Santa Barbara, CA 93106-5070
G. E. Lucas G. R. Odette

134-136. University of California, Dept. of Chemical, Nuclear, and Thermal Engineering, Los Angeles, CA 90024
M. A. Abdou N. M. Ghoniem S. Sharafat

137. University of Illinois, Dept. of Nuclear Engineering, Urbana, IL 61801
J. Stubbins

138. University of Michigan, Dept. of Nuclear Engineering, Ann Arbor, MI 48109
T. Kammash

139. University of Missouri, Department of Nuclear Engineering, Rolla, MO 65401
A. Kumar

140-141. University of Tennessee, Dept. of Materials Science and Engineering, 427-B Dougherty Bldg., Knoxville, TN 37996-2200
P. K. Liaw C. J. McHargue

142-143. University of Wisconsin, Nuclear Engineering Dept., 1500 Johnson Drive, Madison, WI 53706
J. B. Blanchard G. L. Kulcinski

144. Helsinki University of Technology, Laboratory of Engineering Materials, Puumiehenkuja 3, SF-02150 Espoo, Finland
H. Hänninen

145-147. Hokkaido University, Faculty of Engineering, Kita 13, Nishi 8, Kita-ku, Sapporo 060, Japan
Heischichiro Takahashi Somei Ohnuki Akira Okada

148-149. Japan Atomic Energy Research Institute, Tokai Research Establishment, Tokai-mura, Naka-gun, Ibaraki-ken 319-11, Japan
Akimichi Hishinuma K. Noda

150-151. Kyoto University, Institute of Advanced Energy, Gokasho, Uji, Kyoto 611, Japan
Yutai Katoh Akira Kohyama

152. Kyushu University, Dept. of Nuclear Engineering, Faculty of Engineering, Kyushu University 36, Hakozaki, Fukuoka 812, Japan
C. Kinoshita

153. Kyushu University, Research Institute for Applied Mechanics, Kasuga, Fukuoka 816, Japan
Naoaki Yoshida

154-155. Muroran Institute of Technology, Dept. of Metallurgical Engineering, 27-1 Mizumoto-cho, Mororan 050, Japan
Toshihei Misawa Akihiko Kimura

156-157. Nagoya University, Dept. of Nuclear Engineering, Furo-Cho, Chikusa-ku, Nagoya 464-01, Japan
Michio Kiritani Tetuo Tanabe

158-161. National Institute for Fusion Science, Furo-cho, Chikusa-ku, Nagoya 464-01, Japan
Osamu Motojima Chusei Namba
Takeo Muroga Nobuaki Noda

162-165. National Research Institute for Metals, Tsukuba Branch, Sengen, Tsukuba-shi, Ibaraki-ken, 305, Japan
Fujio Abe Tetsuji Noda
Josei Nagakawa Haruki Shiraishi

166. PNC Oarai, 4002 Narita, Oarai, Ibaraki 311-13, Japan
Itaru Shibahari

167. Science University of Tokyo, Dept. of Materials Science & Technology, 2641 Yamazaki, Noda City, Chiba Prefecture 278, Japan
Naohira Igata

168. Teikyo University, Otsuka, Hachioji, Tokyo 192-03, Japan
Akira Miyahara

169. Tohoku University, Institute for Materials Research, Katahira 2-2-1, Sendai 980-77, Japan
Hideki Matsui

170-173. Tohoku University, Institute for Materials Research, Oarai Branch, Oarai, Ibaraki 311-13, Japan
Hideo Kayono — Tamaki Shibayama
Hiroaki Kurishita — Tatsuo Shikama

174-175. Tohoku University, Dept. of Nuclear Engineering, Aoba, Aramaki, Sendai 980-77, Japan
Katsunori Abe — Akira Hasegawa

176. Tohoku University, Dept. of Machine Intelligence and Systems Engineering, Aramaki, Aoba-ku, Sendai 980-77, Japan
Tatsuo Kondo

177. Tokai University, Dept. of Nuclear Engineering, 1117 Kitakaname, Hiratsuka-shi, Kanagawa-ken 259-12, Japan
Shiori Ishino

178. University of Tokyo, Dept. of Nuclear Engineering, 3-1, Hongo 7-Chome, Bunkyo-Ku, Tokyo 113, Japan
Naoto Sekimura

179. University of Tokyo, Dept. of Materials Science, 3-1, Hongo 7-Chome, Bunkyo-ku, Tokyo 113, Japan
Yutaka Kohno

180. VTT Manufacturing Technology, P.O. Box 1704, FIN-02044 VTT, Finland
P. Aaltonen

181. Commission of European Communities, Directorate-General for Research Science and Education, Fusion Programme RUE De La Loi 200, B-1049 Brussels, Belgium
F. Cozzani

182-183. Chalk River Nuclear Laboratories, Atomic Energy of Canada, Ltd., Chalk River, Ontario KOJ 1J0, Canada
I. J. Hastings — D. P. Jackson

184-185. Southwestern Institute of Physics, P.O. Box 432, Chenedu 610041, Sichuan, P.R. China
J. P. Qian — Zeng Yu Xu

186. Institute of Atomic Energy, Academia Sinica, P.O. Box 275-51, Beijing, P.R. China
J. Yu

187. Riso National Laboratory, Materials Dept., P.O. Box 49, DK-4000, Roskilde, Denmark
B. N. Singh

188. Centre d'Etudes Nucleaires, Saclay, DLPC/SMCM, Commissariat a l'Energie Atomique, 91191 Gif-Sur-Yvette, Cedex, France
N. Roux

189. Commission for European Communities, Joint Research Centre, I.A.M. Ispra Establishment, 21020 Ispra (Varese), Italy
P. Fenici

190. EURATOM/CIEMAT Fusion Association, Avenida Complutense 22, 28040, Madrid, Spain
E. R. Hodgson

191. Paul Scherrer Institute, CH-5232 Villigen, Wuerenlingen PSI, Switzerland
M. Victoria

192. Harwell Laboratory, B393, Radiation Damage Dept., Oxfordshire, OX11 ORA, United Kingdom
C. A. English

193. Metallurgical and Nuclear Consultant, 9A Cumnor Rise Road, Cumnor Hill, Oxford OX2 9HD, United Kingdom
D. R. Harries

194. Hahn-Mietner-Institut fur Kernforschung Berlin, Postfach 390128, Glienicker Str. 100, D-14109, Germany
H. Wollenberger

195. Institut fur Festkorperforschung Forschungszentrum Jülich, Postfach 1913, D-52425 Jülich, Germany
H. Ullmaier

196-198. ITER Garching Joint Work Site, Max-Planck-Institute für Plasmaphysik, Boltzmannstrasse 2, D-85748 Garching bei München, Germany
V. Barabash G. Kalinin R. Parker

199-200. ITER Naka Joint Work Site, 801-1 Mukouyama, Naka-machi, Naka-gun, Ibaraki-Ken, 311-01, Japan
M. Huguet (2)

201-204. ITER San Diego Joint Work Site, 11025 N. Torrey Pines Road, La Jolla, CA 92037
V. Chuyanov F. Puhn
S. J. Piet P. Smith

205-206. Kernforschungszentrum Karlsruhe, Postfach 3640, 75 Karlsruhe 1, Germany
M. Dalle-Donne (INR) K. Ehrlich (IMF-II)

207. Max-Planck-Institut für Plasmaphysik, Boltzmannstrasse 2, D-85748 Garching bei München, Germany
Patrick Lorenzetto

208. A. A. Baikov Institute of Metallurgy, USSR Academy of Sciences, Leninsky Prospect 49, Moscow, Russia
L. I. Ivanov

209. CRISM "Prometey," Naberezhnava r. Monastyrick 1, 193167, St. Petersburg, Russia
V. V. Rybin

210. D. V. Efremov Institute of Electro-Physical Apparatus, Scientific Technical Center "Sintez,"189631, St. Petersburg, Russia
S. A. Fabritsiev

211. Kharkov Institute of Physics & Technology, Radiation Damage and Materials Dept., Akademicheskaya 1, 310108 Kharkov, Ukraine
I. M. Neckludov

212-214. V. I. Lenin Research Institute of Atomic Reactors, 433510 Dimitrovgrad-10, Ulyanovsk Region, Russia
V. Kazakov A. S. Pokrovsky V. K. Shamardin

215. Korea Advanced Institute of Science and Technology, Department of Nuclear Engineering, DaeDukDanji, Taejon, 305-701, Korea
I-S. Kim

216-217. Korean Atomic Energy Research Institute, P.O. Box 105, Yusung, Taejon, 305-600, Korea
Thak-Sang Byun Jun Hwa Hong

218. Seoul National University, Dept. of Nuclear Engineering, 56-1 Shinrim-Dong, Kwanak-Ku Seoul, 151-742, Korea
K. H. Chung

219. Sung Kyun Kwan University, Dept. of Metallurgical Engineering, 300 Chunchun-dong, Jangan-gu, Suwon, 440-746, Korea
J. G. Han

220. Department of Energy, DOE Oak Ridge Field Office, P.O. Box 2008, Oak Ridge, TN 37831-6269
Assistant Manager for Energy Research and Development

221. Department of Energy, DOE Oak Ridge Field Office, P.O. Box 2008, Oak Ridge, TN 37831-6269
S. D. Frey

222. Department of Energy, Office of Basic Energy Sciences, Washington, D.C. 20585
R. J. Gottschall

223-228. Department of Energy, Office of Fusion Energy, Germantown, MD 20874

S. E. Berk	W. F. Dove	W. Marton
N. A. Davies	R. McKnight	F. W. Wiffen

229. Department of Energy, Richland Operations Office, P.O. Box 550, MS-K850, Richland, WA 99352
J. Turner

230-231. Department of Energy, Office of Scientific and Technical Information, Office of Information Services, P.O. Box 62, Oak Ridge, TN 37831
For distribution by microfiche as shown in DOE/OSTI-4500-R75, Distribution Categories UC-423 (Magnetic Fusion Reactor Materials) and UC-424 (Magnetic Fusion Energy Systems)